ISSN 2188-5001

MATERIALS DESIGN AND
CHARACTERIZATION LABORATORY

SUPERCOMPUTER CENTER

ACTIVITY REPORT 2016

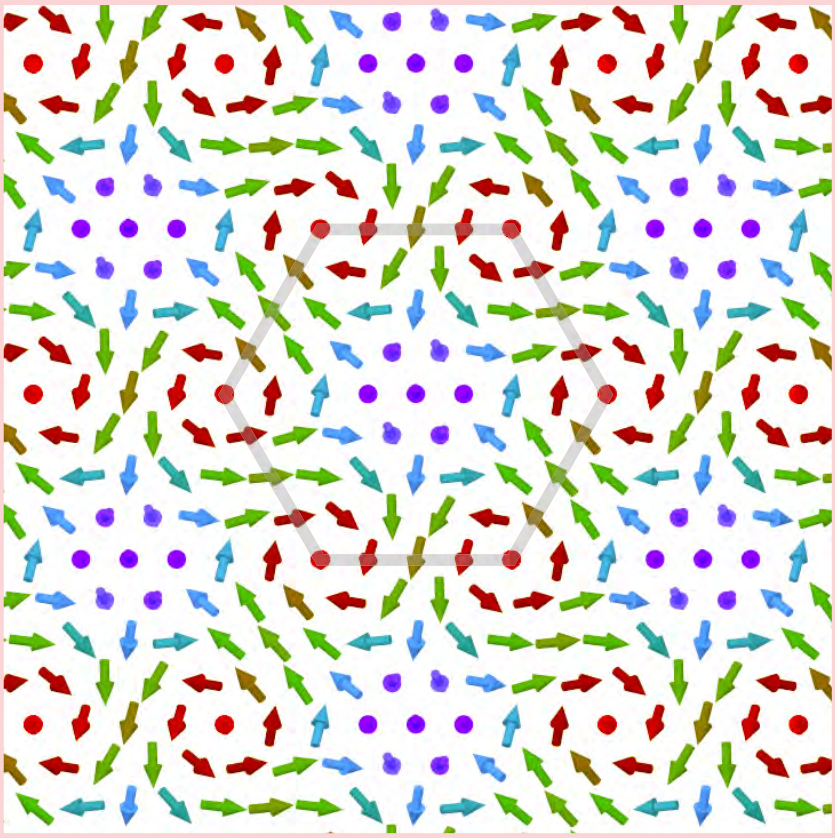

INSTITUTE FOR SOLID STATE PHYSICS
THE UNIVERSITY OF TOKYO

Materials Design and Characterization Laboratory (MDCL)

The MDCL was established as the third research facility of the Institute for Solid State Physics (ISSP) when the latter was reorganized in May 1996. Its aim is to promote material science with an emphasis on the "DSC cycle", where DSC stands for design, synthesis and characterization, three processes for developing new materials.

The MDCL consists of two sections, Materials Design (MD) section and Materials Synthesis and Characterization (MSC) section. The Supercomputer Center of the ISSP (SCC-ISSP) is placed in the MD section, while in the MSC section there are seven laboratories for joint use; Materials Synthesis Laboratory, Chemical Analysis Laboratory, X-ray Diffraction Laboratory, Electron Microscope Laboratory, Electromagnetic Measurement Laboratory, Spectroscopy Laboratory, and High-Pressure Synthesis Laboratory.

Almost all the facilities of the MDCL are open to scientists in Japan through the User Programs conducted by two steering committees of the MDCL. One is the steering committee of the SCC-ISSP, under which the Supercomputer Project Advisory Committee is placed for reviewing proposals. The other is the steering committee of the MSC facilities. More than half of the members of these committees are from the outside of ISSP.

PREFACE

The Supercomputer Center (SCC) is a part of the Materials Design and Characterization Laboratory (MDCL) of ISSP. Its mission is to serve the whole community of computational condensed-matter physics of Japan providing it with high performance computing environment. In particular, the SCC selectively promotes and supports large-scale computations. For this purpose, the SCC invites proposals for supercomputer-aided research projects and hosts the Steering Committee, as mentioned below, that evaluates the proposals.

The ISSP supercomputer system consists of two subsystems: System B, which is intended for more nodes with relatively loose connections. In July, 2015, the SCC replaced the two supercomputer subsystems (SGI Altix ICE 8400EX and NEC SX-9) to one new system (System B, SGI ICE XA/UV hybrid system). The system B consists of 1584 CPU nodes, 288 ACC nodes, and 19 FAT nodes. The CPU node has 2CPUs (Intel Xeon). The ACC node has 2CPUs (Intel Xeon) and 2GPUs (NVIDIA Tesla K40). The FAT node has 4CPUs (Intel Xeon) and large memory (1TB). The system B have totally 2.6 PFlops theoretical peak performance. System C - FUJITSU PRIMEHPC FX10 was installed in April, 2013. It is highly compatible with K computer in Kobe. System C consists of 384 nodes, and each node has 1 SPARC64TM IXfx CPU (16 cores) and 32 GB of memory. The system C have totally 90.8 TFlops.

The hardware administration is not the only function of the SCC. Since 2015, the SCC has started “Project for advancement of software usability in materials science”. In this project, for enhancing the usability of the ISSP supercomputer system, we perform some software-advancement activity such as implementing a new function to an existing code, releasing a private code on Web, and writing manuals. Two target programs were selected in fiscal year 2016 and developed software were released as Komega (Kω) and mVMC. The SCC has also started a service for porting users’ materials science software to General Purpose GPUs (GPGPU) since 2015. Three programs were selected for the GPGPU porting in fiscal year 2016.

All staff members of university faculties or public research institutes in Japan are invited to propose research projects (called User Program). The proposals are evaluated by the Steering Committee of SCC. Pre-reviewing is done by the Supercomputer Project Advisory Committee. In fiscal year 2016, totally 244 projects were approved. The total points applied and approved are listed on Table. 1 below. Additionally, we supported post-K and other computational materials science projects through Supercomputing Consortium for Computational Materials Science (SCCMS).

The research projects are roughly classified into the following three (the number of projects approved):

First-Principles Calculation of Materials Properties (117)
Strongly Correlated Quantum Systems (30)
Cooperative Phenomena in Complex, Macroscopic Systems (97)

All the three involve both methodology of computation and its applications. The results of the projects are reported in 'Activity Report 2016' of the SCC. Every year 3-4 projects are selected for “invited papers” and published at the beginning of the Activity Report. In the Activity Report 2016, the following three invited papers are included:

"Development of First-Principles Simulation of Material Structure and Electronic Properties",

Shinji TSUNEYUKI

"Massively Parallel Monte Carlo Simulation of a Possible Topological Phase Transition in Two-Dimensional Frustrated Spin Systems",

Tsuyoshi OKUBO

"Irreversible Markov-Chain Monte Carlo Methods",

Koji HUKUSHIMA

June 22, 2017

Hiroshi Noguchi
(Chairman of the steering committee, SCC, ISSP)

CONTENTS

PREFACE

1 OUTLINE **1**

1.1 Supercomputer System 1
1.2 Project Proposals 1
1.3 Committees 2
1.4 Staff 6

2 STATISTICS OF FISCAL YEAR 2016 **7**

2.1 System Statistics 7
2.2 Queue, Job, and User Statistics 7
2.3 Project for Advancement of Software Usability in Materials Science 8
2.4 GPGPU Support Service 12

3 RESEARCH REPORTS **13**

3.1 Invited Articles 13
3.2 First-Principles Calculation of Material Properties 37
3.3 Strongly Correlated Quantum Systems 156
3.4 Cooperative Phenomena in Complex Macroscopic Systems 196
3.5 SCCMS Projects 282
3.6 Software Advancement Projects and GPGPU Support 313

4 PUBLICATION LIST **320**

ISSP Joint Research Projects 321
SCCMS Projects 355
Doctor Theses 359
Master Theses 361

1 Outline

1.1 Supercomputer System

In SY2016, the ISSP supercomputer center provided users with two types of systems:

System B - SGI ICE XA/UV hybrid system is a massively-parallel supercomputer with three types of compute nodes: 19 “Fat” nodes, 1584 “CPU” nodes, and 288 “ACC” nodes. “Fat” nodes are each comprised of four Intel Xeon E5-4627v3 CPUs (10 cores/CPU) and 1 TB of memory. “CPU” nodes have two Intel Xeon E5-2680v3 CPUs (12 cores/CPU) and 128 GB of memory. “ACC” nodes have two nVIDIA Tesla K40 GPUs in additon to two Xeon E5-2680v3 CPUs and 128 GB of memory. System B achieves 2.6 PFLOPS in theoretical peak performance with high power efficiency. The subsystem comprised of only CPU nodes ranks 61st on the November 2015 Top 500 List, which is a ranking based on total performance measured by the HPL benchmark. The subsystem of ACC nodes ranks 104th on the Top 500 List, and it also ranks 23rd on the Green 500 List, which is a ranking based on performance per watt of electrical power consumption. The compute nodes communicate to each other through FDR Infiniband. The Fat nodes are interconnected in fat tree topology, while the CPU and ACC nodes are connected in enhanced hypercube topology. System B entered official operation on Aug. 21, 2015.

System C - FUJITSU PRIMEHPC FX10 has been in service since April, 2013. It is highly compatible with K computer in Kobe. System C consists of 384 nodes, and each node has 1 SPARC64TM IXfx CPU (16 cores) and 32 GB of memory. The total system achieves 90.8 TFlops theoretical peak performance.

SY2016 was the second year of the operation of the current System B and the last year of System C.

For further details, please contact ISSP Supercomputer Center (SCC-ISSP).

[Correspondence: center@issp.u-tokyo.ac.jp]

1.2 Project Proposals

The ISSP supercomputer system provides computation resources for scientists working on condensed matter sciences in Japan. All scientific staff members (including post-docs) at universities or public research institutes in Japan can submit proposals for projects related to research activities on materials and condensed matter sciences. These proposals are peer-reviewed by the Advisory Committee members (see Sec. 1.3), and then the computation resources are allocated based on the review reports. The leader of an approved project can set up user accounts for collaborators. Other types of scientists, including graduate students, may also be added. Proposal submissions, peer-review processes, and user registration are all managed via a web system.

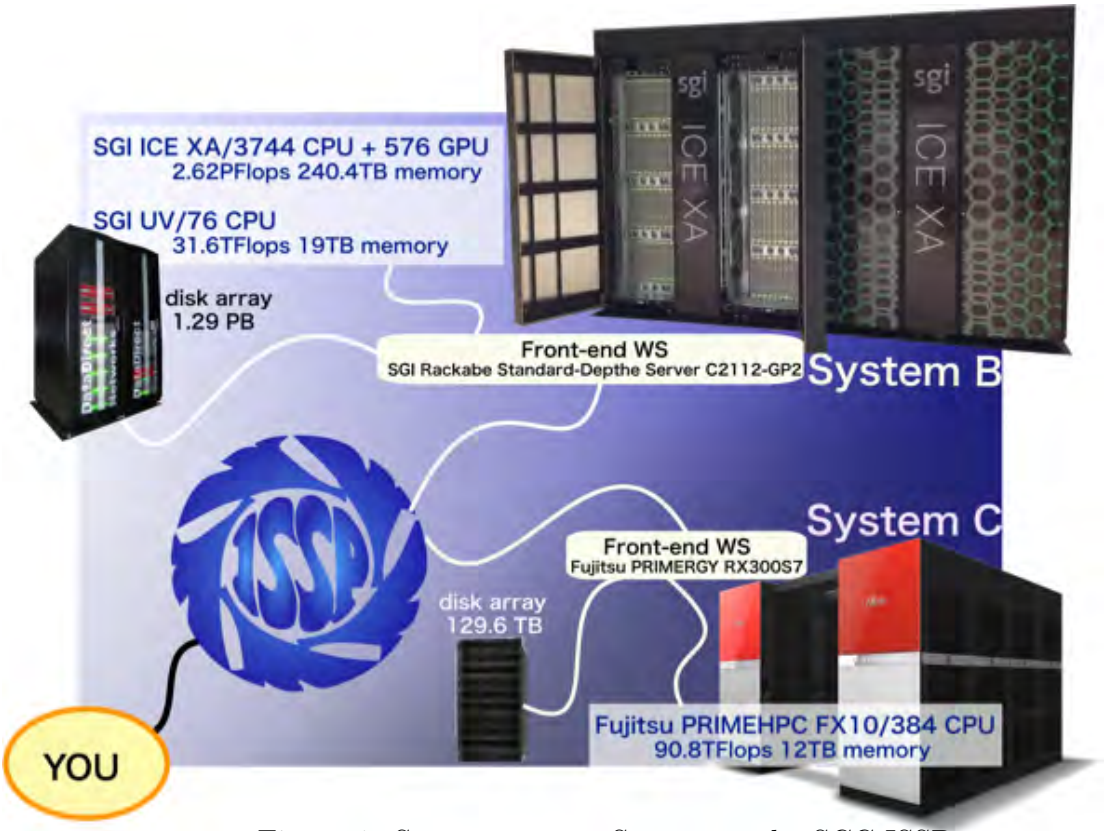

Figure 1: Supercomputer System at the SCC-ISSP

The computation resources are distributed in a unit called "point", determined as a function of available CPU utilization time and consumed disk resources. There were calls for six classes of research projects in SY 2016. The number of projects and the total number of points that were applied for and approved in this school year are listed in Table 1.

In addition, from SY 2016, ISSP Supercomputer is providing 20% of its computational resources for Supercomputing Consortium for Computational Materials Science (SCCMS), which aims at advancing parallel computations in condensed matter, molecular, and materials sciences on the 10-PFlops K Computer and the exascale post-K project. Computer time has also been alloted to Computational Materials Design (CMD) workshops, as well as for Science Camps held in ISSP for undergraduate students.

1.3 Committees

In order to fairly manage the projects and to smoothly determine the system operation policies, the Materials Design and Characterization Laboratory (MDCL) of the ISSP has organized the Steering Committee of the MDCL and the Steering Committee of the SCC-ISSP, under which the Supercomputer Project Advisory Committee (SPAC) is formed to review proposals. The members of the committees

Table 1: Classes of research projects in SY 2016

Class	Maximum Points		Application	# of Proj.	Total points			
					Applied		Approved	
	Sys–B	Sys–C			Sys–B	Sys–C	Sys–B	Sys–C
A	100	100	any time	9	0.9k	0.9k	0.9k	0.9k
B	1k	500	twice a year	50	41.7k	8.2k	29.1k	7.2k
C	10k	2.5k	twice a year	166	1387.8k	164.7k	679k	126.7k
D	10k	2.5k	any time	7	59k	5k	33.3k	3k
E	30k	2.5k	twice a year	12	350k	30k	219.5k	26.5k
S	–	–	twice a year	0	0	0	0	0
SCCMS				32	218.9k	103.5k	218.9k	103.5k
Total				276	2058.3k	312.3k	1180.7k	267.8k

- Class A is for trial use by new users; proposals for Class A projects are accepted throughout the year.
- Proposals for projects in Classes B (small), C (mid-size), E (large-scale), and S (exceptional) can be submitted twice a year. Approved projects in Classes A, B, C, and E continue to the end of the school year.
- In Class D, projects can be proposed on rapidly-developing studies that need to perform urgent and relatively large calculations. An approved project continues for 6 months from its approval.
- Class S is for projects that are considered extremely important for the field of condensed matter physics and requires extremely large-scale computation. The project may be carried out either by one research group or cooperatively by several investigators at different institutions. A project of this class should be applied with at least 10,000 points; there is no maximum. We require group leaders applying for Class S to give a presentation on the proposal to the Steering Committee of the SCC-ISSP. Class S projects are carried out within one year from its approval.
- Project leaders can apply for points so that the points for each system do not exceed the maximum point shown in this table.

in SY 2016 were as follows:

Steering Committee of the MDCL

HIROI, Zenji	ISSP (Chair person)
KATO, Takeo	ISSP
KAWASHIMA, Naoki	ISSP
MORI, Hatsumi	ISSP
NAKATSUJI, Satoru	ISSP
NOGUCHI, Hiroshi	ISSP
SUGINO, Osamu	ISSP
KIMURA, Kaoru	Univ. of Tokyo
YOSHIMOTO, Yoshihide	Univ. of Tokyo
SAWA, Hiroshi	Nagoya Univ.
KAGEYAMA, Hiroshi	Kyoto Univ.
MORIKAWA, Yoshitada	Osaka Univ.
OKUMURA, Hisashi	NINS-RSCS
OTSUKI, Tomi	Sophia Univ.
TAKEDA Mahoto	Yokohama Natl. Univ.

Steering Committee of the SCC-ISSP

NOGUCHI, Hiroshi	ISSP (Chair person)
KAWASHIMA, Naoki	ISSP
SUGINO, Osamu	ISSP
TSUNETSUGU, Hirokazu	ISSP
KATO, Takeo	ISSP
MASUDA, Takatsugu	ISSP
KASAMATSU, Shusuke	ISSP
MORITA, Satoshi	ISSP
WATANABE, Hiroshi	ISSP
HATANO, Naomichi	Univ. of Tokyo
IMADA, Masatoshi	Univ. of Tokyo
NAKAJIMA, Kengo	Univ. of Tokyo
TSUNEYUKI, Shinji	Univ. of Tokyo
YOSHIMOTO, Yoshihide	Univ. of Tokyo
MOHRI, Tetsuo	Tohoku Univ.
MORIKAWA, Yoshitada	Osaka Univ.
OTSUKI, Tomi	Sophia Univ.
OKUMURA, Hisashi	NINS-RSCS
HOSHI, Takeo	Tottori Univ.
SUZUKI, Takafumi	Univ. of Hyogo
YATA, Hiroyuki	ISSP
FUKUDA, Takaki	ISSP

Supercomputer Project Advisory Committee

NOGUCHI, Hiroshi	ISSP (Chair person)
KATO, Takeo	ISSP
KAWASHIMA, Naoki	ISSP
OZAKI, Taisuke	ISSP
SUGINO, Osamu	ISSP
TSUNETSUGU, Hirokazu	ISSP
MASUDA, Takatsugu	ISSP
KASAMATSU, Shusuke	ISSP
MORITA, Satoshi	ISSP
WATANABE, Hiroshi	ISSP
HATANO, Naomichi	Univ. of Tokyo
HUKUSHIMA, Koji	Univ. of Tokyo
IKUHARA, Yuichi	Univ. of Tokyo
IMADA, Masatoshi	Univ. of Tokyo
IWATA, Jun-Ichi	Univ. of Tokyo
MIYASHITA, Seiji	Univ. of Tokyo
MOTOME, Yukitoshi	Univ. of Tokyo
NAKAJIMA, Kengo	Univ. of Tokyo
OGATA, Masao	Univ. of Tokyo
OSHIYAMA, Atsushi	Univ. of Tokyo
TODO, Synge	Univ. of Tokyo
TSUNEYUKI, Shinji	Univ. of Tokyo
WATANABE, Satoshi	Univ. of Tokyo
YOSHIMOTO, Yoshihide	Univ. of Tokyo
ARITA, Ryotaro	RIKEN-CEMS
NEMOTO, Koji	Hokkaido Univ.
AKAGI, Kazuto	Tohoku Univ.
KAWAKATSU, Toshihiro	Tohoku Univ.
MOHRI, Tetsuo	Tohoku Univ.
SHIBATA, Naokazu	Tohoku Univ.
YANASE, Yoichi	Niigata Univ.
ISHIBASHI, Shoji	AIST
OTANI, Minoru	AIST
KOBAYASHI, Kazuaki	NIMS
TATEYAMA, Yoshitaka	NIMS
HATSUGAI, Yasuhiro	Univ. of Tsukuba
KOBAYASHI, Nobuhiko	Univ. of Tsukuba
OKADA, Susumu	Univ. of Tsukuba
ONO, Tomoya	Univ. of Tsukuba
YABANA, Kazuhiro	Univ. of Tsukuba
ODA, Tatsuki	Kanazawa Univ.
SAITO, Mineo	Kanazawa Univ.
HIDA, Kazuo	Saitama Univ.
NAKAYAMA, Takashi	Chiba Univ.

FURUKAWA, Nobuo	Aoyama Gakuin Univ.
MATSUKAWA, Hiroshi	Aoyama Gakuin Univ.
TAKANO, Hiroshi	Keio Univ.
YAMAUCHI, Jun	Keio Univ.
YASUOKA, Kenji	Keio Univ.
TOMITA, Yusuke	Shibaura Inst. Tech.
OTSUKI, Tomi	Sophia Univ.
OBATA, Shuji	Tokyo Denki Univ.
TADA, Tomofumi	Tokyo Tech.
HOTTA, Takashi	Tokyo Metropolitan Univ.
TOHYAMA, Takami	Tokyo Univ. of Sci.
WATANABE, Kazuyuki	Tokyo Univ. of Sci.
HAGITA, Katsumi	National Defense Academy
KONTANI, Hiroshi	Nagoya Univ.
MASUBUCHI, Yuichi	Nagoya Univ.
OKAMOTO, Yuko	Nagoya Univ.
SHIRAISHI, Kenji	Nagoya Univ.
TANAKA, Yukio	Nagoya Univ.
KAWAKAMI, Norio	Kyoto Univ.
KAWAMURA, Hikaru	Osaka Univ.
KUROKI, Kazuhiko	Osaka Univ.
KUSAKABE, Koichi	Osaka Univ.
MORIKAWA, Yoshitada	Osaka Univ.
OGUCHI, Tamio	Osaka Univ.
SHIRAI, Koun	Osaka Univ.
YOSHIDA, Hiroshi	Osaka Univ.
YOSHINO, Hajime	Osaka Univ.
YUKAWA, Satoshi	Osaka Univ.
SAKAI, Toru	JAEA
SUGA, Seiichiro	Univ. of Hyogo
SUZUKI, Takafumi	Univ. of Hyogo
TATENO, Masaru	Univ. of Hyogo
HOSHI, Takeo	Tottori Univ.
YASUDA, Chitoshi	Univ. of the Ryukyus
OKUMURA, Hisashi	NINS-RSCS

1.4 Staff

The following staff members of the SCC-ISSP usually administrate the ISSP Supercomputer.

NOGUCHI, Hiroshi	Associate Professor (Chair person)
KAWASHIMA, Naoki	Professor
SUGINO, Osamu	Associate Professor
WATANABE, Hiroshi	Research Associate

KASAMATSU, Shusuke	Research Associate
NOGUCHI, Yoshifumi	Research Associate
MORITA, Satoshi	Research Associate
YATA, Hiroyuki	Technical Associate
FUKUDA, Takaki	Technical Associate
ARAKI, Shigeyuki	Technical Associate

2 Statistics (School Year 2016)

2.1 System and User Statistics

In the following, we present statistics for operation time taken in the period from April 2016 to March 2017 (SY 2016). In Table 2, we show general statistics of the supercomputer system in SY 2016. The total number of compute nodes in System B, and C is 1891 and 384 respectively. Consumed disk points amount to about 2% and 3% of the total consumed points in System B and C respectively. Roughly 20% of the total points in System B and 40% of that in System C were consumed by SCCMS projects. This means that about 20% of the total computational resources in this school year were actually used by SCCMS projects.

In the left column of Fig. 2, availabilities, utilization rates, and consumed points in each system are plotted for each month. Throughout the school year, the utilization rates were very high. Especially in System B, they were exceeding 90% throughout most of the year.

The user statistics are shown in the right column of Fig. 2. The horizontal axis shows the rank of the user/group arranged in the descending order of the execution time (hour×nodes). The execution time of the user/group of the first rank is the longest. The vertical axis shows the sum of the execution time up to the rank. From the saturation points of the graphs, the number of "active" users of each system is around 250, and 60 for System B and C respectively. The maximum ranks in the graphs correspond to the number of the users/groups that submitted at least one job.

2.2 Queue and Job Statistics

Queue structures of System B and C in SY 2016 are shown in Table 3. In System B, users can choose from three types of compute nodes; jobs submitted to queues with "cpu", "acc", and "fat" at the end of their queue names are submitted to CPU, ACC, and Fat nodes, respectively. See Sec. 1.1 for a description of each type of compute node. The user then has to choose the queue according to the number of nodes to use and the duration of their calculation jobs. Queue names starting with "F" are for jobs taking 24 hours or less, while those starting with "L" can run much longer up to 120 hours. More nodes are allotted to "F" queues in order to maximize the turnaround time of user jobs. The queue names starting with "i" are used for interactive debugging of user programs and the elapsed time limit is

Table 2: Overall statistics of SY 2016

	System-B	System-C
total service time ($\times 10^3$ node·hours)	16035	3327.0
number of executed jobs	397032	19461
total consumed points ($\times 10^3$ point)	642.2	82.4
CPU points ($\times 10^3$ point)	630.8	79.6
disk points ($\times 10^3$ point)	11.3	2.8
total exec. time ($\times 10^3$ node·hours)	14598.4	1860.3
availability	97.2%	97.3%
utilization rate	91.0%	57.5%

30 minutes. The number following "F", "L", or "i" correspond to the number of nodes that can be used by one user job.

In System C, the "F" and "L" queues are set up similarly to System B. In addition, a debug queue is set up for short debugging jobs utilizing 1 to 4 CPUs, and an interactive queue that can use 1 to 4 CPUs is also available.

To prevent overuse of the storage, points are charged also for usage of disk quota in the three systems, as shown in Table 4. Disk points are revised often for optimal usage of the resources by examining usage tendencies each year.

Although we do not mention here in detail, to promote utilization of the massively parallel supercomputer, background queues ("B4cpu", "B36cpu", "B144cpu", "B18acc", "B72acc", and "B2fat") which charge no points for the jobs have also been open in System B.

The number of jobs, average waiting time, and total execution time in each queue are shown in Table 5. In both System B and C, a large portion of jobs have been executed in "F" queues. The largest amount of the execution time has been consumed in the large-scale "F144cpu" queue, but substantial number of jobs were run in every queue, suggesting that a wide variety of user needs are met by this queuing scheme. In most of these queues, the queue settings meet the user's tendencies in that the waiting times are on the order of the elapsed-time limit. The acc queues have relatively short waiting times, but we expect that to change as more users get accustomed to using GPGPUs.

2.3 Project for advancement of software usability in materials science

From School Year 2015, the supercomputer center (SCC) has started "Project for advancement of software usability in materials science". In this project, for enhancing the usability of the supercomputer system in ISSP, we perform some software-advancement activity such as implementing a new function to an existing code, releasing a private code on Web, writing manuals. Target programs are publicly offered in December and selected in the review by the Steering Committee

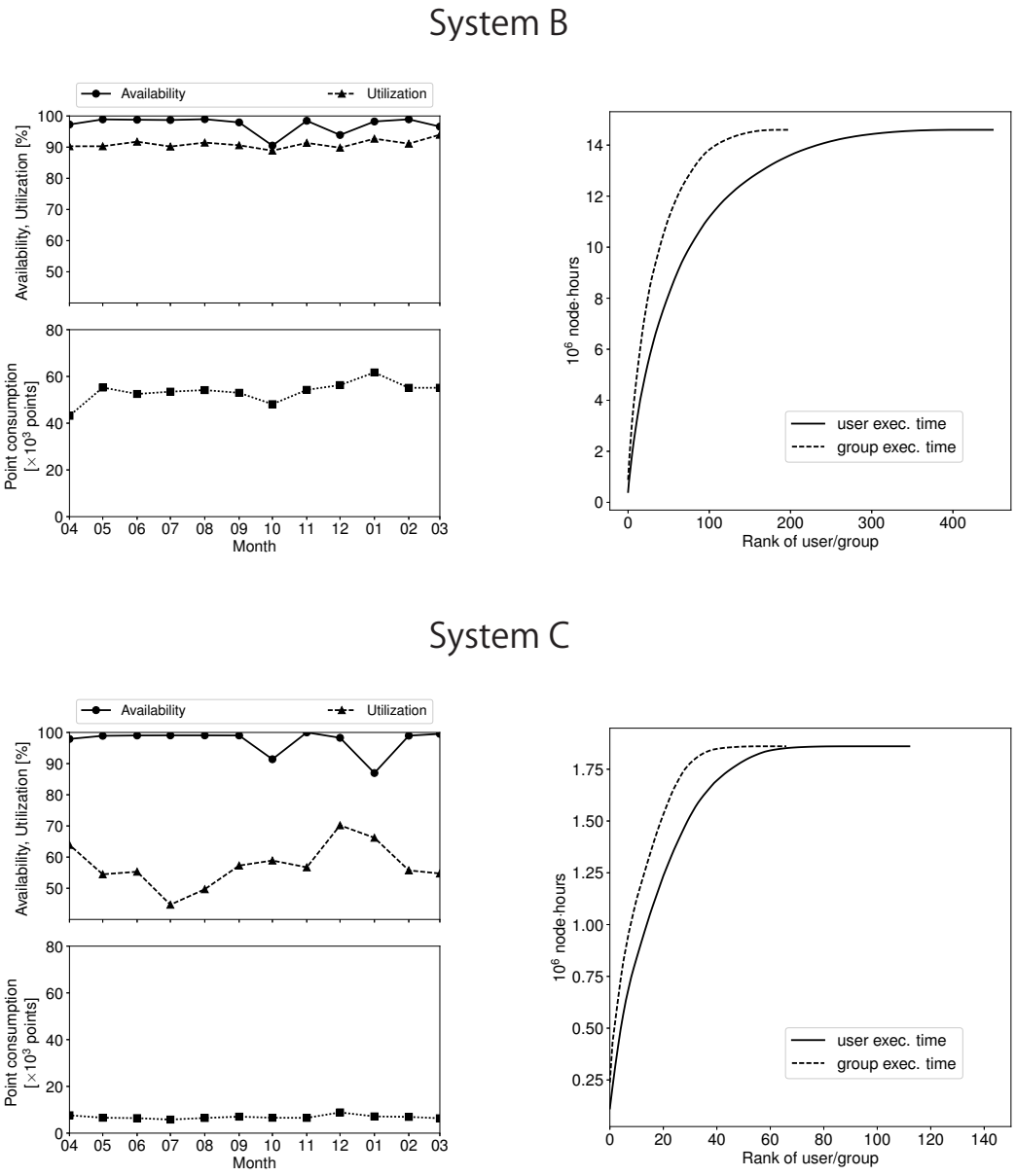

Figure 2: Left: Availabilities, utilization rates and point consumptions of each month during SY 2016. Right: User statistics. The horizontal axis shows the rank of the user/group arranged in the descending order of the execution time (hour×nodes). The vertical axis shows the sum of the execution time up to the rank.

Table 3: Queue structures in SY 2016

System–B

queue name	Elapsed time limit (hr)	# of nodes /job	# of nodes /queue	Memory limit (GB)	job points /(node·day)
F4cpu	24	1–4	216	120/node	1
L4cpu	120	1–4	108	120/node	1
F36cpu	24	5–36	288	120/node	1
L36cpu	120	5–36	144	120/node	1
F144cpu	24	37–144	1008	120/node	1
L144cpu	120	37–144	144	120/node	1
i18cpu	0.5	1–18	72	120/node	1
F18acc	24	1–18	108	120/node	2
L18acc	120	1–18	54	120/node	2
F72acc	24	19–72	144	120/node	2
i9acc	0.5	1–9	36	120/node	2
F2fat	24	1–2	17	1000/node	4
L2 fat	120	1–2	6	1000/node	4
i1fat	0.5	1	2	1000/node	4

System–C

queue name	Elapsed time limit (hr)	# of nodes /Job	# of nodes /queue	job points /(node·day)
debug	0.5	1-4	24	1
interactive	0.5	1-4	24	1
F12	24	2-12	60	1
F96	24	2-12	288	1
L12	120	24-96	24	1
L96	120	24-96	192	1

* The available memory size is limited to 28 GB per one CPU.

Table 4: Disk points of System B and C

		point/day
System B	`/home`	$0.001 \times \theta(q - 300)$
	`/work`	$0.0001 \times \theta(q - 3000)$
System C	`/home`	$0.05 \times \theta(q - 10)$
	`/work`	$0.005 \times \theta(q - 100)$

* q is denoted in unit of GB.
* $\theta(x)$ is equal to the Heaviside step function $H(x)$ multiplied by x, i.e., $xH(x)$.

Table 5: Number of jobs, average waiting time, total execution time, and average number of used nodes per job in each queue.

System-B

queue	# of Jobs	Waiting Time (hour)	Exec. Time ($\times 10^3$ node·hour)	# of nodes
F4cpu	179051	33.32	1227.13	1.59
L4cpu	8018	44.28	541.52	1.91
F36cpu	21986	24.71	1424.16	13.63
L36cpu	1266	79.09	770.36	16.49
F144cpu	11256	28.61	7040.09	87.93
L144cpu	273	170.56	951.20	112.62
i18cpu	55870	0.60	104.88	8.98
F18acc	36569	9.20	499.59	1.80
L18acc	2616	11.09	174.25	1.78
F72acc	2034	30.72	712.90	51.96
i9acc	8346	0.15	3.49	3.41
F2fat	6539	35.34	76.03	1.05
L2fat	394	25.49	23.76	1.24
i1fat	4943	0.09	0.82	1.00

System-C

queue	# of Jobs	Waiting Time (hour)	Exec. Time ($\times 10^3$ node·hour)	# of nodes
F12	8628	2.43	266.62	5.71
L12	181	18.74	40.39	8.35
F96	4677	7.64	1399.77	42.67
L96	78	31.00	141.65	63.58
debug	4826	0.07	2.74	3.22
interactive	705	0.00	0.18	1.62

Table 6: List of Project for advancement of software usability in materials science for SY 2016.

Software	Project Proposer
Novel numerical solvers for large-scale material computations with shifted Krylov-subspace theory	Takeo Hoshi Tottori University
Development of open-source software for many-variable variational Monte Carlo method	Takahiro Misawa The University of Tokyo

of SCC. The projects are carried out by the software development team composed of three members in ISSP. In SY 2016, two projects are selected as listed in Table 6.

2.4 GPGPU Support Service

As noted in Sec. 1.1, ACC nodes with graphics processing units (GPU) were introduced in System B in School Year 2015. Since GPUs were introduced in the ISSP Supercomputer center for the first time, many programs developed or utilized by users of this center have not been programmed for GPU computing. To help users take advantage of GPUs, the supercomputer center has started a service for porting users' materials science software to General Purpose GPUs (GPGPU). After a call for proposals (which will usually be in December), target programs for the next school year are selected by the Steering Committee of SCC. The porting service is carried out on each program for about two months; the coding is performed by engineers from the computer vender suppling the ISSP supercomputer system, and ISSP staff oversee the progress of the project and manage necessary communications with the proposer. Copyrights of the resulting software basically belong to the proposers, but the supported contents might be published under agreement with the proposer. In SY 2016, three projects are selected as listed in Table 7.

Acknowledgments

The staffs would like to thank Prof. Takafumi Suzuki (now at University of Hyogo) for developing WWW-based system (SCM: SuperComputer Management System) for management of project proposals, peer-review reports by the SPAC committee, and user accounts. We also thank Ms. Reiko Iwafune for creating and maintaining a new WWW page of the ISSP Supercomputer Center.

Table 7: List of supported software and project proposers for the GPGPU support service for SY 2016.

Software	Project Proposer
Acceleration of molecular dynamics calculation codes based on fast multipole method by GPGPU	Yoshimichi Andoh Nagoya University
GPU Implementation of Car-Parrinello Molecular Dynamics using Real-space DFT (RS-CPMD)	Yasuteru Shigeta University of Tsukuba
GPGPU implementation of many-variable variational Monte Carlo method	Takahiro Misawa The University of Tokyo

3 RESEARCH REPORTS

3.1 Invited Articles

Development of First-Principles Simulation of Material Structure and Electronic Properties 14

Shinji TSUNEYUKI

Massively Parallel Monte Carlo Simulation of a Possible Topological Phase Transition in Two-Dimensional Frustrated Spin Systems 20

Tsuyoshi OKUBO

Irreversible Markov-Chain Monte Carlo Methods 29

Koji HUKUSHIMA

Development of First-Principles Simulation of Material Structure and Electronic Properties

Shinji TSUNEYUKI
Department of Physics, the University of Tokyo
7-3-1 Hongo, Bunkyo-ku, Tokyo 113-0033
Institute for Solid State Physics, the University of Tokyo
5-1-5 Kashiwa-no-ha, Kashiwa, Chiba 277-8581

Abstract

I discuss the grand challenges in first-principles material simulation and briefly review two of our trials to solve them. The first one is the development of the transcorrelated method, a correlated wave function theory applicabl to condensed matter. The second one is a general scheme for calculating lattice thermal conductivity.

1 Introduction

First-principles electronic structure calculation based on the density functional theory (DFT) is widely used not only in the analysis of material structure and its electronic state but also for theoretical prediction of material properties. As the scope of its application expands, however, we find there are many problems still remaining.

Firstly, accuracy and reliability of total energy and energy spectrum obtained by the present DFT are sometimes insufficient for the research of strongly correlated electronic systems, spin states or magnetic orders, optical properties, structure of molecular crystals and so on. Although there have been reported various succesful attemps such as combination of DFT, downfolding techniques and accurate simulation of simplified model Hamiltonian for low-energy electrons, first-principles method, which is general in the sense of DFT, is still missing.

Secondly, calculable system size is quite limited despite advances in massively parallel supercomputers. This is because the computational cost of DFT essentially scales as order N^3 with N being the number of atoms. So-called order-N methods have been developed for large-scale structural simulations, but calculation of the energy spectrum needs additional process with high calculation load.

Thridly, researh on non-equilibrium dynamics often needs large-scale and long-time dynamical simulation, or otherwise requires some ingenuity. Chemical reaction, thermal transport and structure formation like crystal growth are such examples.

Finally, prediction of material structure is a very important challenge considering increasing importance of computer simulations in new material development. Recent activities on materials informatics have further increase its importance.

For years, we have developed various methods with collaborators to tackle the problems mentioned above. In this article, I briefly review two important methods among them. The developments were mainly done by Masayuki Ochi (Section 2) and Terumasa Tadano (Section 3).

2 Wave-function theory for condensed matter

Wave function theory (WFT) is not often applied to first-principles calculation of condensed matter, since the Hartree-Fock (HF) method, virtually the only available method except for quantum Monte Carlo methods, fails to describe finite density of states at the Fermi level of metals and seriously overestimates the band gap of semiconductors. WFT-based approaches are, however, systematically improvable and this is a great advantage against the density functional theory (DFT). Therefore some groups have been revisiting WFT to go beyond the present DFT calculation.

The transcorrelated (TC) method first developed by S.F. Boys and N.C. Handy [1, 2] is a unique approach to correlated electrons with Slater-Jastrow-type many-body wavefunctions. In TC, by using similarity transformation of the Hamiltonian with the Jastrow factor, HF-like self-consistent-field (SCF) equations called TC-SCF equations are derived for one-electron wave functions in the Slater determinant together with their orbital energies, which are very helpful for intuitive understanding of the electronic state of matter. Thus we have so far developed the TC method for periodic systems [3, 4, 5, 6, 7, 8, 9, 10, 11].

In the TC method, a many-body wavefunction of the system Ψ is formally factorized as $\Psi = F\Phi$. $F = \exp(-\sum_{i,j(\neq 1)} u(x_i, x_j))$ is a Jatrow factor representing two-body electron correlation and Φ is defined as $\Phi = \Psi/F$. The eigenstate equation for the total Hamiltonian $\mathcal{H}$, $\mathcal{H}\Psi = E\Psi$ leads $\mathcal{H}_{\rm TC}\Phi = E\Phi$ with $\mathcal{H}_{TC} \equiv F^{-1}\mathcal{H}F$. Note that this is just a similarity transformation and mathematically exact. The Jastrow factor has been widely used in the variational Monte Carlo method for correlated electrons with variations of the Jastrow function $u(x, x')$. In our study we usually adopt a simple form:

$$u(x, x') = \frac{A}{|\mathbf{r} - \mathbf{r}'|}\left\{1 - \exp\left(-\frac{|\mathbf{r} - \mathbf{r}'|}{C_{\sigma,\sigma'}}\right)\right\}, \quad (1)$$

$$A = \sqrt{\frac{V}{4\pi N}} \times \sqrt{1 - \frac{1}{\varepsilon}}, \quad (2)$$

$$C_{\sigma,\sigma'} = \sqrt{2A}(\sigma = \sigma'), \sqrt{A}(\sigma \neq \sigma'), \quad (3)$$

where V and N are the volume of the cell and the number of electrons, respectively, and ε is the static dielectric constant. Improvement of u is discussed in Ref.[7]. The transcorrelated Hamiltonian $\mathcal{H}_{\rm TC}$ is a non-Hermitian and contains effective two-body and three-body interactions.

Then we use the HF approximation and adopt a single Slater determinant of one-electron wavefunction $\phi_i(\mathbf{r})$ $(i = 1-N)$ for the manybody function Φ. The TC-SCF equation for $\phi_i(\mathbf{r})$ is similar to the HF-SCF equation, with which $\phi_i(\mathbf{r})$ in the Slater determinant can be optimized for the Jastrow function F:

$$\begin{aligned}
&\left(-\frac{1}{2}\nabla_1^2 + v_{\rm ext}(x_1)\right)\phi_i(x_1) \\
&+\sum_{j=1}^{N}\int dx_2 \phi_j^*(x_2) v_{\rm 2body}(x_1, x_2) \\
&\times det[\phi_i(x_1), \phi_j(x_2)] \\
&-\frac{1}{2}\sum_{j=1}^{N}\sum_{k=1}^{N}\int dx_2 dx_3 \phi_j^*(x_2)\phi_k^*(x_3) \\
&\times v_{\rm 3body}(x_1, x_2, x_3) \\
&\times det[\phi_i(x_1), \phi_j(x_2)\,\phi_k(x_3)] = \sum_{j=1}^{N}\epsilon_{ij}\phi_j(x_1). \quad (4)
\end{aligned}$$

Here $v_{\rm ext}(x_1)$ is the external potenial from nuclei or pseudopotentials. $v_{\rm 2body}$ and $v_{\rm 3body}$ are effective two-body and three-body potentials derived from the Jastrow function u:

$$\begin{aligned}
v_{\rm 2body}(x_1, x_2) &= \frac{1}{|\mathbf{r}_1 - \mathbf{r}_2|} \\
&+\frac{1}{2}\sum_{i=1}^{2}[\nabla_i^2 u(x_1, x_2) - (\nabla_i u(x_1, x_2))^2 \\
&+2\nabla_i u(x_1, x_2)\cdot\nabla_i], \quad (5) \\
v_{\rm 3body}(x_1, x_2, x_3) &= \nabla_1 u(x_1, x_2)\cdot\nabla_1 u(x_1, x_3)
\end{aligned}$$

$$+\nabla_2 u(x_2,x_1)\cdot\nabla_2 u(x_2,x_3)$$
$$+\nabla_3 u(x_3,x_1)\cdot\nabla_3 u(x_3,x_2). \quad (6)$$

The orbital energy matrix ϵ_{ij} can be made triangular (by orbital orthogonalization) or diagonal (by biorthogonal formulation), when Koopmans' theorem holds for the diagonal elements. Since $\mathcal{H}_{\rm TC}$ preserves the crystal symmetry of the original Hamiltonian $\mathcal{H}$, we can obtain band structure of the crystal with taking account of the electron correlation through F.

To solve the TC-SCF equation and to calculate the total energy, we need to evaluate three-body integrals for $v_{\rm 3body}$. Since each term of $v_{\rm 3body}$ is a product of two-body functions, computational cost for the three-body integrals can be reduced to the order of two-body integrals in the HF method [6]. Thanks to this algorithm, computational cost of the TC method has come to be within the reach of supercomputers or PC clusters.

So far we have shown that the TC method is actually a good and alternative approach to condensed matter: it is applicable to metals in principle [3], much improves the HF band structure of semiconductors [4, 6, 7], and is compatible with post-HF methods such as the configuration interaction method for calculating photo-excitation spectrum including the excitonic effect [5, 8] and also Møller-Plesset perturbation theory [9]).

Very recently, we have developed a new iterative scheme to solve the TC-SCF equations to further reduce the comutational cost and memory [10], which enabled us to apply the TC method with biorthogonal formalism to a transition metal oxide ZnO for the first time. Calculated band gap, valence band width and position of the narrow 3d band were in better agreement with experimental data than several other conventional methods including the G_0W_0 method (see Table 1) [11].

3 Anharmonic phonons and lattice thermal conductivity

Lattice thermal conductivity is a key parameter in the figure of merit for thermoelectric materials. It is also important from the viewpoint of device technology, since thermal management is necessary to avoid thermal breakdown of nano-scale devices. Therefore, it is highly desirable for material and device development to calculate it from first principles.

Lattice thermal conductivity can be evaluated by molecular dynamic simulation (MD) with Kubo formula, non-equilibrium MD with Fourier's law, or by Boltzman transport equation (BTE) usually with the single-mode relaxation-time approximation (RTA). MD needs large simulation cell comparable with phonon-scattering length and long-time simulation corresponding to the relaxation time of phonons. Since the phonon-scattering length and the relaxation time can reach 10^{-9}s and 10^{-6}m, respectively, in some cases, it is difficult to use first-principles MD except for materials with low thermal conducltivity or at high temperature [21]. It should also be noted that we cannot easily check and assure the appropriateness of the calculation condition of MD.

On the other hand, by BTE with the single-mode RTA, the lattice thermal conductivity can be accurately estimated by the following formula:

$$\kappa_L^{\mu,\nu}(T)=\frac{1}{\Omega N}\sum_{\mathbf{q},\mu} c_{\mathbf{q}}(T)v_{\mathbf{q}}^{\mu}v_{\mathbf{q}}^{\nu}\tau_{\mathbf{q}}(T). \quad (7)$$

Here, Ω is the volume of the unit cell, $c_{\mathbf{q}}$, $v_{\mathbf{q}}$ and $\tau_{\mathbf{q}}$ are the constant-volume specific heat, the group velocity, and the relaxation time of phonons with wave vector $\mathbf{q}$, respectively. N is the mumber of q points. The relaxation time $\tau_{\mathbf{q}}=[2\Gamma_{\mathbf{q}}(\omega_{\mathbf{q}})]^{-1}$ can be calculated by

$$\Gamma_{\mathbf{q}}(\omega)=\frac{\pi}{2N}\sum_{\mathbf{q}',\mathbf{q}''}\frac{\hbar|\Phi(-\mathbf{q},\mathbf{q}',\mathbf{q}'')|^2}{8\omega_{\mathbf{q}}\omega_{\mathbf{q}'}\omega_{\mathbf{q}''}}$$
$$\times[(n_{\mathbf{q}'}+n_{\mathbf{q}''}+1)\delta(\omega-\omega_{\mathbf{q}'}-\omega_{\mathbf{q}'})$$
$$-2(n_{\mathbf{q}'}-n_{\mathbf{q}''})\delta(\omega-\omega_{\mathbf{q}'}+\omega_{\mathbf{q}'})], \quad (8)$$

Table 1: Characteristic values in the band structure of ZnO obtained by various first-principles methods and experiments. All values are in eV. (Ref.[11])

	Band gap	O2p bottom	Zn3d average/bottom
LDA	0.7	$\cdots$	$\cdots/-5.8$
HSE03[a]	2.1	-4.9	$\cdots/-6.5$
G_0W_0 (LDA)[b]	2.4	-5.2	$\cdots/-6.5$
G_0W_0 (HSE03)	3.2[a], 3.46[c]	$\cdots$	-6.21[c]$/-7.2$[a]
AFQMC[d]	3.26(16)	$\cdots$	$\cdots$
VMC[e]	3.8(2)	$\cdots$	$\cdots$
HF	11.4	-5.7	$-9.1/-9.9$
Biorthogonal TC	3.1	-5.1	$-9.3/-9.7$
Expt.	3.4[f]	-5.3[f], -5.2[g]	-7.5[c,h], -8.6[i], -8.81[g]/–

[a]Ref.[12], [b]Ref.[13], [c]Ref.[14], [d]Ref.[15], [e]Ref.[16], [f]Ref.[17], [g]Ref.[18], [h]Ref.[19], [i]Ref.[20].

where the three-phonon scattering matrix element $\Phi(-\mathbf{q}, \mathbf{q}', \mathbf{q}'')$ is calculated from third-order force constants in the potential energy function of atoms. As the third-order force constants are considered to be short-range, they can be calculated with a periodic cell containing relatively small number of atoms. Although we need to use many $\mathbf{q}$-points in eq.(8), we can easily check the convergence of calculation in the BTE-RTA approach. Another advantage of the BTE-RTA approach is that, once we know $\Phi(-\mathbf{q}, \mathbf{q}', \mathbf{q}'')$, temperature dependence of the thermal conductivity is easily obtained from the same $\Phi(-\mathbf{q}, \mathbf{q}', \mathbf{q}'')$. Furthermore mode-dependent analysis of the phonon relaxation can be easily done by eq.(8). These are the reason we often use the BTE-RTA approach instead of MD.

To get anharmonic force constants we developed a general and efficient method based on a first-principles molecular dynamics simulation: the simulation cell typically contains a few tens of atoms and the simulation time is of the order of 10^{-12}s. The third-order force constants derived from the simulation were then used for calculation of the lattice thermal conductivity of various materials (see Fig. 1)[22, 23, 24]. It should be noted that a wide range of lattice thermal conductivity including the temperature dependence is accurately calculated with the present scheme.

The calculation of $SrTiO_3$ shown in Fig. 1 is a special case to be mentioned. $SrTiO_3$ exhibits phase transformation at 105 K and has cubic symmetry above the transition temperature. Frequencies of some phonon modes are calculad to be imaginary with the cubic structure, showing that the cubic phase is not stable statically and has highly anharmonic potential energy surface. In this case we cannot use eqs.(7)-(8) as they are. Thus we introduced the self-consistent-phonon (SCPH) approach to calculate phonon frequencies realized by thermal fluctuation. With the method, we succeeded in quantitative calculation of temperature-dependent *real* phonon frequencies as observed in experiments, and with these frequencies, we obtained the lattice thermal conductivity of $SrTiO_3$ in Fig. 1, which agreed well with experiments [24, 25].

The simulation software named ALAMODE developed by T. Tadano is published as an open source software [26].

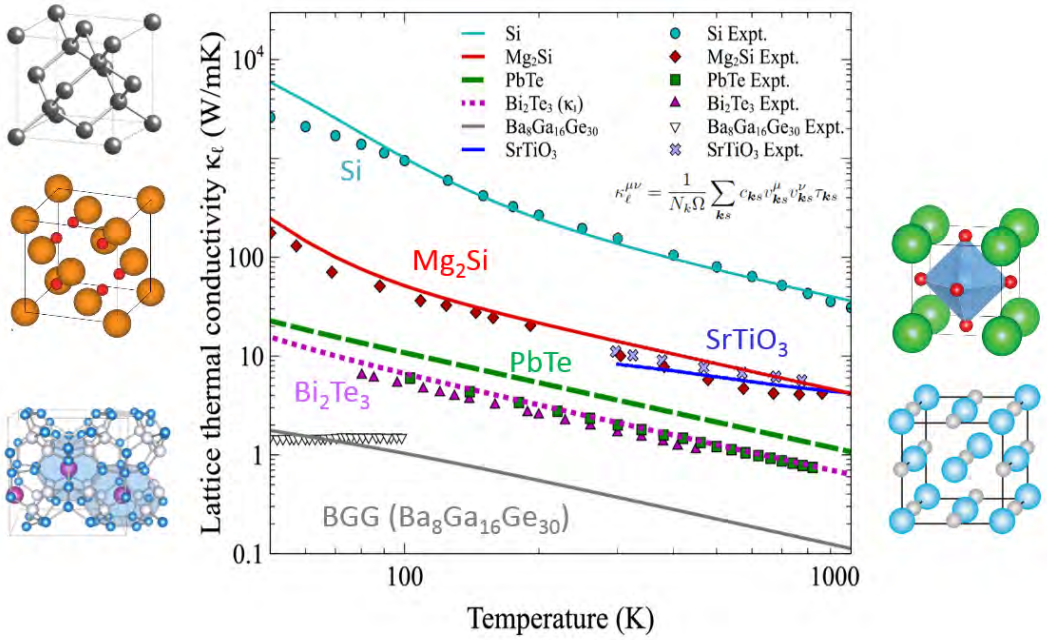

Figure 1: Temperature dependence of the lattice thermal conductivity of various materials obtained by simulation withom BTE-RTA (lines) and by experiments (symbols). (See Refs.[22,23,24] and references therein.)

4 Summary

Supported by rapidly advancing computers, first-principles material simulation is nowadays an indispensable tool for material science. As the simulation extends its application, however, we have come to face with its limitations and challenges. After summarizing the challenges in four direction in the introduction, I reviewed two of our trials to solve some of the challenges. Firstly I reviewed the idea and recent development of the transcorrelated method. It is the wave function theory for correlated electronic systems, which enables us to calculte not only the total energy but also the electronic energy spectrum accurately. Secondly I reviewed the method to calculate lattice thermal conductivity. It is general, accurate and applicable to even a high-symmetry crystal realized by thermal fluctuation at high tempetature. Itroduction of the SCPH approach further expands the scope of its application.

Acknowledgement

The development and calculation reviewed in this article are partly done using the facilities of the Supercomputer Center, Institute for Solid State Physics, The University of Tokyo.

References

[1] S.F. Boys and N.C. Handy, Proc. R. Soc. London, Ser. A 309, 209 (1969); ibid. 310, 63 (1969); ibid. 311, 309 (1969).

[2] N.C. Handy, Mol. Phys. 21, 817 (1971).

[3] N. Umezawa and S. Tsuneyuki, Phys. Rev. B 69, 165102 (2004).

[4] R. Sakuma and S. Tsuneyuki, J. Phys. Soc. Jpn. 75, 103705 (2006).

[5] S. Tsuneyuki, Prog. Theo. Phys. Suppl. 176, 134 (2008).

[6] M. Ochi, K. Sodeyama, R. Sakuma and S. Tsuneyuki, J. Chem. Phys. 136, 094108 (2012).

[7] M. Ochi, K. Sodeyama and S. Tsuneyuki, J. Chem. Phys. 140, 074112 (2014).

[8] M. Ochi and S. Tsuneyuki, J. Chem. Theory Comput. 10, 4098 (2014).

[9] M. Ochi and S. Tsuneyuki, Chem. Phys. Lett. 621, 177-183 (2015).

[10] M. Ochi, Y. Yamamoto, R. Arita and S. Tsuneyuki, J. Chem. Phys. 144, 4109 (2016).

[11] M. Ochi, R. Arita, and S. Tsuneyuki, Phys. Rev. Lett. 118, 026402 (2017).

[12] A. R. H. Preston, B. J. Ruck, L. F. J. Piper, A. DeMasi, K. E. Smith, A. Schleife, F. Fuchs, F. Bechstedt, J. Chai and S. M. Durbin, Phys. Rev. B 78, 155114 (2008).

[13] M. Usuda, N. Hamada, T. Kotani, and M. van Schilfgaarde, Phys. Rev. B66, 125101 (2002).

[14] L. Y. Lim, S. Lany, Y. J. Chang, E. Rotenberg, A. Zunger and M. F. Toney, Phys. Rev. B86, 235113 (2012).

[15] F. Ma, S. Zhang and H. Krakauer, New J. Phys. 15, 093017 (2013).

[16] J. Yu, L. K. Wagner and E. Ertekin, J. Chem. Phys. 143, 224707 (2015).

[17] *Numerical Data and Functional Relationships in Science and Technology*, edited by K. H. Hellwege and O. Madelung, Landolt-Bornstein, New Series, Group III, Vols. 17a and 22a (Springer, Berlin, 1982).

[18] L. Ley, R. A. Pollak, F. R. McFeely, S. P. Kowalczyk and D. A. Shirley, Phys. Rev. B9, 600 (1974).

[19] R. A. Powell, W. E. Spicer and J. C. McMenamin, Phys. Rev. Lett. 27, 97 (1971).

[20] C. J. Vesely, R. L. Hengehold and D. W. Langer, Phys. Rev. B5, 2296 (1972)

[21] S. Stackhouse, L. Stixrude, B.B. Karki, Phys. Rev. Lett. 104, 208501 (2010).

[22] T. Tadano, Y. Gohda, and S. Tsuneyuki, J. Phys.: Condens. Matter **26**, 225402 (2014).

[23] T. Tadano, Y. Gohda, and S. Tsuneyuki, Phys. Rev. Lett. **114**, 095501 (2015).

[24] T. Tadano and S. Tsuneyuki, Phys. Rev. B **92**, 054301 (2015).

[25] T. Tadano and S. Tsuneyuki, submitted to J. Phys. Soc. Jpn.

[26] T. Tadano, "ALAMODE", http://sourceforge.net/projects/alamode/, http://ma.cms-initiative.jp/ja/listapps/alamode/alamode

Massively parallel Monte Carlo simulation of a possible topological phase transition in two-dimensional frustrated spin systems

Tsuyoshi OKUBO*
Institute for Solid State Physics, University of Tokyo
Kashiwa-no-ha, Kashiwa, Chiba 277-8581

Abstract

In two-dimensional frustrated Heisenberg spin systems, a topological defect, so called Z_2-vortex, often appears as an elemental excitation from magnetically ordered non-collinear ground states. In this paper, we investigate a possible topological phase transition driven by binding-unbinding of Z_2-vortices, the Z_2-*vortex transition* by means of massively parallel Monte Carlo simulations. In order to avoid the failure of global update Monte Carlo simulations in frustrated spin systems, we consider an effective model of the Z_2 vortex transition, where $SO(3)$ matrices ferromagnetically interact each other on the $L \times L$ square lattice. We calculate an order parameter, the vorticity modulus, up to $L = 16384$. By extrapolating the data into the thermodynamic limit, we estimate the upper bound of the transition temperature as $T/J \simeq 0.27$. On the other hand, the spin correlation length at this temperature is estimated at least 20000 lattice spacings. Because the present system is limited $L = 16384$, we need further careful analysis to conclude the existence of the finite-temperature topological phase transition.

1 Introduction

Recently, frustrated magnets have attracted much interest [1–4]. Frustrated interactions often introduce two kinds of interesting features to spin systems. Firstly, in several frustrated systems, the classical ground states are macroscopically degenerated due to the competitions of interactions. These systems do not develop magnetic long-range order even at zero temperature. They have been considered to reveal possible quantum spin liquids as their ground state if we introduce strong quantum fluctuation typically appeared in the case of $S = 1/2$. Typical examples of such macroscopically degenerated ground state can be seen in the two dimensional kagomé lattice or in the three dimensional pyrochlore lattice.

Secondly, even if frustrated spin systems have magnetically ordered ground state, spins often cant from each other forming non-coplaner or non-collinear. A typical example showing non-collinear structure is the triangular lattice antiferromagnetic Heisenberg model. The ground state of the model is so called 120-degree structure where spins cant 120 degrees each other (see Fig. 1(a)). Such kind of canted structures often introduce novel phenomena to frustrated spin systems.

In two-dimensional frustrated Heisenberg spin systems with non-collinear ground state, a topologically stable point defect, Z_2 vortex, often plays an important role in their ordering.

*Present address: Department of Physics, University of Tokyo, Bunkyo-ku, Tokyo 113-0033.

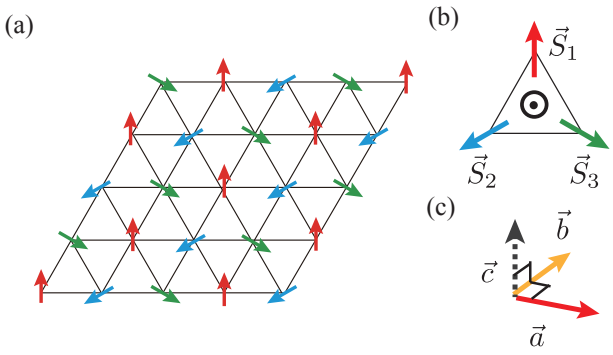

Figure 1: (a)Schematic view of 120-degree structure on the triangular lattice. (b) A local 120 degree structure together with the vector chirality $\kappa \propto \vec{S}_1 \times S_2$ perpendicular to the plane. (c) A local $SO(3)$ vectors $\vec{a}, \vec{b}$, and $\vec{c}$ defined from a local 120-degree structure.

A possible topological phase transition driven by binding-unbinding of the Z_2 vortices was proposed by Kawamura and Miyashita about 30 years ago [5]. In this Z_2-vortex transition, the spin correlation length keeps finite. At the Z_2-vortex transition temperature T_v, only the vortex correlation length characterizing the typical separation of the free vortices diverges. This is a sharp contrast to the case of the Berezinskii – Kosterlitz – Thouless (BKT) transition in two dimensional XY spin systems, where the spin correlation length diverges together with the vortex correlation length below the transition temperature [6, 7].

The nature of the possible Z_2-vortex transition has been investigated typically on the triangular-lattice Heisenberg antiferromagnet [5, 8–10]. Recent Monte Carlo (MC) simulation up to $L = 1536$ suggested the occurrence of Z_2-vortex transition at a finite temperature $T_v/J \simeq 0.285$ with a finite spin-correlation length $\xi \simeq 2000$ [8]. However, the existence of topological phase transition has not been fully resolved because the estimated spin correlation length at T_v is larger than the maximum system size $L = 1536$. In order to clarify the true nature of the Z_2-vortex transition, we need larger systems beyond the spin-correlation length at the transition temperature.

However the increase of the system sizes is not so easy because the cluster update MC techniques such as Swendsen-Wang and Wolff algorithms [11, 12] do not work efficiently in the case of frustrated spin systems. By using local update, typically we suffered from *critical slowing down* which means the relaxation time behaves as

$$\tau \propto L^z, \tag{1}$$

where z is usually $z \geq 2$. Thus, if we increase the systems size by twice as $L' = 2L$, we at least need four times long MC steps than that of L in order to obtain sufficient statistics. In addition, we also need to cover the increase of computational cost par unit MC step which is usually proportional to L^2 in the case of two-dimensional systems.

In order to overcome these difficulties, we consider the following strategy. First, we change the model from original frustrated triangular lattice model to a low temperature effective model where we consider $SO(3)$ rotational matrices as elemental degree of freedoms. As we see in the followings, in this effective model the $SO(3)$ matrices interact each other ferromagnetically and their is no explicit frustration. Thus we can introduce a cluster algorithm which seems to work well at least for smaller system [13, 14]. Second, in order to cover the increase of computational costs, we introduce MPI parallelization of a cluster MC algorithm based on the real space division. Note that in contrast to the local update MC, we need a global communication to determine the cluster structure in the case of global update.

By combining these two techniques, we perform massively parallel MC simulations for the system sizes up to $L = 16384$, which is ten times larger than the previous numerical simulations. It turns out that if we assume the existence of phase transition, the transition temperature T_v is estimated to be actually finite

by using finite size scaling. On the other hand, the spin correlation length at the estimated T_v is larger than the maximum system size $L = 16384$. Thus we need further studies to confirm the existence of Z_2 vortex transition without doubt.

The rest of the paper is organized as follows. In Sec. 2 we introduce an effective model of the Z_2-vortex transition. Then we describe numerical methods to investigate the model in Sec. 3. The main results are provided in Sec. 4. Finally, we give concluding remarks and future issues in Sec. 5.

2 Model

In order to investigate the possible Z_2-vortex transition, we consider an effective model which describes low temperature properties of several frustrated Heisenberg systems, *e.g.* the triangular lattice antiferromagnet Heisenberg model [14,15]. The Hamiltonian of the triangular lattice antiferromagnetic Heisenberg model is given by

$$\mathcal{H} = J \sum_{\langle i,j \rangle} \vec{S}_i \cdot \vec{S}_j, \tag{2}$$

where $\vec{S} = (S_x, S_y, S_z)$ is a three-component unit-vector, $J > 0$, and $\sum_{\langle i,j \rangle}$ means the sum over the nearest-neighbor pairs on the triangular lattice.

The ground state of the model is the 120-degree structure. Note that a "direction" of a 120-degree structure on a triangle can be characterized by a $SO(3)$ matrix. For example, we construct three orthogonal unit vectors $\vec{a}$, $\vec{b}$, and $\vec{c}$ as

$$\begin{aligned} \vec{a} &= \vec{S}_1 \\ \vec{c} &\propto \vec{S}_1 \times \vec{S}_2 \\ \vec{b} &= \vec{c} \times \vec{a}, \end{aligned} \tag{3}$$

(see Fig. 1(b,c)). Thus, a low-temperature effective model of the triangle lattice Heisenberg model is given by

$$\mathcal{H}_{\text{eff}} = -\sum_{\langle i,j \rangle_t} \left(p_1 \vec{a}_i \cdot \vec{a}_j + p_1 \vec{b}_i \cdot \vec{b}_j + p_3 \vec{c}_i \cdot \vec{c}_j \right), \tag{4}$$

where a set of vectors $(\vec{a}_i, \vec{b}_i, \vec{c}_i)$ is located at a upper triangle of the original triangular lattice and $\sum_{\langle i,j \rangle_t}$ is the sum over the nearest-neighbors on the coarse grained triangular lattice formed by upper triangles. Note that interaction coefficients p_1 and p_3 are non-negative (ferromagnetic), and p_3 is generally different from p_1 because $\vec{c}$ is perpendicular to the original 120-degree structure, while $\vec{a}$ and $\vec{b}$ are on the plane formed by the 120-degree structure. In a previous study done by Kawamura and Kikuchi, they used a model with $p_3 = 0$ [15]. Because the the model only has ferromagnetic interactions, the underlying lattice structure might be irrelevant to the nature of the ordering. Thus, hereafter we consider the model on the square lattice for the simplicity.

By introducing a 3×3 matrix R_i as $R_i = (\vec{a}_i, \vec{b}_i, \vec{c}_i)$, the Hamiltonian is transformed into the form as

$$\mathcal{H}_{\text{eff}} = -\sum_{\langle i,j \rangle} \text{Tr } R_i^t P R_j, \tag{5}$$

where P is a diagonal matrix $P = \text{diag } (p_1, p_1, p_3)$. From this notation, we can see that the Hamiltonian is unchanged under the transformation

$$R_i' = U R_i V, \tag{6}$$

where U is a $SO(3)$ rotational matrix and V is a $O(2)$ rotational matrix which mixes $\vec{a}$ and $\vec{b}$. Thus, the effective model often called as $SO(3) \times O(2)$ model. At the special parameter $p_3 = p_1$ the model becomes $SO(3) \times SO(3)$ symmetric, *i.e.*, the Hamiltonian is unchanged under the transformation (6) with both of U and V are $SO(3)$ matrices.

Because the effective model has Z_2-vortices as topological defects independent on the value of p_3, here we concentrate to the case $p_3 = p_1$.

In this special case, the $SO(3) \times SO(3)$ model can be mapped onto so called RP^3 model [14]. In the RP^3 model *four-component* unit vectors $\vec{S}_i = (S_{i,0}, S_{i,1}, S_{i,2}, S_{i,3})$, interact through the ferromagnetic biquadratic interaction as

$$\mathcal{H}_{RP^3} = -\tilde{J} \sum_{\langle i,j \rangle} \left(\vec{S}_i \cdot \vec{S}_j \right)^2 . \qquad (7)$$

The effective spin $\vec{S}$ is related to the matrix R through the relation

$$R_{kl} = 2 \left(S_k S_l - \frac{1}{4} \delta_{k,l} \right) + 2 \sum_{m=1}^{3} \epsilon_{klm} S_0 S_m + 2 \left(S_0^2 - \frac{1}{4} \right) \delta_{kl}. \qquad (8)$$

A general RP^{n-1} model defined as n-component spin system interacting thorough the biquadratic term has been investigated, *e.g.*, as a model for liquid crystals [13, 16–18]. In the case of $n = 2$, the model is equivalent to the XY model and it exhibits the BKT transition on two-dimensional lattices. For $n \geq 3$, the two dimensional RP^{n-1} models have Z_2-vortex excitations and they could exhibit the Z_2-vortex transition, although no clear evidence of the transition has been reported. In the limit of $n \to \infty$, the model is soluble:the model exhibits a finite temperature first-order phase transition [17].

3 Method

In order to investigate the RP^3 model on the $L \times L$ square lattice, we perform MC simulations. Because the Hamiltonian contains no frustrated interactions, conventional cluster algorithms are likely to work efficiently. Actually, Kunz and Zumbach have proposed a Wolff-Swendsen-Wang type cluster algorithm for general RP^{n-1} models [13] and Caffarel *el al.*, have extended it to $SO(3) \times O(2)$ model [14]. In their algorithm, first we generate a random (unit) vector $\vec{e}$ in $O(n)$ space, and then we calculate the projection of $\vec{S}_i$ onto the $\vec{e}$ as $\sigma_i = \vec{S}_i \cdot \vec{e}$. Finally, we perform the Swendsen-Wang cluster algorithm [11] by constructing clusters defined through effective Ising variables σ_i.

Indeed, the Wolff-Swendsen-Wang algorithm for the RP^{n-1} and the $SO(3) \times O(2)$ models have worked efficiently at least for smaller system sizes [13, 14]. On the other hand, for systems of $L = O(1000)$, we found that the relaxation of Z_2-vortex degree of freedoms feel a kind of critical slowing down and the total relaxation time scaled as $\tau \propto L^z$, where $z \simeq 2$. Thus, for the present model the cluster algorithm works not surprisingly well, although it can largely reduce the relaxation time from that of the local updates.

In order to investigate much larger sizes than the previous simulations, we also implemented MPI parallelization of the Wolff-Swendsen-Wang algorithm. We split the two-dimensional square lattice into $M \times M$ cells, and a MPI process is assigned to each cell (see Fig. 2). In total, we have M^2 MPI processes. A MPI process store the information of spins in its cell. Different from the local update methods, we need global communication to perform the cluster algorithm. For this purpose, we implemented a simple hierarchical communication, known as the butterfly type communication.

In Fig. 3, we show benchmark results of our code performed at the K computer and the previous ISSP super computer, Kashiwa. We performed the benchmark up to 16384 MPI processes (2048 nodes) at the K computer and up to 1024 MPI processes (128 nodes) with the flat MPI parallelization. Although the parallelization efficiency is lower than the ideal scaling for large nodes, we can get sufficient speed-up by using MPI parallelization. Based on benchmark calculations, we performed the product calculations *e.g.* of the largest size $L = 16384$ on 512 node of the K computer.

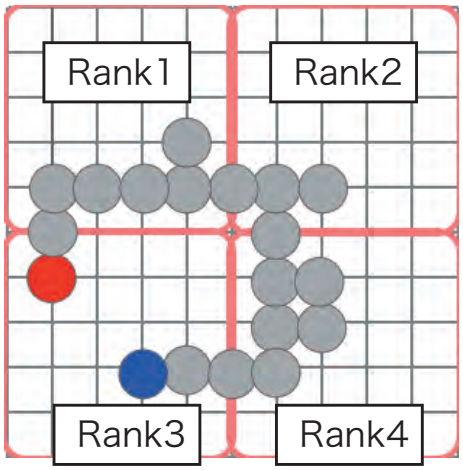

Figure 2: Schematic view of assignment of MPI processes on the square lattice together with a cluster determined by *e.g.* Wolff-Swendsen-Wang algorithm. Because two sites on a cell could be connected through the all other cells, we need information of the whole system to detect the cluster structure.

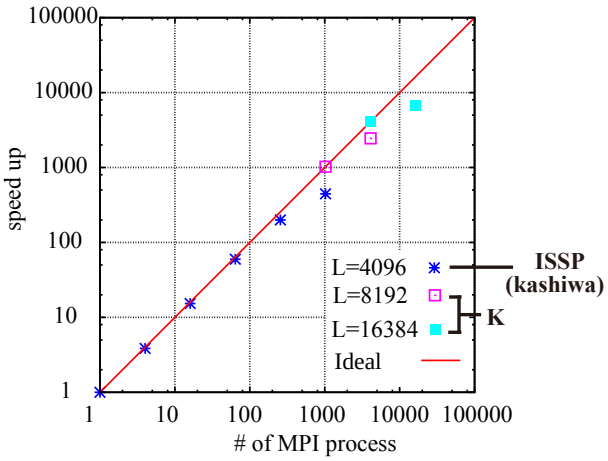

Figure 3: Benchmark results of MPI parallelized cluster MC method for RP^3 model. The speed up is the inverse of elapsed time normalized at 1, 1024, and 4096 MPI processes for $L = 4096$, 8192, and 16384, respectively. In this benchmark calculation, we include not only the MC updates but also calculation of observable. The calculations performed at the K computer and ISSP super computer (Kashiwa) with flat MPI parallelization.

4 Results

By using parallel Wolff-Swendsen-Wang algorithm, we performed MC simulation of the RP^3 model on the square lattice up to $L = 16384$. The calculations have been performed in the K computer and the system B in ISSP University of Tokyo.

In Fig. 4, we show the vortex density n_v for various system sizes. We define vortices on every elemental plaquet of the square lattice, and n_v is defined as the ratio between the number of vortices and the volume L^2. The vortex density does not show strong size dependence and it rapidly varies around $T/\tilde{J} \simeq 0.28$. In the low temperature phase, the vortices appear only as pairs and the vortex density is expected to be described by the thermal activation of such pairs. The inset of Fig. **??** shows the semi-log plot of n_v as a function of $\tilde{J}/T$. For $T \gtrsim 0.28\tilde{J}$, we see clear deviation from the low-temperature behavior $n_v \propto e^{-\mu/T}$, indicating at least something happens in the vortex sector around $T/\tilde{J} \simeq 0.28$. However, note that n_v contains information from both of free and paired vortices, while Z_2-vortex transition is governed by a binding-unbinding of free vortices. At the phase transition, the density of the free vortices becomes zero, while n_v keeps finite due to the contribution from paired vortices. Thus, we need a proper order parameter for Z_2-vortex transition rather than n_v.

In order to further clarify the existence of Z_2-vortex transition, here we investigate the so called *vorticity modulus* as an order parameter of the topological phase transition [10, 15]. The vorticity modulus is conceptually defined through the free energy deference between the cases with and without a free vortex [15]. The free energy difference V is expected to show logarithmic size dependence for sufficiently large L as

$$V = C + v \log L, \tag{9}$$

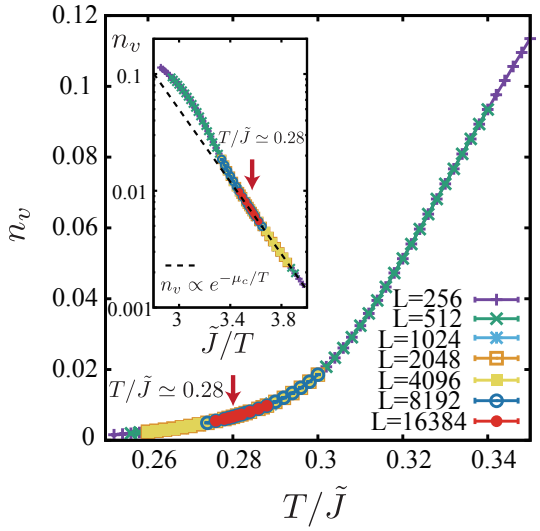

Figure 4: Temperature dependence of the vortex density. Red arrows indicate the position of $T/\tilde{J} = 0.28$, where the vortex density rapidly varies. The inset shows the vortex density in the semi-log plot as a function of $1/T$.

and the coefficient v before $\log L$ is the vorticity modulus. In the thermodynamic limit, the vorticity modulus is equal to zero ($v = 0$) for $T > T_v$ and it is finite ($v > 0$) for $T < T_v$. Thus we can determine the transition temperature T_v through size and temperature dependence of the vorticity modulus es.

In actual calculation, we assume a simple vortex structure and calculate the free energy difference at size L, $V(L)$, through the fluctuation in the equilibrium configurations under the periodic boundary condition;it is similar to the conventional calculation of the helicity modulus [10]. Then, we extract the vorticity modulus v by using $V(L)$s of two system sizes L_1 and L_2 as

$$v(L_1, L_2) \equiv \frac{V(L_1) - V(L_2)}{\log L_1/L_2}. \qquad (10)$$

In Fig. 5, we plot thus obtained vorticity moduluses for various sizes, where we set $L_2 = L_1/2$. As we expect, for sufficiently high temperature $v \simeq 0$, and for $T \lesssim 0.28\tilde{J}$, $v > 0$. We also see that as decreasing the temperature, v becomes negative sightly higher temperature before $v > 0$. It might be a finite size effect comes from *e.g.* the size dependence of C term in Eq. (9). However, owing to this negative part, we can easily define a characteristic temperature $T_v(L)$ as the temperature where v change the sign, which is expected to converge to the true transition temperature T_v in the thermodynamic limit.

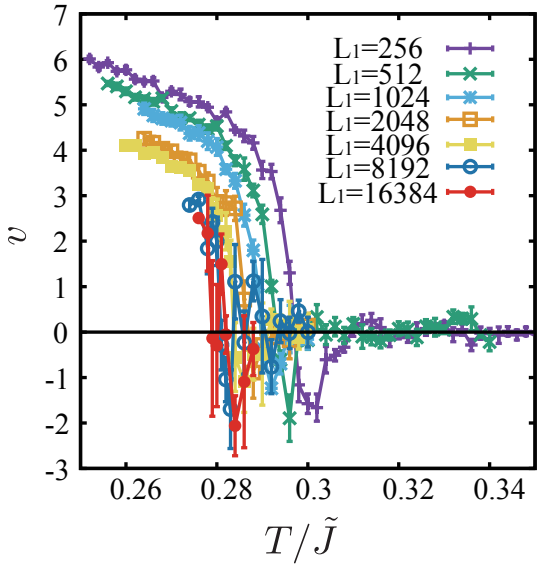

Figure 5: Vorticity moduluses obtained by MC simulations for $128 \le L \le 16384$. The vorticity modulus is calculated through Eq. (10) by setting $L_2 = L_1/2$.

In Fig. 6, we plot the the characteristic temperature $T_v(L)$ as a function of the system size, where we set $L = (L_1 + L_2)/2$. Because the correlation length for vortices ξ_v, which could be defined as characteristic separation length of the free vortices, diverges exponentially at T_v as

$$\xi_v \propto \exp\left[\frac{A}{(T - T_v)^{\alpha}}\right] \qquad (T > T_v), \qquad (11)$$

we expect that $T_v(L)$ converges to T_v by logarithmic form as

$$T_v(L) = T_v + a\,[\log(L/L_0)]^{-\frac{1}{\alpha}} \qquad (12)$$

[8]. In the previous MC simulation of the triangular lattice antiferromagnetic Heisenberg

model, α was estimated as $\alpha = 0.42 \pm 0.15$ [8]. The estimated α is not so different from $\alpha = 0.5$, which is the case of BKT transition. Note that even if there is no Z_2 vortex transition, Eqs. (11) and (12) are applicable by setting $T_v = 0$ and $\alpha = 1$ [19].

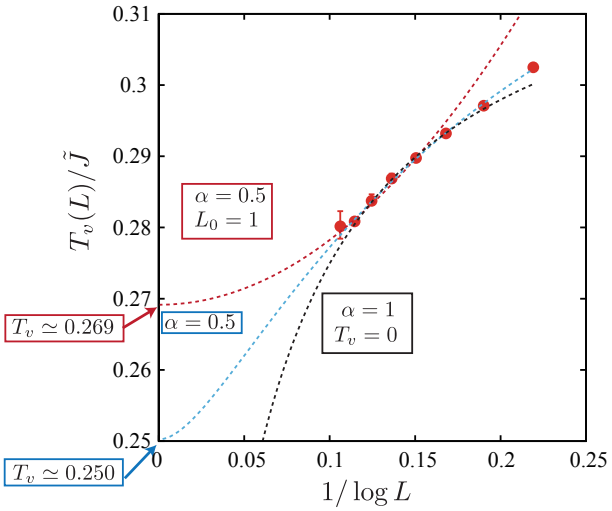

Figure 6: Extrapolation of characteristic temperature $T_v(L)$ to the thermodynamics limit. Based on Eq. (12), we extrapolated the data by assuming three kind of situations: (red) $(\alpha = 0.5, L_0 = 1)$, (blue) $(\alpha = 0.5)$, and (black) $(\alpha = 1, T_v = 0)$.

Based on Eq. (12), we extrapolate $T_v(L)$ to the thermodynamic limit by assuming $\alpha = 0.5$ or $\alpha = 0$, which correspond to assuming finite temperature Z_2-vortex transition or no Z_2-vortex transition, respectively. In the former case, we also try two extrapolations by fixing $L_0 = 1$ or freely change L_0 because $L_0 = 1$ was used in the analysis of the triangular lattice antiferromagnetic Heisenberg model [8]. The fitting curves are also plotted in Fig. 6. The two curves assuming $\alpha = 0.5$ give $T_v/\tilde{J} \simeq 0.269$ and $T_v/\tilde{J} \simeq 0.250$ for fixed $L_0 = 1$ and free L_0 cases, respectively. There extrapolation indicate that if we assume the existence of the Z_2 vortex transition, indeed we obtain finite transition temperature. However, note that the fitting curve obtained by assuming $\alpha = 1.0$ and $T_v = 0.0$ seems to be not bad except for the largest size data. Unfortunately, the statistical error of the largest size is rather large and it is difficult to exclude the possibility of no phase transition from the present data set.

In addition, as we can see from the "spin" correlation length[1] plotted in Fig. 7, even at the higher estimation of the transition temperature, $T_v/\tilde{J} = 0.269$, the correlation length seems to be longer than the largest system size of the present simulation, $L = 16384$. It means that although we investigated the model ten times larger than the previous simulations, the situation remains unclear for persons skeptical about the Z_2-vortex transition because we cannot ruled out the possibility of "fictitious order" due to smaller systems sizes than the spin correlation length. Thus, we probably need much larger scale calculations to conclude the existence of the Z_2-vortex transition without doubt. From the present data, we only conclude that the upper bound of the Z_2-vortex transition is $T_v/\tilde{J} = 0.27$.

5 Conclusion

In this paper, we investigated the possible topological phase transition , the Z_2-vortex transition, in two-dimensional frustrated Heisenberg spin systems. The most characteristic feature of the Z_2-vortex transition is that the spin correlation length at the phase transition keeps finite and only the topological nature, existence of free vortices, changes at the phase transition. In order to clarify the existence of transition and to distinguish with a cross over by numerical simulations, we need to calculate larger systems than the spin correlation length at the transition temperature. We attacked this challenging problem by investigating the RP^3 model on the square lattice as an effective model for the Z_2-vortex transition.

[1] Here we define correlation length through the ferro nematic correlation of $\vec{S}_i$ in RP^3 model, or equivalently through the ferromagnetic correlation of $\vec{a}$, $\vec{b}$, or $\vec{c}$ in $SO(3) \times SO(3)$ model.

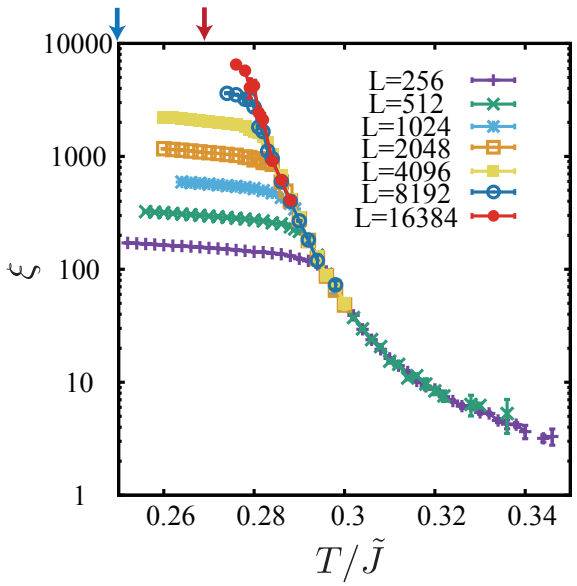

Figure 7: "Spin" correlation length of RP^3 model for various system sizes. red and blue arrows indicate the position of estimated T_vs, $T_v/\tilde{J} \simeq 0.269$ and $T_v/\tilde{J} \simeq 0.250$, respectively.

By using massively parallel cluster MC simulation, we successfully equilibrated the system up to $L = 16384$. We extrapolated the characteristic temperature to the thermodynamic limit by assuming the scaling of the Z_2-vortex transition, and obtained an upper limit of the transition temperature $T_v/\tilde{J} \simeq 0.27$. However, when we extrapolated the data by assuming no phase transition, it also gave us satisfactory fittings. In addition, the spin correlation length at T_v seems to be clearly beyond the maximum size $L = 16384$. These analysis indicates that although we have performed ten times larger size than the previous MC simulation, it is still difficult to show the existence of Z_2-vortex transition without doubt.

Acknowledgement

This work was done in collaboration with Naoki Kawashima at ISSP, University of Tokyo. The numerical calculations were performed on the K computer at RIKEN, on System B (both of Kashiwa and Sekirei) and on System C at ISSP, University of Tokyo, through supports of the HPCI System Research project (hp150116) and the Computational Materials Science Initiative (CMSI) supported by Ministry of Education, Culture, Sports, Science, and Technology, Japan. The present work is financially supported by JSPS KAKENHI No. 15K17701.

References

[1] *Frustrated Spin systems* edited by H.T. Diep, (World Scientific Publishing, Singapore, 2004).

[2] *Introduction to Frustrated Magnetism* edited by C. Lacroix, P. Mendels, and F. Mila, (Springer, Berlin, 2011).

[3] Special Topics on Novel States of Matter Induced by Frustration, edited by H. Kawamura, J. Phys. Soc. Jpn. **79**, 011001-011012 (2010).

[4] L. Balents, Natreu **464**, 199 (2010).

[5] H. Kawamura and S. Miyashita, J. Phys. Soc. Jpn. **53** 4138 (1984).

[6] V. L. Berezinskii, Sov. Phys. JETP **32**, 493 (1971).

[7] J. M. Kosterlitz, and D. J. Thouless, J. Phys. C: Solid State Phys. **6**, 1181 (1973).

[8] H. Kawamura, A. Yamamoto, and T. Okubo, J. Phys. Soc. Jpn. **79**,023701 (2010).

[9] T. Okubo and H. Kawamura, J. Phys. Soc. Jpn. **79**,084706 (2010).

[10] B. W. Southern and H.-J. Xu, Phys. Rev. B **52** R3836 (1995).

[11] R. H. Swendsen and J.-S. Wang, Phys. Rev. Lett. **58** 86 (1987).

[12] U. Wooff, Phys. Rev. Lett. **62** 361 (1989).

[13] H. Kunz and G. Zumbach, Phys. Rev. B **46**, 662 (1992).

[14] M. Caffarel, P. Azaria, B. Delamotte, and D. Mouhanna, Phys. Rev. B **60**, 014412 (2001).

[15] H. Kawamura and M. Kikuchi, Phys. Rev. B **47** 1134 (1993).

[16] P. A. Lebwohl and G. Lasher, Phys. Rev. A **6**, 426 (1972).

[17] H. Kunz and G. Zumbach, J. Phys. A **22**, L1043 (1989).

[18] Y. Tomita, Phys. Rev. E **90**, 032109 (2014).

[19] P. Azaria, B. Delamotte, and D. Mouhanna, Phys. Rev. Lett. **68**, 1762 (1992).

Irreversible Markov-Chain Monte Carlo methods

Koji HUKUSHIMA
Department of Basic Science, University of Tokyo
3-8-1 Komaba, Meguro-ku, Tokyo 153-8902

Abstract

We review irreversible Markov chain Monte Carlo (MCMC) methods, which violate detailed balance and yet still converge to a given target probability distribution. One way to construct an irreversible Markov chain is to enlarge the sampling space from the original space used in the reversible one. The idea is often referred to as "lifting". Two independent irreversible MCMC methods, belonging to the lifting MCMC, are discussed.

1 Introduction

Markov chain Monte Carlo (MCMC) methods have been intensively used as sampling tools from a high-dimensional probability distribution in a wide area of physics, biology and statistical sciences. In particular, MCMC methods are one of the non-peturbative analysis methods for many-body problems in the research field of statistical physics and condensed matter. Some advanced algorithms based on extended ensemble method [2] such as the multicanonical method [3], the simulated tempering [4, 5] and the exchange MC method [6] or parallel tempering, allows us to study more complex systems with rugged free-energy landscape, which are difficult to equilibriate by a simple MCMC algorithm with local update.

Since the seminal paper by Metropolis *et al.* in 1953 [1], most of the MCMC algorithms are on the basis of the Metropolis strategy, in which a Markov chain of the random variables to be sampled makes the target distribution an invariant distribution. Then, one may often impose the detailed balance condition (DBC) for Markov chain, called a reversible MCMC method. It is, however, not always necessary to construct the MCMC method using DBC. One of the pioneering works has been done by Suwa and Todo[7, 8], in which a systematic construction procedure is proposed for the MCMC algorithm without DBC, but with the global balance condition, called an irreversible MCMC method. They showed that the proposed method is able to bring about several times reduction in the correlation time of Potts model and a quantum spin model. Subsequently, Turitsyn *et al.* [9] and Fernandes and Weigel [10] have proposed another type of MCMC method without DBC separately and they also found a qualitative improvement in efficiency of the MCMC method in a mean-field Ising model. Furthermore, from a completely different context in statistical physics, another MCMC algorithm breaking DBC, called event-chain Monte Carlo algorithm, has been developed mainly for interacting particle systems.

These works have attracted a great deal of attention to the MCMC algorithms without DBC. The Markov chain dynamics with DBC exhibits diffusive behavior in sampling space, which yields slowing down close to phase transitions. We expect that it would be helpful to have some inertia effect by breaking DBC as if the sugar in a cup of coffee is spread faster using a spoon to stir the cup. In the framework of DBC, a useful guiding principle for constructing an efficient MCMC algo-

rithm is given by Peskun's theorem [11]. According to the theorem, it turns out that an MCMC algorithm is improved in quality by reducing a rejection probability in the sense that asymptotic variance of any observable becomes small. The strategy of Suwa-Todo algorithm follows this line. In general, however, no such a principle is satisfied in the case of the MCMC method without DBC. Therefore, it would be worth establishing an intrinsic principle of the MCMC method without DBC. In the mathematics literature[19], the idea of lifting is discussed as a promising way to introduce an irreversible MCMC method by enlarging sampling space from the original one. In fact, some of the above-mentioned MCMC algorithms without DBC belong to the lifting MCMC method[18].

In the present report, we make a review on irreversible MCMC methods, in which the basic idea and an implementation of the algorithm are discussed. In particular, we focus our attention to two different irreversible MCMC methods, one with a skew detailed balance condition (SDBC) [9] and the event-chain MCMC method.

2 Irreversible MCMC with skew detailed balance condition

2.1 Skew detailed balance conditions

In this section, we review an irreversible MCMC method with the skew detailed balance condition originally proposed by Turitsyn, Chertkov and Vucelja [9]. Here, an Ising spin system is used for the purpose of illustration. It is straightforward to extend the method to any discrete state models [12] such as the Potts model. A state of the Ising model with N spins is specified by a vector $\boldsymbol{\sigma} = (\sigma_1, \ldots, \sigma_N)$ with $\sigma_j \in \{-1, +1\}$ for $j = 1, \ldots, N$. The target distribution $\pi(\boldsymbol{\sigma})$ for finding the state $\boldsymbol{\sigma}$ in the statistical physics is often proportional to the Boltzmann factor $\exp(-\beta E(\boldsymbol{\sigma}))$ where β is an inverse temperature and E is the energy of the system to be studied. The main aims of the MCMC methods are to generate samples of the state from the target distribution $\pi(\boldsymbol{\sigma})$, and to calculate an expectation value of a function $\hat{f}$ under the target distribution, e.g. $\langle \hat{f} \rangle_\pi = \sum_{\boldsymbol{\sigma}} \pi(\boldsymbol{\sigma}) f(\boldsymbol{\sigma})$ where $f(\boldsymbol{\sigma})$ is the realization of $\hat{f}$ with the state $\boldsymbol{\sigma}$ and $\sum_{\boldsymbol{\sigma}}$ denotes the summation over 2^N states.

In the lifting technique, the state space is doubled by introducing an additional Ising variable $\epsilon \in \{-1, +1\}$, which is called a lifting parameter. The state in the enlarged state space is denoted by $X = (\boldsymbol{\sigma}, \epsilon) \in \{-1, +1\}^{N+1}$ and the corresponding probability distribution $\tilde{\pi}$ is assumed to be independent of the lifting parameter ϵ:

$$\tilde{\pi}(\boldsymbol{\sigma}, \epsilon) = \tilde{\pi}(\boldsymbol{\sigma}, -\epsilon) = \frac{\pi(\boldsymbol{\sigma})}{2}. \tag{1}$$

We consider a single spin-flip update for both the original spin $\boldsymbol{\sigma}$ and the lifting parameter ϵ as an elementary process in the Markov chain. Let F_j be a spin-flip operator on the j-th site: $F_j\boldsymbol{\sigma} = (\sigma_1, \ldots, -\sigma_j, \ldots, \sigma_N)$. A transition rate per unit time from state $(\boldsymbol{\sigma}, \epsilon)$ to $(F_j\boldsymbol{\sigma}, \epsilon)$ is denoted as $w_j(\boldsymbol{\sigma}, \epsilon)$ and that from state $(\boldsymbol{\sigma}, \epsilon)$ to $(\boldsymbol{\sigma}, -\epsilon)$ is $\lambda(\boldsymbol{\sigma}, \epsilon)$. Using these transition rates, the balance condition (BC) is expressed as

$$\sum_j w_j(F_j\boldsymbol{\sigma}, \epsilon)\tilde{\pi}(F_j\boldsymbol{\sigma}, \epsilon) - \sum_j w_j(\boldsymbol{\sigma}, \epsilon)\tilde{\pi}(\boldsymbol{\sigma}, \epsilon) + \lambda(\boldsymbol{\sigma}, -\epsilon)\tilde{\pi}(\boldsymbol{\sigma}, -\epsilon) - \lambda(\boldsymbol{\sigma}, \epsilon)\tilde{\pi}(\boldsymbol{\sigma}, \epsilon) = 0.$$

This ensures that $\tilde{\pi}$ is the unique invariant distribution of the Markov chain. For the determination of the transition rate $w_j(\boldsymbol{\sigma}, \epsilon)$, we impose SDBC given by

$$\tilde{\pi}(\boldsymbol{\sigma}, \epsilon) w_j(\boldsymbol{\sigma}, \epsilon) = \tilde{\pi}(F_j\boldsymbol{\sigma}, -\epsilon) w_j(F_j\boldsymbol{\sigma}, -\epsilon). \tag{2}$$

This requires that the stochastic flow from state $(\boldsymbol{\sigma}, +\epsilon)$ to $(F_j\boldsymbol{\sigma}, +\epsilon)$ is balanced out

by that from $(F_j\boldsymbol{\sigma}, -\epsilon)$ to $(\boldsymbol{\sigma}, -\epsilon)$. In general, this condition breaks the detailed balance conditions (DBC): $\tilde{\pi}(\boldsymbol{\sigma}, \epsilon) w_j(\boldsymbol{\sigma}, \epsilon) = \tilde{\pi}(F_j\boldsymbol{\sigma}, \epsilon) w_j(F_j\boldsymbol{\sigma}, \epsilon)$. As a specific solution of (2) , the transition rate $w_j(\boldsymbol{\sigma}, \epsilon)$ is given by

$$w_j(\boldsymbol{\sigma}, \epsilon) = \frac{1}{2}\alpha \left(1 - \sigma_j \tanh \beta h_j\right)\left(1 - \delta\epsilon\sigma_j\right), \tag{3}$$

where α is a time constant and h_j is a local field acting on the site j. The possible range of δ is -1 to 1 and DBC is recovered in (3) with $\delta = 0$. The transition rate is equivalent to the conventional heat-bath transition rate under a virtual external field ϵH with $H = \frac{1}{\beta} \operatorname{arctanh} \delta$. Thus, the lifting parameter ϵ represents the direction of the virtual field in this case. While ϵ is coupled to the local order parameter σ_j in this transition rate, one can replace it with any other linear function of σ_j such as a local energy $\sigma_j h_j$. The choice of the transition rate might affect the efficiency of the MCMC method, depending on the model system to be studied, but this has not been clarified yet at this moment.

By using SDBC, BC is rewritten as

$$\lambda(\boldsymbol{\sigma}, \epsilon) - \lambda(\boldsymbol{\sigma}, -\epsilon) = \sum_j \left(w_j(\boldsymbol{\sigma}, -\epsilon) - w_j(\boldsymbol{\sigma}, \epsilon)\right). \tag{4}$$

The explicit form of the transition rate for ϵ flip is not unique. Turitsyn *et al.* [9] have proposed the transition rate as

$$\lambda(\boldsymbol{\sigma}, \epsilon) = \max\left(0, \sum_j \left(w_j(\boldsymbol{\sigma}, -\epsilon) - w_j(\boldsymbol{\sigma}, \epsilon)\right)\right), \tag{5}$$

which is referred to as the Turitsyn-Chertkov-Vucelja (TCV) type. Another type of $\lambda(\boldsymbol{\sigma}, \epsilon)$ is also given as

$$\lambda(\boldsymbol{\sigma}, \epsilon) = \sum_j w_j(\boldsymbol{\sigma}, -\epsilon), \tag{6}$$

which is referred to as the Sakai-Hukushima 1 (SH_1) type [13]. These transition rates are available for a general class of the Ising models.

2.2 Irreversible Metropolis-Hastings algorithm

In this subsection, we explain an actual procedure in MCMC simulations which is based on Metropolis-Hastings algorithm [14]. Let $X^{(n)}$ be the state in the enlarged state space after n iterations. The irreversible MCMC method starts with an arbitrary initial state $X^{(0)}$ and iterates the following steps for $n = 1, 2, \ldots$:

(a) Suppose that the current state $X^{(n)} = (\boldsymbol{\sigma}, \epsilon)$ and choose a site j at random.

(b) Accept the new state as $X^{(n+1)} = (F_j\boldsymbol{\sigma}, \epsilon)$ with the probability $w_j(\boldsymbol{\sigma}, \epsilon)$.

(c) If it is rejected, accept the ϵ flipped state as $X^{(n+1)} = (\boldsymbol{\sigma}, -\epsilon)$ with an acceptance rate

$$A(\epsilon \to -\epsilon; \boldsymbol{\sigma}) = \frac{\frac{1}{N}\lambda(\boldsymbol{\sigma}, \epsilon)}{1 - \frac{1}{N}\sum_j w_j(\boldsymbol{\sigma}, \epsilon)}. \tag{7}$$

(d) If it is also rejected, set $X^{(n+1)} = X^{(n)}$. Return to (a) and repeat the steps (a)–(d).

It is proved that these steps satisfy BC [12]. One MC step is defined as N iterations of the steps (a)–(d). To evaluate the acceptance rate in step (c), the summation with respect to the site is necessary and its computational complexity is of the order of N. In practice, once the summation is evaluated at the initial condition, it is sufficient to update the value of the summation when the spin-flip process is accepted. The complexity for the update is of the order of one in statistical-mechanical models with short range interactions.

2.3 Some applications

We demonstrate that the irreversible MCMC method explained above works efficiently in a statistical-mechanical model. Fig. 1 presents time dependence of autocorrelation function of the magnetization in a one-dimensional Ising

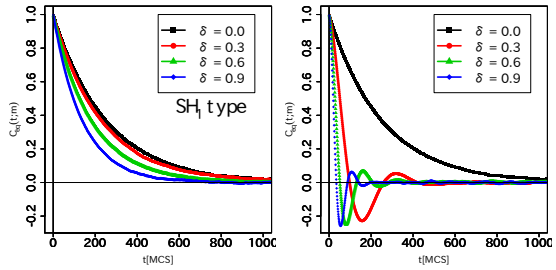

Figure 1: Time evolution of autocorrelation function of the magnetization density in the one-dimensional Ising model for different values of δ, which is a parameter representing the deviation from DBC. The chosen values of parameter in the simulations are $N = 2^7$, $\alpha = 10^{-2}$, $\gamma = 0.6$. The transition probability used is the SH_1(left) and TCV(right) types. Quoted from Ref. [13].

model using two different transition probabilities for SH_1 type (left) and TCV type (right). The autocorrelation decays fast with increasing the value of δ, indicating that breaking DBC makes the relaxation accelerate. Interestingly, oscillating behavior is clearly observed for TCV type. This is an intrinsic effect of the violation of DBC, never seen in the MCMC methods with DBC. The similar behavior is also found when the TCV type probability is applied to the mean-field Ising model[9]. These studies suggest that the dynamical exponent z could be reduced for the TCV type in the Ising models both in one dimension and the mean-field limit. However, such significant improvement of the efficiency is not confirmed in two- and three- dimensional Ising models[12].

On the other hand, the performance evaluation of the lifting MCMC methods has been extensively studied for an one-dimensional random walk problem. Several works showed that the diffusive dynamics in the problem is qualitatively changes by the lifting[19, 17]. While, no theoretical general criterion has not been established, it seems that an one-dimensional structure in the sampling space is necessary for the irreversible MCMC method with SDBC to work effectively.

2.4 Irreversible simulated tempering

Another interesting application is to combine the irreversible MCMC algorithm with the extended ensemble methods. In particular, the transition graph of the simulated tempering is exactly the same as that of the random walk problem. Thus, one may expect that SDBC makes the dynamics in the simulated tempering change qualitatively. Here we discuss the simulated tempering with SDBC[15, 16].

In the simulated tempering, the inverse temperature is treated as a random variable as well as the configuration $\boldsymbol{\sigma}$. More specifically, β takes R different values $\{\beta_r\}_{r=1}^R$ that should be determined before simulation. In addition, a lifting variable $\varepsilon \in \{+, -\}$ is also introduced to the system in the irreversible simulated tempering. Thus, a state in the irreversible simulated tempering is specified by $(\boldsymbol{\sigma}, \beta_r, \varepsilon)$. Accordingly, the target distribution is given as

$$P_{\mathrm{IST}}(\boldsymbol{\sigma}, \beta_r, \varepsilon) \propto \exp[-\beta_r E(\boldsymbol{\sigma}) + g_r], \qquad (8)$$

where g_r denotes a weight factor depending only on the inverse temperature.

An explicit update scheme of the irreversible simulated tempering algorithm consists of two steps. One is the update scheme of an original configuration $\boldsymbol{\sigma}$ for a fixed inverse temperature and the lifting variable with a conventional MCMC algorithm such as the Metropolis-Hastings algorithm and cluster algorithms. The other is the update scheme of the inverse temperature and the lifting variable for fixed $\boldsymbol{\sigma}$, described as follows:

(a) Let the current state be $(\boldsymbol{\sigma}, \beta_r, \varepsilon)$ and the candidate of the next inverse temperature β_l is determined with the probability $q_{r,l}^{(\varepsilon)}$ given as follows:

$$q_{1,2}^{(\varepsilon)} = q_{R,R-1}^{(\varepsilon)} = 1, \qquad (9)$$

$$q_{r,r\pm1}^{(\varepsilon)} = \frac{1 \pm \delta\varepsilon}{2}, \qquad (10)$$

for $1 < r < R$, and $q_{r,l}^{(\varepsilon)} = 0$ otherwise.

(b) Accept the next state $(\boldsymbol{\sigma}, \beta_l, \varepsilon)$ with the probability $W_{r,l}^{(\varepsilon)}$ given by

$$W_{r,l}^{(\varepsilon)} = \min\left[1,\ \frac{q_{l,r}^{(-\varepsilon)}}{q_{r,l}^{(\varepsilon)}} \frac{P_{\mathrm{IST}}(\boldsymbol{\sigma}, \beta_l, -\varepsilon)}{P_{\mathrm{IST}}(\boldsymbol{\sigma}, \beta_r, \varepsilon)}\right]. \tag{11}$$

(c) If the trial (b) is rejected, flip the lifting variable ε with the probability $\Lambda_r^{(\varepsilon)}$ given by

$$\Lambda_r^{(\varepsilon)} = \frac{\max\left[0,\ \varepsilon \sum_{\varepsilon'=\pm} \sum_{l \neq r} \varepsilon' q_{r,l}^{(-\varepsilon')} W_{r,l}^{(-\varepsilon')}\right]}{\left(1 - \sum_{l \neq r} q_{r,l}^{(\varepsilon)} W_{r,l}^{(\varepsilon)}\right)} \tag{12}$$

and set $(\boldsymbol{\sigma}, \beta_r, -\varepsilon)$ as the next state.

(d) If the trial (c) is also rejected, set the current state as the next state.

Note that the acceptance probability satisfies SDBC with respect to the target distribution $P_{\mathrm{IST}}(\boldsymbol{\sigma}, \beta_r, \varepsilon)$ and the global balance condition is fulfilled in the above procedure. The parameter δ in the proposal probability $q_{r,l}^{(\varepsilon)}$ controls the violation of DBC. When δ is set to zero, DBC is restored.

In Ref. [15], the irreversible simulated tempering algorithm has been applied to the two-dimensional ferromagnetic Ising model as a benchmark. It is numerically shown that the relaxation dynamics of the inverse temperature qualitatively changes from diffusive to ballistic behavior by violating DBC and consequently the autocorrelation time of the magnetization is reduced several times compared to the conventional simulated tempering for the case with an ideal choice of the weight factors. Thus, it is confirmed that the violation of DBC can improve the efficiency of simulated tempering algorithm. It is worth investigating whether the irreversible simulated tempering works effectively in a complex system such as spin glasses.

3 Event-chain Monte Carlo

The event-chain Monte Carlo (ECMC) algorithm is also one of the algorithms breaking DBC and is based on the idea of the lifting. The ECMC is proposed originally for hard-sphere systems[20] and is subsequently generalized for more general particle systems such as soft-sphere and LennardJones particles[22, 23], and continuous spin systems such as XY and Heisenberg spin models[24, 25]. This efficient algorithm enables us to simulate about 10^6 particles for the hard-sphere systems[21] and 10^6 spins for frustrated Heisenberg spin systems[26] in equilibrium. In this section, we describe the ECMC algorithm for particle systems and continuous spin systems.

3.1 Event-chain algorithm

We first explain the ECMC algorithm for hard-sphere systems in d dimensions. In the algorithm, the lifting parameter is defined as $U = (i, \vec{v})$ with i and $\vec{v}$ being the particle index and d dimensional vector, respectively. The particle i specified by the lifting parameter U moves along the direction $\vec{v}$ in U until it collides with another particle, and once the collision occurs the collided particle starts to move along the same direction $\vec{v}$. Consequently, many particles are moved along the same vector $\vec{v}$ until the total displacement of particles reaches ℓ, which is a tuning parameter of this algorithm. The displacement until the collision is uniquely determined by the configuration and the vector $\vec{v}$, and thus the dynamics of particles is deterministic for a given $\vec{v}$, the initial particle i, and ℓ. This algorithm breaks detailed balance because particles move along the same direction $\vec{v}$ and never go back to the former position [20].

For the hard-sphere systems, the pair potential is 0 for non-overlapping configurations and infinity for otherwise. Then, one can easily define a collision event as the time when the distance between the moving particle i and

another particle is twice of the particle radius. However, for general particle systems with an interaction potential such as Lennard–Jones systems, the pair potential for arbitrary distance always takes a finite value, and thus an event of collision cannot be defined in the same manner as the case of hard-sphere systems. The determination of a collision is essential for generalizing the ECMC method to more general interacting systems. This is possible by using three concepts[23]; the factorized Metropolis probability, infinitesimal moves, and an event-driven Monte Carlo scheme [27]. With the help of the factorization of the Metropolis transition probability, one can determine whether a proposal of a new state is accepted or not for each interacting pair independently, and the proposal is accepted only if all the interacting pairs accept it. If a new state is proposed by infinitesimally changing from the current state, then at most a particle interacting with the moving one reject the proposal; the probability that more than two pairs simultaneously reject the proposal with infinitesimal displacements is higher-order infinitesimal. Thus, we determine a collision as the probabilistic rejection which is caused by up to one interacting pair. Furthermore, an event-driven Monte Carlo scheme [27] allows us to compute the displacement until a collision efficiently. Consequently, a collision is defined in a probabilistic manner, and the ECMC algorithm is generalized for particle system with interaction potentials.

3.2 ECMC for general interacting systems

We present the ECMC algorithm for more general systems including some interacting particles system and also interacting spins systems in Algorithm 1. The Hamiltonian of the system considered in the algorithm is given by

$$H\left(\vec{x}_0, \cdots, \vec{x}_{N-1}\right) = \sum_{i<j} E_{ij}\left(\vec{x}_i, \vec{x}_j\right),$$

Algorithm 1 ECMC for more general potentials

Input N, ℓ, $\{\vec{x}_0, \cdots, \vec{x}_{N-1}\}$, $\{E_{ij}(\vec{x}_i, \vec{x}_j)\}_{i,j=0,\cdots,N-1}$, β
for $t \geq 0$ **do**
  $(i, \vec{v}) \leftarrow$ RANDOM(N, p)
  $s \leftarrow 0$
  while $s < \ell$ **do**
    $(\delta, j) \leftarrow$ DISPLACEMENT$(i, \vec{v})$
    if $s + \delta < \ell$ **then**
      $(\vec{x}_i, s) \leftarrow (T_{\vec{v}}(\delta)\,\vec{x}_i, s + \delta)$
      $i \leftarrow j$
    else
      $(\vec{x}_i, s) \leftarrow (T_{\vec{v}}(\ell - s)\,\vec{x}_i, \ell)$
    end if
  end while
end for
function RANDOM(N, p)
  Sample i uniformly from $\{0, \cdots, N-1\}$
  Sample $\vec{v}$ uniformly from $\{\vec{v}_0, \cdots, \vec{v}_{p-1}\}$ **return** $(i, \vec{v})$
end function
function DISPLACEMENT$(i, \vec{v})$
  for $k \in \{0, \cdots, N-1\} \setminus \{i\}$ **do**
    Sample r uniformly from $(0, 1]$
    Compute δ_k that satisfies

$$r = \exp\left(-\beta \int_0^{\delta_k} \max\left[0, \frac{\partial E_{ik}\left(T_{\vec{v}}(s)\,\vec{x}_i, \vec{x}_k\right)}{\partial s}\right] \mathrm{d}s\right)$$

  end for
  $j \leftarrow \arg\min_k \delta_k$
  $\delta \leftarrow \delta_j$ **return** (δ, j)
end function

where $\vec{x}_i$ represents a position vector of i-th particle for particle systems, or components of i-th spin for continuous spin systems. In the algorithm, p is the number of degrees of freedom per one particle or one spin, and $\{\vec{v}_i\}_{i=0,\cdots,p-1}$ is a set of linearly independent vectors. The state $\vec{x}_i$ is updated by an operator $T_{\vec{v}}(s)$; for particle systems $T_{\vec{v}}(s)\,\vec{x}_i = \vec{x}_i + s\vec{v}$, and for continuous spin systems $T_{\vec{v}}(s)\,\vec{x}_i = R_{\vec{v}}(s)\,x_i$ where $R_{\vec{v}}(s)$ is a rotation matrix around the vector $\vec{v}$ with an angle s. In this way, spin systems and particle systems are described by an ECMC algorithm on an equal footing.

It turns out that the ECMC algorithm out-

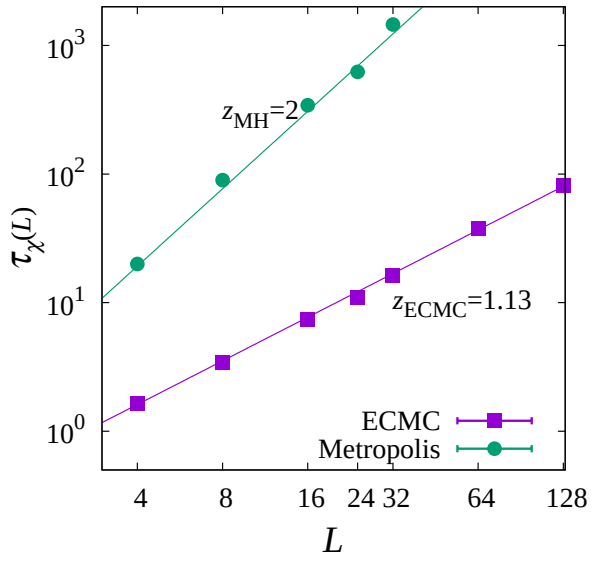

Figure 2: Linear-size dependence of characteristic time of susceptibility autocorrelation function in a three-dimensional Heisenberg ferromagnetic model obtained by ECMC and Metropolis-Hastings algorithm[25].

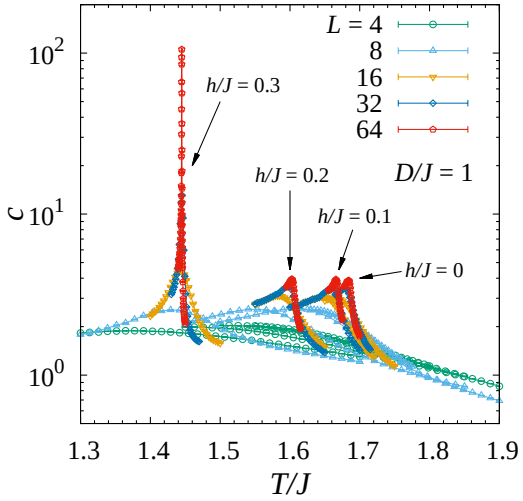

Figure 3: Temperature dependence of the specific heat of a three-dimensional chiral helimagnetic model under the external field h and the amplitude of DM interaction $D/J = 1$. The lattice is a cuboid and the total number of spins is $N = 8L^3$.

performs other conventional algorithms in various systems [20, 22, 28, 24], and one can simulate very large systems consisting of about 10^6 particles or spins in equilibrium by using the algorithm. We applied ECMC to a ferromagnetic Heisenberg ferromagnetic model in three dimensions, in which the algorithm reduces the value of the dynamical critical exponent z from $z = 2$ to $z \simeq 1$ [25], shown in Fig. 2. In contrast to cluster algorithms, the ECMC method works efficiently for frustrated spin systems. In fact, using a large scale simulation with ECMC, phase transitions in a Heisenberg spin model of a chiral helimagnet with the Dzyaloshinskii–Moriya (DM) interaction in three dimensions are studied[26]. In the presence of a magnetic field perpendicular to the axis of the helical structure, it is found that there exists a critical point on the temperature and magnetic-field phase diagram and that above the critical point the system exhibits a phase transition with strong divergence of the specific heat and the uniform magnetic susceptibility.

Quite recently, the ECMC algorithms have been developed for further generalization, which allows to simulate systems with three- and multi-body interactions. It is, however, still difficult to perform systems with anisotropic interactions. A naive implementation leads to multiple collisions yielding that the event chain splits into many chains, which is difficult to handle. In order to extend the ECMC algorithm for more complex systems such as polymers and protein problems, a certain key concept is required is required.

Acknowledgment

The author thanks Y. Sakai, Y. Nishikawa, W. Krauth and M. Michel for valuable discussions. The present report is based on a collaborative work with them, and it is supported by Grants-in-Aid for Scientific Research from MEXT, Japan (Grant Nos. 25610102 and 25120010).

References

[1] N. Metropolis, A. W. Rosenbluth, M. N. Rosenbluth, A. H. Teller, and E. Teller, J. Chem. Phys. **21**, 1087 (1953).

[2] Y. Iba, Int. J. Mod. Phys. C **12** 623–56 (2001).

[3] B. A. Berg and T. Neuhaus, Phys. Rev. Lett. **68** 9–12 (1992).

[4] E. Marinari and G. Parisi, Europhys. Lett. **19** 451–8, 1992.

[5] A. P. Lyubartsev, A. A. Martinovski, S. V. Shevkunov, and P. N. Vorontsov-Velyaminow, J. Chem. Phys. **96**, 1776 (1992).

[6] K. Hukushima and K. Nemoto, J. Phys. Soc. Jpn. **65**, 1604–8, 1996.

[7] H. Suwa and S. Todo, Phys. Rev. Lett. **105**, 120603 (2010).

[8] S. Todo and H. Suwa, J. of Phys.: Conf. Ser. **473**, 012013 (2013).

[9] K. S. Turitsyn, M. Chertkov, and M. Vucelja, Physica D **240**, 410 (2011).

[10] H. C. M. Fernandes and M. Weigel, Comput. Phys. Comm. **182**, 1856–9 (2011).

[11] P. H. Peskun, Biometrika **60**, 607–12 (1973).

[12] K. Hukushima and Y. Sakai, J. of Phys.: Conf. Ser. **473**, 012012 (2013).

[13] Y. Sakai and K. Hukushima, J. Phys. Soc. Jpn. **82** 064003 (2013).

[14] W. Hastings, Biometrika **57**, 97 (1970).

[15] Y Sakai and K Hukushima, J. Phys. Soc. Jpn. **85**, 104002 (2016).

[16] Y. Sakai and K. Hukushima, J. of Phys.: Conf. Ser. **750**, 012013 (2016).

[17] Y. Sakai and K. Hukushima, Phys. Rev. E **93**, 043318 (2016).

[18] M. Vucelja, Ame. J. Phys. **84**, 958 (2016).

[19] F. Chen, L. Lovasz, and I. Pak, Proc. ACM symp. on Theory of Computing, 275 (1999).

[20] E. P. Bernard, W. Krauth and D. B. Wilson Phys. Rev. E **80** 056704 (2009).

[21] E. P. Bernard and W. Krauth, Phys. Rev. Lett. **107** 155704 (2011).

[22] E. A. J. F. Peters and G. de With, Phys. Rev. E **85**, 026703 (2012).

[23] M. Michel, S. C. Kapfer and W. Krauth, J. Chem. Phys.**140**, 054116 (2014)

[24] M. Michel, J. Mayer and W. Krauth, Europhys. Lett. **112**, 20003 (2015).

[25] Y. Nishikawa, M. Michel, W. Krauth and K. Hukushima, Phys. Rev. E **92**, 063306 (2015).

[26] Y. Nishikawa and K. Hukushima, Phys. Rev. **B94**, 064428 (2016).

[27] A. B. Bortz, M. H. Kalos and J. L. Lebowitz, J. Comput. Phys.**17**, 10 (1975).

[28] M. Isobe and W. Krauth, J. Chem. Phys. **143**, 084509 (2015).

[29] J. Harland, M. Michel, T. A. Kampmann and J. Kierfeld, Europhys. Lett. **117**, 30001 (2017).

3.2 First-Principles Calculation of Material Properties

First-principles statistical thermodynamics simulations on the structure and reactivity of heterogeneous catalysts

Teruo HIRAKAWA, Fahdzi MUTTAQIEN, Sasfan Arman WELLA, Yuji HAMAMOTO, Kouji INAGAKI, Hidetoshi Kizaki, and Yoshitada MORIKAWA

Department of Precision Science and Technology,

Osaka University, Yamada-oka, Suita, Osaka 565-0871

In our research project, we investigated chemical reactions at surfaces and interfaces including CO_2 adsorption and hydrogenation on Cu surfaces, naphthalene on graphite surfaces, ligand-free Suzuki-Miyaura cross coupling reactions in aqueous solutions, and stability of Pd atoms dissolved into $LaFeO_3$ perovskite oxides. In the present report, we explain some of our recent progresses.

The Suzuki-Miyaura reaction (SMR) is one of the most efficient palladium-catalyzed cross-coupling reactions for the formation of carbon-carbon bonds, in particular for the formation sp^2-sp^2 carbon-carbon of biaryls in organic synthesis [1-3]. The SMR has been developed mainly with ligands, especially phosphine ligands to make the palladium catalyst stable and optimize its reactivity in an organic solvent.

The SMR without any ligands, that is "ligand free" in a water solvent, was suggested, and it has been attracting enormous interest recently [4-6]. Most theoretical studies for the SMR reported so far, used a simple solvent model to simulate the cross coupling mechanisms in an organic solvent. In these studies, the solvent effect is approximately treated using a polarizable continuum model (PCM). However, solvent molecules may play important roles in ligand-free Pd cross coupling reactions. explicitly including solvent. Thus, in the present study we focus on the oxidative addition step of the SMR in a water solvent explicitly including solvent molecules in our calculation models and perform full quantum mechanical molecular dynamics (MD) simulations[7].

All of the calculations are based on the density functional theory (DFT) within the generalized gradient approximation (GGA-PBE) as implemented in the STATE-Senri code [8]. We used ultrasoft pseudo potentials and a plane-wave basis set with cutoff energies of 25 Ry and 225 Ry for wave functions and charge densities, respectively.

The results show that the energy barrier on the oxidative addition step is quite low especially for PhBr, which is significantly different from the conventional SMR with ligands in organic solvents. This may be the reason why the SMR in water without any ligands can achieve a high TON and low-leaching of the Pd catalyst. Conversely, the barrier of the oxidative addition for PhCl is sizable, indicating that the reaction can proceed at room temperature or above, but the rate is rather slow compared with PhBr. Therefore, the lifetime of the η^2 complex of PhCl-Pd is elongated, causing the sintering of Pd to degrade the catalyst. We observed that the activation barriers of the oxidative addition of PhX to the PdX^- anion complex are similar to those of the oxidative addition of PhX to a single $Pd^{(0)}$ atom in a water solvent. The final state of the oxidative addition step, however, becomes significantly destabilized by the additional coordination of a halogen anion to the central Pd atom, and this should have an important effect for the following transmetalation step. The coordination of anions to the Pd atom should also prevent the aggregation of the Pd atom to form the Pd black. Therefore, the halogen anion can act as a "ligand" in a ligand-free system.

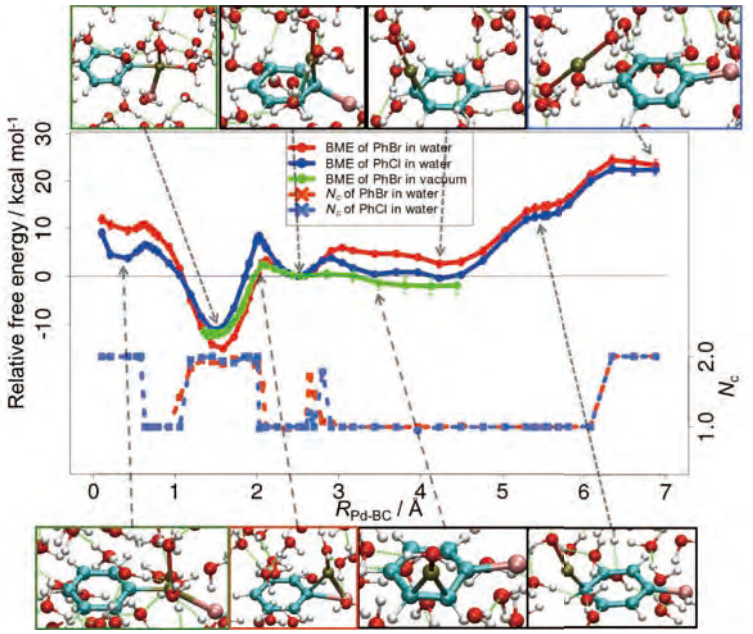

Fig. 1. Relative free energy profile and the number of coordinated H_2O to Pd for the oxidative addition step. The top and bottom panels show snapshots of the oxidative addition

References

[1]. N. Miyaura and A. Suzuki, J. Chem. Soc., Chem. Commun., **19**, 866–867 (1979).

[2]. N. Miyaura, K. Yamada, and A. Suzuki, Tetrahedron Lett., **20**, 3437–3440 (1979).

[3]. N. Miyaura, A. Suzuki, Chem. Rev., **95**, 2457–2483 (1995).

[4]. M.D. Smith, A.F. Stepan, C. Ramarao, P.E. Brennan, S.V. Ley, Chem. Commun., 2652–2653 (2003).

[5]. S.P. Andrews, A.F. Stepan, H. Tanaka, S.V. Ley, M.D. Smith, Adv. Synth. Catal., **347**, 647–654 (2005).

[6]. N.J. Hill, M.D. Bowman, B.J. Esselman, S.D. Byron, J. Kreitinger, N.E. Leadbeater, J. Chem. Educ., **91**, 1054–1057 (2014).

[7]. T. Hirakawa, Y. Uramoto, D. Mimura, A. Takeda, S. Yanagisawa, T. Ikeda, K. Inagaki, and Y. Morikawa, J. Phys. Chem. B, **121**, 164-173 (2017).

[8]. Y. Morikawa, Phys. Rev. B, **51**, 14802 (1995).

Analyses on atomic structure magnetism and electronic structure in spintronics materials and molecular magnets

Tatsuki ODA[1,2], Tomosato KANAGAWA[2], Nurul IKHSAN[2],
Yosuke FUNATO[2], Hasan Al RASYID[2], Masao OBATA[2]
[1]*Institute of Science and Engineering, Kanazawa University, Kanazawa, Ishikawa 920-1192*
[2]*Graduate School of Natural Science and Technology, Kanazawa University, Kanazawa, Ishikawa, 920-1192*

We studied the several topics involved with this project; Rashba's effect of surface, magnetic anisotropy and its electric field (EF) effect in the thin film related with spintronic devices, and magnetic effects in molecular system. We also developed a method of van der Waals density functional (vdW-DF) approach for magnetic systems. These investigations have been done by employing the home-made density functional code, which has run efficiently in the architectures in Systems B in ISSP.

Rashba's effect of surface

The heavy-element-covered semiconductor surfaces show a giant Rashba-type spin splitting and many experiments have been reported for spintronics applications. We found the peculiar magnetic configuration in momentum space (spin texture) around the Fermi level for the surface band of Tl/Si(110). This is novel, compared with the normal Rashba spin texture, in which the spin lies along concentric circles in plane. The spin texture obtained forms an alignment to the direction perpendicular to the mirror plane of system. This may be very useful for spintronics application because of the suppressed spin scattering. The silicon based materials are still recommended as a new material in the next generation electronics (spintronics). Such research has been published in the collaboration with the experimental group of photoemission measurement [1].

The Rashba's effect obtained in Tl/Si(110) is explained in a combination of two usual Rashba spin textures. The one arises from the origin in the momentum space, and the other from the cross point which has both the mirror and glide-plane symmetries. At the middle point between the two, the spin direction tends to align within the surface plane along the direction perpendicular to the mirror plane. In such region, fortunately, the surface single band can form the small hole pocket with a peanut form. This enable us to have a single uniform spin valley when adjusting the Fermi level. These theoretical results not only agree well with the experimental result, but also work efficiently as a useful guide for the accomplishment of experimental measurement.

Magnetic anisotropy and electric field effect

Magnetic anisotropy energy (MAE) and its EF effect were investigated in the slab system of Cr/Fe/MgO by using first-principles calculation. Such system keeps the Fe/MgO interface and has a possibility to improve the perpendicular magnetic anisotropy by introducing intrinsic deflections from the under layer (Cr). We estimated MAEs and votage-control magnetic anisotropy (VCMA)

coefficient and analyzed the electronic structures. The calculation results revealed a more concrete relation between electronic structures and MAE, compared with the previous achievements. The publishing paper is now in preparation.

The slab system which consists of a part of spintronics device, PtCo/ZnO, has been studied. This may be categorized to one of multi-ferroic interfaces. This is because one can expect an electric polarization from ZnO and a magnetism from PtCo metal. By introducing the external electric field or magnetic field, one can control a multi-function of such interface. The first paper, published in the collaboration with the experimental group of magnetic tunnel spectral [2], theoretically reported interface models of different electric polarizations in ZnO layer, as shown in Fig.1. This can be made by the effective screened medium (ESM) method, which easily allows the electric polarization in slab system. At the barrier layer (ZnO), a monotonic variation superpositioned on a rapid oscillation indicates an internal depolarization electric field opposite to the respective polarization. Note that this field cancels out the polarization to maintain a zero electric flux. The publishing paper which describes effects on spin-orbit interaction in the magnetic layer is now in preparation.

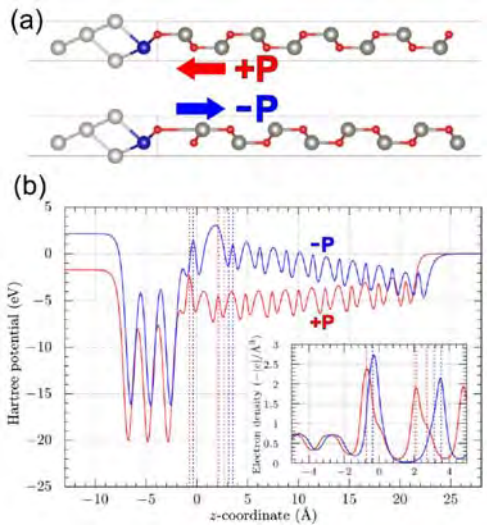

Figure 1. (a) Slab models for the electric polarizations and (b) electrostatic potential profiles along the layer thickness.

Van der Waals density functional approach

The vdW-DF approach is one of promising methods to overcome the problem that the density functional approach, such as local density approximation or generalized gradient approximation, cannot describe van der Waals (vdW) force properly. We have proposed the extension of vdW-DF to spin-polarized (magnetic) systems, vdW-DF-SGC (SGC stands for spin-polarization-dependent gradient correction), and demonstrated the usefulness. We also focused on the effect of SGC which described the spin dependent semi-local electron correlation effect, and found that it plays an important role in antiferromagnetic interactions.

Another spin van der Waals method (svdW-DF) was developed in 2015. The relation between vdW-DF-SGC and svdW-DF should be clarified in several applications. Therefore we also implemented this method in the house-DFT code, and investigated the oxygen systems and the absorption system which contains magnetic materials, namely, graphene on Ni(111) surface. Comparing these results with those of our method, we found that the svdW-DF also corrected the antiferromagnetic coupling and gave almost the same binding property as the vdW-DF-SGC.

[1] E. Annese, et al., Chem. Phys. Rev. Lett. 117 (2016) 16803.
[2] M. Belmoubarik et al., Appl. Phys. Lett., **109** (2016) 173507.

Exciton wave function analysis for [n]CPPs (n = 3-16)

Yoshifumi NOGUCHI

Institute for Solid State Physics,

The University of Tokyo, Kashiwa-no-ha, Kashiwa, Chiba 277-8581

As cycloparaphenylenes molecules (CPP), known as the shortest armchair-type carbon nanotube with hydration terminated edges, were successfully synthesized experimentally in 2008 [1], their structural and optical properties have attracted attention. As one of the interesting features, it has been reported that the optical gap is sensitive to the molecular size in the photo emission spectra but is insensitive to the same in the photoabsorption spectra. However, the theoretical studies within the framework of time-dependent density functional theory (TDDFT) have never successfully explained this experimental fact.

In this study, we applied the first-principles *GW*+Bethe-Salpeter method to [*n*]CPPs (*n* = 3-16) and discussed the optical properties [2]. The simulated spectra are in a good agreement with the experimental UV-vis absorption spectra particularly from the viewpoints of the peak positons and peak heights. More importantly, the results are consistent with the experimentally observed insensitivity of the optical gap to the molecular size. As the first exciton (S_1) is dark (or experimentally invisible) for all the sizes, the experimentally observed molecular size insensitivity is for the higher excitons ($i \geq 2$). To investigate the first dark and bright excitons in detail, we estimated the expectation value for an arbitrary operator (O) by using the exciton wave functions ($\Psi^i(r_1, r_2) = \sum_{e,h} A^i_{e,h} \psi_e(r_1) \psi^*_h(r_h)$), where $A^i_{e,h}$ is the eigenvector obtained when the Bethe-Salpeter equation is solved and $\psi_e(\psi_h)$ is the LDA wave function at the excited electron (created hole) level [3]. The overlap strength between the electron and hole wave functions (Λ), the exciton size (d_{exc}), the electron-hole separation distance ($d_{e\rightarrow h}$), the electron (hole) delocalization (σ_e, σ_h), and the exciton binding energy (E^b) exhibit common features for larger sized CPPs ($n \geq 9$). These observations nicely explain why the optical gap is insensitive to the molecular size.

References

[1] R. Jasti, J. Bhattacharjee, J. B. Neaton, and C. R. Bertozzi: J. Am. Chem. Soc., **130** (2008) 17646.

[2] Y. Noguchi and O. Sugino: J. Chem. Phys. **146** (2017) 144304.

[3] D. Hirose, Y. Noguchi, and O. Sugino: J. Chem. Phys. **146** (2017) 044303.

Development of first-principles electronic-structure and transport calculation method based on real-space finite-difference approach

Tomoya ONO
Center for Computational Sciences, University of Tsukuba
Tenno-dai, Tsukuba, Ibaraki 305-8577

1 Introduction

SiC is attracted much attention due to its excellent physical properties, such as a high thermal conductivity, high breakdown strength, and large band gap. However, unlike Si metal-oxide-semiconductor field-effect transistors (MOSFETs), SiC-MOSFETs, primarily of the n-channel type, suffer from unacceptably low carrier mobility. Large amount of defects at SiC/SiO_2 interface, which are generated in oxidation process, is expected to be one of the origins for the low carrier mobility.

Among various polytypes, 4H-SiC, in which Si and C atoms can occupy one of three positions along the $[1\bar{1}00]$ direction, normally labelled ABCBAB... is the most widely used polytype for SiC-MOSFETs. Within these four bilayers, there are two inequivalent lattice sites, usually known as h (hexagonal) and k (quasi-cubic) based on the site occupied by the Si atoms in the neighboring bilayers. It is found that interface type determines whether conduction band edge (CBE) internal-space states at the interface are affected by the presence of O defects, as with h type, or not, as with k type.[1]

In this study, we performed first-principles calculation to investigate how the electron scattering property of the SiC/SiO_2 interface changes depending on the stacking of SiC bilayers at the interface, i.e. h and k types, and when O atoms are subsequently introduced.[2]

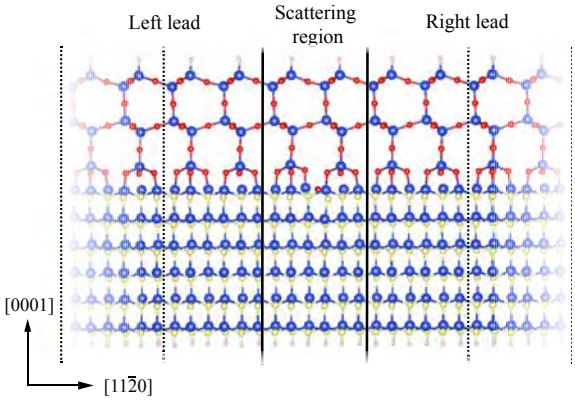

Figure 1: Schematic image of the transport-calculation model. The boundary between the scattering region and the semi-infinite leads is distinguished by solid lines. Supercells of leads are bounded by dotted lines. Blue, yellow, red, and white spheres are Si, C, O, and H atoms, respectively. Reprinted with permission from Ref. 3.

2 Method

Calculations are carried out using RSPACE.[3] To perform the transport calculation, we adopt the Green's function method and the Landauer-Büttiker formalism within the framework of density functional theory. Figure 1 illustrates schematics of the computational models used for the transport calculations, in which the whole system is divided into three parts: a left lead, a central scattering region, and a right lead. The central

scattering region is composed of the SiC/SiO_2 interface including the oxygen related structures or carbon-related defects. We investigate three models, one O atom O_{if}, two O atoms O_{sub}+O_{if}, and VCO_2, which appears after introducing three excess O atoms and removing a CO molecule to relieve the interface stress caused by lattice constant mismatch. The left (right) lead is a semi-infinite slab along the $[11\bar{2}0]$ ($[\bar{1}\bar{1}20]$) direction and its atomic structures correspond to those of the initial interface. The other details of the computational method are introduced elsewhere.[2]

3 Results

Figures 2 and 3 show the channel current with respect to the applied bias. A significant reduction of the current due to the existence of the O atoms is observed for the h type while the amount of the current is unaffected for the k type. This is because the local density of states (LDOS) at CBE is very sensitive to insertion of the O atoms in the case of h type. Two physical phenomena combine to prevent electron transmission in the h type. First, the internal-space states appear from the top of the interface in the h type. Second, the energy level of the internal-space states is shifted upward by the Coulomb interaction with inserted O atoms or defects.

For comparison, the transmissions through the h and k types with carbon-related defects are also examined. Similarly to the case of the oxygen-related structures, it is found that the transmission at the h type is markedly decreased. It is surprising that the oxygen-related structures, which are naturally generated at the SiC/SiO_2 interface during dry oxidation, cause the electron scattering because the oxygen-related structures considered here have been reported to be electrically inactive. According to the discussion about the LDOS at the interface, the internal-space states will play important role for the carrier scattering

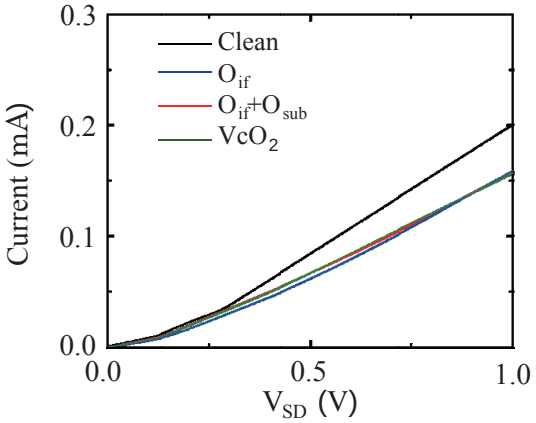

Figure 2: Calculated channel current for h type.

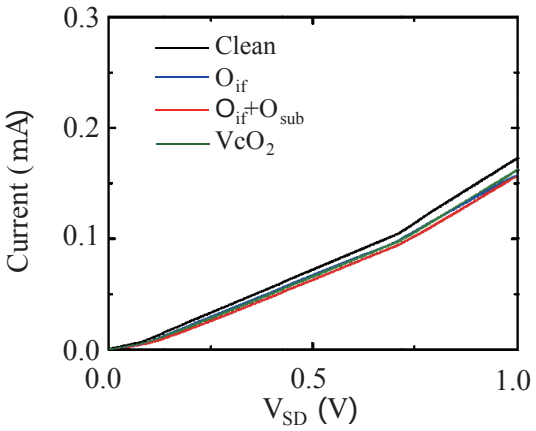

Figure 3: Calculated channel current for k type.

at the n-channel MOSFET.

References

[1] C. J. Kirkham and T. Ono: J. Phys. Soc. Jpn. **85** (2016) 024701.

[2] S. Iwase, C. J. Kirkham and T. Ono: Phys. Rev. B **95** (2017) 041302.

[3] K. Hirose, T. Ono, Y. Fujimoto, and S. Tsukamoto: *First Principles Calculations in Real-Space Formalism, Electronic Configurations and Transport Properties of Nanostructures* (Imperial College, London, 2005).

Analyses on protein-folding process by automatic detection of structural transitions with molecular dynamics simulations

Yasuteru SHIGETA

Center for Computational Sciences,

University of Tsukuba, 1-1-1 Tennodai, Tsukuba, Ibaraki 305-8577, Japan

Structural transitions of proteins are strongly related to biological functions. In order to theoretically reproduce the structural transitions of proteins at the atomic level, molecular dynamics (MD) simulations have been widely used to generate atomic trajectories as time-series data for the structural transitions. If one can ideally perform sufficiently long-time MD simulations, the atomic trajectories would be utilized for analyzing the biological functions and calculating several physical properties on an equal footing, since the Ergodic hypothesis indirectly guarantees that the sufficiently long-time trajectories include structural transitions relevant to the biological functions and might be regarded as a statistically reliable ensemble.

However, conventional timescales of the biological functions are in a range within the order of milliseconds to seconds, which are far from the accessible timescales of conventional MD simulations, i.e. the order of nanoseconds to microseconds. As a strategy for enhancing the conformational sampling of the conventional MD simulations and reproducing these kinds of biologically important rare events, special purpose machines like Anton series enable one to perform extremely long-time MD simulations but the usages of these special purpose machines are limited. Also, the conformational transitions relevant to the biological functions are stochastic processes. It does not ensure that the long-time MD simulations inevitably capture the essential conformational transitions during every MD simulation. Therefore, one might perform several long-time MD simulations starting from distinct initial structures to remove dependence on initial conditions. That is why it is desirable to develop enhanced conformational sampling methods for reproduction of biologically important rare events instead of conventional MD simulations.

As an alternative conformational sampling method to CMD, the Parallel Cascade Selection MD (PaCS-MD) [1] and variants have been proposed by our group as a distributed computing for generating structural transition pathways between a given reactant and product under a condition that the both end-point structures are known *a priori*. In PaCS-MD, the initial structures are selected from obtained snapshots by referring to a structural similarity

of them with respect to the product at the end of each cycle. By repeating the cycles of conformational resampling from the reasonably selected structures, PaCS-MD generates candidates of structural transition pathways from the reactant to the product. To efficiently perform PaCS-MD, the number of the initial structures, n_{initial}, is one of essential parameters. However, it has not been clarified how the choice of n_{initial} affects conformational sampling efficiency of PaCS-MD.

In this work, the conformational sampling efficiency was assessed by changing n_{initial} in performing PaCS-MD. As the assessments, we addressed how a number of initial structures, n_{initial}, affected the conformational sampling efficiency. It is confirmed that the large n_{initial} accelerated the structural transitions. In contrast, the small n_{initial} showed a high conformational sampling efficiency as an accumulated simulation time over cycles, indicating that the both n_{initial}s are suitable for promoting the structural transitions [2].

Besides the PaCS-MD, we have also proposed TaBoo SeArch (TBSA) algorithm [3]. In TBSA, an inverse histogram of the original distribution projected onto a set of reaction coordinates is constructed from trajectories, and rarely occurring states of the protein are statistically selected as new initials based on the inverse histogram, and resampling via restarting MD simulations. In this process, a definition of the inverse histogram, which characterizes the rarely occurring states, is crucial for an efficiency of TBSA.

In this work, we also propose a simple modification of the inverse histogram to further accelerate the convergence of TBSA. As demonstrations of the modified TBSA, hydrogen bonding rearrangements of Met-enkephalin, large-amplitude domain motion of Glutamine binding protein, and folding processes of a B domain of *Staphylococcus aureus* Protein A are shown. In all demonstrations, it is numerically proven that the modified TBSA successfully reproduced these biologically important rare-events with nanosecond-order computational costs, although a set of microsecond-order canonical MD simulations failed to reproduce them, indicating the high efficiency of the modified TBSA[4].

References

[1] R. Harada, Kitao, *J. Chem. Phys.*, **139**, 035103 (2013).

[2] R. Harada, Y. Shigeta, *Chem. Lett.* ***in press*** (2017).

[3] R. Harada *et al. J. Comput. Chem.*, **36**, 763 (2015) and *Chem. Phys. Lett.*, **630**, 68 (2015).

[4] R. Harada, Y. Takano, Y. Shigeta, *J. Chem. Theor. Comput.* **12**, 2436(2016).

DFT sampling studies on interfacial reactions in catalysts and batteries

Yoshitaka TATEYAMA

Center for Green Research on Energy and Environmental Materials (GREEN), National Institute for Materials Science (NIMS), 1-1 Namiki, Tsukuba, Ibaraki 305-0044; Elements Strategy Initiative for Catalysts & Batteries (ESICB), Kyoto University, Goryo-Ohara, Nishikyo-ku 615-8245.

Transformation of energy management systems via success of efficient utilization of renewable energy and CO_2 zero emission is an urgent challenge in our society. To step toward its realization, improvement of energy storage and conversion is indispensible. However, establishments of high-efficiency techniques as well as high reliability are not satisfactory yet for practical implementation. Due to the difficulty in the experimental observations, these atomistic mechanisms are still open questions.

We addressed such issues with well-optimised first-principles calculations. Regarding the CeO_2/Pt particle/H_2O catalytic interface, we found the electron transfer between the oxide and the metal cluster, basicity of the CeO_2 surface, and the fast proton/hydroxide transfer upon the oxide interface [1]. The observed atomistic mechanism gives an insight into the catalytic reactions upon the oxide materials.

For the battery field, we have examined microscopic origins of the interfacial resistance (e.g. space-charge layer model, reaction layer model) as well as the buffer layer effect in solid-state batteries (SSBs) by using first-principles DFT+U calculations [2]. As a representative model system, $LiCoO_2$ (LCO), β-Li_3PS_4 (LPS), and $LiNbO_3$ (LNO) were selected for cathode, sulfide electrolyte, and buffer layer, respectively. We carried out first-principles calculations of the several possible interface configurations and obtained the stable structures and the electronic states. Besides, we calculated the site-dependent Li chemical potentials with respect to Li metal. The results indicate that the Li depletion can proceed at the beginning of the charge process, which may correspond to the space-charge layer scenario, and the interposition of buffer layer can suppress the depletion. Furthermore, we evaluated the interfacial ion diffusion by examining possible exchange of cations between the cathode and the electrolyte. The results show that the Co and P exchange is preferred at the LCO/LPS interface, and the LNO interposition can suppress these mixings

(Fig.1). Interestingly, the Li-depletion tendency still exists under these circumstances [2]. Therefore, the Li-depletion is likely to be a major factor of the interfacial resistance. These aspects would be useful for future improvement of the interfacial resistance of SSBs

We are keeping intensive collaborations with the experimentalists as well as the industries, and solving crucial issues for fundamental science and industrial application on the atomic scale. In the near future, our computational researches may play a decisive role in the transformation of energy management in our society.

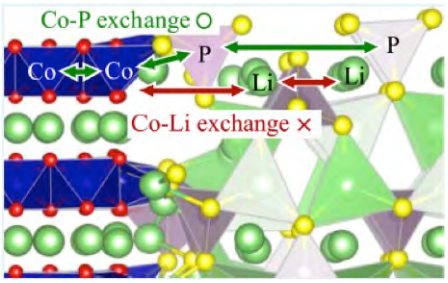

Fig. 1: Schematic picture of cation exchange at the LCO cathode / LPS electrolyte interface. The Co-P exchange turns out to be energetically preferable.

References

[1] M. F. Camellone, F. N. Ribeiro, L. Szabova, Y. Tateyama, S. Fabris, J. Am Chem. Soc. **138**, 11560-11567 (2016).

[2] J. Haruyama, K. Sodeyama, Y. Tateyama, ACS Appl. Mater. Interfaces, **9** 286-292 (2017).

.

First-principles calculations of iron solid solution effects on the lattice thermal conductivity of lower mantle minerals

Haruhiko DEKURA

Geodynamics Research Center

Ehime University, 2-5 Bunkyo-cho, Matsuyama 790-8577, Japan

Iron-bearing Bridgmanite $(Mg,Fe)SiO_3$ would be the most constituent mineral in the earth's lower mantle. Determination of the phonon transport property, *i.e.*, lattice thermal conductivity (κ), of the material should be therefore a key to understanding the dynamics and evolution of the earth's deep interior. Lattice anharmonicity owing to the phonon-phonon interaction strongly relates the phonon transport. The primary purpose of this project in this period is to determine the anharmonic properties of the iron-bearing system at deep mantle pressure conditions.

We have performed density-functional theoretic calculations combined with the LDA+*U* method [1] and have extracted the large number of harmonic and anharmonic force constants (AFC) by numerical derivatives of the adiabatic potential surface [2]. The simulation cell of $(Mg_{0.9375},Fe^{2+}_{0.0625})SiO_3$ that includes totally 160 atoms was adopted in this study. The ferrous iron was treated in the high spin state ($S = 2$). Since the crystal point group symmetry is broken associated with the incorporation of the iron atoms as impurities into the system, the number of SCF calculations is enormous (more than 10,000). The use of the supercomputers in ISSP allowed us to deal with it.

During this period, by the use of supercomputer (system B), we have finished the determination of the *3rd* order AFC at 100 GPa relevant to an earth's lowermost mantle condition. Using the calculated force tensors, we have solved the phonon Boltzmann transport equation and have succeeded in describing κ at temperatures ranging from 300 K to 4000 K [3]. To the best of our knowledge, this is the first time to predict solid solution effects on κ of Fe-bearing lower mantle minerals by fully *ab initio* calculations.

References

[1] T. Tsuchiya and X. Wang: J. Geophys. Res. **118** 83 (2013).

[2] H. Dekura and T. Tsuchiya, Phys. Rev. B **95**, 184303 (2017).

[3] H. Dekura and T. Tsuchiya, *in prep* (2017).

First-principles study of quantum transport in nanostructures

NOBUHIKO KOBAYASHI
Institute of Applied Physics, University of Tsukuba
1-1-1 Tennodai Tsukuba Ibaraki 305-8573

1 Introduction

The aim of this project is to reveal charge, heat and spin transport in materials from first-principles. Quantum nature is essential in nanoscale systems, and atomistic analysis based on detailed electronic states calculations are indispensable to discuss the transport property. In order to analyze transport properties, we have developed the nonequilibrium Green's function (NEGF) method, and the time dependent wave-packet diffusion (TD-WPD) method. Using these methods, we have investigated charge, head and spin transport properties of materials.

2 Charge Transport

The recent progress in the fabrication technology of organic single-crystal semiconductors and thin-film field-effect transistors with very high carrier mobility up to 40 cm^2/Vs requires us to elucidate the mechanisms of carrier transport in organic semiconductors, which are assemblies of p-conjugate molecules weakly bonded by van der Waals interactions. Observations of the crossover from the hopping transport of localized carriers to bandlike transport with a diffusive nature are expected to provide us with clues allowing us to reveal the carrier transport mechanisms.

We studied the carrier coherence factor α and the thermally induced fluctuations of transfer energies with neighboring molecules. The thermal fluctuation effects of molecular motion have been discussed for transport properties of organic semiconductors. We analyzed numerical data of transfer energy fluctuations of pentacene at various temperatures and pressures. We showed that the value of Δ t/t is approximately 20% at room temperature, and that the effect of thermal fluctuations is significant and therefore reduces the electronic coherence. Moreover, plotting the temperature dependence of Δ t/t, we showed that the value rapidly decreases towards 10%, which is favorable for the emergence of coherent electronic states. These calculations show that reducing the dynamic disorder resulting from thermal fluctuations is important to observe coherent charge transport. Thus, synthesizing molecules with steric hindrance is crucial to achieving full coherence under ambient conditions. [1]

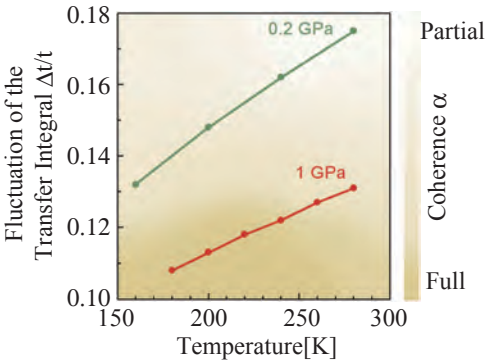

Figure 1: Reduction of the relative thermal fluctuation Δ t/t of the transfer integral at high pressure and low temperature for pentacene. [1]

3 Thermoelectricity

Highly efficient thermoelectric materials have been attracting much attention because of their potential applications, especially for energy harvesting by waste heat. A challenge is to improve the relatively low conversion ef-

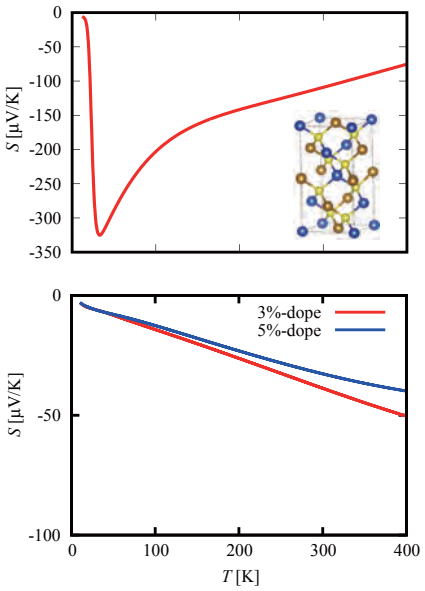

Figure 2: The Seebeck coefficients of CuFeS2 and the doped systems. [2]

ficiency, which is a function of the figure of merit $ZT = \sigma S^2 T/\kappa$. It is difficult to simply enhance ZT because of the typical trade-off between the Seebeck coefficient and electrical conductivity, and a material that should conduct electricity well, without conducting heat, is also somewhat paradoxical.

We analyze the thermoelectric properties of a magnetic semiconductor CuFeS2 based on density functional theory. We reproduces the Seebeck coefficient of CuFeS2, such as a peak structure at a low temperature and weak temperature dependence around room temperature, and elucidated the mechanism of the high performance thermoelectric material. Furthermore, we discuss the temperature dependence of the doped systems.[2]

4 O(N) Method

We developed the O(N) TD-WPD method for the quantum transport calculation of huge systems of up to 100 million atoms a decade or so ago.We calculated the conductance and the mobility of the system with micron-order lengths at room temperature based on the Kubo-Greenwood formula. Using this method we can study the transport properties from diffusive to ballistic regimes including the effect of realistic electron-phonon scattering, and determine the mean free path and relaxation time

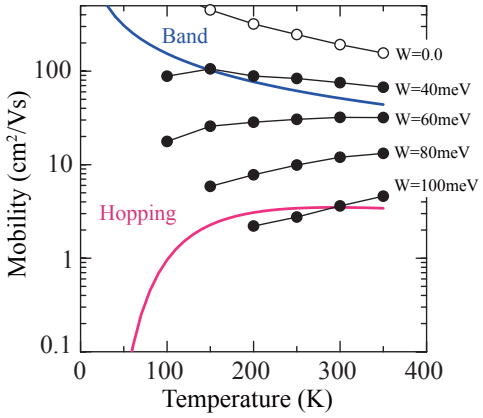

Figure 3: Calculated mobility of a rubrene single crystal along the a axis as a function of temperature for several magnitudes of static disorder W. [3]

from an atomistic viewpoint. We performed DFT calculations of electronic structures and interactions between molecules of pentacene and rubrene single-crystal organic semiconductors including the effect of the van der Waals interaction, and applied the TD-WPD method to the analysis of transport properties of the organic semiconductors.

We have studied charge transport using the TD-WPD method with maximally localized Wannier functions based on density functional theory including van der Waals interactions. The strong electron-phonon interactions due to thermal fluctuation are appropriately included as intrinsic effects. We analyzed the transport properties of pentacene and rubrene single crystals. We also find the temperature-dependent behavior from bandlike to thermally activated behavior due to extrinsic disorder effects, which correspond to experimental observations.

References

[1] K. Sakai, Y. Okada, T. Uemura, J. Tsurumi, R. Hausermann, H. Matsui, T. Fukami, H. Ishii, N. Kobayashi, K. Hirose and J. Takeya, NPG Asia Materials, 8, e252 (2016).

[2] H.Takaki, K.Kobayashi, M.Shimono, N.Kobayashi, K.Hirose, N.Tsujii, T.Mori, Appl. Phys. Lett. 110, 072107 (2017)

[3] H.Ishii, N.Kobayashi, K.Hirose, Phys. Rev. B 95, 035433 (2017)

Theoretical Analyses on Ionic Transport Properties, Electrical Properties and Interfacial Electronic States of Nanostructures

Satoshi WATANABE
Department of Materials Engineering, the University of Tokyo
7-3-1 Hongo, Bunkyo-ku, Tokyo, 113-8656

1 Introduction

For designing and controlling novel nanoscale information and energy devices, our understanding is still insufficient especially on complicated situations and phenomena at nanoscale, such as the effects of interface between novel two-dimensional materials and substrates and ionic transport in metal-oxide heterostructures.

So we have been performing theoretical analyses on these topics based on atomic/electronic level simulations (mainly based on density functional theory (DFT)), taking various nanostructures as target systems. In the followings, some of our results in the fiscal year 2016 are described.

2 Electric field effects in organic molecular layers

Organic semiconductors have attracted increasing attention as promising materials for electronic devices. In α-ω-dihexyl sexithiophene (DH6T) crystal, one of the most famous molecules for organic semiconductor, fluorescence-yield X-ray adsorption spectra (FY-XAS) have taken under the external electric fields [1].

To understand the electric field effects seen in the observed spectra, we have performed theoretical analysis based on DFT calculations (using Quantum-Espresso package) [2]. Comparing the results with/without electronic fields, we have found that the change of total density of states (DOS) is similar to the projected DOS at the hexyl group in DH6T layer. This means that the charge polarization induced by the electric field is mainly localized at the hexyl group in the DH6T molecule, which is in good agreement with the experiment [1]. We conclude that the external electric field is strongly screened by the hexyl group which makes the changes in the electronic state in the thiophene backbone negligible.

3 Search for relevant 2D substrates for Germanene and stanene

Germanene and stanene have attracted much attention recently and have been synthesized on several substrates like Al(111), Au(111) and Pt(111). However, they still lack suitable semiconducting substrates that can preserve their fascinating electronic properties and topology.

We have explored such substrates by using the combination of DFT calculations (using Quantum-Espresso package) and data mining of Inorganic Crystal Structure Database [3]. We have found several candidates including some of the CdI_2-type materials, CuI, and GaGeTe. All of them can preserve the quasi-free-standing geometry, stability and band structure of germanene or stanene. Among them, CdI_2 and ZnI_2 can open a band gap of 0.16-0.18 eV in germanene, larger than

all 2D substrates previously found manually, while preserving Dirac-cone-like band structures. The mobility of supported germanene is as high as 1-8 $\times$ 10^5 cm^2/Vs. Moreover, the Z_2 invariants of germanene on CuI and stanene on CaI_2 are found to be non-trivial. In addition, from the analysis of germanene on substrates based on a low-energy tight-binding Hamiltonian, strong linear correlations are found among the effective electric field, external Rashba coefficient and charge transfer.

4 Li Diffusion in amorphous Li_3PO_4

Deeper understand on atom diffusion is necessary for further development of some of novel information and energy devices. Simulations based on DFT are powerful for this, but are computationally very heavy for certain systems such as amorphous materials. So we have explored the applicability of neural network potentials (NNP), a recently developed machine learning technique, to studying atom diffusion in amorphous materials, using Li_3PO_4 as a benchmark system [4].

We adopted the NNP proposed by Belher and Parrinello [5], and used about 17,000 Li_3PO_4 structures and corresponding DFT energies (calculated using VAPS package) to train our NNP, and 28,000 structures as independent testing data. The residual mean square error (RMSE) of NNP is 7.6 meV/atom for the training dataset and 6.5 meV/atom for the testing dataset.

Our NNP can reproduce the DFT results of Li atom diffusion paths, barrier energies, diffusion coefficients and effective activation energies in amorphous-Li_3PO_4. For example, the average barrier energies are 0.58 eV and 0.56 eV in the DFT and NNP calculations, respectively, and the mean absolute error of barrier energy prediction is 0.05 eV. We would like to note that the calculation speed of NNP is about 3 to 4 orders of magnitude faster than DFT.

References

[1] H.S. Kato, H. Yamane, N. Kosugi and M. Kawai: Phys. Rev. Lett. **107** (2011) 147401.

[2] T. Moriya, E. Minamitani and S. Watanabe: in preparation.

[3] Z. Ni, E. Minamitani, Y. Ando and S. Watanabe: submitted to Phys. Rev. B.

[4] W. Li, Y. Ando, E. Minamitani and S. Watanabe: in preparation.

[5] J. Behler and M. Parrinello: Phys. Rev. Lett. **98** (2007) 146401.

First Principles Calculations of Muon and Positron in Solids

Mineo SAITO

Institute of Science and Technology, Kanazawa University

Kakuma, Kanazawa, 920-1192 Japan

Recently, the spin polarized positron annihilation experiment attracted scientific interests because it provides useful information on electron spin polarization. We study the momentum densities of the ferromagnet Fe. The two dimensional momentum densities of majority and minority spins are found to have strong anisotropy, i.e., the momentum densities on the Σ line are larger than those on the Δ line. We analyze the origin of this anisotropy based on the group theory. For this purpose, we develop a code that can identify irreducible representations of spin-polarized bands. We find that the number of the totally symmetric bands on the Σ line are larger than those on the Δ line. We conclude that this difference in the number of the totally symmetric bands is the origin of the fact that the momentum densities on the Σ line are larger than those on the Δ line since only the totally symmetric bands contribute to the momentum densities. The difference in the number is due to the fact that the symmetry on the Σ line (C2v) is lower than that on the Δ line (C4v).

We next study the one dimensional momentum density distribution. The distribution of the majority spin is found to be broader than that of the minority spin (Fig. 1). This difference between the two spins is expected to be due to the fact that the distribution in space in the majority spin is narrower than that of the minority spin.

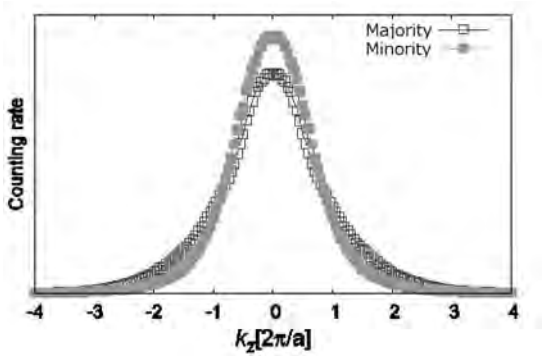

Fig. 1 One dimensional momentum density in Fe

We also study muon in GaN. A paramagnetic neutral muonium was observed and the hyperfine structure was found to show strong anisotropy [1]. We find that the Fermi contact term is small compared with the cases of Si and GaAs and the dipole term induces the anisotropy.

[1] K. Shimomura et al., Phys. Rev. Lett., 92,135505 (2004).

Exploration of structure motifs characterizing metal oxides

Kazuto AKAGI

WPI-Advanced Institute for Materials Research,

Tohoku University, Katahira, Aoba-ku, Sendai, Miyagi 980-8577

We continued the exploration of key structural motifs in metal oxides leading to their properties as preparation for data driven approach.

Polaron and hydrogen in a-HfO_2

Hafnium oxide is a high dielectric constant material used as a gate insulator in modern transistors. However, charge trapping centers in its complicated amorphous structure degrades the electrical performance. Therefore, in-depth understanding of the electronic structure of this material is needed. The molecular dynamics calculations were performed in both the classical and first-principles ways to model the amorphous structures hosting different defects. Screened hybrid functional (HSE06) was used to investigate the geometrical and electronic structures.

First, it turned out that extra electron/holes in the amorphous hafnium oxides (a-HfO_2) can be trapped spontaneously on intrinsic structural precursors like longer Hf-O bonds or under-coordinated atoms. Electrons can get trapped in deep states in the gap. These results show deep polaron in amorphous oxides are inherent and do not require any bond rupture to form precursor sites [1].

The interaction of hydrogen atom (H) in a-HfO_2 was also investigated. Hydrogen in many wide gap crystalline oxides exhibits negative-U behavior with the +1 or −1 charge states lower in energy for all Fermi-level positions. The obtained results demonstrate that hydrogen in a-HfO_2 also gives negative-U feature, with charged states being the most thermo-dynamically stable at all Fermi level positions. However, a metastable atomic hydrogen can share an electron with intrinsic electron trapping precursor sites forming a [e^-_{tr} + O–H] center, which is lower in energy on average by about 0.2 eV. These electron-trapping sites can affect both the kinetics and thermodynamics of the interaction of hydrogen with a-HfO_2 and the electrical behaviour of amorphous hafnia films in CMOS devices.

Shallow Acceptor Level in Rh:$SrTiO_3$

Photocatalytic water splitting uses sunlight to produce hydrogen from water. Rh-doped $SrTiO_3$ (Rh:$SrTiO_3$) has the potential for visible-light water splitting due to the formation of in-gap states. It is known that the valence state of Rh can be changed between +4 and +3,

and only Rh^{3+} provides photocatalytic activity [2]. The photo-carrier lifetime measurement found Rh^{3+}:$SrTiO_3$ has a longer carrier lifetime of about 10ps, which indicates there must be an impurity level close to the conduction band bottom, forming a shallow acceptor level. Since the valence state of Rh can be controlled by the introduction of oxygen vacancies (Vo) into Rh:$SrTiO_3$, the interaction between Vo and Rh must play an important role in the electronic structure change.

We systematically performed first-principles calculations to search for the origin of this shallow acceptor level considering the various configurations between Vo and Rh dopant. The hybrid-functional (HSE06) was necessary to reproduce experimental band gap and a 4x4x4 $SrTiO_3$ unit cell was used. The obtained results show that Rh exists in +3 state and there is no impurity level near conduction minimum as far as Rh and Vo are in the separate configuration. While Rh located next to Vo can be further reduced to +2/+1 states and this Rh^{3+}-Vo complex results in a gap state within 1eV below conduction band minimum. The origin of this shallow acceptor level was unoccupied dz^2 orbital of Rh (Fig. 1). These results can be well interpreted by the octahedral crystal field theory.

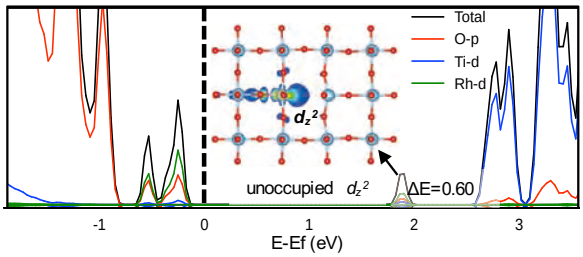

Fig. 1: DOS of the Rh^{3+}-Vo complex and wave-function character of the corresponding shallow acceptor level.

Li_2O_2 formation in a Li-O_2 battery

Li-Air battery is one of the candidates for next generation batteries. Control of the Li_2O_2 formation during discharge is necessary to improve the energy density. It is believed that LiO_2 is formed first and converted to Li_2O_2 +O_2 by self-redox reaction, but even the size dependence has not been clarified.

In order to elucidate it, ab initio random structure search (AIRSS) method developed by C. J. Pickard and implemented to CASTEP was applied to form many Li_nO_{2n} (n=3 to 10) clusters in vacuum (*e.g.* 1,000 samples for n=8) and self-redox events were statistically analyzed. There was no critical threshold for n, but the ratio of $O_2^{2!}$ becomes dominant at $n \gtrsim 9$. Spatial distribution of Li_2O_2 domain seems to be inhomogeneous, but further analysis is on-going.

References

[1] M. Kaviani, J. Strand, V. V. Afanas'ev, A. Sluger, Phys. Rev. B, **94**, 020103(R) (2016).

[2] R. Konta, T. Ishii, H. Kato, and A. Kudo, J. Phys. Chem. B **108**, 8992 (2004).

First-Principles Study of Excited Electron Dynamics of Nanostructures and Positron States at Surfaces

Kazuyuki WATANABE, Yasumitsu SUZUKI, Elena SILAEVA, Satoshi HAGIWARA, Yoshihiro UEDA, Kazuki UCHIDA, Hironari MIYAUCHI, Shota MIYAUCHI, Daisuke IWASAKI
Department of Physics, Tokyo University of Science
1-3 Kagurazaka, Shinjuku-ku, Tokyo 162-8601

In the project we investigated the following six topics this year. 1) Secondary electron emission from nanographene, 2) electron transmission through bilayer graphene (BLG), 3) electron excitation and emission from a nanoribbon under pulsed laser irradiation, 4) dielectric functions of carbon nanotubes with adsorbed water, 5) Bohmian mechanics in the exact factorization of electron-nuclear wave functions, and 6) positron states at Li- and O-adsorbed Fe(001) ferromagnetic surfaces by two-component density functional theory (TCDFT).

1) *Secondary electron emission from nanographene* [1]: We have observed secondary electron emission (SEE) from nanosurface by home-made time-dependent density functional theory (TDDFT) code, KENS. We obtained the incident-electron energy dependence and bilayer effect on the amount of secondary electron (SE) about finite-size graphene flakes. The dynamics of SEE and collective density oscillations, which are electronic excitations induced by electron impact and have a frequency specific to the target graphene flake, were demonstrated numerically. The dynamics of SEE from graphene flakes were also elucidated by the time-dependent occupation numbers of the Kohn-Sham electronic levels, which show consistency with typical properties observed in experiments. We also obtained k-resolved energy spectrum of SEs from various atomic sheets, which are infinite and periodic systems, and revealed relationship between band structure, electron excitation, and SEE. The calculations have been performed using System B.

2) *Electron transmission through bilayer graphene* [2]: We investigated electron scattering by AA-stacked and AB-stacked BLG using KENS code, and obtained energy-dependent transmittances that exhibit an unexpected crossing. The crossing behavior is successfully interpreted using the diffraction intensity distribution of single-layer graphene (SLG). Importantly, the crossing behavior holds for simulated BLG with reduced or increased layer distances compared with the real graphite gap. The present study not only revealed the close relationship between BLG transmittance and SLG diffraction for low-energy electron scattering but also provides relevant knowledge that will be useful for various surface analysis techniques based on electron scattering spectroscopy. The calculations have been performed using System B.

3)*Electron excitation and emission from a nanoribbon under pulsed laser irradiation* [3]: TDDFT simulations of laser-assisted electron excitation and emission from a SiNR were conducted, and the energy spectrum of emitted electrons was obtained. The energy spectrum in the low and intermediate energy regions was successfully interpreted by the excitation dynamics of one-photon and two-photon absorption and by that of multiphoton absorption,

respectively. The calculations have been performed using System B.

4) *Dielectric functions of carbon nanotubes with adsorbed water* [4]: We studied the optical properties of carbon nanotubes (CNTs) with adsorbed water by calculating the dielectric functions of CNTs following water adsorption using density functional theory and random phase approximation. Our calculations reproduced the redshifts of the peak position in the absorption spectrum that were reported in recent experimental studies. We demonstrated that they can be attributed to decreases in the band gaps, which result from electronic coupling between the CNTs and the water molecules. We also performed the calculations based on the many-body perturbation theory, i.e., the GW method and Bethe-Salpeter equation, to take into account the screening and excitonic effects. All calculations were performed with ABINIT code in System B.

5) *Bohmian mechanics in the exact factorization of electron-nuclear wave functions* [5]: The exact factorization theory allows us to define the time-dependent potential energy surfaces (TDPESs) that are responsible for the correlated electron-nuclear dynamics. We are developing a novel first-principle non-adiabatic molecular dynamics simulation method based on the TDPES. We studied whether the propagation of multiple classical trajectories can reproduce the quantum nuclear motion in strong-field processes when their motions are governed by the quantum Hamilton-Jacobi equation derived by applying Bohmian mechanics to the exact factorization theory. We demonstrated that multiple classical trajectories propagated by the force from the gradient of the exact TDPES plus the Bohmian quantum potential can reproduce the strong-field dissociation dynamics of a one-dimensional model of the hydrogen molecular ion. The preliminary calculations that required a lot of memory were performed using System B.

6) *Positron states at Li- and O-adsorbed Fe(001) ferromagnetic surfaces studied by TCDFT* [6]: We investigated the positron states for a ferromagnetic Fe(001) surface with and without Li and O adsorption by using TCDFT, and we determined aniihilation life time τ, binding energies, and the change in the electron work function. τ is found to be sensitive to changes in the electron and positron density distributions, which are induced by adatoms. The spin-polarization fraction at Li- and O-adsorbed Fe(001) surfaces, which are estimated by τ is in good agreement with that at the topmost surfaces obtained by using DFT. Thus, positron density distributions, which are localized around the topmost surface, capture the information of spin states at the topmost surface. Since τ is sensitive to the surface electronic states and spins, spin-polarized positron annihilation spectroscopy can be an important tool for detecting surface magnetization. The calculations have been performed using System B.

References

[1] Y. Ueda, Y. Suzuki, and K. Watanabe, Phys. Rev. B **94**, 035403 (2016).

[2] H. Miyauchi, Y. Ueda, Y. Suzuki, and K. Watanabe, Phys. Rev. B **95**, 125425 (2017).

[3] S. Miyauchi and K. Watanabe, J. Phys. Soc. Jpn **86**, 035003 (2017).

[4] D. Iwasaki, Y. Suzuki, and K. Watanabe, Appl. Phys. Express **10**, 045101 (2017).

[5] Y. Suzuki and K. Watanabe, Phys. Rev. A **94**, 032517 (2016).

[6] S. Hagiwara and K. Watanabe, J. Phys. Soc. Jpn **85**, 114703 (2016).

First-principles study of anomalous thermoelectric effect

Fumiyuki ISHII, Yo Pierre MIZUTA, Hikaru SAWAHATA
Faculty of Mathematics and Physics, Institute of Science and Engineering, Kanazawa University, Kanazawa, 920-1192, Japan

The Berry curvature, a geometric quantity associated with electronic Bloch states of crystalline materials, is one of the key ingredients of various transport phenomena. For example, the behavior of the anomalous Hall effect (AHE) and anomalous Nernst effect (ANE) is sensitively determined by the landscape of Berry curvature in reciprocal space.

The ANE, which is closely related to AHE, is a thermoelectric (TE) effect that generates electric current transversely to the applied temperature gradient.

Our aim is to find or design materials with large ANE, which could be useful in the future realization of highly efficient conversion of waste heat into electric power. As candidate systems that promisingly realize such TE conversion, we have investigated two classes of materials, namely (i) and (ii) described below, in each of which an effective magnetic field that induces AHE and ANE essentially stems from spin-orbit coupling or non-coplanar magnetic configuration.

(i) **(Coplanar) magnetic Heusler alloys** (real systems) :

There have been several studies on Heusler compounds in which time-reversal symmetry is broken due to magnetic order, often resulting in a very large AHE [1]. Since large ANE can be expected as well in such systems if the conductivity of AHE has a strong dependence on Fermi energy, we aim to study the ANE of these compounds as promising candidates for Berry-curvature-driven good TE materials. In preparation for future investigations in such direction, we have clarified the fundamental electronic structure from first-principles using an open-source package OpenMX [2], choosing some of the Co-based Heusler systems.

(ii) **Non-coplanar magnetic structures** (model systems):

Motivated by a previous report of large AHE in a model of *Skyrmion crystal* phase [3], one of non-coplanar magnetic configurations, we studied a similar model from **first-principles**. The procedure was as follows:

1. The electronic structure calculations with OpenMX [2], which supports the assumption of arbitrary magnetic configurations.

2. Identification of *Chern number*=(Band-resolved integration of Berry curvature) characterizing the geometric nature of each band, with our own implementation of a lattice gauge theoretical formalism [4].

3. Construction of a set of Wannier basis via Wannier90 [5] from the Bloch states obtained in the first step.

4. Evaluation of all the transport quantities of interest in the Wannier representation via postprocessing modules of Wannier90 package [6, 7] and some additional integration to evaluate ANE.

In the above procedure, a set of Wannier orbitals was successfully constructed from a large

number of electronic Bloch bands via Wannier90 [5], by exploiting the big memory size of the ISSP Supercomputer for storing large matrices. Subsequent evaluation of the conductivity of AHE from the Wannier orbitals, which required lots of sampling points for integration, was efficiently performed by making use of massive parallelization of the Supercomputer.

These computations revealed a surprisingly large ANE due to the peculiar geometric character of the electronic bands[8]. The variation of such behavior with respect to the magnetic configuration was also examined, which illuminated the uniqueness of the particular configuration of Skyrmion [9].

We hope that our above-described first-principles methods will be widely applied in quest for real materials that realize such noticeable TE effect.

References

[1] J-C. Tung and G-Y. Guo, New J. Phys. **15** (2013) 033014.

[2] T. Ozaki *et al.*, http://www.openmx-square.org/

[3] K. Hamamoto, M. Ezawa, and N. Nagaosa, Phys. Rev. B **92** (2015) 115417.

[4] T. Fukui, Y. Hatsugai, and H. Suzuki, J. Phys. Soc. Jpn.**74** (2005) 1674.

[5] A.A. Mostofi *et al.*, Comput. Phys. Commun. **185** (2014) 2309.

[6] X. Wang *et al.*, Phys. Rev. B **74** (2006) 195118.

[7] G. Pizzi *et al.* , Comput. Phys. Commun. **185** (2014) 422.

[8] Y.P. Mizuta and F. Ishii, Sci. Rep. **6** (2016) 28076.

[9] H. Sawahata, Y.P. Mizuta, and F. Ishii, Poster Q-22, International workshop on nano-spin conversion science & quantum spin dynamics, Tokyo, Oct. 14, 2016.

First-principles calculations of oxide thin-films and heterostructures

Fumiyuki ISHII, Yo Pierre MIZUTA, Hikaru SAWAHATA, Naoya YAMAGUCHI
Faculty of Mathematics and Physics, Institute of Science and Engineering, Kanazawa University, Kanazawa, 920-1192, Japan

Oxides-based thin films and heterostructures are an attractive playground for both basic and applied sciences because of the rich physics that can be manipulated by nano-engineering thier structures.

One example is the thermoelectric (TE) effect: The heat-to-electricity conversion efficiency could be better in two-dimensional(2D) systems such as oxide films compared to 3D bulk [1]. The other example is inverse Rashba-Edelstein effect[2]: The spin-to-charge current conversion at interface of oxide and non-magnetic metals[3].

In the context of magnetism, a whirling magnetic configuration called *Skyrmion crystal* is considered to be more stabilized in 2D than in 3D, which can drive a TE effect named the anomalous Nernst effect (ANE). The ANE is a thermoelectric (TE) effect that generates electric current transversely to the applied temperature gradient due to non-zero *Berry curvature* reflecting the magnetic configuration.

Our idea is, by combining these two, to explore the TE behavior of 2D oxide films when the electrons therein form Skyrmions. As specific ingredients that connect the TE effects and magnetic Skyrmions, we focused on the anomalous Hall effect (AHE) and the related anomalous Nernst effect (ANE), which are among the transverse transport phenomena arising due to non-zero *Berry curvature*, which in turn, can originates from non-coplanar magnetic structures such as Skyrmion crystal.

We chose EuO as a target material, since the appearance of Skyrmion-like state has been experimentally implied there [4]. More specifically, what we considered is a monolayer of EuO on which Skyrmion crystal is formed by unit Skyrmion composed of 4×4 Eu atoms with $S = 7/2$ electronic spin on each.

Firstly, we computed its self-consistent electronic states via OpenMX [5]. Secondly, the geometric (topological) character of each of the obtained bands was analyzed by band-resolved integration of Berry curvature (=*Chern number*) via our implementation of the formalism of Ref. [6, 7]. Thirdly, a set of hundreds of Wannier orbitals was constructed via Wannier90 [8] from the states obtained in the first step, and all the transport quantities of interest were evaluated in the Wannier representation via postprocessing modules of Wannier90 package [9, 10].

In the above procedure, the big memory size of the ISSP Supercomputer was exploited for storing large matrices associated with large number of relavant bands, and the massive parallelization of the computer was essential for the evaluation of ANE, which required a lot of sampling points for integration.

Our study showed the presence of a substantial strength of Berry curvature in the lowest conduction bands, which is reflected in a large ANE when the carriers are doped into those bands. Futhermore, the ANE and the conventional longitudinal Seebeck effect added up constructively to make the transverse TE voltage even larger. This situation, if realized,

would be very beneficial for efficient TE conversion. As a future task, we need to identify energetically stable Skyrmion crystals, unlikely to the present one, which is higher in energy as compared to ferromagnetic state as found in our calculations.

In addition to ANE in magnetic skyrmion, we have studied spin-orbit coupling parameters and spin structures in momentum space (effective magnetic field in momentum space) at the Bismuth surface alloys[11] and interfaces for several oxide systems, such as interfaces of Bi_2O_3/(Cu, Ag, Au). We have focused on Rashba effect and investigated its parameters and the spin structure. We have estimated Rashba coefficients α_R for Bi_2O_3/(Cu, Ag, Au) at 0.37-0.94, 0.48-0.75 and 0.39-0.67 in units of eV·Å respectively, and investigated the sign of the Rashba spin splitting, analyzing spin textures in momentum space. We also discussed a trend of the Rashba parameters for interfaces of Bi_2O_3/(Cu, Ag, Au) compared to that for surface alloys of Bi/(Cu, Ag, Au) [11].

References

[1] L. Hicks and M. Dresselhaus, Phys. Rev. B **47** (1993) 12727.

[2] V.M. Edelstein, Solid State Commun. **73** (1990) 233.

[3] Karube et al, Appl. Phys. Express **9** (2016) 033001.

[4] Y. Ohuchi, Y. Kozuka, M. Uchida, K. Ueno, A. Tsukazaki, and M. Kawasaki, Phys. Rev. B **91** (2015), 245115.

[5] T. Ozaki *et al.*, http://www.openmx-square.org/

[6] T. Fukui, Y. Hatsugai, and H. Suzuki, J. Phys. Soc. Jpn.**74** (2005) 1674.

[7] Y.P. Mizuta and F. Ishii, Sci. Rep. **6** (2016) 28076.

[8] A.A. Mostofi *et al.*, Comput. Phys. Commun. **185** (2014) 2309.

[9] X. Wang *et al.*, Phys. Rev. B **74** (2006) 195118.

[10] G. Pizzi *et al.* , Comput. Phys. Commun. **185** (2014) 422.

[11] N.Yamaguchi, H. Kotaka and F. Ishii, J. Cryst. Growth. *in press*, arXiv:160909782.

Atomic structure and electronic properties of metal/oxide interfaces

Hongping Li[1], Mitsuhiro Saito[1,2], Kazutoshi Inoue[1], Yuichi Ikuhara[1,2]
[1]*Advanced Institute for Materials Research, Tohoku University, Sendai, Miyagi, 980-8577*
[2]*Institute of Engineering Innovation, The University of Tokyo, Yayoi, Tokyo, 113-8656*

Metal/oxide hetero-interfaces are common and important in engineering devices. Their microstructure often plays a critical role in the macroscopic properties. To obtain atomic-scale understanding of the impact of buried interface behavior on electronic properties, it is of great importance to perform precise examinations of the local atomic structure and the detailed bonding characteristics at the metal/oxide interface. However, it is difficult to simply describe the nature of the interfacial bonding by a particular chemical bonding state due to their dissimilar electronic and crystal structures. In this work, we combined the high-resolution and scanning transmission electron microscopy with the first-principles DFT calculations to systematically investigate the atomic-scale structure and their bonding mechanism of the largely mismatched Pd/ZnO interface.

The molecular beam epitaxy method was applied to grow a thin film of Pd on both ZnO (0001) and ZnO ($000\bar{1}$) surfaces and found a successful epitaxial growth between largely mismatched lattices (18%) [1]. The atomic model of the hetero-interface contained 968 atoms. The first-principles DFT calculations have been performed using the Vienna ab-initial simulation package (VASP). We applied the projector augmented-wave method with a plane wave cut-off energy of 400 eV. Geometry optimization was performed using the PBE functional with a $1 \times 1 \times 1$ Gamma point centered k-point grid. All atoms in the supercells were fully optimized with respect to interatomic force tolerance of 1.0×10^{-4} eV/Å. By estimating the adhesion energies, it has been revealed that two different Zn-terminated interfaces are formed between Pd and polarized ZnO, and their large lattice misfit was accommodated periodically by the incoherent interface. Charge density analysis showed that effective chemical bonding was formed along the interface from covalent bonding to ionic bonding according to their site-dependent character. This study opened up a novel avenue to straightforward understanding of the largely mismatched metal/oxide heterointerfaces, which is particularly important in designing interface structure and properties, and uncovering the origin of interface-related phenomena [2].

References

[1] M. Saito, T, Wagner, G. Richter, and M. Rühle, "High-resolution TEM investigation of structure and composition of polar Pd/ZnO interfaces", Phys. Rev. B, 80, 134110 (2009).

[2] H. Li, D. Yin, M. Saito, K. Inoue, C. Chen and Y. Ikuhara, "Atomic structure and electronic properties of metal/oxide interfaces", (2017), preprint.

Theoretical Design for Topological Materials Based on First-Principles Simulation

Kunihiko YAMAUCHI
ISIR-SANKEN, Osaka University, Ibaraki, Osaka 567-0047

Topological matters are known as a new class of materials which exhibits quantum-Hall-like behavior. As aiming at finding novel topological insulators, we have explored the possibility to engineer the coupling of spin and valley physics in ferroelectric transition-metal oxide heterostructures. After we surveyed about hundred combinations between $5d$ element perovskite and ferroelectric host perovskite, we finally found $BiAuO_3/BiAlO_3$ combination as the best candidate material for the topological spin-valley ferroelectric system as shown in Figure 1.

In the wide energy gap of host $BiAlO_3$, Au-e_g orbital states forms the 2D graphene-like molecular-orbital bands with Dirac cone at the K point of the hexagonal Brillouin zone. Due to the ferroelectric ionic distortion, breaking of space-inversion leads to the spin splitting of the Dirac cone bands and results in the ideal spin-valley coupling both at the conduction and valence bands. We showed that the polar structural distortion is also responsible for a topological transition from a topological-insulating phase to a trivial band insulator. The spin-valley physics is influenced by the topological band inversion in a nontrivial way. When the valley-dependent spin polarization of both conduction and valence bands is preserved, a change of the Berry curvature and of spin-valley selection rules is predicted, leading to so-called spin-valley Hall effects.[1]

We have also studied theoretically Weyl semimetals in order to support ARPES experiments performed in Tohoku University. Trigonal tellurium crystalizes in the chiral crystal structure with infinite helical chains along the [001] axis. The chirality, *i.e. lack of the mirror and inversion symmetries*, allows the presence of the Weyl points at the symmetric points, such as the H point. By DFT computation, we successfully reproduced the electronic bandstructure which had been observed through ARPES measurement.[2]

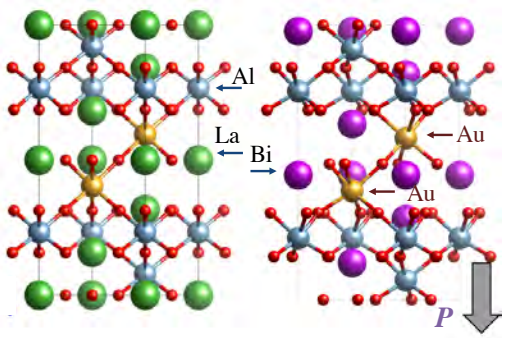

Figure 1: Theoretically designed ferroelectric topological oxide heterostructure.

References

[1] K. Yamauchi, P. Barone, S. Picozzi, Phys. Rev. B **95**, 035146 (2017).

[2] K. Nakayama, M. Kuno, K. Yamauchi, S. Souma, K. Sugawara, T. Oguchi, T. Sato, and T. Takahashi, Phys. Rev. B **95**, 125204 (2017).

The role of Ti interstitial in adsorption of O_2 on reduced rutile TiO_2 (110) surface

Kenji Yasuoka

Department of Mechanical Engineering,

Keio University, Kohoku, Yokohama, Kanagawa 223-8522

TiO_2(110), a wide-gap semiconductor, have attracted considerable attention due to its potential applications as solar cell, photocatalysis and biocompatible materials. Among many surface reactions, adsorption of O_2 was studied as a surface model reaction. It have been reported that reducing TiO_2(110) surface enhances O_2 absorption rate[1]. This change in absorption rate was explained by excess electrons. Until recent, surface bridging-oxygen vacancy was attributed main source of these excess electrons. However, recent experimental result suggested that subsurface Ti interstitial (Ti_{int}) is the main source of these excess electrons [2]. The influence of excess electrons introduced by Ti_{int} for O_2 absorption is still an open question. In order to study the chemistry of this surface, we have performed ab initio molecular dynamics simulation (AIMD).

As a result of AIMD, we were able to obtain the spatial distribution of excess electrons. The change in the distribution by time is shown in Figure 1. Taking account the fact that excess electrons induce by magnetic moment of $\pm 1.0\ \mu_B$, the location of excess electrons were analyzed using the magnetic moment. The vertical lines represent hopping of excess

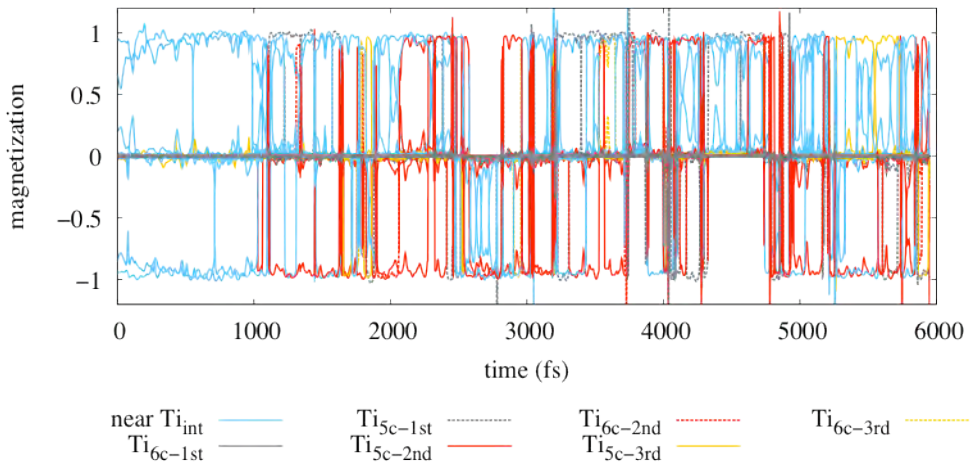

Figure 1: Change in the magnetic moment of a particular Ti site. Coloring is done by the group of Ti sites.

electrons, indicating that spontaneous excess electron hopping is occurring. Furthermore, excess electrons have shown stability in the near-surface region, suggesting that excess electrons introduced by Ti_{int} can contribute to the absorption of O_2.

References

[1] Y. Yoon, Y. Du, J. C. Garcia, Z. Zhu, Z. Wang, N. G. Petrik, G. A. Kimmel, Z. Dohnalek, M. A. Henderson, R. Rousseau, N. A. Deskins, and I. Lyubinetsky: ChemPhysChem. **16** (2015) 313-321.

[2] S. Wendt, P. T. Sprunger, E. Lira, G. K. H. Madsen, Z. Li, J. Ø. Hansen, J. Matthiesen, A. Blekinge-Rassmussen, E. Lægsgaard, B. Hammer, and F. Besenbacher: Science **320** (2008) 1755.

Surface reactions of hydrogen and oxygen on oxide materials

WILSON AGERICO DIÑO

Department of Applied Physics, Osaka University, Suita, Osaka 565-0871, Japan

Center for Atomic and Molecular Technologies Osaka University, Suita, Osaka 565-0871, Japan

Joining and Welding Research Institute, Osaka University, Ibaraki, Osaka 567-0047, Japan

We investigated oxygen ion migration in oxide materials using supercomputer system at ISSP.

Our original code “NANIWA” has allowed us to investigate various quantum states appeared in the reactions. In addition to electronic states, which can be calculated by conventional methods, NANIWA can simulate motions and stationary states of nuclei based on quantum theory. Therefore, this method is applicable to analyze quantum effects like tunneling, and has been successful to reveal reaction mechanisms in the atomic level.

Ceria based materials have been attracting considerable attention as a potential candidate for solid oxide fuel cells (SOFCs). Rare earth doping and lattice strain have been discussed as important factors to reduce the operating temperature of SOFC.

Oxygen ion migration in ceria based materials is essentially affected by covalent interactions resulting from the delocalization of electrons to oxygen sites. We investigated migration barrier for oxygen ion in ceria-based materials using density functional theory based calculation with Hubbard U correction [1]. From our calculations, we emphasized that the treatment of 4f electrons with variable occupancy is crucial for describing the covalent interactions. Furthermore, we conducted quantum dynamics calculation for oxygen ion migration in Sm doped ceria using NANIWA. We identified 4% lattice compression of Sm doped ceria as the optimum for oxygen ion migration. Making use of the quantum effects in oxygen ion migration, we successfully achieved reduction of SOFC operation temperature from 600ºC to 300ºC.

References

[1] M. Alaydrus, M. Sakaue, H. Kasai: Phys. Chem. Chem. Phys. 18 (2016) 12938.

Development and Application of Extended Ensemble Method Coupled with First-Principles Electronic Structure Calculations

Masaaki Araidai

Institute of Materials and Systems for Sustainability, Nagoya University
Furo-cho, Chikusa-ku, Nagoya, 464-8603

First-principles calculation method is a powerful tool to obtain electronic states and optimized atomic configurations in nanoscale. They have achieved many great successes for revealing experimentally inaccessible microscopic processes. In general, electronic states and optimized atomic configurations are calculated at zero temperature from a few initial guesses which can capture the nature of system of interest. Therefore, thermodynamical or statistical aspects of system are often missing in the first-principles electronic-states calculations. There are many physical and chemical phenomena induced by complex motion of a great number of atoms or molecules with charge transfer. Accordingly, free energy calculation method coupled with the first-principles electronic-states calculation method is essential for understanding those kinds of phenomena.

In this project, we developed multicanonical Monte Carlo (MUCA-MC) simulation code[1] coupled with VASP (Vienna ab-initio simulation package) code[2]. We refer to the code as MUCA-MC-VASP hereafter. In the code, the multicanonical weight is generated by the Wang-Landau algorithm[3].

Figure 1 shows the potential of mean force of Lennard-Jones fluids. There are 108 argon atoms in the system. We are aiming at the reproduction of the results, using the MUCA-MC-VASP code. Figure 2 shows the wall time per one MC sweep (dotted line) and parallelization efficiency (solid line) as a function of the number of random walkers. The wall time is the average value over 500 MC sweeps. It is immediately obvious that our code possesses an excellent parallelization efficiency.

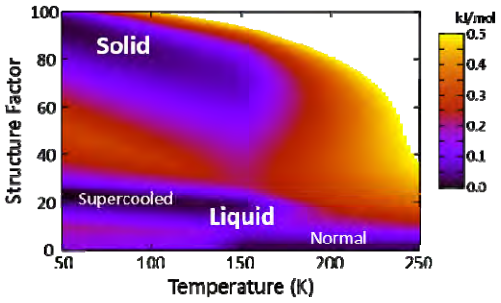

Fig.1 Potential of mean force of Lennard-Jones fluids.

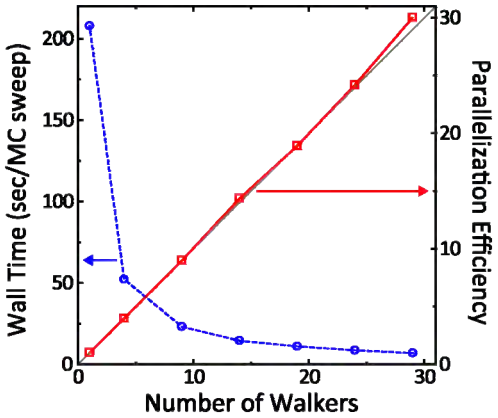

Fig.2 Wall time and parallelization efficiency of the developed code.

After the reproduction, we plan to apply the developed code to redox reaction at solid-gas interface, electrochemical reaction at solid-liquid interface, atomic diffusion process on surface, thermodynamical stability of matter, and so on.

This work was supported by Grants-in-Aid for Scientific Research (Grant No. 16K17551) from MEXT of Japan.

References

[1] B. A. Berg and T. Neuhaus, Phys. Rev. Lett. **68**, 9 (1992).
[2] G. Kresse and J. Hafner, Phys. Rev. B **47**, 558 (1993).
[3] F. Wang and D. P. Landau, Phys. Rev. Lett. **86**, 2050 (2001).

Large-scale computational simulations of non-equilibrium transport phenomena

Yoshihiro Asai, Marius Bürkle, Jun-ichi Ozaki

Research Center for Computational Design of Advanced Functional Materials,

National Institute of Advanced Industrial Science and Technology (AIST),

Central 2, Umezono 1-1-1, Tsukuba, Ibaraki 305-8568

We have studied the following subjects in non-equilibrium transport in terms of large-scale computational simulations:

1-1) Transport calculations based on an order-N DFT method for large channel materials.

1-2) Phonon transport calculation based on the first-principles DFT theory.

1-3) Comparisons of first-principles transport calculations with conductance measurements using scanning tunneling microscope molecular break junction experiments.

2-1) Time-dependent density matrix renormalization group study of the electric conductance of strongly correlated Hubbard chain.

In the following we outline these subjects and give the main results:

1-1) Non-equilibrium Green's function (NEGF) techniques were combined with the order-N code CONQUEST for large scale transport calculations. The method has been applied to highly conducting polymers of length between 50 nm to 100 nm (Fig. 1).【1. (Unpublished)】

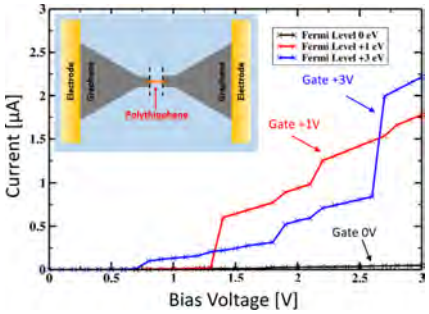

Fig. 1 Calculated I/V for different gate voltages

1-2) Ballistic phonon transport calculations based on (i) first-principles methods and (ii) classical molecular dynamic simulations were made for two terminal devices with a single molecule as a channel material.【2.】

1-3) Using accurate first-principle (DFT+Σ) based calculations of the conductance we investigated the orbital selection rule for molecular conductance, showing excellent agreement with experiment.【3.】

2-1) The electric conductance of Hubbard chain bridging two electrodes at finite bias

voltage was studied, using massive parallel computer simulations. The time-dependent density matrix renormalization group [4] is adopted to simulate the real-time dynamics of electric transport changing bias voltage. Here we have used the real-space parallelization [5] to overcome the expensive calculation cost.

Fig. 2 shows a differential conductance as a function of bias voltage at various wire length (site number) for a non-particle-hole-symmetric wire [6]. The differential of I-V curve oscillates with a length-dependent period. The period is an increasing function of the wire length.

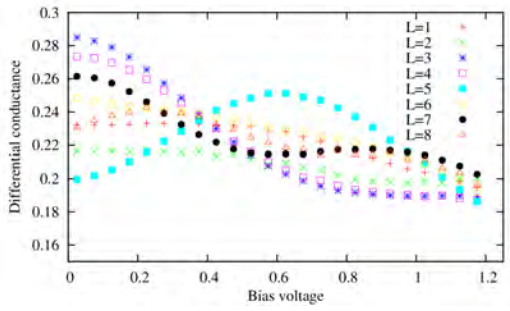

Fig.2: Differential conductance of Hubbard chain

References

[1] Unpublished

[2] M. Buerkle, Y. Asai, **Sci. Rep.**, 7, 41898 (2017)

[3] M. Buerkle, L. Xiang, G. Li, A. Rostamian, T. Hines, S. Guo, G. Zhou, N. Tao, Y. Asai, **J. Am. Chem. Soc.,** 139 (8), 2989 (2017)

[4] S. R. White and A. E. Feiguin, Phys. Rev. Lett. 93, 076401 (2004).

[5] E. M. Stoudenmire and S. R. White, Phys. Rev. B 87, 155137 (2013)

[6] J. Ozaki and Y. Asai, in preparation

Development & Application of Rational Drug Design Method using First-Principles Calculations & Bioinfomatics

Vladimir Sladek and Hiroaki TOKIWA

Research Center for Smart Molecules, Department of Chemistry,

Rikkyo University, 3-34-1 Nishi-Ikebukuro, Toshima, Tokyo 7-8501

We have applied energy interaction analysis based on the first-principles calculations using the energy decomposition techniques: SAPT (Symmetry Adapted Perturbation Theory) [1] and the FMO – PIEDA (Fragment Molecular Orbital – Pair Interaction Energy Decomposition Analysis) [2] to Golgi α-mannosidase II (GM) system. The GM is a pharmaceutical target for the design of inhibitors with anti-cancer activity. The known potent GM inhibitors enter complex interactions with Zn^{2+} ion and the active-site amino acids, many of which contain ionisable functional groups. In our project, the physical insight into the ligand···receptor interactions was provided for a large GM active-site cluster. Protonation dependent molecular recognition in Golgi α-mannosidase is demonstrated for five inhibitors and mannose, as a model for native GM substrate. The Zn^{+2} ion and Asp472 induce the key interactions with the deprotonated inhibitors (bearing an amino group in neutral state) followed by Asp92 and Asp341. This interaction pattern is consistent for all of the studied inhibitors and is similar to the interaction pattern of the enzyme native substrate – mannose. The interactions with the Zn^{+2} ion become repulsive for the protonated states of the inhibitors (bearing an amino group with +1 charge) and the importance of Asp92 and Asp204 raises considerably while the interactions with Asp472 and Asp341 are modified slightly. The interaction pattern for the protonated ligands seems to have an oxocarbenium transition state-like character rather than a Michaelis complex of GM. The electrostatic interactions with amino acids coordinating the zinc ion are of key importance for both the neutral and protonated states of the inhibitors. The ligands diol group which coordinates zinc is an essential structural feature of the potent inhibitors which is consistent with experimental findings. Based on the calculations either the protonated or deprotonated state of the ligand may be the active form of the GM inhibitor exhibiting different interacting patterns.

References

[1] R. Bukowski, et al., Chem. Phys. Lett., **414** (2005) 111.

[2] D. G. Fedorov, et al., Phys. Chem. Chem. Phys., **14** (2012) 7562

Reduction of Rare Metals in Fuel Cell Catalysts and Oxygen Sorption Materials

Yuji KUNISADA

Center for Advanced Research of Energy and Materials, Faculty of Engineering, Hokkaido University, Sapporo, Hokkaido 060-8628

We investigated the Pt adsorption and diffusion properties on non-metal element doped graphene and local electronic structure of oxygen sorption materials, , with the aid of the first principles calculation based on the density functional theory (DFT).

At first, we investigated adsorption and diffusion properties of a single Pt atom on non-metal element doped graphene. We performed the total energy and electronic structure calculations using VASP code. We installed parallelized VASP with Intel® MPI Library and Intel® Math Kernel Library. We found that the adsorption energies increase by non-metal element doping into graphene lattice. We also calculated the dopant dependence of diffusion constants of a single Pt atom at 100 ℃ which is operating temperature of typical polymer electrolyte fuel cell. From these calculations, we found that the non-metal dopants in graphene can prevent the surface diffusion of a single Pt atom.

We also investigated the electronic structure deference of Ca_2AlMnO_5, which is one of the promissing oxygen sorption materials, between before and after oxygen sorption. [2] We obtained the electron energy loss (EEL) spectra with scanning transmission electron microscopy (STEM) and DFT calculation. From comparison of these results, we clarified the pre-edge peak strength of O-K edge spectra depend on the oxygen sorption states.

In addition, we investigated the hydrogen absorption properties of Al(111) subsurfaces, the interface properties of hematite, and dielectric properties of α-Al_2O_3.

References

[1] S. Hasegawa, Y. Kunisada, N. Sakaguchi: submitted.

[2] G. Saito, Y. Kunisada, K. Hayami, T. Nomura, N. Sakaguchi: Chem. Mater. 29 (2017) 648.

[3] Y. Kunisada, N. Sakaguchi: J. Jpn. Inst. Met. Mater. 80 (2016) 570.

[4] G. Saito, Y. Kunisada, T. Nomura, N. Sakaguchi, T. Akiyama: Phys. Chem. Miner. 43 (2016) 749.

[5] N. Sakaguchi, L. Tanda, Y. Kunisada: Ultramicroscopy 169 (2016) 37.

Determination of geometric and electronic structures of organic crystals from first-principles

Susumu Yanagisawa

Department of Physics and Earth Sciences, University of the Ryukyus

1 Senbaru, Nishihara, Okinawa, Japan 903-0213

There years, there have been discussions on the possible band-like transport in the organic crystals, and the mechanism of the charge carrier transport in organic semiconductors is still under the intense debate. In order to predict the charge carrier transport properties, it is crucial to obtain theoretically the accurate crystal structure. The intermolecular distance and the molecular orientation angle have been proposed to impact the electronic properties [1]. In this study, by using oligoacene crystals as examples, we showed that the recent variant of the van der Waals density functional (vdW-DF)[2] is able to predict accurate crystal geometries and cohesive properties of organic crystals. We also demonstrated that by using the calculated crystal structure it is also possible to calculate the accurate electronic structure based on the *GW* approximation [3].

We first performed the structural optimizations and determined the stable structures for naphthalene, anthracene, and tetracene single crystals by using vdW-DF, as implemented in the Vienna ab-initio simulation package (VASP) [4]. In the present work, we carefully checked the convergence of the result with respect to the number of **k**-points, the cutoff energy, and the convergence threshold for the Hellmann-Feynman forces and stresses, presenting the converged results and comparison with the experimental values obtained at low temperatures. All the computations were done at the system B of ISSP supercomputer system with largest CPU cores of 432.

We performed the band structure calculation using the *GW* space-time code [5]. The code has been modified for parallel calculation with thousands of CPU cores. The *GW* calculations were based on the norm-conserving pseudopotentials and plane-wave basis set, and the starting wave functions were generated with the GGA-PBE exchange-correlation using the STATE code [6]. In addition to the one-shot *GW* (G_0W_0) calculation based on the PBE wave functions, we performed the partially self-consistent *GW* calculations in which the eigenvalues constructing the Green's functions replaced with the previous iteration (ev*GW*). The convergence of the calculated band gap (band width) with respect to the number of empty states, **k**-point sampling, and plane-wave

cutoff was estimated to be within 0.05 (0.01) eV.

To elucidate how the molecular configuration affects the intermolecular transfer integrals, we analyze the electronic structures in detail by using the maximally localized Wannier function [7].

It was found that the theoretical cell lengths and volumes are in general underestimated. The calculated cell lengths and cell angle of naphthalene and anthracene were on average deviated by less than 0.7 % from the experimental diffraction data measured at 8-15 K. On the other hand, relative errors of those of tetracene were 1.0 % compared to the experimental values measured at 175 K. The result indicates that the calculated cell lengths and volumes, corresponding to those at 0 K, are close to the experimental values at low temperature. We also found that inclusion of the zero-point vibrational energy by the multi **k**-point phonon calculation may remedy the underestimation.

The theoretical band gaps within G_0W_0 were slightly underestimated compared to the experimental values determined with the photoconductivity measurement, and they were improved by including the partial self-consistency.

The appreciable dispersion of the highest-occupied (HOMO) and lowest-unoccupied molecular orbital (LUMO) bands was elucidated by the in-phase or out-of-phase stacking of the neighboring HOMOs or LUMOs, and the tight-binding approximation employing the nearest-neighbor transfer integrals described well the first-principles band structure. It was also found that only slight geometrical relaxation caused by the sliding of the molecule along the molecular long axis alters the signs of the transfer integrals between the herringbone-arranged molecules. The result highlights the subtle balance between the transfer integral or the band width and the molecular arrangement in the crystal unit cell.

References

[1] V. Coropceanu et al.: Chem. Rev. **107** (2007) 926.

[2] I. Hamada: Phys. Rev. B **89** (2014) 121103(R).

[3] S. Yanagisawa and I. Hamada: J. Appl. Phys. **121** (2017) 045501.

[4] G. Kresse and D. Joubert: Phys. Rev. B **59** (1999) 1758.

[5] M. M. Rieger, L. Steinbeck, I. D. White, H. N. Rojas, and R. W. Godby: Comput. Phys. Commun. **117** (1999) 211.

[6] Y. Morikawa, H. Ishii, and K. Seki: Phys. Rev. B **69** (2004) 041403(R).

[7] N. Marzari, A. A. Mostofi, J. R. Yates, I. Souza, and D. Vanderbilt: Rev. Mod. Phys. **84** (2012) 1419.

First-principles meta-dynamics analysis of Catalyst Referred Etching method (analysis on dissociative adsorption of water molecule and etching reaction at interface between Pt and material surface)

Kouji INAGAKI

Graduate School of Engineering, Osaka University,

Yamada-oka 2-1, Suita, Osaka 565-0871

We investigated reaction mechanisms of chemical etching processes in a surface smoothening technique named Catalyst Referred Etching (CARE)[1], in which etching is invoked by approaching a catalyst (e.g. Pt) surface to material surface (e.g. wide band-gap semiconductors) in an etching solution (e.g. aqueous HF solution for SiC etching or pure water for GaN etching). In SiC-HF system, we have already obtained findings in the previous study with respect to SiC back-bond cleavage and simultaneous dissociative adsorption of HF molecule as the first step of etching process. The reaction barrier is clarified to be strongly lowered by the existence of Pt catalyst [2]. In this project, we analyzed H_2O splitting reaction on 3c-GaN(111) surface with respect to the distance between Pt catalyst and GaN. We find that a dissociative adsorption onto OH terminated kinked-GaN surface occurs in the presence of Pt catalyst (Fig. 1) with almost no barrier (~0.2eV). By subsequent approach of Pt to GaN surface, Ga-N bond cleavage with H-terminating the cleaved N atom occurs with a small barrier (~0.8eV), which is effectively smaller than the barrier in no-Pt reaction (1.4eV). It is concluded that first H_2O dissociation with cleaving Ga-N bond is effectively facilitated by approach of Pt, i.e., the reaction barrier reduced from 1.4eV to 0.8eV.

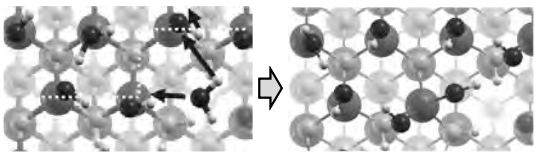

Fig. 1: H_2O dissociative adsorption at kink-site of GaN surface with Pt catalyst. OH adsorbs at kink-Ga and H adsorbs at O atom in OH termination.

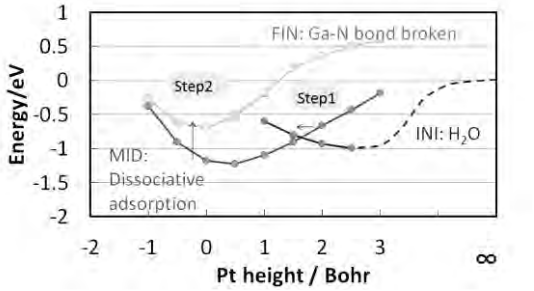

Fig. 2: Relative total energy change with respect to the position of Pt catalyst. Pt height origin is determined by the most stable Pt atom adsorption height. At Pt height 2 Bohr, H_2O dissociative adsorption (Fig.1). At around 0 to -1 Borh, Ga-N bond break take place and N is terminated by H atom in OH termination.

References

[1] H.Hara, et al., J.Electron.Mater. 35 (2006) L11.

[2] P. V. Bui, et al. Curr. Appl. Phys., 12 (2012) S42.

[3] P. V. Bui, et al. Appl Phys.Lett.107(2015)20160.

Protonic Activity on the Hydrated Surface of Acidic and Basic Oxide Catalyst for CO_2 Conversion Processes

Ryuhei Sato and Shu Yamaguchi

Department of Materials Engineering,

The University of Tokyo, Bunkyo-ku, Hongo, Tokyo 113-0032

Proton activity on oxide surface is paid considerable attention for the application to metal/oxide catalysts such as Cu/ZnO for methanol synthesis. The efficiency of methanol synthesis ($CO_2 + 6H^+ + 6e^- \rightarrow CH_3OH + H_2O$) highly depends not only on the Red-Ox property but also on the acid-base property on oxide surfaces. Therefore, in recent years, the acidity of hydroxyl groups on oxide surfaces has been studied, although there are few report about the effect of acidic molecule adsorption on surface acidity. Here, we studied the change in acidity by the adsorption of CO_2, HCOOH, and CH_3OH.

First, we analyzed the adsorption of CO_2, HCOOH, and CH_3OH on bare cubic ZrO_2 (110) surface by *ab initio* molecular dynamic (AIMD) simulation. Subsequently, by introducing H_2O molecules above ZrO_2 surface terminated by those species, hydration reactions are analyzed by AIMD simulation. All the simulations were performed by home-made code written by F. Shimojo et al. [1]. The GGA/PBE functional and PAW method were employed with L4cpu and L36cpu queues.

After 10,000-step (2.4 ps) simulation for adsorption of each organic molecule on the bare surface, bidentate and polydentate carbonates, bidentate and monodentate formate, and methoxy groups are observed on the surface, the structure of which well agrees with that predicted from Fourier transform infrared spectroscopy measurement (FT-IR). These adsorbates except methoxy groups hardly interact with H_2O molecules, monodentate hydroxyl group ($Zr\text{-}OH^-$), and chemisorbed H_2O molecules on the Zr ions ($Zr\text{-}OH_2$) after the hydration. Therefore, these adsorbates are very weak conjugate base and inert to the acid-base reactions. In addition, by analyzing the radial distribution function and bond overlap population (RDF and OVP) between O and H atoms in H_2O adsorbates, it is confirmed that the acidity of H_2O adsorbates on Zr ion sites, $Zr\text{-}OH_2$ and $Zr\text{-}OH^-$, is constant regardless of the adsorption of organic molecules. pH at point of zero charge (pH_{PZC}) and acidity constant (pKa_0) for deprotonation reaction on O ion sites are estimated using $pKa_1 - pH_{PZC,H_2O}$, pKa for deprotonation reaction of $Zr\text{-}OH_2$ normalized by pH_{PZC} on hydrated cubic ZrO_2 surface without any organic molecules,

obtained from previous simulations[2]. Figure 1 shows the calculated change in pH_{PZC} as a function of the coverage of organic molecules on the surface. Note that the similar reduction of pKa_0 as a function of the coverage is observed in all hydration reactions on the surface terminated by carbonate and its derivatives, which suggests the reduction of basicity on surface oxide ions. It is also found that pH_{PZC} is reduced to the degree of 1.5 pH unit by CO_2 adsorption, which is comparable with the results obtained by an electro-kinetic measurement [3]. The extent of the decrease in pH_{PZC} by HCOOH and CH_3OH adsorption is much smaller, although HCOOH molecules themselves are stronger acid than CO_2 in aqueous solution. Therefore, further discussion on the difference between chemisorption of adsorbates on Brønsted and Lewis acid site is now under way to reveal the chemistry of surface acidity and basicity.

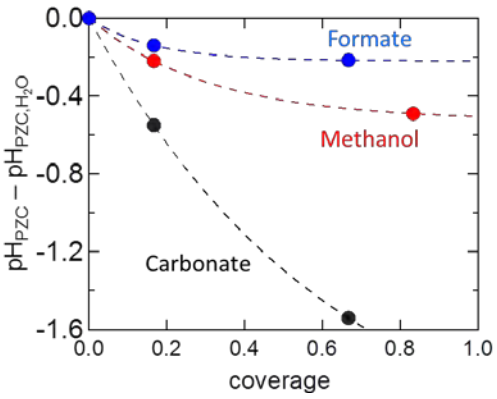

Figure 1. Estimated pH_{PZC} normalized by $pH_{PZC,H2O}$, pH_{PZC} on the organic-molecule-free hydrated surface, as a function of organic molecule coverage.

References

[1] F. Shimojo, R.K. Kalia, A. Nakano, P. Vashishta, *Comp. Phys. Comm.* **140** (2001) 303.

[2] R. Sato, S. Ohkuma, Y. Shibuta, F. Shimojo, S. Yamaguchi: *J. Phys. Chem. C*. **199** (2015) 28925.

[3] C. Su, D.L. Suarez *Clays and Clay Miner.*, **45** (1997) 814.

Ab initio study for nano catalysts based on abundant elements

Tetsuya TAKETSUGU
Faculty of Science, Hokkaido University
N10W8, Sapporo, Hokkaido 060-0810

Heterogeneous catalysts used in automotive gas exhausts control, water gas shifts, and fuel cells rely mostly on the precious metals (PMs) such as Pt, Rh, Pd. Due to their high cost and limited amounts, to reduce or even replace these metals is emergent issues in industry. To that end, we perform density functional theoretical (DFT) computations using ISSP supercomputers to understand the chemical mechanisms in conventional catalysts as well as to design novel catalysts with abundant elements. Specifically, our project focuses on the three-way catalysts (TWC) and fuel cells with water-gas shifts (WGS) and oxygen reduction reactions (ORR). In TWC, NO_x is reduced while CO and CH (hydrocarbons) are oxidized at the same time under the drastic temperature and oxygen concentration changes. With such extreme conditions, only Pt, Rh, and Pd turned out to be effective. To understand the reason as well as to clarify the possible chemical reaction pathways for TWC, we investigate the catalytic activities of these metals by using the slab model under the periodic boundary condition to model surfaces. Whereas to test the abundant elements, we focus on transition metals with 3d electrons (TM^{3d}) that are generally abundant and cost-effective. Although some of bulk TM^{3d} are known to inactive for TWC, we shed light on the nano-size effect, meaning we test nano-sized TM^{3d} such as clusters or islands on an oxide substrate. As for fuel cells, we focus on a hexagonal boron nitride (h-BN) sheet having a 2-dimensional structure similar to graphene. h-BN itself is inert but a carbon doping alters its reactivity. In a previous study, it was found that carbon doped BN sheet work as catalysts [1].

For PM surfaces and supported nano-sized TM^{3d} systems, DFT computations with periodic boundary conditions were performed using the PBE functional with PAW basis sets as implemented in VASP. It should be noted that the calculations for some of the latter system require massive parallelization using about 100 nodes. We considered PM-surfaces of flat (111) and (100) and steps and edges. Until now, we have obtained optimized slab structures and molecule-adsorbed structures and some of reaction pathways. For supported nano-sized TM^{3d} systems, we have obtained optimized structures for one TM^{3d} atom doping with pristine and O-defective oxide substrates and some adsorption states of small molecules. For calculations including transition metals with localized d- or f- electrons, we used +U technique to account for the localized electrons. We have also tried hybrid functionals such as HSE06 but using those functionals are computationally too demanding to the present purpose. For computations on h-BN (7×7) surface using SIESTA, a charge density difference comparing the pristine and doped h-BN indicate the large area would be activated for oxidation reactions.

References

[1] M. Gao, A. Lyalin, and T. Taketsugu, J. Phys. Chem. C **120**, 15993 (2016).

Accurate evaluation of electron-phonon coupling in sulfur-hydride superconductors

Ryosuke AKASHI
Department of Physics, University of Tokyo
Hongo, Bunkyo-ku, Tokyo 133-0033

In this project, we calculated the electron-phonon coupling strength responsible for the phonon-mediated superconductivity in sulfur hydride systems H_xS and also in another sulfide BiS_2 superconductor. These two superconducting compounds have attracted tremendous interest since their recent discovery [1–3], and we have addressed their origins of the superconducting transition from the viewpoint of accurate first-principles simulation. In the theory of phonon-mediated superconducting mechanism [4, 5], an essential quantity for accurate estimation of the superconducting transition temperature (T_c) is the following Eliashberg function

$$\alpha^2F(\omega) = \frac{1}{N(E_F)} \sum_{nn'\mathbf{kq}\lambda} |g^{\lambda\mathbf{q}}_{n\mathbf{k}+\mathbf{q}n'\mathbf{k}}|^2 \delta(\omega - \omega_{\lambda\mathbf{q}}) \delta(\varepsilon_{n\mathbf{k}+\mathbf{q}} - E_F) \delta(\varepsilon_{n'\mathbf{k}} - E_F). \quad (1)$$

Here, E_F, $N(E_F)$, $g^{\lambda\mathbf{q}}_{n\mathbf{k}+\mathbf{q}n'\mathbf{k}}$, $\omega_{\lambda\mathbf{q}}$, $\varepsilon_{n\mathbf{k}}$, denotes the Fermi energy, electronic density of states at the Fermi level, electron-phonon coupling matrix element, phonon frequency and the electron one-particle energy eigenvalue in the normal state, respectively. For example, there is a practical approximate formula of T_c, called McMillan-Allen-Dynes formula [6, 7], derived from the Eliashberg equations [5]

$$T_c = \frac{\omega_{ln}}{1.2} \exp\left[-\frac{1.04(1+\lambda)}{\lambda - \mu^*(1+0.62\lambda)}\right], \quad (2)$$

where λ and ω_{ln} represent the electron-phonon coupling strength and typical frequency of phonons contributing to the electron pairing. Parameter μ^* represents the effective pair-breaking repulsion and called Coulomb pseudopotential [8]. The former coupling parameters are defined with $\alpha^2F(\omega)$ as

$$\lambda = 2\int d\omega \frac{\alpha^2F(\omega)}{\omega}, \quad (3)$$

$$\omega_{ln} = \exp\left[\frac{2}{\lambda}\int d\omega \ln\omega \frac{\alpha^2F(\omega)}{\omega}\right] \quad (4)$$

Although $\alpha^2F(\omega)$ is thus essential for theoretical estimation of superconducting T_c, accurate calculation of this requires enormous computational cost; we used the system B (sekirei) for overcoming this difficulty.

The calculations of the phonon and electron-phonon coupling properties were carried out based on the density functional perturbation theory [9] as implimented with the plane-wave basis in QUANTUM ESPRESSO code package (5.0.3)(Ref. [10]). The Fermi-surface intergral was performed with the optimized tetrahedron method [11]. The GGA-PBE [12] and LDA-PZ [13] exchange-correlation potentials were used for the H_xS and BiS_2 systems, respectively. Parallelization was performed with respect to **k** points (*-npool* option) as implemented in *ph.x* code. The calculations were mainly done in System B (sekirei). Typical computational time was, for example, $\lesssim$16 hours per **q** point with 9 nodes and *-npool 9*.

In the last year, we performed the calculations for $H_{13}S_5$ and $H_{31}S_{11}$ (see Ref. [14]):

We further calculated the coupling for more various compounds. These H_xS systems with $2 \leq x \leq 3$ are the new crystalline phases found by the author and coworkers, called "Magnéli" phases in analogy to the well-known Magnéli phases in transition-metal oxides [15]. We found that the electron-phonon coupling shows monotonic increase as the hydrogen ratio x is increased (Table I). Using a first-principles method to calculate T_c based on the density functional theory for superconductors (SCDFT [16, 17]), we showed that this increase yield gradual increase of T_c. Remarkably, this behavior explains the experimentally observed pressure-induced behavior of T_c, which was unprecedented in the previous theoretical studies. This achievement has been published in Physical Review Letters [18].

TABLE I. Sulfur hydride "Magnéli phases" at high-pressure: First-principles calculated electron-phonon coupling parameters and superconducting transition temperature.

	H_7S_3	$H_{10}S_4$	$H_{13}S_5$	$H_{31}S_{11}$
H-ratio	0.70	0.714	0.722	0.738
Pressure (GPa)	130	180	190	200
λ	0.936	1.162	1.303	1.478
$\omega_{\ln}$ (K)	893	1218	1289	1355
$T_c^{\mathrm{SCDFT}}(K)$	41	80	107	121

Also, we calculated the electron-phonon coupling in BiS_2-layered superconductor $LaO_{0.5}F_{0.5}BiS_2$(Ref. [2, 3]). Previous studies have shown that this system is possibly subject to lattice distortion and/or charge-order instability, sensitively depending on the environment [19–21]. We therefore adopted the supercell configuration to treat these possibilities. The size of supercell (20 atoms) and multiple number of orbitals (especially of La and Bi) render the calculation cost enormous; namely, calculation of the electron-phonon coupling matrix element in Eq. (1) requires much time and therefore it becomes difficult to get their values on dense **q**-point meshes. In order to accelerate the convergence of the calculation with respect to the **q**-mesh, we applied the recently developed method of postprocessing rescaling [22]. The convergence of the calculations were also cross-checked with the results using the optimized tetrahedron method [11]. As shown in Fig. 1, the rescaled values show modest converging trend to the values calculated with the tetrahedron method. The good agreement between the results with the rescaling and optimized tetrahedron methods indicates the reliable convergence. First-principles study based on these data has been submitted to a journal [24].

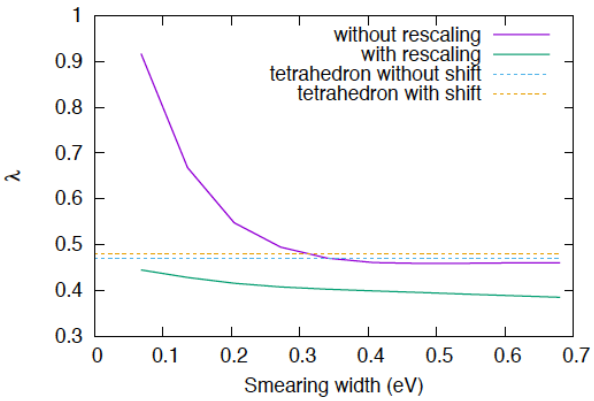

FIG. 1. Electron-phonon coupling in $LaO_{0.5}F_{0.5}BiS_2$ calculated from the first principles. Solid curves represent the calculated values of λ (Eq.(3)) using the Gaussian smearing approximation for the delta functions [23] with and without the rescaling method [22]. This calculation was carried out with the 4×4×2 **q** point mesh. The rescaled values show modest converging trend to the values calculated with the tetrahedron method using the 4×4×2 **q** point meshes with and without a half shift (dashed lines).

[1] A. P. Drozdov, M. I. Eremets, and I. A. Troyan, V. Ksenofontov, and S. I. Shylin, Nature (London) **525**, 73 (2015).

[2] Y. Mizuguchi, H. Fujihisa, Y. Gotoh, K. Suzuki, H. Usui, K. Kuroki, S. Demura, Y. Takano, H. Izawa, and O. Miura, Phys. Rev. B **86**, 220510 (2012).

[3] Y. Mizuguchi, S. Demura, K. Deguchi, Y. Takano, H. Fujihisa, Y. Gotoh, H. Izawa, and O. Miura, J. Phys. Soc. Jpn. **81**, 114725 (2012).

[4] A. B. Migdal, Sov. Phys. JETP **7**, 996 (1958).

[5] G. M. Eliashberg, Sov. Phys. JETP **11**, 696 (1960); D. J. Scalapino, in *Superconductivity* edited by R. D. Parks, (Marcel Dekker, New York, 1969) VOLUME 1; J. R. Schrieffer, *Theory of superconductivity; Revised Printing*, (Westview Press, Colorado, 1971).

[6] W. L. McMillan, Phys. Rev. **167**, 331 (1968).

[7] P. B. Allen and R. C. Dynes, Phys. Rev. B **12**, 905 (1975).

[8] P. Morel and P. W. Anderson, Phys. Rev. **125**, 1263 (1962).

[9] S. Baroni, S. de Gironcoli, A. Dal Corso, and P. Giannozzi, Rev. Mod. Phys. **73**, 515 (2001).

[10] P. Giannozzi *et al*, J. Phys.: Condens. Matter **21**, 395502 (2009); http://www.quantum-espresso.org/.

[11] M. Kawamura, Y. Gohda, and S. Tsuneyuki, Phys. Rev. B **89**, 094515 (2014).

[12] J. P. Perdew, K. Burke, and M. Ernzerhof, Phys. Rev. Lett. **77**, 3865 (1996).

[13] J. P. Perdew and A. Zunger, Phys. Rev. B **23**, 5048 (1981).

[14] R. Akashi, in *Activity report 2015* (Supercomputer Center, Institute for Solid State Physics, 2016).

[15] A. Magnéli, Acta Cryst. **6**, 495 (1953).

[16] M. Lüders, M. A. L. Marques, N. N. Lathiotakis, A. Floris, G. Profeta, L. Fast, A. Continenza, S. Massidda, and E. K. U. Gross, Phys. Rev. B **72**, 024545 (2005).

[17] M. A. L. Marques, M. Lüders, N. N. Lathiotakis, G. Profeta, A. Floris, L. Fast, A. Continenza, E. K. U. Gross, and S. Massidda, Phys. Rev. B **72**, 024546 (2005).

[18] R. Akashi, W. Sano, R. Arita, and S. Tsuneyuki, Phys. Rev. Lett. **117**, 075503 (2016)

[19] T. Yildirim, Phys. Rev. B **87**, 020506(R) (2013).

[20] X. Wan, H. C. Ding, S. Y. Savrasov, and C. G. Duan, Phys. Rev. B **87**, 115124 (2013).

[21] T. Tomita, M. Ebata, H. Soeda, H. Takahashi, H. Fujihisa, Y. Gotoh, Y. Mizuguchi, H. Izawa, O. Miura, S. Demura, K. Deguchi, and Y. Takano, J. Phys. Soc. Jpn. **83**, 063704 (2014).

[22] T. Koretsune and R. Arita, arXiv:1610.09441.

[23] M. Methfessel and A. T. Paxton, Phys. Rev. B **40**, 3616 (1989).

[24] C. Morice, R. Akashi, T. Koretsune, S. S. Saxena, and R. Arita, arXiv:1701.02909.

Microscopic Structure and Dynamics of Solutions Faced to Solid Materials Using First-Principles and Classical Molecular Dynamics

Ken-ichi FUKUI

Department of Materials Engineering Science, Graduate School of Engineering Science, Osaka University, Machikaneyama, Toyonaka, Osaka 560-8531

Microscopic structure of the electric double layer (EDL) formed at aqueous solution / electrode interfaces is important for fundamental understanding of the electrochemical processes occur at the electrodes. It is essential to model EDL focusing on orderings and mobility of water and solute ions. Previous investigations showed that several hydration layers were formed at the interface and density profiles of water changed depending on the electrode potential [1], and the stiffness of such hydration layers also depended on the electrolyte ion species as well as the potential [2]. To evaluate microscopic dynamics of water and ions and their networking in the EDL theoretically, we have investigated the various aqueous solution / graphite electrode interfaces by molecular dynamics (MD) simulation.

Each simulation cell contains two graphite electrodes and 0.5 M sodium halide aqueous solution between them (ca. 5×5×9 nm^3)(Fig.1). Electrode potential is applied by assigning uniform electric charge on each surface graphite carbon atom (1.83, 3.66, 5.49, 7.32 /μC cm^{-2}, which corresponds to 0.34, 0.72, 1.16, 1.61 V vs. pzc potential by solving the Poisson's equation).

Density profiles of water molecules (H and O atom) (Fig.1) show that hydration layers are formed at the graphite electrode interface independent of electrolytes. For the case of hydrophobic HOPG without apparent charge at the pzc potential, two stable alignments are known at the 1st layer (0 ~ 5 Å): one is the parallel alignment and the other is the one H up alignment with some preference to the former one. Fig. 1 clearly shows that hydrophobic I^- ion more favors the interface: it is closely related to its weaker coordination to water molecules.

We also analyzed mobility of a water molecule in the 1st layer by diffusion coefficient (Fig.2) as an index of effective hydrogen bonding networks. By applying positive potential to (positive charge on) HOPG, portion of H-up water molecules increases, which also favors the coordination to hydrophilic halide (F^-). Thus, more positive electrode potential and decrease water mobility in the 1st layer.

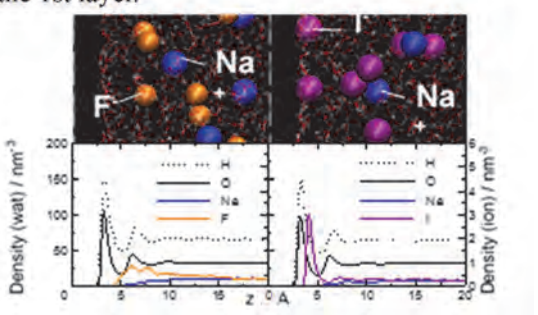

Fig. 1: Snapshots and density profiles of electrolytes at positively charged HOPG surface. (+5.49 μC cm^{-2}, left : NaFaq / right : NaIaq).

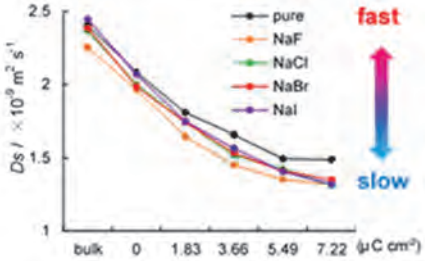

Fig. 2: Diffusion coefficient of water in the 1st layer depending on electrolytes and potential.

References

[1] M. Toney, et al., *Nature* **31**, 444 (1994).
[2] T. Utsunomiya, Y. Yokota, T. Enoki, K. Fukui, *Chem Commun.* **50**, 15337 (2014).

Ab initio molecular dynamics simulation of graphene/water interfaces

Tatsuhiko OHTO

Graduate School of Engineering Science,

Osaka University, 1-3 Machikaneyama, Toyonaka, Osaka 560-8531

Ab initio MD (AIMD) is a powerful tool to describe heterogeneous systems such as the water/solid interface, Although AIMD is computationally expensive, it describes electronic states beyond classical force fields,[1] which is important for interfaces. We calculated graphene/water interfaces with AIMD to reveal the interfacial structure of water. We accumulated 100 ps trajectories by using the CP2K code [2]. The analysis is ongoing together with experiments.

In addition to the simulation of graphene/water interfaces, we studied the interfacial structure of room temperature ionic liquids (RTILs).[3] RTIL interfaces controls many of the unique properties of RTILs, such as the high capacitance of RTILs and the efficiency of charge transport between RTILs and electrodes. RTILs have been experimentally shown to exhibit interfacial molecular layering structures over a 10 Å length scale. However, the driving force behind the formation of these layered structures has not been resolved. Here, we report *ab initio* molecular dynamics simulations of imidazolium RTIL/air interfaces along with force field molecular dynamics simulations. We find that the π+–π+ interaction of imidazolium cations enhances the layering structure of RTILs, despite the electrostatic repulsion.

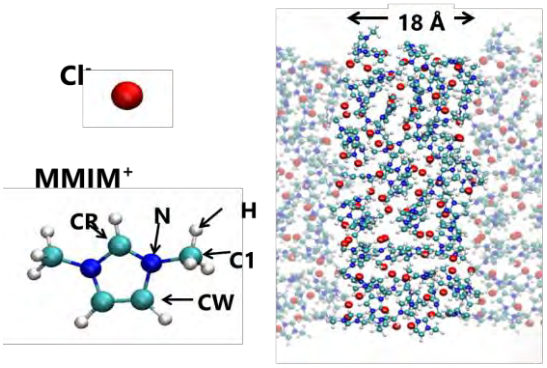

Fig. 1: Structures of RTIL and the RTIL-air interface.

References

[1] T. Ohto et al. Phys. Chem. Chem. Phys. **19**, 6909 (2017).

[2] The CP2K developers group, http://cp2k.berlios.de/

[3] T. Fujie et al. Phys. Chem. Chem. Phys. **19**, 2805 (2017).

First-principles calculation of anharmonic effects of phonons and related properties in solids

Terumasa TADANO
International Center for Young Scientists, National Institute for Material Science
Sengen, Tsukuba, Ibaraki 305-0047

Intermetallic clathrates are promising materials for thermoelectric applications because of their unusually-low lattice thermal conductivity (LTC) values [1]. Our previous computational study on a type-I clathrate $Ba_8Ga_{16}Ge_{30}$ (BGG) showed that the low LTC values can be attributed to the increased Umklapp scattering of heat-carrying acoustic phonons induced by rattling guest atoms [2]. While this study clearly unveils the role of three-phonon scattering processes in BGG, the effect of the quartic anharmonicity is still unclear, which is believed to be significant due to large atomic displacements of rattlers.

To elucidate the actual role of the quartic anharmonicity in BGG, we have performed the self-consistent phonon (SCP) calculations in which the following equations were solved self-consistently [3]:

$$\Omega_{\boldsymbol{q}\nu}^2 = \omega_{\boldsymbol{q}\nu}^2 + 2\Omega_{\boldsymbol{q}\nu} I_{\boldsymbol{q}\nu},$$
$$I_{\boldsymbol{q}\nu} = \sum_{\boldsymbol{q}'\nu'} \frac{\Phi(\boldsymbol{q}\nu; -\boldsymbol{q}\nu; \boldsymbol{q}'\nu'; -\boldsymbol{q}'\nu')}{4\Omega_{\boldsymbol{q}\nu}} \langle Q^*_{\boldsymbol{q}'\nu'} Q_{\boldsymbol{q}'\nu'} \rangle$$

Here, $\omega_{\boldsymbol{q}\nu}$ is the phonon frequency within the harmonic approximation, $\Omega_{\boldsymbol{q}\nu}$ is the temperature-dependent phonon frequency that includes the effect of the quartic anharmonicity in the mean-field level, $\Phi(\boldsymbol{q}\nu; -\boldsymbol{q}\nu; \boldsymbol{q}'\nu'; -\boldsymbol{q}'\nu')$ is the reciprocal representation of quartic force constants, and $\langle Q^*_{\boldsymbol{q}'\nu'} Q_{\boldsymbol{q}'\nu'} \rangle$ is the temperature-dependent displacement factor of the normal coordinate $Q_{\boldsymbol{q}\nu}$. Solving the SCP equation for BGG was a great numerical challenge because of a large number of phonon modes, i.e. $N_\nu = 162$. To make the computation feasible, we have developed an MPI-based code for calculating all elements of $\Phi(\boldsymbol{q}\nu; -\boldsymbol{q}\nu; \boldsymbol{q}'\nu'; -\boldsymbol{q}'\nu')$ in parallel.

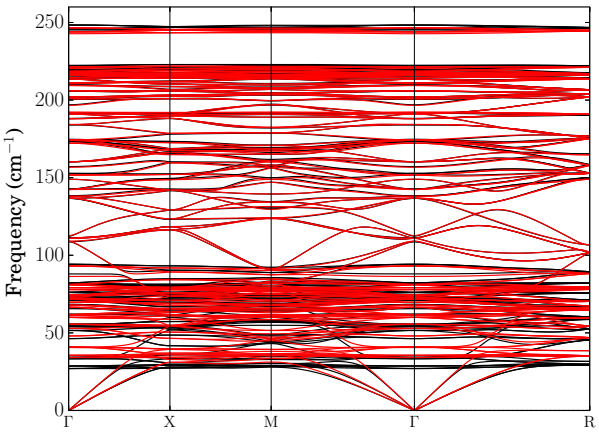

Figure 1: Anharmonic phonon dispersion of BGG at 300 K (red) compared with the harmonic dispersion curves (black)

Figure 1 shows the anharmonic phonon dispersion of BGG calculated at 300 K. As can be seen in the figure, the frequency renormalization by the quartic anharmonicity is almost negligible except for the low-lying rattling modes around 30 cm^{-1}, for which the phonon frequency is slightly increased. We have also calculated LTC of BGG by solving the Boltzmann transport equation (BTE) using the SCP lattice dynamics wavefunctions and found that the small change in the rattling frequencies considerably affects the LTC values as shown in Fig. 2. Interestingly, the quartic anharmonicity reduces the scattering

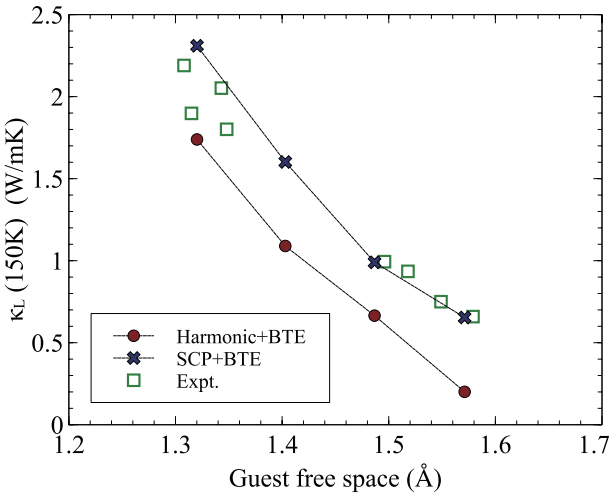

Figure 2: Correlation between the guest-free-space of the rattling atoms and the lattice thermal conductivity in BGG and other Ge clathrates. The experimental values are adapted from Ref. [4].

channel of the three-phonon interactions and therefore increases the LTC values. Moreover, we have found that the quartic anharmonicity is essential for explaining the observed correlation between the guest-free-space of the rattling atoms and the LTC values as shown in the figure [5].

References

[1] T. Takabatake *et al.*: Rev. Mod. Phys. **86** (2014) 669.
[2] T. Tadano, Y. Gohda, and S. Tsuneyuki: Phys. Rev. Lett. **114** (2015) 095501.
[3] T. Tadano and S. Tsuneyuki: Phys. Rev. B **92** (2015) 054301.
[4] K. Suekuni *et al.*: Phys. Rev. B **77** (2008) 235119.
[5] T. Tadano and S. Tsuneyuki, in preparation.

Atomistic simulation of nonlinear optical response in solids

Yasushi SHINOHARA

Photon Science Center,

The University of Tokyo, Hongo, Bunkyo-ku, Tokyo 113-8656

Interactions between light and electrons in solids is one of the most active fields in optical science, in which the electronic motion in attosecond scale is encoded in optical responses. We have developed an atomistic simulation method for describing ultrafast electronic response triggered by intense and short light field, using information derived by density-functional theory (DFT).

We have developed a theoretical framework temporally evolving one-body density matrix without interaction between electrons but with coupling to a time-dependent electric field based on the velocity gauge. Matrix elements of one-body Hamiltonian and momentum operator are taken from orbitals at self-consistent-solution of DFT with the local-density approximation (LDA), by all-electron LAPW code, Elk [1]. Since number of active bands are around a few hundreds, instantaneous Hamiltonian is easily diagonalizable by LAPACK routines. Time-propagation of the equation of motion is performed by an exponential propagator relying on explicit diagonalization on each time-step, to realize efficient temporal integration.

We apply the framework to an unexpected problem appeared in high-order harmonic generation (HHG) experiments in εGaSe crystal [2]. We perform a calculation such that 30 thousand time-step, 64x64x12 k-point mesh, and 103 bands as active space, covering 39 eV frequency ranges. To correct underestimation of the band gap due to LDA, scissors operator is introduced downshifting all valence bands by the amount of 1.2 eV to obtain experimental band gap 2.0 eV. Our simulation successfully captures whole part of experimental outcomes including the unexpected behavior. By analysis based on intensity dependence, we pin down the physical interpretation for the unexpected signal as higher-order nonlinear process showing up because of significantly nonlinear response.

References

[1] http://elk.sourceforge.net/

[2] Keisuke Kaneshima, Yasushi Shinohara, Kengo Takeuchi, Nobuhisa Ishii, Kotaro Imasaka, Tomohiro Kaji , Satoshi Ashihara , Kenichi L. Ishikawa, and Jiro Itatani, in preparation.

First-Principles Molecular-Dynamics Study of Structural and Electronic Properties of Covalent Glasses under Pressure

Fuyuki SHIMOJO, Akihide KOURA, Masaaki MISAWA, and Emina RYUO

Department of Physics, Kumamoto University, Kumamoto 860-8555

SiO_2 glass has been well known to be an archetypal three-dimensional network-forming glass and a material of great interest in various research fields. In particular, numerous experimental and theoretical studies on permanent densification have been carried out since its discovery in the 1950s [1]. However, the microscopic mechanism of permanent densification has not been clarified yet.

To clarify the microscopic structure of densified SiO_2 glass, we have conducted first-principles molecular-dynamics simulations on the decompression process of SiO_2 glass in its relaxed state from high pressures up to 40 GPa. When decompressed from high pressures above at least 15 GPa, the density and structure always converge to those of densified glass, while the coordination number of Si decreases to four rapidly. This is in good agreement with previous experimental studies and strongly suggests that densified glass behaves as a high-pressure polymorph of SiO_2 glass.

In comparison of ordinary glass, the coordination number of densified glass is almost the same, i.e. 4, which indicates that the glass consists of SiO_4 tetrahedra. However, the ring size distribution shows that the network of densified glass is formed from smaller size rings than ordinary glass. This result suggests that permanent densification is caused by the reconstruction of the network structure to a smaller one. Also, the O-Si-O angle distribution shows that SiO_4 tetrahedra of densified glass are deformed.

The difference in the bonding properties between densified and ordinary glasses is estimated with a population-analysis method. It is suggested that the Si-O bond becomes less covalent due to the rearrangement of network, which is in remarkable agreement with previous experimental studies [2].

It is concluded from this study that fully densified glass recovered from a pressure above 15 GPa has a small network structure consisting of deformed SiO_4 tetrahedra with less covalent Si-O bonds.

References

[1] P. W. Bridgman and I. Šimon: J. Appl. Phys. **24**, 405 (1953).

[2] D. Wakabayashi, N. Funamori, and T. Sato: Phys. Rev. B **91**, 014106 (2015).

Large scale ab initio calculations on the fundamental processes of solar energy convergence devices and on designing principles for new materials

Koichi YAMASHITA

Department of Chemical System Engineering, School of Engineering,

The University of Tokyo, 7-3-1, Hongo, Bunkyo-ku, Tokyo 113-8656

Recently, perovskite oxides and oxynitrides have been attracting wide attention since they are promising candidates for highly efficient water splitting photocatalysts. However, their activity still remains low, and further investigations such as theoretical calculations on these materials have not been fully done yet. Here, we investigated several perovskite oxides and oxynitrides which have been actively studied to achieve visible light responsive overall water splitting, or studied due to their novel features such as metallic properties.

First, we have investigated $CaTaO_2N$, an oxynitride photocatalyst which have succeeded in overall water splitting under visible light irradiation [1]. Here, we focused on the impacts of the atomic arrangement of O^{2-} and N^{3-} (= anion orderings) on its band structure. Bandgaps, carrier effective masses, and band edge positions of $CaTaO_2N$ with various anion orderings were calculated using density functional theory (DFT), which is implemented in VASP code. As a result, we found that anion orderings significantly impacts on their valence band structures due to the different orbital overlap between N 2p and Ta 5d bands (Fig. 1).

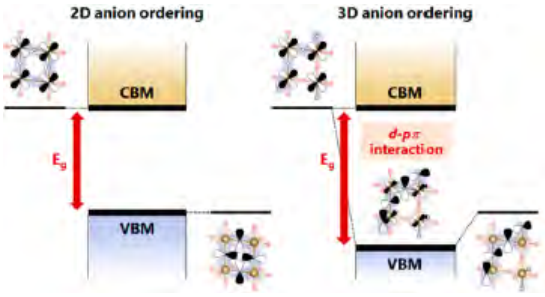

Fig. 1: Schematic diagram of the impact of anion orderings on the valence band structures of $CaTaO_2N$ [2].

Second, we have studied on $SrNbO_3$, a novel metallic photocatalyst with d^1 electronic structure [3], which was also reported to generate both H_2 and O_2 individually under sacrificial reagenst. However, there have been controversial arguments on the photoexcitation path of $SrNbO_3$ among three relevant bands, a fully occupied band (B_{-1}), a partially empty conduction band (CB), and a higher level unoccupied band (B_1). Here, by means of DFT based calculations on the imaginary part of its dielectric function, we revealed that photoexcitation around its optical gap 1.9 eV is

constituted of CB→B_1 transitions from the imaginary part of dielectric function (Fig. 2).

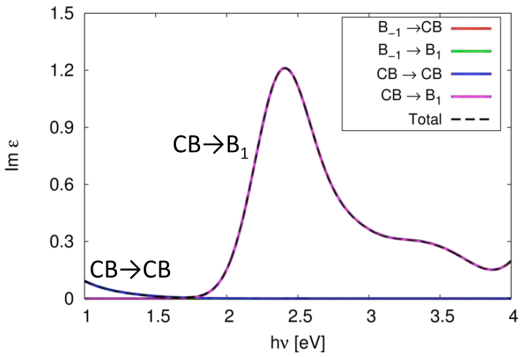

Fig. 2: Calculated imaginary part of dielectric function of each band of $SrNbO_3$.

Third, we have investigated $BaTaO_2N$, an oxynitride photocatalyst which can generate H_2 and O_2 individually with sacrificial reagent under visible light up to 660 nm [4]. In this study, we mainly focused on its carrier lifetime, since its band edge position is already suitable for water splitting. By means of electron-phonon coupling calculation, which is done by the combination of QUANTUM ESPRESSO and YAMBO codes, we found that the carrier lifetime of $BaTaO_2N$ is about 1~10 fs, which is shorter than those of other semiconductors[5], and thus their electronic structures around the band edges need to be modified to retard the relaxation of the carriers.

References

[1] J. Xu, C. Pan, T. Takata, K. Domen: Chem. Commun. **51** (2015) 7191.

[2] A. Kubo, G. Giacomo, K. Yamashita: Chem. Mater. **29** (2017) 539.

[3] X. Xu, C. Randorn, P. Efstathiou, and J. T. S. Irvine: Nat. Mater. **11**, 595 (2012)

[4] M. Hojamberdiev, K. Yubuta, J. J. M. Vequizo, A. Yamakata, S. Oishi, K. Domen, K. Teshima: Cryst. Growth Des. **15** (2015) 466.

[5] H. Kawai, G. Giorgi, A. Marini, and K. Yamashita: Nano Lett. **15(5)** (2015) 3103.

First-principles analysis of the dielectric response of defective interfaces

Shusuke Kasamatsu

Institute for Solid State Physics,

The University of Tokyo, Kashiwa-no-ha, Kashiwa, Chiba 277-8581

Surfaces of and interfaces between materials are sources of various functionalities in nanoelectronics and energy conversion devices. Control of surface and interface properties, which can sometimes be enormously different from bulk, is a key issue for device performance and durability. However, progress in this regard is hindered by lack of knowledge of the microscopic mechanisms for modifications of properties such as permittivity, conductivity, and reactivity at surfaces and interfaces. This year, we focused on how ion vacancies near metal/oxide interfaces affect the dielectric constant. We employ the orbital-separation approach [1,2] that we implemented in VASP code [3] for consideration of the dielectric response of metal/insulator/metal capacitors under bias.

In this work, we considered hydroxyapatite ($Ca_{10}(PO_4)_6(OH)_2$; HAp), which comprises up to 50% of human bone and is a well-studied biomaterial for medical use. It is also an intriguing material in that it exhibits proton conductivity [4], as well as ferroelectricity at the nanoscale [5]. Figure 1 shows the Cu/HAp/Cu model considered in this work and its inverse permittivity profiles with one OH^- ion vacancy at the positions indicated by arrows. We find that the position of the defects significantly affects the permittivity profile. However, it is difficult to understand the underlying mechanism due to rather large relaxation of the lattice induced by introduction of a single vacancy.

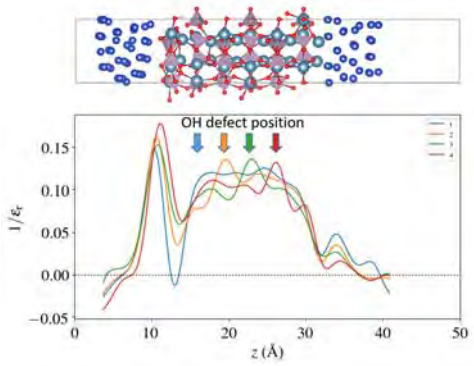

Figure 1 Cu/HAp/Cu model and the calculated inverse permittivity profile with OH^- vacancies.

References

[1] S. Kasamatsu et al., Phys. Rev. B **84** (2011) 085120.

[2] S. Kasamatsu et al., Phys. Rev. B **92** (2015) 115124.

[3] G. Kresse et al., Phys. Rev. B **54** (1996) 11169.

[4] M. Yashima et al., J. Phys. Chem. C **118** (2014) 5180.

[5] S. B. Lang, Phase Transitions **89** (2016) 678.

Theory of molecular Rydberg states by light-mass impurities in semiconductors: tunneling current and strong luminescence properties

Takashi NAKAYAMA
Department of Physics, Chiba University
1-33 Yayoi, Inage, Chiba 263-8522

Tunneling field-effect transistor (TFET) is one of the promising candidates for replacing conventional Si-MOSFETs and realizing energy-saving future devices. However, the current is low for Si-TFETs because the tunneling corresponds to weak indirect transitions between valence and conduction bands. Recent experiments showed that the tunneling current is remarkably enhanced by the codoping of Al and N impurities. However, it has not been clarified why such codoping increases the current. One purpose of the present project is to clarify what electronic structures are realized by various cation+anion pairs and answer this question using the first-principles calculation. On the other hand, it was also found in recent experiments that N or O-atom doping into III–V and II–VI semiconductors promotes strong optical transitions useful for solar-cell applications. The other purpose is to clarify why so strong transition occurs in N/O-doped III-V/II-VI semiconductors.

We first doped III+N and III-O pairs in a large unit cell made of 521/1024 Si atoms as shown in Fig.1(a) and studied which type of pair structure is the most stable using the formation energy. We found that the nearest-neighboring substitutional pair is the most stable for Al+N, Ga+N, and In+N dopings. This is because both III and N atoms have four-coordination covalent bonds as shown in Fig.1(b) and there is no electron-occupied state in the band gap of Si as shown in Fig.2(a). In cases of B+N, Be+O, and Mg+O dopings, on the other hand, the substitutional+interstitial pair with a coordination number of three shown in Fig.1(c) is the most stable. This occurs due to the small atomic radius of these dopants and the lower energies of

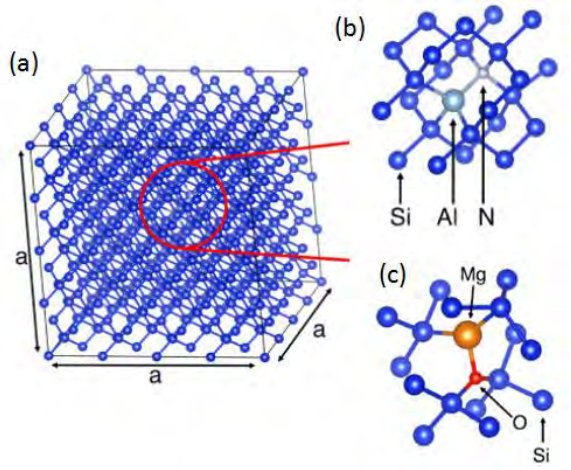

Fig.1. (a) Bulk Si_{512} unit cell adopted in the present calculation. The most stable configurations of (b) Al+N and (c) Mg+O pairs embedded in Si.

N-2p and O-2p dangling bonds.

Then, we consider what electronic structures are produced by these pair dopants. Figures 2(a) and 2(b) show band structures of Al+N and Mg+O doped Si. In both figures, there appear electronic states in the band gap of Si. The electron-unoccupied state around 0.5 eV in the band gap of Al+N doped Si is mainly made of a N-3s orbital that is strongly hybridized with the conduction-band states of Si and is weakly localized around N with a localization length of around 20Å as shown in Fig. 2(c). In case of Mg+O dopant, on the other hand, the electron occupied state appears around 0.2 eV above the top of the valence bands of Si. This state is mainly made of a Mg-3s orbital that is slightly hybridized with the valence bands of Si. These band-gap states can increase the band-to-band transitions.

Next, we consider the tunneling-current feature

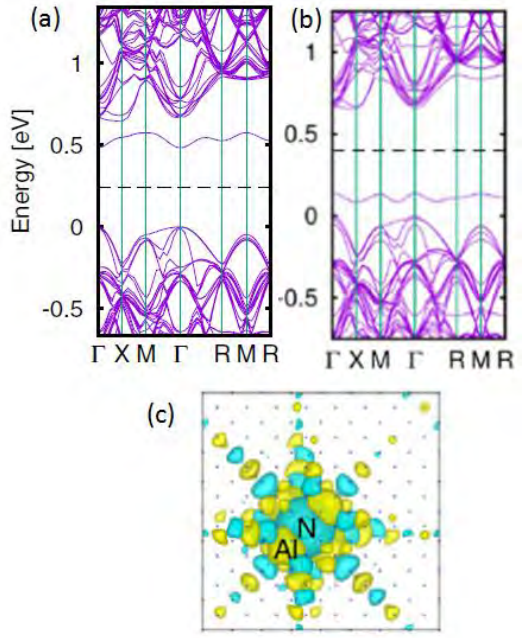

Fig.2. Calculated band structures of (a) Al+N and (b) Mg+O doped Si_{512}. Dashed line corresponds to the boundary between electron occupied and unoccupied bands. (c) Wavefunction of N-related unoccupied state that appears in the band gap of Al+N doped Si. Small dots indicate the positions of Si atoms.

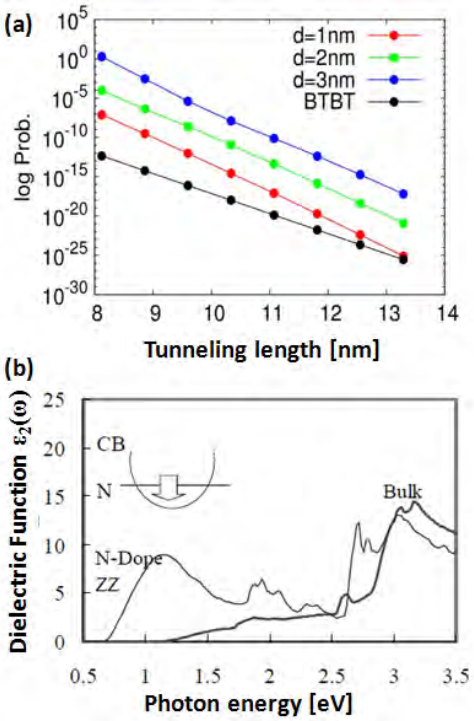

Fig.3. (a) Calculated tunneling probability between valence and conduction bands at Si p/n junction, as a function of p-i-n junction length *L*. BTBT corresponds to transition without dopants, while the others to those with Al+N dopants. (b) Photo-absorption spectra of N-doped InP as a function of photon energy. Inset shows schematic band structure.

when the Al+N pairs are doped in Si p-i-n device structures. Figure 3(a) shows the calculated tunneling probability as a function of tunneling length *L* between p and n-type Si layers, where we used calculated electronic states and assumed the constant applied voltage of 3.0 volt. From this figure, we know that the probability increases with decreasing *L* and that the probability is much larger for Al+N doped case compared to the band-to-band transition (BTBT) without doping. This is because the weakly localized electronic states shown in Fig.2(c) act as stepping stones for the tunneling transitions between the p- and n-Si layers.

Finally, we consider optical transition when N atom is doped in InP. Figure 3(b) shows calculated photo-absorption spectra as a function of photon energy. We can see that the absorption is markedly enhanced around/below the direct band gap of InP. This occurs due to the weakly localized N-orbital states that are hybridized with the conduction bands of host InP.

From these calculations, we can conclude that all these unique conductive and optical properties of N/O doped systems originate from the large electron negativity of N/O atoms. In fact, when we consider other V-family dopants such as P and As with III atoms, we have no electronic states in the band gaps of semiconductors.

All these calculations were performed using the xTAPP and VASP codes. In order to realize calculations for the present impurity-doped systems, because the system is made of a large number of atoms (500-1000 atoms), the advanced computing facility having higher-speed CPU (more than 100G Flops), larger-size memory (around 100GB), larger-size strange (more than 1.0TB), and a multi-task operation is indispensable. These conditions are realized only by the supercomputing systems of the ISSP.

Ab initio calculation for superconducting parameters

Kazuma NAKAMURA
Quantum Physics Section, Kyushu Institute of Technology
1-1 Sensui-cho, Tobata, Kitakyushu, Fukuoka, 804-8550

We estimated superconducting transition temperature T_c of weak-coupling material Al and strong-coupling one Nb from first principles via the McMillan-Allen-Dynes formula as

$$T_c = \frac{\omega_{\log}}{1.2} \exp\left[-\frac{1.04(1+\lambda)}{\lambda - \mu^*(1+0.62\lambda)}\right] \qquad (1)$$

where $\omega_{\log}$ is the characteristic phonon frequency, λ is the electron-phonon coupling, and μ^* is the Coulomb pseudo potential. The program code for the parameter derivation was made originally.

First-principles calculations were performed using `Tokyo Ab-initio Program Package` (`xTAPP`) with plane-wave basis sets, where norm-conserving pseudopotentials and the generalized gradient approximation of the exchange-correlation potential with partial core correction were employed. The cutoff energies for the wave function and charge densities are 36 and 144 Ry for Al and 64 and 256 Ry for Nb, respectively, and 21×21×21 k-point sampling was employed. The integral over the Brillouin zone was evaluated by the Methfessel-Paxton method with a broadening of 0.27 eV for Al and 0.81 eV for Nb. The density of states at the Fermi energy was estimated to be 0.185/eV/spin for Al and 0.837/eV/spin for Nb, which are consistent with the past estimate.

Phonon calculations were performed with the help of `PHONOPY` with the supercell approach. The 4×4×4 and 8×8×8 supercells were employed for Al and Nb, respectively. The electron-phonon coupling λ was evaluated with the frozen-phonon approximation and calculated for the 2×2×2 q phonon modes and the 21×21×21 k wave functions. The Coulomb pseudo potential μ^* was evaluated within the random-phase approximation using the *ab initio* many-body perturbation code `RESPACK`.

Figure 1 displays *ab initio* phonon dispersion for Al and Nb, which are compared with experimental data (blue dots) [1, 2]. The Debye frequency was estimated as 448.73 K for Al and 298.69 K for Nb.

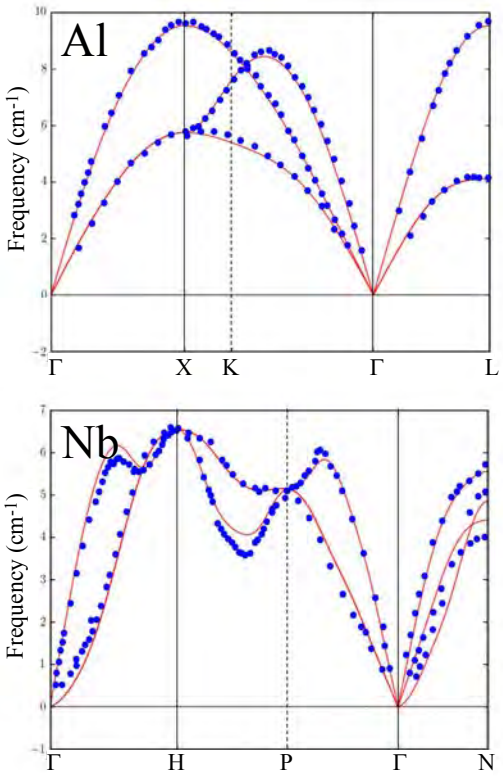

Figure 1: Calculated *ab initio* phonon dispersion of Al and Nb, where blue dots denots experimental data taken from Ref. [1] for Al and Ref. [2] for Nb.

Table 1 compare our calculated superconducting parameters ($\omega_{\log}, \lambda, \mu^*, T_c$) with other theoretical [3, 4, 5, 6, 7] and experimental values [8, 9]. Our code gives reasonable agreements with the past data. We note that the μ^* of Ref. [4] is set to reproduce the experimental T_c.

Table 1: Calculated superconducting parameters of Al and Nb.

Al	$\omega_{\log}$ (K)	λ	μ^*	T_c (K)
present	248	0.46	0.10	2.0
Ref. [3]	308	0.42	0.11	1.4
Ref. [4]	270	0.44	0.12	1.2
Ref. [5]	-	0.45	-	-
Ref. [6]	-	0.45	-	-
Ref. [7]	-	-	0.10	-
Expt.	-	0.42 [8]	-	1.2 [9]

Nb	$\omega_{\log}$ (K)	λ	μ^*	T_c (K)
present	199	1.36	0.14	18.2
Ref. [3]	164	1.31	0.13	14.5
Ref. [4]	185	1.26	0.21	10.5
Ref. [5]	-	1.33	-	-
Ref. [7]	-	-	0.13	-
Expt.	-	1.22 [8]	-	9.3 [9]

References

[1] R. Stedman, G. Nilsson, Phys. Rev. **145**, 492 (1966).

[2] M. Holt, P. Czoschke, H. Hong, P. Zschack, H. K. Birnbaum, T.-C. Chiang, Phys. Rev. B **66**, 064303 (2002).

[3] R. Akashi, K. Nakamura, R. Arita, M. Imada, Phys. Rev. B **86**, 054513 (2012).

[4] S. Y. Savrasov, D. Y. Savrasov, Phys. Rev. B **54**, 16487 (1996).

[5] R. Bauer, A. Schmid, P. Pavone, D. Strauch, Phys. Rev. B **57**, 11276 (1998).

[6] M. M. Dacorogna, M. L. Cohen, P. K. Lam, Phys. Rev. Lett. **55**, 837 (1985); P. K. Lam, M. M. Dacorogna, M. L. Cohen, Phys. Rev. B **34**, 15065 (1998).

[7] K.-H. Lee, K. Chang, M. L. Cohen, Phys. Rev. B **52**, 1425 (1995); K.-H. Lee, K. Chang, Phys. Rev. B **54**, 1419 (1996).

[8] For a review, see, e.g., E. L. Wolf, in *Principles of Electronic Tunneling Spectroscopy* (Oxford University Press, New York, 1985).

[9] N. W. Ashcroft and N. D. Mermin, Solid State Physics (Thomson Learning, Singapore, 1976).

Large-scale device-material research by massively parallel electronic structure calculation and data science

Takeo Hoshi and Hiroto Imachi (*)

Department of Applied Mathematics and Physics, Tottori University,

4-101 Koyama-Minami, Tottori 680-8550, Japan;

(*) Present affiliation: *Preferred Networks, Inc.*

The present project was carried out for the joint research between electronic structure calculations and data science. Mathematical studies and first principle studies were also carried out. The main collaborators are Yusaku Yamamoto (U. Elec. Comm.) and Kentaro Kinoshita (Tokyo U. Sci.).

The large-scale electronic-state and transport calculations were carried out for flexible organic devices. [1-4] Our parallel electronic structure calculation code ELSES (http://www.elses.jp) was used for 10^8-atom condensed polymers and presents a transport mechanism through the dynamical small polymer networks. Quantum transport was carried out by the wavepacket dynamics for hole. The calculations are realized with *ab initio* based tight-binding formulations.

Figure 1 shows a preliminary result for our machine learning research [3,4]. A classification analysis of the disordered polymer structures with the k-means clustering method, a typical data scientific analysis method. The analysis will be used as a prescreening procedure of real transport simulations. A part of the research was realized by the collaboration with Weichung Wang (National Taiwan U.).

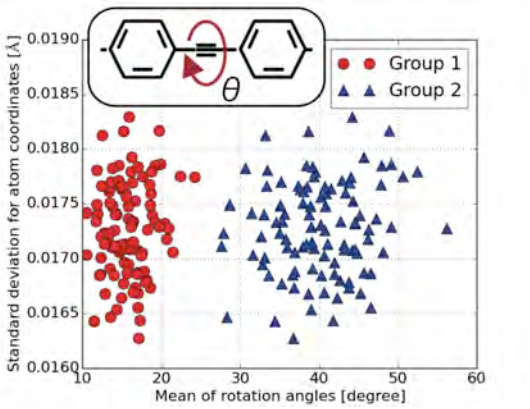

Fig. 1 A data scientific analysis (classification problem) for disordered organic polymer structures.

As mathematical studies, we analyzed convergence properties of the serial block Jacobi method for the symmetric eigenvalue problems and proved its quadratic convergence [5]. We also implemented the block Jacobi method on the system B at ISSP and showed that it is faster than ScaLAPACK under certain conditions. [6]

First principle calculations with experiments were carried out for Resistive Random Access Memory (ReRAM). [7,8] Practical use of ReRAM depends on thorough

understanding of the resistive switching (RS) mechanism in transition metal oxides (TMOs). We discusses what determines resistance values in a Pt/polycrystalline TMOs (NiO, CoO, MgO)/Pt ReRAM structures by using both experiments and first-principles calculations with a first-principles calculation program PHASE/0. Electrical measurements suggest that the RS is caused in the grain boundaries of TMO films. First-principles calculations indicate that slight displacements of atoms with a small energy change of 0.04 eV per atom on the surfaces exposed in the grain boundaries can drastically change conductivities. We newly propose the tiling model, in which grain surfaces are composed by insulating and conductive micro surface structures, and the surface resistances are determined by the tiling patterns. The research was collaborated with Satoru Kishida (Tottori U), Takahiro Yamasaki, and Takahisa Ohno (NIMS).

References

[1] H. Imachi, S. Yokoyama, T. Kaji, Y. Abe, T. Tada, T. Hoshi, 'One-hundred-nm-scale electronic structure and transport calculations of organic polymers on the K computer', AIP Conf. Proc. 1790, 020010, 4pp. (2016)

[2] T. Hoshi, H. Imachi, K. Kumahata, M. Terai, K. Miyamoto, K. Minami and F. Shoji, 'Extremely scalable algorithm for 10^8-atom quantum material simulation on the full system of the K computer', Proc. ScalA16 in SC16, pp.33-40, (2016).

[3] H. Imachi, Y. M. Tsai, T. Hoshi, W. Wang, 'A data scientific research on organic polymer device materials', in *The 19th Asian Workshop on First-Principles Electronic Structure Calculations*, National Chiao Tung University, Hsinchu, Taiwan, 31. Oct.- 2. Nov. (2016).

[4] H. Imachi, 'Numerical methods for large-scale quantum material simulations', D. Thesis, Tottori University, 17. Jan. (2017).

[5] S. Kudo, Y. Yamamoto, M. Becka, M. Vajtersic, 'Performance analysis and optimization of the parallel one-sided block Jacobi SVD algorithm with dynamic ordering and variable blocking', Concurrency and Computation: Practice and Experience, to appear (DOI : 10.1002/cpe.4059)

[6] G. Oksa, Y. Yamamoto, M. Vajtersic, 'Asymptotic quadratic convergence of the serial block-Jacobi EVD algorithm for Hermitian matrices', Numerische Mathematik, to appear (DOI : 10.1007/s00211-016-0863-5).

[7] T. Moriyama, T. Yamasaki, S. Hida, T. Ohno, S. Kishida, and K. Kinoshita, 'Switching mechanism in resistive random access memory by first-principles calculation using practical model based on experimental results', Jpn. J. Appl. Phys., Accepted.

[8] T. Moriyama, T. Yamasaki, T. Ohno, S. Kishida, and K. Kinoshita, 'Resistance given by tiling grain surface with micro surface structures inpolycrystalline metal oxide', J. Appl. Phys. Vol. 120, 215302 (2016)

Search for magnet and spintronics materials based on materials informatics

Tomoki YAMASHITA
Center for Materials Research by Information Integration, National Institute for Materials Science
Sengen, Tsukuba, Ibaraki 305-0047

Sm-Co and Nd-Fe-B intermetallic compounds are known for high-performance rare-earth permanent magnets which are one of the key materials in magnetic and energy conversion devices. For material search of permanent magnets, developments of basic methods with data-driven approaches have been highly desired because of the rapid growth of supercomputer performances. One of difficulties in finding new permanent magnet materials is how to predict the complex crystal structures. For example, the best magnet, $Nd_2Fe_{14}B$, contains 68 atoms in the unit cell. This system is quite difficult to predict the crystal structure because number of configuration explosively increases as atoms increase. In this study, we have developed and investigated methods of crystal structure predictions to overcome those difficulties. First, random search algorithm in combination with structure optimization technique using first-principles calculations was employed. Furthermore, Bayesian optimization method was added to accelerate crystal searches.

Crystal structure prediction simulations were tested for Y_2Co_{17} by using both random search algorithm and Bayesian optimization. In the random search simulations, we randomly generated several hundreds of crystal structures. For the generated structures, total energy calculations and structure optimization were carried out using the density functional theory with the projector-augmented wave method [1], as implemented in the VASP code [2]. We carried out several random search simulations using supercomputer system at ISSP. Total number of calculated structures was several thousands. We checked efficiency of Bayesian optimization by using the structure and energy data set obtained by random search simulations. Our simulations with Bayesian optimization show highly efficient results compared to the random search alogrithm.We succeeded developing a new algorithm for crystal structure prediction.

References

[1] P.E. Blöchl: Phys. Rev. B **50** (1994) 17953.

[2] G. Kresse and J. Furthmüller: Phys. Rev. B **54** (1996) 11169.

Theoretical study on electrode materials for sodium ion batteries

Atsuo YAMADA

Department of Chemical System Engineering,

The University of Tokyo, Hongo, Bunkyo-ku, Tokyo 113-8656

Sodium ion batteries have received much attention in recent years due to its abundance and potential low cost, which may offer large scale applications such as smart grids and electric vehicles. With a purpose of developing electrode materials, we have studied (i) intrinsic electrochemical properties of $Na_2Fe_2Si_2O_7$ and (ii) reaction mechanism of the hard carbon.

A sodium pyrosilicate $Na_2Fe_2Si_2O_7$ is an appealing cathode materials which was successfully synthesized in our group. However, very limited reversible capacity was observed at present. Towards practical utilizations, we applied density functional theory calculations to elucidate the intrinsic bulk properties of $Na_2Fe_2Si_2O_7$ such as volume change, voltage, electronic structure, and charge carrier transport. From our calculations, volumetric change during charging-discharging process, Na-ion migration energy, and polaron migration energy are found to be reasonable for active electrochemical intercalations at room temperature. Therefore, the origin of limited reversible capacity remains to be determined, and further work is necessary to activate this intriguing cathode material.

Hard carbon is one of the most promising anode material for the sodium-ion battery owing to its large reversible capacity. However, the reaction mechanism has not been fully elucidated. We built several models of hard carbon with a graphene sheet that have typical point defects (MV, DV, SW). Then the sodiation and lithiation potential of the alkali adatom on the defective graphene was calculated. As a result, it was found that the adsorption potential of alkali ions was increased to positive values by introduction of defects. In particular, MV and DV enhanced adsorption, and its effects were not dependent on alkali species. Consequently, it was revealed that charge-discharge reaction at high potential of hard carbon is caused by adsorption / desorption of alkali ions to defects.

All the calculations were performed using VASP code. The GGA/PBE functional and PAW method were employed for all the calculations. We used F4cpu, F18acc and F36cpu queues.

Spontaneous Distortion via Quantum-well Induced Ferromagnetism in Pd(100) Ultrathin Films

Shunsuke SAKURAGI,[1] Hiroyuki KAGESHIMA,[2] and Tetsuya SATO[1,*]
[1]*Department of Applied Physics and Physico-Informatics, Keio University, Hiyoshi, Yokohama 223-0061*
[2]*Interdisciplinary Graduate School of Science and Engineering, Shimane University, Nishikawatsu-cho, Matsue 690-8504*

Recently, we found the appearance of ferromagnetism in the ultrathin film of Pd(100) periodically depending on the film thickness [1]. The period was consistent with the first-principles calculation, which predicted the appearance of ferromagnetism based on *d*-electron quantum-well states in Pd(100). From the surface x-ray diffraction experiments, we have shown the appearance of ferromagnetism in Pd(100) films promotes the atomically flat film growth which is accompanied by spontaneous lattice expansion. In order to clarify the origin of the correlation between magnetism and crystal structure, we performed the density functional calculation [2].

The PHASE/0 program using the PAW method to the spin-polarized local density approximation reported was used. The values of lattice constant converged to 3.84 Åfor fcc bulk Pd, and we used this value for film shaped Pd(100). To evaluate the magnetism of Pd(100) ultrathin films, the slab of Vacuum(2 monolayers)/Pd(N monolayers)/Vacuum(3 monolayers), $56 \times 56 \times 1$ k-points, and 36 Ry of cut off energy were used. Based on this, we calculated the difference of total energies between paramagnetic and ferromagnetic states where the spin polarization is fixed to a curtain value in freestanding Pd(100).

Based on the density functional calculation, we discovered that when the ferromagnetism was appeared in Pd(100) ultrathin films due to increase of the density of states near the Fermi energy induced by quantum-well states, Pd films expanded the lattice constant in order to suppress the increase in kinetic energy of electrons accompanied by occurring of the exchange splitting. This finding reveals an effect that the transition metal spontaneously regulates the electronic states; i.e., inverse mechanism of Stoner's theory, in order to stabilize ferromagnetic state. This energy gain due to stabilizing of ferromagnetic state reduces the surface energy of Pd(100) films, and makes the film flat and uniform structure. This mechanism can explain our surface x-ray diffraction experiments, and indicates the existence of closely relationship between magnetism, crystal structure, and quantum-well states which are the specific electronic states of confined electrons in nanoscale films. This finding gives us the key to understanding the origin of ferromagnetism in nano-film shaped metals, and thus, this indicates the possibility of creating a nano-material with a desired magnetism by processing nonmagnetic metals artificially.

References

[1] S. Sakuragi *et al.*: Phys. Rev. B **90** (2014) 054411.

[2] S. Sakuragi, H. Tajiri, H. Kageshima, and T. Sato: arXiv:1612.06216.

Structural analysis of titanium dioxide by first-principles calculation

Kanako YOSHIZAWA

Research Organization for Information Science and Technology,

Kobe, Hyogo 650-0047

Titanium dioxide (TiO_2) has attracted an increasing amount of attention in recent years due to its numerous technological applications. TiO_2 is a widely used photocatalytic material with many potential application in electronics, optoelectronics, and photovoltaics. It is well-known that TiO_2 can lose oxygen, resulting in the formation of both bulk and surface vacancies. Impurity hydrogen (H) and oxygen vacancy (V_O) affect electronic properties of TiO_2 and we study the effect of H doping of it.

Therefore, we pay attention to the effect of H doping of TiO_2, and there are excess electrons accompanying H or V_O. It is known that the electrons can localize at Ti 3d orbitals, forming Ti^{3+} ions [1, 2]. The trapped electrons form small polarons that consist of the electrons coupled to the distortion of the lattice around the Ti^{3+} ions.

We examine the electronic structure of H in rutile TiO_2 by using DFT calculation. We calculated using VASP package [3] on System B and C in ISSP. The large scale calculation was carried in 216-atom supercell with HSE hybrid functional in DFT. The spin density for a localized electron in Ti site is shown in Figure. It is verified that the excess electrons are described as localized small polaron by DFT calculation.

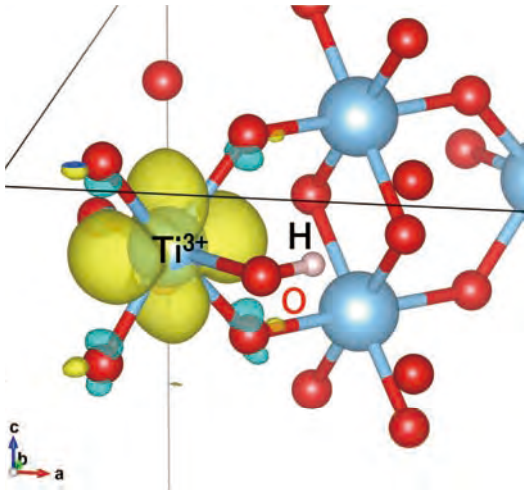

Figure: Spin density of a localized electron (small polaron) in Ti, forming Ti^{3+} ions in rutile TiO_2 by DFT calculation.

References

[1] A. Janotti, C. Franchini, J. B. Varley, G. Kresse, and C.!G. Van de Walle, Phys. Status Solidi RRL **7**, 199 (2013).

[2] F. Filippone, G. Mattioli, P. Alippi, and A. Amore Bonapasta, Phys. Rev. B **80**, 245203 (2009).

[3] http://www.vasp.at.

First-Principles Calculations of Electron and Spin Device Materials

Hiroyoshi MOMIDA, Motoyuki HAMAGUCHI, Hiroshi KATSUMOTO
Institute of Scientific and Industrial Research, Osaka University
8-1 Mihogaoka, Ibaraki, Osaka 567-0047

We have studied electronic properties of future electron and spin device materials using the first-principles method. In the fiscal year 2016, we have mainly investigate piezoelectric properties of wurtzite materials [1] using the supercomputer systems. We have also studied electronic structures of layered topological materials which consist of Bi_2Se_3 and PbSe layers [2]. In this project, the first-principles calculations were performed by using the HiLAPW code. The calculations are based on the density functional theory with the all-electron full-potential linearized augmented plane wave method.

Piezoelectricity of wurtzite materials

We perform the first-principles calculations of the piezoelectric constants of w-$Sc_xAl_{1-x}N$ in all the ranges of x. We find that piezoelectric e constants (e_{33}) of the w-$Sc_xAl_{1-x}N$ materials can be significantly enhanced as x increases from 0 to 0.75. In addition to the e_{33} enhancement, the elastic constant (C_{33}) softening due to the Sc substitution can contribute to the piezoelectric d constant (d_{33}) enhancement in the x ranges up to about 0.75. The wurtzite-type $Sc_xAl_{1-x}N$ materials have been experimentally obtained for x less than about 0.43, and our results predict that wurtzite-type $Sc_xAl_{1-x}N$ with higher x have a strong potential to further enhance the piezoelectric constants. Such higher piezoelectric $Sc_xAl_{1-x}N$ could be experimentally realized if we could stabilize the wurtzite-type phases at the high x range against the cubic-type phases, for example, by doping an additional third element. We also study the element dependences on piezoelectricity in w-$A_{0.5}B_{0.5}N$ (A = Sc, Y, La and B = Al, Ga, In). The result shows that Sc, Y, and La have the strongest effect on the enhancement of piezoelectric d constants in AlN, GaN, and InN, respectively. The calculated results are partly published in the journal [1].

Topological states in layered materials

Recently, interesting electronic structures of $(PbSe)_5(Bi_2Se_3)_6$, which forms a natural heterostructure consisting of a topological insulator and and an ordinary insulator, have been experimentally studied by the angle-resolved photoemission spectroscopy [3]. We have theoretically studied electronic band structures of $(PbSe)_5(Bi_2Se_3)_6$, showing this material can have topological interface states in the bulk [2].

We partially used the system to clarify Li-ion battery reaction mechanism in transition-metal oxide cathodes and spectroscopic properties of circular dichroism in chiral materials, and the computations were partly done by Motoyuki Hamaguchi and Hiroshi Katsumoto in collaboration with Tamio Oguchi.

References

[1] H. Momida, A. Teshigahara, and T. Oguchi: AIP Advances **6** (2016) 065006.

[2] H. Momida *et al.*: in preparation.

[3] K. Nakayama *et al.*: Phys. Rev. Lett. **109** (2012) 236804.

The effect of Cu addition to Nd-Fe-B magnets studied by first-principles calculations

Yasutomi TATETSU

The University of Tokyo, Hongo, Bunkyo, Tokyo 113-0033

Nd-Fe-B sintered magnets are used in various kinds of applications, mostly in motors since they have the largest $(BH)_{max}$ among other permanent magnets. However, the magnetic instability, especially the coercivity decrease at high temperatures, is a critical issue in order to keep its good performance. Controlling the grain boundary phase by annealing processes or doping some elements is the most effective way in terms of improving the coercivity of Nd-Fe-B magnets.

We performed first-principles calculations for the Cu-doped $Nd_2Fe_{14}B/Nd_4O$ systems using a computational code OpenMX [1] in order to understand these electronic and magnetic structures. We chose Nd_4O as the subphase, which existence around the grain boundaries is confirmed by the experimental and theoretical studies [2, 3]. One Cu atom is existing around the interface of the grain-boundary-model structures. By calculating the formation energies of these model structures, we found that the models with Cu existing at the interstitial space and Fe site at the interface are energetically stable compared to the non-Cu-doped model structure. Especially, in the model with Cu at the Fe site at the interface, the magnetic anisotropy K_1 of Nd near Cu at the interface is improved due to Cu, which is in good agreement with experimental results (see Figure) [4]. We conclude that adding Cu to Nd-Fe-B magnets works effectively in terms of improving the magnetic anisotropy K_1 of Nd atoms at the interface of Nd-Fe-B magnets since the magnetic anisotropy of Nd is strongly related to the coercivity of Nd-Fe-B magnets [5].

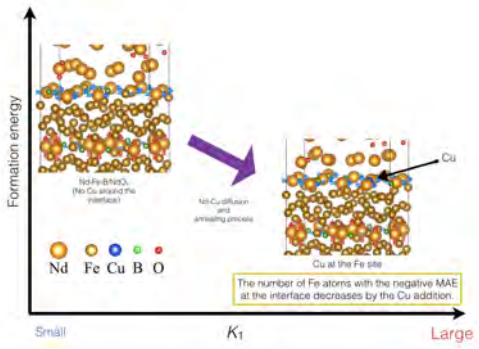

Figure: Schematic image of the relationship between the formation energy and the magnetic anisotropy of Nd at the interface based on our theoretical study.

References

[1] http://www.openmx-square.org

[2] T. Fukagawa and S. Hirosawa, J. Appl. Phys. **104**, 013911 (2008).

[3] H. Misawa, Dr. Thesis, Faculty of Science, The University of Tokyo, Tokyo, (2015).

[4] H. Sepehri-Amin *et al*., Acta Mater. **60**, 819 (2012).

[5] Y. Tatetsu, S. Tsuneyuki, and Y. Gohda, Phys. Rev. Appl. **6**, 064029 (2016).

Development and application of the large-scale *GW* calculation code

Ikutaro HAMADA

Center for Green Research on Energy and Environment Materials ,

National Institute for Materials Science, 1-1 Namiki, Tsukuba 305-0044

The electronic structure method based on density functional theory (DFT) has been used to study a wide range of materials, including bulk insulators, semiconductors, metals, and interfaces, and proven accurate and useful for in the researches of chemistry, physics, and materials science. However, DFT within the local density and generalized gradient approximation is known to suffer from sevral drawbacks, such as the band-gap underestimation. To get rid of the shortcomings of semilocal DFT, many-body perturbation theory within the GW approximation has been used to calculate more accurate electronic structure. Despite the theoretical and methodological development, the applicability of the GW method is limited, because of its complexity.

To overcome the limitation and apply the GW method to calculate accurate electronic structure of large-scale systems such as nanoparticles, aqueous solutions, and interfaces, an efficient method has been developed: The method uses the eigenpotential of static dielectric matrix as an efficient basis set for the polarizability, and the Lanczos method is used to compute the frequency dependent polarizability of Green's function. The latter allows one to perform efficient frequency integration to calculate the electron self-energy, and to avoid the plasmon-pole approximation. The above algorithms are implemented in the WEST code [1].

In this work, we extend the applicability of the WEST code. We have introduced the spin-orbit coupling to WEST in a nonperturbative way, and accurate calculations of electronic properties of molecules and materials containing heavy elements are possible [2]. We also introduced general k-points WEST for efficient and accurate calculations of solids. A systematic benchmark calculations are under progress [3].

References

[1] M. Govoni and G. Galli, J. Chem. Theory Comput. 11, 2680-2696 (2016).

[2] P. Scherpelz, M. Govoni, I. Hamada, and G. Galli, J. Chem. Theory Comput. 12, 3523 (2016).

[3] I. Hamada, M. Govoni, and G. Galli (in preparation)

Ab initio molecular dynamics study of static structure of glasses

Akihide KOURA

Student Affairs Department,

Kumamoto University, Kurokami, Kumamoto, Kumamoto 860-8555

We have studied static structure, electronic and dynamic properties of liquid, crystal, and glassy systems. In this project, we focused on the static structure of network forming glasses under pressure by using *ab initio* molecular dynamics simulations.

We have studied the static structure of ternary silver germanium triselenide ($Ag_x(GeSe_3)_{1-x}$) glass (x = 0.15, 0.33, 0.5). At $x \geq 0.33$, these glasses show properties of super ionic conductor, in which silver atoms migrate inside the $GeSe_3$ network glass. It is suggested experimentally that silver atoms make chain-like fragments at the concentration $x = 0.5$ [1], however, stable sites of silver atoms are still unclear. Our simulations confirmed that silver atoms replace germanium atoms. Furthermore, three-body bond angle distributions for Ge-Se-A (A=Ge, Ag) and Se-A-Se are wider than those without silver atoms. Ag-Ag fragments consisting of weak covalent bonds are confirmed not only at the concentration $x = 0.5$ but also x = 0.33 and 0.15. However, in the present simulation, only 6 silver atoms exist in the system at x = 0.15, so we need to enlarge the system to remove the problem of size dependence.

We have also studied the pressure dependence of the static structure of liquid GeTe [2]. The pressure and temperature ranges are from 0 to 250 GPa and 1000 to 4000 K, respectively. Liquid GeTe has a semiconducting property at ambient condition. With increasing pressure, the semiconductor-metallic transition occurs at approximately 12 GPa. At ambient and low pressure range up to 12 GPa, there exists Peierls-type distortion, where atoms are threefold-coordinated, even in the liquid state. However, the distortion disappears at about 12 GPa, and coordination numbers (CN) increases with increasing pressure. Finally, CN reaches 13.7 at approximately 250 GPa, which is quite similar to that of CsCl-type bcc crystalline state with taking the second neighbor into account.

References

[1] K. Ohara, *et al.*: J. Phys. Soc. Jpn. **79** (2010) Suppl. A, 141.

[2] A. Koura and F. Shimojo: submitted to LAM-16 conference proceedings.

First-Principles Molecular Dynamics Study of Biomolecule Synthesis Induced by Meteorite Impacts on Primitive Ocean

Kohei Shimamura

Graduate School of System Informatics,

Kobe University, 1-1 Rokkodai, Nada-ku, Kobe 657-8501

Whereas recent experimental simulations suggested that meteorite impacts on primitive ocean could provide a large amount of various biomolecules such as proteinogenic amino acids, the production process has not been well understood. To address this issue from the atomistic viewpoint, we have performed first-principles molecular dynamics in combination with multi-scale shock technique (MSST) simulations, where the MSST method was used to reproduce the behavior of moving atoms in shock waves. Since impact velocities of meteorites generally exceed the sound speed, a shock waves are generated.

In this study, in particular, we focused on investigation of how the production of ammonia, which is important nitrogen source for most biomolecules, is produced by the meteorite impacts [1-2]. We firstly prepared a calculation model consisting of nitrogen, water, and metallic iron contained in the meteorite, which imitated the environment of the early Earth. We applied a shock wave to this model to reproduce a meteorite impact and investigate the detailed production reaction pathways using population analysis.

We found that meteorite impacts of meteorites could drive three ammonia production mechanisms. The two are associative and dissociative mechanisms of nitorgen on the iron surface. The former and the latter are the mechanisms as seen in the catalysis of nitrogenase enzyme and in the Haber-Bosch process, respectively, both of which are currently supplying a large amount of ammonia to life. Meanwhile, in the remaining one mechanism, ammonia was produced away from the iron surface by reduction of nitrogen through the formation of hydrazine. Hydrazine has been regarded as an important precursor in the electrocatalytic synthesis of ammonia.

The emergence of such multiple production mechanisms capable of providing a large amount of ammonia induced by the meteorite impacts would have played a key role in the origin of life on Earth.

References

[1] K. Shimamura, F. Shimojo, A. Nakano, and S. Tanaka: Sci. Rep. **6** (2016) 38953.

[2] K. Shimamura, F. Shimojo, A. Nakano, and S. Tanaka: Phys. Chem. Chem. Phys. accepted.

Search and realization of novel electronic properties of solid surfaces and small particles

Takeshi INAOKA
Department of Physics and Earth Sciences, Faculty of Science, University of the Ryukyus, 1 Senbaru, Nishihara, Okinawa 903-0213

In first-principles calculations of semiconductor surfaces, we usually assume a periodic array of slabs, and describe the electronic structure in terms of a plane-wave basis set. Recent remarkable progress of supercomputers has realized those large-scale slab calculations which can adequately treat surface-resonance states extending deeply into the substrate. On the other hand, strain engineering is expected to achieve higher operation performance of Si devices through modification of the band structure, since the conventional downsizing approach is showing its limitations. Using the program package 'Vienna Ab initio Simulation Package' (VASP) [1,2], we analyzed the strain effect on the electronic structure of the Si(001)-2x1 surface.

Presence of a dynamic dipole moment in the gap between the scanning tunneling microscope (STM) tip and the substrate produces a giant dynamic dipole moment through formation of the localized surface plasmons (LSPLs). It is reported that vibration-induced structures appear around the cutoff energy in the light-emission spectra from this enhanced dipole. Assuming a dynamic dipole moment in the STM gap, we examined the effect of phonon vibration of an admolecule on the LSPLs, and consequently on the enhanced total dipole moment.

(1) Compressive strain effect on the electronic structure of the Si(001)-2x1 surface [3]

Last year, we investigated the biaxial strain effect on the electronic structure of the Si(001)-2x1 surface. This year, we have examined the effect of uniaxial compressive strain in the $[\bar{1}10]$ (fundamental period) direction and in the [110] (twofold period) direction. We assumed a 30 atomic-layer slab, and terminated dangling bonds on the other side by hydrogen atoms. We considered normal tensility and internal strain in structure optimization under the normal-stress free condition.

As an example of the results, figure 1 shows the valence-band dispersion on the $\bar{\Gamma}-\bar{J}'$ line of the surface Brillouin zone when 2% uniaxial compression is applied in the $[\bar{1}10]$ direction. The $\bar{\Gamma}-\bar{J}'$ line corresponds to the compression direction. In this strain direction, a small-effective-mass band protrudes at the valence-band top. The dispersion of this protruding band agrees with that of the bulk band when the same strain is applied. This indicates that this band originates from the valence band of the semi-infinite system. The red circles represent the surface or surface-resonance states which can be identified

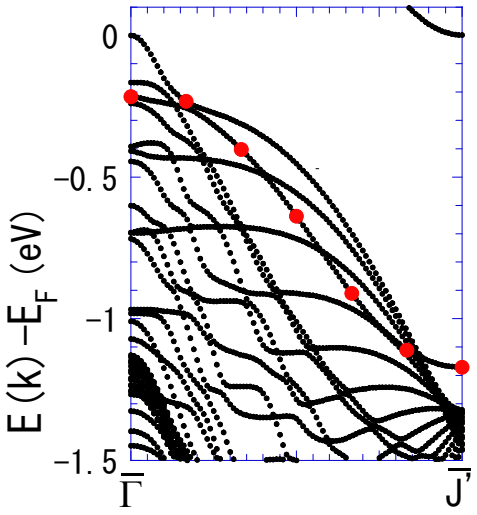

Fig. 1 Valence-band dispersion of the Si(001)-2x1 surface on the $\bar{\Gamma}-\bar{J}'$ line of the surface Brillouin zone under 2% uniaxial compressive strain in the $[\bar{1}10]$ direction. The red circles represent surface or surface-resonance states.

by analyzing the charge-density distribution of each state. These states are found to penetrate into the valence band of the semi-infinite system except near the $\bar{J}$' point. The protruding dispersion in the strain direction is the same for uniaxial compression in the [110] direction.

In each of these strain directions, the wave function at the top of this protruding band is connected closely in the strain direction, and this strong coupling is correlated with the energy increase of this valence-top state due to the compression. When the uniaxial compression is applied in the axis direction of the asymmetric surface dimer, buckling in the dimer becomes stable, which leads to the energy lowering of the surface (resonance) states relative to the valence band of the semi-infinite system.

(2) STM-enhanced dynamic dipole moments coupled with adsorbate vibration at substrate or tip surfaces [4]

We investigated the effect of phonon vibration of an admolecule in the STM gap on the enhanced total dipole for three models. In the model A, we considered the vibration of the dynamic point dipole near the substrate surface. In the models B and C, we assumed that the dipole arises from a tunneling current between an admolecule and the substrate or tip surface. In the model B (C), the admolecule is at the substrate (tip) surface. In any of the three models, the phonon vibration of an admolecule in the gap produces a series of the resonance modes, each of which is shifted in energy from the corresponding mode involving no phonon by a multiple of the phonon energy $\hbar\omega_p$. If we pay attention to the intensity ratio of the phonon-shift resonance to that of the no-shift resonance as an indicator of detectability of the shifted resonance, the phonon effect is most remarkable in the model C, because the vibration of the admolecule is closest to the tip.

Presence of a dynamic dipole p_0 of angular frequency ω in the gap gives rise to an enhanced dipole $p_0 F_k(\omega)$ with angular frequency $\omega + k\omega_p$ (k=0, ±1, ±2) including phonon shifts. Figure 2 exhibits the ω dependence of $|F_k(\omega)|$ in the model C for k=0 and ±1 when the tip and substrate are made of silver. The gap distance D, the tip curvature radius R, the height of the admolecule position h_0, the phonon energy $\hbar\omega_p$, and the phonon vibration amplitude a_p are taken to be D=10 Å, R=200 Å, h_0=7 Å, $\hbar\omega_p$=0.1 eV, and a_p =1 Å, respectively. The dynamic dipole in the gap induces the LSPLs, which leads to a strongly enhanced total dipole. The resonance-peak energy of k=1 (-1) is lower than (higher) than the corresponding peak energy of k=0 by $\hbar\omega_p$. The resonance intensity of the phonon-shifted peak is considerable in this model, because the phonon vibration of the admolecule is close to the tip.

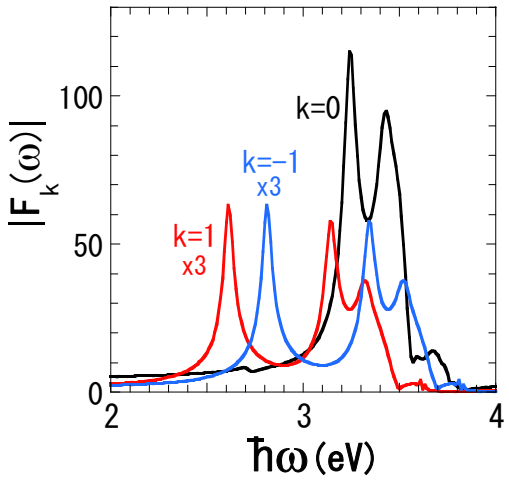

Fig. 2 ω dependence of the dipole enhancement $|F_k(\omega)|$ for k=0 and ±1 in the model C where an admolecule at the tip surface vibrates with $\hbar\omega_p$=0.1 eV.

References

[1] G. Kresse and J. Hafner: Phys. Rev. B **47** (1993) 558-561.
[2] G. Kresse and J. Furthmüller: Comput. Mat. Sci. **6** (1996) 15-50.
[3] T. Inaoka, S. N. Takeda, and T. Shirasawa: to be prepared.
[4] T. Inaoka and Y. Uehara: submitted to J. Appl. Phys.

Hybrid ab initio QM/MM calculations of biological systems

Masaru TATENO

Graduate School of Life Science, University of Hyogo

To theoretically analyze the electronic structures that are relevant to the functional mechanisms of crucial biological macromolecular systems, we employed *ab initio* quantum mechanics (QM) calculations that are coupled to molecular mechanics (MM) classical calculations, with respect to the entire structures of the systems solvated with the explicit water. In our hybrid *ab initio* QM/MM calculations, our interface program is employed to connect highly-parallelized engines, gamess and amber, for the QM and MM calculations, respectively.

This FY, we analyzed the detailed electronic structural changes in the enzymatic reaction of a novel biological catalyst, and the analysis revealed the dynamical properties in the electronic structure. Interestingly, our findings are likely to be characteristic to biological macromolecular catalytic systems.

Here, our previous works should be introduced briefly: Our previous hybrid *ab initio* QM/MM MD simulations of leucyl-tRNA synthetase (LeuRS) complexed with the cognate tRNA that was mis-aminoacylated (threonyl) revealed that unexpectedly, the reaction of an "RNA-protein complex" is a "ribozymal" (RNA enzyme) self-cleavage reaction (not via a "protein enzyme"), but one in which the protein also plays a critical role. This was a novel catalyst, which operates via cooperation of the "RNA enzyme" (the mis-aminoacylated threonyl-$tRNA^{Leu}$) and protein (LeuRS), and thus was referred to as "hybrid ribozyme/protein catalyst".

In the present study, we investigated the dynamical changes that occur in the electronic structure of the catalytic site during the reaction, and observe dramatic rearrangements of functional importance in the molecular orbitals (MOs). The following two changes are particularly noteworthy.

One concerns the MO that contains a contribution from the nucleophile (a water molecule). It initially has a much lower energy than the HOMO, but it is activated as the reaction proceeds until it becomes the reactive HOMO. The other involves the reactive LUMO of anti-bonding character that emerges in the bond rupture that leads to products.

We term these processes dynamical induction of the reactive HOMO (**DIRH**) and LUMO (**DIRL**), respectively. In the complex environment of a biological macromolecule, the reactive HOMO and LUMO are likely to be hidden, and so these systems must implement DIRH and DIRL mechanisms that expose them. Thus, we conjecture that this is a characteristic feature that is specific to biological systems.

LeuRS is also a member of an enzyme family composed of aminoacyl-tRNA synthet-

ases (aaRSs). Eukaryotic aaRSs form a huge supercomplex composed of 20 types of aaRSs, each of which is corresponding to each of 20 amino acids, and thereby constitute a complicated reaction network. In general, most biological systems involve such biochemical reaction networks.

Analysis of such biochemical reaction networks has been a crucial target in various interdisciplinary fields, such as biophysics, complex systems, biochemistry, cell biology, etc., for a long time. Notably, theoretical analyses as well as experimental approaches have recently been important increasingly as a crucial issue of systems biology and bioinformatics, to understand the relationships between cellular responses/phenotypes and molecular mechanisms in detail.

This FY, we also analyzed the kinetics of biochemical reaction network systems. For this aim, we first decomposed cellular biochemical reaction cascades into building blocks, and investigated the mathematical features (e.g. the stability of the systems) of such elementary reaction units and their combinations, which are actually involved in real signal transduction cascades.

More specifically, in our present analysis, we focused on effects of the presence and absence of a positive feedback loop (PFL) that is combined with the above- mentioned elementary reaction cycles, by theoretically exploring the mathematical stability. As a consequence, we have discovered all the conceivable transitions, including the transition from the bistability (b) to the monostability (m) (i.e., the b→m transition), as well as the m→b transition, that were induced by the PFL, depending on the parameter values.

Since in the previous works, the PFL reportedly induced only the latter, i.e., the m→b transition, this analysis is the first report to address the b→m transition induced by the PFL. Employing the resultant data, we also analyzed the detailed mechanisms of the b→m transition. As a result, the origin of the b→m transition was identified to be the significantly lower Michaelis-Menten constant in the PFL.

Moreover, based on the resultant data, we propose possible biological systems (e.g. iPS cell) where this type of transition may be induced, and discuss functional roles of the b→m transition, based on the mechanism that we theoretically elucidated. In this manner, this analysis also provides a new perspective in systems biology and complex systems, and a novel viewpoint to understand experimental data concerning the signal transduction network cascades, etc.

Further achievements of this FY are also cited as [3-5].

References

[1] J. Kang, H. Kino, M. J. Field, and M. Tateno: *J. Phys. Soc. Jpn*. **86** (2017) 044801.

[2] J. Kang and M. Tateno: *J. Phys. Soc. Jpn*. in press.

[3] A. Sugimoto, J. Kang, T. Sumi, and M. Tateno: *J. Phys. Soc. Jpn*. in press.

[4] J. Kang, K. Yamasaki, K. Sano, K. Tsutsui, K. M. Tsutsui, and M. Tateno: *J. Phys. Soc. Jpn*. **86** (2017) 014802.

[5] S. Shimada, K. Shinzawa‐Itoh, J. Baba, S. Aoe, A. Shimada, E. Yamashita, J. Kang, M. Tateno, S. Yoshikawa and T. Tsukihara: *EMBO J.*, **86** (2017) 291-300.

Novel Structures of Liquid Metal under Ultrahigh Pressures: ab initio Molecular-Dynamics Simulations

Satoshi OHMURA

Research Center for Condensed Matter Physics,,

Hiroshima Institute of Technology Saeki-ku, Hiroshima, 731-5143

We have studied static and dynamical properties of liquid metal and liquid semiconductor under extreme conditions (high pressure and high temperature) by *ab initio* molecular dynamics (MD) simulations. This year, we focused on liquid sodium under ultrahigh pressure and pressure induced metallization of liquid sulfur.

In the simulation, the electronic state was calculated using the projected augmented wave (PAW) method within the framework of density functional theory (DFT), in which the generalized gradient approximation was used.

From this simulation, it was found that liquid Na has asymmetric structure under ultra-high pressure at about a few hundred gigapascal. For liquid sodium, previous theoretical study suggested that pressure induced structural and electronic transition occur, analogous those observed in solid sodium. The relationship between this transition and the new structure observed in this study is currently under investigation.

We also performed *ab initio* MD simulation for liquid sulfur to investigate mechanisms of pressure induced metallization in liquid semiconductor. It is well known that, at a temperature near the melting point, liquid sulfur is molecular liquid which consists of eight membered-ring molecules. When pressure increases, the ring breaks and forms chain and finally metallization occurs by breaking the chain. In this study, our *ab initio* MD simulations clarified the details of mechanism of the ring breakage and metallization under high pressure.

In addition to these liquids, we investigated charge dynamics in I-containing organic molecules under X-ray free electron laser (X-FEL) irradiation by a nonadiabatic quantum-mechanical MD simulation that incorporates electronic transitions through a surface-hopping approach. From the result of this simulation, it was found that holes generated in I by the X-FEL irradiation transfer from the iodine to the molecular counterpart in ~5 fs [1].

References

[1] K. Nagaya, K. Motomura, E. Kukk, Y. Takahashi, K. Yamazaki, S. Ohmura *et al.*, *Farad, discuss*. **194** (2016) 53

Exploring active sites of "Real" model catalysis via first principle calculations

Wataru Mizukami
Department of Advanced Materials Science and Engineering, Faculty of Engineering Sciences
Kyushu University, 6-1 Kasuga-Park, Fukuoka, 816-8580, Japan

Bimetallic nanoparticles have been attracted a lot of attention as potentially tunable catalysts such as for exhaust emission control or fuel cells. This year we studied electronic structures of bimetallic nanoparticles consisting of Pt and Rh/Pd using *ab initio* density functional theory (DFT). We employed the Vienna Ab initio Simulation Package (VASP) version 5.4.1 for DFT calculations, where it was vital to utilize parallel computing with more than hundreds of cores for the description of a nanoparticle whose diameter exceeds 2.5 nm. Three kinds of bimetallic structures, i.e., core-shell, random-alloy, and core-randomly-alloyed-shell structures, were considered in this study. The d-band centers, which are an index of the oxygen reduction reaction catalytic activity, were estimated from their density of states. We observed that the d-band center at the outermost layer of bimetallic core-shell nanoparticles quickly converged to that of pure monometallic's by increasing the number of shell atoms. We are currently constructing Behler-Parrinello neural-network potentials [1] for the bimetallic nanoparticles using the data obtained this year by Atomistic Machine-learning Package (AMP) of Prof. Andrew Peterson and his coworkers at Brown University[2]. We expect that the force fields will enable us to estimate of vibrational entropy contributions to the stability of those nanoparticles, and to model more realistic structures.

Furthermore, we worked on refining a protocol for finding a transition state (TS) structure on a metal surface. Though tremendous efforts have been devoted to develop the TS structure optimization techniques in first principle simulations, still there is considerable room for improvement; a robust and computationally efficient method for locating TS is highly desirable to investigate chemical reactions on the surface of a large nanoparticle. Here we focused on a three-step strategy which combines Nudged Elastic Band (NEB), and Climbing-Image-NEB (CI-NEB) and the dimer method, examining various initial vectors for the dimer method. The VTST tools of Henkelman's group were used with VASP for NEB, CI-NEB and the dimer method. The calculations were performed on the GPGPU nodes of the ISSP system B. We employed eight surface reactions on Pt(100) surface [3] as a benchmark set to see the effects of the initial modes. We found that our improved initial vector reduced the computational costs for the dimer method by 17% on average.

References

[1] J. Behler and M. Parrinello: Phys. Rev. Lett. **98** (2007) 146401.

[2] A. Khorshidi and P.A. Peterson: Comput. Phys. Commun. **207** (2016) 310.

[3] A. Nikodem, A.V. Matveev, B.X. Zheng, and N. Rösch: J. Chem. Theory Comput. **9** (2012) 588.

First-Principles Study on New Group-IV Semiconductor Alloys

Yuki NAGAE and Masashi KUROSAWA

Graduate School of Engineering, Nagoya University,

Furo-cho, Chikusa-ku, Nagoya 464-8603

Group-IV semiconductor alloys have been one of the promising materials for optoelectronic applications of intra- and interchip optical wirings in silicon-based high-performance large-scale integrated circuits. Si-Sn binary alloy ($Si_{1-x}Sn_x$) is an interesting material since its energy bandgap (E_g) is theoretically expected to correspond to a wavelength (1550 nm; E_g=0.8 eV) that is preferable for optical communication applications [1]. However, the formation of high-Sn-content $Si_{1-x}Sn_x$ alloy is still a great challenge owing to the low thermal equilibrium solubility limit of Sn atoms in Si bulk (~0.1%) [2]. Recently, we have experimentally achieved the formation of polycrystalline $Si_{1-x}Sn_x$ (poly-$Si_{1-x}Sn_x$) and epitaxially grown $Si_{1-x}Sn_x$ (epi-$Si_{1-x}Sn_x$) layers on insulators with a Sn content as high as 40% [3, 4]. On the other hand, some theoretical calculations have been examined for predicting the energy band structure of $Si_{1-x}Sn_x$. These studies mainly investigated the threshold Sn content causing indirect-direct crossover, which is expected to be 31–55% [5–9]. To design the energy band alignment needed to realize multi-quantum-well (MQW) structures composed of $Si_{1-x}Sn_x$ layers with various Sn contents, the investigation of not only the E_g of $Si_{1-x}Sn_x$ alloy but also the valence and conduction band offsets is important to the design of both electron and hole confinement structures for enhancing carrier recombination. Ranjan and Das [10] and Menéndez and Kouvetakis [11] used a regression model based on the elastic theory to predict the valence band offset (VBO) of strained $Ge_{1-x-y}Si_xSn_y$ using the referenced deformation potential.

In this work, we performed density functional theory (DFT) calculation to predict the VBOs of $Si_{1-x}Sn_x$ with various Sn contents while considering the atomic displacement and configuration with Sn atomic incorporation into Si. We theoretically investigated the VBO of $Si_{1-x}Sn_x$ only by the first-principles calculation of the electronic properties of $Si_{1-x}Sn_x$. In order to examine the consistency of our theoretical prediction, we compare our theoretical data with some experimental data [3, 4] and conventional results of $Si_{1-x}Sn_x$.

We investigated the energy band offset of $Si_{1-x}Sn_x$ alloy and compared it with conventional theoretical estimation and experimental results. By estimating the CNL of each $Si_{1-x}Sn_x$ alloy, we could compare it with the VBO of $Si_{1-x}Sn_x$ alloys with different Sn contents (Fig. 1). As a result, we estimated the bowing tendency of the VBO of $Si_{1-x}Sn_x$ due to the effect of the variation in atomic configuration on the electronic state of $Si_{1-x}Sn_x$; we estimated a bowing parameter of

1.15±0.02 eV. The obtained Sn content dependence of VBO showed a similar tendency to the experimental results of $Si_{1-x}Sn_x$ with Sn content ranging between 0 and 40%, which cannot be ignored for designing band alignment. By estimating the energy band offset using calculations of E-***k*** dispersion and the VBO, we could estimate the dependences of the VBM and CBM in the entire Sn content range not only in the low-Sn-content region; we could also find the possibility of making type-I MQW with a suitable E_g for optoelectronic applications.

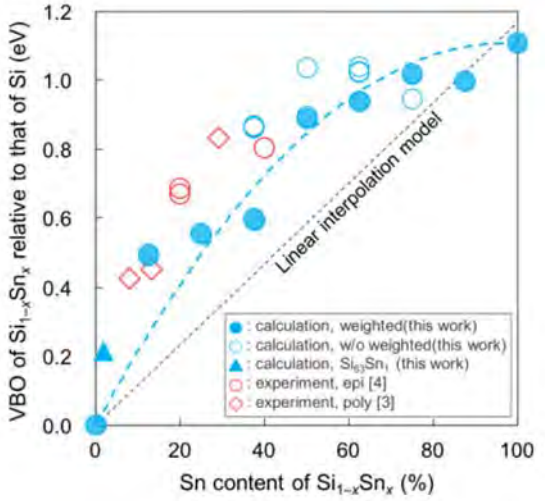

Fig.1: VBO of $Si_{1-x}Sn_x$ relative to the VBM of Si. The closed blue circles are calculation results weighted by the formation probability of each $Si_{1-x}Sn_x$. The open blue circles represent all atomic configurations of $Si_{1-x}Sn_x$ (not weighted). The red circles and diamonds correspond to experimental values of epi-$Si_{1-x}Sn_x$ [4] and poly-$Si_{1-x}Sn_x$ [3], respectively. The values estimated with the interpolation model by Sun [12] are indicated as reference. The closed blue triangle is for calculated $Si_{63}Sn_1$ as reference in this work.

References

[1] P. Moontragoon, R. A. Soref, and Z. Ikonic, J. Appl. Phys. **112**, 073106 (2012).

[2] T. B. Massalski, in Binary Alloy Phase Diagrams, ed. J. L. Murray, L. H. Bennet, and H. Baker (American Society for Metals, Metals Park, OH, 1986).

[3] M. Kurosawa, M. Kato, T. Yamaha, N. Taoka, O. Nakatsuka, and S. Zaima, Appl. Phys. Lett. **106**, 171908 (2015).

[4] M. Kato, M. Kurosawa, T. Yamaha, N. Taoka, O. Nakatsuka, and S. Zaima, presented at 9th Int. Conf. Silicon Epitaxy and Heterostructures (ICSI 9), 2015.

[5] R. A. Soref and C. H. Perry, J. Appl. Phys. **69**, 539 (1991).

[6] J. Tolle, A. V. G. Chizmeshya, Y. Y. Fang, J. Kouvetakis, V. R. D'Costa, C. W. Hu, J. Menéndez, and I. S. T. Tsong, Appl. Phys. Lett. **89**, 231924 (2006).

[7] P. Moontragoon, Z. Ikonic, and P. Harrison, Semicond. Sci. Technol. **22**, 742 (2007).

[8] N. Amrane and M. Benkraouda, Am. J. Mater. Sci. Eng. **1**, 12 (2013).

[9] Y. Nagae, M. Kurosawa, S. Shibayama, M. Araidai, M. Sakashita, O. Nakatsuka, K. Shiraishi, and S. Zaima, Jpn. J. Appl. Phys. **55**, 08PE04 (2016).

[10] R. Ranjan and M. K. Das, Opt. Quantum Electron, **48**, 201 (2016).

[11] J. Menéndez and J. Kouvetakis, Appl. Phys. Lett. **85**, 7 (2004).

[12] G. Sun, R. A. Soref, and H. H. Cheng, J. Appl. Phys. **108**, 033107 (2010).

[13] Y. Nagae, M. Kurosawa, M. Araidai, O. Nakatsuka, K. Shiraishi, and S. Zaima, Jpn. J. Appl. Phys. **56**, 04CR10 (2017).

Study of Charge-trapping Site of High Performance Polymer Electret Material

Seonwoo KIM and Yuji SUZUKI

The University of Tokyo, 7-3-1 Hongo, Bunkyo-ku, Tokyo 113-8656

Electret is a dielectric with quasi-permanent charge, and it can generate electrostatic field without additional voltage supply. Electret energy harvester have electrodes covered with electret material. External vibration causes relative movement of electrodes, leads electrons to flow through load circuit connected to electrodes. Enhancing electret's performance and understanding alignment behavior of anisotropic dielectric fluid [1] are considered to be promising method to improve power output of electret energy harvester. In this report, the authors portrait on attempt to develop high-performance electret material with analytical approach.

Electret's performance can be evaluated by its characteristics such as charge density, long-term stability, and dielectric breakdown voltage. Even electrets materials satisfying these respects were reported within these years [2], theoretical model to estimate / evaluate performance of electret material is not yet developed. In this research, as a first step, electron trapping site of polymer electret has been studied.

Amorphous polymer CYTOP (Asahi Glass Co., Ltd) is studied with ab-initio computational software package NWChem [3]. Basis set of 6-31G* was used to express effect of polarization of fluorine. B3LYP density functional is used to solve the Schrodinger equation. Figure 1. shows image of CYTOP monomer. As an early step, CTL-A and CTL-S is studied. Oligomer systems are made with 4 CYTOP monomers, combined with different end-group (COOH for CTL-A, CF_3 for CTL-S). After pre-process of molecular dynamic rough geometry optimization is made, the geometry of the system is precisely optimized with ab-initio method. After geometry optimization, the energy of systems is calculated before/after charge is trapped. The calculation is

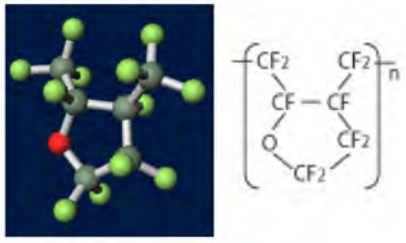

Fig. 1. CYTOP monomer

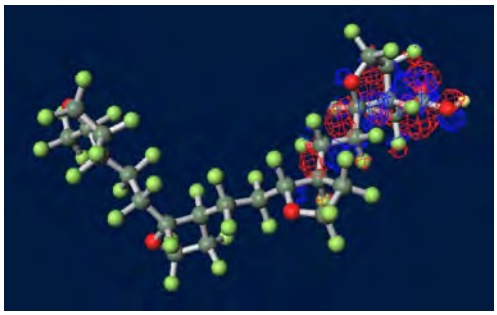

Fig. 2. Localization of trapped electron near carboxyl acid (CTL-A)

performed with SGI ICE XA ISSP system B F4cpu nodes. Every calculation was held with 4 nodes. In case of CTL-A, the calculation costs of geometry optimization are 02:46:16(Wall time), 66:18:13(CPU time). For energy calculation, 0:29:31(Wall time), 11:43:36(CPU time).

With calculated orbital energy, site of trapped charge is visualized. Fig. 2. shows the case of CTL-A. Charge concentration near carboxyl end is significant. In the case of CTL-S, the localization tendency was not shown.

References

[1] K. Kittipaisalsilpa et al.: 29th IEEE Int. Conf. Micro Electro Mechanical Systems (MEMS'16), Shanghai, pp. 37-40 (2016)

[2] K. Kashiwagi et al.: J. Micromech. Microeng. **21** (2011) 125016.

[3] M. Valiev et al.: Comput. Phys. Commun. **181** (2010) 147.

Magnetization Processes Based on Magnetic Dipole Moments

Shuji OBATA
School of Science & Engineering, Tokyo Denki University
Ishizaka, Hatoyama, Hiki, Saitama 350-0394, Japan

The electronic binding energies J_{ij} of 3d electrons in transition metals are induced from the tight binding interactions of the directed magnetic moments $\boldsymbol{\mu}_i$ bonded in the Hunts rule. These 3d and 4s electrons construct eigenstates in external field environments. The magnetization processes are calculated by use of the Hamiltonian

$$\hat{H} = \sum_{i \le j} J_{ij} \hat{\boldsymbol{\mu}}_i \cdot \hat{\boldsymbol{\mu}}_j + \sum_{i \le j} W_{ij} + \sum_j \boldsymbol{\mu}_j \cdot \boldsymbol{H} \qquad (1)$$

including magnetic dipole moment interactions composed of classical-spin magnetic fields

$$W_{ij} = \frac{1}{4\pi\mu_0 d_{ij}^3}\{(\boldsymbol{\mu}_i \cdot \boldsymbol{\mu}_j) - 3(\boldsymbol{\mu}_i \cdot \boldsymbol{e}_{ij})(\boldsymbol{\mu}_j \cdot \boldsymbol{e}_{ij})\}. \qquad (2)$$

The third term is magnetization energy in the external field $\boldsymbol{H}$. Distance vector is set as $\boldsymbol{d}_{ij}=\boldsymbol{e}_{ij}d_{ij}$ between the dipole moments at i and j. The static field energies J_{ij} do not affect to the hysteresis energy transitions for $\boldsymbol{H}$. Thus in this study, magnetization processes are simulated in a Fe3O4 doughnut film using the Hamiltonian

$$\hat{H} = \sum_{i \le j} W_{ij} + \sum_j \boldsymbol{\mu}_j \cdot \boldsymbol{H}. \qquad (3)$$

This energy system produces the domain structures, the magnetization curves and the Barkhausen effects, which fairly coincide with the experimental data. The dipole moment freedom is tentatively selected to 26 directions to compose the energy minimum structures.[1][2]

The Fe_3O_4 hysteresis curve is shown in Fig.1, where H_C coincides with experimental data. At the external field $\mu_0 H$=-0.06T marked in Fig.1 as ○, the domain structures by $\boldsymbol{\mu}_i$. $\boldsymbol{H}$ are drawn in Fig.2, where the total energy map by Eq.(3) is drawn in Fig.3 as -3.0×10^{-23} J: dark blue ~ 3.0×10^{-23} J: read. In these simulated results, diagonal zig-zag domain walls are not observed as in experimental data. This miss match indicates the necessity of molecular spin states obtained using the interactions J_{ij} using Eq. (1).

In the ISSP system, the Fortran programs of the nano-Fe_3O_4 magnetizations are executed by about 500 line programing. The used times are about 18 hours using a large scale PC system for drawing the Fig.1~3. The programing for many PC cluster system are developing now.

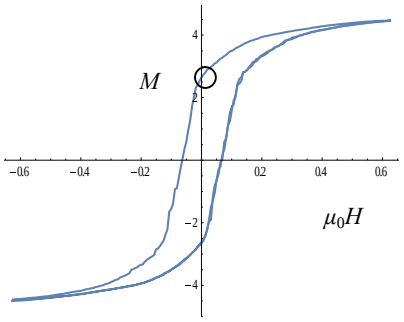

Fig.1. Fe_3O_4 hysteresis curve of a thin film ring : R=16,r=4, y=3 lattices.

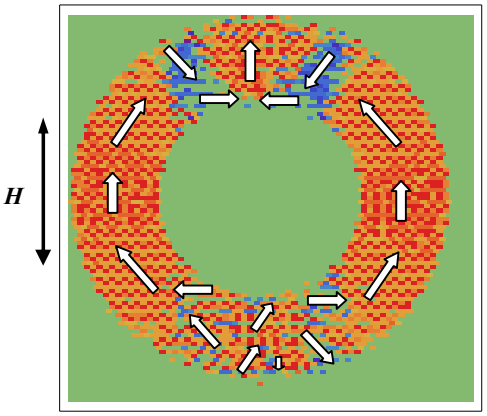

Fig.2. Fe_3O_4 spin direction structures in the ring system. Ordered aria are domains.

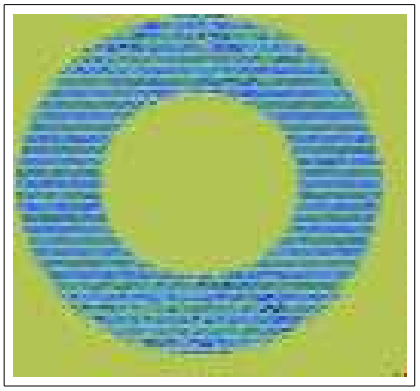

Fig.3. Fe_3O_4 energy map in the ring system. The variations are small.

1) S. Obata: Mater. Trans. **55** No 10 (2014) 1591-8.
2) S. Obata: IEEJ Trans. FM, **133** No 9 (2013) 489.

Molecular Dynamics Simulation of Organic Semiconductors

Kazume NISHIDATE and Masayuki HASEGAWA
Faculty of Engineering, Iwate University
Ueda 4-3-5, Morioka, Iwate 020-8551

We have investigated the energetics and work function (WF) of graphene (GR) with depositing pentacene ($C_{22}H_{14}$, PEN) and perfluorinated pentacene ($C_{22}F_{14}$, PFP) using the electronic structure calculations based on the density functional theory (DFT) with van der Waals (vdW) corrections[1]. Where the molecules are chemically adsorbed on the metals by exchanging electrons or forming hybridized orbitals, while they are physisorbed on GR through the vdW interactions in the flat laying configurations.

To study the WF of GR covered by the organic molecules, we put two PEN or PFP molecules on GR sheet to obtain plane averaged results for the local potential. The coverages are 0.75 ML (PEN) and 1.01 ML (PFP). Where the DFT-D2, DFT-D3, and the optB86b-vdW gave the same results for the adsorption configurations since the vdW corrections only affect the energetics but not the electric structure in direct way. A special attention was paid to the computational conditions to obtain converged results. We used the Γ-centered 4×4×1 Monkhorst-Pack k-point mesh and very high cutoff energy of 1 keV. Present result for the WF for GR (4.23 eV) is compared to the experimental value (4.3 eV) and as well as to the theoretical value reported by other reseach group (4.26 eV) showing a good consistency. When the PEN molecules are adsorbed on GR, the vacuum level is shifted downward (-0.06 eV), whereas the vacuum level shift is upward (+0.10 eV) in the adsorption of the PFP molecules on GR. This tendency is different from that of the PFP adsorbed on the Au(111), Cu(111), and Ag(111) surfaces where only the negative vacuum-level shifts have been predicted. It has been known that the electronic structure is only weakly perturbed by the benzene adsorption on GR. This is also the case in the adsorption of PEN and PFP molecules on GR. Energy diagrams obtained in the present study are shown in the Figure 1.

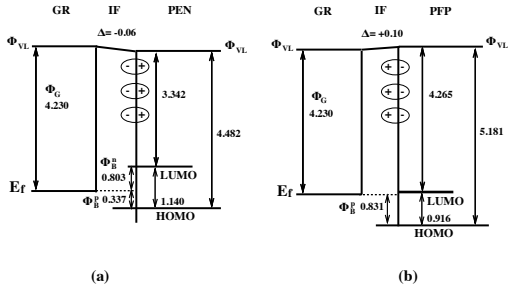

Figure 1: Energy diagrams for (a) PEN on GR and (b) PFP on GR. The vacuum levels Φ_{VL} are shifted by Δ through the dipole layers induced at the interface to the molecular surface. E_f is the Fermi level and Φ_G is the WF of the pristine graphene. Φ_B^p (Φ_B^n) is the hole (electron) injection barrier from GR to the molecules. All the energy values are in units of eV.

References

[1] K. Nishidate, N. Yoshimoto, P. Chantngarm, H. Saito and M. Hasegawa: Molecular Physics, Vol. 114, 2993-2998, 2016.

First principles calculations of electronic structures, magnetism, and electric field effects in metal thin films and organometallic complexes

Kohji NAKAMURA

Department of Physics Engineering,

Mie University, Tsu, Mie 514-8507

***Electric field effect to magnetism of metal thin films**:* Magnetocrystalline anisotropy (MCA) at Fe/MgO interfaces with insertions of 3d (Co, Ni), 4d (Ru, Rh, Pd), and 5d (Os, Ir, Pt) elements in an external electric field was investigated.[1] The MCA energy and the electric-field-induced MCA modification is found to dramatically depend on the inserted elements. Large MCA modification may be achieved by heavy-metal insertions, in which the strength of spin-orbit coupling of inserted elements and the position of the Fermi level relative to *d*-band level play key roles.

Search for the ground-state electronic configurations of organometallic molecules: The ground-state electronic configurations of the organometallic metallocenes, MCp2, M = V, Cr, Mn, Fe, Co, and Ni, were investigated using constraint density functional theory combined with non-empirical U_{eff} approach in linear-response theory.[2] The relative stability of the various *d*-orbital electronic configurations is found to be sensitive to the U_{eff} values. Using the calculated non-empirical U_{eff} values, the electronic configurations are in agreement with the experiments: $^4A_{2g}$, $^3E_{2g}$, $^6A_{1g}$, $^1A_{1g}$, $^2E_{1g}$, and $^3A_{2g}$ for the VCp_2, $CrCp_2$, $MnCp_2$, $FeCp_2$, $CoCp_2$, and $NiCp_2$, respectively

Electric-field-driven superconductivity at diamond (110): Hole states in an electric-field-driven superconductivity at diamond(110) were examined.[3] The surface-bound hole states, confined near the surface by an application of external electric field, is found to play a key role in superconductivity. Indeed, there is a critical electric field for observing the superconductivity, which attributes to the second surface-bound hole state. It further demonstrated that the transition temperature of superconductivity reaches to about 1K at electric field of 1.2V/Å, which corresponds to the surface carrier density of about $6\times10^{13}\mathrm{cm}^2$.

References

[1] K. Nakamura at.al., J. Magn. Magn. Mater. **429** (2017) 214.

[2] K. Nawa et.al., Phys. Rev. B **94** (2016) 0351361.

[3] T. Hattori et.al., submitted.

Development and application of first-principles simulator for time-dependent electron-transport calculation

Yoshiyuki EGAMI
Division of Applied Physics, Faculty of Engineering, Hokkaido University
Kita 13, Nishi 8, Kita-ku, Sapporo, Hokkaido 060-8628

Nowadays, computational simulations with a high accuracy and efficiency have attracted much attention in both science and technology. For example, in the research and development of electronic devices, such numerical investigations play important roles to understand relationship between atomic and electronic structures of materials and electric, magnetic and optical characteristics of devices. A large number of notable studies using first-principles calculations have been performed so far to elucidate the relationship. However, most of the calculations are based on the density functional theory which describes the static characteristics of electrons in the steady state, and there remains to be discussed a time-dependent behavior of electrons.

In order to demonstrate the time-dependent transport properties of electrons through the nanoscale materials, we developed the impulse response (IR) method [1] based on the real-space finite-difference approach [2] within the framework of the time-dependent density functional theory. In this subject, for the IR method, we have worked on the improvement of the efficiency of parallel computing in the spatial dimensions since we cannot parallelize the calculations in the direction with respect to time due to the sequential evolution of scattering wave functions. This work has been performed with a few hundred cores on FUJITSU PREMEHPC FX10 in System C.

On the other hands, we have calculated the electron transport properties of the molecular junction consisting of a transition metal complex molecule using the conventional time-independent electron transport simulator[3, 4] in order to compare the characteristics obtained by the IR method. As the results, in a $Mn(dmit)_2$ molecular junction, spin-dependent properties are observed owing to the spin polarization derived from Mn atom, which are suitable as a spin filtering device. In particular, for a down-spin electron transport depending on the relative angle θ between two planar ligands, a non-monotonic behavior with θ in the conductance spectrum is found. It is confirmed that the d-orbitals of Mn atom plays a key part to exhibit such behavior. This work has been performed on System B.

References

[1] Y. Egami and K. Hirose: JPS Conf. Proc. **1**, 016012 (2014).

[2] K. Hirose *et al.*: *First-Principles Calculations in Real-Space Formalism*, (Imperial College Press, London, 2005).

[3] Y. Egami, K. Hirose and T. Ono: Phys. Rev. E **82**, 56706 (2010)..

[4] Y. Egami, S. Iwase, S. Tsukamoto, T. Ono and K. Hirose: Phys. Rev. E **92**, 033301 (2015).

Magic Angles in Energetics of Graphene Bilayer

Kazuyuki Uchida

Department of Physics,

Kyoto Sangyo University, Kyoto

Energetics for bilayer of graphene disks has been explored, to analyze the magic angles where the system has locally minimal energy. In this work, we have successfully clarified physical origin of the magic angles. This is the first time that magic angles are seriously discussed for interfaces where van-der Waals interactions are playing a dominant part.

We have calculated energy E for bilayers of graphene disks a function of the twist angle θ between the two layers. In Fig. 1, we show our model used in this work. The nearest-neighbor C-C bond length within a layer is fixed to be 1.42Å. The bond angle among the three nearest neighbor C atoms within a layer is fixed to be 120°. The inter-layer distance is fixed to be 3.35Å. We have used Lenard-Jones potential to describe van-der Waals interactions between the two layers.

We have found that the energy E oscillates as a function of the twist angle θ between the two layers, which is consistent with a previous report [1]. We have compared the atomic structures of the systems which have the locally minimal energy and that of the system which have the locally maximal energy, finding that Moire patterns in the stacking structures of the two layers are closely related with the energy of the systems. Detail will be shown elsewhere [2].

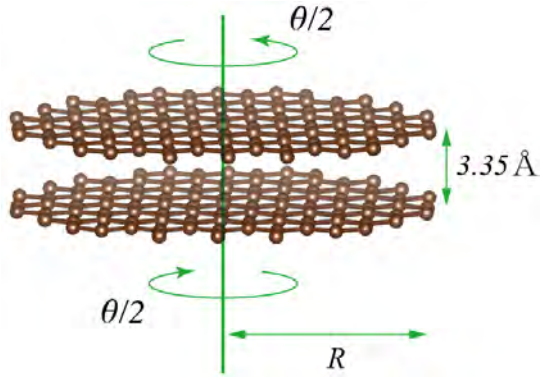

Fig. 1: Bilayer of graphene disks.

References

[1] Bin Liu Min-Feng Yu, and Yonggang Huang, PRB **70**, 161402(R) (2004).

[2] in preparation.

Atomic structures and electronic properties of atomic-layered materials

Yoshitaka FUJIMOTO
Depertment of Physics, Tokyo Institute of Technology
Oh-okayama, Meguro, Tokyo 152-8551

Graphene shows various unique electronic properties. In particular, graphene possesses very high carrier mobilities, and therefore is expected to be a potential device material for future nanoelectronics. Graphene is reported to be sensitive to adsorbates, and is also good candidates for promising sensor applications due to the high carrier mobility as well as the high sensitivity to adsorbates.

We here report polluting or toxic gas (NO and NO_2) adsorption effects on energetics and electronic properties of B-doped and N-doped graphene bilayers using first-principles electronic-structure calculations in the framework of the density-functional theory [1]. It is found that NO and NO_2 molecules are adsorbed with chemical bonds on the B-doped graphene bilayer. It is also found that the charge transfer takes place between the NO or the NO_2 molecule and the B-doped graphene layer.

We examine the stabilities of the NO and NO_2 molecules adsorbed on the B- and N-doped graphene bilayers. For the N-doped cases, NO and NO_2 molecules are not chemically but physically adsorbed with relatively small adsorption energies (E_a) as well as the long distances (d) between the molecule and the dopant atom ($d > 2.6$ Å). For the B-doped cases, the NO and NO_2 molecules can bind chemically with the large adsorption energies ($|E_a| > 1.1$ eV) as well as the short distances ($d < \sim 2$ Å). Interestingly, the B atom protrudes from the planar graphene sheet when the NO_2 molecule binds with a chemical bond between the O atom in the NO_2 molecule and the B atom in the B-doped graphene bilayer, whereas it still resides in the planar sheet when the NO molecule binds with a chemical bond between the N atom in the NO molecule and the B atom in the graphene layer.

We also exmaine the electronic properties of the NO and NO_2 molecules adsorbed on the B-doped graphene bilayer. The adsorption of the NO (NO_2) molecule clearly induces the charge transfers between the N (O) atom in the NO (NO_2) molecule and the B atom in the graphene due to the orbital hybridizations between the NO (NO_2) molecule and the B-doped graphene bilayer. Interestingly, by the NO molecule adsorption, electrons move from the NO molecule to the B-doped graphene with an amount of ~ 0.03 electrons, while for the adsorption of the NO_2 molecule, they move from the B-doped graphene to the NO_2 molecule with an amount of $\sim$ 0.18 electrons. It can be seen that the charge transfer in the case of the adsorption of the NO_2 molecule is considerably larger than that in the case of the NO molecule. This is because the distance between the NO_2 molecule and the B-doped graphene is shorter compared with that between the NO molecule and the B-doped graphene.

We further exmaine work functions of the B-doped bilayer graphenes with adsorptions of the NO and the NO_2 molecules. Our calculated work function of the pristine AB-stacked bilayer graphene is 4.50 eV. When the B atom is doped into the graphene bilayer, the work function increases to $\sim$ 5 eV since a B atom has one deficit electron compared with a C atom. When the NO_2 molecule is adsorbed, its work function further increases up to beyond 5 eV. On the other hand, when the NO molecule is adsorbed, the work function diminshes dramatically below that of the pristine bilayer

graphene. The variation of the work function induced by the adsorption of different types of adsorbates is mainly attributed to the charge transfer: In the case of the NO_2 molecule, the charge transfer takes place from the B-doped graphene layer into the NO_2 molecule, whereas it takes place from the NO molecule into the B-doped graphene layer.

In summary, we have examined adsorption effects of the polluting gas molecules on the energetics and the electronic properties of B-doped and N-doped graphene bilayers using first-principles density-functional calculations. The NO and NO_2 molecules can bind with chemical bonds on the B-doped graphene bilayer. By the adsorptions of the NO molecule and the NO_2 molecule, the charge transfers take place between the NO (NO_2) molecule and the B-doped graphene layer. The B-doped graphene bilayer is expected to be useful as sensors for the NO and the NO_2 molecules.

References

[1] Y. Fujimoto and S. Saito, Chem. Phys. **478**, 55 (2016).

Study on electronic structures in perovskite-type lead-halide mixed crystals

Takayuki Makino

Department of Electric and Electronics Engineering,

University of Fukui, Bunkyo Fukui, Fukui 910-8557

Perovskite type halide compound is known to exhibit several interesting properties. They are , for example, strong excitonic effect and photovoltaic action. Deeper understandings for mixed crystal are important from both technological and basic viewpoints [1]. In this research, we intend to compare calculation and experimental data.

We have used the Quantum-ESPRESSO package to optimize the crystal structure and perform the band structure calculations. In this work, we use a set of the optimized norm-conserving Vanderbilt pseudopotentials generated by Schlipf and Gygi. We also confirmed the unit cell size necessary for the mixed crystal calculations. Flow chart is shown at the right hand side We confirmed that evaluated bandgap energy is similar to that evaluated by Brivio *et al*[2].

We then moved into study of the electronic structure perovskite-lead chloride compound. As has been done for perovskite iodides, we optimized crystal structural parameters, followed by the calculation of electronic structures. The research plan of FY 2017 covers the mixed crystals between iodide and chloride. We are calculating the electronic states, though the calculation is now at its beginning. Specifically, it aims to determine the dependence of Cl concentration and their positions.

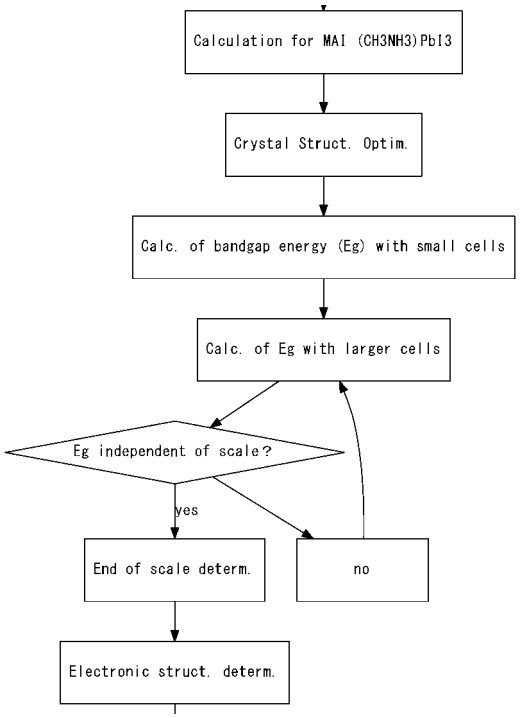

References

[1] J. H. Heo and S. H. Im: Nanoscale **8** 2554 (2016).

[2] F. Brivio *et al.*, APL Materials **1**, 042111 (2013).

Theoretical analysis of H/D isotope effect in hydrogen-bonded organic conductor

Masanori TACHIKAWA

Quantum Chemistry Division,

Yokohama City University, Seto 22-2, Kanazawa-ku, Yokohama 236-0027, Japan

We have performed the computational analysis of H/D isotope effect on the novel hydrogen-bonded material, catechol-fused ethylenedithio-tetrathiafulvalene (H_2Cat-EDT-TTF) (H-TTF) [1]. H-TTF is a hydrogen-bonded π-electron system which was found to reveal *C*2/*c* symmetry in 50-293 K, while its isotopologue, κ-D_3(Cat-EDT-TTF)$_2$ (D-TTF), showed the phase transition at 185 K from *C*2/*c* to *P*-1. To elucidate the origin of such difference, we calculated the potential energy curves (PECs) for the hydrogen transfer along the H-bonds in these conductors. We found that both the π-stacking and the hydrogen nuclear quantum effect drastically affected the hydrogen transfer energy. With taking account of both effects, we obtained symmetric single-well effective PEC for H-TTF, which indicated that the hydrogen was always located at the center of the H-bond. By contrast, the effective PEC of D-TTF was low-barrier double-well, indicating that the position of the H-bonded deuterium would change according to the temperature. We concluded that the π-stacking and the nuclear quantum effect were the key factors for the appearance of phase transition only in D-TTF [2].

We also theoretically investigated a significant contraction of the hydrogen-bonding O…O distance upon H/D substitution in recently developed purely organic crystals, κ-H_3(Cat-EDT-ST)$_2$ (H-ST) and its isotopologue κ-D_3(Cat-EDT-ST)$_2$ (D-ST). The optimized O…O distance in H-ST was found to be longer than that in D-ST due to the anharmonicity of the potential energy curve along the O–H bond direction, which was in reasonable agreement with the experimental trend [3].

References

[1] T. Isono, H. Kamo, A. Ueda, K. Takahashi, A. Nakao, R. Kumai, H. Nakao, K. Kobayashi, Y. Murakami, H. Mori: Nat. Commun. **4** (2013) 1344.

[2] K. Yamamoto, Y. Kanematsu, U. Nagashima, A. Ueda, H. Mori, and M. Tachikawa, Phys. Chem. Chem. Phys. (Communication), **18** (2016) 29673-29680.

[3] K. Yamamoto, Y. Kanematsu, U. Nagashima, A. Ueda, H. Mori, and M. Tachikawa, Chem. Phys. Lett., in press (2017).

Strain of β-$FeSi_2$(100) ultra-thin film

Ken HATTORI
Graduate School of Materials Science, Nara Institute of Science and Technology
Takayama, Ikoma, Nara 630-0192

Using scanning tunneling microscopy (STM) and low-energy electron diffraction (LEED), author's group has been studied the epitaxial growth of β-$FeSi_2$(100) nano-films on Si(001) prepared in ultra-high vacuum [1]. The β-$FeSi_2$[010] and [001] directions are Si⟨110⟩ with lattice mismatches of +1.5% and +2.0%, respectively. The spot-intensity profiles in the LEED measurements have suggested the β-$FeSi_2$ surface structure; 1) the stacking of the surface top-layer of Si, 2nd-layer of Fe, 3rd-Fe, 4th-Si, 5th-Fe and repetition of Si/Fe/Fe/Si/Fe layers to bulk, and 2) in-plane relaxation of top-layer Si atoms from a rectangle configuration in the ideal to a square one in the real reconstruction.

The structure was also confirmed by the comparison with the STM simulation images calculated using Simulation Tool for Atom TEchnology (STATE)-Senri [2] in SCC-ISSP system; four Si atoms in the square configuration forms one atomic protrusion in the STM calculation. Recently the authors' group has confirmed such a slab structure using high-angle annular dark-field scanning transmission electron microscopy (HAADF-STEM) in atomic resolution. The HAADF-STEM showed β-$FeSi_2$(100) nano-films consists of units of the quintuple layers (QL) (Si/Fe/Fe/Si/Fe) with a bottom Si layer on a Si(001) substrate. Figure 1 shows a model for β-$FeSi_2$(100) with 3 QL on Si(001). The red and green balls are Fe and Si in *beta*-$FeSi_2$, respectively. The cyan, orange, pink and green balls are 1st-, 2nd-, 3rd- and 4th/5th-layer atoms in Si, respectively.

Interestingly, the STM and HAADF-STEM displayed the bending of β-$FeSi_2$ over Si substrate steps; the bending strain was estimated to be ∼3–4% in the ratio of the height difference (Δz) to length (L). On the other hand, the in-plane compression of β-$FeSi_2$ was smaller than the ideal values (1.5% and 2.0%) within the error. These experimental results suggest the relaxation of the in-plain compress strain by the bending formation.

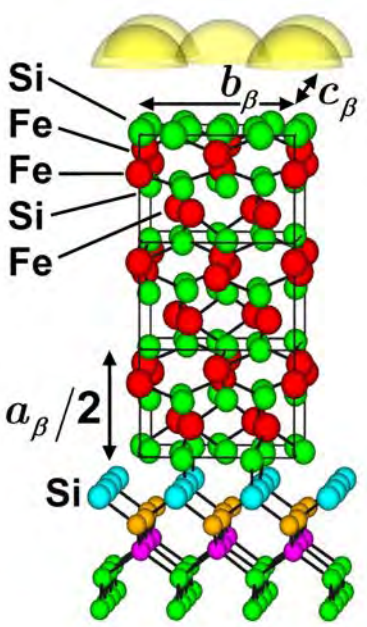

Figure 1: A model of β-$FeSi_2$(100) with three quintuple layers (QL) on Si(001). Red and green balls represent Fe and Si atoms, respectively, in β-$FeSi_2$. Cyan, orange, pink and green balls represent 1st, 2nd, 3rd and 4th/5th-layer Si atoms, respectively, in Si. a_β, b_β and c_β denote unit-lengths of β-$FeSi_2$[100], [010] and [001], respectively. Yellow hemispherical balls represent schematic atomic protrusions in the STM calculation.

In this project we calculated energy increases by the compression and bending of free-standing β-$FeSi_2$(100) using STATE-Senri.

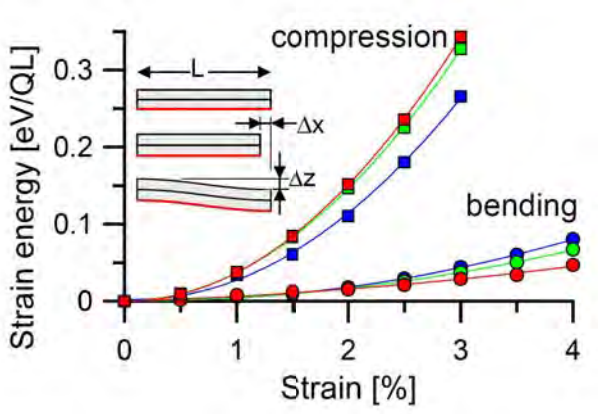

Figure 2: Calculated strain energies of β-$FeSi_2$(100). Blue, green and red squares (circles) represent energy increases divided by QL number for 1, 2 and 3 QL models, respectively, as a function of compression (bending) strain, $|\Delta x|/L$ ($\Delta z/L$).

The compression models were (100)1×1 units for 1 QL, 2 QL and 3 QL with the bottom Si layer consisting of 6, 11, and 16 layers having 32, 56, and 80 atoms, respectively. The atomic positions in the bottom layer were fixed to those with the same relative x and y components normalized by unit lengths in [010] and [001], respectively, to the stable bulk structure. The other positions were relaxed at the residual force of $\leq$0.05 eV/ Å,

Troullier-Martins norm-conserving pseudo potentials were used for Si and Fe atoms. The wave functions and charge densities were expanded by a plane-wave set with cut-off energies of 25 and 225 Ry, correspondingly. 4×4×1 k-points mesh was used for the k-space integration. The spin polarization was not taken into account in the calculations. The blue, green and red squares in Fig. 2 displays the energy increases divided by the number of QL for 1, 2 and 3 QL models, respectively, as a function of the compression ($|\Delta x|/L$) from the stable structures with L.

Similarly the energy increases by the bending strain were calculated as shown by blue, green and red circles in Fig. 2, for 1, 2 and 3 QL (100)1×1 units, respectively. Here, z components of the fixed bottom layer atoms were modulated by $(|\Delta z|/2)\cos(\pi x/L)$, thus, the actual calculations were done with 2×1 units under 2×4×1 k-points mesh.

Figure 2 indicates that the energy increases in the compression at 1.5–2.0% are larger than those in the bending at 3–4%, which implies that the nano-film system is prefer to bend in order to release the large energy increase due to the compression strain, in principle. We should note here that the stable in-plain lattice constants depend on the film thickness. For the 3 QL model, the [010] and [001] lattice constants were 0.3% smaller than the bulk ones, but the above trend is not changed. Figure 2 also indicates no drastic difference in energy per QL for the 1-3 QL models.

The author thank Prof. Morikawa in Osaka University, Dr. Yanagisawa in Ryukyu University, and Dr. Hamada in NIMS for their great support in STATE-Senri calculations.

References

[1] O. Romanyuk, K. Hattori, M. Someta, and H. Daimon: Phys. Rev. B **90** (2014) 155305.

[2] Y. Morikawa: Phys. Rev. B **63** (2001) 033405, and references therein.

First-principles study on the defects in semiconductors

Jun YAMAUCHI
Faculty of Science and Technology, Keio University
3-14-1 Hiyoshi, Kohoku-ku, Yokohama-shi, Kanagawa 223-8522

As the size of devices on integrated circuits decreases, the behavior of dopant atoms make relatively larger effect on the device performance. Especially, it is very important to understand the unfavorable defects including the dopant atoms. The experimental observations on each defect is extremely difficult. One of the major difficulties for detecting dopant configurations is the very weak signals from the defects of very low concentration comparing to those from the matrix semiconductors. However, recently, as a solution for the above problem, it is suggested to use powerful synchrotron radiation facilities to measure the X-ray photoelectron spectroscopy (XPS) signals of defects. On the other hand, there have been few reliable first-principles core-level XPS calculations for impurity defects in semiconductors, because the local potential boundary condition of defect model systems has not yet been sufficiently evaluated. To obtain reliable shifts in the XPS binding energy, it is necessary to take a sufficiently large supercell for a defect.

To investigate the dependence of the substrate semiconductors on the XPS binding energies, we carried out a comprehensive study on the As 3*d* core-level XPS binding energies for As defects in crystalline Si using a first-principles calculation with careful evaluation of the local potential boundary condition for the model system. To represent a core hole in the 3d orbitals, we adopted the arsenic pseudopotential including the 3d orbitals as valence ones, and the spherical hole approximation assuming that one core hole occupies degenerated core states equally. It is found that the effect of this approximation on the relative XSP binding energy is negligible. We adopted cubic supercell corresponding to 1000 Si atoms and also considered the charged state and spin effect. The code used in this study is xTAPP, which is a hybrid paralleled density functional theory calculation program with plane-wave basis[1].

It is found that, while the spin polarization does not make large effect on the formation and XPS binding energy of defects, the charge state change those energies up to several tenth of eV in some cases. Among the examined defect structures, vacancy related defects, where one vacancy is surrounded by substitutional arsenic atoms, well explain the experimentally observed XPS peak.

References

[1] xTAPP (eXtended Tokyo Ab initio Program Package)
(http://xtapp.cp.is.s.u-tokyo.ac.jp)

[2] J. Yamauchi, Y. Yoshimoto, and Y. Suwa: J. Appl. Phys. **119** (2016) 175704.

Effects of heavy elements in surface nanostructures

Yoshihiro GOHDA
Department of Materials Science and Engineering, Tokyo Institute of Technology
J1-3, Nagatsuta-cho 4259, Midori-ku, Yokohama 226-8502, Japan

Spin-orbit coupling of heavy elements, especially in nanostructures, has potentials of novel physical properties. For example, bilayer Bi(111) films have been predicted theoretically as two-dimensional topological insulators [1]. In recent experiments, atomically-flat Bi(110) ultrathin films have successfully grown on Si(111)$\sqrt{3}\times\sqrt{3}$-B surfaces [2]. Since Si(111)$\sqrt{3}\times\sqrt{3}$-B surfaces have no dangling bonds, properties of Bi ultrathin films are expected to be similar to those of freestanding one. Contrary to previous studies [3], where even-layer thickness films have stable black-phosphorous-like structures and odd-layer ones have less-stable bulk-like structures, the preference of even-layer thickness was not obtained [2]. Furthermore, it is difficult to distinguish black-phosphorous-like structures and bulk-like structures by scanning-tunneling-microscope images.

In the present study, the atomic structures and electronic properties of Bi(110) ultrathin films are studied by first-principles calculations using the OpenMX code [4], where pseudo-atomic orbitals and norm-conserving pseudopotentials are used. For even-layer thickness films, we obtained black-phosphorous-like structures, which is consistent with previous studies [3]. In contrast, for odd-layer thickness ones with 5 monolayers or more, the optimized structures have characteristics of both black-phosphorous-like and bulk-like structures. The atomic structure together with the electron-density rearrangement compared to the isolated atoms are shown for the 5-monolayer case in Fig. 1 (a). The outermost two monolayers form the black-phosphorous-like structure, whereas the inner one monolayer has essentially no chemical bonding with neighboring layers. The formation energy relative to the bulk Bi as a function of the thickness of the films is shown in Fig. 1 (b). The formation energy decreases as the thickness increases. Furthermore, our result demonstrates that there is no clear preference for even or odd numbers of the layer-thickness, as far as the thickness is more than 5 monolayers. As the spin-orbit coupling of Nd dominates the magnetic anisotropy of Nd-Fe-B permanent magnets [5], the spin-orbit coupling of other heavy elements including Bi should be useful to control the anisotropy of magnetic materials, which must be an interesting target of further studies.

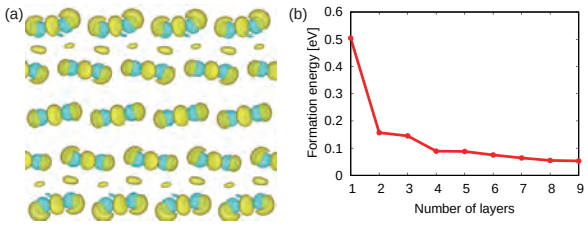

Figure 1: (a) The atomic structure together with the electron-density increase compared to the isolated atoms for the 5-monolayer case and (b) the formation energy per atom relative to the bulk Bi as a function of the thickness of the films.

[1] S. Murakami, Phys. Rev. Lett. **97**, 236805 (2006); M. Wada, S. Murakami, F. Freimuth, and G. Bihlmayer, Phys. Rev. B **83**, 121310(R) (2011).
[2] I. Kokubo, Y. Yoshiike, K. Nakatsuji, and H. Hirayama, Phys. Rev. B **91**, 075429 (2015).
[3] T. Nagao, J. T. Sadowski, M. Saito, S. Yaginuma, Y. Fujikawa, T. Kogure, T. Ohno, Y. Hasegawa, S. Hasegawa, and T. Sakurai, Phys. Rev. Lett. **93**, 105501 (2004).
[4] T. Ozaki, Phys. Rev. B. **67**, 155108 (2003).
[5] Y. Tatetsu, S. Tsuneyuki, and Y. Gohda, Phys. Rev. Appl. **6**, 064029 (2016).

Geometric and electronic structures at edge of 2-dimensional honeycomb sheets

Noriaki TAKAGI[1], Ryuichi ARAFUNE[2], Naoya KAWAKAMI[1], and Emi MINAMITANI[3]

[1]*Department of Advanced Materials Science, University of Tokyo Kashiwa-no-ha, Kashiwa, Chiba 277-8561,*

[2]*International Center for Materials Nanoarchitectonics, National Institute for Materials, Science, 1-1 Namiki, Ibaraki 304-0044,*

[3]*Department of Materials Engineering, The University of Tokyo, 7-3-1 Hongo, Bunkyo-ku, Tokyo 113-8656, Japan..*

The discovery graphene has fueled the competition to explore exotic new honeycomb materials and to uncover their hidden properties. One-atom layer honeycomb sheets consisting of heavy elements such as Bi, Si, Ge and Sn atoms have gathered lots of attention. These materials are promising candidates of two-dimensional (2D) topological insulator because the large spin-orbit interactions open the energy gaps, leading to the topological edges states [1, 2].

Recently, we have investigated the geometric and electronic structures of Bi thin films grown on Si(111) and Au(111) substrates mainly by using scanning tunneling microscopy (STM). We found that the Bi thin films on Si(111) have two types of step edges; One shows a regular step edge and the other exhibits a reconstruction. Interestingly, the latter reconstructed edge hosts a localized 1D electronic state [3]. In addition, we found the superstructure formed by the Bi adsorption on Au(111). We carried out density functional theory (DFT) calculations (1) to construct the structural model of the reconstructed edge in Bi films on Si(111) and elucidate the origin of the 1D state and (2) to construct the structure model of the superstructure for Bi on Au(111).

The DFT calculations were carried out by the plane-wave-based Vienna Ab initio Simulation Package (VASP) [4, 5] with the projected augmented wave method [6]. While we did no find reasonable structural model for the reconstructed Bi edge yet, we found a good model for the superstructure of Bi on Au(111).

Reference

[1] S. Murakami: Phys. Rev. Lett. **97**, 236805 (2006).

[2] M. Ezawa, Phys. Rev. Lett. **109**, 055502 (2012).

[3] N. Kawakami, C.-L. Lin, M. Kawai, R. Arafune and N. Takagi, Appl. Phys.

Lett. **107**, 031602 (2015).
[4] G. Kresse and J. Furthmüller: Phys. Rev. B **56**, 11169 (1996).
[5] G. Kresse and J. Furthmüller: Comput. Mater. Sci. **6**, 15 (1996).
[6] P. E. Blöchl: Phys. Rev. B **24**, 17953 (1994) 17953.

Adsorbed states of magnetic molecules at solid surfaces

Noriaki TAKAGI[1] and Emi MINAMITANI[2]

[1]*Department of Advanced Materials Science, University of Tokyo*

Kashiwa-no-ha, Kashiwa, Chiba 277-8561

[2]*Department of Materials Engineering, The University of Tokyo, 7-3-1 Hongo,*

Bunkyo-ku, Tokyo 113-8656, Japan.

Adsorption of metal phthalocyanines (MPcs) on solid surfaces has gathered considerable attention because these molecules exhibit unique properties [1-3]. MnPc, FePc and CoPc are typical members of MPc family and the adsorption of these molecules on solid surfaces has been intensively studied. Recently, we have investigated the magnetism of FePc on noble metal surfaces, especially the relation between the spin state and the molecule-surface (Mol-S) interaction, by using scanning tunneling microscopy (STM) and spectroscopy (STS) and photoelectron spectroscopies. We have elucidated that the S=1 spin state of the bulk FePc is converted when the molecule directly contacts Cu(110) [4]. In contrast, the S=1 state is preserved by inserting atom-thick oxide layer between the molecule and the Cu substrate [4] On Au(111). two unpaired spins of S=1 FePc exhibit Kondo effect because of the exchange coupling with the substrate electrons [5,6]. These examples indicate the spin state is sensitive to the molecule-surface interactions.

To understand systematically the relation of the spin state and the Mol-S interaction, we investigated the spin state of FePc on Ag(111) by using soft X-ray photoelectron spectroscopy (SXPS) together with the density-functional theory (DFT) calculations. The evolution of SXPS spectra as a function of the amount of adsorbed FePc molecules shows that the S=1 spin state is converted to S=0 for the monolayer regime, and that S=1 preserves in the second layer on the monolayer. We performed the DFT calculations by using the plane-wave-based Vienna Ab initio Simulation Package (VASP) [7,8] with the projected augmented wave method [9]. The DFT calculations have found that the adsorption of FePc on Ag(111) changes the S=1 spin state of bulk FePc to S=0, consistent with the SXPS results. The present results show that there is a boundary between Ag and Au in the 11th group of periodic table concerning the conversion of S=1 to S=0 upon the adsorption.

Reference

[1] R. Bonnett: Chem. Soc. Rev. **24**, 19 (1995).

[2] C. C. Lanznoff and A. B. P. Lever: *Phthalocyanines, Properties and*

Applications (Wiley, New York, 1996).
[3] K. Kadish, and R. Guillard: *Applications of Phthaloyianines, The Porphyrin Handbook* (Academic Press, San Diego, 2003).
[4] N. Tsukahara *et al*.: Phys. Rev. Lett. **102**, 167203 (2009).
[5] N. Tsukahara *et al*.: Phys. Rev. Lett. **106,** 187401 (2011).
[6] E. Minamitani *et al*.: Phys. Rev. Lett. **109**, 086602 (2012).
[7] G. Kresse and J. Furthmüller: Phys. Rev. B **56**, 11169 (1996).
[8] G. Kresse and J. Furthmüller: Comput. Mater. Sci. **6**, 15 (1996) 15.
[9] P. E. Blöchl: Phys. Rev. B **24**, 17953 (1994).

Study on an automatic derivation technique of first-principles effective model based on the many body electron theory

Hirofumi SAKAKIBARA

Department of Applied Physics and Mathematics,

Tottori University, Koyama-cho, Tottori, Tottori 680-8552

The derivation of effective model is one of the central issues in the condensed matter physics. Especially in the low-temperature physics, the effective model is can be constructed by truncating the space which constructs the energy eigenvalues around the Fermi level. However, the states spanning such space are affected by electron process in higher energy scales. Therefore, we have to obtain the whole electron band structure before the truncation of the effective model.

By recent development of the implementation technique of the first-principles calculation and the computational resources, we can obtain the electron band structure for each material by several ours of calculation. Furthermore, the recent studies on the Hubbard-type model have shown that the critical temperature of high-Tc cuprates can be estimate as the realistic values and the systematics with the curvature of the Fermi surface is reproduced [1,2]. Therefore, if we can systematically construct the effective model from the first-principles calculations, we have possibilities to salvage the new superconducting materials from the material database in principle.

To this end, we have firstly improved the derivation system of effective model. We have suggested the modified random phase approximation (named mRPA) method to overcome some difficulties recognized in the constrained RPA.

For the benchmark of mRPA, we have estimated the Hubbard interaction U in the HgBa2CuO4, which is the typical single-band high-T_c superconductor. As a result, the U in mRPA is larger than the value in cRPA (U_{cRPA}=2.0eV, U_{mRPA}=3.9eV). The reasons are follows: On one hand, in cRPA, the

screening effect by long-ranged Coulomb interaction is completely discarded [3]. On the other hand, even mRPA can treat the range truncation of the interaction exactly in principle, our recent test in the mRPA does not take any off-site interaction. In the future study including the off-site interaction in mRPA, the value of U may be modified to become close to the appropriate value of the single-band (extended) Hubbard model, which has been studied to reproduce the low-energy process in the cuprates superconductors.

References

[1] H. Sakakibara et al: Phys. Rev. Lett. **105** (2010) 057003.

[2] H. Sakakibara et al: Phys. Rev. B **89** (2014) 224505.

[3] H. Sakakibara et al: J. Phys. Soc. Jpn. **86** (2017) 044714.

Ab initio calculations of impurity states in the silicon cluster superlattice

Nozomi ORITA, Yasushi IWATA
National Institute of Advanced Industrial Science and Technology
Tsukuba Central 2, Tsukuba, Ibaraki 305-8568

Recently, Iwata *et al.* found out the crystallographic coalescence of silicon (Si) clusters into a bcc superlattice structure with a lattice constant of 2.134 nm by direct deposition of a Si cluster beam on a graphene substrate[1]. In the past year, we obtained a good model structure for the bcc Si cluster superlattice by *ab initio* calculations using OpenMX [2]. That structure is composed of Si_{211} clusters and the lattice constant is 2.167 nm, which is in good agreement with the experimental value, 2.134nm[3, 4]. The obtained structure and the band structure of the bcc Si_{211} cluster superlattices are shown in Fig. 1.

This year, we have investigated the effect of impurities for the bcc Si_{211} cluster superlattice. The Si_{211} cluster has 18 symmetrically equivalent atomic sites. An atom for each equivalent site was substituted by a boron (B) or a phosphorus (P) atom and the stable structure and the electronic state were calculated. The obtained band structures of the $Si_{210}B_1$ and $Si_{210}P_1$ cluster superlattices in which the each central Si atom of the Si_{211} cluster was substituted by the impurity are shown in Fig. 2. The impurity states are hidden in the surface states in the vicinity of the Fermi level and those band structures are almost same as that of the Si_{211} cluster superlattice. We obtained similar band structures for impurities at the other 17 equivalent sites.

We also calculated surface-oxidized $Si_{210}B_1$ and $Si_{210}P_1$ cluster superlattices. In those calculations, the twelve oxygen atoms terminate

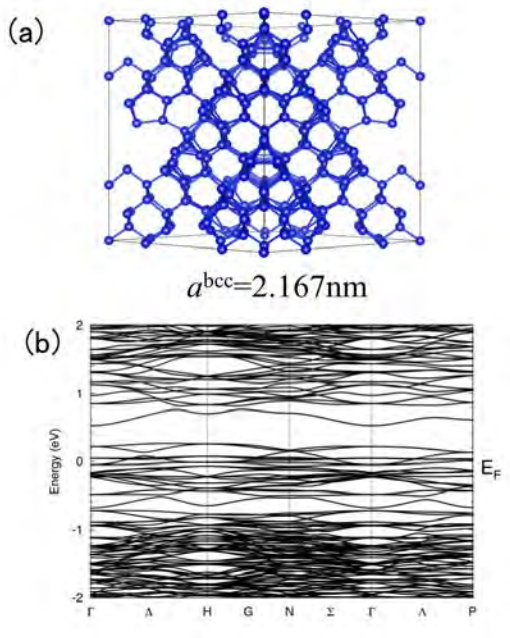

Figure 1: Crystal structure (a) and band structure (b) of the bcc Si_{211} cluster superlattices. E_F denotes the Fermi level

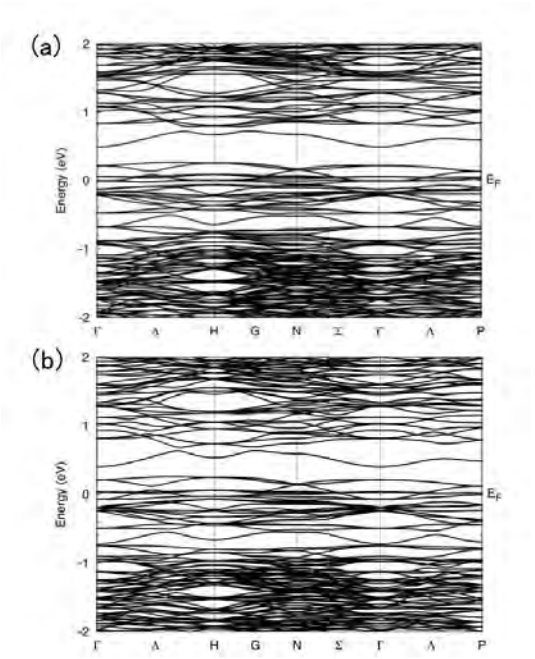

Figure 2: Band structures of the $Si_{210}B_1$ (a) and the $Si_{210}P_1$ (b) cluster superlattices. The impurity is located at the center of the cluster. E_F denotes the Fermi level

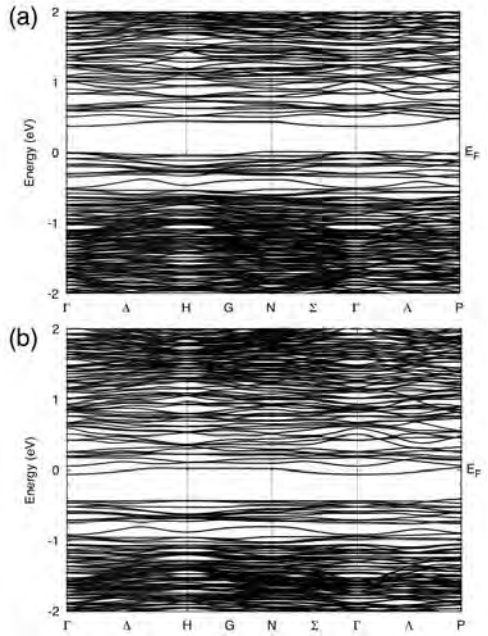

Figure 3: Band structures of the surface-oxidized $Si_{210}B_1$ (a) and $Si_{210}P_1$ (b) cluster superlattices. The B or P is located at the center of the cluster. E_F denotes the Fermi level

dangling bonds on the surface. The obtained band structures for a B and a P atom at the center of the clusters are shown in Fig. 3. In those cases, the B-doped and the P-doped surface-oxidized Si cluster superlattices indicate a p-type and an n-type conductivety, respectively. However, in some cases, depending on the position of the impurity, the B-doped and the P-doped surface-oxidized Si cluster superlattices became an n-type and a p-type semiconductor, respectively.

References

[1] Y. Iwata, K. Tomita, T. Uchida, and H. Matsuhata, Cryst. Growth Des. **15** (2015) 2119.

[2] T. Ozaki *et al.*, http://www.openmx-square.org/

[3] Y. Iwata, N. Orita, T. Uchida, and H. Matsuhata, Proc. Advanced Materials World Congress 2015, Chapter 10, p. 5.

[4] Y. Iwata, N. Orita, T. Uchida, H. Amekura, J. Hasegawa, K. Horioka, and H. Matsuhata, EMN Meeting on Quantum Matter 2016.

Study of interaction between radiation damage and interstitial atom

Kazuhito Ohsawa

Institute for Applied Mechanics,

Kyushu University, Kasuga-koen, Kasuga, Fukuoka 816-8580

Metal properties usually deteriorate by the presence of hydrogen (H). In particular, the degradation of Fe, W, and their alloys by H is paid attention in the field of irradiation damage, which is related to the safety of fusion and fission reactors. Stable configurations of H atoms trapped in a mono-vacancy have been reported in some previous works. So, we investigated stable configurations of di-vacancy in BCC transition metals and H trapped in the di-vacancy. Formation energies of di-vacancy and vacancy hydrogen complex (VHC) are estimated by first-principle calculations based on density functional theory.

It is possible to be two types of di-vacancies in BCC lattice, as shown in Fig. 1. In Fe lattice, <100> di-vacancy is more stable than <111> di-vacancy. While, <111> di-vacancy is more stable in Cr, Mo, W lattice.

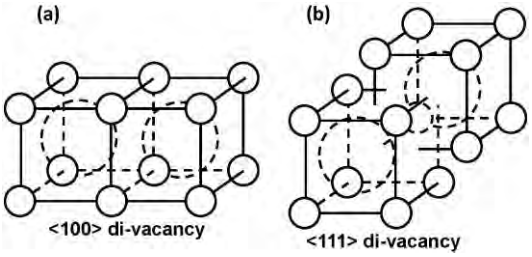

Fig. 1: Two types of di-vacancies in BCC lattice.

The binding energies of di-vacancy and VHC are calculated, as shown in Fig. 2. The di-vacancy formation $V + V \rightarrow V_2$ is usually exothermic reaction. But di-vacancy in W is unstable. Binding energies of VHC are also calculated in the case of $VH_6 + VH_6 \rightarrow V_2H_{12}$. The presence of H usually enhances di-vacancy formation except for Cr. In particular, W and its alloys will be installed in fusion reactors which are exposed to intense H plasma. The abnormal properties of vacancy type lattice defects in W materials will be an important subject in the field of plasma facing material.

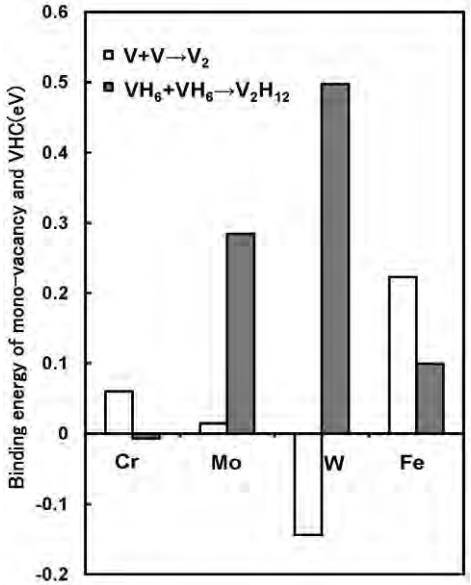

Fig. 2: Binding energy of V and VH_6.

Study on structure, formation, and physical properties of multiatomic vacancies and clusters of 2D semiconductors

Hiroyuki KAGESHIMA
Interdisciplinary Graduate School of Science and Engineering, Shimane University
Nishi-Kawatsucho, Matsue, Shimane 690-8504

Our project has been focused on the physical and structural properties of defects, surfaces and interfaces of two dimensional (2D) semiconductors such as graphene, h-BN, and transition metal dichalcogenide (TMD). MoS_2 is one of the 2D semiconductors consisting of two elements as h-BN is. In addition, the projected atomic structure of MoS_2 is honeycomb as that of h-BN is. Therefore, it is expected that physical properties of MoS_2 is similar to those of h-BN. We study properties of MoS_2 vacancies based on the first-principles method and compare them with those of h-BN vacancies [1, 2]. The calculations were performed based on the first-principles calculation with the GGA density functional, plane wave bases, and pseudopotentials. Program package PHASE [3] was employed.

The results show that vacancies for both h-BN and MoS_2 are more stable when they are more negatively charged (Fig. 1). Almost all of the calculated vacancies prefer the negative charge states to the neutral and positive charge states. In addition, they show that the vacancy atomic structures change with the charge states. We successfully explain both of these properties based on gap state properties. The highest occupied states for the neutral states are located close to the valence band maximum in band gap, and many vacancy states appear in the band gap as unoccupied states.

Our results also show that the anion vacancies are much easily formed for MoS_2. The formation energy of V_S is only 0.64 eV in the Mo-rich condition at conduction band minimum. The reason comes from the rather strong ionic nature of chemical bonds of MoS_2. On the other hand, the rather strong covalent nature of chemical bonds of h-BN enlarges the formation energy of anion vacancies.

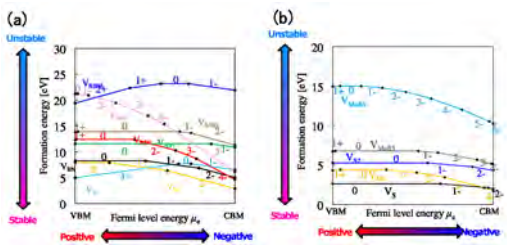

Figure 1: Charge state dependent formation energies of vacancies (a) of h-BN in the N-rich condition and (b) of MoS_2 in the S-rich condition. The numbers along lines show the charge states.

References

[1] S. Urasaki, and H. Kageshima, Jpn. J. Appl. Phys. **56**, 025201 (2017).

[2] S. Urasaki and H. Kageshima, 2016 International Conference on Solid State Devices and Materials, Tsukuba, Japan, PS-13-02.

[3] https://azuma.nims.go.jp/cms1

First-Principles study on the electric-double layer capacitance of MXene compound Ti_2CT_x

Yasunobu ANDO

CD-FMat,

AIST, Tsukuba Central 2, 1-1-1 Umezono, Tsukuba, Ibaraki, 305-8568

MXenes are a new, large family of layered materials synthesized from MAX phases by simple chemical treatments. Due to their enormous variations, MXenes have attracted great attention as promising candidates as anode materials for next-generation secondary batteries. However, specific capacitance of MXene supercapacitors is lower than that of active-carbon ones. Theoretical investigation of the electric-double layer (EDL) at electrode interfaces is necessary to improve their capacitance.

Ab initio molecular dynamics (AIMD) simulation based on the density functional theory (DFT) is performed to estimate the EDL capacitance from a potential profile V(z) and a charge distribution q(z) induced by the ions at water- Ti_2CT_2 (T=O, F) interfaces. Potential profiles V(z) of both Ti_2CO_2 and Ti_2CF_2 decrease about 1.0 eV steeply in a region of only 3 Å from a Ti layer, which is the same profile at the platinum interfaces. On the other hand, induced charge distribution q(z) depends on the species of surface termination. Induced electrons are introduced at Ti layers in the case of O surface termination. However, Ti_2CF_2 is not capable to store electrons at Ti layers because it is mono-valence anions. It indicates that effective surface-position of MXenes depends on the surface terminations. Our results are revealed that small induced charge leads the low EDL capacitance at MXene interfaces. This is because interface polarization due to strong interaction between water and Ti_2CT_x induces net charge. The surface net charge hinders the introduction of ion-induced charges.

Electronic structure of light rare earth permanent magnets

Akai Group[a,b]
[a] *Institute for Solid State Physics, University of Tokyo*
Kashiwa-no-ha, Kashiwa, Chiba 277-8581
[b] *Elements Strategy Initiative Center for Magnetic Materials,*
National Institute for Materials Science,
Sengen, Tsukuba, Ibaraki 305-0047

Introduction There has been a surge in the interest on high-temperature magnetic anisotropy of $4f$-$3d$ intermetallics as motivated by practical applications of them as permanent magnets. Permanent magnets need strong magnetization and accordingly strong coercivity: magnetic anisotropy is considered to be the intrinsic origin of the coercivity. Magnetization mostly comes from $3d$-electrons in Fe or Co and leading-order magnetic anisotropy is contributed from $4f$-electrons in rare earth elements, while sub-leading $3d$-electron magnetic anisotropy can also be of relevance at high temperatures. We are developing *ab initio* understanding of magnetic anisotropy toward a quantitative understanding and control of magnetic properties of several representative compounds in permanent magnets. Here $4f$-electrons pose also a methodological challenge in *ab initio* calculations.

Target materials and methods In today's champion magnet, Nd-Fe-B alloy, the main phase is made of $Nd_2Fe_{14}B$ [1] which has 68 atoms, 4 formula units, in the complicated unit cell. Utilizing OpenMX and AkaiKKR [2], we have gone through the electronic states of $R_2Fe_{14}B$ permanent magnet compounds and RCo_5 compounds (R=rare earth) with the latter being a reference material to have our own theoretical insights in a relatively easy way. Thus complicated nature in the Nd-Fe-B champion magnets is being resolved one by one. Relativistic calculations to calculate magnetic anisotropy for $R_2Fe_{14}B$ can be computationally expensive but manageable with OpenMX, which implements $O(N)$ methods. Great variety of magnetic properties in $R_2Fe_{14}B$ depending on the species of R has been known [3] to which KKR-CPA as implemented in AkaiKKR is suitable for systematically tracking the trends among rare earth with $(R_{1-x}R'_x)_2Fe_{14}B$ where $0 \leq x \leq 1$ can be continuously swept. Significant part of our computational projects was launched in the latter half of the fiscal year 2016 and here we report

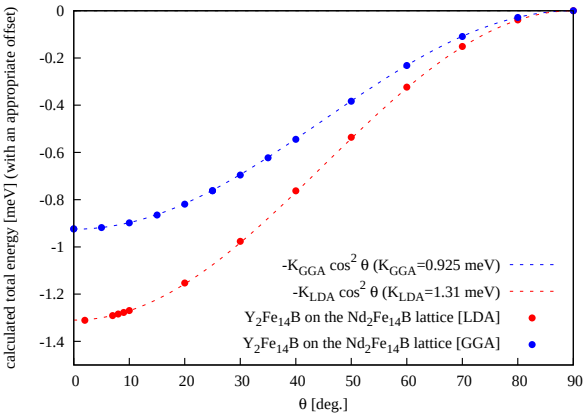

Figure 1: Calculated total energy for $Y_2Fe_{14}B$ artificially constructed on the experimental lattice of $Nd_2Fe_{14}B$ [1] as a function of the angle, θ, between the total magnetization and the c-axis. This is obtained with OpenMX fully relativistic runs with constrained non-collinear spin orientation.The energy gain in $\theta = 0$ reflects $3d$-electron magnetic anisotropy in $R_2Fe_{14}B$ (R=rare earth) The data was obtained on system B in March 2017 at the cost of $O(10^2)$ points overall.

our progress up to the anisotropy of d-electrons (as shown in Figs. 1 and 2) and magnetization (as shown in Fig. 3). Results concerning the magnetic anisotropy from $4f$-electrons are now being elaborated to be out in a separate few publications in the near future.

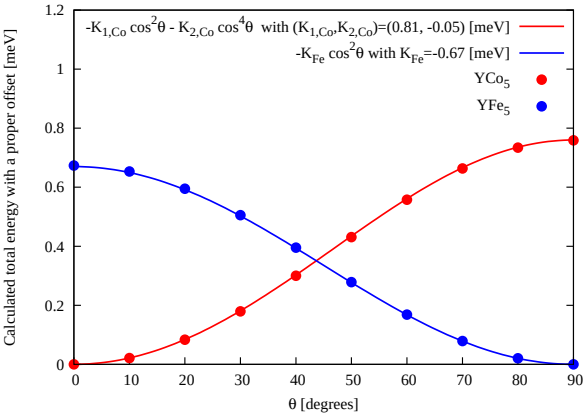

Figure 2: Calculated total energy for YT_5 (T=Co,Fe) on an computationally optimized lattice with OpenMX as a function of the angle, θ, between the total magnetization and the c-axis. The data collection procedure is the same as is applied for the data shown in Fig. 1.

Results [1/2]: magnetic anisotropy The leading-order uni-axial magnetic anisotropy can be described by the following term [4]:

$$\mathcal{H}_{\rm aniso} = -K_1 \cos^2\theta, \qquad (1)$$

where θ is the angle between the bulk magnetization in the ferromagnetic order and an easy-axis, which is c-axis for the present cases of $R_2Fe_{14}B$ (R=Nd, Pr, and Y) and R'Co_5 (R'=Y). Calculated results for $3d$-electron contribution in $R_2Fe_{14}B$ as shown in Fig. 1 indicates $K \simeq 1$ [meV/formula unit] which amounts to 0.7 [MJ/m^3] [1]. The result is in good agreement with the experimental number for $Y_2Fe_{14}B$ near the ground state, $K \simeq 0.8$ [MJ/m^3] [3].

Trends in $3d$-electron magnetic anisotropy have been inspected with the case of RCo_5 as shown in Fig 2. We make the following observations.

1. a higher-order term, $(-K_2 \cos^4\theta)$, contributes to the Co-anisotropy on top of the leading-order one written as Eq. (1). The quantitative relation between them, $K_2/K_1 \simeq -0.06$, seems to be in a reasonable agreement with the experimental result $K_2/K_1 \simeq -0.02$ as had been found in a past work [5].

2. Co and Fe contributes the opposite sign of anisotropy.

Implication of the second observation is serious for permanent magnet applications: a possible optimization of magnetization could be reached via the celebrated Slater-Pauling curve which points to a material-design principle that an appropriate mixture of Fe and Co would give us the best magnetization. We see that uni-axial magnetic anisotropy could be sacrificed during such course of magnetization optimization. Thus a non-trivial generalization of the Slater-Pauling curve is to be sought after where the overall performance in both of magnetization and anisotropy would be optimized.

Results [2/2]: magnetization Practical application of $Nd_2Fe_{14}B$ often involves alloys such as $(Nd_{1-x}Dy_x)_2Fe_{14}B$ in elevating the high-temperature coercivity to an industrially acceptable level or $(Nd_{1-x}Pr_x)_2Fe_{14}B$ when a light-rare-earth alloy is taken as the raw ingredients to fabricate a low-cost magnet. Thus it is important to address the intrinsic magnetism of such alloys, being at least of technological relevance. Also the known variation of magnetic properties with respect to the species of rare earth in $R_2Fe_{14}B$ [3] is to be put under a good theoretical control to come up with another material design principe to make the best use of rare-earth mixtures. Along these lines of motivations we have looked at the magnetization of $(Nd_{1-x}Pr_x)_2Fe_{14}B$ as shown in Fig. 3 to computationally interpolate the stoichiometric limits utilizing AkaiKKR. Mass generation of the data to explore the overall magnetic trends in (R,R')$_2Fe_{14}B$ is now under progress to be combined with machine-learning approach and reference experimental data: the idea is to distill potentially useful composition candidates which could have been overlooked

[1] Experimental lattice constants for $Nd2Fe_{14}B$ (a=8.8 [Å] and c=12.20 [Å]) [3] are tentatively taken here.

(a) Open core results

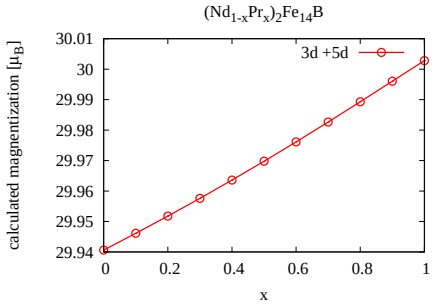

(b) manually adding $g_J\sqrt{J(J+1)}$

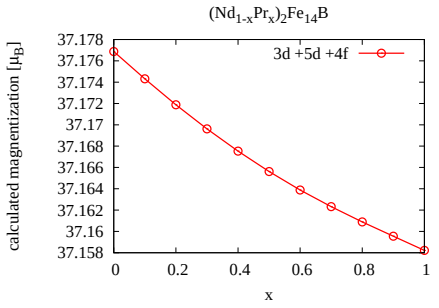

Figure 3: Calculated magnetization per formula unit of $(R_{1-x}R'_x)_2Fe_{14}B$ (R=Nd,R'=Pr) as a function of the composition parameter. Alloying of Nd and Pr has been described within Coherent Potential Approximation (CPA) and the data are collected utilizing AkaiKKR. (a) Open core results to show the *d*-electron contribution and (b) 4f-electron contribution has been included by manually adding $g_J\sqrt{J(J+1)}$ $[(g_J, J) = (8/11, 9/2)$ for Nd and $(4/5, 4)$ for Pr] as appropriately weighted with x.

on all-manual work done by strictly-limited human power.

Discussions We have successfully captured the qualitative trends in magnetization and magnetic anisotropy among $Y(Co,Fe)_5$ and $R_2Fe_{14}B$ (R=Nd, Pr, Y), while absolutely correct description on a quantitative level is yet to be achieved by a more comprehensive incorporation of realistic energy scales. Possible improvements might come in the following two-fold way:

1. Electronic correlation in 3*d*-bands, however small in an intermetallic compound, is not quite negligible. In order to describe such many-body physics, DFT+U or self-interaction correction can be done and are partly in progress in bringing the calculated results closer to experimentally known data.

2. The true macroscopic properties of permanent magnets involves extrinsic effects coming from classical dipolar magnetic fields. In principle they can also be incorporated in *ab initio* simulations while description of microstructure and various defects on the mesoscopic scale involves non-trivial physics on other level.

Conclusions and outlook Trends in magnetism among rare-earth permanent magnet compounds has been successfully addressed *ab initio* and the combined calculation framework (AkaiKKR+OpenMX) has been put onto our mass data production line with stoichiometric data points addressed with OpenMX and compositional interpolation taken care of with AkaiKKR. Together with a few schemes of implementation of *ab initio* description of $4f$-electron anisotropy by fully relativistic calculations, we expect that the mass data generation would take another few $O(10^4)$ points on system B in the upcoming fiscal year.

References

[1] J. F. Herbst: Rev. Mod. Phys. **63** (1991) 819.

[2] both available via MateriApps http://ma.cms-initiative.jp/ja/listapps and runs out of the box on System B.

[3] S. Hirosawa, Y. Matsuura, H. Yamamoto, S. Fujimura, M. Sagawa, and H. Yamauchi: J. Appl. Phys. **59** (1986) 873.

[4] M. Matsumoto, H. Akai, Y. Harashima, S. Doi, and T. Miyake, J. Appl. Phys. **119** (2016) 213901.

[5] J. M. Alameda, D. Givord, R. Lemaire, and Q. Lu: J. Appl. Phys. **52** (1981) 2079.

First-principles molecular spin dynamics theory of the complex magnetic structures in Mn-Pt alloys

Takashi UCHIDA
Hokkaido University of Science
4-1, 7-15, Maeda, Teine-ku, Sapporo 006-8585

Mn-Pt alloys show four different types of antiferromagnetic (AF) structures below their Néel temperatures depending on the composition and temperature. Mn_3Pt with Cu_3Au structure shows D-phase (triangular structure) and F-phase (collinear AF) . MnPt with CuAu-I structure shows II-phase (collinear AF) and III-phase (collinear AF). We have recently applied the first-principles molecular spin dynamics (MSD) method to Mn_3Pt and explained the magnetic phase transitions from the D-phase to a high-temperature ordered phase in terms of the temperature dependence of the electronic structure [1]. As a preparation for the systematic study on the disordered alloys $Mn_{3-x}Pt_{1+x}$ ($x = 0 \sim 1$), in the present research, we have investigated the electronic and magnetic structures of ordered MnPt alloy.

The MSD theory is formulated by incorporating the first-principles TB-LMTO Hamiltonian into the MSD approach for itinerant magnets on the basis of the functional integral method and the isothermal MSD technique [1, 2]. The MSD approach allows us to determine automatically the magnetic structure of a large system with several hundred atoms in a unit cell at finite temperatures. In the present MSD analysis, we solved the isothermal MSD equations of motion by using site-dependent effective medium. We used the recursion method to calculate the local electronic structure in determining the effective medium and in calculating magnetic forces at each time step of the MSD equations of motion. We utilized the MPI parallel calculation scheme in the recursion calculation. The site-dependent effective medium is determined by the local coherent potential approximation (CPA) equation. In the present case with tetragonal lattice, we have included the orbital dependence of the effective medium and the charge potential which is determined by the charge neutrality condition at each site. The magnetic structure is calculated on the supercell with $4 \times 4 \times 4$ CuAu-I unit lattice, which is embedded in a large cluster consisting of $5 \times 5 \times 5$ supercells, each of which are connected by the periodic boundary condition. The lattice parameter was fixed to the room temperature value [3].

The calculated magnetic structure of MnPt at 25 K was shown to be a collinear AF structure (II-phase) in agreement with experiment [3]. The calculated d-electron density of states (DOS) reveals a dip at the Fermi energy, being consistent with the previous LMTO calculation [4] with assuming the magnetic structure of II-phase.

References

[1] T. Uchida, N. Kimura, and Y. Kakehashi: J. Korean Phys. Soc. **62** (2013) 1748; Y. Kakehashi, S. Akbar, and N. Kimura, Phys. Rev. B**57** (1998) 8354.

[2] T. Uchida, Y. Kakehashi, and N. Kimura: J. Magn. Magn. Mater. **400** (2016) 103.

[3] E. Krén *et al.*: Phys. Rev. **171** (1968) 574.

[4] A. Sakuma: J. Phys. Soc. Jpn. **69** (2000) 3072.

Calculation of polarons, vibration modes, and positron trapping from first principles

Hannes Raebiger
Department of Physics, Yokohama National University
Graduate School of Engineering
Tokiwadai, Hodogaya-ku, Yokohama 240-8501

We employ first principles calculations to study not only electronic behavior, but also vibration modes in solids, and positron trapping in molecules. Solids are mainly studied by density-functional theories, whereas molecular systems are studied by Hartree-Fock theory. We push the limits of electronic structure theory, also by including positronic densities via multi-component theory [1], as well as by explicit calculation of nuclear wavefunction in order to investigate non-adiabatic phenomena at phase transitions [2].

Positron trapping in molecules

Positrons are a versatile to probe various properties of diverse materials. Positrons are used not only to probe defects in bulk materials [3] and recently also for medical purposes, including positron emission tomography [4]. The latter involves positron trapping to organic molecules, which is a poorly studied field. Moreover, for clinical applications, this positron trapping cannot be modeled by study of isolated molecules in vacuum, so we focus on the effect of an aqueous environment to the positron trapping properties of organic molecules. It is well known that in addition to negative ions, also strongly polar molecules may bind positrons [5]. We investigate positron binding to glycine (Gly) and its zwitterion (GlyZI) form, and their aqueous complexes $\mathrm{Gly} \cdot n\,\mathrm{H_2O}$ and $\mathrm{GlyZI} \cdot n\,\mathrm{H_2O}$, and show that also these systems do exhibit a critical dipole moment μ_{cr}, such that molecules with dipole moment $\mu > \mu_{\mathrm{cr}}$ bind positrons. However, we demonstrate that μ is not a sufficient quantity to describe binding properties to such complex systems, and that positron binding to molecular systems also strongly depends on the intramolecular bonding [6].

Localization of vibration modes around defects in 2D materials

2D and quasi-1D bulk materials have unique phonon properties, which allow, e.g., to determine sample thickness based on shifts in typical vibration modes [7]. In collaboration with experiment, we show that defects in $\mathrm{MoS_2}$ give rise to new Raman active vibration modes, which are unique to different types of defects [8]. We discover new vibration modes, which are both localized near defect sites, as well as scattered, such as to exhibit large vibration amplitudes far away from the defects. Thus, we have shown that Raman spectroscopy combined with first principles caluation offer a non-invasive probe to observe both defect species, as well as to evaluate defect concentrations etc.

Non-adiabatic metal-insulator transition in magnetic semiconductors

Mn-doped GaAs is an important and widely studied material for magnetic semiconductors. In addition to its exotic magnetic properties,

it exhibits a critical metal-insulator transition (MIT) as Mn concentration x is increased up to, and beyond $\sim 1\%$. We study this material by self-interaction corrected density-functional calculations [9], and for the first time, reproduce a critical MIT in a first principles calculation [2]. We find both delocalized, metallic states Φ_M, as well as localized, insulator states Φ_I, whose relative stability depends on x: Φ_M is stable for $x > 1\%$, and Φ_I is stable for $x < 1\%$. Moreover, around the critical concentration $\sim 1\%$, both states coexist. We calculate the adiabatic potential energy surface that joins these states, which exhibits an anharmonic double-well structure. We then numerically evaluate nuclear wavefunctions for nuclear motion Q along this adiabatic potential, showing that the system must be described by an anharmonic superposition state $c_I(Q)\Phi_I + c_M(Q)\Phi_M$ [2]. Thus, the MIT criticality in this system arises due to excitonic phases [**?**]; this implies that for critical x, Mn-doped GaAs is an excitonic insulator, and in this sense, our work proves the realization of an excitonic insulator material.

References

[1] M. Tachikawa: Chem Phys. Lett. **350** (2001) 269.

[2] S. Bae and H. Raebiger: Phys. Rev. B (Rapid Communications) **94** (2016), 241115(R).

[3] F .Tuomisto and I. Makkonen: Rev. Mod. Phys. **85** (2013) 1583.

[4] M. Reivich et al.: Circ. Res. **44** (1979) 127.

[5] O. Crawford, Proc. Phys. Soc. (London) **91** (1967) 279.

[6] M. Nummela, H. Raebiger, D. Yoshida, and M. Tachikawa: J. Phys. Chem. A **120** (2016) 4037.

[7] K. Osada S. Bae M. Tanaka H. Raebiger K. Shudo T. Suzuki: J. Phys. Chem. C **120** (2016) 4653.

[8] S. Bae, N. Sugiyama, T. Matsuo, H. Raebiger, K. Shudo, K. Ohno: Phys. Rev. Applied **7** (2017) 024001.

[9] S. Lany and A. Zunger: Phys. Rev. B **80** (2009) 085202.

[10] W. Kohn: Phys. Rev. Lett. **19** (1949) 416.

Search for new electronic properties of new nanoscale interfaces

Katsuyoshi KOBAYASHI
Department of Physics, Ochanomizu University
2-1-1 Otsuka, Bunkyo-ku, Tokyo 112-8610

We started a theoretical study on the electronic states of IV-VI monolayers on alkaline-earth chalcogenide surfaces in 2015. We performed more detailed study on the same system in 2016.

It was theoretically proposed by several groups that IV-VI monolayers are two-dimensional (2D) topological crystalline insulators (TCIs). However, it was also pointed out that the planar structure of free standing IV-VI monolayers is not stable, and the TCI states are broken by structural deformation [1]. In order to maintain the planar structure of IV-VI monolayers we consider the system of IV-VI monolayers supported by substrates. First we consider alkali halide surfaces for supports. However, it was found that the interaction between IV-VI monolayers and alkali halides is weaker than that between IV-VI monolayers. This means that single IV-VI layers are not stable on alkali halide surfaces. Therefore we consider alkaline-earth chalcogenide surfaces as a candidate for supports having strong interaction with IV-VI monolayers. In 2015 we performed energetic calculations using 1×1 unit cell. In 2016 we extend the calculations up to 2×2 unit cell. For the total-energy calculations we used the VASP code.

The IV-VI monolayers investigated are GeS, GeSe, GeTe, SnS, SnSe, SnTe, PbS, PbSe, and PbTe. The alkaline-earth chalcogenides are MgO, MgS, MgSe, CaO, CaS, CaSe, CaTe, SrO, SrS, SrSe, BaO, and BaS. Various combinations of these monolayers and supports are investigated. We found that the combinations favorable for stable IV-VI monoalyers on surfaces are SnTe-SrS, SnTe-SrSe, SnTe-CaTe, SnTe-BaS, SnSe-CaS, SnSe-CaSe, SnS-MgSe, and GeSe-MgSe. In the structural optimization we found a structure of IV-VI monolayers shown in Fig. 1. This structure consists of tetragons and octagons of IV-VI networks. It is essentially the same structure as those found theoretically for Bi monolayers [2, 3, 4].

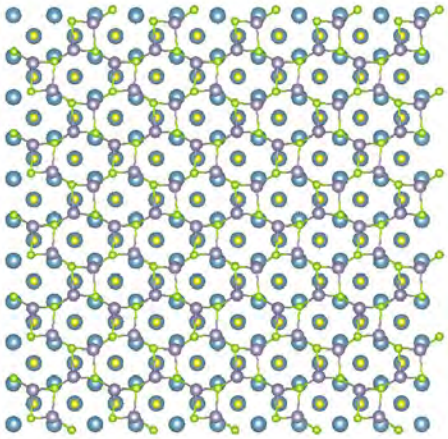

Figure 1: Top view of a tetragonal-octagonal structure of IV-VI monolayer on an alkaline-earth chalcogenide surface. The tetragonal-octagonal structure is shown by the network.

References

[1] K. Kobayashi: Surf. Sci. **639** (2015) 54.

[2] L. Kou *et al.*: 2D Materials **2** (2015) 045010.

[3] P. Li and W. Luo: Sci. Rep. **6** (2016) 25423.

[4] F. Ersan *et al.*: Phys. Rev. B **94** (2016) 245417.

Thermo-Chemical Wear Mechanism of Diamond Cutting Tools

Yutaka Uda, Shoichi Shimada

Osaka Electro-Communication University, Hatsu-cho, Neyagawa, Osaka 572-8530

Sakuro Honda

Technology Research Institute of Osaka Prefecture, Ayumino, Izumi, Osaka 594-1157

Diamond is the only ideal cutting tool material for high efficient ultraprecision cutting of accurate three-dimensional metal works such as molds for precise optical components with high aspect ratio. However, it is well known that diamond cutting tools show severe wear in cutting of heat-resistant materials such as ferrous metals and nickel. On the other hand, in cutting of electroless nickel deposits, in which 10-14% phosphorus (P) is solid-soluted, remarkably less tool wear is observed than in case of pure nickel [1,2]. However, the essential mechanisms of tool wear and its suppression by P addition have not yet been understood well. To understand these mechanisms, first principles analyses were carried out using double-grid method for real-space electronic-structure calculations package RSPACE [3].

The $C_{10}H_{14}$ cluster was used as the model of diamond (100) surface. The dangling bonds other than that of the radical carbon atom at the bottom layer of diamond were terminated by hydrogen atoms. The atomic and back bond populations of the radical carbon were 4.11 and 0.894, respectively. The thin Ni (100) surface model was composed of 24 Ni atoms. The dimension of the model $x \times y \times z$ was $2a \times 2a \times a$, where a is lattice constant of Ni. The atomic populations of all Ni atoms were 10.0. The model has periodic boundaries in x and y directions and aperiodic boundary in z direction. The Ni-P surface model was prepared by randomly distributing of 6 P atoms at the octahedral holes of the Ni model. The atomic populations of Ni atoms decreased from 9.29 to 9.72 and those of P atoms increased from 6.28 to 6.39. The result suggests that strong ionic bonding occur between Ni and P atoms.

The atomic and bond populations in combined structures of diamond with Ni after optimization are shown in Fig.1. White and yellow figures express atomic and bond populations, respectively. By the interaction with Ni, the atomic population of radical carbon increases to 4.91 and those of Ni atoms interacting with radical carbon decreases

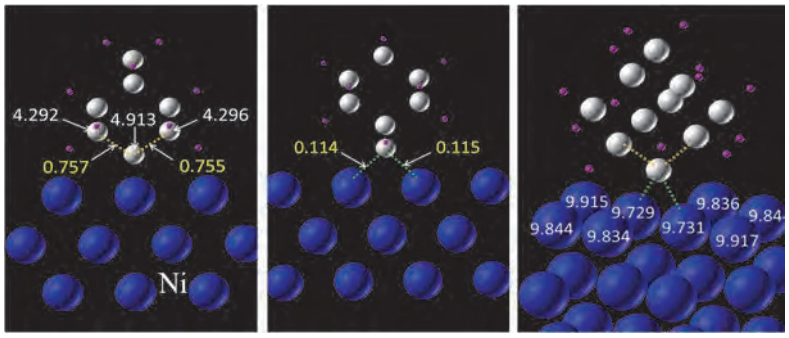

Fig. 1 Atomic and bond populations in combined structure of diamond with Ni surface after optimization.

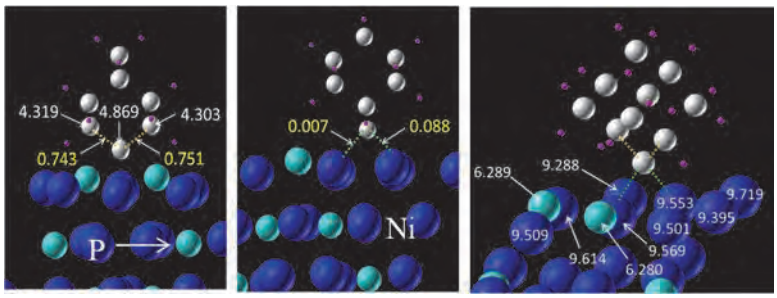

Fig.2 Atomic and bond populations in combined structure of diamond with Ni surface after optimization.

to 9.73. The result suggests that the strength of ionic bond between carbon and Ni increases. As the population of back bonds of radical carbon decrease to 0.76 from the original value of 0.89, the strength of covalent bond of back bonds decreases and the radical carbon has a chance to dissociate from the diamond surface when it has a large kinetic energy due to cutting temperature. On the other hand, in case of interacting with Ni-P, both of decrease of back bond population and increase of atomic population of radical carbon are remarkably suppressed as shown in Fig.2.

The dissociation energy of the radical carbon was estimated as shown in Figure 3. Diamond model is lifted up from optimum stable structure leaving the radical carbon on work surface. By optimization after lifting of a certain distance, the radical carbon moves toward the main body of diamond. However, at a lift up distance larger than the critical value, the radical carbon stays on the work surface. The dissociation energy of the radical carbon can be estimated from the difference between the total energy of the combined structure at the critical lift up distance and that of optimum stable structure. Although the atomic structure was not optimized in pulling up process, the dissociation energies of radical carbon by different work materials can be relatively compared. The dissociation energies estimated are 5.01eV and 5.70eV when the diamond is contacting with Ni and Ni-P, respectively. The results suggest that the essential wear mechanism is the dissociation of carbon atoms on diamond surface due to the interaction with nickel atoms on work surface. P atoms addition reduces the dissociation because the interaction is suppressed.

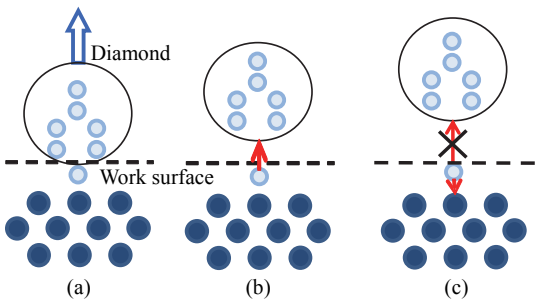

Fig.3 Estimation of dissociation energy of radical carbon atom interacted with work surface.

References

[1] C.K. Syn, J.S. Taylor, R.R. Donaldson: Proc. SPIE, **676** (1986) 128.

[2] J.M. Oomen, L. Eisses: Precision Engineering, **14**, (1992) 206.

[3] K. Hirose, T. Ono: First-Principles Calculations in Real-Space Formalism – Electronic Configurations and Transport Properties of Nanostructures -, Imperial College Press, London, (2005).

Electron-Phonon Interactions in Isotopic Diamond Superlattice

Yuki Bando, Masayuki Toyoda, and Susumu Saito
Department of Physics, Tokyo Institute of Technology
2-12-1 Ookayama, Meguro-ku, Tokyo 152-8550 Japan

The isotopic diamond superlattices that are periodic arrays of layers of carbon isotopes, such as ^{12}C and ^{13}C, with diamond structure, have been known to confine carriers to the layers of the lighter isotope (^{12}C) due to the isotope effect on the electron-phonon interaction [1]. This phenomena has a great potential to realize the band-gap engineering in diamonds and to utilize diamonds as electronic devices. In this study, the electron-phonon interactions have been quantitatively investigated for the isotope diamond superlattices using the adiabatic Allen-Heine-Cardona calculations based on the density functional perturbation theory [2]. The calculations were performed by using ABINIT code [3] on the cpu nodes of system B. The visualized images of the crystal structures were created by using XCrySDen [4].

Figure 1(a) shows the crystal structures of the superlattices. The stacking direction is along [001] and each structure is labeled as $\{m,n\}$ that means it consists of periodic arrays of m atomic layers of ^{12}C and n atomic layers of ^{13}C. The tetragonal unit cells of the superlattices have a lower symmetry than the original $Fd\bar{3}m$ symmetry and thus the electron-phonon interaction would modify the electronic structure in such a way that it breaks the original symmetry. One of such examples is schematically shown in Fig. 1(b), where the six identical electron pockets in diamonds are separated into two groups in superlattices: two pockets along Γ-Z line and four along Γ-M line.

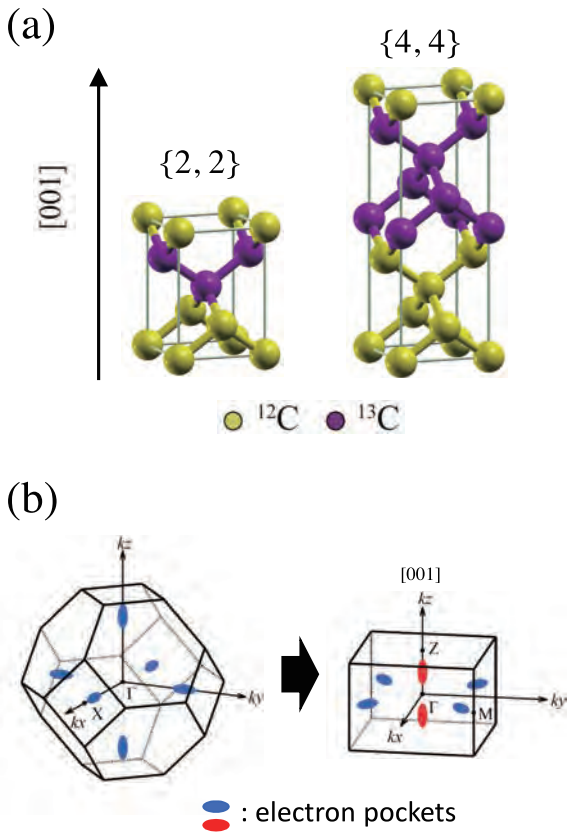

Figure 1: (a) Tetragonal unit cells of {2,2} and {4,4} isotope diamond supperlattices (see text for the definition of the labels). (b) Schematic image of the electron-pockets in the fcc (simple diamond) and tetragonal (superlattices) Brillouin zones.

The zero point renormalization (ZPR) of the Kohn-Sham band gap has been calculated for the isotope superlattices. Figure 2 shows the calculated Kohn-Sham eigenvalues around the valence band (VB) top and conduction band

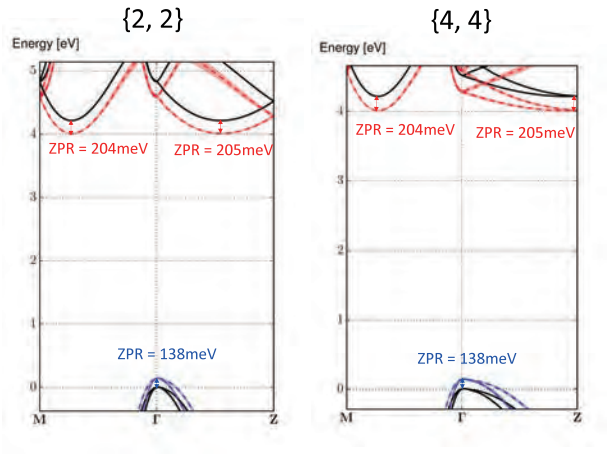

Figure 2: Calculated zero-point renormalized Kohn-Sham eigenvalues of the valence bands (blue) and conduction bands (red). The Kohn-Sham eigenvalues without renormalization are also plotted by the black line for comparison.

(CB) bottoms, as well as the renormalized eigenvalues. The Kohn-Sham band structure is shown by the black solid lines and the renormalized band structure is by the colored (red for CB and blue for VB) dashed lines. For both of the {2,2} and {4,4} systems, the renormalization of the indirect band-gap is 342 meV. This value is in exact agreement with the renormalization of the band gap calculated for a simple diamond lattice of a carbon isotope with a virtual mass number $^{12.5}$C. This result shows that the isotope effect is mass-averaged, being consistent with our previous study of the phonon modes of the this layer isotope superlattices.

Interestingly, we found that there is a slight difference in the ZPR of the CB bottoms between those along Γ-M and Γ-Z lines. The difference is as small as 1 meV, but it might possibly be due to the symmetry breaking as discussed above. In order to confirm this symmetry breaking ZPR effect, further study is necessary.

References

[1] H. Watanabe, C.E. Nebel, and S. Shikata, Science **324** (2009) 1425.

[2] S. Ponce, et al, Phys. Rev. B **90** (2014) 214304

[3] X. Gonze, et.al, Computer Physics Communications **180** (2009) 2582-2615

[4] A. Kokalj, Comp. Mater. Sci., **28** (2003) 155.

Theoritical reserch on dissociation of N_2 for designing new ammonia catalysis supporting Ru

Yoichi KAMIHARA
Department of Applied Physics and Physico-Informatics, Keio University
3-14-1 Hiyoshi, Yokohama, Kanagawa 223-8522

In the Haber-Bosch process NH_3 is synthesized from gaseous N_2 and H_2 with an Fe-based catalyst for over 100 years[1]. In 21st century, it has been reported that Ru-loaded $[Ca_{24}Al_{28}O_{64}]^{4+}(e^-)_4$ (Ru/C12A7:e^-) works as an efficient catalyst for NH_3 synthesis[2]. C12A7:e^-, the first room temperature stable electride, which has a low work function (2.4 eV) comparable to that of potassium metal, with chemically and thermally stability. C12A7:e^- contains 12Ca-Al-O cage structures in a unit cell. In this report, three virtual Ru/C12A7:e^- lattices are modeled by layered slab models. These N_2 adsorption energies are quantified for these models.

A first reaction step in the synthesis of ammonia is

$$N_2 + 2(*) \longrightarrow 2N(*) \quad (1)$$

where $(*)$ stands for an empty site on the surface. The adsorption energies (E_{ad}) of nitrogen were calculated using

$$E_{ad} = 2E_{N-Ru/C12A7} - 2E_{Ru/C12A7} - E_{N_2} \quad (2)$$

where $E_{Ru/C12A7slab}$ and $E_{N-Ru/C12A7}$ stand the total energies of the Ru/C12A7 clean surface and Ru/C12A7 surface with an adsorbed nitrogen atom respectively. E_{N_2} is the total energy of a nitrogen molecule.

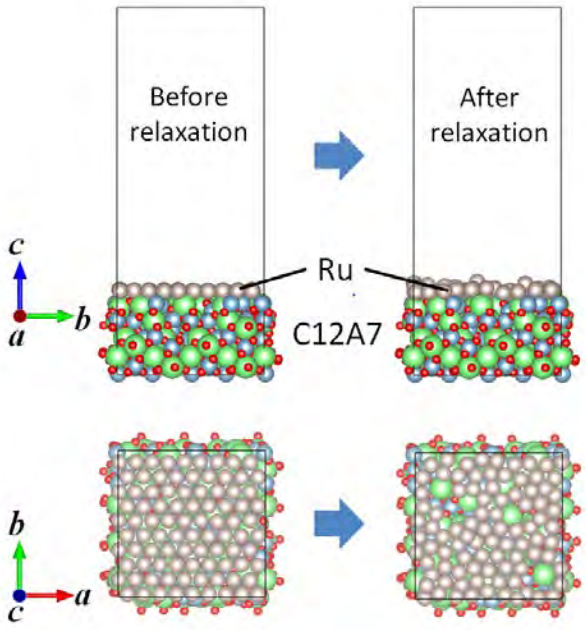

Figure 1: Structure of slab model of 1 Ru layer on C12A7 before and after optimization of internal structure. Green, blue and red symbols represent Ca, Al and O ions, respectively.

Each calculation has been carried out based on density functional theory (DFT) using Projector Augmented Wave (PAW) method[3] implemented in the Vienna *ab-initio* Simulation Package (VASP)[4]. Generalized gradient approximation (GGA) of Perdew-Burke-Ernzerhof (PBE) functional[5] was adopted for exchange-correlation energy.

The Ru supported by C12A7 surface were

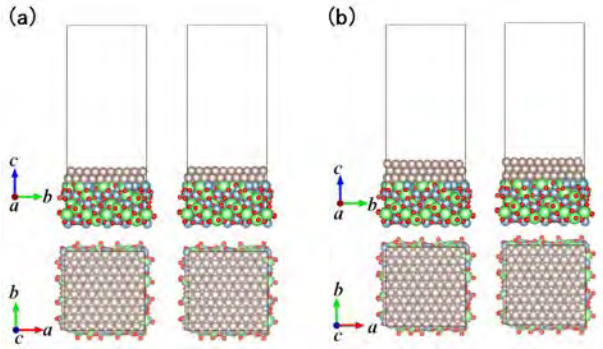

Figure 2: Structure of slab model of 2 and 3 Ru layers on C12A7 before (left) and after (right) optimization of internal structure. Green, blue and red symbols represent Ca, Al and O ions, respectively.

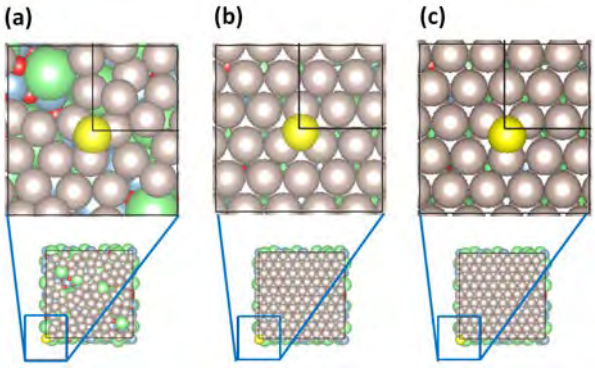

Figure 3: The configurations of the surfaces adsorbed nitrogen atoms on (a)1 Ru layer model (b)2 Ru layers model (c)3 Ru layers model. Green, blue, red and yellow symbols represent Ca, Al, O and N ions, respectively.

modeled as periodically repeating C12A7, Ru (0001) and vacuum for simplify the system. Supercell was made by $(2 \times 2 \times 1)$ of C12A7 unitcell, N layer(s) $(N = 1, 2, 3)$ of Ru (0001) surface (90 atoms per layer) and vacuum region of 4.2 nm. The energy cut off for plane waves was 500 eV. The Brillouin zone was sampled at the Γ point only. Fractional occupancies of the bands were obtained allowed using a Gaussian smearing method with width $\sigma = -0.05$[6].

Fig. 1, Fig. 2(a) and Fig. 2(b) show the schematic image of slab structures of 1, 2 and 3 layer(s) of Ru on C12A7 before and after optimization of internal structures for the lattices respectively. For 1 Ru layer model, Ru atoms move along the C12A7 surface. Therefore C12A7 surface is partially exposed to vacuum. As for 2 and 3 Ru layers model, such an atomic coordination's movement are smaller than that of 1 Ru layer model.

After ionic optimization, a nitrogen atom laid on a hollow site of the obtained surface model of N layer(s) $(N = 1, 2, 3)$ of Ru (0001) on C12A7(Fig. 3). Adsorption energies E_{ad} of 1 Ru layer model, 2 Ru layers model and 3 Ru layers model are calculated as -1.74 eV, -0.21 eV and -0.48 eV respectively. A nitrogen atom is more stable when it adsorbed on the surface of 1 Ru layer model, than that of 2 or 3 Ru layers model.

In our calculation, the supporting C12A7makes matrix structures composed of several Ru atoms and the Ca-Al-O cages. The matrix surface structures would works to enhance the catalytic activity in the process of dissociative adsorption for 1 Ru layer model. As for 2 and 3 layers model, further calculation is required.

References

[1] F. Haber: Z. Elektrochem. Angew. P. **16** (1910) 244.

[2] M. Kitano, *et al.*: Nature Chemistry **4** (2012) 934.

[3] P. E. Blöchl: Phys. Rev. B **50** (1994) 17953.

[4] G. Kresse and J. Hafner: Phys. Rev. B **47** (1993) 558.

[5] J. P. Perdew, K. Burke and M. Ernzerhof: Phys. Rev. Lett. **77** (1996) 3865.

[6] `https://cms.mpi.univie.ac.at/vasp/vasp/Finite_temperature_approaches_smearing_methods.html`

Ab-initio Analysis on Structures of Amorphous Iron Oxide for Secondary Battery

Kenji TSURUTA, Keiichi MITANI, Satoshi OHMURA[a], and Atsushi ISHIKAWA

Graduate School of Natural Science and Technology, Okayama University, Okayama 700-8530
[a] Department of Civil Engineering and Urban Design, Hiroshima Institute of Technology, Hiroshima 731-5193

Corundum-structure hematite α-Fe_2O_3 is one of the most common mineral on the earth, and plays important roles in various industrial sectors such as steel, medical and electronics. Especially, hematite nanoparticles have recently attracted much attention for lithium-ion batteries, sensors, biomedical, and photoelectro-chemical (PEC) applications. In addition, the iron-oxide nanoparticles are found in nature as biogenous secondary materials [1]. It has been identified that the biogenous iron-oxide has an amorphous structure containing several impurities such as Si and P. They have exhibited to possess high capacity in using anode material of Li-ion secondary battery.

In the present study, we investigate structural properties of a Si/P co-doped hematite using the density-functional theory. The generalized gradient approximation (GGA) + *U* functional, the Perdew-Burke-Ernzerhof functional for the local spin density approximation of exchange-correlation, and the projector-augmented wave based pseudo-potential for the core electrons have been employed for the electronic-structure calculations. The ab-initio molecular dynamics simulations with the *NPT* ensemble have been performed to obtain thermal equilibrium states of the Si/P co-doped systems of an anti-ferromagnetic (AFM) state at the room temperature, as well as a non-doped amorphous structure modeled by rapid quenching from high-temperature (3000K) melt. We have adopted the Vienna Ab initio Simulation Package (VASP) for these ab-initio simulations.

The pair distribution functions $g_{\alpha\beta}$ for the co-doped and the non-doped amorphous Fe_2O_3 models are shown in Fig. 1. In $g_{OO}(r)$ of the amorphous Fe_2O_3, the peak in the vicinity of r = 1.5Å indicates that oxygen dimers are formed in a disordered structure of the iron oxide at the AFM state. This feature is consistent with previous theoretical calculations for Fe_2O_3[2]. We find that all the $g_{\alpha\beta}(r)$ agree very well with each other; overlaps between both distributions for Fe-Fe, O-O and Fe-O are 97.5%, 95.8% and 98.7% respectively. Thus the Si/P co-doping has been shown to be an efficient route for amorphization of iron oxides.

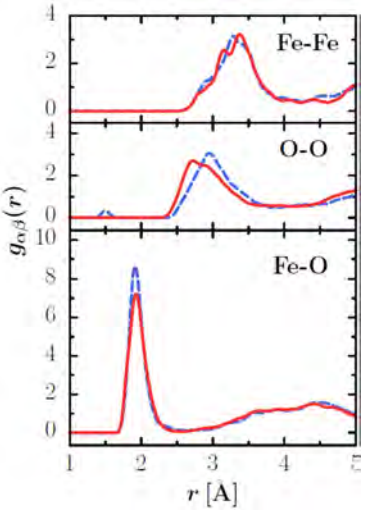

Fig. 1: Partial pair distribution functions $g_{\alpha\beta}(r)$ for non-doped amorphous (dashed lines) and Si/P co-doped Fe_2O_3 (solid lines).

References

[1] H. Hashimoto *et al.*, ACS Appl. Mater. Interface **6**, 5374-5378 (2014).

[2] M. Misawa *et al.*, J. Phys. Soc. Jpn. **83**, 105002 (2014).

First-Principles Momentum Dependent Local Ansatz and Application to Momentum Distribution Function and Quasiparticle Bands in Fe Compounds

Yoshiro KAKEHASHI
Department of Physics and Earth Sciences, Faculty of Science, University of the Ryukyus, 1 Senbaru, Nishihara, Okinawa, 903-0213, Japan

Quantitative aspects of the density functional theory (DFT) are well-known to become unstable with increasing Coulomb interaction strength as found in ϵ-Fe, Fe-pnictides, and cuprates. In order to describe correlated electrons quantitatively and to remove the difficulties in the DFT, we have recently proposed the first-principles momentum dependent local ansatz (MLA) wavefunction theory on the basis of the tight-binding LDA+U Hamiltonian [1].

In the first-principles MLA, we introduce the three kinds of momentum dependent correlators (*i.e.*, intra-orbital correlator, inter-orbital charge-charge correlator, and inter-orbital spin-spin correlator), and takes into account all the two-particle excited states with the momentum-dependent amplitudes, so that it describes exactly the weak interaction limit, and describes well correlated electrons from the weak to strong Coulomb interaction regime.

In this project, we have performed the numerical calculations of the ground-state properties of iron-group transition metals from Sc to Cu using the first-principles MLA.

We found large Hund's rule correlation energy in Mn and Fe (3000 K), which are missing in the magnetic energy calculations in the LDA+DFT. The Hund rule correlations also enhance the amplitudes of local moments. We found that calculated amplitudes of local moments quantitatively explain the experimental values estimated from the inner core photoelectron spectroscopy and susceptibility [2].

We also found large deviation of the momentum distribution function from the Fermi-Dirac function in the late transition metals. Figure 1 shows a systematic change of the mass enhancement factors m^*/m calculated from the jump of the momentum distribution function. We found significant enhancement of m^*/m in the late transition metals. The result explains a systematic change of the experimental data obtained from the low-temperature specific heats [2].

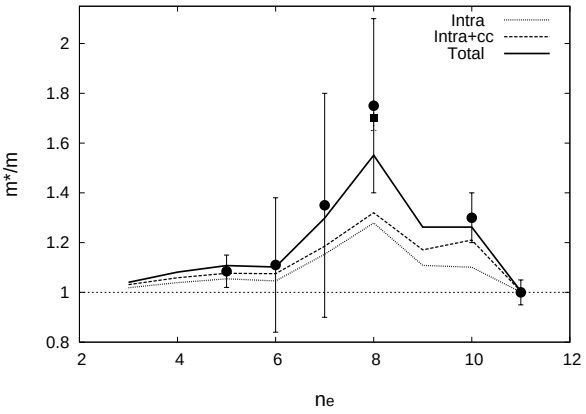

Figure 1: Calculated mass enhancement factor (m^*/m, solid curve) as a function of conduction electron number n_e. Experimental results: closed circles, closed squares.

References

[1] Y. Kakehashi and S. Chandra, J. Phys. Soc. Jpn. **85**, 043707 (2016); **85**, 064714 (2016).

[2] Y. Kakehashi and S. Chandra, J. Phys. Soc. Jpn. **85**, 084708 (2016); **86**, 034711 (2017).

Electronic State and Proximity Effects around Interface in Layered Superlattices

Kunitomo HIRAI
Department of Physics, Nara Medical University
Kashihara, Nara 634–8521

The purpose of the present research is to elucidate characteristics of electronic state in superlattices with layered structures, in particular, to illustrate proximity effects of each layer on adjacent layers in the superlattices. This research of a first-principles electronic structure calculation is performed by means of the Korringa-Kohn-Rostoker (KKR) Green function method within the framework of the local spin density (LSD) functional formalism.

The calculation by means of the KKR method was so far carried out for superlattices of ferromagnetic layers with nonmagnetic spacer layers such as Fe/Cr, Fe/V, Fe/Cu, ... ones, with magnetizations of two successive Fe layers being aligned parallel or antiparallel. Oscillatory interlayer exchange coupling between ferromagnetic layers with respect to spacer thickness was investigated, and relation between bulk effects inherent in the spacer layer and the proximity effects due to the ferromagnetic layers was analyzed. In the calculation, every atom in a monolayer stacked in the superlattices is assumed to be equivalent, and there is one site in each monolayer. This assumption can be justified for the superlattices with ideal interfaces without structure, but not for those with realistic interfaces with structures like steps, islands, or such, and hence there are two or more sites in each monolayer for the superlattices with realistic interfaces.

A need of the calculation for superlattices with more sites in each monolayer arises also for layered superlattices of ordered alloys or compounds, which now attract broad interests particularly in viewpoint of spintronics. We then start preparation of the calculation for superlattices with more sites in each monolayer, which results in increase of the number of atoms in a unit cell and involves vast increase of computation times. In the preparation of the calculation, installation of parallelization with use of the OpenMP into program codes of the KKR methods is intended, together with parallelization with use of the MPI which was already achieved, that is, installation of hybrid parallelization is intended.

The installation of the OpenMP has not been achieved within the present term, which was the last one, and it is really unfortunate that the proximity effects in the superlattices with realistic interfaces are not amply investigated. In the last place, I thank the Supercomputer Center, Institute for Solid State Physics, the University of Tokyo for the longtime use of its facilities.

3.3 Strongly Correlated Quantum Systems

Numerical Studies on Finite-Temperature Properties of Superconductivity in Cuprates

Dai Kubota, Kota Ido, Kensaku Takai, Huihai Zhao, Yusuke Nomura,
Takahiro Ohgoe, and Masatoshi Imada
Department of Applied Physics, University of Tokyo
Hongo 7-3-1, Bunkyo-ku, Tokyo 113-8656

Superconductivity in cuprates has attracted extensive attention since its discovery. In bulk, the discovery of (short-ranged) charge order has raised renewed interest in the relationship between pseudogap and superconductivity [1]. At interfaces, several exotic phenomena which are not observed in the bulk has been reported. For example, at the interface of La_2CuO_4 (insulator) and $La_{2-x}Sr_xCuO_4$ (metal), it has been shown that the transition temperature (T_c) of the interface superconductivity is anomalously pinned around the maximum T_c in bulk (~ 42 K) irrespective of doping concentration x in the metallic layers [2].

As for the interfaces, a previous study using high-accuracy many-variable variational Monte Carlo (mVMC) method [3] has given an explanation for the anomalous behavior of T_c at interfaces [4]. This study has revealed that the doping concentration at the interface is self-optimized to the optimal doping by the interlayer phase separation, which leads to the pinned superconducting order parameter at zero temperature. The pinned superconducting order parameter at $T = 0$ naturally explains the pinning of T_c.

The interlayer phase separation is realized to avoid the charge inhomogeneity within the layer. The instability for intralayer phase separation or charge inhomogeneity in bulk has been suggested by the mVMC calculations at $T = 0$. It has also revealed that the phase separation and associated uniform charge fluctuations play an important role in realizing high T_c superconductivity [5]. However, to discuss the relationship between charge instability and T_c, it is advantageous to perform finite-temperature calculations which can directly calculate T_c. It is also an important problem to investigate whether the instability for the phase separation persists to finite temperatures. Therefore, in this project, we extend the study to finite temperatures and investigate the microscopic origin for charge instability and the role of charge fluctuations in the superconductivity.

For this purpose, we study multi-layer Hubbard model defined as

$$\begin{aligned} H = &-t \sum_{\langle i,j\rangle,\nu,\sigma} (c^\dagger_{i\nu\sigma} c_{j\nu\sigma} + \text{h.c.}) \\ &- t_z \sum_{i,\sigma,\langle\nu,\nu'\rangle} (c^\dagger_{i\nu\sigma} c_{i\nu'\sigma} + \text{h.c.}) \\ &+ U \sum_{i,\nu} n_{i\nu\uparrow} n_{i\nu\downarrow} - \sum_{i\nu} \epsilon_\nu n_{i\nu}, \end{aligned} \tag{1}$$

where $c_{i\nu\sigma}$ ($c^\dagger_{i\nu\sigma}$) is an annihilation (creation) operator of an electron with spin σ at ith site on νth layer. The number operators are defined as $n_{i\nu\sigma} = c^\dagger_{i\nu\sigma} c_{i\nu\sigma}$, and $n_{i\nu} = n_{i\nu\uparrow} + n_{i\nu\downarrow}$. The chemical potential ϵ_ν can be layer-dependent in the simulation for interfaces. t (t_z) is the intralayer (interlayer) transfer. The onsite Coulomb interaction U is set to $U = 8t$.

We apply the cellular dynamical mean field theory (CDMFT) [6] to this model. In the cDMFT, we solve the cluster impurity problem

embedded in self-consistently determined bath sites. The impurity problem is analyzed by exact diagonalization method extended to finite temperatures [7]. As a result, we have obtained several solutions: d-wave superconductivity (d-SC), antiferromagnetic (AF) phase, and the coexistence between d-SC and AF. We have calculated the grand canonical potential for these phases and found that there exists instability for phase separation also at finite temperature. If we make interfaces, this intralayer phase separation will be avoided by the interlayer phase separation, and the stable interface superconductivity will emerge.

It will also be interesting to perform finite-temperature calculations using the mVMC. We have already formulated finite-temperature variational Monte Carlo (FT-VMC) scheme [8]. Combining mVMC with the tensor-network will further improve the accuracy [9]. Studies in this direction is under way.

References

[1] G. Ghiringhelli *et al.*, Science **337**, 821 (2012); J. Chang *et al.*, Nat. Phys. **8**, 871 (2012).

[2] J. Wu *et al.*, Nat. Mater. **12**, 877 (2013).

[3] D. Tahara and M. Imada, J. Phys. Soc. Jpn. **77**, 114701 (2008).

[4] T. Misawa *et al.*, Sci. Adv. **2**, e1600664 (2016).

[5] T. Misawa and M. Imada, Phys. Rev. B **90**, 115137 (2014).

[6] A. I. Lichtenstein and M. I. Katsnelson, Phys. Rev. B **62**, R9283 (2000); G. Kotliar *et al.*, Phys. Rev. Lett. **87**, 186401 (2001).

[7] S. Sakai *et al.*, Phys. Rev. Lett. **116**, 057003 (2016).

[8] K. Takai *et al.*, J. Phys. Soc. Jpn. **85**, 034601 (2016).

[9] H.-H. Zhao *et al.*, arXiv:1703.03537.

Creation and Control of Skyrmions with Different Topological Numbers in Itinerant Magnets

Ryo Ozawa, Yasuyuki Kato, and Yukitoshi Motome
Department of Applied Physics, University of Tokyo 113-8656 Hongo, Bunkyo-Ku, Tokyo

A magnetic Skyrmion, which is a swirling noncoplanar spin texture, has been intensively studied not only from the viewpoint of fundamental physics but also for potential applications to magnetic devices, mainly owing to the robustness protected by the topological nature. Most of previous studies thus far have been concerned primarily with the Skyrmions with topological number of one ($n_{\rm sk} = 1$). For further extensions of potential applications, other types of Skyrmions have been desired, both experimentally and theoretically.

In this study, we explore a new type of Skyrmions in a fundamental model for itinerant magnets by large-scale simulation. We here focus on the stabilization mechanism not by the competition between ferromagnetic and Dzyaloshinskii-Moriya interactions, which has been intensively studied for the conventional Skyrmions with $n_{\rm sk} = 1$, but by the Fermi surface instability, existing ubiquitously in itinerant magnets. Specifically, we study the ground state and finite-temperature properties of the Kondo lattice model on a triangular lattice by a recently-developed efficient algorithm based on both the kernel polynomial method (KPM) and the Langevin dynamics (LD) [1], which we call the KPM-LD simulation. For the KPM-LD simulation, we utilize massive parallel processing by general-purpose computing on graphics processing units (GPGPU) to perform the sparse matrix operations in the KPM. The GPGPU calculations on an ACC node of the system B at ISSP achieve $\sim$350 times faster KPM-LD simulation compared with the CPU calculation on a single core.

We find that a Skyrmion crystal with unusual high topological number $n_{\rm sk} = 2$ is stabilized even without magnetic fields [2]. This is in stark contrast to the Skyrmions in the previous studies, which have $n_{\rm sk} = 1$ and become thermodynamically stable only in nonzero magnetic fields. We also reveal that the Skyrmion crystal state with $n_{\rm sk} = 2$ shows successive phase transitions with multiple digital changes of $n_{\rm sk}$ from two to one, and to zero while increasing an external magnetic field (see Fig. 1).

Furthermore, we find that by raising temperature the topological charge in the Skyrmion crystal with $n_{\rm sk} = 2$ decreases gradually from two to zero. This is also contrast to a rather rapid change in the Skyrmion crystal with $n_{\rm sk} = 1$ [3].

Finally, we emphasis that the large-scale simulations using the massive GPGPU system were crucially important for the finding of this new high-topological-number Skyrmion. This is because the itinerant electron systems are rather sensitive to the finite-size effect in general, and stabilizing the true ground state often fails in small systems. Our results of multiple digital switching of topological number $n_{\rm sk}$ can bring about a great impact on the active fields in spintronics.

References

[1] K. Barros and Y. Kato, Phys. Rev. B **88**, 235101 (2013).

[2] R. Ozawa, S. Hayami, and Y. Motome, Phys. Rev. Lett. **118**, 147205 (2017).

[3] R. Ozawa, Y. Kato, S. Hayami, and Y. Motome, JPS 2017 Annual (72nd) Meeting (19pC24-9).

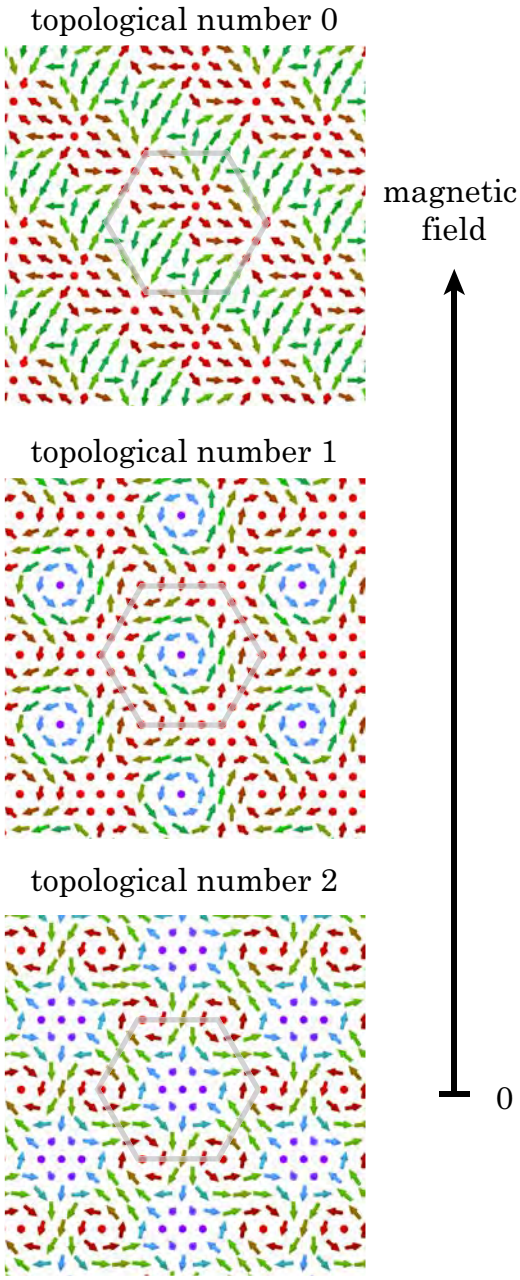

Figure 1: Spin configurations of a $n_{\mathrm{sk}} = 2$ Skyrmion crystal (bottom), a $n_{\mathrm{sk}} = 1$ Skyrmion crystal (middle), a $n_{\mathrm{sk}} = 0$ vortex crystal (top). They are switchable by an external magnetic field.

Theoretical study of novel quantum phenomena in strongly-correlated spin-orbit coupled systems

Yukitoshi MOTOME

Department of Applied Physics,

The University of Tokyo, Bunkyo, Tokyo 277-8581

We have theoretically studied novel quantum phenomena arising from the competition and cooperation between strong electron correlations and spin-orbit coupling. In this project, we have been making substantial progress on the following four topics. We summarize the main achievements for each topic below.

(i) *Spin dynamics, exotic phase transitions, and thermal transport in the Kitaev model*: The Kitaev model, whose ground state is exactly given by a quantum spin liquid with long-range entanglement, is believed to well describe magnetic properties of spin-orbital entangled Mott insulators, such as iridates, ruthenates, and rhodates. For providing theoretical inputs for experiments in these compounds, we have studied the fundamental physics associated with the quantum spin liquid nature in the Kitaev model. Performing the quantum Monte Carlo simulation in a Majorana fermion representation, we obtained the quantitative results for the magnetic Raman scattering [1,2], the temperature and energy dependences of spin dynamics [3-5], an exotic liquid-to-liquid transition by introducing the Ising interaction [6], and thermal transport [7].

(ii) *Vortex crystals, skyrmions, and chiral soliton lattices in spin-charge coupled systems*: Itinerant frustration has been attracted much attention as a source of noncollinear and noncoplanar spin textures. We have explored such spin textures in a fundamental model for itinerant magnets, the Kondo lattice model. Performing large-scale Langevin dynamics simulation with the kernel polynomial method and variational calculations, we discovered a vortex crystal state as a generic ground state in the weak coupling limit [8], a skyrmion crystal with a high topological number [9,10], and collinear multiple-Q states [11]. We constructed an effective model for understanding of the stabilization mechanism [12]. We also studied the magnetotransport in a chiral soliton lattice by quantum Monte Carlo simulation [13].

(iii) *Nonreciprocal and off-diagonal responses in spontaneously parity broken systems*: The spin-orbit coupling brings about rich phenomena, in particular, in the system with spatial inversion symmetry breaking. We have studied nonreciprocal and off-diagonal responses in such systems. We clarified that

asymmetric magnon excitations arise with an antiferromagnetic ordering on a zigzag chain [15]. We summarized a review type article on this topic [16]. We also studied multiferroic properties in a compound composed with low-symmetric square cupolas of Cu $S = 1/2$ spins in collaboration with experimental groups [17].

(iv) *ab initio study of atomically-thin materials with strong spin-orbit coupling*: To further explore intriguing phenomena by the spin-orbital entanglement, we have initiated a project on the basis of *ab initio* calculations supplemented by model analyses. Studying a family of the monolayer form of transition metal trichalcogenides, we predicted that the compounds will show peculiar multiple Dirac cones near the Fermi level due to the lattice geometry and orbital anisotropy. Furthermore, we found that they become topologically nontrivial magnets by electron correlation and carrier doping [18].

References

[1] J. Nasu, J. Knolle, D. L. Kovrizhin, Y. Motome, and R. Moessner: Nature Physics **12** (2016) 912.

[2] 東京大学大学院工学系研究科 プレスリリース (2016.07.05 付)

[3] J. Yoshitake, J. Nasu, and Y. Motome: Phys. Rev. Lett. **117** (2016) 157203.

[4] J. Yoshitake, J. Nasu, Y. Kato, and Y. Motome: preprint (arXiv:1704.02707).

[5] S.-H. Do, S.-Y. Park, J. Yoshitake, J. Nasu, Y. Motome, Y. S. Kwon, D. T. Adroja, D. J. Voneshen, K. Kim, T.-H. Jang, J.-H. Park, K.-Y. Choi, and S. Ji: preprint (arXiv:1703.01081).

[6] J. Nasu, Y. Kato, J. Yoshitake, Y. Kamiya, and Y. Motome: Phys. Rev. Lett. **118** (2017) 137203.

[7] J. Nasu, J. Yoshitake and Y. Motome: preprint (arXiv:1703.10395).

[8] R. Ozawa, S. Hayami, K. Barros, G-W. Chern, Y. Motome, and C. D. Batista: J. Phys. Soc. Jpn. **85** (2016) 103703.

[9] R. Ozawa, S. Hayami, and Y. Motome: Phys. Rev. Lett. **118** (2017) 147205.

[10] 東京大学大学院工学系研究科 プレスリリース (2017.04.05 付)

[11] S. Hayami, R. Ozawa, and Y. Motome: preprint (arXiv:1703.07690).

[12] S. Hayami, R. Ozawa, and Y. Motome: Phys. Rev. B **94** (2016) 024424.

[13] S. Okumura, Y. Kato, and Y. Motome: preprint (arXiv:1704.01708).

[14] Y. Sugita and Y. Motome: J. Phys. Soc. Jpn. **85** (2016) 073709.

[15] S. Hayami, H. Kusunose, and Y. Motome: J. Phys. Soc. Jpn. **85** (2016) 053705.

[16] S. Hayami, H. Kusunose, and Y. Motome, J. Phys.: Cond. Matter **28** (2016) 395601.

[17] Y. Kato, K. Kimura, A. Miyake, M. Tokunaga, A. Matsuo, K. Kindo, M. Akaki, M. Hagiwara, M. Sera, T. Kimura, and Y. Motome: Phys. Rev. Lett. **118** (2017) 107601.

[18] Y. Sugita, T. Miyake, and Y. Motome: preprint (arXiv:1704.00318).

Thermal pure quantum state study on finite-temperature properties of quantum spin liquids

Takahiro Misawa
Institute for Solid State Physics, University of Tokyo
Kashiwa-no-ha, Kashiwa, Chiba 277-8581

The two-dimensional Hubbard model with geometrical frustrations is one of the simplest theoretical models that describes competition and cooperation of the strong electronic correlations and the geometrical frustrations. In this model, due to the next-nearest neighbor hopping t', which induces the next-nearest neighbor antiferromagnetic interactions, the competition between two magnetic phases occurs: Simple Néel state becomes stable when t' is small compared to the nearest neighbor hopping t while stripe state becomes stable for large t' region ($t'/t \sim 1$). Several theoretical calculations for the ground states of the frustrated Hubbard model including its strong coupling limit, i.e., frustrated J_1-J_2 Heisenberg, have been done so far. Most of previous calculations suggest that quantum spin liquid states actually appear [1, 2, 3, 4, 5] around intermediate region ($t'/t \sim 0.75$ or $J_2/J_1 \sim 0.5$). In spite of the huge amount of the studies for the ground states, there are few unbiased theoretical studies on the finite-temperature properties of the frustrated Hubbard model due to the lack of the efficient theoretical method.

Recently, efficient numerically unbiased method for calculating finite temperature properties in quantum systems is proposed [6]. In this method, it is shown that the calculation within small number of pure states instead of the full ensemble average is sufficient for accurate estimate of finite-temperature properties. Such pure states are called thermal pure quantum (TPQ) states and they are easily generated by performing the imaginary-time evolution of the wave function.

By using the TPQ method, we systematically study finite-temperature properties of the frustrated Hubbard model. As a result, around $t'/t \sim 0.75$, we find the evidence of the spin liquid states from the calculations on temperature dependence of the spin correlations and entropy. The present unbiased and detailed numerical calculations also offer an experimental criterion of closeness to the spin liquid phase: Finite-temperature entropy at moderate temperatures $T/t \sim 0.1$ significantly correlates with closeness to the spin liquid phase. We also find that such signatures of quantum spin liquid states can be observed in an ab initio models [7] for spin-liquid candidates $EtMe_3Sb[Pd(dmit)_2]_2$.

A part of calculation is done by using open-source software $\mathcal{H}\Phi$ [8].

References

[1] T. Kashima and M. Imada, J. Phys. Soc. Jpn. **70**, 3052 (2001).

[2] T. Mizusaki and M. Imada, Phys. Rev. B **74**, 014421 (2006).

[3] L. F. Tocchio, F. Becca, A. Parola, and S. Sorella, Phys. Rev. B **78**, 041101 (2008).

[4] H.-C. Jiang, H. Yao, and L. Balents, Phys. Rev. B **86**, 024424 (2012).

[5] W.-J. Hu, F. Becca, A. Parola, and S. Sorella, Phys. Rev. B **88**, 060402 (2013).

[6] S. Sugiura and A. Shimizu, Phys. Rev. Lett. **108**, 240401 (2012).

[7] K. Nakamura, Y. Yoshimoto, and M. Imada, Phys. Rev. B **86**, 205117 (2012).

[8] https://github.com/QLMS/HPhi.

Topological phases and nonequilibrium phenomena in strongly correlated electron systems with strong spin-orbit interaction

Norio KAWAKAMI
Department of Physics, Kyoto University
Kitashirakawa, Sakyo-ku, Kyoto 606-8502

Many quantum phases compete in systems with coexisting spin-orbit interaction and electron correlation. Particularly, topologically nontrivial band structures, which are classified by topological invariants, have attracted much attention experimentally and theoretically.

We have studied the impact of strong correlations on the surface states of a three-dimensional topological Kondo insulator. [1] Correlations are strongly increased at the surface and at low enough temperature T, the surface f electrons are energetically confined into a narrow window around the Fermi energy. While light and heavy surface states coexist, with increasing temperature, the latter becomes incoherent.

We have studied the modification of the competition between the Kondo effect and the RKKY interaction in f-electron materials by the superlattice structure. [2] The quantum critical point between the magnetic phase and the Fermi-liquid phase depends on the structure of the f-electron superlattice.

By analysing a bilayer Kane-Mele-Hubbard model with lattice distortion and interlayer spin exchange interaction under cylinder geometry using real-space dynamical mean field theory (R-DMFT) with continuous-time quantum Monte Carlo (CTQMC), we have demonstrated that a topological Mott insulating (TMI) state emerges. [3] The TMI state, which hosts gapless edge modes only in collective spin excitations, evolves from the ordinary spin-Hall insulating state with increasing the Hubbard interaction before it undergoes a phase transition to a trivial Mott insulator.

We have studied the reduction of topological classification in free fermions. In a bilayer honeycomb lattice model by taking into account temperature effects using R-DMFT+CTQMC, we have shown that even when the reduction occurs, the winding number ν defined by the Green's function can take a nontrivial value at $T = 0$, which is consistent with the absence of gapless edge modes due to edge Mott behaviors. [4] Furthermore, we have proposed a heavy fermion superlattice system as a test bed for the reduction of topological classification in free fermions. [5]

References

[1] R. Peters, T. Yoshida, H. Sakakibara, and N. Kawakami: Phys. Rev. B **93**, 235159 (2016).

[2] R. Peters, Y. Tada, and N. Kawakami: Phys. Rev. B **94**, 205142 (2016).

[3] T. Yoshida and N. Kawakami: Phys. Rev. B **94**, 085149 (2016).

[4] T. Yoshida and N. Kawakami: Phys. Rev. B **95**, 045127 (2017).

[5] T. Yoshida, A. Daido, Y. Yanase, and N. Kawakami: Phys. Rev. Lett. **118**, 147001 (2017).

Novel phenomena of correlated topological phases

Tsuneya Yoshida

Department of Physics, Kyoto University,

Sakyo-ku, Kyoto 606-8502

In this decade, topological insulators/superconductors have attracted much attention due to their interesting phenomena arising from topology of the ground state wave functions. So far, electron correlations have been neglected in most of studies of topological phases. Recently, however, it became clear that topological insulators can emerge even in strongly correlated systems. Furthermore such systems are expected to show new phenomena arising from electron correlation and topology. Therefore, understanding impact of electron correlation on topological insulators is one of the most important issues of condensed matter systems.

In our study, we have addressed this issue by making used of dynamical mean field theory (DMFT)[1-4] as well as bosonization approach[5]. Here, in particular, we focus topological phases in heavy-fermion systems.

(i) $CeCoIn_5$/$YbCoIn_5$ superlattice systems as a test bed for reduction of topological classification. Classifying of topological phases, i.e., examining how many topological phases exist under given symmetry, has provided useful information for searching topological materials. In 2010, Fidkowski and Kitaev revealed that the classification result may change in the presence of electron correlations; for instance, topological superconductors of symmetry class BDI can show topological phases characterized by an arbitrary integer, while there are only eight distinct topological phases in the presence of electron correlations. Namely, in this case, electron correlations reduce number of possible topological phases. The aforementioned reduction of topological classification is new phenomenon. Unfortunately, however, no candidate material has been reported so far. In our study, we have searched a candidate material which can show the reduction of topological classification. As the result, we have found the $CeCoIn_5$/$YbCoIn_5$ superlattice system can be the candidate material for the reduction of topological classifications $Z \times Z \rightarrow Z \times Z_8$[5]. Furthermore, we have analyzed finite temperature effects in a bi-layer honeycomb lattice model showing the reduction $Z \rightarrow Z_4$ by using DMFT+ continuous-time quantum Monte Carlo[2].

(ii) Temperature effects on topological Kondo insulators. Although the topological structure is well-defined only at zero

temperature, understanding finite temperature effects on topological insulators is important form a practical view point; any experiment is carried out at finite temperatures. Besides that, in heavy fermion systems, various intriguing behaviors have been reported for finite temperature regions due to the Kondo effect.

In our study, applying DMFT + numerical renormalization group method to the Kane-Mele Kondo lattice model[4], we have demonstrated that finite temperature effects can restore gapless edge modes even when gapless edge modes are destroyed at zero temperature. Furthermore, combining first principle calculation and the dynamical mean-field theory, we have revealed that the effective mass at the edge becomes much heavier than that in the bulk for SmB6, which may explain inconsistency of the mass between ARPES measurement and transport measurement[3].

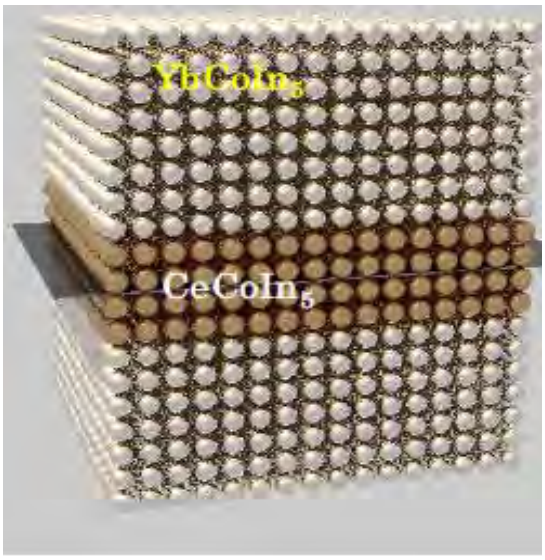

Fig. 1: Sketch of $CeCoIn_5/YbCoIn_5$ superlattice.

References

[1] Tsuneya Yoshida and Norio Kawakami: Phys. Rev. B **95** (2017) 045127.

[2] Tsuneya Yoshida and Norio Kawakami: Phys. Rev. B **94** (2016) 085149.

[3] Robert Peters, Tsuneya Yoshida, Hirofumi Sakakibara, and Norio Kawakami: Phys. Rev. B **93** (2016) 235159.

[4] Tsuneya Yoshida, Robert Peters and Norio Kawakami: Phys. Rev. B **93** (2016) 045138.

[5] Tsuneya Yoshida, Akito Daido, Youich Yanase, and Norio Kawakami: Phys. Rev. Lett. **118** (2017) 147001.

Competitions of superconducting, antiferromagnetic and charge orders in electron-phonon coupled systems

Takahiro OHGOE

Department of Applied Physics, The University of Tokyo,

7-3-1 Hongo, Bunkyo-ku, Tokyo 113-0033

In a class of strongly-correlated materials, the interplay between electron correlations and electron-phonon interactions is believed to induce novel phenomena such as the unconventional high-Tc s-wave SC in the alkali-doped fullerenes [1]. To establish the roles of phonons in a wide range of stongly correlated materials, we need a flexible method which can accurately treat strong electron-electron and electron-phonon interactions on an equal footing. In previous study, we proposed an extended many-variable variational Monte Carlo method [2] for electron-phonon coupled systems [3].

In this work, by using the many-variable variational Monte Carlo method, we study competitions of strong electron-electron and electron-phonon interactions in the ground state of Holstein-Hubbard model on a square lattice [4]. At half filling, an extended intermediate metallic or weakly superconducting (SC) phase emerges, sandwiched by antiferromagnetic (AF) and charge order (CO) insulating phases (Fig. 1). By the carrier doping into the CO insulator, the SC order dramatically increases for strong electron-phonon couplings, but largely hampered by wide phase separation (PS) regions. Superconductivity is optimized at the border to the PS.

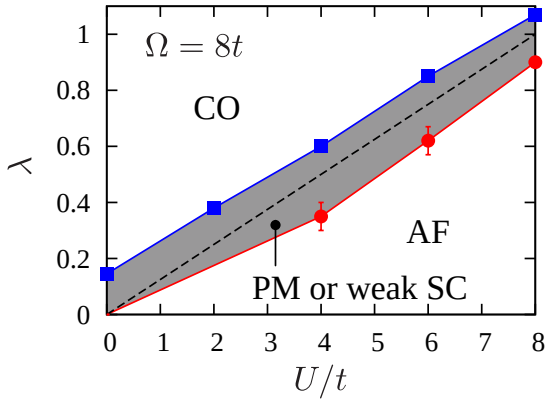

Fig. 1: Ground-state phase diagram of the Holstein-Hubbard model on a square lattice in the U/t-λ plane. Here, U/t is the on-site Coulomb interaction divided by the hopping amplitude, and λ is the dimensionless electron phonon interaction.

References

[1] Y. Nomura, S. Sakai, M. Capone, and R. Arita, Sci. Adv. 1, e1500568 (2015)

[2] D. Tahara and M. Imada, J. Phys. Soc. Jpn. **77**, 1140701 (2008)

[3] T. Ohgoe and M. Imada, Phys. Rev. B **89**, 195139(2014)

[4] T. Ohgoe and M. Imada, arXiv:1703.0889

DMFT study for the valence skipping and charge Kondo effect induced by pair hopping interaction

Akihisa Koga
Department of Physics, Tokyo Institute of Technology
Ookayama, Meguro, Tokyo 152-8551

Valence skipping has been observed in some compounds containing the group III, IV, V or VI element such as Bi or Tl. In these valence skipping elements, the ionic states with closed shell are stable rather than non-closed shell states. Recently, it has been reported that Tl-doped PbTe exhibits Kondo-like behavior in the resistivity in spite of the absence of magnetic impurities [1]. Moreover, superconductivity is also observed in this material at low temperatures [1, 2, 3], implying that the the valence skipping nature and charge Kondo effect [4] play a key role for the emergence of the superconductivity.

In previous theoretical works, the valence skipping nature has been explained by an effective negative Coulomb interaction [5]. On the other hand, recently, the valence skipping and charge Kondo effect have successfully been described, by introducing the impurity Anderson model with the pair hopping interaction, instead of the negative Coulomb interactions [6]. This indicates the importance of the pair hopping term for understanding the valence skipping behaviors and charge Kondo effect. However, it remains unclear how the pair hopping interaction affects physical properties in the lattice systems beyond the impurity model.

To investigate the valence skipping phenomenon and charge Kondo effect induced by pair hopping interaction in lattice systems, we analyze the extended Falicov-Kimball model on the Bethe lattice as follows:

$$\begin{aligned}\mathcal{H} = & -t \sum_{\langle i,j\rangle,\sigma} c^{\dagger}_{i\sigma} c_{j\sigma} + \epsilon_d \sum_{i,\sigma} n^d_{i,\sigma} \\ & + U_{cd} \sum_{i,\sigma,\sigma'} n^c_{i\sigma} n^d_{i\sigma'} \\ & - J_{ph} \sum_i (d^{\dagger}_{i\uparrow} d^{\dagger}_{i\downarrow} c_{i\uparrow} c_{i\downarrow} + \text{H.c.}), \end{aligned} \quad (1)$$

where $c_{i\sigma}$ ($d_{i\sigma}$) is the annihilation operator of a conduction (localized) electron with spin $\sigma(=\uparrow,\downarrow)$, respectively. $n^c_{i\sigma}(= c^{\dagger}_{i\sigma} c_{i\sigma})$ and $n^d_{i\sigma}(= d^{\dagger}_{i\sigma} d_{i\sigma})$ are the number operators of a conduction electron and an electron occupying the localized orbital at site i. t is the hopping integral of the conduction electrons between the nearest-neighbor sites, and U_{cd} and J_{ph} are the interorbital Coulomb interaction and pair hopping interaction, respectively. We assume that the localized orbital d corresponds to the electronic orbital of valence skipping elements.

In the work, we have used dynamical mean-field theory (DMFT) to clarify the stability of the charge Kondo effect in the lattice system. Here, we have made use of the continuous-time quantum Monte Carlo (CT-QMC) method with the double expansion technique as an impurity solver [7]. In this technique, we numerically perform the diagrammatic expansion for both hybridization between the impurity and bath, and the pair hopping term on an equal footing. This enables us to avoid the negative sign problem in the CT-QMC simulations. Moreover, we used the ALPS library preinstalled in the ISSP su-

percomputer system, which facilitates a parallelization in the present calculations [8].

We calculate the electron occupancy at each orbital and pseudo-spin correlations between the conduction and impurity orbitals introduced in Ref. [6]. We have found the charge ordered and s-wave superconducting phases. Performing the systematic calculations, we have clarified that the former (latter) is stabilized by the interaction U_{cd} (J_{ph}). In addition, we have found that the charge Kondo state appears in the strong pair hopping region.

References

[1] Y. Matsushita, H. Bluhm, T. H. Geballe, and I. R. Fisher, Phys. Rev. Lett. **94**, 157002 (2005).

[2] Y. Matsushita, P. A. Wianecki, A. T. Sommer, T. H. Geballe, and I. R. Fisher, Phys. Rev. B **74**, 134512 (2006).

[3] K. Nakayama, T. Sato, T. Takahashi, and H. Murakami, Phys. Rev. Lett. **100**, 227004 (2008).

[4] A. Taraphder and P. Coleman, Phys. Rev. Lett. **66**, 2814 (1991).

[5] T. Yanagisawa, I. Hase, Physica C **24-26**, 494 (2013)

[6] H. Matsuura and K. Miyake, J. Phys. Soc. Jpn. **81**, 113705 (2012).

[7] P. Werner, A. Comanac, L. de'Medici, M. Troyer and A. J. Millis, Phys. Rev. Lett. **97**, 076405 (2006)

[8] B. Bauer *et al.*, J. Stat. Mech. **2011**, P05001 (2011).

Numerical Studies on Excitation Spectra of Strongly Correlated Topological Materials

Youhei YAMAJI
Quantum-Phase Electronics Center and Department of Applied Physics, The University of Tokyo
Hongo, Bunkyo-ku, Tokyo 113-8656

The Kitaev's quantum spin liquid has attracted much attention as a rare example of controlled spin liquid ground state in correlated electron systems. An experimentally observable signature of proximity to the Kitaev's quantum spin liquid phase is a continuum in spin excitation spectra [1]. To examine the spin excitation spectra in the vicinity of the Kitaev's spin liquid phases, we employ the shifted Krylov subspace methods [2] and simulate dynamical spin structure factors of an *ab initio* effective hamiltonian of Na_2IrO_3 [3] and other related hamiltonians [4].

Below, we briefly touch on the shifted Krylov subspace method. Excitation spectra are given by taking imaginary parts of Green's functions defined as,

$$G^{AB}(\zeta) = \langle 0|\hat{A}^\dagger(\zeta - \hat{H})^{-1}\hat{B}|0\rangle. \tag{1}$$

To evaluate the above formula, the Lanczos method is widely employed. However, convergence of the Lanczos method often suffers from truncation errors. We have another option: We solve a linear equation by employing a conjugate gradient (CG) method, instead of explicitly calculating the resolvent of $\hat{H}$. The CG methods find the solution in a Krylov subspace, as follows. First, by introducing the following three vectors,

$$|\lambda\rangle = \hat{A}|0\rangle, \tag{2}$$
$$|\rho\rangle = \hat{B}|0\rangle, \tag{3}$$
$$|\chi(\zeta)\rangle = (\zeta - \hat{H})^{-1}|\rho\rangle, \tag{4}$$

we rewrite $G^{AB}(\zeta)$ as

$$G^{AB}(\zeta) = \langle\lambda|\chi(\zeta)\rangle. \tag{5}$$

To obtain the unknown vector $|\chi(\zeta)\rangle$, we solve the following linear equation,

$$(\zeta - \hat{H})|\chi(\zeta)\rangle = |\rho\rangle. \tag{6}$$

When the linear dimension of the matrix $\hat{H}$, $N_{\rm H}$, is too large to store the whole matrix in the memory, the linear equation is solved iteratively, for example, by using the CG methods. At nth iteration, the conjugate gradient algorithm initialized with $|\chi_0(\zeta)\rangle = |\rho\rangle$ finds an approximate solution $|\chi_n(\zeta)\rangle$ within a n-dimensional Krylov subspace $\mathcal{K}_n(\zeta - \hat{H}, |\rho\rangle) = \mathrm{span}\{|\rho\rangle, (\zeta - \hat{H})|\rho\rangle, \ldots, (\zeta - \hat{H})^{n-1}|\rho\rangle\}$. At each steps, the CG-type algorithms search the approximate solution $|\chi_n(\zeta)\rangle$ to minimize the 2-norm of the residual vector,

$$|\rho_n(\zeta)\rangle = (\zeta - \hat{H})|\chi_n(\zeta)\rangle - |\rho\rangle. \tag{7}$$

We note that one needs to solve Eq.(6) essentially once at a fixed complex number $\zeta = \omega + i\delta$ to obtain whole spectrum $-\mathrm{Im}G^{AB}(\omega + i\delta)$. Due to the shift invariance of the Krylov subspace [2], namely, $\mathcal{K}_n(\zeta - \hat{H}, |\phi\rangle) = \mathcal{K}_n(\zeta' - \hat{H}, |\phi\rangle)$ for any complex number $\zeta' \neq \zeta$, we can obtain $|\chi(\zeta')\rangle$ from $|\chi(\zeta)\rangle$ without performing time-consuming matrix-vector products [2]. The Krylov subspace methods utilizing the shift invariance are called the shifted Krylov subspace methods. The several shifted Krylov subspace methods are available through a numerical library $\mathcal{K}\omega$ [5].

As a typical example of the excitation spectra in the proximity to the Kitaev's spin liquid phase, we show dynamical spin structure factors of the *ab initio* effective hamiltonian of Na_2IrO_3 [3] in Fig.1. The contiuum spectra up to the typical energy scale of Na_2IrO_3, 30 meV, is a signature of the proximity. We also apply the shifted Krylov subspace method to simulating excitation spectra of the Kitaev-Γ model [4], which is relevenat to another Kitaev material α-$RuCl_3$.

To further examine the relevance of the the *ab initio* effective hamiltonian to Na_2IrO_3, the ground state properties of the *ab initio* effective hamiltonian are examined by combining tensor network approaches and exact diagonalization [6]. The proximity to the quantum spin liquids, other than the Kitaev's one, is also clarified in the t-t' Hubbard model [7]. These simulations have offered not only deeper understanding of the proximity to the spin liquid, but also benchmark results on newly implemented functions of $\mathcal{H}\Phi$ [8, 9].

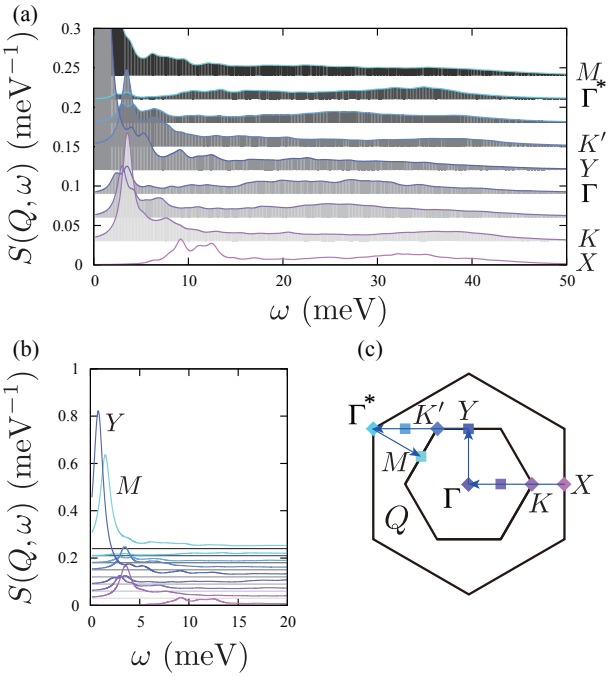

Figure 1: (a) Dynamical spin structure $S(Q,\omega)$ factors shifted vertically depending on Q. (b) Expansion of low-energy spectra. There are prominent peaks at the momenta Y and M, which correspond to zigzag orders observed in experiments. (c) Brillouin zone of Na_2IrO_3. Here, Γ* corresponds to the standard Néel order.

References

[1] A. Kitaev, Annals Phys. **321** (2006) 2 (2006); J. Knolle, D. L. Kovrizhin, J. T. Chalker, and R. Moessner, Phys. Rev. Lett. **112** (2014) 207203.

[2] A. Frommer, Computing **70** (2003) 87.

[3] Y. Yamaji, T. Suzuki, T. Yamada, S. Suga, N. Kawashima, and M. Imada: Phys. Rev. B **93** (2016) 174425.

[4] A. Catuneanu, Y. Yamaji, G. Wachtel, H.-Y. Kee, and Y. B. Kim: arXiv:1701.07837.

[5] `https://github.com/issp-center-dev/Komega`

[6] T. Okubo, K. Shinjo, Y. Yamaji, N. Kawashima, S. Shigetoshi, T. Tohyama, and M. Imada: arXiv:1611.03614.

[7] T. Misawa and Y. Yamaji: arXiv:1608.09006.

[8] M. Kawamura, K. Yoshimi, T. Misawa, Y. Yamaji, S. Todo, and N. Kawashima: arXiv:1703.03637; accepted by Comput. Phys. Commun.

[9] `https://github.com/QLMS/Hphi/releases`

Monte Carlo approach to correlated electron and spin systems

Shintaro HOSHINO
RIKEN Center for Emergent Matter Science (CEMS), Wako 351-0198, Saitama, Japan

The discovery of a new type of ordered state of condensed matter is certainly an important and rare event. It is even nicer if the properties of this unconventional ordered state convincingly explain recent puzzling experimental results on an interesting class of correlated electron materials. In our recent work for correlated electrons using the supercomputer at Institute for Solid State Physics (ISSP), we show that certain types of three-orbital lattice systems, with degenerate orbital degrees of freedom, can spontaneously break the orbital symmetry in such a way that the electrons in a subset of orbitals are Mott insulating, while the electrons in the remaining orbitals are metallic (spontaneous orbital selective Mott transition). This state occurs in systems with effectively negative Hund coupling, such as fulleride compounds, and it can explain the origin of the puzzling "Jahn-Teller metal phase" that has been experimentally detected in $Rb_xCs_{3-x}C_{60}$ [1].

Alkali doped fulleride compounds [2, 3, 4] have attracted much attention due to their unconventional high Tc (∼38K) superconductivity. It is important to understand the properties of these correlated systems in the vicinity of the Mott phase, and to clarify the connection of the unconventional metal states to the superconducting instability. It has been suggested that the Jahn-Teller metal [1], which appears between the Mott insulating and unconventional superconducting phase of A_3C_{60}, may be characterized by the coexistence of itinerant and localized electrons.

To understand this peculiar behavior, we have analyzed the multiorbital Hubbard model with antiferromagnetic Hund coupling relevant to fulleride superconductors. For theoretical analysis, we have used the dynamical mean-field theory combined with the continuous-time quantum Monte Carlo method (hybridization expansion algorithm) [5]. This is suitable for strongly correlated three-dimensional electron systems such as fulleride compounds. The quantum Monte Carlo simulation has been performed efficiently by a parallel computing using the supercomputer facilities of ISSP.

Analyzing the multiorbital Hubbard model, we have numerically mapped out the phase diagrams which are shown in Fig. 1 together with the sketches for expermental phase diagrams [6]. Our results have succeeded to capture the characteristic phases observed in fulleride superconductors, including Jahn-Teller metal phase which is here identified as a spontaneous orbital selective Mott (SOSM) state. This ordered state is not characterized by any conventional one-body order parameter (it has no ordinary orbital moment, with broken orbital symmetry), but by a many-body operator. It is a so-called composite order, and it can also be viewed as an odd-frequency order because the symmetry-breaking appears in the time-dependence of certain correlation functions. The spontaneous orbital-selective Mott state is therefore a diagonal-order version of the concept of odd-frequency superconductivity.

References

[1] R.H. Zadik et al., Sci. Adv. **1**, e1500059 (2015).

[2] A.F. Hebard et al., Nature **350**, 600 (1991).

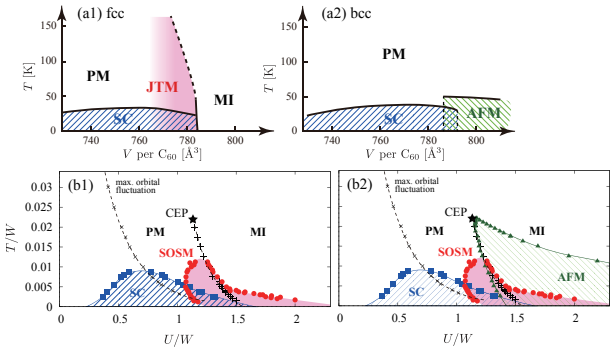

Figure 1: Sketches of the experimental phase diagrams for (a1) fcc and (a2) bcc fullerides based on Refs. [3, 1]. Panels (b1) and (b2) show the phase diagrams of the three-orbital Hubbard model for negative Hund coupling, without and with staggered orders, respectively. The former phase diagram corresponds to the fcc lattice since the geometrical frustration suppresses the staggered orders in a wide temperature range. See Ref. [6] for more detail.

[3] Y. Takabayashi et al., Science **323**, 1585 (2009).

[4] M. Mitrano et al., Nature **530**, 461 (2016).

[5] E. Gull et al., Rev. Mod. Phys. **83**, 349 (2011).

[6] S. Hoshino and P. Werner, arXiv:1609.00136, accepted for publication in Phys. Rev. Lett.

Numerical Studies on Models of Unconventional Superconductors

KAZUHIKO KUROKI
Department of Physics, Osaka University
1-1 Machikaneyama, Toyonaka, Osaka, 560-0043, Japan

In this report, we present two of the studies, related to superconductivity due to electron correlation, performed in our group in 2016 fiscal year using the supercomputer at ISSP.

SUPERCONDUCTIVITY IN SYSTEMS WITH ELECTRON AND HOLE BANDS

In the early days of the theoretical studies of the iron-based superconductors, the nesting of the Fermi surface was considered to be the key for the superconductivity. However, later experiments have suggested that high T_c is obtained when the nesting is degraded, or even in the absence of the nesting. In a previous study, we have pointed out that superconductivity is enhanced, even if the nesting is not good, if the magnitude of the hopping integrals is in good match with the inverse Fourier transformation of the gap function from momentum space to real space[1]. The importance of the real space picture implies that the states away from the Fermi level also plays an important role, since the inverse Fourier transformation from momentum space to real space involves all the states within the Brillouin zone, namely, the states away from the Fermi level.

Extending the above picture, we have studied how the finite energy spin fluctuation can act as a pairing glue. We apply the fluctuation exchange approximation to Hubbard type models possessing electron and hole bands, and compared them with the Hubbard model on a square lattice with a large Fermi surface[2]. As models with the electron and hole bands, we consider the five orbital model for the hydrogen doped 1111 iron-based superconductor, constructed in ref.1, and also a bilayer model with bonding and antibonding bands. In these models with electron and hole bands, superconductivity is optimized when the Fermi surface nesting is degraded to some extent, and finite energy spin fluctuations around the nesting vector develops. This is in contrast to the case of the square lattice model, where superconductivity is more enhanced for better nesting. The difference lies in the robustness of the nesting vector, namely, in models with electron and hole bands, the wave vector at which the spin susceptibility is maximized is fixed even when the nesting is degraded, whereas when the Fermi surface is large, the nesting vector varies with the deformation of the Fermi surface.

ELECTRON-HOLE ASYMMETRY OF THE ELECTRON CORRELATION STRENGTH IN THE CUPRATE SUPERCONDUCTORS

Recent experiments have revealed a remarkable difference in the phase diagram of the cuprate superconductors between hole- and electron-doped materials. Previously, there has been an understanding that pseudogap exists in both hole-doped and electron-doped cuprates. However, recent experiment shows that the pseudogap disappears in the electron-doped cases if the antiferromagnetism is suppressed by appropriate annealing process[3]. Hence, in the absence of the antiferromagnetism, there is an electron-hole asymmetry regarding the presence/absence of the pseudogap. Since the pseudogap can be considered as a hallmark of strong correlation, it seems that the strength of the electron correlation is apparently different between the electron and the hole-doped cases. One may consider that the origin of this asymmetry lies in the difference in the effective electron-electron interaction strength between the hole- and electron-doped materials. However, a recent first principles estimation[4] has revealed that many of the hole-doped cuprates have on-site U comparable to those in the T-type electron doped systems. A typical example with a moderate U is $HgBa_2CuO_4$, in which T_c is very high ($\sim$ 100K) and a pseudogap is observed. Therefore, it is difficult to explain the electron-hole asymmetry in the diagram by their interaction strength.

Given this background, we have analyzed the one-particle spectrum of the single band model of a cuprate superconductor using dynamical mean field theory with two kinds of impurity solvers : iterated perturbation theory and continuous time quantum Monte Carlo methods[5]. We have found that the electron-hole asymmetry of the electron correlation effect can exist even under common interaction strengths and the band structure between the hole- and electron-doped systems. Although there exists an asymmetric feature of the density of states, this alone cannot account for the remarkable asymmetry observed experimentally. An important finding is that the presence of the strong correlation effect, strong enough to produce a Mott insulating state

at half-filling, is necessary to understand the experimental observation. To be more precise, the combination of the Mottness and the asymmetry of the DOS results in a discontinuous electron-hole asymmetry of the one-particle spectrum. The fact that the present results are obtained under a common value of U between the hole and the electron-doped cases implies that the electron correlation effect is less visible in the electron-doped regime. In this sense, it can be said that the origin of the electron-hole asymmetry of the cuprates is the asymmetry of the "visibility" of the strong correlation effect.

[1] K. Suzuki, H. Usui, S. Iimura, Y. Sato, S. Matsuishi, H. Hosono, and. K. Kuroki, Phys. Rev. Lett. **113**, 027002 (2014).
[2] M. Nakata, D. Ogura, H. Usui and K. Kuroki, submitted.
[3] M. Horio *et al.*, Nat. Commmun. **7**, 10567 (2016).
[4] S. Jang, H. Sakakibara, H. Kino, T. Kino, K. Kuroki, and M.J.Han, Sci. Rep. **6**, 33397 (2016).
[5] R. Mizuno, M. Ochi, and K. Kuroki, submitted.

Research on Kondo effect in the Peierls-Anderson model

Dai MATSUI and Takashi HOTTA
Department of Physics, Tokyo Metropolitan University
1-1 Minami-Osawa, Hachioji, Tokyo 192-0397

After the discovery of magnetically robust heavy-fermion phenomenon in Sm-based filled skutterudites [1], non-magnetic Kondo effect due to electron-phonon interaction has attracted renewed attention in the research field of condensed matter physics. To promote our understanding on electronic properties of cage-structure compounds, it has been considered that *rattling*, i.e., local anharmonic oscillation of guest atom in the cage, plays a key role through the coupling with conduction electrons. Such rattling-induced phenomena have been frequently discussed on the basis of the Holstein-type model with the linear coupling between electron density and atomic displacement [2], given by $H_{\rm H} = g\rho x$, where g indicates an electron-phonon coupling, ρ is local electron density, and x denotes the displacement of atom. On the other hand, since localized electrons exist on the vibrating atom in the cage and conduction electrons originate from the atoms forming the cage, it is important to consider Peierls-type phonon in the hybridization between localized and conduction electrons, given by $H_{\rm P} = g\sum_{\boldsymbol{k},\sigma} x(d_\sigma^\dagger c_{\boldsymbol{k}\sigma} + {\rm h.c.})$, where $d_\sigma^\dagger$ and $c_{\boldsymbol{k}\sigma}$ denotes the annihilation operators of localized and conduction electrons, respectively, σ is spin, and $\boldsymbol{k}$ indicates wave vector.

In this research, we discuss the Kondo effect in the Peierls-Anderson model. The Hamiltonian is given by

$$H = \sum_{\boldsymbol{k}\sigma} \varepsilon_{\boldsymbol{k}} c_{\boldsymbol{k}\sigma}^\dagger c_{\boldsymbol{k}\sigma} + H_0, \tag{1}$$

where $\varepsilon_{\boldsymbol{k}}$ is the dispersion of conduction electron and H_0 includes the hybridization and local terms, given by

$$\begin{aligned} H_0 = {} & U n_\uparrow n_\downarrow + E_d \rho + \omega a^\dagger a \\ & + U_{\rm dc} \sum_{\boldsymbol{k},\boldsymbol{k}',\sigma} c_{\boldsymbol{k}\sigma}^\dagger c_{\boldsymbol{k}'\sigma} \rho \\ & + V_{\rm P} \sum_{\boldsymbol{k}\sigma} (a + a^\dagger)(d_\sigma^\dagger c_{\boldsymbol{k}\sigma} + {\rm h.c.}). \end{aligned} \tag{2}$$

Here U denotes the Coulomb interaction between localized electrons, $n_\sigma = d_\sigma^\dagger d_\sigma$, $\rho = n_\uparrow + n_\downarrow$, E_d is the energy level of localized electron, a is the annihilation operator of Peierls phonon, ω is the phonon energy, $U_{\rm dc}$ indicates the Coulomb interaction between localized and conduction electrons, and $V_{\rm P}$ denotes the phonon-assisted hybridization. Note that the energy unit is a half of the conduction bandwidth, which is set as unity in the following calculations. In this unit, we set $U = 1$ and $\omega = 0.1$. As for E_d, we set $E_d = -U/2$ to consider the case of half filling at an impurity site. Then, we change $V_{\rm P}$ and $U_{\rm dc}$ to investigate electronic and phononic properties. We also note that it is useful to define the non-dimensional coupling constant α through $V_{\rm P} = \sqrt{\alpha}\omega$. Roughly speaking, the cases of $\alpha < 1$ and $\alpha > 1$ correspond to the weak- and strong-coupling regions, respectively.

Here we note the conserved quantity in the Peierls-Anderson model, in addition to charge and spin. Namely, we define parity P as

$$P = \rho + N_{\rm ph} \bmod 2, \tag{3}$$

where $N_{\rm ph}$ indicates the phonon number. The states with $P = 0$ and 1 correspond to even and odd parity ones, respectively. We note that the eigenstates of H_0 are characterized by P in addition to total charge and spin. Note also that for $U_{\rm dc} = U/2$, it is possible to obtain the exact solution of H_0 (the two-site problem) by using Lang-Firsov transformation. We find that even and odd parity states are exactly degenerate for $U_{\rm dc} = U/2$.

To investigate the electronic and phononic properties of H at low temperatures, we usually discuss the corresponding susceptibilities, entropy, and specific heat. For the diagonalization of the impurity Anderson model, we employ a numerical renormalization group (NRG) method, in which we logarithmically discretize the momentum space so as to efficiently include the conduction electrons near the Fermi energy. The conduction electron states are characterized by "shells" labeled by N, and the shell of $N = 0$ correspond to the two-site case described by H_0. Then, after some algebraic calculations, the Hamiltonian is transformed into the recursive form

$$H_{N+1} = \sqrt{\Lambda} H_N + \xi_N \sum_\sigma (c^\dagger_{N\sigma} c_{N+1\sigma} + c^\dagger_{N+1\sigma} c_{N\sigma}), \quad (4)$$

where Λ is a parameter used for logarithmic discretization, $c_{N\sigma}$ denotes the annihilation operator of the conduction electron in the N-shell, and ξ_N indicates the "hopping" of the electron between N- and $(N+1)$-shells, expressed by

$$\xi_N = \frac{(1+\Lambda^{-1})(1-\Lambda^{-N-1})}{2\sqrt{(1-\Lambda^{-2N-1})(1-\Lambda^{-2N-3})}}. \quad (5)$$

In the NRG calculation, we keep M low-energy states for each renormalization step. In this study, we set $\Lambda = 5.0$ and $M = 2000$.

In the weak-coupling region, we obtain the standard spin Kondo effect for $U_{\rm dc} < 1$, while the singlet even-parity state appears for $U_{\rm dc} > 1$. On the other hand, in the strong-coupling region, we find the Schottky-type specific heat.

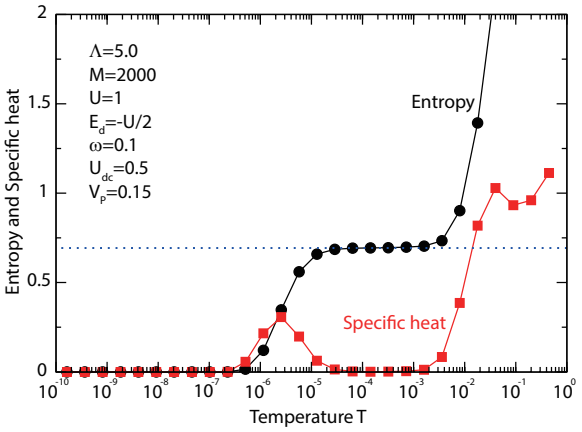

Figure 1: Entropy $S_{\rm imp}$ (solid circle) and specific heat $C_{\rm imp}$ (solid square) for $U = 1$, $E_d = -U/2$, $U_{\rm dc} = 0.5$, $V_{\rm P} = 0.15$, and $\omega = 0.1$. The dotted line indicates $\log 2$.

In Fig. 1, we show typical results for entropy and specific heat in the strong-coupling region for $U_{\rm dc} = U/2$. We observe the plateau of $\log 2$ and the release of this entropy leads to the peak in the specific heat. Note that this entropy release is due to the lift of parity doublet, not due to the Kondo effect. In fact, when we evaluate the energy difference Δ between even and odd parity states for 4-site case, it is found that the peak temperature is in proportion to Δ. This phenomenon is, of course, characterized by the change of parity susceptibility, but this is only a theoretical quantity. For the comparison with experimental results, we propose the measurement of the electric dipole susceptibility, which reproduces the temperature dependence of parity susceptibility in the strong-coupling region.

References

[1] S. Sanada, Y. Aoki, H. Aoki, A. Tsuchiya, D. Kikuchi, H. Sugawara, and H. Sato: J. Phys. Soc. Jpn. **74** (2005) 246.

[2] T. Hotta: J. Phys. Soc. Jpn. **78** (2009) 073707.

Magnetic properties in the Hubbard model on the Honeycomb Lattice by variational cluster approximation

Atsushi Yamada
Department of Physics, Chiba University
Chiba 263-8522, Japana, Chiba 277-8581

A spin liquid state, which is a purely non-magnetic Mott insulator without spontaneously broken spatial or spin symmetry, has attracted a lot of interest. This state is realized in geometrically frustrated systems like the charge organic transfer salts κ-(BEDT-TTF)$_2$X[1] and Cs_2CuCl_4.[2] A simple theoretical model of these compounds is the Hubbard model on the an-isotropic triangular lattice, and spin liquid state is in fact found in this model.[3] A spin liquid could arise also in the intermediate coupling region of strongly correlated systems between a semimetal and ordered state, because in this case a correlation-driven insulating gap might open before the system becomes ordered. This possibility might be realized in the half-filled Hubbard model on the honeycomb lattice.

We have studied the magnetic and metal-to-insulator transitions by variational cluster approximation using 10-site and 16-site clusters as a reference system. Parts of numerical calculations were done using the computer facilities of the ISSP. We found that $U_{\rm AF} = 2.7$ and $U_{\rm MI} = 3.0$ for 10-site cluster, and $U_{\rm AF} = 2.7$ and $U_{\rm MI} = 3.2$ for 16-site cluster.[5] This result also rules out the existence of the spin liquid in this model. Both the magnetic and non-magnetic metal-to-insulator transitions are of the second order. Our results agree with recent large scale Quantum Monte Carlo simulations.[4]

References

[1] Y. Shimizu, K. Miyagawa, K. Kanoda, M. Maesato, and G. Saito, Phys. Rev. Lett. **91**, 107001 (2003); Y. Kurosaki, Y. Shimizu, K. Miyagawa, K. Kanoda, and G. Saito, Phys. Rev. Lett. **95**, 177001 (2005).

[2] R. Coldea, D.A. Tennant, A.M. Tsvelik, and Z. Tylczynski, Phys. Rev. Lett. **86**, 1335 (2001); R. Coldea, D.A. Tennant, and Z. Tylczynski, Phys. Rev. Lett. **68**, 134424 (2003).

[3] T. Yoshioka, A. Koga, and N. Kawakami, Phys. Rev. Lett. **103**, 036401 (2009); P. Sahebsara and D. Sénéchal, Phys. Rev. Lett. **100**, 136402 (2008); L.F. Tocchio, H. Feldner, F. Becca, R. Valenti, and C. Gros, Phys. Rev. B **87**, 035143 (2013); A. Yamada, Phys. Rev. B **89**, 195108 (2014); L.F. Tocchio, C. Gros, R. Valentí, F. Becca, Phys. Rev. B **89**, 235107 (2014); A. Yamada, Phys. Rev. B **90**, 235138 (2014).

[4] S. Sorella, Y. Otsuka, and S. Yunoki, Sci. Rep. **2**, 992 (2012); F. F. Assaad and I. F. Herbut, Phys. Rev. X **3**, 031010 (2013); F. Parisen Toldin, M. Hohenadler, F. F. Assaad, and I. F. Herbut, Phys. Rev. B **91**, 165108 (2015).

[5] A. Yamada, Int. J. Mod. Phys. B **30**, 1650158 (2016).

Monte Carlo simulation of ^{4}He adsorbed on substrates[*]

Yuichi MOTOYAMA
Institute for Solid State Physics, University of Tokyo
Kashiwa-no-ha, Kashiwa, Chiba 277-8581

A system of ^{4}He atoms adsorbed on a substrate such as a graphite is an ideal two-dimensional interacting bosonic system. Greywall [1] studied ^{4}He on a graphite by measuring heat capacity and drew a phase diagram consisting of 1/3 solid phase, fluid and solid coexistence phase, normalfluid and superfluid coexistence phase, and normal fluid phase. This diagram is compatible with that of a hardcore Bose-Hubbard model with nearest neighbor repulsion on a triangular lattice in quality. On the other hand, Pierce and Manousakis [2] performed path integral quantum Monte Carlo (PIQMC) calculation of ^{4}He on a graphite and reported that solid-vacuum coexistence phase extended to very low density at very low temperature, and there is no superfluid phase.

Aiming to perform larger simulation, we tried to obtain an effective lattice Hamiltonian for ^{4}He atoms on a graphite surface, because PIQMC for continuous space has not been yet parallelized but PIQMC for lattice system is already massively parallelized [3]. We have at least three ways to obtain parameters of an effective Hamiltonian. The first one is starting from adsorption sites, that is, to use the tight-binding representation to build an effective model. In this representation, we compare worldlines of continuous space system with that of lattice system. Another method is to discretize continuous space. This is straightforward but obtained effective model including many interactions, say, n-th nearest neighbor coupling. The last strategy is brute force method, which is to search for parameters reproducing results, such as melting point, from continuous space Monte Carlo method.

In this study, we adopted the first strategy and tried to estimate a hopping constant t of an effective model as the following way. First, we performed continuous space Monte Carlo simulation and obtained imaginary-time trajectories (snapshots) of a ^{4}He atom. Second, we regarded a circle centered on an adsorption site with a fixed radius dr as a "site" of an effective model. Next, we counted the number of hopping from one "site" to another "site" and calculated mean time between hopping, $\langle \mathrm{d}t \rangle$. Finally, we estimated the hopping constant of an effective hardcore Bose-Hubbard model on a triangular lattice t as $t = 1/(6\langle \mathrm{d}t \rangle)$, where 6 is the coordination number of a triangular lattice. Figure 1 shows dr dependence of the estimated hopping constant of an effective model for ^{4}He on a graphite surface. If particles are tightly bounded to "site", t will saturate before a "site" completely covers a hexagon of carbons (d$r \sim 1.42$Å). ^{4}He on a graphite, however, is not the case, and so this system cannot be represented by the tight-binding model.

References

[*] This work has been done in collaboration with A. Masaki-Kato and N. Kawashima.

[1] D. S. Greywall, Phys. Rev. B **47**, 309 (1993).

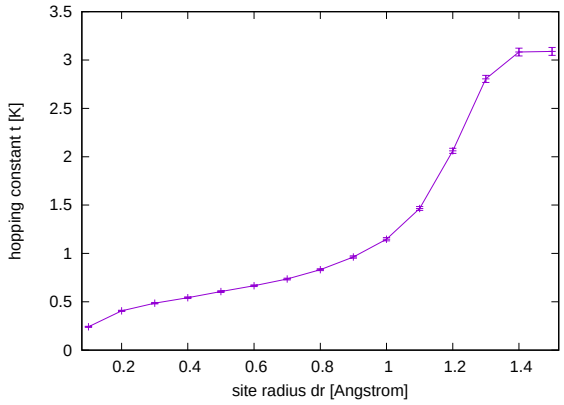

Figure 1: "site" radius dr dependence of the estimated hopping constant t of an effective lattice model for ^{4}He on a graphite surface.

[2] M. E. Pierce and E. Manousakis, Phys. Rev. B **62**, 5228 (2000).

[3] A. Masaki-Kato, T. Suzuki, K. Harada, S. Todo, and N. Kawashima, Phys. Rev. Lett **112**, 140603 (2014).

First-principles study on strong electron correlations in 5d transition metal oxides

Hiroshi Shinaoka
Department of Physics, Saitama University
Sakura-ku, Saitama-shi, Saitama, Japan, 338-8570

In recent years, novel properties of $5d^5$ pyrochlore iridates have been studied extensively theoretically and experimentally. We have studied metal-insulator and magnetic transitions in $Y_2Ir_2O_7$ by means of the local density approximation+dynamical mean-field method (DFT+DMFT). [2] For this study, we implemented a quantum Monte Carlo impurity solver based on the hybridization expansion algorithm [1], which can treat complex hybridization functions. This year, we have further implemented the measurement of various correlation functions such as two-particle Green's function in the solver. This new feature will be useful for investigating dynamical spin-orbital correlations in these compounds. The code has been published as an open-source software licensed under GPLv3. [3] The code is built on an updated version of the core libraries of ALPS (Applications and Libraries for Physics Simulations) [ALPSCore libraries].

We used the new impurity solver to investigate a $5d^4$ pyrochlore oxide, $Y_2Os_2O_7$. This compound is the first $5d^4$ pyrochlore oxide whose low-T properties have been reported experimentally. In the presence of strong spin-orbit coupling (SOC), the three t_{2g} orbitals are split into an upper $j_{\rm eff}$=1/2 doublet and a lower $j_{\rm eff} = 3/2$ quartet. If the SOC is strong enough, a d^4 configuration will be a trivial band insulator with four electrons filling the lower $j_{\rm eff} = 3/2$ manifold. Surprisingly, it has been reported that $Y_2Os_2O_7$ is an magnetically active insulator whose magnetic susceptibility follows a Curie-Weiss-like law below room temperature but does not show any magnetic long-range order down to 10 K. This may indicate the existence of a novel insulating phase induced by strong electron correlation and geometrical frustration.

We first figured out a U-$J_{\rm H}$ phase diagram (U is onsite Coulomb repulsion and $J_{\rm H}$ is Hund's coupling). In the DFT+DMFT calculations, we used a rotationally invariant Slater-Kanamori interaction. We constructed maximally localized Wannier functions for t_{2g} manifold. Most of the simulations were carried out on the system B.

We plot the spectral function at $\omega = 0$ computed with $\beta = 40$ eV ($T \simeq 290$ K) in Fig. 1. The spectral weight $A(\omega = 0)$ vanishes around $U = 2$ eV for reasonable values of $J_{\rm H}/U = 0.1$–0.2. For (possibly unphysical) large values of the Hund's coupling, the system enters into a metallic phase where the above mentioned single-particle picture is not valid due to strong hybridizations between the two manifolds.

Now we focus on the results obtained with $J_{\rm H}/U = 0.1$. We plot computed momentum-resolved spectral function $A(k, \omega)$ in Fig. 1. It is clearly seen that as U increases the system exhibits a Lifsitz transition to a band insulator where quasi-particle bands still survive. To investigate the magnetic properties more closely, we computed the correlation function $\langle \hat{M}(\tau)\hat{M}(0)\rangle$ in imaginary time, where $\hat{M}$ is a local magnetic moment operator (including spin and orbital contributions). We used

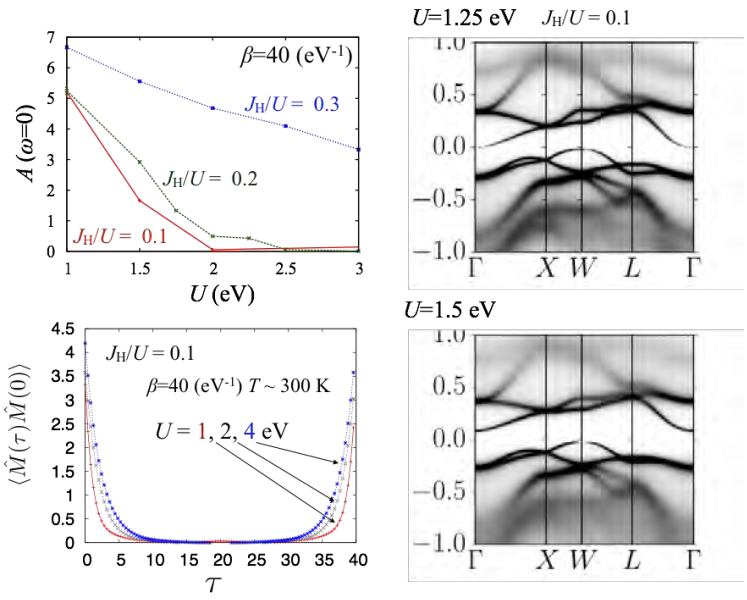

Figure 1: Spectral weight at $\omega = 0$, the momentum-resolved spectral weight $A(k, \omega)$, and the imaginary-time correlation function of magnetic moments.

the ability of the impurity solver to compute two-particle correlation functions. As shown in the figure, the correlation function quickly decays toward $\tau = \beta/2$, indicating that the ground state is magnetically inactive (.i.e., the ground state is a nonmagnetic band insulator). These results contradict the experimental results. This may indicate the important of non-local correlation functions beyond the DFT+DMFT approximation.

This work on $Y_2Os_2O_7$ was done in collaboration with Youhei Yamaji (University of Tokyo).

References

[1] P. Werner, A. Comanac, L. def Medici, M. Troyer, A. Millis, Phys. Rev. Lett. **97**, 076405 (2006).

[2] H. Shinaoka, S. Hoshino, M. Troyer, P. Werner, Phys. Rev. Lett. **115**, 156401(1-5) (2015).

[3] H. Shinaoka, E. Gull, P. Werner, Computer Physics Communications **215**, 128–136 (2017).

Topological symmetry in two-body scattering in strongly correlated electron systems

Koichi KUSAKABE
Graduate School of Engineering Science, Osaka University
1-3 Machikaneyama, Toyonaka, Osaka 560-8531

1. Introduction

Topological symmetry found in materials causes symmetry protected two-particle interaction processes. In curious materials, *e.g.* nanographene and cuprate superconductors, we often find a selected set of relevant orbitals, where the scattering processes among them are strongly optimized to cause "exchange-mediated correlation effects" and "the enhanced super processes". We can derive the scattering strength and specialty of the resulted electron state via the multi-reference density functional theory (MR-DFT).

2. The A-space formulation of MR-DFT

In our MR-DFT,[1, 2] we define a set A of orbitals for the correlated electron sub-system. This is usually done by obtaining the Kohn-Sham orbitals via a self-consistent calculation. A projection operator P_A giving a representation state $|\Psi_A\rangle \equiv P_A|\Psi\rangle = |\Phi_A\rangle \times |\Phi_0\rangle$ is defined for the MR ground state $|\Psi\rangle$, where $|\Phi_0\rangle$ is an uncorrelated filled state and $|\Phi_A\rangle$ is the strongly correlated state in the effective model. The representation state is determined via a many-body effective Hamiltonian in a form of

$$\left(\hat{H}_A + \hat{h}_B + \hat{H}_{\rm super}\right)|\Psi_A\rangle \quad = \quad E|\Psi_A\rangle. \quad (1)$$

Here, the third term in the Hamiltonian represents the super processes, which may describe screening, super exchange, pair hopping, and all of renormalized effective interactions.

$$\hat{H}_{\rm super} = P_A\hat{H}_{AB} \left(E - \hat{H}_A - \hat{h}_B - P_B\hat{H}_{AB} - \hat{H}_{BA}\right)^{-1} \hat{H}_{BA}P_A.$$

This Brillouin-Wigner-type determination equation is exact for a MR-DFT model where inter-particle interactions are subtracted in the un-correlated sub sets for both of the filled and empty orbitals in $|\Phi_0\rangle$.[3]

3. A spin-exchange process for Kondo's screening in nanographene

A set of topologically protected zero modes is found for a series of nanographene molecules called the vacancy-centered arm-chair-edged hexagonal nanographene (VANG).[4] These modes are producing a protected Kondo screening promoting formation of the stable singlet ground state with strong entanglement between a quasi-localized electron and Dirac electrons by the super process. This protection is caused by a topological protection of zero modes found in VANG.[5] When the molecule is deformed, if a mirror symmetry axis is preserved, the singlet formation via the exchange scattering is maintained.

The VANG molecules provides us a unique opportunity for fabrication of efficient hydrogen storage materials.[6, 7, 8] We have derived a special chemical reaction against hydrogen adsorption on VANG, where the barrier height is much reduced than conventional storage materials composed of organic hydrides.

We offered new fabrication and design methods of edges states at the armchair edges,[9] which is promising for controllable quantum device. This example is explained by the topological argument by Ryu-Hatsugai.

4. Materials dependence of cuprate superconductors

A self-doping effect between outer and inner CuO_2 planes (OPs and IPs) in multi-layer cuprate superconductors is investigated theoretically. When one considers a three-layer tight-binding model of the Hg-based three-layer cuprate derived from the single-reference DFT, the electron concentration tends to be large in the OP compared to the IP, which is opposite to the experimental fact. While the two-particle self-consistent approach for multi-layer systems by Nishiguchi[10] derives decrease in the double occupancy (instability for the antiferromagnetic phase) apparently in OP than IP in a three-layer Hubbard model, which corresponds to the strongly correlated phase of MR-DFT.

To explore material dependence of layered cuprate superconductors, we examine effective two-particle interactions for Hg1201 and Tl1201, where Tl1201 having a nearly half value of T_c of Hg1201 even at the optimal oxygen concentration. Although the $3d_{x^2-y^2}$ band, the Fermi surface, and its Wannier-orbitals are similar for these superconductors, there is an apparent difference in the unoccupied levels above E_F. Based on our MR-DFT, effective two-particle exchange interactions are estimated to derive enhancement in intra-layer exchange interactions for $HgBa_2CuO_4$, (Fig. 1) while it is weakened in $TlBaLaCuO_5$ and furthermore it is weak in $TlBa_2CuO_5$. The characteristic difference in the band structure is correlated with oxygen contents in the buffer layer. We also comment on the similar feature in triple-layered compounds. Our spin-fluctuation enhancement mechanism in an electron-correlation regime is consistent with the experimental fact.[3]

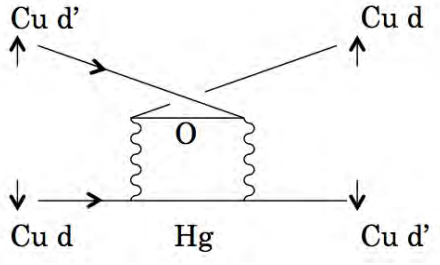

Figure 1: The super exchange mechanism giving material dependence for the layered cuprate superconductors.

Acknowledgement

The author (K.K.) is grateful to Prof. I. Maruyama, Dr. K. Nishiguchi, Mr. S. Miyao, Mr. S. Gagus Ketut, Mr. N. Morishita in physics groups, and Prof. T. Enoki, Prof. T. Mori, Prof. M. Kiguchi, Prof. K. Takai, Prof. S. Fujii, Mr. M. Ziatdinov, and Mr. Y. Kudo in chemistry groups. This work was partly supported by KAKENHI (No. 2610752, 26400357, 16HH00914).

References

[1] K. Kusakabe and I. Maruyam, J. Phys. A: Math. Theor. **44**, 135305 (2011). [2] K. Kusakabe and I. Maruyam, Japanese patent No. 5447674. [3] S. Teranishi, S. Miyao, K. Nishiguchi, K. Kusakabe, arXiv:1704.06559. [4] N. Morishita, G.K. Sunnardianto, S. Miyao, K. Kusakabe, J. Phys. Soc. Jpn., **85**, 084703 (2016). [5] S. Miyao, N. Morishita, G.K. Sunnardianto, K. Kusakabe, J. Phys. Soc. Jpn. **86**, 034802 (2017). [6] G.K. Sunnardianto, I. Maruyama, K. Kusakabe, J. Comput. Theor. Nanosci. **13**, 4883 (2016). [7] G.K. Sunnardianto, I. Maruyama, K. Kusakabe, Advanced Science, Engineering and Medicine, **8**, 421 (2016). [8] G.K. Sunnardianto, I. Maruyama, K. Kusakabe, Int. J. Hydrogen Energy (2017) in press. [9] M. Ziatdinov, H. Lim, S. Fujii, K. Kusakabe, M. Kiguchi, T. Enoki, and Y. Kim, Phys. Chem. Chem. Phys. **19**, 5145-5154 (2017). [10] K. Nishiguchi, S. Teranishi, K. Kusakabe, arXiv:1704.04867.

References

[1] K. Kusakabe and I. Maruyam, J. Phys. A: Math. Theor. **44**, 135305 (2011).

[2] K. Kusakabe and I. Maruyam, Japanese patent No. 5447674.

[3] S. Teranishi, S. Miyao, K. Nishiguchi, K. Kusakabe, arXiv:1704.06559.

[4] N. Morishita, G.K. Sunnardianto, S. Miyao, K. Kusakabe, J. Phys. Soc. Jpn., **85**, 084703 (2016).

[5] S. Miyao, N. Morishita, G.K. Sunnardianto, K. Kusakabe, J. Phys. Soc. Jpn. **86**, 034802 (2017).

[6] G.K. Sunnardianto, I. Maruyama, K. Kusakabe, J. Comput. Theor. Nanosci. **13**, 4883 (2016).

[7] G.K. Sunnardianto, I. Maruyama, K. Kusakabe, Advanced Science, Engineering and Medicine, **8**, 421 (2016).

[8] G.K. Sunnardianto, I. Maruyama, K. Kusakabe, Int. J. Hydrogen Energy (2017) in press.

[9] M. Ziatdinov, H. Lim, S. Fujii, K. Kusakabe, M. Kiguchi, T. Enoki, and Y. Kim, Phys. Chem. Chem. Phys. **19**, 5145-5154 (2017).

[10] K. Nishiguchi, S. Teranishi, K. Kusakabe, arXiv:1704.04867.

Quantum Monte Carlo simulation and electronic state calculations in correlated electron systems

Takashi YANAGISAWA
Electronics and Photonics Research Institute
National Institute of Advanced Industrial Science and Technology (AIST)
AIST Central 2, 1-1-1 Umezono, Tsukuba 305-8568

We investigated the two-dimensional Hubbard model by adopting improved wave functions that take into account intersite correlations beyond the Gutzwiller ansatz. Our wave function is an $\exp(-\lambda K) - P_G$-type wave function, which is inspired by the wave function used in quantum Monte Carlo methods. The wave function can be improved systematically by multiplying by P_G and $e^{-\lambda K}$ where K is the kinetic-energy operator.

The single-band Hubbard model is given by

$$H = \sum_{ij\sigma} t_{ij} c^{\dagger}_{i\sigma} c_{j\sigma} + U \sum_{i} n_{i\uparrow} n_{i\downarrow}, \qquad (1)$$

where t_{ij} are transfer integrals and U is the on-site Coulomb energy. The transfer integral t_{ij} is non-zero $t_{ij} = -t$ for nearest-neighbor pair $\langle ij \rangle$ and $t_{ij} = -t'$ for next-nearest neighbor $\langle\langle ij \rangle\rangle$. Otherwise t_{ij} vanishes. We denote the number of sites as N and the number of electrons as N_e. The energy unit is given by t.

The well-known Gutzwiller wave function is given by $\psi_G = P_G \psi_0$ where P_G is the Gutzwiller operator defined by $P_G = \prod_j (1 - (1-g) n_{j\uparrow} n_{j\downarrow})$ with the variational parameter g in the range of $0 \le g \le 1$. The one way to improve the wave function is to take account of nearest-neighbor doublon-holon correlation: $\psi_{d-h} = P_{d-h} P_G \psi_0$. We can take into account inter-site correlations by multiplying P_J such as $P_J P_{d-h} P_G \psi_0$.

In the other way, we can take account of inter-site correlation by multiplying the kinetic operator to the Gutzwiller function in order to improve the wave function. A typical wave function of this type is written as[1]

$$\psi_\lambda \equiv \psi^{(2)} = e^{-\lambda K} P_G \psi_0, \qquad (2)$$

where K is the kinetic term in the Hamiltonian: $K = \sum_{ij\sigma} t_{ij} c^{\dagger}_{i\sigma} c_{j\sigma}$ and λ is a variational parameter to be optimized to lower the energy. This wave function is further improved by multiplying the Gutzwiller operator again:

$$\psi^{(3)} \equiv P_G \psi_\lambda = P_G e^{-\lambda K} P_G \psi_0. \qquad (3)$$

The expectation values are evaluated by using the variational Monte Carlo method.

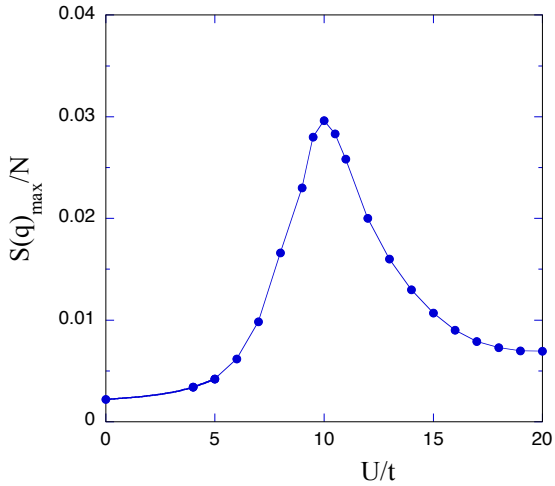

Figure 1: Spin correlation function as a function of U in units of t on 10×10 lattice. The number of electrons is $N_e = 88$ and we set $t' = 0.0$. We used the periodic boundary condition in one direction and the anti-periodic one in the other direction.

The trial wave function $P_{d-h} P_G \psi_0$ was used to develop the physics of Mott transition following the suggestion that the Mott transition occurs due to doublon-holon binding. We examined the Mott transition with the wave function $e^{-\lambda K} P_G \psi_0$[4] because the variational

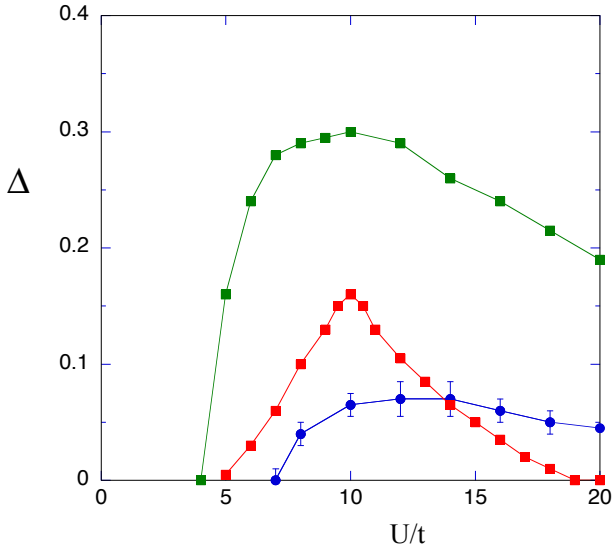

Figure 2: Superconducting and antiferromagnetic order parameters as functions of U in units of t on 10×10 lattice. The number of electrons is $N_e = 88$ and $t' = 0.0$. The solid circles show the SC gap for the improved wave function. The squares represent the antiferromagnetic order parameter, where the upper curve is for the Gutzwiller wave function and the lower curve is for the improved wave function. The boundary condition is periodic in one direction and anti-periodic in the other direction.

energy by this wave function is much lower than that of the doublon-holon wave function.

The $\mathbf{q} = (\pi, \pi)$ component of $S(\mathbf{q})$ is shown in Fig.1, where $S(\mathbf{q})$ is defined as

$$S(\mathbf{q}) = \frac{1}{N} \sum_{ij} e^{iq\cdot(r_i - r_j)} \frac{1}{4} \langle (n_{i\uparrow} - n_{i\downarrow})(n_{j\uparrow} - n_{j\downarrow}) \rangle. \tag{4}$$

$S(\mathbf{q})$ has a maximum at $\mathbf{q} = (\pi, \pi)$. The calculations were performed using the improved wave function ψ_λ. $S(\pi, \pi)$ has a peak near $U \simeq 10t$. The spin correlation is suppressed when U is extremely large begin larger than the bandwidth. There is a crossover from weakly to strongly correlated regions as U increases. The antiferromagnetic correlation induced by U is reduced for hole doping when U is large. begin greater than the bandwidth.

The optimized superconducting order parameter Δ increases as U increases, and also has a maximum at some U. We show Δ and the antiferromagnetic (AF) order parameter as functions of U in Fig.2. The superconducting correlation is developed in the region where the AF correlation is suppressed. The reduction of the antiferromagnetic correlation the strongly correlated region suggests the existence of a large antiferromagnetic spin fluctuation. The development of a superconducting correlation is understood to be induced by spin and charge fluctuations that are induced by the process to gain the kinetic energy. The charge fluctuation induced by the kinetic operator is appreciable and helps electrons to form pairs. The spin fluctuation in the strongly correlated region should be distinguished from that in a weakly correlated region. The latter is the conventional spin fluctuation.

The improved wave function gives results that are qualitatively different from those obtained by the simple Gutzwiller function. In particular, the picture of the stability of the antiferromagnetic state is crucially changed when we employ wave functions with intersite correlations.

References

[1] T. Yanagisawa et al., J. Phys. Soc. Jpn. 67, 3867 (1998).

[2] T. Yanagisawa, Phys. Rev. B75, 224503 (2007) (arXiv: 0707.1929).

[3] T. Yanagisawa, New J. Phys. 15, 033012 (2013).

[4] T. Yanagisawa and M. Miyazaki, EPL 107, 27004 (2014).

[5] T. Yanagisawa, J. Phys. Soc. Jpn. 85, 114707 (2016).

[6] I. Hase, T. Yanagisawa and K. Kawashima, Nanoscale Research Letters 12, 127 (2017).

[7] T. Yanagisawa, I. Hase and K. Odagiri, Phys. Lett. A381, 737 (2017).

Study of skyrmion in frustrated magnets with inversion symmetry

Satoru Hayami
Department of Physics, Hokkaido University, Sapporo, 060-0810

Noncollinear and noncoplanar magnetic structures including skyrmions and vortices act as emergent electromagnetic fields and lead to novel electronic and transport properties. Recently, theoretical studies have shown that such noncoplanar multiple-Q orderings are realized in the ground state in spin-charge coupled systems, such as the Kondo lattice model [1, 2]. The instability toward these magnetic orderings originates from higher-order multiple spin interactions beyond the Ruderman-Kittel-Kasuya-Yosida (RKKY) interaction, which appears after tracing out the itinerant electron degree of freedom. The interplay between charge and spin degrees of freedom, however, results in a variety of multiple spin interactions and its analysis becomes more complicated in the higher-order terms. Thus, it is crucial to elucidate essential contributions among effective magnetic interactions in itinerant magnets and construct a fundamental effective model for further exploration of exotic magnetic orderings.

In this project, in order to clarify the minimal ingredient to capture the essential physics in itinerant magnets, we derive a minimal effective spin model. First, we begin with a Kondo lattice model consisting of itinerant electrons and localized spins on square and triangular lattices, which is given by

$$\mathcal{H} = -\sum_{i,j,\sigma} t_{ij} c^{\dagger}_{i\sigma} c_{j\sigma} + J \sum_{i,\sigma,\sigma'} c^{\dagger}_{i\sigma} \boldsymbol{\sigma}_{\sigma\sigma'} c_{i\sigma'} \cdot \mathbf{S}_i, \quad (1)$$

where $c^{\dagger}_{i\sigma}$ ($c_{i\sigma}$) is a creation (annihilation) operator of an itinerant electron at site i and spin σ. In the first term, we consider hopping elements between nearest-neighbor sites, $t_{ij} = t_1$, and third-neighbor sites, $t_{ij} = t_3$, although qualitative features derived from the model in Eq. (1) are expected to hold for other choices of the hopping elements, e.g., second-neighbor hopping instead of t_3, whenever the bare magnetic susceptibility shows multiple maxima at symmetry-related wave numbers. In the second term, $\boldsymbol{\sigma} = (\sigma^x, \sigma^y, \sigma^z)$ is the vector of Pauli matrices, $\mathbf{S}_i$ is a localized spin at site i which is regarded as a classical spin with length $|\mathbf{S}_i| = 1$, and J is the exchange coupling constant.

Carefully examining the higher-order perturbations in terms of the spin-charge coupling J in Eq. (1), we have obtained an effective spin model composed of the bilinear and biquadratic interactions with particular wave numbers dictated by the Fermi surface as follows [3]:

$$\mathcal{H} = 2\sum_{\nu} \left[-\tilde{J} \mathbf{S}_{\mathbf{Q}_\nu} \cdot \mathbf{S}_{-\mathbf{Q}_\nu} + \tilde{K} (\mathbf{S}_{\mathbf{Q}_\nu} \cdot \mathbf{S}_{-\mathbf{Q}_\nu})^2 \right], \quad (2)$$

where the sum is taken for $\nu = 1, 2$ $(1, 2, 3)$ for the square (triangular) lattice, and $\mathbf{Q}_\nu$ are the wave numbers for the multiple peaks of the bare susceptibility; $\tilde{J}$ and $\tilde{K}$ are the coupling constants for bilinear and biquadratic interactions in momentum space, which originate from the RKKY interaction ($\propto J^2$) and higher-order interaction ($\propto J^4$), respectively.

By performing the Monte Carlo simulation for the model in Eq. (2), we have shown that our model provides a unified understanding of unconventional multiple-Q magnetic orders previously found in the Kondo lattice

model in Eq. (1) [1, 2]. Moreover, by applying an external magnetic field to our effective model, we have found a variety of field-induced multiple-Q phases including different types of double(triple)-Q states on the square (triangular) lattice. Our findings will serve as a guide for exploring further exotic magnetic orderings in itinerant magnets.

References

[1] R. Ozawa, S. Hayami, K. Barros, G.-W. Chern, Y. Motome, and C. D. Batista, J. Phys. Soc. Jpn. **85**, 103703 (2016).

[2] R. Ozawa, S. Hayami, and Y. Motome, Phys. Rev. Lett. **118**, 147205 (2017).

[3] S. Hayami, R. Ozawa, and Y. Motome, preprint (arXiv: 1703.07690).

Numerical analysis on a transverse-field Ising Kondo lattice model

Kazumasa HATTORI, Kohei SUZUKI

Department of Physics, Tokyo Metropolitan University,

1-1 Minami-osawa, Hachioji, Tokyo 192-0397, Japan

Ferromagnetic superconductors have attracted great attentions in condensed matter physics both in theory and experiments in the last decade. Uranium-based heavy-fermion compounds such as UGe_2, URhGe, and UCoGe show unconventional superconductivity within their ferromagnetic phases and show very interesting behaviors in magnetic fields [1]. A special attention in our work is paid to the existence of the second superconducting dome in URhGe under the transverse magnetic field (against the Ising axis of the ferromagnetism). We have analyzed one-dimensional Kondo lattice model with a single-ion anisotropy and transverse magnetic field by means of the density matrix renormalization group.

In order to speed up the calculations, we have utilized the spin-parity eigenvalue that remains even in our very anisotropic Kondo lattice Hamiltonian under transverse fields. Using the eigenstates, we can block-diagonalize the full Hamiltonian and also the density matrix. We find several phases under the transverse fields such as a ferromagnetic, antiferromagnetic, Tomonaga-Luttinger liquids (TLL), gapped Kondo-plateau, charge-density wave, and fully polarized states. The ferromagnetic state appears for lower filling and larger Kondo coupling J regime, while the gapped Kondo-plateau state appears in a wide range of the electron filling for large J. The TLL appears in a broad range of the transverse field strength between the ordered (or the Kondo-plateau) states and fully-polarized state.

To understand the connections between the ferromagnetism and superconductivity in the U-based superconductors, we will need further analyses of the various phase boundaries appearing in the phase diagram and achieve much higher precision for the analysis about the superconducting correlation functions.

References

[1] See, a recent review: D. Aoki and J. Flouquet, J. Phys. Soc. Jpn. **81**, 011003 (2012).

Electronic structure calculations of strongly correlated Ce compounds using the dynamical mean-field theory

Junya OTSUKI
Department of Physics, Tohoku University, Sendai 980-8578

4f electrons in rare-earth ions behaves as a localized moment and/or an itinerant electron depending on materials and situations. First-principles calculations based on density functional theory (DFT) give descriptions of *either* localized or itinerant state. Interesting phenomena such as heavy fermions and exotic superconductivities, however, emerge in the intermediate regime, where 4f electrons show *dual* itinerant and localized characters. In its descriptions, inclusion of many-body effects is essential. For this purpose, we perform dynamical mean-field theory (DMFT) calculations on the top of DFT results.

Here, we give a brief descriptions of our computation scheme and a setup on the ISSP supercomputer. The calculation scheme is summarized in Fig. 1. We first perform DFT calculations within LDA/GGA using `WIEN2k` package on a local computer. The Bloch states are projected to Wannier orbitals to define an effective lattice Hamiltonian using `DFTTools` [1] of `TRIQS` library [2]. Thus obtained Hamiltonian parameters and information of the material are transfered to the supercomputer and plugged into DMFT calculations. Within DMFT, the local correlation effect is evaluated through an effective Anderson impurity model, which is solved by continuous-time quantum Monte Carlo method [3] in `ALPSCore` implementation [4]. This calculation is repeated until convergence is reached. All the above packages are compiled in `C++14` mode of `gcc` version 5.1.0 to keep compatibility with the

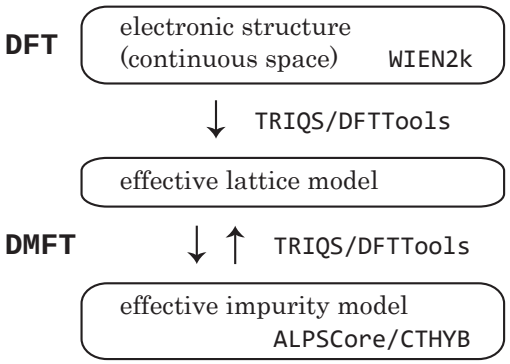

Figure 1: A flow chart of the DFT+DMFT scheme and softwares used in each step.

`TRIQS`-based softwares, which are written with the `C++14` standard.

We have done test calculations of the DMFT loop. Low-temperature calculations of order 100K are expected for Ce-based compounds. Further computations are necessary to obtain results that can be compared with experiments.

References

[1] M. Aichhorn *et al.*, Comp. Phys. Comm. **204**, 200 (2016).

[2] O. Parcollet *et al.*, Comp. Phys. Comm. **196**, 398 (2015).

[3] E. Gull *et al.*, Rev. Mod. Phys. **83**, 349 (2011).

[4] H. Shinaoka, E. Gull, P, Werner Comp. Phys. Commun. **215**, 128 (2017).

Microscopic theory for magnons of chiral magnets

Naoya ARAKAWA

Center for Emergent Matter Science, RIKEN, Wako, Saitama 351-0198

Magnons are quasiparticles describing low-energy physics of magnets. The understanding for nonchiral magnets, such as ferromagnets and antiferromagnets, has been developed. In contrast to the understanding for nonchiral magnets, the understanding for chiral magnets is developing; chiral magnets are magnets having the finite spin scalar chirality. In particular, it is unclear about the differences between magnons of nonchiral and chiral magnets and the differences between magnons of different chiral magnets.

To advance the understanding for chiral magnets, we studied the magnon dispersion and specific heat for chiral magnets on the pyrochlore lattice [1]. This study was done by using the linearized-spin-wave approximation for an effective model of pyrochlore magnets for the weak spin-orbit coupling; the effective model consists of the Heisenberg interactions and the Dzyaloshinsky-Moriya interactions. As the chiral magnets, we considered the all-in/all-out (AIAO) type chiral magnets and the three-in-one-out (3I1O) type chiral magnets.

There are two main results. First, we show that in all the chiral magnets considered, there is no gapless excitation in the magnon dispersion curves. Since a gapless excitation exists in nonchiral magnets, this result demonstrates that the absence and presence of the gapless excitations is the difference between magnons of chiral and nonchiral magnets. Second, we show that magnons for the 3I1O type chiral magnets possess not only the quasiacoustic branches of the magnon dispersion but also the optical branch, while the branches for the AIAO type chiral magnets are all quasiacoustic. Here a quasiacoustic branch increases with the displacement from $\boldsymbol{q}=\boldsymbol{Q}$, with the ordering vector $\boldsymbol{Q}$, and an optical branch decreases with the displacement. The above difference demonstrates the difference between magnons of different chiral magnets.

The facilities of the Super Computer Center were useful because the pyrochlore magnets offer the systematic numerical calculations to study the magnon properties due to the complex structure. We thus acknowledge support from the Super Computer Center.

References

[1] N. Arakawa: Magnon dispersion and specific heat of chiral magnets on the pyrochlore lattice, submitted to PRB.

Intradimer charge degree of freedom, magnetism, and superconductivity in κ-type molecular conductor

Hiroshi WATANABE
Waseda Institute for Advanced Study, Waseda University
1-6-1 Nishi Waseda, Shinjuku-ku, Tokyo 169-8050

The family of quasi two-dimensional molecular conductors κ-(BEDT-TTF)$_2$X has been extensively studied as a typical example of strongly correlated electron system. Due to the strong hybridization, two BEDT-TTF molecules facing each other can be regarded as a dimer and form an anisotropic triangular lattice with one hole per dimer (effective 1/2-filled system). Depending on the monovalent anion X, they show various quantum phases such as antiferromagnetic and spin-liquid dimer-Mott insulators, and superconductivity (SC) [1]. Owing to the similarities in the experimental phase diagrams, κ-(BEDT-TTF)$_2$X system is often compared with high-T_c copper oxides, which exhibit Mott metal-insulator transition and SC [2]. One of the theoretical models common to them is the two-dimensional Hubbard model, and the 1/2-filled case has been heavily studied. Early works suggested SC near the Mott insulating phases, but some of the recent numerical works do not support such results, and cast doubt on the simple "Mott" picture believed in κ-(BEDT-TTF)$_2$X for years.

Although the effective 1/2-filled dimer model well describes the Mott physics, recent experimental and theoretical studies suggest the importance of intradimer charge degree of freedom which are neglected in the dimer model. The intradimer charge degree of freedom leads to charge fluctuations within the dimers and should affect the electronic structure and mechanisms of emergent phenomena. Here, we theoretically study the phase competition in κ-(BEDT-TTF)$_2$X by taking account the intradimer charge degree of freedom. We consider a 3/4-filled four-band extended Hubbard model including onsite (U) and intersite Coulomb interactions (V_{ij}) with κ-type geometry with the largest hopping integral t_{b_1} as an energy unit. The ground state properties are studied with the variational Monte Carlo (VMC) method. The Gutzwiller-Jastrow type wave function is used for the VMC trial wave function. The system sizes for calculation are from 288 (4×12×6) to 1152 (4×24×12).

In the ground state phase diagram of the model parameters for X=Cu[N(CN)$_2$]Br, we find the SC state near the border between the dimer-Mott and charge-ordered states (Fig. 1) [3]. The extended-s+$d_{x^2-y^2}$-wave symmetry is favored and the gap function changes its sign depending on the band [4, 5]. Without the intersite Coulomb interactions, SC is difficult to arise since not only the spin fluctuation but also the charge fluctuation is important for the stability of SC. Our result supports the importance of intradimer charge degree of freedom and leads to a unified view of κ-(BEDT-TTF)$_2$X.

References

[1] K. Kanoda: J. Phys. Soc. Jpn. **75** (2006) 051007.

[2] R. H. McKenzie: Science **278** (1997) 820.

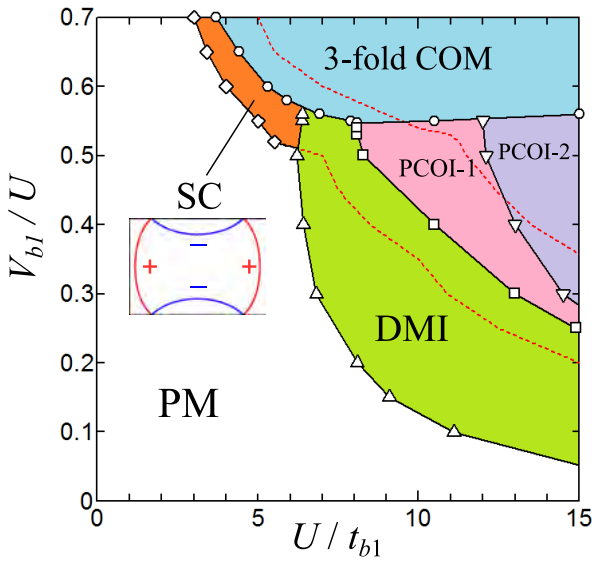

Figure 1: Ground-state phase diagram of the 3/4-filled extended Hubbard model for κ-(BEDT-TTF)$_2$X. PM, DMI, PCOI, 3-fold COM, SC denote paramagnetic metal, dimer-Mott insulator, polar charge-ordered insulator, 3-fold charge-ordered metal, and superconductivity, respectively.

[3] H. Watanabe, H. Seo, and S. Yunoki: J. Phys. Soc. Jpn. **86** (2017) 033703.

[4] K. Kuroki, T. Kimura, R. Arita, Y. Tanaka, and Y. Matsuda: Phys. Rev. B **65** (2002) 100516(R).

[5] D. Guterding, M. Altmeyer, H. O. Jeschke, and R. Valentí, Phys. Rev. B **94** (2016) 024515.

3.4 Cooperative Phenomena in Complex Macroscopic Systems

Tensor Network Study of Frustrated Quantum Spin Systems*

Naoki KAWASHIMA

Institute for Solid State Physics,

The University of Tokyo, Kashiwa-no-ha, Kashiwa, Chiba 277-8581

Tensor network states (TNS) are quantum wave function whose matrix elements are represented by partially contracted tensor products of many tensors. They are used as variational ansatz and turned out to be useful. The resulting optimized wave function is very accurate when the entanglement is not very strong. Even when it is strong, as is the case with the state near the quantum criticality, it still is competitive with other conventional numerical methods. One of the advantages of the tensor network method is that it is free from the negative sign problem inherent to the quantum Monte Carlo simulation. As a result, it may be possible, at least in principle, to compute frustrated quantum spin systems or fermionic systems within computation time that depends on the system size only polynomially. In our project using the ISSP supercomputer, we planned to (i) optimize and parallelize the tensor network based renormalization group (RG) method, and (ii) carry out computation on the kagome lattice antiferromagnet and related models.

As for the optimization and development of the RG method based on the TNS representation, we examined the simplest framework, i.e., the tensor RG proposed by Levin and Nave [1]. While this framework is generally taken as the O(D^6) method for the square lattice, we discovered that, by introducing the partial singular value decomposition (SVD), we can squeeze it down to O(D^5) keeping the result unchanged. Our benchmark calculation showed the expected scaling up to the parallelization with 10,000 cores.

We also carried out tensor network computation based on the corner transfer matrix framework for kagome antiferromagnet and generalized Kitaev-Heisenberg model. As for the kagome antiferromagnet, we obtained very small or vanishing gap at zero field, consistent with the spin liquid nature of the ground state, and identified the nature of the 1/3 magnetization plateau. As for the generalized Kitaev-Heisenberg model, we clarified the phase diagram that is supposed to represent Na2IrO3. [2]

References

[*] This work has been done in collaboration with T. Okubo and S. Morita

[1] Michael Levin, Cody P. Nave: Phys. Rev. Lett. 99, 120601 (2007).

[2] Tsuyoshi Okubo, Kazuya Shinjo, Youhei Yamaji, Naoki Kawashima, Shigetoshi Sota, Takami Tohyama, and Masatoshi Imada: arXiv:1611.03614.

Nonuniqueness of local stress tensor of multibody potentials in molecular simulations

Koh M. NAKAGAWA and Hiroshi NOGUCHI
Institute for Solid State Physics, University of Tokyo, Kashiwa, Chiba 277-8581

Microscopic stress fields are widely used in molecular simulations to connect discrete molecular systems and continuum mechanics. The calculation method of local stress for pairwise potentials are well established but that for multibody potentials are still under debate. Recently, decomposition methods of multibody forces to central force pairs between the interacting particles have been proposed (called central force decomposition, CFD) [see Fig. 1(b)] [1, 2]. Their method satisfies the local conservation of translational and angular momentum and yields symmetry stress tensor $\sigma_{\alpha,\beta} = \sigma_{\beta,\alpha}$.

We introduced a force center of a three-body potential and proposed two alternative force decompositions that also satisfy the conservation of translational and angular momentum [3]. For three-body forces, three lines drawn along the force vectors $\mathbf{f}_i$ from the particle positions $\mathbf{r}_i$ $(i \in 1, 2, 3)$ always meet at one position owing to the angular-momentum conservation. We call this position the force center, $\mathbf{r}_c$. Then the three-body forces are decomposed to three central force pairs between the particle positions and the force center (called force center decomposition, FCD) [see Fig. 1(c)]. By combining CFD and FCD, the force center is set at arbitrary positions (called hybrid decomposition, HD) [see Fig. 1(d)]. For four-body or more-body potentials, the forces can be decomposed by HD.

We compared the force decomposition by stress-distribution magnitude and discuss their difference in the stress profile of a bilayer membrane using coarse-grained (dissipative particle dynamics) and atomistic molecular dynamics simulations. For the atomistic model, DOPC lipids was simulated using CHARMM36 force field and GROMACS 5.1. The lateral stress profile across the lipid bilayers is strongly dependent on the choice of the decomposition methods while the normal stress is constant and independent of the decompositions.

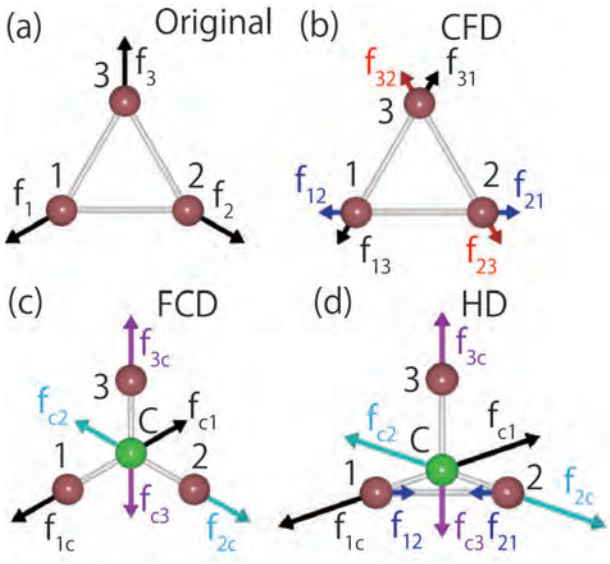

Figure 1: Force decomposition for area expansion forces. (a) Original forces. (b) CFD. (c) FCD. (d) HD. The green gray sphere represents the force center, $\mathbf{r}_c$.

References

[1] N. C. Admal and E. B. Tadmor, J. Elast. **100**, 63 (2010).

[2] J. M. Vanegas, A. Torres-Sánchez, and M. Arroyo, J. Chem. Theory Comput. **10**, 691 (2014).

[3] K. M. Nakagawa and H. Noguchi: Phys. Rev. E **94**, 053304 (2016).

Morphology of high-genus fluid vesicles

Hiroshi NOGUCHI
Institute for Solid State Physics, University of Tokyo, Kashiwa, Chiba 277-8581

The nucleus of a eukaryotic cell is surrounded by a nuclear envelope. The nuclear envelope consists of two bilayer membranes connected by many lipidic pores, which are supported by a protein complex called nuclear pore complex (NPC). Nuclear pores have an approximately uniform distribution in the nuclear envelope. Hence, the nuclear envelope is a spherical stomatocyte with a high genus. In order to clarify the formation mechanism of the nuclear envelope, we simulated the morphology of high-genus vesicles by dynamically triangulated membrane methods.

First, we investigated the vesicle morphology of genus $0 \leq g \leq 8$ in the absence of NPCs [see Fig. 1(a)–(f)] [1]. For $g \geq 3$, bending-energy minimization without volume or other constraints produces a circular-cage stomatocyte, where the pores are aligned in a circular line on an oblate bud [see Fig. 1(a)]. As osmotic pressure is imposed to reduce the vesicle (perinuclear) volume, the vesicle transforms to the spherical stomatocyte (nuclear envelope shape) [see Fig. 1(d)]. In the lipid vesicles, the area difference ΔA of two monolayers of the bilayer is different from the preferred value ΔA_0 determined by the lipid number of both monolayers. This effect is taken into account by the area-difference elasticity (ADE) energy: $K_{\rm ade}(\Delta A\_\Delta A_0)^2/2$. With increasing ΔA_0, the vesicle transforms from the circular-cage stomatocyte into discocyte continuously via pore opening [see Fig. 1(b)] at the large volume as seen in genus-0 vesicles. Surprisingly, however, at the small volume, the vesicle exhibits a discrete transition from polyhedron to discocyte [see Figs. 1(e) and (f)].

Next, we modeled the pore size constraint by the NPC as a ring which the membrane cannot penetrate [2]. When the pore is restricted as a small size, the aligned pores move to the end of the vesicle under the bending-energy minimization as shown in Fig. 1(g). Interestingly, the pore-constraint itself rather presents the formation of the spherical stomatocyte. We found that the spherical stomatocyte is formed by a small perinuclear volume, osmotic pressure within nucleoplasm, and/or repulsion between the pores. When the ADE energy is accounted, the endoplasmic-reticulum-like tubules can grow from the spherical stomatocyte [see Fig. 1(i)].

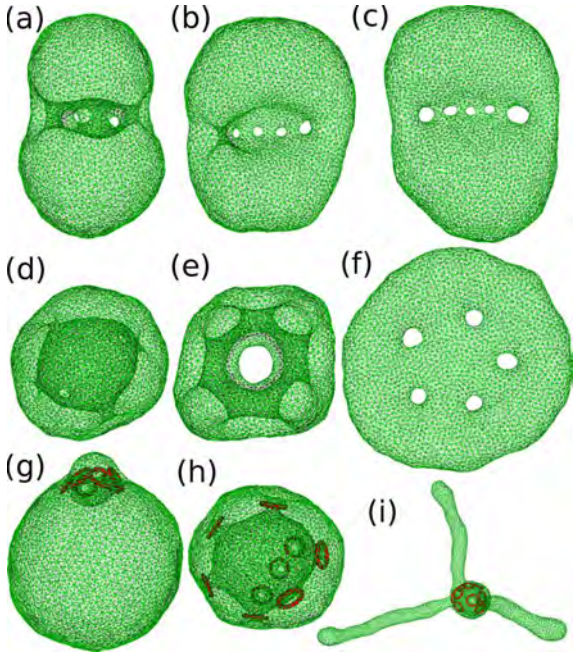

Figure 1: Snapshots of high-genus vesicles (a–f) with no pore-size constraint and (g–h) with pore-size constraint. (a–g) $g = 5$. (h,i) $g = 8$.

References

[1] H. Noguchi: EPL **112**, 58004 (2015).

[2] H. Noguchi: Biophys. J. **111**, 824 (2016).

Thermal properties of spin-S Heisenberg-Kitaev models on a honeycomb lattice

Takafumi SUZUKI

Graduate School of Engineering,

University of Hyogo, Shosha, Himeji, Hyogo 670-0083

In this project, we have studied thermal properties of spin-S Heisenberg-Kitaev (HK) models on a honeycomb lattice. It has been shown for the S=1/2 case that a spin liquid state, namely Kitaev's spin liquid (KSL), is stabilized when the Heisenberg interaction is weak enough [1]. The low-energy excitations of this KSL are characterized by Majorana fermions resulting from fractionalization of quantum spins. In the Kitaev model, where the Heisenberg interaction is absent, this fractionalization is observed as a two-peak structure in the temperature dependence of the specific heat C(T) [2]. We reported that the two-peak structure of C(T) survives in the magnetic ordered phase, if the system is located in the vicinity of the KSL phase, and this offers criteria for measuring the closeness to the KSL phase [3]. Similarly, it has been indicated that C(T) of the HK model in the large S limit (HK model written by classical spins) also shows a two-peak structure [4].

In this study, we have calculated C(T) for spin-S HK models and found that the origin of two peaks is quite different between the quantum and classical limits. The difference is evident in the higher temperature peaks in C(T). For the quantum spin S=1/2, the higher temperature peak is well developed. As the spin S increases, the high temperature peak shrinks and the prominent two-peak structure disappears for $3/2 < S$. In the classical limit, the high temperature peak remains as a shoulder structure. In order to discuss the details of the spin-S dependence for C(T), we have applied the Jordan-Wigner transformation to the spin-S Kitaev model. The obtained results show that the model can be composed by kinetic terms of itinerant Majorana fermions and coupling terms of local gauge field with the itinerant Majorana fermions. The difference from the S=1/2 case is the number of colors for Majorana fermions. As S increases, the number of interactions between different-colored fermions increases. This can suppress the development of the higher temperature peak in C(T).

References

[1] A. Kitaev, Ann. Phys. **321**, 2 (2006).

[2] J. Nasu, M. Udagawa and Y. Motome, Phys. Rev Lett. **113**, 197205 (2014).

[3] Y. Yamaji, et al., Phys. Rev B **93**, 174425 (2016).

[4] C. Price and N. Perkins, Phys. Rev Lett. **109**, 187201 (2012).

Multiscale Simulation of Polymer Melts

Takahiro MURASHIMA

Department of Physics,

Tohoku University, Aoba-Ward, Sendai, Miyagi 980-8578

We have been developing a multiscale simulation method to solve flow dynamics of entangled polymer melt [1]. This simulation consists of macroscopic fluid particle simulation and microscopic polymer dynamics simulation. Each fluid element at the macroscopic simulation has a microscopic simulator describing the internal degrees of freedom of the fluid element. The momentum and energy transfers among the fluid elements are considered through the macroscopic fluid dynamics simulation. Therefore, massively parallel computing are available for updating the microscopic degrees of freedom.

This year, the macroscopic simulation part are updated. In order to treat a large number of fluid elements, the macroscopic fluid simulation part must be parallelized. Using FDPS [2], the parallelization of macroscopic fluid particle simulation part is succeeded in a short period of time. The code has been tested on system-B and system-C at ISSP, and then the production run has been done on K Computer. We have obtained a good parallel efficiency for the multiscale simulation. The details are summarized in Ref. [3].

References

[1] T. Murashima, T. Taniguchi: EPL **96** (2011) 18002.

[2] M. Iwasawa et al.: Publ. Astron. Soc. Jpn. **68** (2016) 54.

[2] T. Murashima: Microsyst. Technol. (2017). Doi:10.1007/s00542-017-3414-x.

Development of a parallel quantum Monte Carlo Method and Study of novel quantum phenomena in quantum lattice models

Akiko Masaki-Kato

Riken, Hirosawa, Wako, Saitama, 351-0198

We have developed parallelizable quantum Monte Carlo algorithm with nonlocal update[1] based on worldline algorithm and have studied quantum spin and lattice boson systems using massive parallel computer simulations.

This year, we especially focused on development of finite size scaling form for the parallelizable multi-worm algorithm (PMWA) what we proposed in Ref. [1]. In PMWA, a term corresponding to the transverse magnetic field is artificially introduced in the target Hamiltonian as the source field Γ of worms, and finally Γ is extrapolated to 0 limit after finishing the simulation. Unfortunately extrapolation rules are nontrivial and have to be considered about each case. In addition, there is a problem when we try to apply PMWA to critical phenomena because the correlation length is cut off by worms which are discontinuities of worldlines. In the critical region, the correlation length grows rapidly as it is close to the critical point. Consequently, usual FSS for critical phenomena does not work. We firstly solved this problem in the off-critical region by inventing a form of scaling formula based on the idea of finite size scaling (FSS) derived from renormalization group theory instead of the extrapolation process. Secondly, in the critical region, we found FSS fomula that can be used in PMWA by incorporating Γ as a scaling field (e.g. Γ works as a relevant field when the transition in case of XY universality, while treating Γ as irrelevant field in the case of Ising universality). I demonstrated to apply this finite worm+size scaling having two variables, Γ and T, to the finite temperature transition of superfluid using the Bayesian scaling tool [2]. The accuracy becomes higher than conventional worm algorithm when we use large system sizes with nontrivial parallelization.[3]

References

[1] A. Masaki-Kato et al., *Phys. Rev. Lett*. **112**, 140603 (2014).

[2] Kenji Harada, *Phys. Rev*. E **92**, 012106 (2015).

[3] A Masaki-Kato and N. Kawashima, unpublished.

The effect of bond-randomness on the quantum magnetisms in low dimension

Tokuro SHIMOKAWA and Hikaru KAWAMURA

Faculty of Science, Osaka University Machikane-yama, Toyonaka Osaka 560-0043

S=1/2 antiferromagnetic Heisenberg model on the kagome lattice with nearest-neighbor interaction are well known as a candidate of the possible realization of a quantum spin liquid (QSL) state. In spite of the tremendous efforts, the true natures still remain unclear.

In this study, we investigated the thermal properties of the S=1/2 kagome antiferromagnet by means of Hams-de Raedt (thermal pure quantum state) method [1-3]. This method enables us to compute exact finite-temperature physical quantities for larger lattice sizes (up to about 40 spins) than those treated by the conventional exact diagonalization method and the negative sign problem does not occur.

We identified the additional 3rd and 4th peaks in the low-temperature specific heat and found that the 3rd peak is associated with a crossover phenomenon occurring between the QSL states with distinct magnetic short-ranged orders (SROs). The static spin structure showed that the low-temperature state is associated with q=0 SRO, while the high-temperature one with the$\sqrt{3}\times\sqrt{3}$ SRO[4].

Our specific heat we obtained here seems to be not comparable to the recent experimental results in herbertsmithite. This fact may imply that some additional ingredients such as bond-randomness [5] or a symmetry reduction [6] are needed.

Our numerical calculations have been performed by using CPU and FAT nodes of system B. The parallel computing technique with OpenMP has been employed.

References

[1] M. Imada and M. Takahashi, J. Phys. Soc. Jpn. **55**, 3354 (1986).

[2] A. Hams and H. De Raedt, Phys. Rev. E **62**, 4365 (2000).

[3] S. Sugiura and A. Shimizu, Phys. Rev. Lett. **111**, 010401 (2013).

[4] T. S and H. Kawamura, J. Phys. Soc. Jpn. **85**, 113702 (2016).

[5] T. S., *et al*, Phys. Rev. B **92**, 134407 (2015).

[6] A. Zorko, *et al*, Phys. Rev. Lett. **118**, 012720 (2017).

Critical behavior of the classical Heisenberg antiferromagnet on the stacked-triangular lattice

Hikaru Kawamura, and Yoshihiro Nagano

Graduate School of Science, Osaka University, Toyonaka 560-0043

The notion of universality is now standard in statistical physics of phase transition. Namely, it has been well established that critical behaviors of various continuous transitions can be classified into small number of universality classes determined by the basic properties of the system such as the spatial dimensionality and the symmetry of the system. In standard bulk magnets in three dimensions (3D), the number of spin components *n* dictates the underlying symmetry of the system, i.e., *O(n)* symmetry, where *n=1,2,3* correspond to the Ising, *XY* and Heisenberg universality classes.

It was suggested by one of the present authors in as early as mid-80's that there might exist new universality classes different from the standard *O(n)* classes in certain frustrated magnets, i.e., *O(n)×O(2) chiral universality classes* [1,2]. While this theoretical proposal was met by the supports from some experiments [3], numerical simulations [4-6] and analytical calculations including the renormalization-group (RG) calculations [7] and the conformal bootstrap method [8], a counter view that the transition might actually be weakly first order has also been presented [9,10], and the situation still remains not entirely clear.

In this year's project, we undertake a new set of large-scale Monte Carlo simulations on the antiferromagnetic classical Heisenberg on the 3D stacked-triangular lattice, a typical model expected to belong to the n=3 chiral universality class. We can go over to lattice sizes much larger than the previous works on the same model, i.e., up to 384^3 versus 60^3~90^3.

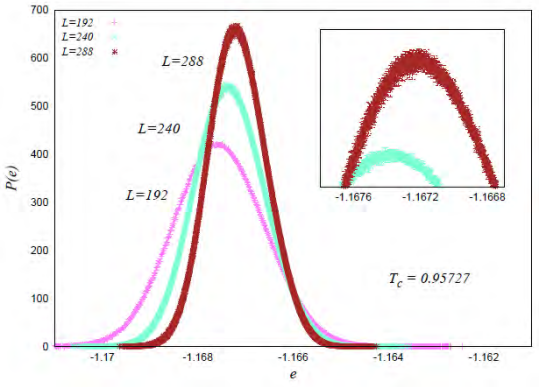

Fig1: The energy histogram at the transition point *Tc*=0.95727 for the sizes *L*=192, 240and 288.

In Fig.1, we show the energy distribution function at the transition temperature estimated to be *Tc*=0.95727, which persists to exhibit a single-peak structure characteristic of a continuous transition. Double-peak structure characteristic of a first-order transition has

never been observed, in sharp contrast to the previous work on the same model for smaller sizes [9]. Thus, we conclude that the transition is continuous.

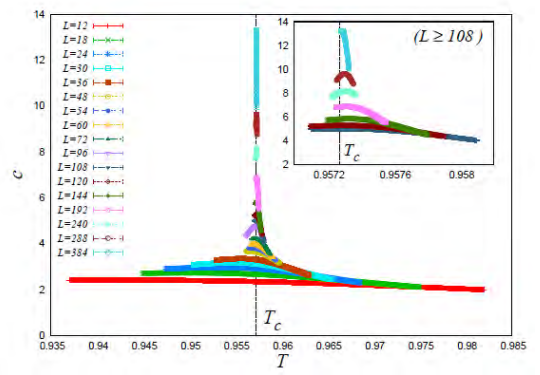

Fig.2: The temperature and size dependence of the specific heat.

In Fig.2, we show the temperature and size dependence of the specific heat. A sharp peak characteristic of a phase transition is observed. In fact, the analysis of the dimensionless quantities such as the correlation-length ratio has revealed the existence of a rather large correction to leading scaling in this model, described by a small correction-to-scaling exponent ω. Indeed, we find that the two correction-to-scaling exponents ω_1 and ω_2 provide satisfactory fits to all the data taken by our simulations, with ω_1=0.02 and ω_2=0.05.

Then, other spin exponents are estimated to be α=0.35(1), β=0.29(6), γ=1.1(1), ν=0.551(4), η=0.07(23) whereas the chirality exponents to be β_κ=0.37(3), γ_κ=0.91(6) and η_κ=0.35(10). Among various previous estimates claiming a continuous transition, our presents estimates are best compared with the 6th order massive RG calculation by A. Pelissetto et al. [7], α=0.35(9), β=0.30(2), γ=1.06(5), ν=0.55(3), η=0.073(94) whereas the chirality exponents to be β_κ=0.38(10), γ_κ=0.89(10) and η_κ=0.38(20). Our new computation then strongly supports the view that the stacked-triangular-lattice Heisenberg antiferromegnet lies in the new *O(3)*×*O(2)* chiral universality class.

[1] H. Kawamura, J.Phys.: Condens. Matter **10** (1998) 4707.

[2] H. Kawamura, J.Phys.Soc.Japan **54** (1985) 3220; **61** (1992) 1299.

[3] D. Beckmann, J. Wosnitza, H. v. Lohneysen, and D.Visser, Phys. Rev. Lett **71** (1993) 2829.

[4] T. Bhattacharya, A. Billoire, R. Lacaze and Th.Jolicoeur, J.Physique I **4** (1994) 181.

[5] A. Mailhot, M.L. Plumer and A. Caille, Phys. Rev. B **50** (1994) 6854.

[6] D. Loison and H.T. Diep, Phys. Rev. B **50** (1994) 16453.

[7] A. Pelissetto, P.Rossi, and E.Vicari, Phys. Rev. B **63** (2001) 140414.

[8] Y. Nakayama, and T. Ohtsuki, Phys. Rev. D **91** (2015) 021901.

[9] V.Thanh Ngo, and H.T. Diep, Phys. Rev. E **78** (2008) 031119.

[10] M. Tissier, B. Delamotte, and D. Mouhanna, Phys. Rev. Lett. **84** (2000) 520.

Seismic properties of the inhomogeneous one-dimensional Burridge-Knopoff model mimicking the subduction zone

Hikaru Kawamura and Maho Yamamoto

Graduate School of Science, Osaka University, Toyonaka, Osaka 560-0043

An earthquake is a stick-slip dynamical instability of a pre-existing fault driven by the motion of a tectonic plate. Numerical simulations of earthquakes based on a simplified statistical model, the so-called Burridge-Knopoff (BK) model, has been popular in statistical physics and provided much information about statistical properties of earthquakes. Some of the properties of the BK model was reviewed in Ref.[1].

In recent years, on the basis of the BK model combined with the rate-and-state dependent friction (RSF) law now standard in seismology, our group has studied slow-slip phenomena, including afterslips and silent (slow) earthquakes where the sliding velocity is several orders of magnitude smaller than that of the high-speed rupture of main shocks. Indeed, the simple BK model combined with the RSF law has turned out to be capable of describing rich seismic phenomena including such slow slips within a single unified framework, only with a few fundamental frictional and elastic parameters, the relative magnitude of the frictional parameters a and b appearing in the RSF law, in particular. When the velocity-strengthening parameter a is comparable or moderately greater than the frictional weakening parameter b, main shocks accompany slow afterslips, while, when a is considerably greater than b, silent earthquakes occur without any high-speed rupture.

In the subduction zone, it has been known that the high-speed rupture of main shocks occurs in the shallower part while aseismic slips dominate in the deeper part, slow slips occurring in between. Such inhomogeneous occurrence is likely to be caused by the spatial change of the frictional parameter a/b. In this year's project, we studied the seismic properties of the inhomogeneous 1D BK model where the frictional parameters a/b are set non-uniform, i.e., $a>>b$ in the deeper part but $a<<b$ in the shallower part. We find that, in certain parameter range, main shocks in the shallower part are almost always preceded by slow slips in the deeper part. This observation gives some hope of the possible forecast of earthquakes by monitoring slow slips in the deeper region.

References

[1] For review, see, H. Kawamura, T. Hatano, N. Kato, S. Biswas and B.K. Chakrabarti, Rev. Mod. Phys. 84, 839-884 (2012).

Numerical Diagonalization Study on the Quantum Spin Liquid in Frustrated System

Tôru SAKAI[1,2,3], Hiroki NAKANO[1,2], Tokuro SHIMOKAWA[4], and Alisa Shimada[5]
[1]*Graduate School of Material Science, University of Hyogo, Kouto, Kamigori, Hyogo 678-1297, Japan*
[2]*Research Center for New Functional Materials, University of Hyogo, Kouto, Kamigori, Hyogo 678-1297, Japan*
[3]*Synchrotron Radiation Research Center, Kansai Photon Science Institute, Quantum Beam Science Research Directorate, National Institute for Quantum and Radiological Science and Technology (QST) SPring-8, Kouto, Sayo, Hyogo 679-5148, Japan*
[4]*Okinawa Institute of Science and Technology Graduate University, Okinawa 904-0495, Japan*
[5]*Graduate School of Science, Kyoto University, Kyoto 606-8502, Japan*

The S=1/2 kagome-lattice antiferromagnet is one of interesting frustrated quantum spin systems. The systems exhibit the quantum spin liquid behavior, which was proposed as an origin of the high-Tc superconductivity. The spin gap is an important physical quantity to characterize the spin liquid behavior. Whether the S=1/2 kagome-lattice antiferromagnet is gapless or has a finite spin gap, is still unsolved issue. Because any recently developped numerical calculation methods are not enough to determine it in the thermodynamic limit. Our large-scale numerical diazonalization up to 42-spin clusters and a finite-size scaling analysis indicated that the S=1/2 kagome-lattice antiferromagnet is gapless in the thremodynamic limit[1]. It is consistent with the U(1) Dirac spin liquid theory of the kagome-lattice antiferromagnet[2, 3]. On the other hand, some density matrix renormalization group (DMRG) calculations supported the gapped Z2 topological spin liquid theory[4, 5]. Our recent numerical diagonalization analysis on the magnetization process of a distorted kagome-lattice antiferromagnet indicated that the perfect kagome-lattice system is just on a quantum critical point[6]. It would be a possible reason why it is difficult to determine whether the perfect kagome-lattice antiferromagnet is gapless or gapped. The magnetization process will be also discussed[7, 8, 9].

References

[1] H. Nakano and T. Sakai: J. Phys. Soc. Jpn., 2011, 80, 053704.

[2] Y. Ran, M. Hermele, P. A. Lee and X. -G. Wen: Phys. Rev. Lett., 2007, 98, 117205.

[3] Y. Iqbal, F. Becca, S. Sorella and D. Poilblanc: Phys. Rev. B ,2013, 87, 060405(R).

[4] S. Yan, D. A. Huse and S. R. White: Science, 2011, 332, 1173.

[5] S. Nishimoto, N. Shibata and C. Hotta: Nature Commun., 2013, 4, 2287.

[6] H. Nakano and T. Sakai: J. Phys. Soc. Jpn., 2014, 83, 04710.

[7] H. Nakano and T. Sakai: J. Phys. Soc. Jpn., 2015, 84, 063705.

[8] T. Sakai and H. Nakano: Phys. Rev. B, 2011, 83, 100405(R).

[9] T. Sakai and H. Nakano: POLYHEDRON 126 (2017) 42.

Novel Field Induced Transitions in Low-Dimensional Quantum Spin Systems

Tôru SAKAI[1,2,3], Hiroki NAKANO[1,2], Tokuro SHIMOKAWA[4], and Alisa Shimada[5]
[1]*Graduate School of Material Science, University of Hyogo, Kouto, Kamigori, Hyogo 678-1297, Japan*
[2]*Research Center for New Functional Materials, University of Hyogo, Kouto, Kamigori, Hyogo 678-1297, Japan*
[3]*Synchrotron Radiation Research Center, Kansai Photon Science Institute, Quantum Beam Science Research Directorate, National Institute for Quantum and Radiological Science and Technology (QST) SPring-8, Kouto, Sayo, Hyogo 679-5148, Japan*
[4]*Okinawa Institute of Science and Technology Graduate University, Okinawa 904-0495, Japan*
[5]*Graduate School of Science, Kyoto University, Kyoto 606-8502, Japan*

The S=1/2 distorted diamond chain is one of interesting frustrated low-dimensional quantum spin systems. The candidate material azurite $Cu_3(CO_3)_2(OH)_2$ was revealed to exhibit a field-induced spin gap at 1/3 of the saturation magnetization in the high-field magnetization measurement[1]. In the present study we take the additional monomer-monomer interaction into account in the distorted diamond spin chain. The nimerical exact diagonalization and the level spectroscopy analysis indicated that the monomer-monomer interaction makes the 1/3 magnetization plateau appear in wider parameter regions[2].

Using the same analysis we also investigated the effect of the monomer-monomer interaction on the S=1/2 distorted diamond spin chain. The obtained ground state phase diagram is much more consistent with the experimental result of the azurite, rather than the previous phase diagram[3].

References

[1] H. Kikuchi, Y. Fujii, M. Chiba, S. Mitsudo, T. Idehara, T. Tonegawa,K. Okamoto, T. Sakai, T. Kuwai and H. Ohta: Phys. Rev. Lett. 94 (2005) 227201.

[2] K. Okamoto, T. Tonegawa and T. Sakai: J. Phys. Soc. Jpn. (Letters) 85 (2016) 063704.

[3] K. Okamoto, T. Tonegawa, Y. Takahashi and M. Kaburagi: J. Phys.: Cond. Mat. 11 (1999) 10485.

Applicability of scaling law in the magnetic refrigeration

Ryo TAMURA
International Center for Materials Nanoarchitectonics,
National Institute for Materials Scinece
1-1 Namiki, Tsukuba, Ibaraki, 305-0044

Cooling phenomena are widely used in everyday, such as food storage and medical treatment, and also in technology for next-generation electronics, such as hydrogen-fuel cells and quantum information processing. Thus, high-performance cooling technology has been actively developed for many fields. The magnetic refrigeration is a promising candidate for a next-generation cooling technology[1, 2, 3, 4, 5], which can solve environmental and noise problems.

In magnetic materials, the change of magnetic entropy is induced by applying magnetic field. In the magnetic refrigeration, the magnetic entropy change at the phase transition point is mainly used. Because the magnetic entropy density in the magnetic materials is higher than that of gas refrigeration, it is possible that higher refrigeration efficiency is obtained by the magnetic refrigeration than the gas refrigeration. Then, searching for high-performance magnetic refrigeration materials which exhibit a large magnetic entropy change has been done exhaustively.

For the magnetic refrigeration materials where the second-order phase transition occurs, the magnetic entropy change ΔS_{M} can be predicted by using the scaling law which is given by

$$\Delta S_{\mathrm{M}} \propto |H|^n, \tag{1}$$

where H is the magnetic field. Furthermore, n is obtained by

$$n = 1 + \frac{\beta - 1}{\beta\delta}, \tag{2}$$

where β and δ are the critical exponents of each magnetic material. However, this scaling law is not guaranteed for larger magnetic fields. Thus, it is necessary to quantify the limits where the scaling laws would remain applicable for researches on magnetic refrigeration. For this purpose, we investigated the magnetic field dependence of the magnetic entropy of (a) a mean-field model with Curie temperatures ranging from 46 to 336 K, (b) experimental data for Gd, and (c) a 3D-Ising model which is beyond the mean-field approximation.

From the results, we found that the scaling law remains applicable up to the magnetic field which is obtained by $\mu_0 H_{\mathrm{mag}} \times 8\%$ T. Here, H_{mag} is defined by $k_{\mathrm{B}} T_{\mathrm{c}} / g J \mu_{\mathrm{B}}$ where $k_{\mathrm{B}}, T_{\mathrm{c}}, g, J$, and μ_{B} are the Boltzmann constant, the Curie temperature, the g-factor, the magnetic quantum number, and the Bohr magneton, which is the characteristic values of each magnetic material. In this range, the predictions of magnetic entropy change by the scaling law remain within errors of 5 %, which is smaller than the experimental error margin. Thus, for magnetic refrigeration materials whose Curie temperature is close to room temperature, scaling laws at the Curie temperature would be applicable for the magnetic field range available at conventional laboratories, that is, smaller than 10 T[6]. From the

results, it was shown that the scaling law is sufficiently practical for development of the high performance magnetic refrigeration materials.

This work is the collaboration work with Carlos Romero-Muñiz (Universidad Autónoma de Madrid), Shu Tanaka (Waseda University), and Victorino Franco (Universidad de Sevilla).

References

[1] A. M. Tishin and Y. I. Spichkin: *The Magnetocaloric Effect and its Applications* (Taylor & Francis, London, 2003).

[2] K. A. Gschneidner and V. K. Pecharsky: Annu. Rev. Mater. Sci. **30** (2000) 387.

[3] R. Tamura, T. Ohno, and H. Kitazawa: Appl. Phys. Lett. **104** (2014) 052415.

[4] R. Tamura, S. Tanaka, T. Ohno, and H. Kitazawa: J. Appl. Phys. **116** (2014) 053908.

[5] S. Toyoizumi, H. Kitazawa, Y. Kawamura, H. Mamiya, N. Terada, R. Tamura, A. Dönni, K. Morita, and A. Tamaki: J. Appl. Phys. **117** (2015) 17D101.

[6] C. Romero-Muñiz, R. Tamura, S. Tanaka, and V. Franco: Phys. Rev. B **94** (2016) 134401.

2D Scattering Pattern Analysis on Coarse Grained MD Model of Filled Hydrogel

Katsumi HAGITA

Department of Applied Physics,

National Defense Academy, 1-10-20, Hashirimizu, Yokosuka, Kanagawa 239-8686

Recently, small angle scattering experiments to observe 2D scattering patterns of filler filled polymer materials are widely performed. For systems with anisotropic axis, 2D scattering patterns analysis is a powerful tool to obtain information of nm-scale structures. When anisotropic axis is x, reasonable approximations of 2D scattering patterns $I(q_x, q_{||})$ can be calculated by circular average $I(\boldsymbol{q})$ for q_y-q_z, where $q_{||}^2 = q_y^2+q_z^2$ and $I(\boldsymbol{q})$ is a square of 3d Fourier transformation of densities.

It is considered that coarse grained (cg) MD simulations with bead spring model based on Kremer-Grest model [1] are effective tools to simulate nm-structures in systems with sub-micron meter dimensions. Recently, we examined changes of 2D scattering patterns of spherical nanoparticles in rubbers by the cgMD with uniaxial elongation [2]. We considered the cgMD is effective for fillers in hydrogels.

Shibayama and co-workers had been reported 2D scattering patterns of clays in clay-filled hydrogels under uniaxial elongation [3,4]. We developed cgMD model for this system. In our model, a disc-like clay filler consists of 177 particles, polymer chains are modeled by Kremer-Grest model, and explicit solvent are not considered. For simulations of hydrogels, density of polymers and fillers are much smaller than those for simulations of rubbers. During pseudo-reaction process, ends of polymer chains are bonded to other ends or particles of clays. After the pseudo-reaction, we elongated the PBC box with constant volume condition.

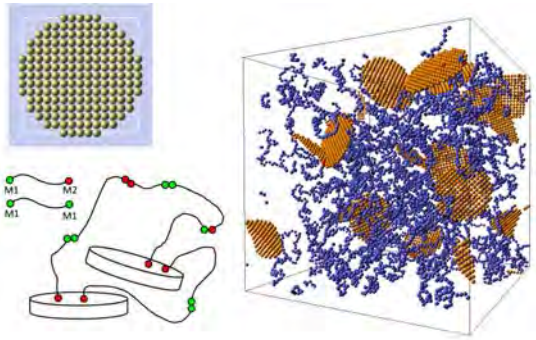

Fig. 1: Cartoon of cgMD model of clay-filled hydrogels.

We performed cgMD simulations for various densities of clays and polymers. We used LAMMPS package [5] as MD solver. Almost calculations planed in our D-class proposal are performed by using supercomputers under the JHPCN proposals in

FY2015 and 2016 in order to save computing resources for Solid State Physics.

Figure 2 shows one of results of our cgMD simulations. Here, clay-density dependence on stress-strain relation is in good agreement with those measured by tensile experiments. The obtained 2D scattering patterns are consistent with those reported by Shibayama group [3, 4]. As results, we confirmed relationship between structure and mechanical function. Detail calculations and analyses are in progress.

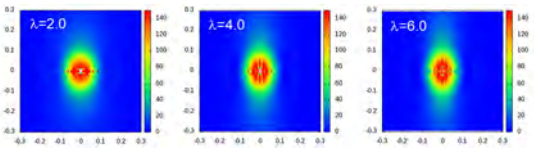

Fig. 2: 2D scattering patterns of clay-filled hydrogels by cgMD simulations of uniaxial elongation.

We also considered 2D scattering patterns of spherical nano-particles in hydrogels. In cgMD simulations, spherical aggregations of particles are used instead of disc-like clay. Examples of obtained 2D scattering patterns are presented in Fig. 3. In Fig. 3, system size dependence is examined. Here, number of fillers are 512, 4096, and 32768. We considered 4096 fillers are required to observe 2D scattering patterns. Detail calculations and analyses are in progress.

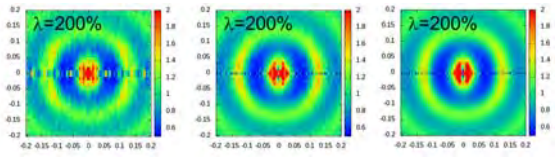

Fig. 3: Dependence of system size on 2D scattering patterns of spherical-filler filled hydrogels by cgMD simulations of uniaxial elongation.

In addition, 2D scattering pattern can be used as an indicator of nanovoids in filler-filled polymer nanocomposites. Recently, we had reported creation and growth of nanovoids in elongated rubbers [6]. In our preliminary calculations, peaks corresponding to nanovoids can be observed in 2D scattering patterns. Detail calculations and analyses are in progress.

References

[1] K. Kremer, G. S. Grest: J. Chem. Phys. **92** (1990) 5057.

[2] K. Hagita, H. Morita, M. Doi, H. Takano: Macromolecules **49** (2016) 1972-1983.

[3] S. Miyazaki, T. Karino, H. Endo, K. Haraguchi, M. Shibayama: Macromolecules **39** (2006) 8112–8120.

[4] T. Nishida, H. Endo, N. Osaka, H.-J. Li, K. Haraguchi, M. Shibayama: Phys. Rev. E **80** (2009) 030801.

[5] S. Plimpton: J. Comp. Phys. **117** (1995) 1.

[6] K. Hagita, H. Morita, H. Takano, Polymer, **99** (2016) 368-375.

Efficient Sampling Simulation of the Soft Modes Significantly Contribute to Protein Properties

Duy TRAN, Kazuhiro TAKEMURA, Hisham DOKAINISH, Jacob SWADLING, Hiroaki HATA, Kenichiro TAKABA, Chika SATO, and Akio KITAO
Institute of Molecular and Cellular Biosciences, University of Tokyo

Here we report dissociation and association simulation of a protein-protein complex using Parallel Cascade Selection Molecular Dynamics (PaCS-MD[1]).

Simulating dissociation and association processes of protein-protein complexes using classical molecular dynamics simulation remains highly challenging. Typically, biased forces are used to accelerate these processes. However, biased forces sometimes mislead protein complexes to unnatural metastable states. Moreover, changes in environments, e.g., ionic or electrostatic interactions lead to changes in the free energy landscape of the substrate[2]. Therefore, unbiased and slow-growth simulation methods for association and dissociation might yield better structures of the protein-protein complexes. Here we present a method based on PaCS-MD for generating the dissociation and association pathways without using any biased forces. PaCS-MD conducts cycles of multiple short MD simulations in parallel, which allows us to explore local conformational states. Snapshots closest to target configurations are chosen as the inputs for the next cycle. Our flexible docking method based on PaCS-MD can take advantage of highly distributed computing.

We have applied our method to the complex of the transactivation domain of p53 (TAD-p53) protein and MDM2 protein. We simultaneously performed association and dissociation simulations using the

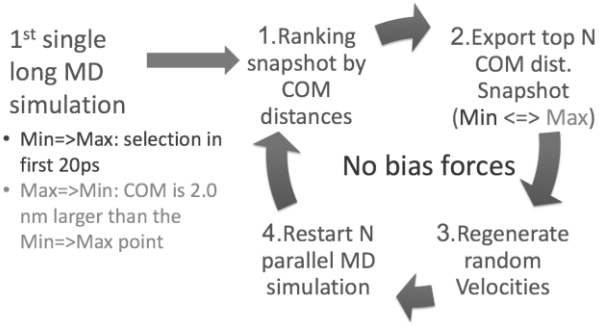

Fig 1. Workflow of flexible-body docking method based on PaCS-MD

center of mass distance (d) as a selection parameter to enhance the motion toward the bound structure of the TAD-p53/MDM2 (Fig. 1). We used the switching condition between dissociation and association and vice versa as follows: if association did not progress for 20 ps, association will switch to dissociation. When d reaches at the point 2.0 nm longer than the last switching point, association simulation will start. A time step of 1fs was used with velocity Verlet integration in all of our simulations together with the MTTK barostat[3] and Nosé-Hoover thermostat [4,5].

After performing 274 cycles, we examined all the conformations of TAD-p53 and MDM2 if structures similar to the crystal complex structure were generated. Figure 2 shows the all-atom RMSD of TAD-p53 from the crystal structure (PDB id 1YCQ). The RMSD minimum that we achieved was 0.429 nm. Although not using the biased force, TAD-p53 found the correct binding cavity. We clustered all the bound conformation to check the variation of

the structures. We identified 4 representative structures among all the bound conformations as shown in Figure 3a. Figure 3b shows the lowest RMSD structure of TAD-p53. Although the two key π-π stacking interactions were not formed, their contacts are in agreement with the crystal structure. The binding interface RMSD of TAD-p53 between the best structure and the crystal structure is 0.243 nm.

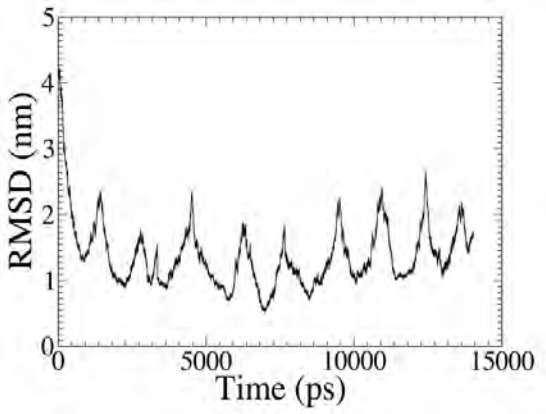

Fig 2. RMSD of TAD-p53 from the crystal structure in concatenated trajectory

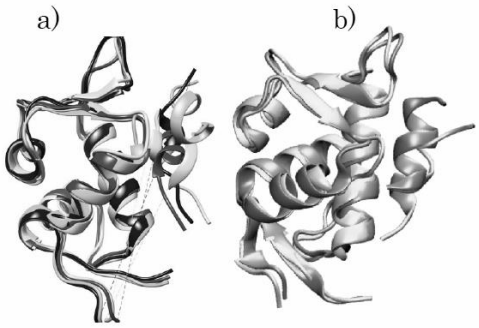

Fig 3. Conformations of the bound structure. a) Representative structure. b) Lowest RMSD structure of TAD-p53 after least square fitting of MDM2 to the x-ray structure

Next, we constructed the Markov State Model to predict the lowest binding free energy structure. We used the distance RMSD (dRMSD) of simulated TAD-p53 from the initial TAD-p53 of the simulation. We found that the lowest energy minimum is situated at dRMSD = 4.21 nm as shown in Fig 4. Interestingly, among the structures at around dRMSD = 4.21 nm, we found that the lowest RMSD structure is identical to the one previously mentioned.

Our proposed method is a promising flexible-body docking method that considers solvation changes during association and flexibility of protein substrate. We would continue to develop our method to reduce the total simulation time needed to reach the structure in agreement with experiment.

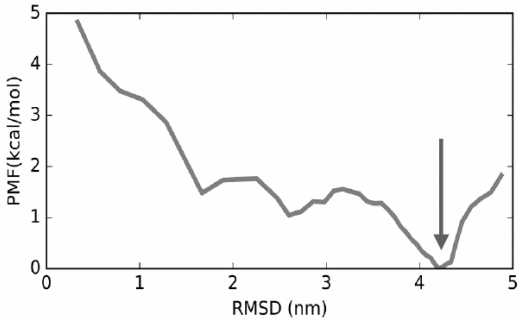

Fig 4. Evolution of PMF with distance RMSD of TAD-p53 after least squre fitting with MDM2

References

(1) Harada, R.; Kitao, A. Parallel Cascade Selection Molecular Dynamics (PaCS-MD) to Generate Conformational Transition Pathway. *J. Chem. Phys.* **2013**, *139* (3).

(2) Kitao, A.; Takemura, K. High Anisotropy and Frustration: The Keys to Regulating Protein Function Efficiently in Crowded Environments. *Curr. Opin. Struct. Biol.* **2017**, *42*, 50–58.

(3) Martyna, G. J.; Tuckerman, M. E.; Tobias, D. J.; Klein, M. L. Explicit Reversible Integrators for Extended Systems Dynamics. *Mol. Phys.* **1996**, *87* (5), 1117–1157.

(4) Hoover, W. G. Canonical Dynamics: Equilibrium Phase-Space Distributions. *Phys. Rev. A* **1985**, *31* (3), 1695–1697.

(5) Nosé, S. A Unified Formulation of the Constant Temperature Molecular Dynamics Methods. *J. Chem. Phys.* **1984**, *81* (1), 511–519.

Magnetization process modified by quantum phonons

Hidemaro SUWA
Department of Physics, The University of Tokyo
7-3-1 Hongo, Bunkyo, Tokyo 113-0033

Under magnetic field, magnetization shows a characteristic curve as a result of interaction. A magnetization curve offers great opportunity for finding the spin energy scale, gaped ground states with magnetization plateaus, magnon interaction, etc. By fitting to model calculation, spin interaction of a material can be well inferred.

Meanwhile, spin-phonon interaction can produce complicated effective spin interaction and non-trivial phenomena [1]. For example, $CuGeO_3$, which is considered as a quasi one-dimensional spin system, has significant spin-phonon interaction because of the edge-sharing CuO_6 octahedra. Its magnetization process [2] with magnetic field shows the complex curve that is not fitted well by a simple spin model. For understanding the nature of the material, it is necessary to study a physical model that has phonon degrees of freedom explicitly.

We studied the magnetization curve of a one-dimensional spin-phonon model by using the worldline quantum Monte Carlo method without any approximation [3]. We found a non-trivial magnetization process that is significantly different from calculation of simple spin models and close to the experimental data. In addition, a new Monte Carlo technique was developed for energy-level and magnetization-curve calculation. We use the projector Monte Carlo approach, preparing various trial states with different quantum numbers. The energy level of each quantum number, e.g., total S^z, is precisely estimated tuning magnetic field in a plausible way. The whole magnetization curve is precisely calculated using this projector technique.

We also calculated the magnon interaction around saturation field. At a magnetic field stronger than the saturation field, the excitation of the spin chain is a magnon. While the magnon interaction of the Heisenberg chain is repulsive, it can be attractive, which leads to a nematic phase. The spin chain with a ferromagnetic J_1 and an antiferromagnetic J_2 interaction has indeed the nematic phase.

We calculated the energy level of several magnon states for the spin-phonon model and found that magnons can attractively interact with each other as a result of the quantum nature of phonons. Our result indicates the existence of the non-trivial nematic phase. Nevertheless, more careful study of the finite-size effect and the thermodynamic limit is needed for a future problem.

As for the computation, we used the system B as the class C (project ID:H28-Cb-0052). Independent worldline quantum Monte Carlo simulations with the worm (directed-loop) algorithm and the geometric optimization were efficiently run by the MPI parallelization.

References

[1] H. Suwa *et al.*: Phys. Rev. Lett. 115 (2015) 080601.

[2] H. Nojiri *et al.*: Phys. Rev. B 52 (1995) 12749.

[3] H. Suwa: Springer Theses (2014).

Monte Carlo Spectral Analysis of Quantum Spin Systems with Emergent Excitation

Hidemaro SUWA
Department of Physics, The University of Tokyo
7-3-1 Hongo, Bunkyo, Tokyo 113-0033

Conventional quantum phase transitions between different ground states of quantum many-body systems can be understood within the Landau-Ginzburg-Wilson (LGW) paradigm, according to which a critical point is described by an order parameter whose fluctuation diverges. Following intriguing numerical results pointing to violations of LGW predictions, the deconfined quantum critical (DQC) point was proposed as a scenario beyond the standard paradigm. Here the low-energy physics is not described directly by order parameters, but by fractional degrees of freedom that emerge (deconfine) on long length scales close to the DQC point. These fractional objects should have prominent signatures in excitation spectra and experimentally accessible spectral functions.

The existence of the DQC point has been addressed in numerous studies of the J-Q model, 3D close-packed loop and dimer models (which provide effective descriptions of quantum spins), and lattice versions of the proposed non-compact CP^1 DQC field theory. Dynamical properties of DQC systems have not been addressed in direct numerical calculations. The J-Q model offers unique opportunities to study deconfined excitations and the quantum dynamics of confinement. The deconfined excitations should be spinons carrying spin $S = 1/2$.

We investigated the level spectrum of the J-Q model at its DQC point [1]. We analyzed gaps extracted from correlation functions, thus characterizing the level spectrum of spinons and scaling behaviors as bound states (magnons) form in the ordered phases. Our study reveals gapless critical $S = 0$ and $S = 1$ excitations at $\mathbf{k} = (0,0), (\pi,0), (0,\pi)$, and (π,π), and all these points are characterized by linear dispersion with a common velocity, thus lending strong support to elementary $S = 1/2$ spinons with dispersion minimum at the above four $\mathbf{k}$-points. Moreover, the scaling of singlet and triplet gaps in the ordered phases exhibits a duality consistent with emergent SO(5) symmetry.

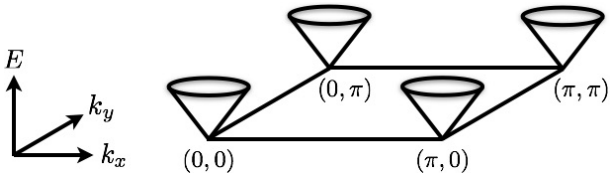

Figure 1: Schematic illustration of the low-lying energy spectrum at the deconfined quantum-critical point. There are four gapless points for both $S = 0$ and 1 excitations, at $\mathbf{k} = (0,0), (\pi,0), (0,\pi)$, and (π,π). Close to these points the modes disperse linearly with the same velocity. The dispersion relation marks the lower edge of a continuum of excitations arising from two essentially deconfined spinons, with the single-spinon dispersion also being the same as the lower edge of the two-spinon continuum. This figure was taken from Ref. [1].

As for the computation, we used the system B as the class C (project ID:H28-Ca-0099). Independent worldline quantum Monte Carlo simulations with the single loop update were efficiently run by the MPI parallelization.

References

[1] H. Suwa, A. Sen, and A. W. Sandvik: Phys. Rev. B **94** (2016) 144416

Screening for Thermal Functional Materials using Materials Infomatics

Junichiro SHIOMI

Department of Mechanical Engineering, The University of Tokyo

7-3-1 Hongo, Bunkyo, 113-8656

Informatics, as the fourth paradigm of science in addition to theory, simulation, and experiment, is gaining great attention in general and interdisciplinary fields of physics which is a powerful approach to search for optimal models, structures, and materials. This year, we focused on designing nanostructures for phonon transport via informatics. We have developed a new materials-informatics (MI) method combining atomistic Green's function approach and Bayesian optimization that realizes highly efficient design of nanostructures with optimal thermal transport, as shown in Fig. 1.

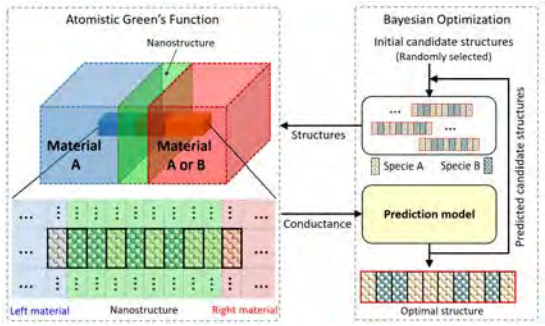

Figure 1: Schematics of the materials informatics method combing Atomistic Green's function (AGF) and Bayesian optimization.

As a case study, we have applied the developed method to design the Si/Ge-composite nanostructures that minimize or maximize interfacial thermal conductance (ITC) across Si-Si and Si-Ge interfaces which are important and realistic for instance in thermoelectrics. We formulate two optimization problems: the first part is optimization of relatively small interfacial region accounting for full degrees of freedom (as shown in Fig. 2) to demonstrate the validity and capability of the current method, and the second part move on to the optimization of larger interfacial region with layered superlattice structures, which is possible to do experiment measurement.

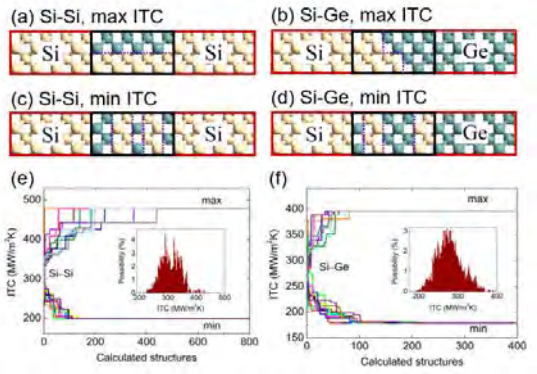

Figure 2: Interfacial Si/Ge alloy structure optimization. (a)-(d) Optimal structures with the maximum and minimum interfacial thermal conductance. (e), (f) The 10 optimization runs with different initial choices of candidates, where the insets show the probability distributions of ITC obtained from calculations of all the candidates.

The optimal structures were obtained by calculating only a few percent of the total candidate structures, considerably saving the computational resources. In addition, the obtained structures are non-intuitive and impacting. The validity and capability of the method are demonstrated by identifying the thin interfacial structures with the optimal Si/Ge configurations among all the possible candidates. Based on the finding that the interfacial structures with minimum ITC take a form of aperiodic superlattice, we extended the search to thicker structures (up to 8.69 nm), and identified non-intuitive structures whose ITCs are significantly smaller than those of the optimal periodic superlattices.

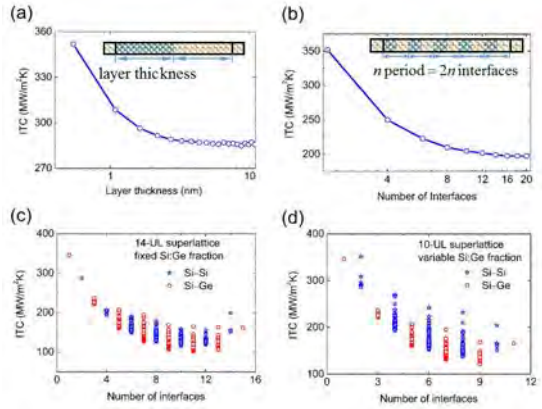

Figure 3: (a), (b) Interfacial thermal conductance versus the layer thickness and number of interfaces. (c), (d) Interfacial thermal conductance versus number of interfaces for cases of 14-unit layer (UL) superlattice with equal Si/Ge layer number and 10-UL superlattice with variable Si/Ge fraction.

Another merit of MI lies in possibility to explore new physics in the course of understanding its output. By performing further systematic analyses, we identified that the small thermal conductance in the aperiodic superlattices originates from their degrees of freedom to mutual-adoptively balance the two competing effects (as shown in Fig. 3): as the layer thickness in superlattice increases, the impact of Fabry–Pérot interference increases, and the rate of reflection at the layer-interfaces decreases. Aperiodic superlattice with spatial variation in the layer thickness has a degree of freedom to realize optimal balance between the above two competing mechanism. Furthermore, the spatial variation enables weakening the impact of constructive phonon interference in relative to that of destructive interference.

In conclusion, we have developed a framework combining atomistic Green's function and Bayesian optimization to design the nanostructure for phonon transport with high efficiency. The present work shows the effectiveness and advantage of material informatics in designing nanostructures to control heat conduction. We believe that the developed novel method, which can be applied to nanostructure design of any materials in principle, would have a broad and impacting appeal to the general scientific and engineering communities, as well as to the general public.

References

S. Ju, T. Shiga, L. Feng, Z. Hou, K. Tsuda, J. Shiomi: Physical Review X, in press (arXiv:1609.04972).

Control of phonon and electron transport properties using mechanical strain

Junichiro SHIOMI

Department of Mechanical Engineering, University of Tokyo,

Hongo 7-3-1, Bunkyo-ku, Tokyo 113-8656

Carbon nanotubes (CNTs) have recently attracted attention as materials for flexible thermoelectric devices. To provide theoretical guideline of how defects influence the thermoelectric performance of CNTs, we have theoretically studied the effects of defects (vacancies and Stone-Wales defects as shown in Fig. 1) on its thermoelectric properties; thermal conductance, electrical conductance, and Seebeck coefficient.

We used a nonequilibrium molecular dynamics simulation and Green's function method to obtain thermal and electrical properties, respectively. We revealed that the defects mostly strongly suppress the electron conductance, and deteriorate the thermoelectric performance of a CNT. By plugging in the results for single CNTs and the intertube-junction properties into the network model, we further show that the figure of merit (*ZT*) increases with decreasing the CNT length regardless of the presence of defects (Fig. 2(a)) and that the defects with realistic concentrations can significantly degrade the thermoelectric performance of CNT-based networks (Fig. 2(b)). Our findings indicate the importance of the improvement of crystallinity of CNTs for improving CNT-based thermoelectrics.

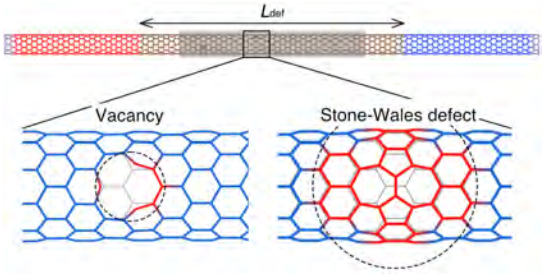

Fig. 1: Analysis model for CNTs with vacancies and Stone-Wales defects.

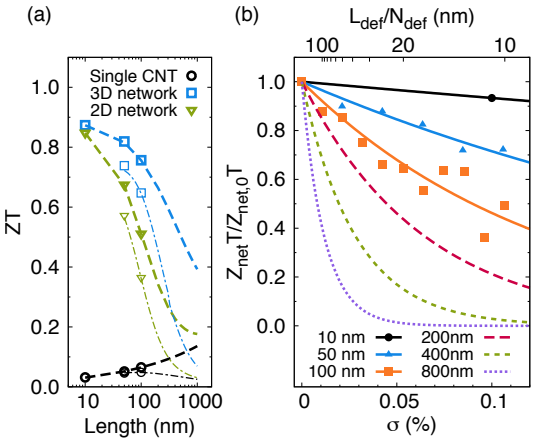

Fig. 2: Figure of merit (*ZT*) of CNT networks. Dependence of (a) the CNT length and (b) defect concentration.

References

[1] M. Ohnishi, T. Shiga, and J. Shiomi: Phys. Rev. B **95**, 155405 (2017).

Numerical study on low-energy states of quantum spin systems

Hiroki NAKANO
Graduate School of Material Science, University of Hyogo
3-2-1 Kouto, Kamigori-cho, Ako-gun, Hyogo 678-1297, Japan

Numerical approaches become more and more important in condensed matter physics because it is generally difficult to estimate physical quantities precisely in systems of many-body problems. From such a motivation, a lot of computational studies have been carried out and contributed much to our deeper understanding of such quantum systems. However, numerical studies are particularly difficult when quantum spin systems in spatial dimensions larger than one include frustrations. The reason for this difficulty comes from the situation that e ectively applicable algorithms are limited. It is well known that such systems cannot be treated by the density matrix renormalization group calculations and the quantum Monte Carlo simulations. Only the numerical diagonalization method based on the Lanczos algorithm is generally applicable for such frustrated quantum spin systems in dimensions larger than one. This method also has a weak point at the same time. This method can treat only very small system sizes. To overcome this disadvantage, we succeeded in developing a hybrid-type parallelized code of Lanczos diagonalization[1]. We examine quantum spin systems using this Lanczos-diagonalization code that we developed as a primary approach.

The primary study of this year in the present project examines the ground state of the $S = 1/2$ Heisenberg antiferromagnet on the triangular lattice with a distortion[2]. The distortion is controlled between the undistorted triangular lattice and the dice lattice[3]. The dice-lattice antiferromagnet does not include frustrations in it; this lattice satis es the Lieb-Mattis theorem[4]. Therefore, the ground state of the Heisenberg antiferromagnet on the dice lattice shows ferrimagnetism with the spontaneous magnetization whose magnitude is one third height of the saturation. In the undistorted triangular lattice, on the other hand, it is widely believed that the ground state shows 120-degree spin structure, which does not show a nonzero spontaneous magnetization. We examine the intermediate region between the two limiting cases by the numerical-diagonalization method. Our diagonalization results suggest that the ground state in an intermediate region between the two limiting cases shows spontaneous magnetizations. The magnitude gradually increases as the distortion is controlled from the undistorted case to the case when there appears the ferrimagnetic state based on the Lieb-Mattis theorem. A similar intermediate state with nonzero spontaneous magnetization is known in the case of a distorted-kagome-lattice antiferromagnet[5], in which an incommensurate modulation appears in this intermediate state. In the present model between the triangular and dice lattices, on the other hand, such an incommensurate modulation is not observed. The spin structure of this nontrivial intermediate state with nonzero spontaneous magnetizations should be examined in future studies. Such studies will contribute to our understandings of this phenomenon and the nontrivial e ect of frustration in magnetic materials.

References

[1] H. Nakano and A. Terai: J. Phys. Soc. Jpn. **78** (2009) 014003.

[2] H. Nakano and T. Sakai: to be published in J. Phys. Soc. Jpn.

[3] A. Jagannathan and A. Szallas: Eur. Phys. J. B **86** (2013) 76.

[4] E. Lieb and D. Mattis: J. Math. Phys. (N.Y.) **3** (1962) 749.

[5] H. Nakano, T. Shimokawa, and T. Sakai: J. Phys. Soc. Jpn. **80** (2011) 043703.

Study on Statistical Physics Toward High-Performance Quantum Information Processing

Shu TANAKA
Waseda Institute for Advanced Study, Waseda University
Nishi-waseda, Shinjuku, Tokyo 169-8050

(I) Topological phase diagram and sweep dynamics of a generalized cluster-Ising model

Topological properties and their related dynamical phenomena are interesting topics in statistical physics, condensed matter physics, and quantum information science. To investigate the robustness of cluster phase which is a candidate for measurement-based quantum computation, we proposed a generalized cluster-Ising model [1]. The Hamiltonian of our model in one dimension is described by

$$\mathcal{H}_{\rm GCI} = \sum_{i=1}^{N}(-J^{XZX}\sigma_i^x\sigma_{i+1}^z\sigma_{i+2}^x + J^{YY}\sigma_i^y\sigma_{i+1}^y + J^{YZY}\sigma_i^y\sigma_{i+1}^z\sigma_{i+2}^y).$$

We completed the ground-state phase diagram of our model, and the topological number of each topological phase is confirmed by numerical calculations [1, 2]. In addition, we considered dynamical properties of our model during interaction sweeps through the critical points of topological phase transition. We observed the topological blocking (or the so-called parity blocking) when we change the interaction so that the topological number changes.

This work was done in collaboration with Takumi Ohta (YITP, Kyoto University), Ippei Danshita (YITP, Kyoto University), and Keisuke Totsuka (YITP, Kyoto University).

(II) Quantum annealing for principal component analysis

Quantum annealing is a promising method for finding the best solution of optimization problems [3, 4]. To investigate novel applications of quantum annealing is a significant topic. We proposed a method to perform the principal component analysis by quantum annealing. We implemented our method to data matrices with hierarchical structure and found that the choice of initial Hamiltonian affects the performance of quantum annealing.

This work was done in collaboration with Yoichiro Hashizume (Tokyo University of Science) and Ryo Tamura (National Institute for Materials Science).

References

[1] T. Ohta, S. Tanaka, I. Danshita, and K. Totsuka: J. Phys. Soc. Jpn. **84** (2015) 063001.

[2] T. Ohta, S. Tanaka, I. Danshita, and K. Totsuka: Phys. Rev. B **93** (2016) 165423.

[3] T. Kadowaki and H. Nishimori, Phys. Rev. E **58** (1998) 5355.

[4] S. Tanaka, R. Tamura, and B. K. Chakrabarti, "Quantum Spin Glasses, Annealing and Computation", Cambridge University Press (2017).

Dynamical DMRG study of spin dynamics in spin-1/2 Inequilateral diamond-chain systems

Takami TOHYAMA
Department of Applied Physics, Tokyo University of Science, Tokyo 125-8585

Frustrated quantum magnets provide various exotic ground states such as gapless spin-liquid and gapped singlet dimer phases. The typical constituent of frustrated magnets is a triangular unit of spin with antiferromagnetic (AFM) interaction for each bond. The spin-1/2 diamond chain, where the triangular unit is connected linearly, is thus regarded as a typical frustrated system in one dimension. The azurite was originally suggested to be such a system, but a recent consensus is that it less frustrated.

Recently, a new highly one-dimensional (1D) diamond chain compound $K_3Cu_3AlO_2(SO_4)_4$ was reported [1]. In this compound, the magnetic susceptibility exhibits a double-peak structure similar to the azurite, but the temperatures of the peaks (50 K and 200 K) are one order of magnitude higher than those in the azurite. In spite of such high characteristic temperatures, there is no magnetic order down to 0.5 K, indicating a possible spin-liquid ground state. It is, thus, important to clarify common features characterizing the distorted diamond-chain compounds in both the azurite and the new compound.

We analyzed the temperature dependence of the magnetic susceptibility in $K_3Cu_3AlO_2(SO_4)_4$ by using the finite-temperature Lanczos and the exact diagonalization methods [2]. The estimated magnetic exchange interactions are found to form strong dimer bond and monomer-monomer chains. The interactions in a diamond Heisenberg model are shown in Fig. **??**. The dimer-bond

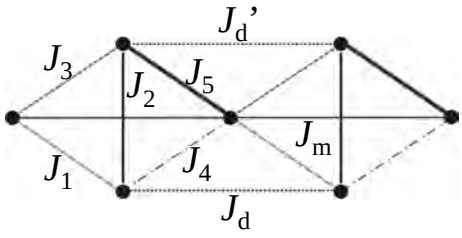

Figure 1: Effective spin model of $K_3Cu_3AlO_2(SO_4)_4$. The circles represent Cu^{2+} ions with spin 1/2. $J_1 = J_3 = J_4 = -30$ K, $J_2 = -300$ K, $J_5 = 510$ K, and $J_m = J_d = J'_d = 75$ K.

position as well as their energy scale is different. The frustration is less effective in $K_3Cu_3AlO_2(SO_4)_4$ than in the azurite and the spin-liquid behavior at low temperatures is attributed to an effective spin-1/2 Heisenberg chain.

Based on the estimated exchange interactions in $K_3Cu_3AlO_2(SO_4)_4$, we calculate the dynamical spin structure factor $S(q,\omega)$ defined by

$$S(q,\omega) = -\frac{1}{\pi N}\mathrm{Im}\,\langle 0|\, S^z_{-q}\frac{1}{\omega - H + E_0 + i\eta}S^z_q\,|0\rangle\,,$$

where q is the momentum for the triangular unit cell, $|0\rangle$ is the ground state of the diamond Heisenberg Hamiltonian H with energy E_0, η is a broadening factor, N is the number of sites, and $S^z_q = N^{-1/2}\sum_i e^{iqR_i}S^z_i$ with R_i being the position of spin i and S^z_i being the z component of $\boldsymbol{S}_i$.

We use the dynamical density matrix renor-

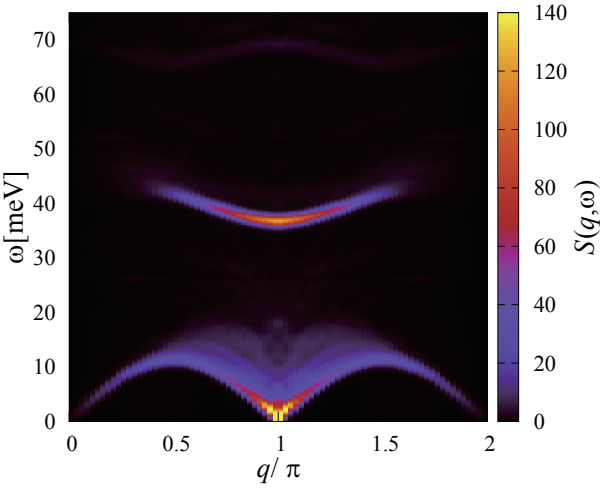

Figure 2: Dynamical spin structure factor $S(q,\omega)$ obtained by DDMRG for a 240-site periodic chain for $K_3Cu_3AlO_2(SO_4)_4$.

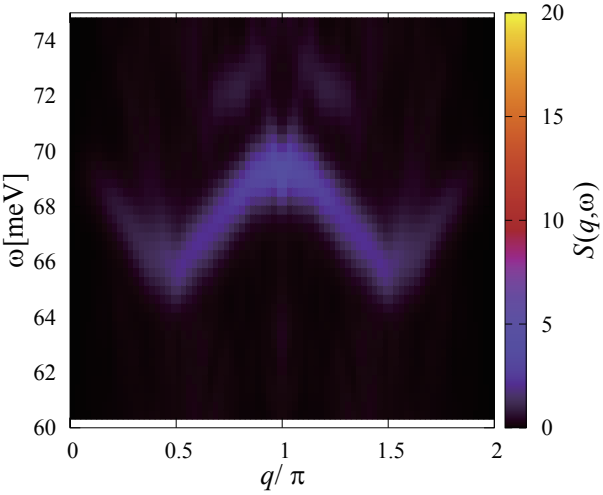

Figure 3: The same as Fig. 2, but higher energy region.

malization group (DDMRG) for a N=240-site periodic chain (80 triangular cells). We use a mutitarget scheme and one of the targets, $(\omega - H + E_0 + i\eta)^{-1} S_q^z |0\rangle$, is evaluated by using a kernel-polynomial expansion method [3]. In our kernel-polynomial expansion method, the Lorentzian broadening given by η is replaced by a Gaussian broadening with half width at half maximum 0.65 meV. In our numerical calculations, dividing the energy interval $[0, 60]$ meV by 186-mesh points and $[60, 75]$ meV by 46-mesh points, we targeted all of the points for each interval at once.

The truncation number $m = 400$ and the truncation error is less than 7×10^{-3}. The value of η is taken to be 0.65 meV.

Figure 2 shows the contour plot of $S(q,\omega)$. At the low-energy region below 10 meV, we find a clear dispersive behavior fitted quite well by $(\pi/2)J\,|\sin q|$ with $J = J_{\rm d}$. This indicates that the lowest-energy branch comes from the 1D Heisenberg chain connected by the $J_{\rm d}$ bond. At high energy region around 40 meV, there is a dispersive structure having a minimum at $q = \pi$. This is nothing but the dispersion of a dimer predominantly formed on the J_5 bond. The dispersion relation is well reproduced by $\omega_q = J_5 + J_{\rm m} \cos q + \frac{1}{4} J_{\rm m}^2 / J_5 (3 - \cos 2q)$. Both the low-energy and high-energy structures have been confirmed for the powder sample of $K_3Cu_3AlO_2(SO_4)_4$ [4].

There are small but dispersive spectral weights around 65 meV. Figure 3 exhibits this energy region. Judging from the energy scale, we assign these structures to be double dimer excitations. These have not yet been observed experimentally and thus detecting them remains to be a challenging problem.

References

[1] M. Fujihala *et al.*: J. Phys. Soc. Jpn. **84** (2015) 073702.

[2] K. Morita *et al.*: Phys. Rev. B, in press.

[3] S. Sota and T. Tohyama, Phys. Rev. B **82** (2010) 195130.

[4] M. Fujihala *et al.*: to be published.

Dynamical scaling analysis for the antiferromagnetic triangular Heisenberg model

Y. Ozeki and R. Tobise

Graduate School of Informatics and Engineering, The University of Electro-Communications

We investigate the topological phase transition expected to appear in the antiferromagnetic (AF) triangular Heisenberg model by the use of the dynamical scaling analysis [1]. In 2D continuous spin systems, while it has been well-known that there is no long-range order with continuous symmetry-breaking, there might be phase transitions for a discrete symmetry-breaking or for a topological phase with no long-range order. In the nonequilibrium relaxation (NER) analysis for the AF triangular XY case [2], two dynamical order parameters are analyzed from a so-called 120° structure. The one is the orientational order parameter defined by the projection of spin vector to the direction of the initial state, $\cos(\theta_i - \theta_{i0})$, and the other is the chiral order parameter defined by the vector product of nearest neighboring spin pair, $\sin(\theta_i - \theta_j)$. It has been found that the chiral order parameter shows a second order transition with a discrete symmetry-breaking (the chiral phase) and the orientational order parameter shows a topological phase transition, the Kosterlitz-Thouless (KT) one.

Similar transitions have been explored in the Heisenberg case, and discussed for a long time [3]. In the present study for the Heisenberg case, we will estimate the transition temperature precisely using the NER method [2] with recently improved dynamical scaling analysis [1]. The chiral order parameter forms a vector, $\vec{m} = \frac{1}{N}\sum_{i\to j} \vec{S}_i \times \vec{S}_j$, where summation is taken over all nearest-neighboring pairs with fixed direction. We simulate the relaxation from a 120° structure in the XY-plane, and measure the z-component and the square of $\vec{m}(t)$.

Calculations are carried out for 2000×2001 triangular lattice with skew boundary condition up to an observation time of 10^5 MCSs. For each temperature, 864 samples are taken for statistical averaging. In the dynamical scaling analysis for the NER method, a general scaling form is examined;

$$m(t, T) = \tau^{-\lambda}\Psi(t/\tau),$$

where $\tau(T)$ is the relaxation time, which is expected to diverge as $\tau(T) = a\exp\left(b/\sqrt{T - T_{\rm KT}}\right)$ for the KT transtion. The resulting scaling plot is shown in Fig. 2 with $T_{\rm KT} = 0.280$ and $\lambda = 0.109$.

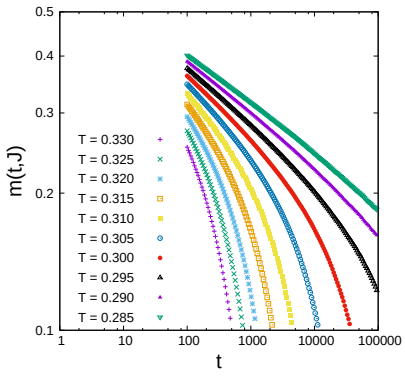

Figure 1: Relaxation of the z-component.

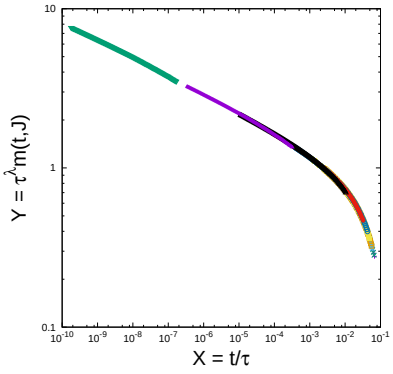

Figure 2: Scaling plot

References

[1] Y. Echinaka and Y. Ozeki, Phys. Rev. E**94** 043312 (2016).

[2] Y. Ozeki and N. Ito, Phys. Rev. B**68** 054414 (2003); Y. Ozeki and N. Ito, J. Phys. A: Math. Theor. **40** R149 (2007).

[3] H. Kawamura and S. Miyashita, J. Phys. Soc. Jpn. **53** 4138 (1984); H. Kawamura, et. al., J. Phys. Soc. Jpn. **79** 023701 (2010).

Development of direct method for quantum respose from microscopic Hamiltonian

Seiji MIYASHITA
Department of Physics, University of Tokyo
Hongo, Bunkyo-ku, Tokyo 113-0033

Quantum response and Quantum dynamics

We have studied the following topics related to quantum response and quantum dynamics.

1. Size- and temperature- dependences of ESR line-shape of the one-dimensional XXZ chain

We introduced a method to decompose the spectrum into contributions specified by the magnetizations of the resonating states, and applied the so-called moment method for each contribution. By making use of it, the size and temperature dependences of the ESR spectrum of the 1DXXZ spin model have been obtained [1].

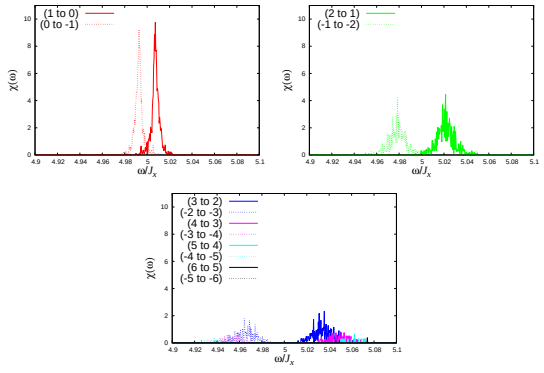

Figure 1: Spectra for classified by the magnetizations ($M = 1, 2$ and others) of transitions at $\beta^{-1} = 100$K.

2. Synergistic effects of the spin-orbit interaction and the external field on the optical conductivity

Synergistic effects of the spin-orbit interaction and the external field on the optical conductivity of the Hubbard model were studied. In one-dimensional noninteracting case ($U = 0$: the tight-binding model), we obtained exact result of the effect as a function of the angle between the directions of the spin-orbit interaction and the external field. For the interacting case, we studied the model numerically and found the angle dependent properties.[2]

3. Population dynamics of the quantum Storner-Wohlfarh model

We have studied the relaxation of metastable state of magnetization under sweeping field in a uniaxial magnetic systems. In the fiscal year, we studied the spin size S dependence of the population dynamics over the adiabatic eigenstates after the Storner-Wohlfarh point, and found some universal aspects of the distribution which survives in the classical limit. We also studied the effect of thermal decoherence on the quantum beating which was found in the previous paper.

4. Thermal distribution of stationary state of periodically driven quantum systems

Properties of periodically driven systems are characterized by the Floquet state, and the quasi-eigenenergy state of Floquet state has been studied from the view point of development of new states under periodic external

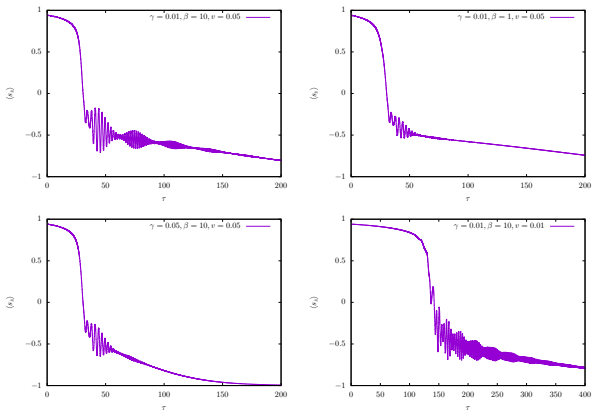

Figure 2: Relaxation of the quantum beating of the quantum Stoner-Wohlfarth model.

field. We have studied the thermal distribution over the quasi-eigenenergy levels, and examined the conditions for the realization of the distribution [3].

5. Thermalization of isolated quantum systems

We formulate this problem as a general problem of the ensemble equivalence [4]. We showed that the system thermalizes when the effective dimension of the initial state is sufficiently large but may be exponentially smaller than the dimension of the Hilbert space.

We also consider the problem of the second law of thermodynamics from the viewpoint of the ensemble equivalence. We proved that the amount of increase of the entropy of the system must be extensively large, i.e. proportional to the system size, by using the large deviation property of the equilibrium state of a macroscopic quantum system [5].

6. Related topics

We also studied cooperative systems, such as the frustrated systems, microscopic mechanisms of the coercive force of permanent magnets, spin-crossover systems, etc. [6, 7, 8, 9].

We also studied fundamental properties of the quantum master equation (QME). Usually QME is perturbatively derived by tracing out the degree of freedom of the thermal bath. We demonstrated this procedure in a spin system. We found that properties obtained by the QME derived by the perturbation method qualitatively agree with the numerical results, but quantitatively they differ each other [10].

References

[1] Hiroki Ikeuchi, Hans De Raedt, Sylvain Bertaina, and Seiji Miyashita, Phys. Rev. B **95**, 024402 (2017).

[2] Adrien Bolens, Hosho Katsura, Masao Ogata, Seiji Miyashita, ArXiv:1704.03153.

[3] Tatsuhiko Shirai, Juzar Thingna, Takashi Mori, Sergey Denisov, Peter Hanggi and Seiji Miyashita, New J. Phys. **18**, 053008 (2016).

[4] Takashi Mori, Phys. Rev. E **94**, 020101(R) (2016).

[5] Takashi Mori, J. Phys. A **49**, 44403 (2016).

[6] Masamichi Nishino, Yuta Toga, Seiji Miyashita, Hisazumi Akai, Akimasa Sakuma and Satoshi Hirosawa, Phys. Rev. B **95**, 094429 (2017).

[7] Masamichi Nishino and Seiji Miyashita, Phys. Rev. B **94**, 184434 (2016).

[8] Yuta Toga, Munehisa Matsumoto, Seiji Miyashita, Hisazumi Akai, Shotaro Doi, Takashi Miyake, and Akimasa Sakuma, Phys. Rev. B **94**, 174433 (2016).

[9] Sasmita Mohakud, Sergio Andraus, Masamichi Nishino, Akimasa Sakuma, and Seiji Miyashita, Phys. Rev. B **94**, 054430 (2016).

[10] P. Zhao, H. De Raedt, S. Miyashita, F. Jin, and K. Michielsen, Phys. Rev. E **94**, 022126 (2016).

Numerical studies of bulk-edge correspondence

Y. Hatsugai
Division of Physics, University of Tsukuba
1-1-1 Tennodai, Tsukuba 305-8571, Ibaraki, Japan

Recent intense studies of topological phases have revealed that variety of materials, that are characteristic but can not be well described by a conventional classification based on a symmetry, is quite wide. They are topological in a sense that topological quantities such as the Chern number or the Berry phase are non trivial for the bulk. However these bulk quantities are mostly hidden and can not be easily observed experimentally. Topological implies hidden. Then experimental tools to identify the phase as non trivial are edge states such as the surface Dirac cones of the topological insulators where the angle resolved photoemission spectroscopy (ARPES) directly measures them. Topologically non trivial bulk induces localized modes when the system has boundaries or geometrical defects. This is the bulk-edge correspondence. We have demonstrated this bulk-edge correspondence in many of quantum systems[1, 2, 3, 4].

One of the recent important developments is that the concept of the topological phase can be extended beyond quantum world into classical systems such as photonic crystals governed by the Maxwell equation and even for the classical mechanics obeying the Newton equation.

We have numerically demonstrate this bulk-edge correspondence without quantum mechanics in two classical systems. One is a three dimensional photonic crystal[5]. The section Chern number defined for a propagating mode with fixed direction can be non zero when the three dimensional system breaks spatial inversion. Then the topological change of the section Chern number implies the existence of the Weyl point that is also reflected by the boundary modes as an example of the bulk-edge correspondence (See Figure 1).

The other one is a classical mechanics. This is just a simple spring mass model arrayed in a diamond lattice. The bulk frequency spectrum has a singular behavior known as a line node protected by the chiral symmetry. These line nodes in the three dimensional Brillouin zone is shown in Figure 2. Topological change of the line nodes induced by the tension change are clearly demonstrated. The symmetry protecting the line nodes of the bulk spectrum also guarantees quantization of the Berry phase of the multibands of the classical system, which directly reflected by momentum dependent boundary modes[6].

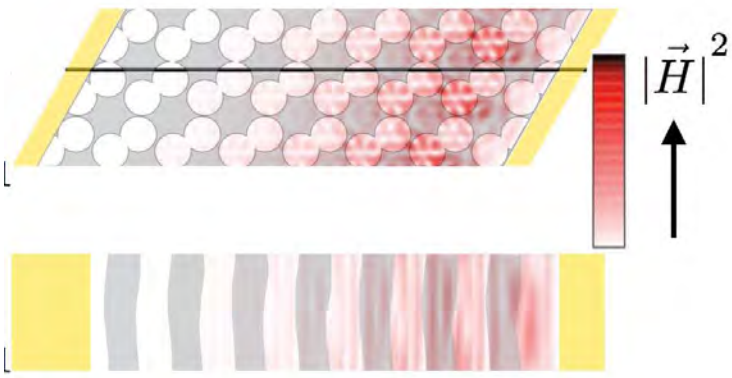

Figure 1: Edge states of a three dimensional photonic crystal without spatial inversion symmetry[5].

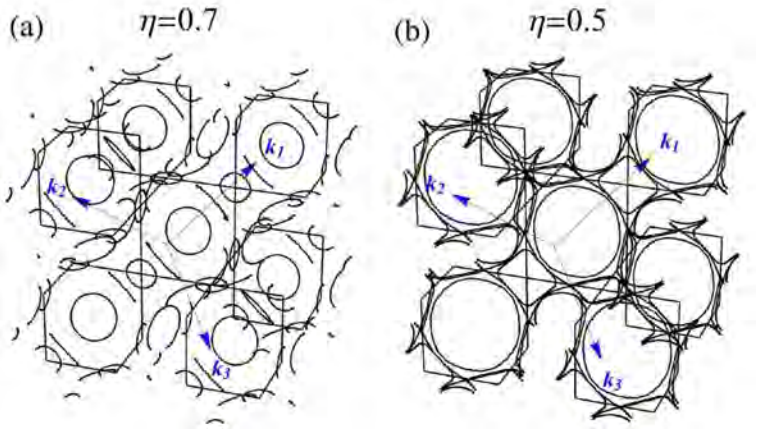

Figure 2: Line nodes of the mechanical diamonds[6] with different tension. Topological phase transition between the phases is clearly demonstrated.

References

[1] Y. Hatsugai, T. Fukui, Phys. Rev. B 94, 041102(R) (2016), DOI: 10.1103/PhysRevB.94.041102

[2] T. Fukui, Y. Hatsugai, J. Phys. Soc. Jpn 85, 083703 (2016), DOI: 10.7566/JPSJ.85.083703

[3] A. Hattori, S. Tanaya, K. Yada, M. Araidai, M. Sato, Y. Hatsugai, K. Shiraishi, Y. Tanaka, J. Phys. Cond. Mat. 29, 115302 (2017), DOI: 10.1088/1361-648X/aa57e0

[4] T. Kawarabayashi, H. Aoki, Y. Hatsugai, Phys. Rev. B94, 235307 (2016), DOI: 10.1103/PhysRevB.94.235307

[5] S. Oono, T. Kariyado, Y. Hatsugai, Phys. Rev. B94, 125125 (2016), DOI: 10.1103/PhysRevB.94.125125 (selected as editors's suggestion)

[6] Y. Takahashi, T. Kariyado, Y. Hatsugai, New J. Phys. 19, 035003 (2017), DOI:10.1088/1367-2630/aa5edb

Role of dimensionality on the glassy fluctuation

Hayato SHIBA
Institute for Materials Research, Tohoku University
Katahira, Aoba-ku, Sendai 980-8577

Dimensionality plays a key role in the physics of solids and liquids. Fluctuation shows up differently in different spatial dimensions, as typically observed in phase transitions. Two-dimensional (2D) crystalline solids often exhibit enhanced fluctuations that span an infinite length that induces long-wavelength structural correlations. A glassy system, on the other hand, lacks the crystalline order and endows the random liquid-like structure. As a consequence, structural (static) correlations cannot represent the dimensionality dependence. We need to look into dynamical aspects to clarify the dimensionality dependence of such systems.

With the use of ISSP supercomputer, we have shown that fluctuation is dependent on the spatial dimensions, but the modality of inherent structural relaxation is similar between 2D and 3D [1]. Extensive simulations are performed for both a 2D binary mixture of 12th-core repulsive potential and a 3D binary mixture of Kob-Andersen-type Lennard-Jones potential, with up to 256,000 and 10,240,000 particles, respectively. We clarified enhancement of 2D fluctuation taking place due to a mechanism similar to Mermin-Wagner theorem for a 2D crystal, by direct calculation of the Debye-asymptote of the vibrational density of states, which also accounts for enhanced fluctuation recently observed in 2D systems [2]. It leads to system-size dependent behavior of the estimated relaxation time and dynamic correlation length in the 2D system in terms of the density-based correlation functions. However, such size dependence is eliminated by introduction of an alternative correlator that characterizes relative rearrangement motions of the particles.

We also treated the glassy dynamics at low-temperature near the jamming and glass transitions. Based on the extensive normal mode analysis of 2D and 3D particle assemblies with large system sizes. In 2D, we have found that the vibrational modes are divided into two groups below the boson peak. One group of the modes converge to the phonons following the Debye law $g_{\rm ex}(\omega) = A_0\omega^2$, and the other to the soft localized modes following another universal non-Debye scaling $g(\omega) \sim \omega^4$. Strikingly, all the non-phonon contributions to the vDOSs at different pressures can be expressed as a universal function of the frequency. In contrast, completely different behaviors are observed in 2D; vibrational modes smoothly converge to phonons without appearance of the group of the soft localized modes [3].

References

[1] H. Shiba, Y. Yamada, T. Kawasaki, and K. Kim, Phys. Rev. Lett. **117**, 245701 (2016).

[2] H. Shiba, T. Kawasaki, and A. Onuki, Phys. Rev. E **86**, 041504 (2012).

[3] H. Mizuno, H. Shiba, and A. Ikeda, submitted.

Metastability and Hysteresis in Chiral Helimagnet

Misako SHINOZAKI and Yusuke KATO
Department of Basic Science, The University of Tokyo
Komaba, Meguro-ku, Tokyo, 153-8902, Japan

The competition between the Heisenberg exchange and the uni-axial Dzyaloshinskii-Moriya (DM) interactions gives rise to a long-period helical magnetic texture called a chiral helimagnetic state. We investigate the thermodynamic properties of the three-dimensional chiral helimagnets under the external field perpendicular to the helical axis using a mean-field method. The winding number, or number of chiral solitons, is essential factor when the finite-size helical systems are considered, and it makes the numerical calculation di cult. To solve the mean-field equations e ciently, we prepare many initial states and solve the equations for each state using a parallel programming.

First, we analyze a phase diagram of the chiral helimagnets particularly paying attention to the order of the phase transition and the crossover phenomena. We found two critical points which separate the first-order and second-order transitions. We evaluate the height of the energy barrier which creates the double minimum structure in the free-energy profile in the first-order transition region. By comparing the height of the energy barrier with thermal energy (i.e. k_BT), we elucidate the condition in which the first-order transition signature is observable. Around the transition temperature at very low field, the magnitude of the local spin moments becomes small, so that a new spin structure called chiral-fan structure is stabilized. We show that the chiral-fan region is related to the crossover line defined on the basis of the susceptibility.

We also analyze a finite-size effect on the physical properties of the chiral helimagnets. The specific heat and susceptibility respectively show the small delta peaks and step-like behavior caused by the discrete change of the winding number at low temperature. Recently, experimental studies have shown hystereses in the magnetization [1, 2] and magneto-resistance [3] using small $CrNb_3S_6$ samples, which often involve step-like behavior. Although these hystereses can be related to the finite-size effect, the relation between the finite-size effect and hysteresis has not been investigated theoretically so far. Using various boundary conditions, we show that many local minima appear in the free-energy profile as the magnetic field increases. By simulating the decreasing external field process numerically, we clarify the relations between these local minima and hystereses.

References

[1] T. Moriya and T. Miyadai, Solid State Commun. **42**, 209 (1982).
[2] K. Tsuruta, M. Mito, Y. Kousaka, J. Akimitsu, J. Kishine, Y. Togawa, H. Ohsumi, and K. Inoue, J. Phys. Soc. Jpn. **85**, 013707 (2016).
[3] Y. Togawa, T. Koyama, Y. Nishimori, Y. Matsumoto, S. McVitie, D. McGrouther, R. L. Stamps, Y. Kousaka, J. Akimitsu, S. Nishihara, K. Inoue, I. G. Bostrem, Vl. E. Sinitsyn, A. S. Ovchinnikov, and J. Kishine, Phys. Rev. B **92**, 220412 (2015).

Predicting a melting curve and structure of melt

Kazuhiro Fuchizaki, Kazuma Okamoto, and Takahiro Sakagami
Department of Physics, Ehime University, Matsuyama 790-8577
Yuta Asano
The Institute for Solid State Physics, The University of Tokyo, Kashiwa 277-8581

We have investigated an effective way with which to predict the accurate location of a phase boundary of a particle system, and arrived at a method that applies nonequilibrium relaxation (NER) [1], which has been established for determining the phase-transition point of a spin system. The method was devised to determine the equilibrium melting curve of the modified Lennard-Jones (mLJ) system [2]. The method, reported first, was further improved, and could predict the location of not only the solid–liquid but also the liquid–gas and solid–gas phase boundaries of the mLJ system. This improved method was then mentioned. Finally, we report our recent important findings, regarding orientational order in liquid SnI_4 and GeI_4, achieved by using the system B of the facility.

A new way for determining a melting curve

To locate the transition point for a particle system, an orthodox way to employ is to compare the free energies of the relevant phases, which are usually evaluated using a thermodynamic integration. The evaluation of free energy consists of multiple stages of computation, and the orthodox way requires much processing cost to identify a single transition point of a particle system. The NER method [1] has been used also as an effective tool with which to locate the equilibrium phase transition point of a system from an equilibrating stage, which is usually discarded from the calculation of equilibrium quantities. It is therefore worth trying to apply the NER method to a particle system to address the high cost of processing.

We first tried to determine a melting curve. To this end, we employed the mLJ system because the accurate melting points are known as a function of pressure [2]. The key for the NER to work properly in determining a transition point is a choice of an appropriate initial state. We prepared a combined system consisting of a solid system (13500 particles were located on the face-centered cubic lattice points in a cube with the density $\rho = 1.0$) and a liquid system (14196 particles in a rectangular parallelepiped brought into a well disordered state at the temperature $T = 10$, a sufficiently high temperature for the mLJ system) as a trial initial state, from which the isothermal–isobaric time evolution was traced conducting a molecular dynamics (MD) simulation to measure ρ of the whole system as a function of time. If a chosen T is higher (lower) than the transition temperature under the pressure p, the whole system would become a liquid (solid) state so that ρ would decrease (increase). The melting point could thus be found with a desired accuracy by choosing such T as ρ hardly relaxes.

The result was satisfactory [3]; the NER method could reproduce the previous melting points [2]. However, a slight discrepancy is recognizable in a low-pressure region ($p < 1$). This discrepancy was removed by taking a slightly lower initial $\rho = 0.95$ for the solid density. (The setting of the initial $\rho = 1.0$ was rather suitable for investigation of the melting points in a high-pressure region.)

Improvement and extension of the method

The important ingredient of the method is preparation of a coexistence state. In the NER method [3], the coexistence state was prepared by "mechanically" combining equilibrium solid and liquid states under isothermal and isobaric conditions. Extreme care must be taken when joining the two states so as not to cause instability at the interface. This is because the equal pressure of the states to be combined is not necessarily a sufficient condition for the states to come to equilibrium in a rectangular parallelepiped simulation box.

This situation was improved in such a way that a solid–liquid coexistence state was generated by elongating the box containing a solid phase in one direction under isothermal conditions. The system has no free surface because of periodic boundary conditions imposed in all directions. The deformation then allows to produce a solid–liquid interface perpendicular to the direction of elongation in the elongated simulation box. Under the isobaric conditions, the interface moves in the simulation box, which is to be completely filled with a solid or a liquid state depending on the temperature. The melting temperature was defined as the midpoint between the two temperatures. The width between the midpoint and the highest (lowest) temperature then gave the probable error associated with the melting temperature thus defined. The melting points thus obtained are plotted in Fig. 1. The result coincides with the one [2] within statistical errors. The method was further extended so as to be assisted by the Clausius–Clapeyron relationship, thereby predicting the nearby melting points. The present method could be adopted to predict also the liquid–gas and solid–gas phase boundaries of the mLJ system. In particular, the triple point was identified to be $T_{\rm t} = 0.611(4)$ (which improved the result [2] by an order of magnitude) and $p_{\rm t} = 0.0013(1)$. Together with the critical point examined based on the renormalization-group approach [4], the phase diagram of the mLJ system is said to be established.

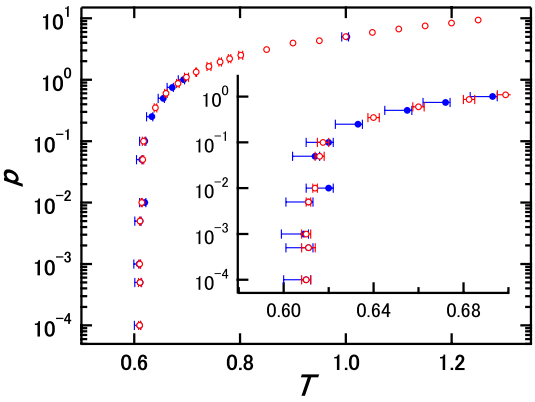

Figure 1: The melting points established from the free-energy balance [2] are designated by blue symbols whereas those obtained through the present method for a 5000-particle mLJ system are designated by red symbols.

Liquid structure of GeI_4 and SnI_4

The structure of these molecular liquids at ambient pressure was closely examined using the reverse Monte Carlo (RMC) method. Liquid structures obtained through the MD simulation [5] as input. We first developed an expedient method [6] for estimating density of liquids from the structure factor as the density is also an important input to the RMC analysis. A possible pressure-induced network formation consisting of molecules with the vertex-to-face orientation was suggested [7].

References

[1] N. Ito: Physica A, **192** (1993) 604; *ibid.* **196** (1993) 591.
[2] Y. Asano and K. Fuchizaki: J. Chem. Phys. **137** (2012) 174502.
[3] Y. Asano and K. Fuchizaki: J. Phys. Soc. Jpn. **86** (2017) 025001.
[4] K. Okamoto and K. Fuchizaki: J. Phys. Soc. Jpn. **86** (2017) 034003.
[5] K. Fuchizaki and Y. Asano: J. Phys. Soc. Jpn. **84** (2015) 064601.
[6] T. Sakagami, K. Fuchizaki, and K. Ohara: J. Phys.: Condens. Matter. **28** (2016) 395101.
[7] T. Sakagami and K. Fuchizaki: J. Phys.: Condens. Matter. **29** (2017) 145102.

A construction of the Markov state model of protein folding using the manifold theory

Takashi YOSHIDOME

Department of Applied Physics,

Tohoku University, 6-6-05, Aoba, Aramaki, Aoba-ku, Sendai 980-8579

Recently, Markov state model (MSM) [1] is a promising model for analyzing long-time behaviors of proteins, which are difficult to investigate using the conventional molecular dynamics (MD) simulations. Its construction consists of the following three steps:

(i) Classification the protein conformations into the major states obtained using MDs,

(ii) Calculation the transition matrix between the states, and,

(ii) Computation physical quantities using the master equation.

Although constructions of a MSM for proteins has been performed for a decade, quantitative performance of the physical quantities was poor at long-time scales [1]. It was considered that an origin of the poor performance is failure of the classification into states (step (i)).

In the present stud, we proposed to use the manifold learning for the classification. To demonstrate its usefulness, we constructed a MSM using MD data to investigate the folding of a protein. First, we performed MD simulations of proteins. Then classifications of the data were conducted using our custom-made software “EMMA” [2] in which the diffusion map method based on the manifold learning was implemented. All computations were performed using the system B (F4cpu, L4cpu, L36cpu, and L2fat) at the Supercomputer Center in the Institute for Solid State Physics at the University of Tokyo. Finally, we constructed a MSM of a protein using the states obtained with the manifold learning.

By comparing a physical quantity obtained using the MSM with that obtained by the MD, we found that the MSM was a high quantitative performance even at long time scales. This result indicates that MSM using manifold leaning is effective.

References

[1] V.S. Pande, K. Beauchamp, and G.R. Bowman, Methods, **99**, (2010).

[2] T. Yoshidome, T. Oroguchi, M. Nakasako, and M. Ikeguchi, Phys. Rev. E, **92**, 032710 (2015).

Utilizing AVX2 instructions for molecular dynamics simulation of Lennard-Jones potential

Hiroshi Watanabe
Institute for Solid State Physics, University of Tokyo
Kashiwa-no-ha, Kashiwa, Chiba 277-8581

Since early 2000s, the increase in the clock rates of computers has stopped. The development of the performance has mainly been achieved by increasing the number of processing cores and the width of SIMD (single instruction, multiple data). The bit length of register is 256 in AVX (Advanced Vector Extensions) and is 512 in AVX-512 instruction sets. It is difficult to generate efficient codes for such architecture automatically, and therefore, a programmer has to write them explicitly. In this report, we describe an algorithm to utilize AVX2 instruction for calculating force of Lennard-Jones potential.

The AVX2 instruction set uses registers with 256-bit width. Each register can contain four 64-bit double-precision floating point numbers like a vector and floating operations can be performed for all elements of the vector simultaneously. The basic idea of utilizing 256-bit registers is as follows, i) unfold a loop by four times, ii) calculate forces of four atom pairs, and iii) store the results. However, a naive implementation of the above procedure is highly inefficient since it involves memory access many times which becomes a performance bottleneck. To address this problem, we change data structure. Figure 1 illustrates how the data are stored in registers. (a) The crucial idea is to prepare four dimensional array for three dimensional system. While we use only three-quarters of memory, we can load three components of coordinate to a register simultaneously. (b) We calculate a relative coordinates by a single subtraction. (c) After calculating relative coordinates of four pairs, we transpose a data. Then taking sum of squares gives for squared distances of for pairs. Then we can calculate forces of four pairs simultaneously.

This optimization gives us 2.23 times speed-up compared to a code without the SIMD optimization. This result shows that the data structure is a key to utilize SIMD instructions effectively. A sample code is available online [1].

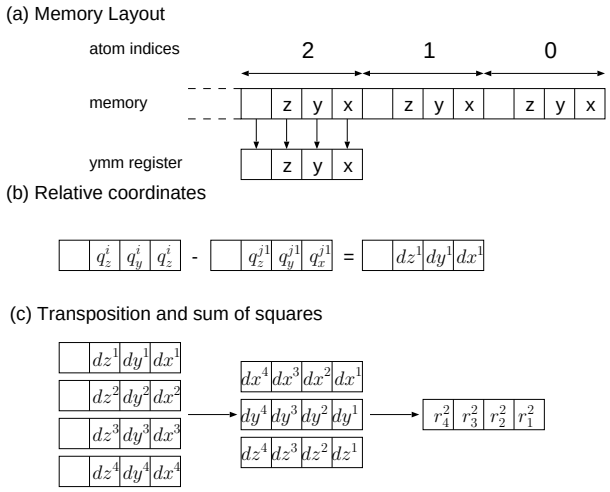

Figure 1: Data layout in registers.

References

[1] `https://github.com/kaityo256/lj_simdstep`

Dynamical ordering of amyloid fibrils by molecular dynamics simulations

Satoru G. Itoh and Hisashi Okumura

Research Center for Computational Science,

Institute for Molecular Science, Okazaki, Aichi 444-8585

The amyloid-β peptide (Aβ) is composed of 39–43 amino-acid residues. Aβ tends to form amyloid fibrils, which are associated with the Alzheimer's disease. To understand amyloid fibril formation, we have performed molecular dynamics (MD) simulations of amyloid fibrils [1, 2, 3].

It was reported that formation of amyloids is accelerated at a hydrophilic/hydrophobic interface such as an air/water interface or an interface between sugar-head groups and hydrocarbon chains of glycolipids. It is necessary to clarify the amyloid formation process at the interface in order to find a remedy for Alzheimer's disease.

To investigate amyloid formation process at the hydrophilic/hydrophobic interface, we performed Hamiltonian replica-permutation molecular dynamics (RPMD) simulations for a full-length Aβ molecule, Aβ40, in the presence of the interface, as shown in Fig. Hamiltonian

As a snapshot shown in Fig. 1, residues in the β1 and β2 regions existed at the interface. Furthermore, these residues tended to form helix structures. These results agree well with experiments.

We will analyze the Aβ conformation at the interface and that in bulk water in more details. We will also discuss effects of the interface on the amyloid formation.

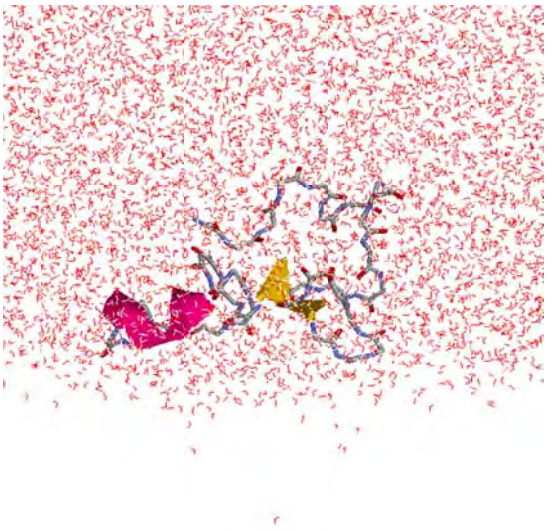

Fig. 1: Snapshot obtained by a Hamiltonian RPMD simulation.

References

[1] H. Okumura and S. G. Itoh: J. Am. Chem. Soc. **136** (2014) 10549.

[2] S. G. Itoh and H. Okumura: J. Phys. Chem. B **118** (2014) 11428.

[3] S. G. Itoh and H. Okumura: J. Comput. Chem. **120** (2016) 6555.

Quantum Monte Carlo study of spin liquids

Yoshi KAMIYA

Condensed Matter Theory Laboratory,

RIKEN, Wako, Saitama 315-0115

As in our proposal, we initially ran world-line Quantum Monte Carlo (QMC) simulations for a toric code in a staggered magnetic field, which corresponds to the anisotropic limit of the honeycomb-lattice Kitaev model in a [001] magnetic field. We obtained the temperature and field dependence of several thermodynamic quantities, such as magnetization. However, later on, we realized that the model can be mapped onto a free fermion model and thus can be solved analytically [1], and we ceased to continue our numerical analysis on this model.

We changed our subject and decided to study an interacting Majorana fermion system to describe Majorana q-bits on the surface of a strong topological insulator that is proximate to an ordinary superconductor with an Abrikosov vortex lattice induced by an external magnetic field; each Majorana degree of freedom corresponds to a zero-mode bound to a vortex [2]. The non-interacting limit at the so-called neutrality point belongs to topological class BDI, in which Majorana fermion bilinear terms are prohibited due to an extra symmetry [3], resulting in a minimal Hamiltonian that comprises only quartic terms. We put such a system on the square lattice (instead of more normal triangular lattices, by assuming for instance an array of impurities), as originally proposed by Chiu and coworkers [4]. By mapping the fermionic system to a quantum spin system using the Jordan-Wigner transformation, we apply the QMC simulations to study the phase diagram as a function of the temperature and a lattice distortion parameter. According to our preliminary investigation, the system without the lattice distortion undergoes a finite-temperature phase transition that induces a sort of density wave order breaking the translational symmetry spontaneously. We believe that this interesting observation deserves an extra investigation and the results will be reported elsewhere.

References

[1] Y. Kamiya, J. Yoshitake, Y. Kato, J. Nasu, and Y. Motome: in preparation.

[2] L. Fu and C. L. Kane: Phys. Rev. Lett. **100** (2008) 096407.

[3] J. C. Y. Teo and C. L. Kane: Phys. Rev. B **82** (2010) 115120.

[4] C-.K. Chiu, D. I. Pikulin, and M. Franz: Phys. Rev. B **91** (2015) 165402.

[5] Y. Kamiya and G.-W. Chern: in preparation.

Stochastic Optimization Approach to Phase Transitions and Structure Search

Synge Todo
Department of Physics, University of Tokyo, Tokyo 113-0033, Japan
Institute for Solid State Physics, University of Tokyo, Kashiwa, 277-8581, Japan

In this project, we developed several new and powerful techniques based on stochastic optimization and other methods for investigating various exotic critical phenomena in strongly correlated systems and determining crystal structure of materials.

Quantum critical phenomena of systems with strong spatial and temporal anisotropy: we have developed a method for evaluating the dynamical exponent z at the quantum critical point by combining the path-integral quantum Monte Carlo method and the stochastic optimization method [1]. By using our novel method, the coupling constant as well as the aspect ratio between the real-space and imaginary-time system sizes are tuned during the simulation, and the critical point, critical amplitude, spin-wave velocity, etc, can be automatically evaluated in a very accurate way. We extended our method to the one-dimensional random Heisenberg model and demonstrated that we can clearly distinguish the random singlet phase from the quantum Griffith phase as the distribution of strength of random bonds is altered.

Spion linear dispersion relation at the deconfined quantum critical point: we performed a large scale simulation of the two dimensional J-Q model and elucidated a linear dispersion relation of spinon by using the path-integral quantum Monte Carlo and generalized moment method [2]. We found a non-trivial degeneracy in singlet and triplet excitations, which suggests the emergence of a higher symmetry than that of the Hamiltonian.

Strange correlator for two-dimensional SPT phase: we developed a new method to calculate the *strange correlator*, which is proposed recently as an order parameter that identifies symmetry protected topological (SPT) phase in one and two dimensional quantum lattice models. It was confirmed that in the $S = 1$ bond-alternating antiferromagnetic Heisenberg chain we can distinguish the Haldane phase from the trivial dimer phase clearly by using the strange correlator. Our method can be applied straightforwardly to the SPT phase in two dimensions.

Critical decay exponent of long-range interacting spin models: using the $O(N)$ cluster algorithm [3], we studied precisely the critical exponents and critical amplitudes of the long-range interacting Ising model on the square lattice. In addition, we have introduced a universal method, the *combined Binder ratio*, by which the leading corrections to scaling can be automatically removed even near the critical decay exponent, and established the phase diagram in which the critical amplitude changes as the effective dimension of the system does according to the changes of decay exponent of the interaction [4]. We also performed a preliminary simulation on the effective dimension at the criticality in the system with spatially correlated random external fields.

Combined optimization method and application to determination of crystal structure: we developed a new method, the combined optimization method (COM), for simultaneously optimizing two cost functions that share the same global minimum point. It was demonstrated that one can reach the global minimum of the sum of multi-valley functions by using the COM with much higher probability than the conventional method, such as the simulated annealing. We have applied our method for the problem of crystal structure determination of the materials. As for the two different cost functions, we introduced the total energy calculated by the simulation (classical force field or the first-principles calculation) and the *crystallinity* that is defined as a difference between the experimental and the calculated X-ray diffraction patterns. We confirmed that we the correct crystal structures can be predicted with much higher probability than the optimization the calculated total energy or the crystallinity alone.

The programs used in the present project have been developed based on the following open-source libraries: ALPS [5, 6], ALPS/looper [7], BCL [8], and worms [9].

References

[1] S. Yasuda, H. Suwa, and S. Todo: Phys. Rev. B **92** (2015) 104411.

[2] H. Suwa and S. Todo: Phys. Rev. Lett. **115** (2015) 080601.

[3] K. Fukui and S. Todo: J. Comp. Phys. **228** (2009) 2629.

[4] T. Horita, H. Suwa, and S. Todo: Phys. Rev. E **95** (2017) 012143.

[5] B. Bauer, L. D. Carr, H. G. Evertz, A. Feiguin, J. Freire, S. Fuchs, L. Gamper, J. Gukelberger, E. Gull, S. Guertler, A. Hehn, R. Igarashi, S. V. Isakov, D. Koop, P. N. Ma, P. Mates, H. Matsuo, O. Parcollet, G. Pawlowski, J. D. Picon, L. Pollet, E. Santos, V. W. Scarola, U. Schollwöck, C. Silva, B. Surer, S. Todo, S. Trebst, M. Troyer, M. L. Wall, P. Werner, and S. Wessel: J. Stat. Mech.: Theo. Exp. (2011) P05001.

[6] http://alps.comp-phys.org/.

[7] http://wistaria.comp-phys.org/alps-looper/.

[8] http://github.com/cmsi/bcl.

[9] http://github.com/wistaria/worms.

Sixteen-beam pinhole topographs.

Kouhei OKITSU
Institute of Engineering Innovation, University of Tokyo
2-11-16 Yayoi, Bunkyo-ku, Tokyo 113-8656

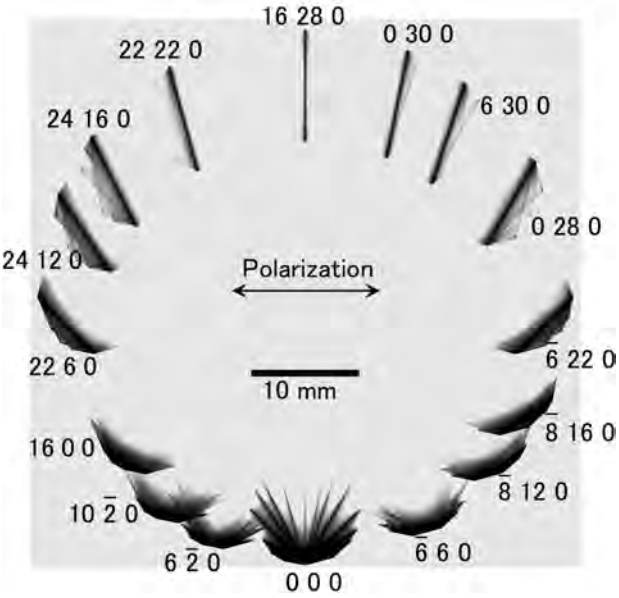

Figure 1: Computer-simulated sixteen-beam pinhole topograph images.

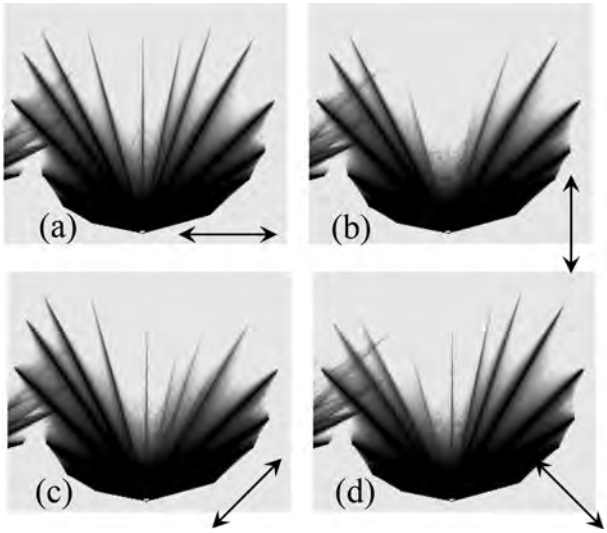

Figure 2: Enlargements of 0 0 0-forward-diffracted images for incident X-rays with (a) vertial, (b) horizontal, (c) +45°-inclined and −45° polarizations.

The present author has derived n-beam Takagi-Taupin equation that describes X-ray wavefields when n X-ray beams ($n \in \{3, 4, 5, 6, 8, 12\}$) are simultaneously strong [1, 2] and has verified it by comparing experimentally obtained pinhole topograph images and computer-simulated ones obtained by numerically solving the equation. Excellent agreements were found between them [3, 4, 5]. This equation can be applied for circular (coplanar) n-beam cases in which n reciprocal lattice nodes are on a circle in reciprocal space.

However, the author found sixteen-, eighteen- and twenty-four-beam circular cases. In this report, the author describes computer-simulated results of a sixteen-beam case.

Figure 1 shows a computer-simulated sixteen-beam pinhole topograph. Horizontally polarized X-rays [a photon energy of 50 keV (wavelength of 0.248 Å)] whose dimension is infinitesimally small (less than 100 μm) were assumed to be incident on a perfect parallel-plate silicon crystal with a thickness of 4.8 mm. An imaging plate (IP) was assumed to be placed 18 mm behind the crystal such that the IP is parallel to the surface of the crystal.

Figure 2 shows 0 0 0-forward-diffracted images with assumptions of the incident X-rays of (a) horizontal (b) vertical (c) +45°-inclined and (d) −45°-inclined linear polarizations. Strong dependence of topograph images

on the polarization state of the incident X-rays is recognized.

It has been found that the Takagi-Taupin n-beam equation the present author has derived and solved [1-5] can be applicable for 'circular n-beam cases' of $n \in \{3, 4, 5, 6, 8, 12, 16, 18, 24\}$.

References

[1] K. Okitsu: Acta Cryst A **59** (2003) 235-244.

[2] K. Okitsu, Y. Yoda, Y. Imai, Y. Ueji, Y. Urano and X.-W. Zhang: Acta Cryst A **62** (2006) 237-247.

[3] K. Okitsu, Y. Imai, Y. Ueji and Y. Yoda: Acta Cryst A **59** (2003) 311-316.

[4] K. Okitsu, Y. Yoda, Y. Imai and Y. Ueji: Acta Cryst A **67** (2011) 557-558.

[5] K. Okitsu, Y. Imai and Y. Yoda: InTech *Recent Advances in Crystallography* (2012) 67-86 [Invited].

Molecular Dynamics Simulation Study of Morphology Control Mechanism of TiO_2 Rutile Crystal by Hydroxy Acid

Hiroki NADA

National Institute of Advanced Industrial Science and Technology (AIST),

16-1 Onogawa, Tsukuba, Ibaraki 305-8569

A molecular dynamics simulation was conducted to elucidate the conformation and dynamics of a glycolate ion at the surface of a TiO_2 rutile crystal using massive parallel computer simulations [1]. The simulation was performed for both the {001} and {110} planes of the crystal.

The simulation suggested that the binding of the glycolate ion at the surface is more stable for the {110} system than for the {001} system. The simulation also suggested that the stable conformation of the glycolate ion near the surface was different for the two planes: the COO^- group of the ion was preferentially oriented toward the liquid water in the {001} system, whereas it was oriented toward the surface in the {110} system (Fig. 1). This anisotropy in the stable conformation of the glycolate ion was attributed not only to a difference in the interaction of the glycolate ion with the surface but also to a difference in the layered structure of water on the surface.

Suppose that the binding of the glycolate ion to the rutile surface hinders the growth there. Then the present simulation agrees with the fact that the growth rate at the {001} plane becomes much larger than that at the {110} plane in the presence of glycolic acid [2]. The simulation also suggests that water is a key for elucidating the anisotropy in the conformation and dynamics of the glycolate ion and, hence, the growth shape of real rutile crystals in the presence of glycolic acid.

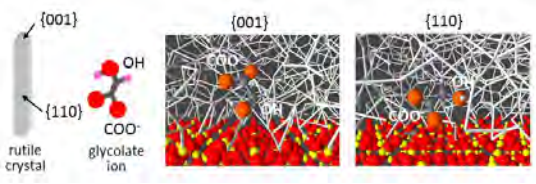

Fig. 1: Snapshots of the glycolate ion, which was stably located near the rutile surface. The white cylinders represent hydrogen bonds between water molecules. Yellow and red spheres represent Ti and O atoms, respectively.

References

[1] H. Nada, M. Kobayashi, and M. Kakihana: J. Phys. Chem. C **120** (2016) 6502.

[2] M. Kobayashi, H. Kato, and M. Kakihana: Nanomater. Nanotechnol. **3** (2013) 1.

Molecular Dynamics Simulation of Ferroelectrics Using a Shell Model II

T. Hashimoto

Research Center for Computational Design of Advanced Functional Materials (CD-FMat), National Institute of Advanced Industrial Science and Technology (AIST), Tsukuba Central 2, 1-1-1 Umezono, Tsukuba, Ibaraki 305-8568, Japan

$BaTiO_3$ is an ABO_3 type perovskite whose solid solution with other A site atoms could be a potential candidate for Pb free piezoelectric materials. $BaTiO_3$ undergoes phase transitions among, listing from high temperature to low temperature, cubic (C), tetragonal (T), orthorhombic (O), and rhombohedral (R) phases.

In this study, we performed molecular dynamics (MD) simulations using the shell model[1, 2]. We used a MD program developed by us. We used the smooth particle mesh Ewald method for computing the Coulomb interactions. We used a MD cell made up with 12×12×12 unit cells. The cutoff length for the nonbonded interactions were 10.0 Å. We used the adiabatic method in which the shells are given a small mass. One MD step (Δt) was 0.1 fs. The Nosé-Hoover chain method and the Parrinello-Rahman method were used for generating constant temperature and constant pressure (NPT) ensembles. The externally applied pressure was set to 0 Pa.

The piezoelectric constants were calculated by[3] $d_{kij} = \frac{1}{k_B T} \langle \Delta M_k \Delta \eta_{ij} \rangle$. Here, $\eta_{ij} = \frac{1}{2}\left(H_0^{t-1} G H_0^{-1} - 1\right)$ is the strain tensor, where $G = H^t H$ with $H = \{\mathbf{a}, \mathbf{b}, \mathbf{c}\}$ representing the MD cell, and H_0 is the reference state of H. $\mathbf{M}$ is the total dipole moment of the MD cell. ΔX represents $X - \langle X \rangle$, where X is M_k or η_{ij}.

The temperature dependences of piezoelectric constants were similar to those obtained by the Landau-Ginzburg-Devonshire (LGD) theory[4]. The shear and some of the longitudinal piezoelectric constants changed dramatically depending on the temperature. This arises from the temperature dependence of the dipole moment and the strain fluctuations. We also calculated the temperature dependences of the longitudinal piezoelectric surface d_{33}^* of $BaTiO_3$. Due to the large temperature dependence of the piezoelectric constants, the d_{33}^* surface changes significantly with temperatures as observed in the $KNbO_3$ study[5]. The detailed results will be published elsewhere.

References

[1] M. Sepliarsky, S. R. Phillpot, D. Wolf, M. G. Stachiotti, and R. L. Migoni, Appl. Phys. Lett. **76** (2000) 3986.

[2] T. Hashimoto and H. Moriwake, Mol. Simul. **41** (2015) 1074.

[3] A. García and D. Vanderbilt, Appl. Phys. Lett. **72** (1998) 2981.

[4] M. Budimir, D. Damjanovic, and N. Setter, J. Appl. Phys. **94** (2003) 6753.

[5] T. Hashimoto and H. Moriwake, J. Phys. Soc. Jpn. **85** (2016) 034702.

Development of tensor network algorithms

Kenji HARADA
Graduate School of Informatics, Kyoto University, Kyoto 606-8501, Japan

The real-space renormalization is an important concept to study the macroscopic behavior of classical and quantum systems. Although some schemes were proposed (Ex. Migdal-Kadanoff approximation), it is hard to improve the accuracy systematically. Recently, the new type of real-space renormalization scheme appears. It is based on a singular value decomposition (SVD). In detail, it is a real-space renormalization on a tensor network. The tensor network is a mathematical framework to describe the partition function of many-body systems. For example, by a path-integral representation of the ground state in a quantum system can be regarded as a tensor network. Thus, the new real-space renormalization scheme on a tensor network has a large potential to study quantum and classical many-body problems.

Levin and Nave [1] proposed the first real-space renormalization scheme on a tensor network which is called a tensor renormalization group (TRG). SVD controls the precision in the coarse-graining step of TRG. In detail, large singular values only remain. It means that the large correlation (entanglement) part between tensors is conserved. However, Levin and Nave's scheme goes to a special structure in a coarse-grained tensor at final. It may not be an expected behavior because the structure of a coarse-grained tensor at a critical point does not have the structure of a coarse-grained tensor of TRG.

To resolve this issue of TRG, Gu and Wen [2] proposed the removing a short-scale entanglement in a coarse-grained step. Evenbly and Vidal [3] improved this idea, and they introduced a new scheme which is called a tensor network renormalization (TNR). In particular, TNR numerically shows the correct structure of a tensor even at a critical point. In both algorithms, the treatment of entanglement is a key. SVD can select the important part of entanglement between two tensors. In this study, I propose the splitting of entanglement on the edge of a tensor network. The new operation can introduce flexibility in a tensor network algorithm. For example, we can do a many-body decomposition of a tensor. We can introduce a removing of a short-scale entanglement in a high-order tensor renormalization group scheme (HOTRG). We checked the structure of a coarse-grained tensor of a new HOTRG scheme numerically. It has the same structure of a coarse-grained tensor in TNR. This new operation has a potential to develop a new tensor network algorithm [4].

References

[1] M. Levin and C. Nave, Phys. Rev. Lett. **99**, 120601 (2007).

[2] Z. C. Gu and X.-G. Wen, Phys. Rev. B **80**, 155131 (2009).

[3] G. Evenbly and G. Vidal, Phys. Rev. Lett. **115**, 180405 (2015).

[4] K. Harada, in preparation.

Development of Parallelized Tensor-Network Library

Satoshi MORITA

Institute for Solid State Physics,

The University of Tokyo, Kashiwa-no-ha, Kashiwa, Chiba 277-8581

Tensor network method is one of numerical methods for quantum and classical many-body systems. To achieve highly accurate simulation for interesting problems, one needs to increase bond dimensions of tensors. However, the computational cost and the amount of memory rapidly increase with bond dimension. Therefore, we are developing parallelized library for tensor calculations [1]. Common operations appearing various tensor network methods are implemented using C++ language with hybrid parallelization (MPI + OpenMP). In our library, a tensor is stored as a matrix on distributed memory and main operations in tensor network methods, “contraction” and “decomposition”, are done by calling routines in ScaLAPACK [2]. We adopted application programming interface similar to NumPy, which is the fundamental Python package with multidimensional array. One can easily translate a Python test code into a parallel C++ code with our library.

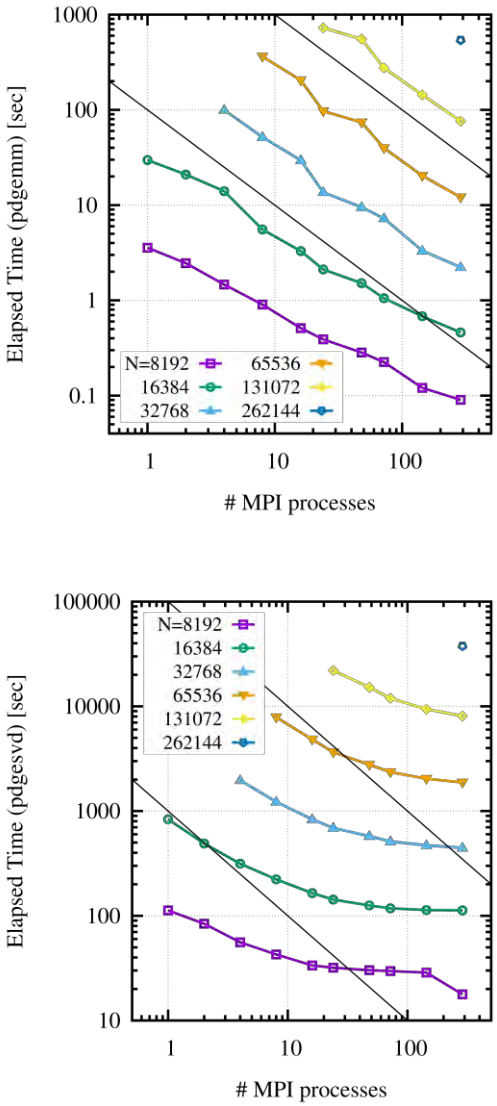

Fig. 1: Benchmark results of matrix-matrix product (top) and singular value decomposition (bottom) on the ISSP System B.

References

[1] https://github.com/smorita/mptensor

[2] http://www.netlib.org/scalapack/

Numerical study of dynamics in Ising spin models with long-range interactions

Yusuke TOMITA
Shibaura Institute of Technology
307 Fukasaku, Minuma-ku, Saitama-City, Saitama 337-8570

Relaxational processes in ordered phases of one-dimensional (1D) Ising models with long-range interactions are investigated by $O(N)$ Monte Carlo simulations [1]. Three types of spin model, the pure ferromagnetic, the diluted ferromagnetic, and the spin glass models, are examined. Through numerical analyses of the 1D Ising model, we examined results derived from the droplet theory[2].

The Hamiltonian of the 1D Ising model with long-range interactions is given by

$$\mathcal{H} = -\sum_{i<j} \frac{J_{ij}}{r_{ij}^{\sigma}} S_i S_j,$$

where σ is the tuning parameter of long-range interaction. Only the nearest neighbor interactions are relevant in the limit of $\sigma \to \infty$, while all the interactions become equivalent when $\sigma = 0$. In the case of the diluted ferromagnetic model ($J_{ij} \geq 0$), the universality class depends on σ in the range of $3/2 < \sigma < 2$. In the smaller-σ region ($\sigma \leq 3/2$), the diluted systems belong to the mean-field model. The Kosterlitz-Thouless transition appears at a finite temperature at the critical point ($\sigma = 2$).

Autocorrelation functions obtained by Monte Carlo simulation exhibited the power law decay as the droplet theory declares. The autocorrelations as functions of a wave number of k and time t, $C(k;t)$, are fitted by

$$C(k;t) = C_0 \frac{\exp[-t/\tau_2(k)]}{[1 + t/\tau_1(k)]^{x(k)}} + C_\infty.$$

The parameter $\tau_1(k)$ provides an indication of the waiting time for starting the power-law decay, and the thermal relaxation time $\tau_2(k)$ indicates the relaxation time to reach the thermally equilibrium value C_∞. Numerical data and fitting results at $\sigma = 0.8$ are shown in Fig. 1.

A marked feature of the autocorrelation functions of the diluted system is that they are placed with roughly equal intervals; the functions are approximately described by

$$C(k;t) \sim k^{-y} C(k = 2\pi/L; t),$$

where y is a constant. This means excited droplets have a fractal-like structure. The fractal-like features does not mean the system is in the Kosterlitz-Thouless phase but the correlation length is smaller than the percolation correlation-length on the diluted lattice. This pseudocritical feature is also observed in disordered ferroelectrics[3].

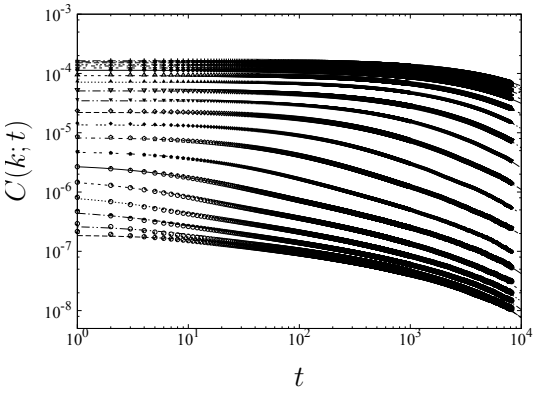

Figure 1: Autocorrelation functions of the diluted ferromagnetic model at $\sigma = 0.8$.

References

[1] K. Fukui and S. Todo, J. Comput. Phys. **228**, 2629 (2009).

[2] Y. Tomita, Phys. Rev. E **94**, 062142 (2016).

[3] A. Koreeda, *et al.*, Phys. Rev. Lett. **109**, 197601 (2012).

Numerical study of random Dirac/Weyl electron systems

TOMI OHTSUKI[1]
TOHRU KAWARABAYASHI[2]
KEITH SLEVIN[3]
KOJI KOBAYASHI[4]
1) Dept. Phys., Sophia University, Chiyoda-ku, Tokyo 102-8554, Japan
2) Dept. Phys., Toho University, Miyama 2-2-1, Funabashi 274-8510, Japan
3) Dept. Phys., Osaka University, Toyonaka, Osaka 560-0043, Japan
4) IMR, Tohoku University, Sendai 980-8577, Japan

Recent discoveries of two-dimensional quantum spin Hall states and three-dimensional (3D) topological insulators (TIs) have inspired extensive research for these novel topological materials. Here we have studied disordered topological insulators as well as Weyl semimetals (WSM). We stacked N layers of two dimensional Chern insulators, and performed comparative studies of TI and WSM, which subtly depends on N, but robust against certain amount of disorder[1].

Weyl semimetal belongs to the unitary class. We have studied the 3D and 4D unitary classes Anderson transition, and obtained the critical exponents with high precision[2].

Topological insulator is realized not only in fermionic systems, but also in bosonic systems. We have shown that bosonic topological insulators are robust against disorder by analysing quantum magnon Hall effect [3].

In addition to the above works, we have demonstrated that the image recognition based on multilayer convolutional neural network (so called deep learning) works well for drawing the phase diagram of disordered topological insulators and Weyl semimetals [4,5]. See Fig. 1.

References

1.Y. Yoshimura, W. Onishi, K. Kobayashi, T. Ohtsuki, K.-I. Imura: Physical Review B **94**, 235414 (2016)
2. K. Slevin, T. Ohtsuki: Journal of the Physical Society of Japan **85**, 104712 (2016)
3. B. Xu, T. Ohtsuki, R. Shindou: Physical Reivew B **94**, 220403(R) (2016)
4. T. Ohtsuki, T. Ohtsuki: Journal of the Physical Society of Japan **85**, 123706 (2016)
5. T. Ohtsuki, T. Ohtsuki: Journal of the Physical Society of Japan **86**, 044708 (2017)
6. S. Liu, T. Ohtsuki, R. Shindou: Physical Review Letters **116**, 066401 (2016)

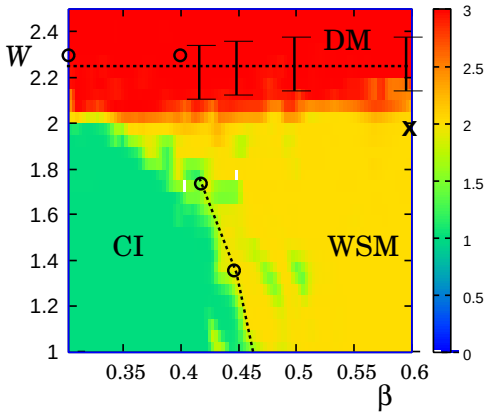

Figure 1: Color map of $P_{\mathrm{CI}}, P_{\mathrm{WSM}}$, and P_{DM}, which are probabilities that the eigenfunctions are judged to belong to the Chern insulator, Weyl semimetal and diffusive metal phases, respectively. The intensity $1\times P_{\mathrm{CI}}+2\times P_{\mathrm{WSM}}+3\times P_{\mathrm{DM}}$ is plotted. Bars with errors and circles ($\circ$) indicate the transfer matrix estimate of the critical points[6], and dotted lines are a guide to the eye. The cross ($\times$) at $(\beta, W)\approx(0.6, 2.0)$ indicates the WSM/DM phase boundary estimated by the scaling of density of states. Taken from [5].

Simulation studies of (i) the significant difference in the dynamics between strong and fragile liquids and (ii) shear thinning in glassy liquids

Akira Furukawa
Institute of Industrial Science, University of Tokyo
Komaba 4-6-1, Meguro-ku, Tokyo 153-8505

(i) We revealed a significant difference in the dynamics between these two types of glass formers through molecular dynamics simulations [1]: In strong glass formers, the relaxation dynamics of density fluctuations is nondiffusive, whereas in fragile glass formers it exhibits diffusive behavior. We demonstrate that this distinction is a direct consequence of the fundamental difference in the underlying elementary relaxation process between these two dynamical classes of glass formers. For fragile glass formers, a density-exchange process proceeds the density relaxation, which takes place locally at the particle level in normal states but is increasingly cooperative and nonlocal as the temperature is lowered in supercooled states. On the other hand, in strong glass formers, such an exchange process is not necessary for density relaxation due to the presence of other local relaxation channels. Our finding provides a novel insight into Angell's classification scheme from a hydrodynamic perspective.

(ii) We proposed a simple mechanism for describing the onset of shear thinning in a high-density glassy liquid: In a shear flow, along the compression axis, the overlap between neighboring particles is more enhanced than that at equilibrium, meaning that the effective size is reduced along this axis. On the other hand, along the extension axis perpendicular to the compression axis, the average structural configurations are stretched, but it does not indicate the expansion of the effective size itself. This asymmetric shear flow effect for particles results in a small reduction of the effective density. Because, in glass-forming liquids, the structural relaxation time strongly depends on the density , even a very small reduction of the effective density should lead to a significant decrease of the relaxation time under shear flow. We predict that the crossover shear rate from Newtonian to non-Newtonian flow behaviors is given by $\dot{\gamma}_{\rm c} = [\rho(\partial\tau_\alpha/\partial\rho)]^{-1}$, which can be much smaller than $1/\tau_\alpha$ near the glass transition point. It is shown that this prediction is consistent with the results of molecular dynamics simulations.

These simulations (i) and (ii) were partially performed at the ISSP Supercomputer Center. The programs are parallelized with a combination of OpenMP and MPI techniques.

References

[1] A. Furukawa and H. Tanaka, Phys. Rev. E, **94**, 052607 (2016).

[2] A. Furukawa, Phys. Rev. E, **95**, 012613 (2017).

Heat Transfer Characteristics of Condensate Film Flow along Vertical Plates with Microscopic Grooves

Takahiro ADACHI
Department of Mechanical Engineering, Akita University
Tegata-Gakuen 1-1, Akita, Akita 010-8502

The characteristics of thin, falling liquid films due to condensation along a vertical plate have been of interest to engineers, for example, in plate-type absorber, plate-type condenser and so on. In order to enhance the heat transfer, fluted parts along the streamwise direction have been established on the plate. This is because the liquid film spreads as thinly as possible over the plate surface since strong surface tension aids in the removal of film from the top to bottom of the fluted parts, thereby producing a very thin liquid film. This is called a drainage effect[1].

On the other hand, little research was done on the film flow along a plate with a grooved part setting perpendicular to the streamwise direction due to some mathematical difficulties. Therefore, our objective in this study is to clarify how the grooved part affects the flow patterns and heat transfer.

We consider a liquid film flow along a plate with a rectangular groove setting perpendicular to the stream-wise direction on its surface. Figure 1 shows a geometry of the problem and the coordinate system. The x-axis is taken to be parallel to the vertical direction and the y-axis to be perpendicular to it. Nondimensional parameters to characterize the plate configuration, height h of the groove, width of the groove w_b, inlet length w_i and outlet length w_o are, using δ_0^* at the inlet as a characteristic length, defined as

$$h = \frac{h^*}{\delta_0^*}, \quad w_b = \frac{w_b^*}{\delta_0^*}, \quad w_i = \frac{w_i}{\delta_0^*}, \quad w_o = \frac{w_o}{\delta_0^*} \quad (1)$$

where we represent physical quantities with their dimensions by attaching a superscript $*$ to them, and the total plate length is $L = w_i + w_b + w_o$. The characteristic length δ_0^* can be derived from Nusselt's film theory such as

$$\delta_0^* = \left(\frac{3\nu_l^* Q^*}{g^*}\right)^{1/3}, \quad (2)$$

where ν_l^*, g^* and Q^* are dynamic viscosity of the fluid, gravitational acceleration and flow rate, respectively.

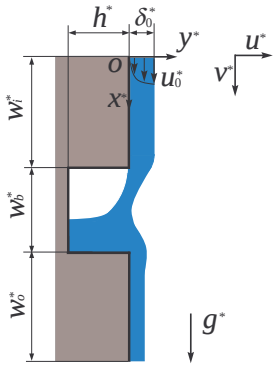

Fig.1 Geometry and coordinates.

We assume that the flow is two-dimensional because the film flow is thin and the depth in the spanwise direction of plate is large enough. Moreover, the fluid is assumed to be incompressible and the shear stress from the gas phase side can be negligible. Then we make non-dimensional the following quantities, by using characteristic length δ_0^* and surface velocity at the reference point as $u_0^* = \rho_l^* g^* \delta_0^{*2}/(2\mu_l^*)$ which is also derive from Nusselt's film theory, as

$$\boldsymbol{x} = \frac{\boldsymbol{x}}{\delta_0^*}, \quad \boldsymbol{u} = \frac{\boldsymbol{u}}{u_0^*}, \quad t = \frac{t^* u_0^*}{\delta_0^*}, \quad p = \frac{p^*}{\rho_l^* \, u_0^{*2}},$$

$$\rho = \frac{\rho^*}{\rho_l^*}, \quad \mu = \frac{\mu^*}{\mu_l^*}. \quad (3)$$

This time, we proceed our calculations not only for liquid phase but also for gas phase. Then, the governing equations for the velocities and pressure are written in non-dimensional forms as

$$\nabla \cdot \boldsymbol{u} = 0, \tag{4}$$

$$\rho \left\{ \frac{\partial \boldsymbol{u}}{\partial t} + (\boldsymbol{u} \cdot \nabla)\boldsymbol{u} \right\} = \rho Fr \boldsymbol{e}_x - \nabla p - \frac{Fr}{Bo}\kappa \nabla H + \frac{1}{Re}\nabla \left[\mu \{ \nabla \cdot \boldsymbol{u} + (\nabla \cdot \boldsymbol{u})^T \} \right], \tag{5}$$

Nondimensional parameters in the equations are the Reynolds number, Flude number and Bond number respectively defined as

$$Re = \frac{u_0^* \delta_0^*}{\nu^*}, \quad Fr = \frac{\delta_0^* g^*}{u_0^{*2}}, Bo = \frac{\delta_0^{*2} \rho^* g^*}{\sigma^*}. \tag{6}$$

First, we solve the governing equations Eq. (4) and (5) for velocity and pressure fields numerically by Highly Simplified Marker and Cell (HSMAC) method using staggered grid system. In addition to HSMAC method for the velocity and pressure fields, we have used a Coupled Level-Set and Volume Of Fluid (CLSVOF) method[2,3] to determine the free surface between gas and liquid phases, wehre we have been dealing with a new approach to impose surface tension effect and discontinuous changes of physical quantities between liquid and gas phases. Namely, Ghost Fluid Method(GFM)[4] are examined as well as CLSVOF Mmethod in our program.

Before, we used CSF(Continuum Surface Force) model proposed by Brackbill et al.[5] in order to express the surface tension effect. In such model, a continuous Heaviside function was used. However in this study, we have used a discontinuous Heaviside function in the Ghost Fluid method defned as

$$\begin{aligned} H(\phi) &= 1, && \text{if } \phi \geq 0, \\ &= 0, && \text{if } \phi \leq 0. \end{aligned} \tag{7}$$

Therefore, we can express the discontinuous changes of density and viscousity between the liquid and gas phased as

$$\rho = \frac{\rho_g^*}{\rho_l^*}(1 - H(\phi)) + H(\phi), \tag{8}$$

$$\mu = \frac{\mu_g^*}{\mu_l^*}(1 - H(\phi)) + H(\phi). \tag{9}$$

This leads to the more realistic calculation results in our study.

1 Results

In this year, we try to calculate the evapolation heat transfer. The treatment for evaporation is the same for condensation, because the direction of the heat flux is different. Figure 2 is the result of film evapolation along the vertical smoothe plate. We can see in the figure that the evaporation bulles are separate from the plate as shown in Fig. 2(a), and the temperature distribution in Fig. 2(b). However, the treatment of evaporation and condensation is basically very difficult, because iteration process in HSMAC spends much time of about 80% to total time in our code. So we are now trying to parallelize the part by using MPI.

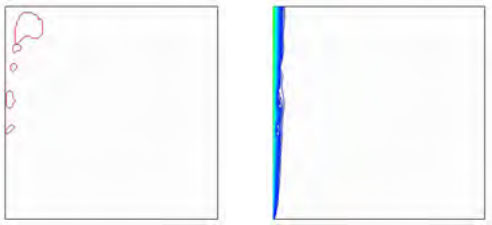

(a) (b)

Fig.2 Evaporation bubbles and temperature distribution.

References

[1] R. Gregorig, Z. Angew. Math. Phys., Vol. 5, (1954) 36.
[2] M. Sussman, E. G. Puckett. J. Comput. Phys., Vol. 162, (200) 301.
[3] G. Son, and N, Hur. Numer. Heat Transf., Part B, Vol. 42, (2002) 523.
[4] G. Son, and V. K. Dhir. Numer. Heat Transf., PArt B, Vol. 52, (2007) 153.
[5] U. J. Brackbill, D. B. Kothe, and C. Zemach. J. Comput. Phys., Vol. 100, (1992) 335.

Cell Crowding Effects in Collective Cell Migration

Katsuyoshi Matsushita
Department of Biological Science, Osaka University
Machikaneyama-cho, Toyonaka 560-0043

The collective cell migration contributes to various biological phenomena including morphogenesis of organs, would healing, and immune response. Therefore, the clarification of its mechanism is a key to understandings of these phenomena. To clarify the mechanism, much effort have been devoted. In particular, they have been intensively investigated on the basis on statistical physics models. In spite of large amount of effort, the understanding of the mechanism is not sufficiently achieved because of the complexity and diversity of biological systems.

A possible mechanism is the mechanism based on collective motions of soft active colloid systems [1]. It is well known that the soft active colloids spontaneously exhibit collective motion for large volume fraction of colloids. This is regarded as a crowding effect of soft active colloids. The crowding mechanism may be a possible mechanism of collective cell migration.

The soft active colloids behave as a self-propelled particle. In contrast, in various collective cell migrations, movement using highly randomly deformations of cell, so-called amoeboid motion, are frequently observed. Because of this difference in motion, the crowding mechanism of soft active colloids is not simply applied to collective cell migration.

To show the applicability of this crowding mechanism to the collective cell migration associated with the amoeboid cells, we utilize a variant of cellular Potts model in which amoeboid cells repulsively interacts with each other and have a motility [2, 3]. We simulate the migration of amoeboid cells with sweeping the number of cells and calculate the order parameter of cell motility M. Here, when M is close to unity, the cells exhibit a collective motion and otherwise do not exhibit it. The data of M is plotted as a function of volume fraction ϕ in Fig. 1. M rapidly increases with ϕ at a threshold volume fraction $\phi = \phi_{\mathrm{C}}$ and gets close to unity at large volume fractions. Therefore, the crowding mechanism is concluded to be applicable to the collective cell migration of amoeboid cells.

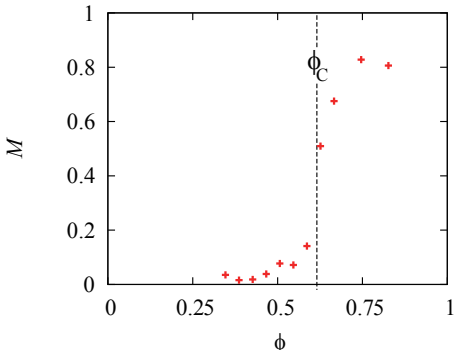

Figure 1: The order parameter of cell motility M as a function of volume fraction..

References

[1] T. Hanke, C. A. Weber, and E. Frey: Phys. Rev. E. **88** 570 (2013).

[2] K. Matsushita, Phys. Rev. E **95**, 032415 (2017).

[3] K. Matsushita, Proc. Sympo. Simul. Traffic Flow **21**, 19 (2015).

Ground-State Phase Diagram of a Frustrated $S=1/2$ Two-Leg Ladder with Different Leg Interactions

Takashi Tonegawa

Professor Emeritus, Kobe Univ. and Visiting Professor, Osaka Prefecture Univ.

This report aims at exploring the ground-state phase diagram of an anisotropic $S=1/2$ two-leg ladder with different leg interactions by using mainly numerical methods. We express the Hamiltonian which describes this system as

$$\begin{aligned}\mathcal{H} = & J_{\rm leg,a}\sum_{j=1}^{L}\vec{S}_{j,a}\cdot\vec{S}_{j+1,a} \\ & +J_{\rm leg,b}\sum_{j=1}^{L}\vec{S}_{j,b}\cdot\vec{S}_{j+1,b} \\ & +J_{\rm rung}\sum_{j=1}^{L}[\vec{S}_{j,a},\,\vec{S}_{j,b}]_{\Gamma}\end{aligned} \tag{1}$$

with

$$[\vec{S}_{j,a},\,\vec{S}_{j,b}]_{\Gamma}\equiv\Gamma\{S^x_{j,a}S^x_{j,b}+S^y_{j,a}S^y_{j,b}\}+S^z_{j,a}S^z_{j,b}\,. \tag{2}$$

Here, $\vec{S}_{j,\ell}=\left(S^x_{j,\ell},\,S^y_{j,\ell},\,S^z_{j,\ell}\right)$ is the $S=1/2$ operator acting at the (j,ℓ) site assigned by rung j and leg $\ell(=a$ or $b)$; $J_{{\rm leg},a}$ and $J_{{\rm leg},b}$ denote, respectively, the magnitudes of the isotropic leg a and leg b interactions; $J_{\rm rung}$ denotes that of the anisotropic rung interaction, the XXZ-type anisotropy being controlled by the parameter Γ; L is the total number of rungs, which is assumed to be even. It should be noted that this system has a frustration when $J_{{\rm leg},a}J_{{\rm leg},b}<0$ irrespective of the sign of $J_{\rm rung}$. Throughout this report, we assume that $J_{\rm rung}=-1.0$ (the rung interaction is ferromagnetic), choosing $|J_{\rm rung}|$ as the unit of energy, and also that $J_{{\rm leg},a}=0.2$.

We [1] have already determined numerically the ground-state phase diagram on the $1/\Gamma$ versus $J_{\rm leg,b}$ plane in the case where the anisotropy of the rung interaction is assumed to be of the XY-type ($\Gamma>1.0$). This phase diagram consists of the Haldane, triplet-dimer, $XY1$ and non-collinear ferrimagnetic (NCFR) [2] phases. In this report, we confine ourselves to the case where the anisotropy of the rung interaction is of the Ising-type ($0.0\le\Gamma\le1.0$). The motivation of treating this case is as follows. When the ferromagnetic rung interaction with Ising-type anisotropy is much stronger than both of two kinds of leg interactions, a pair of $S=1/2$ spins at each rung forms a bound state of two magnons. This may lead, in the frustrated region, to the nematic Tomonaga-Luttinger liquid (TLL) state, which has been extensively investigated in recent years.

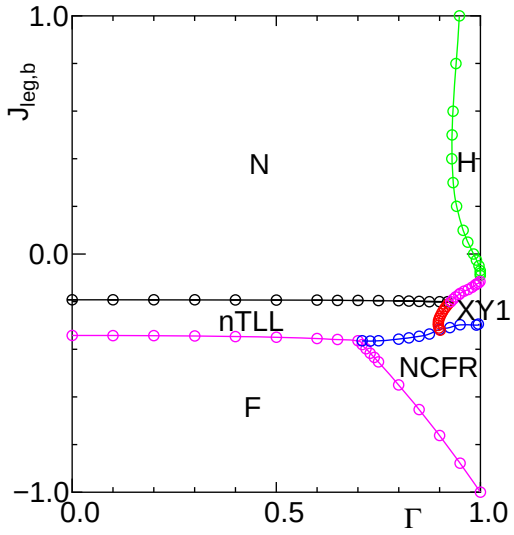

Figure 1: Ground-state phase diagram on the Γ versus $J_{\rm leg,b}$ plane for $J_{\rm rung}=-1$ and $J_{{\rm leg},a}=0.2$. The regions designated by N, H, nTLL, XY1, F and NCFR are, respectively, those of the Néel, Haldane, nematic TLL, $XY1$, ferromagnetic and non-collinear ferrimagnetic phases.

Figure 1 shows our final result for the ground-state phase diagram on the Γ versus $J_{\rm leg,b}$ plane. In this phase diagram six states, that is, the Néel (N), Haldane (H), nematic TLL (nTLL), $XY1$, ferromagnetic (F) and NCFR states, appear as the ground states. It should be emphasized that, as is expected, the nTLL state becomes the ground state in the strong-rung frustrated region.

At this junction, we denote, respectively, by $E_0(L,M;{\rm pbc})$ and $E_1(L,M;{\rm pbc})$ the lowest and first excited energies within the subspace of the Hamiltonian (1) determined by L and M under periodic boundary conditions, where M is the total magnetization which is a good quantum number with the eigenvalues of $M=0,\ \pm1,\ \cdots,\ \pm L$. We have numerically calculated these energies for finite-size systems with up to $2L=28$ spins by means of the exact-diagonalization (ED) method.

The ground-state energy $E_{\rm g}(L)$ is given by the minimum value among $E_0(L,0;{\rm pbc})$, $E_0(L,\pm1;{\rm pbc})$, $\cdots$, $E_0(L,\pm L;{\rm pbc})$, and the ground-sate magnetization $M_{\rm g}(L)$ is the value of M giving $E_{\rm g}(L)$. It is noted that $M_{\rm g}(L)=0$ in the N, H, nTLL and $XY1$ states, $0<M_{\rm g}(L)<L$ in the NCFR state, and $M_{\rm g}(L)=L$ in the F state. Furthermore, we introduce the following three excitation energies:

$$\Delta_{00}^{({\rm p})}(L) = E_1(L,0;{\rm pbc}) - E_0(L,0;{\rm pbc})\,, \quad (3)$$

$$\Delta_{10}^{({\rm p})}(L) = E_0(L,1;{\rm pbc}) - E_0(L,0;{\rm pbc})\,, \quad (4)$$

$$\Delta_{20}^{({\rm p})}(L) = E_0(L,2;{\rm pbc}) - E_0(L,0;{\rm pbc})\,. \quad (5)$$

Let us now discuss how to numerically determine the phase boundary lines shown in Fig. 1. In the following way, we estimate the finite-size critical values of $J_{\rm leg,b}$ (or Γ) for various values of Γ (or $J_{\rm leg,b}$), for each phase transition. Then, the phase boundary line for the transition is obtained by connecting the results for the $L\to\infty$ extrapolation of the finite-size critical values.

Firstly, we employ the level spectroscopy method [3] to estimate the phase boundary lines between two of the N, $XY1$ and nTLL phases. According to this method, the three quantities, $\Delta_{00}^{({\rm p})}(L)$, $\Delta_{10}^{({\rm p})}(L)$ and $\Delta_{20}^{({\rm p})}(L)/2$, should be compared in the $L\to\infty$ limit; the ground state is the N, $XY1$ or nTLL state depending upon whether $\Delta_{00}^{({\rm p})}(L)$, $\Delta_{10}^{({\rm p})}(L)$ or $\Delta_{20}^{({\rm p})}(L)/2$ is lowest among them. Thus, the finite-size critical values for the N-$XY1$, N-nTLL, and $XY1$-nTLL transitions can be evaluated by solving the equations,

$$\Delta_{00}^{({\rm p})}(L) = \Delta_{10}^{({\rm p})}(L) < \Delta_{20}^{({\rm p})}(L)/2\,, \quad (6)$$

$$\Delta_{00}^{({\rm p})}(L) = \Delta_{20}^{({\rm p})}(L)/2 < \Delta_{10}^{({\rm p})}(L)\,, \quad (7)$$

$$\Delta_{10}^{({\rm p})}(L) = \Delta_{20}^{({\rm p})}(L)/2 < \Delta_{00}^{({\rm p})}(L)\,. \quad (8)$$

respectively. It is noted that the tricritical point for the N, $XY1$ and nTLL phases is given by $(\Gamma, J_{\rm leg,b})=(0.927\pm0.001, -0.200\pm0.001)$, at which $\Delta_{00}^{({\rm p})}(L)=\Delta_{10}^{({\rm p})}(L)=\Delta_{20}^{({\rm p})}(L)/2$ holds in the limit of $L\to\infty$.

Secondly, the phase transition between the H and N phase is the 2D Ising-type transition. Therefore, the phase boundary line between these two phases can be estimated by the phenomenological renormalization group (PRG) method [4]. That is to say, we numerically solve the PRG equation,

$$L\Delta_{00}^{({\rm p})}(L) = (L+2)\Delta_{00}^{({\rm p})}(L+2)\,, \quad (9)$$

to calculate the finite-size critical values.

Thirdly, it is apparent that the finite-size critical values of the phase transition between the F and nTLL phases are estimated from the equation,

$$E_0(L,L;{\rm pbc}) = E_0(L,0;{\rm pbc})\,, \quad (10)$$

because $M_{\rm g}(L)=L$ and $M_{\rm g}(L)=0$ in the F and nTLL states, respectively.

Finally, we discuss the phase transition between the F and NCFR phases and that between the NCFR and $XY1$ (or nTLL) phases. The results of the ED calculation show that the former transition is of the second order, that is, it is the transition between the $M=L$ and $M=L-1$ states. Thus, the finite-size critical values can be estimated from

$$E_0(L,L;{\rm pbc}) = E_0(L,L-1;{\rm pbc})\,. \quad (11)$$

The obtained finite-size critical values are naturally independent of L; as is well known, we can derive the analytic formula for them by analyzing the spin-wave dispersion relation. On the other hand, the latter transition is of the first order, that is, it is the transition between the $M>1$ and $M=0$ states. In order to determine the phase transition line of this transition, we have carried out the density-matrix renormalization-group [5] calculations for the system with $2L=72$ spins to estimate $M_{\rm g}(L)$ for various values of $J_{{\rm leg},b}$ with Γ fixed at several values. We suppose that the phase transition line obtained in the $2L=72$ system gives good approximate result at the $L\to\infty$ limit. (See our recent paper [1] for more details.)

This work has been done in collaboration with T. Hikihara, K. Okamoto and T. Sakai.

[1] T. Tonegawa, K. Okamoto, T. Hikihara and T. Sakai: J. Phys.: Conf. Series **828** (2017) 012003.
[2] M. Tsukano and M. Takahashi: J. Phys. Soc. Jpn. **66** (1997) 1153; S. Yoshikawa and S. Miyashita: J. Phys. Soc. Jpn. **74** (2005) Suppl. 71.
[3] K. Okamoto and K. Nomura: Phys. Lett. A **169** (1992) 433; K. Nomura and K. Okamoto: J. Phys. A **27** (1994) 5773.
[4] M. P. Nightingale: Physica A **83** (1976) 561.
[5] S. R. White: Phys. Rev. Lett. **69** (1992) 2863; Phys. Rev. B **48** (1993) 10345.

Randomness Effects on Quantum Spin Systems Coupled to Lattice Degrees of Freedom

Chitoshi YASUDA and Shouta MIYARA
Department of Physics and Earth Sciences, Faculty of Science, University of the Ryukyus, Nishihara, Okinawa 903-0213, Japan

Since the inorganic compound $CuGeO_3$ was synthesized, randomness effects of the spin-Peierls (SP) system have attracted considerable attention. When nonmagnetic impurities are doped in the SP compound, an antiferromagnetic long-range order (AFLRO) is induced. The mechanism is understood by magnetic moments induced near the impurities, which are called 'effective spins'. By substituting nonmagnetic atoms for magnetic atoms, effective spins are induced near the nonmagnetic atoms. Since the effective spins interact through a sea of spin-singlet pairs, the AFLRO is induced [1]. However, an experimental result contradictory to this interpretation was reported: the effective spins are not induced near diluted sites [2]. We need to take lattice degrees of freedom into account in order to investigate positions of the effective spins.

In this project, we investigated the spin-1/2 antiferromagnetic Heisenberg (AFH) model coupled to lattice degrees of freedom. Previous researches on the two-dimensional site-diluted AFH systems have concluded that effective spins are induced near diluted sites at low temperature. However, the experimental result of the SP compound described by the AFH model showed that there is no effective spin near impurities as mentioned above. Thus, in the present work, we examined what kind of situation is the case that the effective spins are not induced near diluted sites, and investigated whether the AFLRO is actually induced or not. The method is the quantum Monte Carlo (QMC) simulation with the continuous-imaginary-time loop algorithm and the program is based on 'Looper' developed by S. Todo *et al* [3]. Since this QMC simulation is suitable to parallel computing, we mainly performed parallel computing with MPI.

At first, assuming two patterns of lattice distortion such that effective spins are induced near diluted sites or not, we compared two ground-state energies. As the result, we found that the effective spins are hard to be induced near diluted sites for the large elastic constant, small interchain interaction, and large concentration of dilution.

Next, we performed self-consistent calculations of lattice-distortion patterns for the one-dimensional finite chains and found that the lattice distortion is described by a hyperbolic tangent function and that soliton-type magnetic moments are induced at the places other than edges. Furthermore, we investigated site-dilution effects in the two-dimensional system consisting of the one-dimensional chains connected by the spin-spin interaction. As the result, the AFLRO was induced. In this calculation, the temperature regarded as zero temperature is lower than that of the site-diluted bond-alternated system. This problem of the large-scale computation becomes serious when the interchain interaction is small.

References

[1] C. Yasuda, *et al.*: Phys. Rev. B **64**, 092405 (2001); J. Phys. Soc. Jpn. **75**, 124704 (2006).

[2] J. Kikuchi, *et al.*: Phys. Rev. Lett. **88**, 037603 (2002).

[3] S. Todo and K. Kato, Phys. Rev. Lett. **87**, 047203 (2001).

Shape Optimization in Conjugate Heat Transfer Problems

Kenichi MORIMOTO

Department of Mechanical Engineering,

The University of Tokyo, 7-3-1 Hongo, Bunkyo-ku, Tokyo 113-8656

We have developed an adjoint-based shape-optimization scheme under the conjugate condition with thermal coupling between the solidified liquid and the solid wall. In order to consider practical applications, we examined the effect of the wall thermal conductivity on the shape optimization, and the regularization effect due to the wall heat conduction. In Ref. [1], in order to develop an adjoint analysis-based shape optimization method for convective boundary-layer flows with complex heat transfer surfaces, as the first step, we have increased the node density of the meshless analyses using parallel computing. A series of numerical simulations of the present shape optimization has been performed using in-house code for broader ranges of the thermo-physical properties. Also, we proposed a new strategy for efficient scheme for dealing with boundary-layer flows.

High-performance turbulent heat exchangers are demanded for energy-saving purposes in various engineering fields such as in automobile industry. Over the past several decades, remarkable advances have been made in the adjoint-based shape optimization methods, but no application to turbulent heat and fluid flow problems has been reported so far. We previously demonstrated the effectiveness of the adjoint-based analysis on the optimization of convective heat transfer problem in the laminar-flow regime. We established a RANS-based adjoint analysis approach (using OpenFOAM) for shape optimization in turbulent heat transfer problems [2].

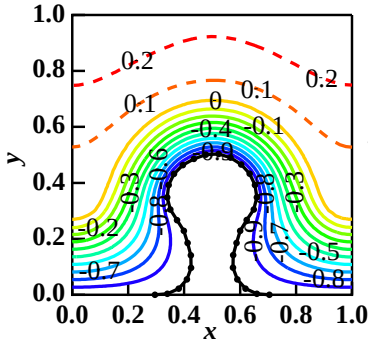

Fig. 1: Meshless computation-based shape optimization.

References

[1] H. Kinoshita, Y. Suzuki, and K. Morimoto, Proc. 9th JSME-KSME Thermal Fluids Eng. Conf. (TFEC9) , Oct. 2017 (accepted).

[2] K. Morimoto, Y. Goto and Y. Suzuki, Proc. 9th JSME-KSME Thermal Fluids Eng. Conf. (TFEC9), Oct. 2017 (accepted).

Structural dynamics of an aldehyde-deformylating oxygenase studied by molecular dynamics simulations

Yuma SUEMATSU and Munehito ARAI

Department of Life Sciences, Graduate School of Arts and Sciences,

The University of Tokyo, Komaba, Meguro, Tokyo 153-8902

Cyanobacteria are known to synthesize alkanes/alkenes corresponding to diesel oils. Because these hydrocarbons are produced from carbon dioxide by photosynthesis, such "bio-energies" are expected to be substitutes for petroleum-based hydrocarbons [1]. In 2010, Schirmer *et al.* revealed that cyanobacteria use two enzymes for two-step production of hydrocarbons from fatty acyl-(acyl carrier protein (ACP)) [2]. In the first step, an acyl-ACP reductase (AAR) reduces acyl-ACP into aldehydes. Then, in the second step, an aldehyde-deformylating oxygenase (ADO) converts aldehydes into alkanes/alkenes. However, ADO has extremely low activity, and its catalytic mechanism has been poorly understood. In general, proteins exert their functions through dynamic motions, and thus, elucidation of structural dynamics of ADO is necessary for understanding the mechanism of the ADO action and improving its catalytic activity.

Here, we performed molecular dynamics (MD) simulations of the ADO protein from *Nostoc punctiforme* PCC 73102. Because ADO is known to bind two metal ions, we performed MD simulations both in the presence and absence of metal ions. In addition, we did simulations in the presence and absence of an alkane molecule, resulting in four types of MD simulations. The crystal structure of the protein was used as an initial structure of simulations.

We found by simulations that the N-terminal region of ADO forms helical structures and interacts with the regions for the substrate entry. Moreover, the simulations suggest that the dynamics of N- and C-terminal regions control the substrate entry. We propose that low activity of ADO is attributed to slow entry of a substrate and slow exit of a product, and changing the dynamics of ADO by mutations at the N-terminal region may improve the catalytic activity of ADO.

References

[1] H. Kudo, R. Nawa, Y. Hayashi, and M. Arai: Biotechnology for Biofuels, **9** (2016) 234.

[2] A. Schirmer, M.A. Rude X. Li, E. Popova, and S.B. del Cardayre: Science, **329** (2010) 559-562.

Designing Kitaev spin liquids in metal-organic frameworks

Masahiko G. YAMADA, Hiroyuki Fujita, and Masaki OSHIKAWA
Institute for Solid State Physics, University of Tokyo
Kashiwa-no-ha, Kashiwa, Chiba 277-8581

We have studied the possiblity to design Kitaev models in real materials. The ground sate of the Kitaev model on the honeycomb lattice is a particular type of spin liquid (called Kitaev spin liquid). Conventional candidate materials, iridates and α-$RuCl_3$, have substantial non-Kitaev direct exchange interactions and show magnetic ordering at lower temperature. We propose metal-organic frameworks (MOFs) with Ru^{3+} (or Os^{3+}) forming the honeycomb lattice as new candidates for an ideal realization of the Kitaev model, where the problematic direct exchange interaction can be suppressed. In order to show the supression of the non-Kitaev interactions, we used a first-principles electronic structure calculation code called OPENMX [1] for the molecular structure of the organic ligands in the proposed MOFs. Although the calculation was a simple one for the molecular orbitals, we used the ISSP supercomputer to speed up the material explorations. From this calucation, we proved the degeneracy of the highest occupied molecular orbitals of the organic ligands in this class of materials, which implies a strong suppression of non-Kitaev interactions. We have estimated the parameters of the spin interactions in MOFs with oxalate-based (or tetraaminopyrazine-based) ligands, and have shown that they are promising candidates to realize Kitaev spin liquids. The great flexibility of MOFs allows generalization to other three-dimensional lattices or heterogeneous structures, for potential realization of various new spin liquids, such as a gapless Weyl spin liquid and a gapped Z2 spin liquid. The details of our work are reported in Ref. [2].

References

[1] T. Ozaki: Phys. Rev. B **67**, (2003) 155108.

[2] M. G. Yamada, H. Fujita, and M. Oshikawa: arXiv:1605.04471 [cond-mat.str-el] (2016).

Microscopic analysis of the Hall effect in superconductors using the augmented quasiclassical equations with the Lorentz force

Takafumi KITA
Department of Physics, Hokkaido University
Sapporo 060-0810, Japan

After the sign change of the Hall conductivity have been observed in some high-T_c superconductors, intensive studies have been performed on *the flux-flow Hall effect* in type-II superconductors theoretically and experimentally. Despite these efforts, a microscopic understanding of the anomalous flux-flow Hall effect is still missing. This may be because the Lorentz force is missing from the standard Eilenberger equations and Ginzburg–Landau equation. In fact, the standard equations cannot describe the Hall effect in superconductors.

Recently, the Lorentz force has been incorporated successfully in a gauge-invariant manner within the real-time Keldysh formalism [1]. The augmented quasiclassical equations in the Keldysh formalism have been used to study charging in the Meissner state with Fermi-surface and gap anisotropies [2], and also to calculate flux-flow Hall conductivity numerically for the s-wave pairing on an isotropic Fermi surface [3]. However, the temperature dependence of the Hall conductivity have not been calculated in Ref. [3].

The flux-flow Hall effect denotes a dissipative nonequilibrium phenomena accompanying motions of vortices and the resulting electric field. It is much more difficult to investigate than the equilibrium Hall effect in superconductors or the Hall effect in metals and semiconductors due to the presences of the spatial inhomogeneity and vortex motion. Hence, it is not surprising to know that a fully microscopic study on the flux-flow Hall effect was started only quite recently by Arahata and Kato [3] for an isolated vortex in an s-wave superconductor.

On the other hand, we derived augmented quasiclassical equations of superconductivity with the Lorentz force in the Matsubara formalism so that the charge redistribution due to supercurrent can be calculated quantitatively [4]. It is still desirable when studying the charging to transform the equations into the Matsubara formalism, in which equilibrium properties and linear responses can be calculated much more easily.

We study the flux-flow Hall effect in a superconductor with an isolated vortex based on the augmented quasiclassical equations of the superconductivity with the Lorentz force [1]. In particular, we calculate the temperature dependence of the Hall angle for electric field induced by a motion of an isolated vortex by transforming the energy variable of the augmented quasiclassical equations in the Keldysh formalism into the Matsubara energy on the imaginary axis. The Hall angle is defined as $\tan\theta_{\rm H} \equiv \langle E_{\rm H}\rangle/\langle E_{\rm O}\rangle$, where $\langle\cdots\rangle$ denotes the spatial average, $E_{\rm O}$ is the longitudinal electric field and $E_{\rm H}$ is the Hall electric field. It is shown that linear responses can be calculated much more easily compared to the approach based on the augmented quasiclassical equations in the Keldysh formalism.

We consider the linear response $\check{g} = \check{g}^{\rm eq} + \delta\check{g}$

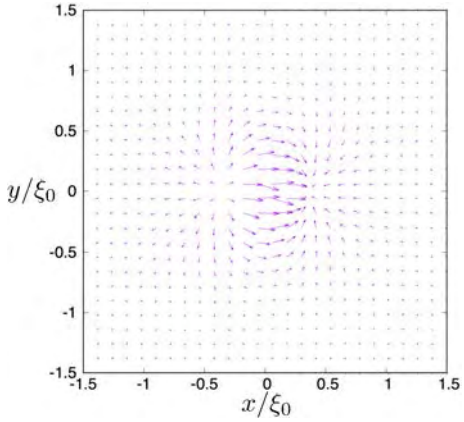

Figure 1: Longuitudinal electric field $\boldsymbol{E}_{\rm O}$ over $-1.5\xi_0 \le x, y \le 1.5\xi_0$ at $T/T_{\rm c} = 0.4$.

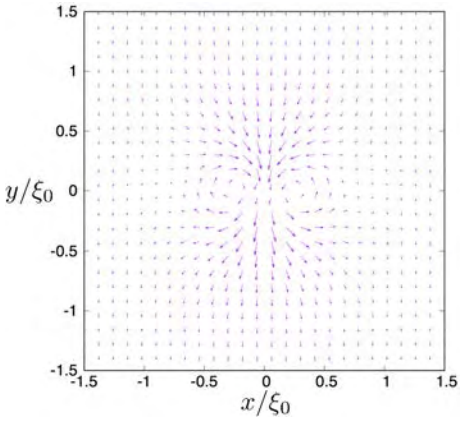

Figure 2: Hall electric field $\boldsymbol{E}_{\rm H}$ over $-1.5\xi_0 \le x, y \le 1.5\xi_0$ at $T/T_{\rm c} = 0.4$.

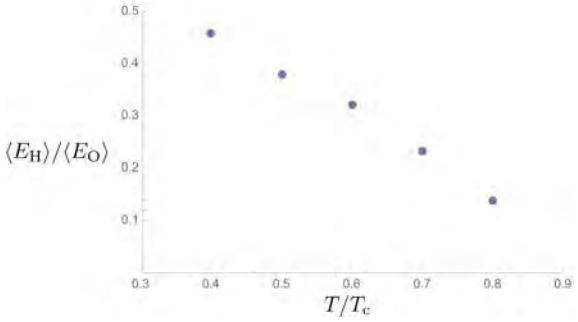

Figure 3: Hall angle $\tan\theta_{\rm H}$ as a function of temperature.

to a spatially uniform but time-dependent perturbation $\delta\boldsymbol{A}^{\rm ex}{\rm e}^{-i\omega t} = \delta\boldsymbol{E}^{\rm ex}{\rm e}^{-i\omega t}/i\omega$ with frequency ω [5]. The limit $\omega \to 0$ will be taken eventually. As shown in Refs. [2, 4], we expand Green's functions in the quasiclassical parameter $\delta \equiv 1/k_{\rm F}\xi_0$ (ξ_0: the the coherence length). With these preliminaries, we solve the augmented quasiclassical equations of superconductivity with the Lorentz force, the gap equation, and Maxwell equations simultaneously in a self-consistent way. We obtain the longitudinal and Hall electric field induced by the vortex motion numerically by standard Runge–Kutta methods.

Figures 1 and 2 plot the longitudinal and Hall electric field induced by the vortex motion in the core region at $T/T_{\rm c} = 0.4$, respectively. They clearly show the existence of the ohmic and Hall resistivity in the flux-flow state. Figure 3 plots the Hall angle as a function of temperature. We observe the decreasing the Hall angle as the temperature is increased from $T = 0$.

We have also developed a new approach to calculate the liner responses in the flux-flow state by transforming the energy variable of the augmented quasiclassical equations in the Keldysh formalism into the Matsubara energy on the imaginary axis. Using it, we confirmed that there exists the ohmic and Hall resistivities caused by the moving isolated vortex in an s-wave superconductor, and obtained the Hall angle as a function of temperature. Thus, we have established a method to study this complicated topic fully microscopically in a tractable manner.

References

[1] T. Kita, Phys. Rev. B **64**, 054503 (2001).

[2] T. Kita, Phys. Rev. B **79**, 024521 (2009).

[3] E. Arahata and Y. Kato, J. Low. Temp. Phys. **175**, 346 (2014).

[4] H. Ueki, W. Kohno, and T. Kita, J. Phys. Soc. Jpn. **85**, 064702 (2016).

[5] T. Kita, J. Phys. Soc. Jpn. **73**, 21 (2004).

Computer-aided synthesis of zeolites

Tatsuya Okubo
Department of Chemical System Engineering, The University of Tokyo
7-3-1 Hongo, Bunkyo-ku, Tokyo 113-8656

Zeolites, a class of crystalline microporous materials composed of T (Si, Al, B, Ga, and others) and O, have been widely used as sorbents and catalysts due to their uniform pore sizes, catalytic activities, and hydrothermal stability. We have utilized the computational resources to describe zeolites and organic structure-directing agents (OSDAs) incorporated in their structures during the synthesis of zeolites. OSDAs are generally bulky and water-soluble organic molecules that interact with negatively charged inorganic species. OSDAs can guide the crystallization of specific zeolite framework since their molecular structures tailor the void spaces having particular sizes and structures. We have developed a scheme to design OSDAs that can fit the cavities in zeolite framework utilizing the combination of molecular modeling and meta-heuristic algorithms. Out first example of this approach designed unconventional OSDAs. With the use of this OSDAs, we synthesized highly nanoporous silica with very rare pore diameter (c.a. 2 nm) as silica and high porosity[1]. This method was useful not only for the synthesis of novel materials but also for the interpretation of experimental results at molecular level. We found that an OSDA possessing carbon chain with particular length crystallizes hierarchically and sequentially intergrown zeolite[2]. The molecular modeling revealed that this unique morphology is likely to be derived from the unusual interaction between the OSDA and zeolite framework[3].

Our computational investigations involved DFT calculation on Quantum ESPRESSO and CP2K, and classical lattice minimization using a program named GULP[4]. We compiled Quantum ESPRESSO and CP2K to efficiently utilize all cores implemented in the system. On the other hand, the computations using GULP generally entail many jobs executed serially, which are inefficient if they are submitted one-by-one. In order to maximize the efficiency of the calculation, we have tried to use GXP[5], Rake, and the other tools to distribute serial jobs over many cores. The approach was successful to efficiently utilize all computational resources given on a batch job by allocating cores to jobs dynamically.

References

[1] K. Muraoka, W. Chaikittisilp, Y. Yanaba, T. Yoshikawa, T. Okubo, Chemical Communications, 2015, 51, 10718.

[2] W. Chaikittisilp, Y. Suzuki, R. R. Mukti, T. Suzuki, K. Sugita, K. Itabashi, A. Shimojima, T. Okubo, Angewandte Chemie International Edition, 2013, 52 (12), 3355.

[3] S. H. Keoh, W. Chaikittisilp, K. Muraoka, R. R. Mukti, A. Shimojima, P. Kumar, M. Tsapatsis, T. Okubo, Chemistry of Materials, 2016, 28, 8997.

[4] J. D. Gale, Journal of the Chemical Society, Faraday Transactions, 1997, 93(4), 629.

[5] K. Taura, et al. Future Generation Computer Systems, 2013, 29(2), 662.

Local structure and phase transition in supercooled cyclohexane

Tomoko MIZUGUCHI[1], Soichi TATSUMI[2], and Susumu FUJIWARA[2]

[1]*Institute for the Promotion of University Strategy, Kyoto Institute of Technology, Matsugasaki, Sakyo-ku, Kyoto 606-8585*
[2]*Faculty of Materials Science and Engineering, Kyoto Institute of Technology, Matsugasaki, Sakyo-ku, Kyoto 606-8585*

A recent experimental result revealed that a first-order phase transition occurs at 154 K in supercooled cyclohexane confined in silica nanopores [1]. This transition is different from that observed in a bulk system in which the liquid-plastic phase transition occurs at 280 K and the plastic-crystal phase transition occurs at 186 K. It is thus suggested to be a liquid-liquid phase transition. To understand the nature of this transition, we carried out all-atom molecular dynamics simulations of supercooled cyclohexane on the ISSP supercomputer system. In this year, we examined the local structures of bulk cyclohexane [2].

All the simulations were conducted with NAMD 2.10 [3] in the isothermal-isobaric (NPT) ensemble at 1 atm and various temperatures. The electrostatic interaction was handled by the smooth particle-mesh Ewald method. The CHARMM force field developed by Vorobyov *et al*. [4] was adopted for cyclohexane. Periodic boundary conditions were applied to the unit cell which contains 1331 cyclohexane molecules.

We first prepared liquid cyclohexane at 320 K, and quenched the system to 60 K with a cooling rate of 10^{11} K/s. The system remained liquid below its melting temperature due to such fast cooling. In experiments, a confined system is used to prevent crystallization. In our simulations, however, a supercooled state can be attained even in a bulk system, thus we examined the local structures of bulk in this work. The system was then heated with a heating rate of 10^{11} K/s, and configurations were collected in the heating process. Starting from the dumped configurations, we carrid out 1-ns equilibration runs and subsequent 1-ns production runs at a variety of temperatures.

The local structures are analyzed in terms of Voronoi polyhedra by using a Voro++ library [5]. We use the Voronoi index $\langle n_3, n_4, n_5, n_6 \rangle$ to identify the type of each polyhedron, where n_i is the number of faces with i vertices. The $\langle 0, 1, 10, 2 \rangle$ type of polyhedra is the most populous at 90 K (glass) and its fraction decreases from 16.5% at 90 K to 4.2% at 290 K (liquid). It is an icosahedron-like cluster and frequently observed in metallic glasses. The full icosahedra $\langle 0, 0, 12, 0 \rangle$ are also observed, but the fraction is smaller than that of $\langle 0, 1, 10, 2 \rangle$. A distorted icosahedron is prefered as a local structure in the glassy state rather than a full icosahedron. This observation is consistent with the studies of metallic glasses.

We plot the fractions of four types of Voronoi polyhedra against temperatures in Figure 1. It clearly shows that the icosahedral structures $\langle 0, 1, 10, 2 \rangle$ and $\langle 0, 0, 12, 0 \rangle$ grow in a supercooled liquid, on the other hand,

crystalline(fcc)-like structures $\langle 0,3,6,4\rangle$ and $\langle 0,3,6,5\rangle$ do not grow when temperature decreases. The fraction of $\langle 0,1,10,2\rangle$ steadily increases with decreasing temperatures, but abruptly stops growing at 170 K. This fact implies that some structural change related to the icosahedral order occurs at this temperature. We cannot conclude clearly that the system is in a supercooled liquid state at this temperature. This issue will be addressed in our future work including a relationship with the liquid-liquid phase transition.

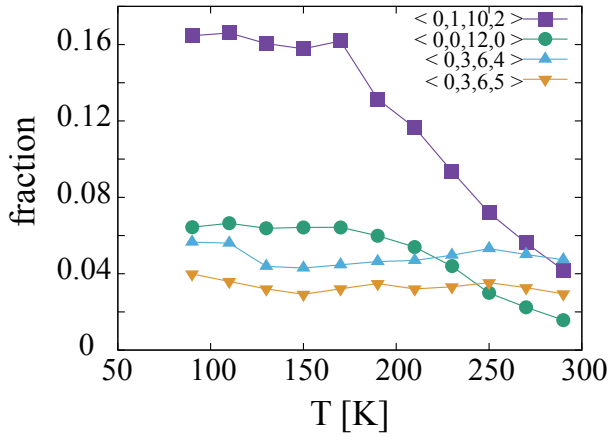

Figure 1: Fractions of four types of Voronoi polyhedra as a function of temperature: distorted icosahedra $\langle 0,1,10,2\rangle$, full icosahedra $\langle 0,0,12,0\rangle$, and fcc-like structures $\langle 0,3,6,4\rangle$ and $\langle 0,3,6,5\rangle$.

References

[1] S. Tatsumi, T. Uehara, and M. Oguni: Netsu Sokutei **42** (2015) 142.

[2] T. Mizuguchi, S. Tatsumi, and S. Fujiwara: Proceedings of JSST 2016 - International Conference on Simulation Technology (2016) 41.

[3] J. C. Phillips, R. Braun, W. Wang, J. Gumbart, E. Tajkhorshid, E. Villa, C. Chipot, R. D. Skeeo, L. Kalé, K. Schulten: J. Comput. Chem. **26** (2005) 1781.

[4] I. Vorobyov, V. M. Anisimov, S. Greene, R. M. Venable, A. Moser, R. W. Pastor, A. D. MacKerell, Jr.: J. Chem. Theory Comput. **3** (2007) 1120.

[5] C. H. Rycroft: Chaos **19** (2009) 041111.

Magnetic excitation and spin transport in frustrated quantum spin chain

Hiroaki ONISHI
Advanced Science Research Center, Japan Atomic Energy Agency, Tokai, Ibaraki 319-1195

The spin nematic state is currently attracting much attension as a novel quantum state. We have studied spin excitation spectra of the spin nematic state in a spin-$\frac{1}{2}$ J_1-J_2 chain with $J_1 < 0$ and $J_2 > 0$ in a magnetic field [1]. Here, we investigate excitation spectra in the quadrupole channel.

To clarify the properties of the spin nematic state from the dynamical aspect, we analyze the dynamical quadrupole structure factor at zero temperature, given by

$$Q^{--}(q,\omega) = -\mathrm{Im}\frac{1}{\pi}\langle 0|Q_q^{--\dagger}\frac{1}{\omega + E_0 - H + \mathrm{i}\eta}Q_q^{--}|0\rangle,$$

where Q_q^{--} is the Fourier transform of $Q_i^{--} = S_i^- S_{i+1}^-$, by exploiting the dynamical DMRG [2]. Note that we calculate the spectral weight at q and ω after one DMRG run with fixed q and ω, so that we need to perform many runs to obtain a full spectrum in a wide range of the q-ω space. The computations are accelerated by parallel simulations utilizing the system B of the ISSP supercomputer.

In Fig. 1, we show results of $Q^{--}(q,w)$ in the spin nematic regime. We find a dispersive mode. We clearly observe gapless excitations with high intensity at $q = \pi$ regardless of the value of magnetization, signaling quasi-long-range antiferro-quadrupole correlations. This indicates that a magnon pair is excited with zero energy, so that bound magnons would contribute to transport. To clarify transport properties, calculations of spin and thermal conductivities by exact diagonalization are on going.

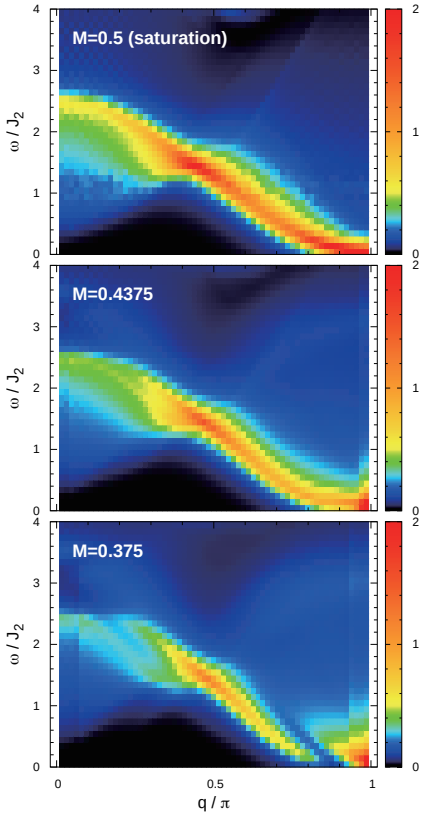

Figure 1: $Q^{--}(q,\omega)$ at several values of magnetization for $J_1 = -1$ and $J_2 = 1$.

References

[1] H. Onishi, J. Phys. Soc. Jpn. **84**, 083702 (2015); J. Phys.: Conf. Ser. **592**, 012109 (2015).

[2] E. Jeckelmann, Phys. Rev. B **66**, 045114 (2002).

Large-scale simulations of semiconductor nanocrystals

Takamichi TERAO

Department of Electrical, Electronic and Computer Engineering,

Gifu University, Yanagido 1-1, Gifu 501-1193

Recently, glassy dynamics in interacting electron systems with geometrical frustration have attracted much attention. It has been pointed out that these frustrated electron systems may show a non-equilibrium relaxation behavior similar to that found in Coulomb glass systems where both many-body electron–electron interactions and randomness of the system are present. The relaxational dynamics of the Coulomb glass model were investigated, and a transition from stationary to non-stationary dynamics at the equilibrium glass transition temperature of the system was observed. At low temperatures, the system exhibits glassy dynamics, and the two-time autocorrelation function shows aging owing to the lack of time translation invariance. Despite these studies, the behavior of electronic systems with geometrical frustration is still not fully understood.

In this study, the hopping electron model on the Kagome lattice was investigated by Monte Carlo simulations. The spatial configuration of electrons on the Kagome lattice when the total energy of the system at a low temperature has been investigated. Because it is difficult to determine the exact ground state by examination of the many possible low-lying states, we employed annealing techniques to obtain an approximate solution. Figure 1 shows a typical snapshot of the electron configuration on the Kagome lattice [1]. Starting with a sufficiently high temperature, the system is cooled gradually until the temperature of the system reaches a sufficiently low target temperature. Filled circles and open circles denote the sites occupied by an electron and vacant sites, respectively. The dashed rectangles in the figure are only for visual aid and denote blocks of occupied neighboring sites that comprise rod-like domains with different orientations.

The dynamics of the electrons in this model were also studied. For this purpose, the mean-square displacement (MSD) of the electrons on the Kagome lattice has been calculated with different temperatures. At a lower temperature, the MSD show deviations from diffusive behavior.

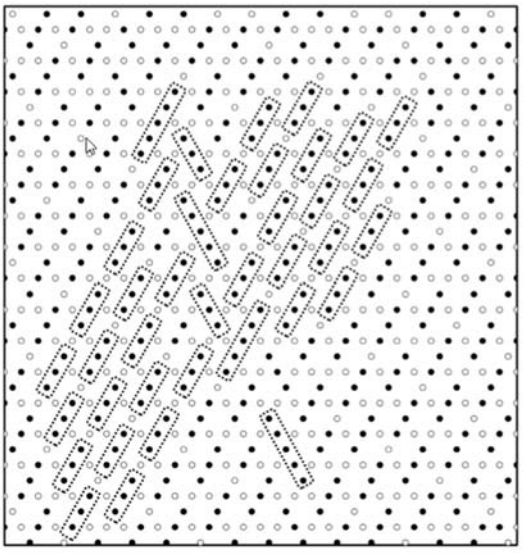

Fig. 1: Snapshot of electrons on Kagome lattice

References

[1] T. Terao: Eur. Phys. J. B **89** (2016) 209.

Calculation of the optical properties of ordered structures of soft materials

Jun-ichi FUKUDA

Department of Physics, Kyushu University, Motooka 744, Nishi-ku, Fukuoka 819-0395

(formerly at AIST, 1-1-1 Higashi, Tsukuba 305-8565)

My main focus in this project was the optical properties of exotic ordered structures exhibited by one of the intensively studied soft materials, a chiral liquid crystal. Particular focus is on the structures found when the liquid crystal is confined between two parallel substrates. I showed previously [1] that a highly chiral liquid crystal under such circumstances exhibit various types of defect structures depending on temperature and the spacing between the substrates. These structures include a hexagonal lattice of half-Skyrmions, and its typical lattice spacing is a few hundred nanometers.

My interest was how these structures can be observed by optical measures. This study was motivated by my experimental collaborators trying to observe such structures of a chiral liquid crystal by conventional optical microscope with high numerical aperture. As the typical periodicity of the structures, a few hundred nanometers, is close to the resolution limit of optical means, experimental observations are highly challenging. So is theoretical interpretation of optical images to be obtained by experiments, because geometrical optics commonly used to explain the principles of optical microscopy is entirely useless. One has to solve the full Maxwell equations for propagating light, and careful consideration is necessary as to under what kind of setup the Maxwell equations must be solved.

It requires a huge amount of numerical resources to calculate the whole optical system using the finite difference time domain (FDTD) method routinely employed for the calculations of optical properties of such structures. Therefore, I carried out calculations of the responses of the system for different wavevectors of incident light, and tried to obtain optical images by combining the results of different calculations. My calculations relied on plane-wave expansions along the directions parallel to the surfaces of the confining substrates, and finite-difference discretization along the normal direction. The latter is carefully formulated so that the energy conservation (that is, the reflectivity and the transimittivity sum up to 1) is rigorously fulfilled up to rounding errors. To reduce the computational cost of solving a large set of linear equations obtained by the discretization

of the Maxwell equations, I made use of the tridiagonal nature of the matrix, which is realized by the finite-difference discretization. The structure of the liquid crystal was determined numerically by minimizing its free energy in terms of a second-rank orientational order parameter [1], and the profile of the dielectric tensor of the liquid crystal appearing in the Maxwell equations is assumed to be a linear function of the orientational order parameter.

The calculated microscope images for a Skyrmion lattice agree almost perfectly with the experimental ones, and I believe that my numerical attempts successfully corroborate the experimental findings. Unfortunately, these results have not yet been published, and therefore I cannot describe the details in this report that will be open to public. Hopefully I will be able to present the details next time.

References

[1] J. Fukuda and S. Žumer, Nature Commun. **2**, 246 (2011); Phys. Rev. Lett. 106, 097801 (2011); Phys. Rev. Lett. 104, 017801 (2010).

Light transport for medical imaging

Manabu Machida
Institute for Medical Photonics Research, Hamamatsu University School of Medicine
1-20-1 Handayama, Higashi-ku, Hamamatsu, Shizuoka 431-3192

We have studied light propagation in random media and sought its application to medical imaging, i.e., optical tomography. The specific intensity of near-infrared light in a random medium such as biological tissue is governed by the radiative transport equation, which is a linear Boltzmann equation. The equation is a first-order differential equation involving an integral term and has six variables, i.e., time t, positions x, y, z, and angular variables θ, φ. Therefore, numerical calculation of the radiative transport equation for a human body requires massive parallel computer simulations. This year, we focused on preparing such parallel computation.

The radiative transport equation is given as follows.

$$\begin{cases} \left(\frac{1}{c}\frac{\partial}{\partial t} + s\cdot\nabla + \mu_a + \mu_s\right) I(x,s,t) \\ \qquad = \mu_s \int_{S^2} p(x,s,s') I(x,s',t)\, ds', \\ \qquad x \in \Omega, \quad s \in S^2, \quad t \in (0,T), \\ I(x,s,t) = g(x,s,t), \\ \qquad (x,s) \in \Gamma_-, \quad t \in (0,T), \\ I(x,s,0) = a(x,s), \quad x \in \Omega, \quad s \in S^2, \end{cases}$$

where c is the speed of light in the medium and $\mu_a(x), \mu_s(x)$ are the absorption and scattering coefficients, respectively. Here, $\Gamma_\pm$ is defined as

$$\Gamma_\pm = \left\{(x,s) \in \partial\Omega \times S^2;\, \pm\nu\cdot s > 0\right\},$$

where ν is the outer unit vector normal to $\partial\Omega$.

In the time-independent case for the slab geometry, we experimentally verified the use of the radiative transport equation in optical tomography [1]. That is, we calculate tomographic images from experimentally obtained data by solving the inverse transport problem using the method of rotated reference frames.

Although the method of rotated reference frames assumes simple geometry such as the slab geometry, obviously the shape of a human body is more complicated. Hence we need to use fully numerical schemes such as finite difference, which are computationally time-consuming but more flexible. Moreover, the number of source-detector pairs that can be used at the clinical stage is usually very limited. To acquire enough information to make tomographic images, it is necessary to conduct time-dependent experiments with the incident beam a short pulse. The introduction of the time-dependence significantly increases the computation time. We began by implementing the time-dependent radiative transport equation for light traveling in a human neck by focusing on a two-dimensional plane in the human neck [2]. In this way, we could test our finite-difference numerical scheme in two-dimensional space. It is now the time to use the supercomputer to bring the calculation to three-dimensional space.

References

[1] M. Machida, G. Y. Panasyuk, Z.-M. Wang, V. A. Markel, and J. C. Schotland: J. Opt. Soc. Am. A **33** (2016) 551.

[2] H. Fujii, S. Okawa, K. Nadamoto, E. Okada, Y. Yamada, Y. Hoshi, and M. Watanabe: J. Appl. Nonlin. Dynamics **5** (2016) 117.

Study of numerical methods for quantum phenonema of anisotoropic superconductors

Yasunari Tanuma
Graduate School of Engineering Science, Akita University, Akita 010-8502

The quantum effects of superconducting phenomena are a key issue in the field of condensed matter physics. While the BCS pairing state is robust against non-uniform systems, unconventional pairing states with other symmetries are rather fragile. The tunneling spectroscopy is an important experimental tool to identify unconventional superconductors. The formation of Andreev bound states (ABS) at the surface of superconductor is attributed to the anisotropy in the pairing states displaying a zero energy peak (ZEP) in the local density of states. In some cases, such bound states have a topological origin due to the bulk-edge correspondence. Therefore, the ZEP in the local density of states. strongly suggests unconventional pairing symmetries. [1]

Theoretically, the tunneling spectroscopy is formulated as the surface density of states of superconductors. The ZEP in high-T_c cuprate superconductors has been found in a number of paper. On the other hand, a splitting of ZEP due to a broken time reversal symmetry state (BTRSS) is reported in several groups. The origin is that an induced subdominant is-wave component near the surface of d-wave superconductor shifts the ABS from zero energy, and then the ZEP splits in two peaks. The BTRSS is sensitive to the atomic-scale surface roughness of the superconductor, and it is not easy to discriminate the subdominant is-wave or id' components from the tunneling spectroscopy. In this stage, it is unclear how the quantum effect of the spin-orbit interaction affects the BTRSS induced near the surface of d-wave superconductors.

In this report, we present a self-consistent calculation of the pair potentials of d-wave superconductors based on the t-Jmodel with the Rashba spin-orbit interaction. Moreover, we have been studied the surface density of states under the self-consistently determined pair potentials. As shown in Figure 1 our results is that the effect of spin-orbit interaction by changing a doping rate has the various shapes of tunneling spectra.

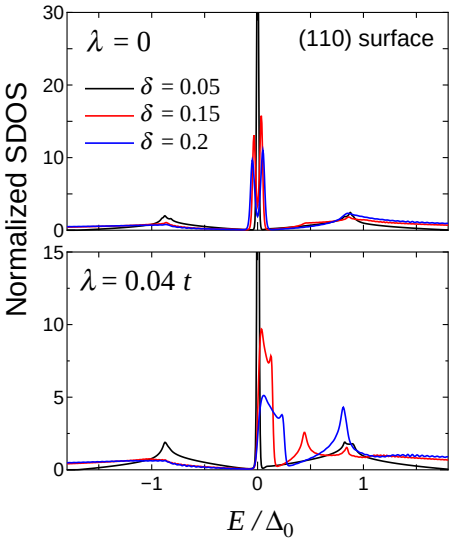

Figure 1: Normalized (110) surface density of states for $J/t = 0.4$. λ is the magnitude of Rashba spin-orbit interaction.

References

[1] Y. Tanaka, M. Sato, and N. Nagaosa: J. Phys. Soc. Jpn. **81** (2012) 011013.

Effects of a magnetic field on spin-lattice-coupled orders in pyrochlore antiferromagnets

Kazushi AOYAMA
Department of Earth and Space Science, Graduate School of Science, Osaka University
Machikaneyama-cho, Toyonaka-shi, Osaka 560-0043

1 Introduction

An antiferromagnet on the pyrochlore lattice which is a three dimensional network of corner-sharing tetrahedra, is a typical example of frustrated magnets. It has been theoretically established that with the nearest-neighbor (NN) antiferromagnetic interaction alone, classical Heisenberg spins on the pyrochlore lattice do not order at any finite temperatures. On the other hand, the corresponding magnets ACr_2O_4 (A=Zn, Cd, Hg, Mg) where the magnetic ion Cr^{3+} with spin-3/2 forms the pyrochlore lattice, undergo a first order Neel transition together with a simultaneous structural transition, which suggests strong spin-lattice coupling (SLC) in this class of antiferromagnets. In this work, we theoretically investigate effects of the SLC originating from site phonons on the spin ordering in the antiferromagnetic classical Heisenberg model on the pyrochlore lattice by means of Monte Carlo (MC) simulations.

Last year, we showed that in the case without magnetic fields, the SLC induces a first-order transition into two different types of collinear magnetic ordered states. The state realized at stronger SLC is cubic symmetric characterized by the magnetic $(\frac{1}{2}, \frac{1}{2}, \frac{1}{2})$ Bragg peaks, while that at weaker SLC is tetragonal symmetric characterized by the $(1, 1, 0)$ ones, each accompanied by the commensurate local lattice distortions [1]. This year, we examined effects of a magnetic field on the spin-latticed-coupled orders.

2 Model and numerical method

The effective spin Hamiltonian in the site-phonon model has been derived elsewhere and is given by $\mathcal{H}_{\rm eff} = \mathcal{H}_0 + \mathcal{H}_{\rm SL}$,

$$\begin{aligned}
\mathcal{H}_0 &= J \sum_{\langle i,j\rangle_s} \mathbf{S}_i \cdot \mathbf{S}_j - \sum_i \mathbf{H} \cdot \mathbf{S}_i, \\
\mathcal{H}_{\rm SL} &= -J\, b \sum_{\langle i,j\rangle} (\mathbf{S}_i \cdot \mathbf{S}_j)^2 \\
&- \frac{J\, b}{2} \sum_i \sum_{j\neq k\in N(i)} \mathbf{e}_{ij} \cdot \mathbf{e}_{ik}\, (\mathbf{S}_i \cdot \mathbf{S}_j)(\mathbf{S}_i \cdot \mathbf{S}_k),
\end{aligned}$$

where J is the antiferromagnetic exchange interaction between NN spins, the dimensionless parameter b measures the strength of the SLC, and $\mathbf{e}_{ij}$ is a unit vector connecting NN sites i and j. In $\mathcal{H}_{\rm SL}$, the first term favors collinear spin state and the second term includes effective further neighbor interactions. $\mathbf{H}$ denotes a magnetic field.

In our MC simulation, we perform 10^6 Metropolis sweeps under periodic boundary conditions at each temperature, where the first half is discarded for thermalization. Our single spin flip at each site consists of the conventional local update and a successive over-relaxation process in which we try to rotate a spin by the angle π around the local mean field. Observations are done in every 5 MC steps and the statistical average is taken over $8-10$ independent runs. Since the cubic unit cell includes 16 sites, a total number of spins N is $N = 16L^3$ for a system size L. In the present

model, we have three parameters, the strength of the SLC b, the temperature T/J, and the magnetic field H/J. A systematic numerical investigation in this parameter space has been done using the facilities of the Supercomputer Center, ISSP, the University of Tokyo.

3 Result and Discussion

As is naively expected, in-field properties of the system depend on the zero-field ordering patterns. Figure 1 shows the results for $b = 0.2$ in the weaker SLC regime. As one can see in Fig. 1 (a), there are three regions classified by the field dependence of the magnetization whose low-temperature behavior is shown in Fig. 1 (b). In the region I, the canted $(1, 1, 0)$-state is realized and the magnetization linearly increases as a function of the magnetic field. The region II corresponds to the 1/2-plateau region in which each tetrahedron takes three-up and one-down collinear spin configuration. The MC snapshot taken at a low temperature in the region II is shown in Fig. 1 (c). The $\uparrow\uparrow\uparrow\downarrow$ chains run along all the six tetrahedral bonds, and this spin state is cubic-symmetric. As the magnetic field is further increased, spins start canting. The onset of this canted state in higher magnetic fields is denoted by the boundary between the regions II and III. All the transitions from the paramagnetic phase to the magnetic ones I, II, and III, are of first order.

From neutron diffraction experiments, it has been known that the zero-field ordered states in most of the spinel chromium oxides basically involve the $(1, 1, 0)$ magnetic patterns as observed in the weak SLC regime in the present model. Furthermore, the cubic-symmetric collinear spin configuration observed in the region II is the same as the experimentally proposed spin structure in the 1/2-plateau region of ACr_2O_4 (A=Cd, Hg). These results suggest that the SLC originating from the site phonons may be relevant to the magnetic ordering in these materials.

Finally, we would like to briefly comment on in-field properties in the stronger SLC regime. As in the case of the weaker SLC, we found the 1/2-plateau in the magnetization curve, but the spin ordering at higher fields are complicated, and this matter needs further detailed investigation.

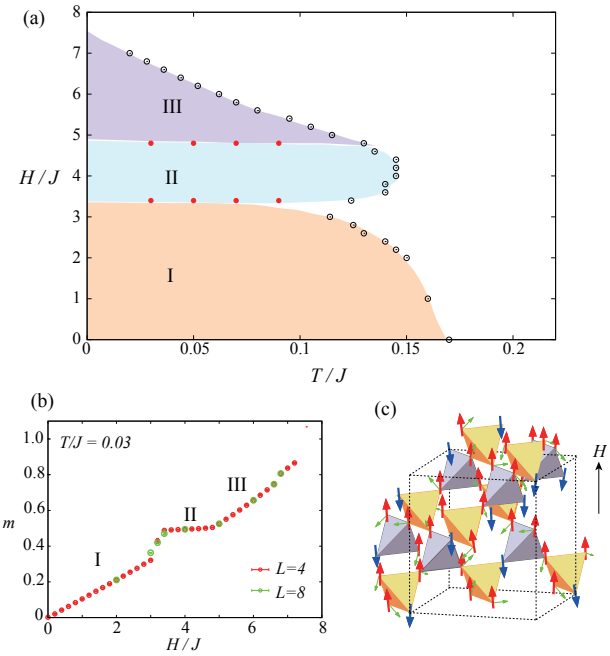

Figure 1: (a) The T-H phase diagram for $b = 0.2$ in the weaker SLC region, and (b) the corresponding magnetization curve at $T/J = 0.03$. (c) Real space spin configurations in the 1/2-plateau region [the region II in (a) and (b)], where a box represents the cubic unit cell.

References

[1] K. Aoyama and H. Kawamura, Phys. Rev. Lett. **116**, 257201 (2016).

Competition between ferroelectric and antiferroelectric order in anisotropic molecular systems

Kyohei Takae and Hajime Tanaka
Institute of Industrial Science, University of Tokyo
4-6-1 Komaba, Meguro-ku, Tokyo 153-8505, Japan

Mesoscopic and glassy dynamics in dielectric materials are of growing interests among soft matter physicists because some complex phenomena in dielectrics such as relaxor behaviour can be understood by the concept of soft matter physics, namely, hierarchical spatio-temporal cooperativity. Here, two or more cooperating/competing phase ordering produces rich physical phenomena. Particularly, we focus our attention on the coupling between polarisation and strain in dielectric materials, and aim to understand their complex behaviour by constructing a simple model exhibiting such mesoscopic dynamics and related phase transitions.

We construct a molecular model exhibiting relaxor-like behaviour and antiferroelectricity. The pair interaction consists of dipolar interaction and Lennard-Jones interaction but slightly modified to realise anisotropic molecular systems. Note that our model corresponds to Stockmayer model if molecular anisotropy vanishes, which is known to exhibit paraelectric–ferroelectric phase transition in crystalline phase. We perform molecular dynamics simulation to study how ferroelectric and antiferroelectric order can be controlled by changing material composition and molecular anisotropy.

Firstly, by introducing non-polar particles as impurities, we examine how ferroelectric order is disturbed by them [1]. By increasing the impurity concentration, we found the destruction of global ferroelectric order. Nevertheless, mesoscopic ferroelectric order still emerge in regions surrounded by the impurities. This result implies the appearance of polar nanoregion is determined by the distribution of impurities in our model. Large polarisation and strain response to external electric field is also observed due to the collective response of mesoscopically ordered regions, indicating a strong polarisation-strain coupling.

Secondly, we vary molecualar anisotropy and examine how antiferroelectric order is stabilised [2]. We determine the phase diagram by comparing the chemical potential of liquid phase, paraelectric crystalline phase, ferroelectric crystalline phase, and antiferroelectric crystalline phase. The chemical potential of the liquid phase is calculated by the Widom particle insertion methods, and that of crystals is obtained by Einstein crystal method. We found the antiferroelectric phase is stabilised for large anisotropy, which results from the coupling between polarisation and strain in our system. The phase transition also induce large lattice deformation, implying the possibility to control polarisation order by external strain.

References

[1] K. Takae and A. Onuki: J. Phys.: Condens. Matter **29** (2017) 165401.

[2] K. Takae and H. Tanaka, in preparation.

Nonequilibirum phase transition in the large scale dense hard sphere molecular dynamics simulation

Masaharu ISOBE
Nagoya Institute of Technology
Gokiso-cho, Showa-ku, Nagoya, 466-8555

The hard disk/sphere systems have been investigated as one of the simplest molecular models in the field of both equilibrium and non-equilibrium statistical physics. In this project, we investigated non-equilibrium phase transition in the hard disk/sphre model system with modern algorithms, especially for Event-Chain Monte Carlo(ECMC) [1] and Event-Driven Molecular Dynamics(EDMD) [2], where we propose the "Hybrid Scheme", namely, ECMC for equilibration and EDMD for calculation of dynamical properties [3, 4].

Facilitation in athermal molecular systems — Efficient algorithm figures out a mystery in supercompressed glassy materials—: One of the grand challenges of statistical physics is to understand whether the essential properties of glass forming materials is fundamentally thermodynamic or dynamic in origin. A perspective that favors a dynamic origin is called Dynamic Facilitation (DF) theory [5, 6, 7]. The concept of "facilitation" is used in general to indicate the ability to activate people in a meeting to exchange ideas and information with a common purpose in business and education. The "facilitation" is also observed in the microscopic molecular systems. DF theory was known to explain a wide range of empirically observed dynamical features of thermal supercooled liquids and glasses. In our present paper, the results of an international collaboration on three continents (Japan, U.S. and U.K.) devoted to investigating the applicability of DF theory to athermal systems, i.e., systems of hard particles where the relevant control parameter is pressure rather than temperature, under "supercompressed" conditions. By employing novel efficient algorithms [1, 2, 3], it was possible to find true equilibrium states and generate the phase diagram of a binary mixture of hard spheres. This allowed to study in detail the equilibrium dynamics of high density systems, showing that slow relaxation at these conditions are consistent with the predictions of DF theory generalized to systems controlled by pressure rather than temperature. In such athermal molecular systems under "super-compressed" conditions — where what is facilitated is the ability of the constituent particles to structurally relax — giving rise to correlated and cooperative dynamics, in a manner predicted by theory [8]. These results should pave the way for understanding thermal and athermal glassy materials from a unified point of view.

References

[1] E. P. Bernard, W. Krauth, and D. B. Wilson: Phys. Rev. E **80** (2009) 056704.

[2] M. Isobe: Int. J. Mod. Phys. C **10** (1999) 1281.

[3] M. Isobe: Mol. Sim. **42** (2016) 1317.

[4] M. Isobe: "Advances in the Comutational Sciences — Proceedings of the Symposium in Honor of Dr Berni Alder's

90th Birthday", edited by Eric Shwegler, Brenda M. Rubenstein, and Stephen B. Libby, World Scientific, **Chapter 6** (2017) 83.

[5] D. Chandler and J. P. Garrahan: Annu. Rev. Phys. Chem. **61** (2010) 191.

[6] L. O. Hedges, R. L. Jack, J. P. Garrahan and D. Chandler: Science **323** (2009) 1309.

[7] A. S. Keys, L. O. Hedges, J. P. Garrahan, S. C. Glotzer, and D. Chandler, Phys. Rev. X, **1** (2011) 021013.

[8] M. Isobe, A. S. Keys, D. Chandler, and J. P. Garrahan: Phys. Rev. Lett. **117** (2016) 145701.

Evaluation of quantum error correction codes' performance against realistic error models

Takanori SUGIYAMA
Graduate School of Engineering Science, Osaka University
Machikaneyama-chou, Toyonaka, Osaka 560-8531

Summary: We have studied a quantum error correction code under realistic error models. We focused on a specific code called a 1D repetition code. We have performed Monte Carlo simulations for evaluating the fault-tolerance of the code against errors with quantum coherence. The numerical results clarified that quantum coherence in errors can weaken the fault-tolerance of 1D repetition code.

Coherence of a bare quantum system is easily broken by environmental noise, and the use of methods for protecting the coherence from the noise is inevitable for implementing large-scale quantum computer. A quantum error correction code (QECC) is one of such methods for protecting logical information of quantum systems (logical qubits), which consist of multiple quantum systems (physical qubits), from noise [1]. By increasing the number of physical qubits, a QECC can make the effect of noise on the logical qubit exponentially small if strength of the noise is less than a threshold.

There are a lot of proposals of QECCs, and currently a 2D planer surface code [2] is considered as a promising candidate [3, 4]. A 2D planer surface code arranges physical qubits in a checkerboard pattern on a 2D plane. As an intermediate step to the realization, experimental groups of UCSB/Google [5] and TU Delft [6] implemented a 1D component of the code, which is called a quantum 1D repetition code. An experimental group of IBM implemented a 2D component of the code [7]. Although the numbers of physical qubits in these experiments are $O(1)$ and not enough for building large-scale quantum computer, the experimental results imply that an implementation of a quantum device using a 2D planer surface code with $O(100)$ physical qubits would be possible in the near future.

In order to check whether the device would work as desired under an effect of environmental noise, we need a theoretical method for evaluating the performance. There are two theoretical approaches to evaluate a performance of QECCs. The standard approach [8] assumes a depolarizing noise model. This approach makes it easier to analyze the performance, but the model assumed is not realistic. The other approach [9], which uses the diamond norm, does not assume specific noise models. However, this approach sacrifices the tightness of the evaluation and greatly underestimates the performance.

We proposed such a new theoretical method for evaluating QECCs' performance. Our method is applicable to both of classical and quantum noises and is tighter than the approach using the diamond norm. We applied our method to a quantum 1D repetition code, which is an important subcode of a 2D planer surface code, and we have numerically evaluated the performance against quantum noise.

We have applied the theoretical results to a classical memory with a quantum 1D repetition code, which does not tolerate an arbitrary noise but is still an important building

block of a 2D planer surface code, and hence has been implemented in recent experiments [5, 6]. We have performed Monte Carlo simulations for calculating the values of the upper bound for the following settings: The numbers of physical qubits, N, are from 5 (3 data-qubits and 2 ancilla-qubits) to 101 (51 data-qubits and 50 ancilla-qubits). The number of error detection cycles is $N-1$. In order to analyze the effect of quantumness in noise, we considered a noise model that is a probabilistic mixture of a bit-flip noise model with error rate p and a unitary noise with a mixing probability c (the case of $c=0$ corresponds to the pure bit-flip noise model). We have phenomenologically allocated the noise on each of the data-qubits and ancilla-qubits. We have chosen the minimum-weight perfect matching algorithm for the decoding and used the Blossom V matching library [10] for the numerical implementation. We performed 4×10^6 repetitions for the Monte Carlo sampling.

Our numerical results have clarified that the performances against quantum noise greatly differs from those against classical noise. In real experiments, c is not zero because there exist the energy relaxation and over/under-rotation during unitary operations on physical qubits. The standard approach is not applicable to realistic settings of experiments. We have provided a new theoretical tool, or a new classical simulator, applicable to QECC-equipped quantum devices with $O(100)$ physical qubits, which would appear in the near future, under realistic assumptions on noise.

Our results can contribute not only to the evaluation of the performance, but also to further improvement of quantum devices. For implementing large-scale quantum computer, it is required to suppress the noise as smaller than the threshold as possible, because we cannot obtain the advantage of the error decreasing via increasing N around the threshold. In order to suppress the noise, which are already tiny in current experiments, we need an appropriate guideline for further improving the design of devices, chips, and pulses. The standard approach is not appropriate for the purpose, because the realistic noise is out of the scope as mentioned above. Our results would provide an appropriate guideline for the purpose, and the detailed analysis on specific physical systems such as superconducting circuits is an open problem to be tackled.

Acknowledgements: The computation in this work has been done using the facilities of the Supercomputer Center, the Institute for Solid State Physics, the University of Tokyo. This work was supported by JSPS Research Fellowships for Young Scientists (PD:H27-276) and the Grant-in-Aid for Young Scientists (B) (No.24700273).

References

[1] D. A. Lidar and T. A. Brun (ed.), *Quantum Error Correction* (Cambridge University Press, 2013)

[2] S. B. Bravyi and A. Y. Kitaev, arXiv:9811052 [quant-ph].

[3] J. M. Martinis, npj Quantum Information **1**, 15005 (2015).

[4] J. M. Gambetta, J. M. Chow, and M. Steffen, arXiv:1510.04375 [quant-ph].

[5] J. Kelly et al., Nature **519**, 66 (2015).

[6] D. Riste et al., Nature Commun. **6**, 6983 (2015).

[7] A. D. Córcoles et al., Nature Commun. **6**, 6979 (2015).

[8] E. Dennis et al., J. Math. Phys. **43**, 4452 (2002).

[9] P. Aliferis, Chap. 5 in *Quantum Error Correction* (Cambridge University Press, 2013)

[10] V. Kolmogorov, Math. Prog. Comp. **1**, 43 (2009)

Analysis of Topological Systems with Real Space Structures

Toshikaze KARIYADO
International Center for Materials Nanoarchitectonics (MANA), NIMS
Namiki, Tsukuba, Ibaraki 305-0044

This year, we have mainly focused on the electronic structure of antiperovskite Ba_3SnO. A_3EO (A=Ca,Sr,Ba and E=Sn,Pb) is predicted to be a topological crystalline insulator, but the first-principles calculation indicates the gap at the Fermi energy is tiny because of the cubic symmetry of the crystal [1]. More specifically, around the k-points of gap minima, the electronic state is described as Dirac fermions. For the stability of the possible topological crystalline insulator phase, it is better to have large gap. Then, in order to find out a way to have a larger topological gap in this series of materials, we investigate (i) the effect of the lattice distortion experimentally found [2], and (ii) possible heterostructures where the A sites are substituted layer-by-layer, both of which break the cubic symmetry, by means of the first-principles calculation.

For the first-principles calculation, we have employed the parallelized version of QuantumEspresso package [3]. In the calculations for the distortion effect, the number of atoms in a unit cell is still not so large, and then, the parallelization is really efficient by using the k-point parallelization. On the other hand, for the heterostructure calculation, especially when the period of layer-by-layer alternation is large, we rather divide each work for a k-point into pieces, and distribute them. This is rather different from the k-point parallelization, but anyway, enables us to calculate the electronic structure with relatively large real space structures.

Figure 1 shows the band structure for Ba_3SnO with the distorted crystal structure. As is expected, the gap at the Dirac nodes becomes visible in this energy scale. (Originally, the Dirac nodes are exactly gapless, or have tiny gap of the order of meV.) However, the deviation of the crystal structure from the original cubic structure itself is not significant, the gap size is still small comparing with the typical energy scale of the band structure. The heterostructure induces the sizable gap depending on the position of the Dirac nodes in the Brillouin zone [4].

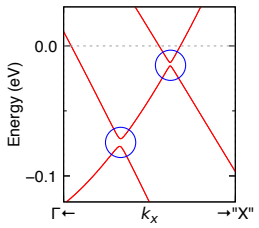

Figure 1: Band structure for Ba_3SnO with distorted structure.

References

[1] T. Kariyado and M. Ogata: J. Phys. Soc. Jpn. **80** (2011) 083704; T. H. Hsieh, J. Liu, and L. Fu: Phys. Rev. B **90** (2014) 081112.

[2] J. Nuss *et al.*: Acta Cryst. B**71** (2017) 300.

[3] P. Giannozzi *et al.*: J. Phys.: Condens. Matter **21** (2009) 395502.

[4] T. Kariyado, in preparation.

Electronic states of bioluminescence related molecules

Miyabi HIYAMA
Institute for Solid State Physics, University of Tokyo
Kashiwa-no-ha, Kashiwa, Chiba 277-8581

In firefly bioluminescence, the emission occurs due to the luciferin-luciferase reaction. Figure 1 shows the reaction process for firefly luciferin-luciferase reaction. In this process, the emitter, Oxyluciferin, is produced by the oxidation reaction of the substrate, Luciferin, via two intermediate molecules which are Luciferyl adenylate (Luciferyl-AMP) and 4-membered dioxetanone (Dioxetanon). According to the previous studies, we found that the protonated/deprotonated chemical species of Oxyluciferin and Luciferin present in aqueous solutions and that the ratio of these concentrations depends on the pH values of solution [1]-[2]. Thus, the molecular structures for intermediate molecules of the luciferin-luciferase reaction could also depend on the pH values of solutions.

In this year, we calculated the electronic potential energies and free energy profiles for Liuciferin, Oxyluciferin, luciferyl-AMP, and Dioxetanon, and their deprotonated chemical species [3] to elucidate this emission process across the pH range of 7-9. All calculations were performed using the GAUSSIAN09 [4] program on system B of Super Computer Center in ISSP.

From these relative free energies, it was found that the oxidation pathway changes from Luciferin → deprotonated Luciferyl-AMP → deprotonated Dioxetanone → Oxyluciferin to deprotonated Luciferin → deprotonated Luciferyl-AMP → Dioxetanone → Oxyluciferin with increasing pH value. This indicates that deprotonation on the hydroxy group of benzothiazole ring occurs during the formation of Dioxetanone at pH 7-8, whereas Luciferin in the reactant has a deprotonated of hydroxy group form at pH 9.

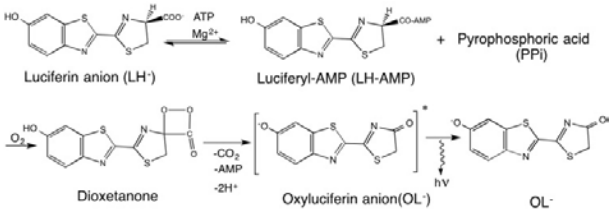

Figure 1: luciferin-luciferase reaction in firefly bioluminesncece

References

[1] Hiyama et al.: Photochem. Photobiol.**91** (2015) 819.; **91** (2015)74. ; **90** (2014) 820.; **90** (2014) 35.; **89**(2013) 571.; **88** (2012) 889.

[2] Hiyama et al.: Chem. Phys. Lett. **577** (2013) 121.

[3] M. Hiyama, H. Akiyama, and N. Koga : Luminescence: The Journal of Biological and Chemical Luminescence (2017) *in press*.

[4] Gaussian 09, Revision D.01, M. J. Frisch et al.

Topological analysis of membrane systems using persistent homology

Fumiko Ogushi
AIMR, Tohoku Unive.
Katahira 2-1-1, Aoba-ku, Sendai, 980-8577

Biological membrane involves wide variety of lipid molecules and forms complicated structures with various concave-convex with large-scale changes in cell-cycle progressions, like membrane fusion, fission, and vesicular transportation, Golgi formations, and so on. In a cell, lipid molecules distribute heterogeneously affecting membranes structures. Moreover, compositions and distributions of lipids are not stationary. Flexibility of lipid redistribution is one of the most important phenomena to overcome the limitation of model membrane to real biological membrane.

This year, we investigated structural features of multi lipid membranes using persistent homology. The multi lipid membrane is made up with water molecules and two different types of lipid molecules, 20:4 PC (DAPC) and diacylglicerol (DAG), which have different Gaussian curvatures. Three structures of membranes, Lamella, Inverse Hexagonal, and Sponge-like structures, are examined by molecular dynamics simulation. Such a complex structures in three dimension are hard to distinguish. Thus, we use persistent homology to analyze membrane morphologies. Persistent homology is an algebraic tool for computing topological features of data. It can systematically characterize geometric objects and capture the topological properties such as rings and cavities, and provide the metrics of these topological properties. In recent years, persistent homology and its graphical representation, persistent diagram, can be computed efficiently [1, 2, 3]. Some types of condensed systems are well distinguished its local structures using persistent homology and PDs [4, 5].

We calculated persistent homology for DAPC, DAG, and water molecules. Comparing with persistent diagrams of equilibrium structures, we succeeded to capture topological features of different membrane systems and localization of DAGs in Sponge-like membranes. Moreover, persistent diagrams show that DAGs in Sponge-like membrane do not form any characteristic formations.

References

[1] Perseus [online] Available at `www.math.rutgers.edu/vidit/perseus.html`

[2] PHAT [online] Available at `https://code.google.com/p/phat`

[3] CGAL [online] Available at `https://cgal.org`

[4] T. Nakamura, Y. Hiraoka, A. Hirata, E. G. Escolar, and Y. Nishiura, Nanotechnology, 26 (2015) 304001.

[5] Y. Hiraoka, T. Nakamura, A. Hirata, E. G. Escolar, K. Matsue, and Y. Nishiura, PNAS, 113, 25, (2016) 7035

Numerical Study of One Dimensional Frustrated Quantum Spin Systems

Kazuo HIDA
Division of Material Science, Graduate School of Science and Engineering
Saitama, Saitama 338-8570

1 Ground-State Phase Diagram of $S = 1$ Diamond Chains[1]

The ground-state phase diagram of a spin-1 diamond chain is investgated. The Hamiltonian is given by,

$$\mathcal{H} = \sum_{l=1}^{L} \Big[\boldsymbol{S}_l \boldsymbol{\tau}_l^{(1)} + \boldsymbol{S}_l \boldsymbol{\tau}_l^{(2)} + \boldsymbol{\tau}_l^{(1)} \boldsymbol{S}_{l+1} + \boldsymbol{\tau}_l^{(2)} \boldsymbol{S}_{l+1} + \lambda \boldsymbol{\tau}_l^{(1)} \boldsymbol{\tau}_l^{(2)} \Big], \quad (1)$$

where $\boldsymbol{S}_l$ and $\boldsymbol{\tau}_l^{(\alpha)}$ $(\alpha = 1, 2)$ are spin operators with magnitude 1. Owing to a series of conservation laws $\forall l$ $[\boldsymbol{T}_l^2, \mathcal{H}] = 0$, where $\boldsymbol{T}_l = \boldsymbol{\tau}_l^{(1)} + \boldsymbol{\tau}_l^{(2)}$, any eigenstate of this system can be expressed using the eigenstates of finite odd-length chains or infinite chains with spins 1 and 2.

The ground state undergoes quantum phase transitions with varying λ as shown in Fig. 1. In addition to the various paramagnetic DCn phases, which consists of clusters with n consecutive nonvanishing T_ls, the Haldane phase and the ferrimagnetic phases with 1/3 and 1/6 of the saturated magnetization are found. Among them, the ferrimagnetic phase with 1/6 magnetization is accompanied by the spontaneous breakdown of translational symmetry. The ground state energy of the DCn phase is calculated by the Lanczos numerical diagonalization and finite-size DMRG methods. That of the DC∞ phase is estimated by the iDMRG method.

Exact upper and lower bounds for the phase boundaries between these phases are also obtained.

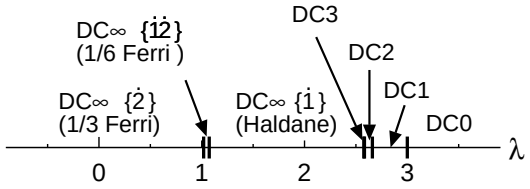

Figure 1: Ground state phase diagram of the $S = 1$ diamond chain..

(collaborator : Ken'ichi Takano)

2 Partial Ferrimagnetism in $S = 1/2$ Heisenberg Ladders with Ferromagnetic-Antiferromagnetic Legs and Antiferromagnetic Rungs[3]

The $S = 1/2$ Heisenberg ladders described by the Hamiltonian

$$\mathcal{H} = -J_1 \sum_{i=1}^{L} \boldsymbol{S}_{i,1} \cdot \boldsymbol{S}_{i+1,1} + J_2 \sum_{i=1}^{L} \boldsymbol{S}_{i,2} \cdot \boldsymbol{S}_{i+1,2} + R \sum_{i=1}^{L} \boldsymbol{S}_{i,1} \cdot \boldsymbol{S}_{i,2} \quad (2)$$

are investigated, where $\boldsymbol{S}_{i,a}$ is the spin-1/2 operator. For $J_1 = J_2$, the rung-dimer state is the exact ground state down to a finite critical value of R as shown by Tsukano and Takahashi[4]. We consider the case $-J_1 < 0$,

$J_2 > 0$ and $R > 0$ in general. The ground-state phase diagram is determined by the Lanczos numerical diagonalization method for $L = 12$ as shown in Fig.2. In the Lieb-Mattis ferrimagnetic phase, $M = L/2 = 6$. In the partial ferrimagnetic phase, $0 < M < L/2$. It is found that the partial ferrimagnetic phase extends over a wide parameter range.

The ground-state phase diagram is studied also analytically based on the mapping onto the nonlinear σ model[5] and the perturbation expansion from the strong-rung limit. The results support the overall phase diagram obtained numerically as shown in Fig. 2.

The finite-temperature susceptibility is also calculated by the canonical thermal pure quantum state method.[6] The χT^2-$T^{1/2}$ plot in Fig. 3 suggests that the susceptibility behaves as $\chi \sim T^{-2}$ in the partial ferrimagnetic phase as well as in the Lieb-Mattis ferrimagnetic phase. This behavior is the same as that of the ferromagnetic Heisenberg chain studied by Takahashi and Yamada.[7]

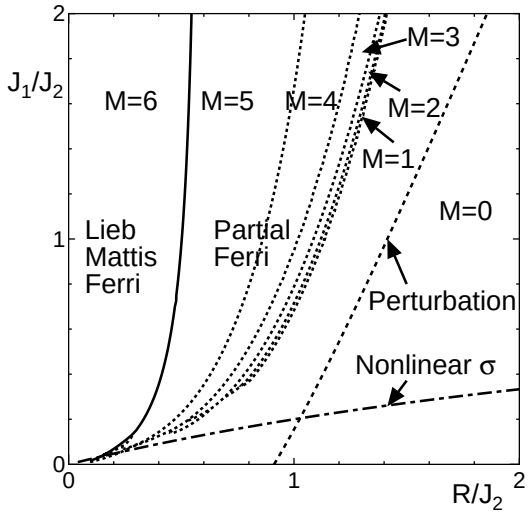

Figure 2: Ground state phase diagram of the $S = 1/2$ Heisenberg ladder (2) with $L = 12$. The spontaneous magnetization is denoted by M. The dashed and dash-dotted lines are the nonmagnetic-partial ferrimagnetic phase boundaries calculated by the perturbation expansion from the strong-rung limit and mapping onto the nonlinear σ model, respectively.

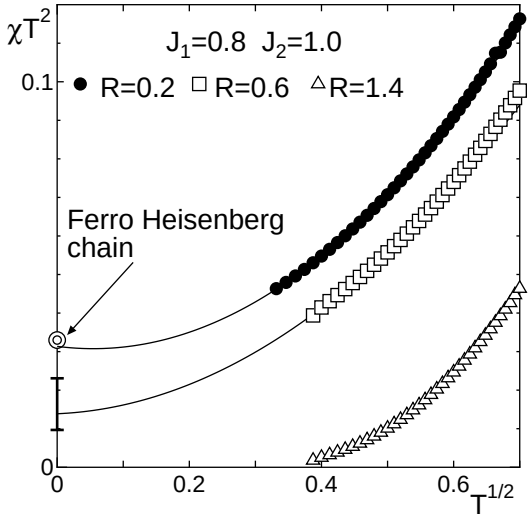

Figure 3: Plot of χT^2 against $T^{1/2}$. The size extrapolation is carried out by the Shanks transform from $L = 8, 10$ and 12.

(collaborator: Kazutaka Sekiguchi)

This work is supported by JSPS KAKENHI Grant Numbers JP25400389 and JP26400411.

References

[1] K. Hida and K. Takano, J. Phys. Soc. Jpn. **86**, 033707 (2017).

[2] K. Takano, K. Kubo, and H. Sakamoto, J. Phys.: Condens. Matter **8**, 6405 (1996).

[3] K. Sekiguchi, Master Thesis, Saitama University (2017) [in Japanese].

[4] M. Tsukano and M. Takahashi, J. Phys. Soc. Jpn. **66**, 1153 (1996).

[5] S. Furuya and T. Giamarchi, Phys. Rev. B. **89**, 205131 (2014)

[6] S. Sugiura and A. Shimizu, Phys. Rev. Lett. **111**, 010401 (2013)

[7] M. Takahashi and M. Yamada, J. Phys. Soc. Jpn. **54**, 2802 (1985).

3.5 SCCMS projects

First-Principles Electronic-Structure Calculations and Device/Process Simulations

G. Mil'nikov, N. Mori
Graduate School of Engineering, Osaka University
Suita Osaka 565-0871
J.-I. Iwata, A. Oshiyama
Department of Applied Physics, The University of Tokyo
Hongo, Tokyo 113-8656

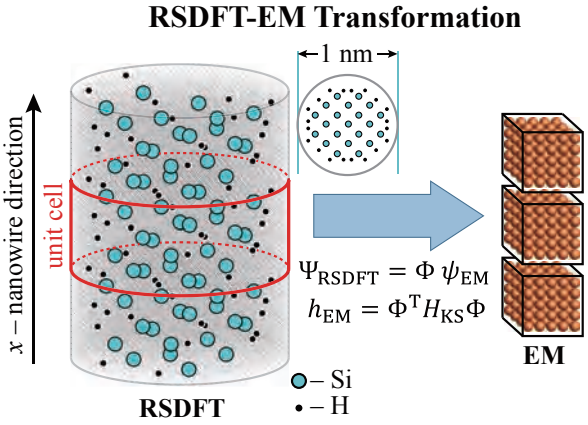

Figure 1: EM transformation of the RSDFT Hamiltonian. The left panel shows mesh points (small gray dots) in three unit cells of a [100] Si nanowire with diameter of 1 nm. The rectangular $N_{\mathrm{RSDFT}} \times N_{\mathrm{EM}}$ real-valued basis matrix Φ is constructed in order to obtain a computationally inexpensive N_{EM}-dimensional model of a quantum chain with Hamiltonian h_{EM} which reproduces the scattering states Ψ_{RSDFT} within the transport energy interval.

With continuing advances in semiconductor fabrication technology, it is predicted that the physical channel length in electronic devices will scales down to sub-10 nm regime. Semiconductor nanowires (NWs) have been recently considered as promising novel devices to realize the scaling merit in the ultra-small scale. However, it is also anticipated that their practical implementation will face technical issues such as characteristics fluctuations. Theoretical study of the device performance of NW transistors requires detailed atomistic transport simulations based of first-principles modeling of semiconductor nanostructures.

We here report on our recent progress in developing a first-principle quantum transport simulator based on the real-space density functional theory (RSDFT) [1] and the Troullier-Martins pseudopotentials [2]. The RSDFT method has been shown to be applicable to large atomic clusters and nanowire structures which enables one to obtain an optimized nanostructure geometry and the Kohn-Sham Hamiltonian in the real-space representation. In this work, we utilize the R-matrix method [3] and perform RSDFT-based non-equilibrium Green's function (NEGF) transport simulations in a ballistic regime

In scope of the R-matrix method, the computational domain is split into a set of fragments (i.e. small clusters of mesh points) and the R-matrix propagation algorithm is used for constructing the Green's function in the close device with no leads attached. The contact self-energies are computed independently at the end of calculation. This would generally involve a difficult numerical task of computing all the outgoing/decaying Bloch states in the leads. However, since the current is actually formed by mobile carriers in a few scattering states, one can make use of an appropriate low-dimension equivalent transport model (EM) to obtain the relevant physical solutions within a transport energy interval (Fig. 1). Small size of the EM representation greatly simplifies atomistic transport simulations [4].

We have developed a parallel computer code for

constructing the EM representation within an arbitrary finite energy interval. The primary low-dimensional atomistic basis is extracted from a set of Bloch states computed at equidistant set of k-points in the Brillouin zone by the FEAST method [5]. Extra basis states are further constructed by minimizing the number of branches in the electronic band structure. Effective algorithms have been developed for optimizing parameters in the variational functional [4] and choice of the initial variational state. The numerical tests in a thin SiNW with diameter of 1 nm have confirmed applicability of the method within a wide energy range in both conduction and valence bands. For an ideal nanostructure, the EM provides an effective quantum chain model with equivalent transport characteristics. In general case, one can still make use of the EM in the lead area in order to compute the equilibrium states in the leads and obtain the contact self-energies in the NEGF formalism. The numerical tests confirm that such mixed EM-RSDFT representation causes no unphysical reflection at the contact interfaces and describes correctly the electron transport through the device channel.

Figure 2 presents an example of calculated IV characteristics in a [100] NW MOSFET with 10 nm gate length and 1 nm channel diameter. In these simulations, we have assumed a continuous dielectric layer in the insulator region and used the bulk parameters to account for polarization effects in the device electrostatics. More accurate analysis would require self-consistent calculation of the polarization charge distribution in the nanostructure which can also be greatly accelerated by implementing the EM representation.

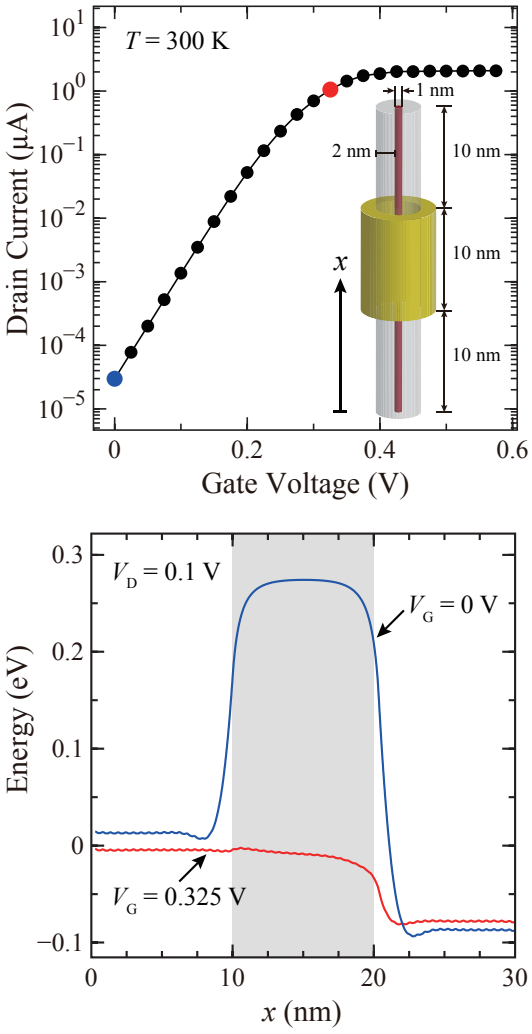

Figure 2: Current-voltage characteristics and potential profiles in a n-SiNW MOSFET. The first-principle RSDFT method is only used in the silicon core region. The oxide layer in the gate region is treated as a continuous dielectric media, and the device electrostatics is calculated using the bulk parameters $\epsilon_{\mathrm{Si}} = 11.9$ and $\epsilon_{\mathrm{SiO_2}} = 3.8$.

References

1. J.-I. Iwata *et al.*,, Journal of Computational Physics 229, 2339 (2010).
2. N. Troullier and J. L. Martins, Physical Review B 43, 1993 (1991).
3. G. Mil'nikov, N. Mori, and Y. Kamakura, Physical Review B 79, 235337 (2009).
4. G. Mil'nikov, N. Mori, and Y. Kamakura, Physical Review B 85, 035327 (2012).
5. E. Polizzi, Physical Review B 79, 115112 (2009).

Nano-Optical Response Theory and Computational Design of Photo-Electronic Functional Devices

Katsuyuki NOBUSADA

Institute for Molecular Science,

Myodaiji, Okazaki, Aichi 444-8585

Optical response of materials provides the basis for understanding their essential physicochemical properties and these optical properties are the key ingredient in developing new optoelectronic or photo-electronic devices. In conventional theoretical approaches to optical response of materials, two conditions are usually assumed:

(i) A scale of wavelength of an incident light is considered to be much longer than the material size, *i.e.*, dipole approximation. Then, a target material is well approximated by a point dipole and the dipole feels a spatially uniform electromagnetic field.

(ii) Electric polarization in material induced by incident light excitation inevitably generates a new electromagnetic field, referred to as an "optical near-filed (ONF)." However, such a self-consistent light-matter (LM) interaction between electron and electromagnetic field dynamics is ignored.

Recent development of nanofabrication and nano-optical techniques requires a more general optical response theory fully taking account of *nonuniform and self-consistent* LM interactions.

We have so far been developing a nano-optical response theory and a computational program to describe full (nonuniform and self-consistent) LM interactions with the aim of understanding the ONF excitation dynamics in nanostructures of more than ten-nanometers in size. Electron dynamics in nanostructures interacting with an electromagnetic field is described by the time-dependent Kohn-Sham equation, whereas electromagnetic field dynamics is represented by the microscopic Maxwell's equations. The nonuniform LM interaction is taken into account in the vector potential and the self-consistent LM interaction is described by solving the electron and electromagnetic field coupled equations self-consistently. The coupled equations are solved numerically by using our developed computational program (GCEED: *Grid-based Coupled Electron and Electromagnetic field Dynamics*). Our computational approach is based on a finite-difference method in real-time and real-space. Since the approach employs very simple algorithms, it is highly suitable for massively parallelized computations. By using GCEED, we elucidated unique optical response phenomena due to the ONF excitation

dynamics. More specifically, second harmonic excitation of a para-dinitrobenzene molecule [1] and direct wave vector excitation of a silicon semiconductor have been investigated. These theoretical findings are expected to design photo-electronic functional devices.

We also launched a project of computational design of heterogeneous catalysts to develop efficient and commercially appealing ones, thus reducing the use of expensive rare catalytic metals [2-4]. The calculations were carried out by using the first-principles Car-Parrinello molecular dynamics approach. The theoretical approach allows us to treat dynamical chemical reaction processes taking account of the effects of temperature and nonequilibrium interactions on a heterogeneous surface or an interface.

References

[1] M. Yamaguchi and K. Nobusada, J. Phys. Chem. C **120**, (2016) 23748.

[2] K. Koizumi, K. Nobusada and M. Boero, *Phys. Chem. Chem. Phys.* **19**, (2017), 3498.

[3] K. Koizumi, K. Nobusada and M. Boero, *Chem. Eur. J.* **23**, (2017) 1531.

[4] K. Koizumi, K. Nobusada and M. Boero, *Phys. Chem. Chem. Phys.* **18**, (2016) 20708.

Superconducting correlations of nonequilibrium states

Kota Ido, Takahiro Ohgoe and Masatoshi Imada

Department of Applied Physics,

The University of Tokyo, Hongo 7-3-1, Bunkyo-ku, Tokyo 113-8656

Realizing superconductivity at room temperature is one of dreams in condensed matter physics. Although the highest superconducting critical temperature T_c at ambient pressure has been recorded in copper oxide superconductors around 130 K decades ago, it has essentially remained unchanged [1]. One reason would be that the strong effective attraction between electronic carriers required for higher T_c unavoidably drives the tendency for charge inhomogeneities. In order to circumvent this difficulty, we need to pursue a new way for controlling and enhancing superconductivity.

Recently, superconducting properties such as gap formations above room temperatures were reported in pump-probe laser measurements with the intension to excite coherent phonons in cuprates [2, 3]. These studies have shed new light on the realization of room-temperature superconductivity by utilizing nonequilibrium conditions.

In this project, we have proposed an alternative possibility ascribed to a mechanism more generic to strongly correlated electron systems. Our strategy is to control electron correlations by using the dynamical localization effect [4], where the electron hopping is effectively suppressed by the intense alternating-current electric field at high frequency. We are also inspired by recent finding that the effective attraction between carriers increases from intermediate to strong coupling regions in strongly correlated electron systems [5].

To achieve our goal, we have performed the many-variable variational Monte Carlo (mVMC) [6, 7] calculations for the Hubbard model on square lattice under laser irradiation introduced by means of the Peierls substitution. The mVMC method is capable of providing us flexible and accurate quantum states in correlated electron systems for not only equilibrium but also nonequlibrium at zero temperature.

As a result, we have found that the superconductivity can be enhanced by strong laser irradiation. We have shown that this enhancement is caused by an intrinsic effect of the dynamical localization. More importantly, this enhancement is numerically achieved without causing substantial charge inhomogeneities in contrast to the equilibrium ground state. We have also found that the dynamical superconductivity is subject to the Higgs oscillations during and after the irradiation. Our findings have revealed a way to enhance superconductivity that is inaccessible in equilibrium in strongly correlated electron systems.

References

[1] B. Keimer *et al.*: Nature **518** (2015) 179.

[2] W. Hu *et al*.: Nat. Mater. **13** (2014) 705.
[3] S. Kaiser *et al*.: Phys. Rev. B **89** (2014) 184516.
[4] D. H. Dunlap and V. M. Kenkre: Phys. Rev. B **34** (1986) 3625.
[5] T. Misawa and M. Imada: Phys. Rev. B **90** (2014) 115137.
[6] D. Tahara and M. Imada: J. Phys. Soc. Jpn. **77** (2008) 114701.
[7] K. Ido, T. Ohgoe, and M. Imada: Phys. Rev. B **92** (2015) 245106.

First-Principles Phase Field Mapping I

Kaoru Ohno

Department of Physics, Faculty of Engineering Science,

Yokohama National University, Tokiwadai, Hodogaya-ku, Yokohama 240-8501

To perform, for example, accurate mapping of first-principles results to phase field models, it would be necessary to perform a lot of first-principles calculations to collect important information on (1) the behavior of variety of chemical reactions and (2) the relationship between the geometrical and electronic structures of various materials. For the purpose of (1), we performed first-principles molecular dynamics simulations of the chemical reactions of carbon monoxide (CO) and hydrogen atoms to produce methanol by using time-dependent density functional theory (TDDFT) and time-dependent GW (TDGW) method in particular for the electronic excited state for the first time [1]. For the purpose of (2), we also performed various (ferromagnetic and anti-ferromagnetic) crystalline phases of MnO_2 [2] and various cap structures shown in Fig. 1, with which one side of the armchair carbon nanotubes are terminated [3], and clarified the relationship between their geometrical and electronic structures. Last, We investigated a mechanism of generating a screw dislocation of graphite and proposed a way to create a carbon nanocoil inside an insulating SiO_2 cylinder with a bottom surface and a pillar at the center [4].

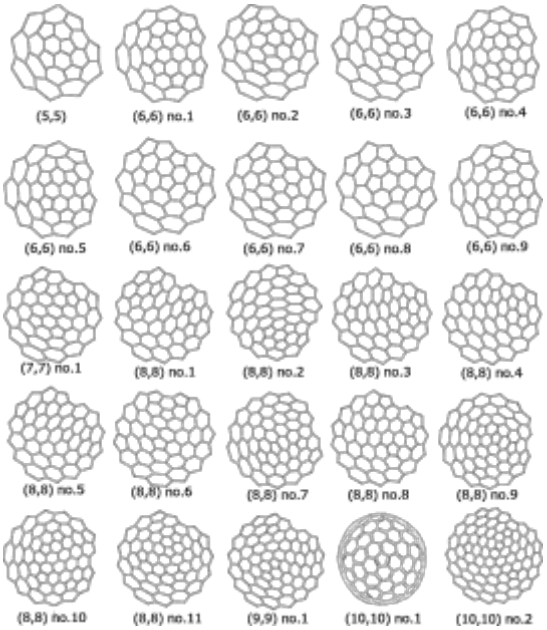

Fig.1 Various cap structures of armchair carbon nanotubes investigated in Ref. [3].

References

[1] T. N. Pham, S. Ono, and K. Ohno, J. Chem. Phys. **144**, 144309;1-6 (2016).

[2] Y. Noda, K. Ohno, and S. Nakamura, Phys. Chem. Chem. Phys. **18**, 13294-13303 (2016).

[3] S. Ono, K. Tanikawa, and K. Ohno, J. Chem. Phys. **145**, 024702;1-6 (2016).

[4] S. Battacharyya, S. Otake, S. Ono, R. Kuwahara, and K. Ohno, Advances in Materials Physics and Chemistry **6**, 113-119 (2016).

First-Principles Phase Field Mapping II

Kaoru Ohno

Department of Physics, Faculty of Engineering Science,

Yokohama National University, Tokiwadai, Hodogaya-ku, Yokohama 240-8501

To perform, for example, accurate mapping of first-principles results to phase field models, it would be necessary to perform accurate and reliable first-principles calculations. For this purpose, we performed self-consistent GW total energy calculation of He dimer with different interatomic distances using TOMBO [1] and derived the adiabatic potential between He atoms. Then, using it, we solved the Schrödinger equation for the two He system and estimated the van der Waals interaction between two He atoms. Surprisingly, the resulting expectation value for the interatomic distance of He dimer is quite large (~ 35 Å) [2]. In order to obtain accurate photoelectron (PE) and photoabsorption spectra, we performed for the first time [3] the self-consistent GWΓ calculation for small molecules using TOMBO. The accuracy of the result is comparable or higher than the result of the multi-reference single & double configuration interaction method as shown in Tables I and II. Last, we proved that the PE spectroscopy and therefore the quasiparticle (QP) theory can be applied to an arbitrary initial excited eigenstate [4]. The validity of the present theory for some initial excited eigenstates is tested using the one-shot GW approximation using TOMBO for several atoms and molecules [4].

TABLE I. Ionization potential (IP), electron affinity (EA), and optical gap E_g^{opt} (corresponding to $^2S \rightarrow {}^2P$ and $^2B_2 \rightarrow {}^2A_1$ transitions) of Na and Na_3 (in units of eV).

	Na			Na_3		
	IP	EA	E_g^{opt}	IP	EA	E_g^{opt}
G_0W_0	5.15	0.41	1.32	4.10	1.14	0.53
GW	5.40	0.33	2.23	4.64	0.51	1.91
LGW	5.23	0.42	2.18	4.48	0.66	1.92
$LGW\Gamma_v$	5.01	0.60	2.00	4.08	1.04	1.57
$LGW\Gamma_W$	5.12	0.58	2.16	4.04	1.15	1.60
MRDCI	4.97[a]	0.44[b]	1.98[b]	3.76[c]	1.07/1.17[b]	1.61[b]
Expt.	5.14[d]	0.55[e]	2.10[f]	3.97[g]	1.02/1.16[h]	1.65[i]

TABLE II. IP, EA, and E_g^{opt} (corresponding to the $^3\Sigma_g^- \rightarrow {}^3\Sigma_u^-$ transition) of B_2, and IP and E_g^{opt} (corresponding to the $^1\Sigma_g^+ \rightarrow {}^1\Pi_u$ transition) of C_2H_2 (in units of eV).

	B_2			C_2H_2	
	IP	EA	E_g^{opt}	IP	E_g^{opt}
G_0W_0	9.21	2.18	2.44	11.05	5.01
GW	9.97	1.76	3.94	11.65	8.39
LGW	9.79	1.94	3.75	11.44	8.23
$LGW\Gamma_W$	9.87	1.91	3.84	11.48	8.25
MRDCI	9.48[a]	2.0[b]	3.85[c]	11.21[d]	(8.06)[e]
Expt.	10.3±0.6[f]	1.8±0.4[g]	3.79[h]	11.49[i]	8.16[j]

References

[1] S. Ono, Y. Noguchi, R. Sahara, Y. Kawazoe, and K. Ohno, Comp. Phys. Commun. **189**, 20-30 (2015).

[2] T. Shoji, R. Kuwahara, S. Ono, and K. Ohno, Phys. Chem. Chem. Phys. **18**, 24477-24483 (2016).

[3] R. Kuwahara, Y. Noguchi, and K. Ohno, Phys. Rev. B **94**, 121116(R)-1;5 (2016).

[4] K. Ohno, S. Ono, and T. Isobe, J. Chem. Phys. **146** (8), 084108;1-15 (2017).

Energy conversion and storage – electric energy

Osamu Sugino

Institute for Solid State Physics,

The University of Tokyo, Kashiwa-no-ha, Kashiwa, Chiba 277-8581

We have studied the structure and catalytic property of a zirconia (ZrO_2) surface, which has been developed as the post platinum cathode material of a future fuel cell. Zirconia is attracted attention because it is very stable but can efficiently catalyze the oxygen reduction reaction (ORR) when partially reduced and doped with nitrogen atoms. To explain how and why ORR occurs, we did a first-principles calculation of the electronic structure using the VASP package implemented in the ISSP supercomputer.

The surface was modeled using ZrO_2(101), which is the most stable among the tetragonal surfaces. The 2x2 ZrO_2(101) was prepared as shown in Fig. 1 and let water molecules adsorb to represent the complex hydrated surface. The slab model was then doped with up to two nitrogen atoms and removed by up to one oxygen atom to mimic the doped and reduced interface. The surface was then covered with ORR intermediates such as O and OH under all possible coverage conditions to investigate the ORR pathways.

The calculated adsorption energy of an oxygen atom is negative indicating that it is not adsorbed on the surface and therefore is nonreactive when undoped. When doped, the

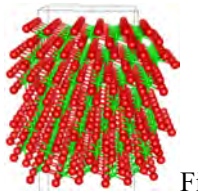

Fig. 1: ZrO2(101) model.

adsorption energy is 0.22 eV for a certain configuration of the impurities, indicating that the surface can be made reactive by doping.

The obtained free-energy profile of ORR shows that the activation barrier of the whole reaction is half an eV because of too weak binding of an oxygen molecule, indicating that the surface is not so reactive even after doping and thus does not model the real catalyst.

Nevertheless, our calculation shows that ORR occurs without being hampered by the two-electron reduction process to produce a hydrogen peroxide in consistent with experiments. Since the two-electron reduction usually occurs on an electrocatalyst of weak oxygen adsorption, such as gold, the zirconia surface is exceptional. We find that this behavior is due to the complex hydrated surface structure; the two-electron reduction is hindered by the OH adsorbed near the reaction site. Note that the complex hydrated structure requires us to use a quite large unit cell for the calculation, which is infeasible with smaller computers.

Slow Dynamics in Ionic Liquids

Hailong Peng and Hayato Shiba
Institute for Materials Research, Tohoku University
2-1-1 Katahira, Aoba-ku, Sendai 980-8577

Ionic liquids (ILs), recently, are attracting tremendous interests both in application and fundamental research, due to their outstanding thermo-physical and chemical aspects. One of the features is the low glass-transition temperature, that can be below the room temperature. Ability of high supercooling endorses ILs promising as electrolytes, solvent for many organic and inorganic liquids. Our focus, here, is to understand the slow dynamics in ILs, especially on the aspect of alkyl-chain length and electrostatic interaction.

The systems we investigate is imidazolium-based ILs, 1-Alkyl-3-methylimidazolium phosphate and borate [1], which is a prototype of hydrophobic and hydrophilic system respectively. For the imidazolium family, a distinguishing pre-peak is found in the static structure factors, indicating a still unclear mesoscopic ordered structure in liquid state (at a length scale about 10 nanometers) [2]. This demands large length scale simulation. On the ISSP clusters, three different system sizes will be investigated, i.e., 1000, 8000, and 27000 ion pairs, which is roughly corresponding to 27000, 216000, and 729000 atoms in the simulation box. As the dynamics of the system is very slow at the temperature near room-temperature, long-time structural relaxation is needed, which will be about 10-100 nanoseconds.

In order to elucidate the role played by the non-charged alkyl-chain and the charges on the head of cations and anions for the dynamics of the system, two series of systems has been numerically investigated. One is systematic change of the chain-length, varying from 2 to 16 carbons on the alkyl chain. The other approach is charge-scaling, where the charges on the ions will be scaled in the range 0.6 to 1 proton. Detailed analysis on the effect of molecular geometry and electrostatics is ongoing, on which we plan forthcoming publications in a near future.

Let us mention brifly our plan. For analysis of the dynamics, usual two- (and four-) point correlation function will be calculated. These correlators would show systematic change as the chain-length and scaled charges. The vibrational density of states is another candidate to be analyzed, in terms of how the extra vibrational modes (e.g. optic modes) affect the relaxation behavior of the system, which is absent in usual glassy systems (e.g. metallic melts, colloids, polymers, and granular materials).

References

[1] X. Zhong, Z. Liu, and D. Cao: J. Phys. Chem. B **115** (2011) 10027.

[2] M. Kofu, M. Nagao, T. Ueki, Y. Kitazawa, Y. Nakamura, S. Sawamura, M. Watanabe, and O. Yamamuro: J. Phys. Chem. B **117** (2013) 2773.

Promotion of joint researches through Project for advancement of software usability in materials science in 2015

Kazuyoshi Yoshimi
Institute for Solid State Physics, University of Tokyo
Kashiwa-no-ha, Kashiwa, Chiba 277-8581

1 Introduction

In fiscal year 2015, the numerical solver package for quantum lattice model $\mathcal{H}\Phi$[1] was developed by "Project for advancement of software usability in materials science" by The Institute for Solid State Physics, The University of Tokyo[2]. By using $\mathcal{H}\Phi$, we can calculate physical quantities in quantum lattice models that are constructed by one- and two-body interactions by using exact diagonalization with Lanczos method and thermal pure quantum states[3]. In fiscal year 2016, we investigated the origin of charge glassy state observed in organic conductors on the basis of the spinless fermion model and also constructed the solver to analyze spin relaxation phenomena in quantum dots.

2 Spinless fermion model

Quasi two dimensional organic conductor theta-type BEDT-TTF salts are considered as typical geometrically charge frustrated system and theoretically studied within the effective quantum models such as extended Hubbard model and spinless Fermion model[4]. Recently, in terms of charge ordering transition and glassy behavior, the importance of long range Coulomb interaction (LRC) is indicated[5].

In this study, we extended $\mathcal{H}\Phi$ to treat the spinless fermion model up to 6×6 sites. Then, we investigated the properties of the ground state by exact diagonalization method on the spinless fermion model with LRC in the presence of the geometrical charge frustration. Furthermore, we also calculated physical quantities at finite temperatures such as charge structure factors, specific heat and entropy by using thermal quantum pure state. From these calculations, we found that with increasing LRC, the wave number dependence of charge structure factors becomes broadened and the release in entropy by decreasing temperature becomes gradual in the intermediate temperature region. These results indicate that, compared to the short-range geometrical charge frustrations, LRC enhances the competition among various types of charge order patterns and thus promotes the metastable states in the intermediate temperature region.

3 General electron model

In experiments of GaAs/AlGaAs quantum dot systems, the spin relaxation rate of the high-spin state is more than 10 times larger than that of the $S = 0$ state. However, this large relaxation rate can not be simply explained by the electron number dependence and the angular momentum selection rule. In this project, we extend the function of $\mathcal{H}\Phi$ to investigate the many-body effect in the high-spin states of quantum dots, and examine how the electron correlation and the spin-orbital interac-

tion influences spin relaxation. Since the number of the two-body interactions becomes enormous in this model, we have first implemented the parallelization on the interaction parts and succeeded in improving the efficiency of calculation. As a result, the calculation of the eigenstates in 32-site systems was achieved within the configuration interaction method on the basis of Fock-Darwin single-particle states. We are now estimating the spin relaxation rate, and will compare experimental results on spin relaxation in the high-spin states of quantum dots in the near future.

4 Acknowledgements

This work was supported by Building of Consortia for the Development of Human Resources in Science and Technology from the MEXT of Japan.

References

[1] M. Kawamura, K. Yoshimi, T. Misawa, Y. Yamaji, S. Todo, N. Kawashima, arXiv:1703.03637.

[2] http://www.issp.u-tokyo.ac.jp/supercom/softwaredev.

[3] S. Sugiura and A. Shimizu, Phys. Rev. Lett. **108**, 240401(2012).

[4] For review, H. Seo, J. Merino, H. Yoshioka and M. Ogata, J. Phys. Soc. Jpn. **75**, 051009 (2006).

[5] T. Mori, J. Phys. Soc. Jpn. **72**, 1469 (2003); K. Kuroki, J. Phys. Soc. Jpn. **75**, 114716 (2006); M. Naka and H. Seo, J. Phys. Soc. Jpn. **83**, 053706 (2014); S. Mahmoudian et al., Phys. Rev. Lett. **115**, 025701(2015).

[6] H. Kiyama and A. Oiwa, private communication.

[7] J. I. Climente, et al. Phys. Rev. B **76**, 085305 (2007).

Many-variable variational Monte Carlo study for interfaces of high-T_c superconductors

Takahiro Misawa
Institute for Solid State Physics, University of Tokyo
Kashiwa-no-ha, Kashiwa, Chiba 277-8581

Recent experiments on interfaces and thin films of the cuprates and iron-based superconductors suggest that they often show better superconducting properties such as higher critical temperatures (T_c) than in the bulk materials. Above all, in a recent experiment on the interfaces of $La_2CuO_4/La_{2-x}Sr_xCuO_4$ (interfaces of the Mott insulator and the metallic phases), unexpected pinning of the T_c has been found [1] by systematically changing the doping rates of the metallic phase. It is noteworthy that pinning $T_c \sim 42$K is nearly the same as the optimal T_c in the bulk $La_{2-x}Sr_xCuO_4$. This behavior is in a sharp contrast with the bulk system where a dome-like doping dependence of T_c has been commonly found in the doping concentration dependence.

To clarify microscopic origin of the unconventional pinning of T_c observed at the interfaces of $La_2CuO_4/La_{2-x}Sr_xCuO_4$, we study multi-layer Hubbard model as an effective model for interfaces of the cuprates by using many-variable variational Monte Carlo method, which properly takes into account both spatial and dynamical quantum fluctuations [2, 3, 4, 5]. We employ the parameter values within the realistic constraint of the cuprate interface suggested from the experimental results and ab initio calculations. Especially, we take into account the effects of inter-layer Sr diffusions as differences in on-site levels around the interfaces.

As a result, we find that pinning of carrier densities and superconducting correlations at the interfaces indeed occur in the multi-layer Hubbard model [6] in essential agreement with the experimental results. We also clarify that the pinning emerges as a consequence of the inter-layer phase separation, which dissolves the inner-layer phase separation. Our result shows that the interfaces provide an ideal tool to enhance and stabilize superconductivity without fine tuning and opens a new way to design the higher-T_c superconductivities.

A part of calculation is done by using open-source software mVMC [3].

References

[1] J. Wu et al., Nat. Mat. 12, 877 (2013).

[2] D. Tahara and M. Imada, J. Phys. Soc. Jpn. 77, 114701 (2008).

[3] http://ma.cms-initiative.jp/en/application-list/mvmc/mvmc

[4] T. Misawa and M. Imada, Phys. Rev. B 90, 115137 (2014).

[5] T. Misawa and M. Imada, Nat. Commun. 5, 5738 (2014).

[6] T. Misawa, Y. Nomura, S. Biermann, and M. Imada, Sci. Adv. 2, e1600664 (2016).

First-principles analyses on adsorption of NH_x on GaN surfaces

BUI THI Kieu My and Yasuteru SHIGETA

Center for Computational Sciences,

University of Tsukuba, 1-1-1 Tennodai, Tsukuba, Ibaraki 305-8577, Japan

Gallium nitride (GaN), which belongs to the III-V family, is attracting tremendous attention recently. Owing to having wide bandgap, GaNis used in optoelectronics, photonics, high power and high temperature operation devices. Having well knowledge about thesurface adsorption and deposition mechanisms for different precursors isnecessary to improve thin-film crystalline quality and growth processrequirements. Using density functional theory (DFT) method, as implemented in real-space density functional theory (RSDFT) [1], we aim to theoretically investigate the reaction mechanism of GaN on (0001) surface from ammonia (NH_3) precursor. The calculated lattice parameters (a = 3.2 Å, c = 5.2 Å) are in accordance with experiments [2]. The 2x2 surface reconstruction structure is obtained. We found that, in agreement with other study [3], Ga add atom is most favorable to form at hcp site, while N add atom is most favorable to form at fcc site. The obtained structures for Ga and N add atom surfaces are shown in Figure 1.

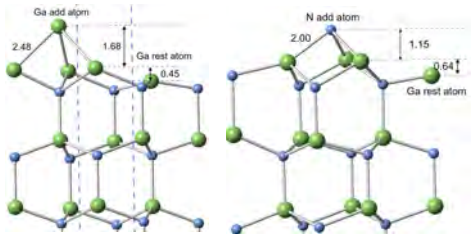

Figure 1: (left) Ga-hcp and (righ) N-fcc add atom configurations. All lengths are in Å.

Table 1: Binding energies of NH_x (x=1,2, and 3) on clean (upper) and Ga adatom (bottom) surfaces.

	On top	Hcp	Fcc	Bridge
NH_3	-0.0479 -0.0465	...	...	...
NH_2	-0.1725 -0.1456	...	...	-0.1768 -0.1196
NH	... -0.2317	-0.2449 -0.1889	-0.2715 -0.2274	...

Next, adsorptions of NH_3, NH_2, and NH on bare and Ga adatom surfaces were studied. We found that on the bare surface, NH_3 is the most favorable to form at on top site, NH_2 is likely to form at the bridge site, and NH is the most stable at the fcc site, respectively. On the Ga adatom surface, all NH_3, NH_2, and NH are the most favorable to form at on top site. The calculated binding energy for NH_3, NH_2, and NH on the bare and Ga adatom surfaces at on the top, hcp, fcc, and br sites are summarized in Table 1. This surface specificity of binding energies suggests that there exist different kinetics during the growth of GaN on surface.

References

[1] J.-I. Iwata *et al*., *J. Comput. Phys.* 2010, **229**, 2339.

[2] H. Schulz, K. Thiemann, Solid State Commun. 1977, **23**, 815.

[3] M. Chugh, M. Ranganathan, *J. Phys. Chem. C* 2016, **120**, 8076.

First-principles calculation of interactions between extreme pulse light and matter

Kazuhiro YABANA

Center for Computational Sciences,

University of Tsukuba, Tsukuba, 351-8577

Interaction between intense and ultrashort laser pulse and solid is one of active subjects in current optical sciences. Employing a few-cycle femtosecond laser pulses, a number of intriguing phenomena reflecting extremely nonlinear light-matter interactions have been observed. We have been developing a first-principles computational method to describe electron dynamics in solids under irradiation of a pulsed electric field based on time-dependent density functional theory, solving time-dependent Kohn-Sham equation in real time for electron orbitals in a unit cell of crystalline solids.

For a quantitative description of light-matter interactions, it is important to employ a potential in the Kohn-Sham equation that describes the band gap of the material adequately. As is well known, a simple local density approximation underestimates the band gap systematically. Recently, a few potentials that describe band gaps reasonably have been proposed. We have investigated computational methods to use such potentials in our code and examined optical responses of dielectrics in both linear and nonlinear regimes [1].

We implemented two potentials in our code, a meta-GGA potential developed by Tran and Blaha and a hybrid functional of Heyd, Scuseria, and Ernzerhof. For the meta-GGA potential, we have found that a predictor-corrector step is essential for a stable time evolution. Since a computation of nonlocal exchange potential in the hybrid functional requires heavy computational costs, we have developed a code that efficiently utilizes GPU.

We applied the code to various optical phenomena. One of such applications is the nonlinear photogalvanic effect [2]. It was found that an extremely intense and ultrashort laser pulse produces a current in dielectrics of wide band gap. We have found that the induced current in such dielectrics shows complex behavior, changing its direction depending on the maximum intensity of the pulse.

References

[1] S.A. Sato et.al, J. Chem. Phys. **143**, 224116 (2015).

[2] G. Wachter et.al, New J. Phys. **17**, 123026 (2015).

Tensor-Network Computation of Generalized Kitaev-Heisenberg Model*

Naoki KAWASHIMA

Institute for Solid State Physics,

The University of Tokyo, Kashiwa-no-ha, Kashiwa, Chiba 277-8581

Realization of Kitaev spin liquid is an active research topic of recent years since Jackeli and Khaliullin pointed out that Iridium compounds may be promising candidates. Among them, an effective quantum spin model for Na2IrO3 was derived [1] from the first-principles calculation, which then was studied by exact numerical diagonalization (ED) of a 24 site cluster. The resulting model contains a parameter, Δ, that controls the proximity to the pure Kitaev model (Δ=0 for the pure Kitaev model, Δ=-28 meV for the first-principle model). According to the exact diagonalization calculation, there are 4 phases; 3 distinct incommensurate magnetically ordered phases and a commensurate ordered phase, so-called zigzag-Z phase.

In our project using the ISSP supercomputer, we carried out tensor-network calculation of the same model, to verify the validity of the small-cluster ED results. In the tensor network calculation, one assumes that the wave function is represented by a partially contracted external product of many tensors, whose elements are obtained by some iterative optimization or variational adjustments. To be more specific, our calculation is based on the iPEPS ansatz that is expected to reproduce the thermodynamic limit results accurately as far as the entanglement is small and the magnetic structure fit in the assumed unit cell. We employed the ``simple update'' technique for optimizing the tensor elements. The accuracy of the method is controlled by the bond dimension, i.e., the dimension of the indices to be contracted. The largest bond dimension we used in the calculation was 9.

While our new results identifies the character of the first-principle model to be the zigzag-Z phase, in agreement with the small cluster ED result, they also revealed that the Δ-phase diagram is significantly different from what had been predicted by the ED result. For example, one of the incommensurate phase turned out to be a commensurate phase with a unit cell of 16 sites.

References

[*] This work has been done in collaboration with T. Okubo, K. Shinjo, Y. Yamaji, S. Sota, T. Tohyama and M. Imada. (arXiv:1611.03614)

[1] Y. Yamaji, Y. Nomura, M. Kurita, R. Arita, and M. Imada, Phys. Rev. Lett. 113, 107201 (2014).

Simulation of organic-inorganic interfaces

Shuji OGATA
Nagoya Institute of Technology
Gokiso-cho, Showa-ku, Nagoya 466-8555, Japan

In the fiscal year of 2016, we have mainly treated two subjects using our hybrid quantum-classical (QM-CL) simulation codes.

Subject 1: The hybrid QM-CL simulation of Si-O bond breaking in silica glass [1]. We perform a hybrid QM-CL simulation of a 4,608-atom silica glass at a temperature of 400 K with either a water monomer or dimer inserted in a void. The quantum region that includes the water and the surrounding atoms is treated by the DFT. During a simulation, the silica glass is gradually compressed or expanded. No Si-O bond breaking occurs with a water monomer until the silica glass collapses.

With a water dimer, we find that Si-O bond breaking occurs through three steps in 3 out of 24 compression cases: (i) H-transfer as $2H_2O \rightarrow OH^- + H_3O^+$ accompanied by the adsorption of OH^- at a strained Si to make it five-coordinated, (ii) breaking of a Si-O bond that originates from the five-coordinated Si, and (iii) H-transfer from H_3O^+ to the O of the broken Si-O bond. A separate DFT calculation confirms that the barrier energy of the bond breaking with a water dimer under compression is smaller than that with a water monomer and that the barrier energy decreases significantly when the silica glass is compressed further.

Subject 2: Moisture-Induced Reduction of Adhesion Strength Between Surface Oxidized Al and Epoxy Resin: Dynamics Simulation with Electronic Structure Calculations [2]. Adhesion strength between metal and epoxy resin is well known to reduce significantly in a moist environment. To theoretically understand its mechanisms, we calculate the shear strength of the interfacial adhesion between the surface oxidized Al and bisphenol-A epoxy resin with a varying number of water molecules or hydroxide ions inserted inbetween using the hybrid quantum-classical simulation method. The quantum region in the hybrid method, which is composed of about thousand atoms at the interface, is treated by the electronic density-functional theory implemented to calculate on a real-space grid. In a typical run using 63 CPU's, it takes about 9 minutes to evolve the atomic dynamics by a timestep; here, the settings of the parallel computation are the -spatial decomposition of 5x5x5, the electronic level parallelization of 2, and the OpenMP parallelization of 4.

It is thereby found that the adhesion strength reduces more significantly as the degree of the moisture content increases, in accordance with the experimental observations. Microscopic analyses find the following key features; (i) The inter-atomic Al-O bond between the Al atom of the oxide and the O atom of the epoxide group in the epoxy resin contributes substantially to the strength of the interfacial adhesion. (ii) Dissociation of the O atom of the epoxide group forming such an Al-O bond is enhanced when an H_2O rather than an OH resides in close proximately to the bond. (iii) The epoxy resin becomes more plastic by incorporating H_2O molecules. Both (ii) and (iii) act to weaken the shear strength of the interfacial adhesion.

References

[1] T. Kouno, S. Ogata, T. Shimada, T. Tamura, and R. Kobayashi, J. Phys. Soc. Jpn. **85** (2016) 054601-1-9.
[2] S. Ogata and Y. Takahashi, J. Phys. Chem. C **120** (2016) 13630-13637.

Large scale calculations on the fundamental processes of organic and perovskite solar cells and their optimization in conversion efficiency

Koichi YAMASHITA

Department of Chemical System Engineering,

The University of Tokyo, Hongo, Bunkyo-ku, Tokyo 113-8656

Organic photovoltaic (OPV) cells and Perovskite solar cells are being eagerly researched and developed. In particular, bulk heterojunction (BHJ) type of the organic photovoltaic cells has many attractive properties. Although exciton dissociation that leads to generation of free carriers has been considered as a key factor in photo-conversion process of OPVs, the fine mechanism of the exciton dissociation against Coulomb interaction has not been fully revealed yet.

Then, we studied three properties; (1) The first one is a “descriptor” of efficiencies of free carrier generation [1, 2]; (2) band bending by deformed structure of organic compound at the interface in the BHJ [3]; and (3) blending effects of electron-donor and –acceptor materials in the BHJ [4]. In these studies, we used our original code named as MolDS [5] implemented for massive parallel computing of semiempirical quantum calculations, especially electronic excites states in large molecular aggregates, by using hybrid (openMP/MPI) parallelization technique.

In the first part, we found that a pair of donor and acceptor exhibits the largest charge-bridging upon photoabsorption, which leads to the highest IQE and PCE. In the second part, we revealed two different dynamics of free carrier generation, prompt (a few picoseconds) generation from excitons that were generated on interfaces and delayed (order of sub-nanoseconds) generation from excitons which migrated to interfaces; the former is dominant but its ratio depends on the domain size of morphologies. Finally, the band bending in OPV due to the structure fluctuations are revealed quantitatively as 0.0, 0.2 or 1.5 eV at the edge-on interface between PCBM and rr-P3HT, rra- P3HT or F-P3HT.

References

[1] M. Fujii, W. Shin, T. Yasuda, and K. Yamashita, Phys Chem Chem Phys, **18**, 9514-9523 (2016).

[2] S. Koda, M. Fujii, S. Hatamiya, K. Yamashita, Theor. Chem. Acc. **135**, 115-124 (2016).

[3] E. Kawashima, M. Fujii, K. Yamashita, Phys Chem Chem Phys, **18**, 26456-26465 (2016).

[4] R. Jono, E. Watanabea, and Mikiya Fujii, K. Yamashita, J. photochem. photobiol., C **330** (2016) 181–185

[5] M. Fujii, K. Nishimra, M. Okuyama, MolDS URL: https:// en.osdn.jp/projects/molds/

Conversion and storage of energy−fuel cells and secondary batteries: Research and development of fundamental technologies of battery simulators.

Susumu OKAZAKI
Department of Applied Chmistry, Nagoya University
Furo-cho, Chikusa-ku, Nagoya 464-8603

The goal of our project is to develop the basic technology of the whole battery simulator. One of the key techniques is molecular-level design of polymer membranes controlling transportation of protons and ions across the membrane with proper stiffness resistant to mechanical deformation under external stress. Such membranes are expected to be widely applicable to the fuel cells used in the industrial products.

On the system B and C, we performed fully atomistic molecular dynamics (MD) calculations of hydrated perfluorosulfonic acid (PFSA) ionomers composed of a hydrophobic polytetrafluoroethylene backbone with hydrophilic side chains terminated by sulfonic acid (its molecular structure is shown in Fig. 1), as a model of proton exchange polymer electrolyte membrane of fuel cells[1]. The morphology of the hydrated polyelectrolyte membranes, depending on the degree of hydration and lengths of backbone monomer and side chains, was investigated. Diffusivity of water molecules in the PFSA membranes, which is closely related to the proton transport in the membranes, was also measured as a function of the degree of hydration. Further, mechanical resistance to the tensile deformation of the polymer membranes was tested.

We found that an increase of hydration changes the morphology of the hydrated PFSA membranes from a channel-network structure to a tortuous layered structure shown in Fig. 2, and that water diffusivity and mechanical resistance to the stress strongly depend on the degree of hydration. These findings will contribute to the development of higher performance fuel−cells and secondary batteries and to the realization of the entire battery simulator in the near future.

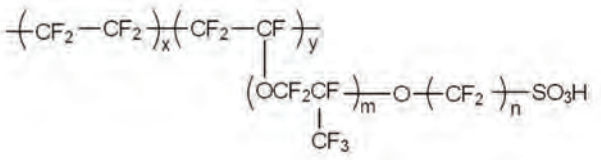

Figure 1: Molecular structure of perfluorosulfonic acid (PFSA) ionomers.

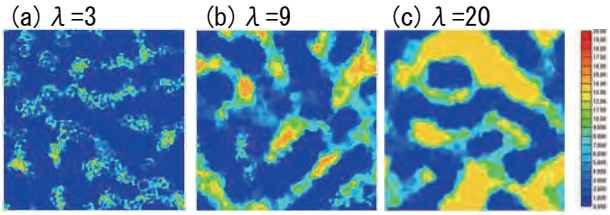

Figure 2: Number density map of sulfonic acid groups, water, and hydronium ions at one cut plane. λ is a mole fraction of water molecule and hydronium ion to sulfonic acid groups.

References

[1] A. T. Kuo, W. Shinoda, S. Okazaki : J. Phys. Chem. C **120** (2016) 25832.

Multiscale simulations of bio-membrane shape-changing dynamics

Kei-ichi OKAZAKI

Institute for Molecular Science,

National Institutes of Natural Sciences, Okazaki, Aichi 444-8585

In the cell, various shape-changing processes of membrane happen. For example, in the process called endocytosis/exocytosis, a vesicle fusion/fission happens with a help of protein machinery. We are interested in these membrane shape transformations driven by proteins.

Molecular simulations of the membrane shape transformation are challenging due to size of the system. All-atom molecular dynamics simulations are quite expensive since total number of atoms can easily exceed one million. Alternatively, we can use coarse-grained models to reduce the computational cost.

In this study, we use a coarse-grained model in which a lipid molecule is represented by three beads, developed by Noguchi and coworkers [1]. The model has been confirmed to reproduce some basic properties of lipid membrane, including spontaneous vesicle formation. As a test calculation, I simulated vesicle formation from flat membrane. Order parameters defined using principal axis clearly quantify the shape transformation.

By using this coarse-grained model, I am trying to reveal how proteins induce the shape transformations. Especially, banana-shaped proteins in the BAR domain family play an important role by generating curvature on the membrane. I am particularly interested in one of the BAR domain proteins called Pacsin [2] that transforms homogeneous vesicles into various shapes.

To simulate this protein-induced shape transformation, I am implementing a coarse-grained protein model in the afore mentioned model. I am considering internal energy such as bond length, bond angle and contact potentials as well as inter-molecule energy such as electrostatic interaction between lipid head groups and charged residues in the protein.

This work is in collaboration with H. Noguchi (ISSP, The University of Tokyo).

References

[1] H. Noguchi and M. Takasu: Biophys. J. **83** (2002) 299-308.

[2] Q. Wang et al.: Proc. Nat. Acad. Sci. **106** (31) (2009) 12700-12705

Excited-state calculations for molecular aggregates based on Green′s function method

Takatoshi Fujita
Institute for Molecular Science
Myodaiji, Okazaki, Aichi 444-8585

Predicting the electronic excited states of large systems with reasonable accuracy remains an ongoing challenge in quantum chemistry. In this project, we aim to develop a theory that can treat excited states of large systems with reasonable accuracy, on the basis of the fragment-based electronic structure theory and many-body Green′s function techniques. As a first step, we have developed a theory to treat non-local excitations in large systems based on the configuration interaction singles (CIS) and fragment molecular orbital (FMO) method. The developed method was applied to organic donor/accepter interfaces.

The present theory is the generalization of the excite-state calculations combining the FMO and transition-density fragment interaction methods [1]; the theory was designed to reproduce low-energy excited state manifold of large systems with small dimension. The aim of the development is to systematically derive a tight-binding exciton Hamiltonian, which can be used to study real-time quantum dynamics combined with quantum dynamics theory. To describe delocalized excited state for the total system, configuration state functions (CSFs) were constructed from localized molecular orbitals by self-consistent field calculations for fragment monomer and dimer, and multi-layer FMO with the CIS method. The excited-state wavefunction of the total system was described as a superposition of fragment CSFs for local excitations and for interfragment charge-transfer excitations. Exploiting those fragment CSFs allows for the efficient truncation of the dimension of excited-state Hamiltonian. The one-electron parts of excited-state Hamiltonian were treated by the FMO-linear combination of molecular orbital (FMO-LCMO) method; the two-electron parts were efficiently treated within FMO framework. In addition, the approximation scheme to calculate two-electron parts was developed in accordance with the electrostatic approximation in the FMO.

As a demonstration, the developed method was applied to an organic donor/accepter interface comprising 24 pentacene and 20 fullerene molecules.The excited states were treated at the FMO-CIS/6-31G** level; the FMO calculation parallelized with the flat MPI was performed in system B using 864 cores. The results were analyzed with correlation correction to the diagonal terms and the screening correction to the long-range Coulomb interactions of the off-diagonal terms. As a next step, the charge separation and recombination mechanisms will be analyzed by combining a quantum dynamics theory.

References

[1] T.Fujita, J. Huh, S K. Saikin, and A. Aspuru-Guzik, J. Phys. Chem. Lett. **7** (2016) 546.

Design of spintronics materials by order-N screened KKR Green's function method

Tetsuya Fukushima
Institute for NanoScience Design, Osaka University, Osaka 560-8531, Japan
Institute for Datability Science, Osaka University, Osaka 565-0871, Japan

This year, we developed a large-scale electronic structure calculation package, KKRnano, where the full potential screened Korringa-Kohn-Rostoker (KKR) Green's function method is optimized by a massively parallel linear scaling (order-N) all electron algorithm [1]. The central part of the screened KKR Green's function method is the solution of the Dyson equation for the Green's functions $G^{nn'}_{LL'}(E)$:

$$G^{nn'}_{LL'}(E) = G^{r,nn'}_{LL'}(E) + \sum_{n''L''L'''} G^{r,nn''}_{LL''}(E)\Delta t^{n''}_{L''L'''}(E)G^{n''n'}_{L'''L'}(E).$$

Here $L = (l, m)$, where l and m are the angular momentum indices. $G^{nn'}_{LL'}(E)$ and $G^{r,nn'}_{LL'}(E)$ are the Green's function elements of the system under study and of a suitable reference system, respectively. $\Delta t^{n}_{LL'}(E) = t^{n}_{LL'}(E) - t^{r,n}_{LL'}(E)$ is the difference between the single site scattering t matrices of the atoms in the true and reference system. In the screened KKR method, a system with strongly repulsive potentials is used as reference system [1], such that the Green's functions $G^{r,nn'}_{LL'}(E)$ decrease very rapidly at large distances $(\boldsymbol{R}^n - \boldsymbol{R}^{n'})$. Contrary to the standard KKR-GF method, KKRnano allows order-N scaling of the computational cost by truncating the Green's function and solving the Dyson equation iteratively, based on the quasi minimal residual method with block-circulant matrix preconditioning. Since the charge density and density of states are directly related to the imaginary part of the Green's function, one can use the KKR-GF method in the framework of density functional theory.

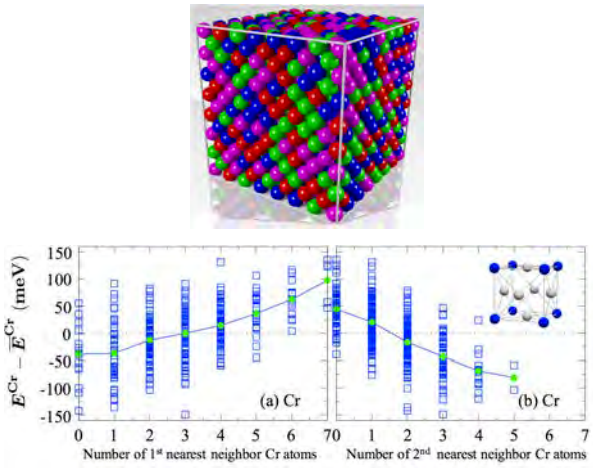

Figure 1: (Upper panel) Crystal structure of HEA CrFeCoNi with the random solid solution phase. (Lower panel)Local energy fluctuations of Cr atoms $(E^{\mathrm{Cr}} - \overline{E}^{\mathrm{Cr}})$ as a function of number of (a) first nearest neighbor Cr atoms $(n^{\mathrm{1st}}_{\mathrm{Cr}})$ and (b) second nearest neighbor Cr atoms $(n^{\mathrm{2nd}}_{\mathrm{Cr}})$. Green points show the average values. The inset in (b) shows the $L1_2$ crystal structure.

We demonstrate large-scale all-electron density functional calculations for a prototype high entropy alloy (HEA) CrFeCoNi by the KKRnano program package [2]. HEA forms an ideal face centered cubic (FCC) or body centered cubic (BCC) random solid solution phase. To describe the randomness and local environment effect, one needs to employ a large

supercell; therefore, it has been recognized that general DFT methods, where the computational costs increase as order-N^3, cannot perform calculations. To overcome this limitation, we have executed the KKRnano program package for a supercell containing 1,343 atoms. We have also presented a new method to calculate "local energies", which is the energetic contribution of each atomic cell to the total energy of the supercell. The local energy gives the useful information for local structural stability. Our supercell calculations show very large variations of the local energies. This leads to fact that the random solid solution is not stable and has a tendency to form an $L1_2$-structure with the Cr-atoms ordered at the corner of the cube and the elements Fe, Co and Ni randomly distributed on the three other FCC sublattices.

References

[1] R. Zeller, J. Phys.: Condens. Matter **20**, (2008) 294215.

[2] T. Fukushima, K. Sato, H. Katayama-Yoshida, M. Ogura, R. Zeller, and P. H. Dederichs, submitted to J. Phys. Soc. Jpn.

Materials exploration for sodium secondary batteries

Hiroki KOTAKA[1], Motoyuki HAMAGUCHI[2], Hiroyoshi MOMIDA[1,2], Tamio OGUCHI[1,2]
[1]*Elements Strategy Initiative for Catalysts and Batteries, Kyoto University*
Katsuragoryo, Kyoto, Kyoto 567-0047
[2]*Institute of Scientific and Industrial Research, Osaka University*
Mihogaoka, Ibaraki, Osaka 567-0047

We have studied the microscopic mechanism of charge/discharge reactions in several battery systems by means of first-principles calculations to explore new sodium secondary batteries. In this year, we focus on Na/SnS and Li/Li$_x$$MTiO_4$ (M=V, Mn, Fe, Co, and Ni) systems.

Tin compounds are known as high-capacity materials in charge/discharge reactions and to have advantages in price and safety for practical applications, being considered as a good candidate for the anode materials of sodium secondary battery. [1, 2] We investigate the electronic mechanism in discharge reactions of Na/SnS system. From experimental works, several stages are involved in conversion reactions starting from SnS. Stable phases in the ternary Na-Sn-S system are searched by assuming a reaction as $(1-x)$SnS+xNa$\rightarrow$Na$_x$Sn$_y$S$_z$+$(1-x-y)$Sn + $(1-x-z)$S. On the basis of the total energies calculated for the reaction, Sn and Na_2S are generated as intermediate products. In addition, generated Sn and newly introduced Na may react to form several alloy phases as $NaSn_5\rightarrow NaSn_2\rightarrow NaSn\rightarrow Na_9Sn_4\rightarrow Na_{15}Sn_4$. This multi-stage discharge reaction may explain discharge voltage-capacity curve measured by Kitajou *et al.* [3] To identify possible phases in the discharge reaction, calculated x-ray absorption spectroscopy spectra for SnS and Na_2S are compared with experimental ones [3] and the existence of Na_2S in the intermediate stage is confirmed.

Li$_x$$MTiO_4$ (M=V, Mn, Fe, Co, and Ni) systems have attracted much attention recently because of a possible candidate for high-voltage and high-capacity cathode materials. In this oxides, since cations M are octahedrally coordinated by O ions and octahedra MO_6 share their ridges, high stability to O dissociation is highly expected. However, measured discharge capacity is extremely lower than theoretical one and complicated processes are involved in the discharge reaction. We estimate the voltage as a function of Li concentration and O-vacancy formation energy for different M systems. From the electronic structure calculations, it is found that a two-stage process associated with M+Ti and M+O takes place depending on the Li concentration. The O-vacancy formation energy becomes decreased as the Li concentration is decreased, implying the increase of the role of O redox in the reaction. This tendency becomes more remarkable in proportional to the number of d electrons in M ions.

References

[1] J. W. Wang *et al.*, Nano Lett. **12**, 5897 (2012).

[2] C. J. Pelliccione *et al.*, J. Phys. Chem. C **120**, 5331 (2016).

[3] A. Kitajou and S. Okada, private communications.

Exploration of novel semiconductors by first-principles screening

Fumiyasu OBA[1,2], Hirofumi AKAMATSU[1], and Yu KUMAGAI[2]

[1]*Laboratory for Materials and Structures, Institute of Innovative Research, Tokyo Institute of Technology, 4259 Nagatsuta, Midori-ku, Yokohama 226-8503, Japan*
[2]*Materials Research Center for Element Strategy, Tokyo Institute of Technology, 4259 Nagatsuta, Midori-ku, Yokohama 226-8503, Japan*

The search for novel semiconductors is increasingly important as the applications of semiconductors become more prevalent. Among the compound semiconductors, nitrides and oxides are especially attractive due to the abundant and environmentally-benign nitrogen and oxygen constituents. Currently commercialized nitride semiconductors are, however, mostly limited to GaN and its based alloys. Several kinds of oxide semiconductors are used in commercial applications such as transparent electrodes and thin-film transistors, but those with improved or different functionalities are required to expand the applications. This situation stimulates not only experimental but also computational, or *in silico*, exploration of novel nitride and oxide semiconductors.

Recently we have discovered a novel nitride semiconductor $CaZn_2N_2$ by first-principles screening of ~ 600 candidate materials in combination with high-pressure synthesis [1]. It is our objective to extend this *in silico* screening approach for the exploration of semiconductors with a wide variety of chemistry, not only nitrides but also others including oxides. In addition, the screening needs to be made more efficiently so that a much larger number of candidate materials can be evaluated within feasible computational time.

Our screening procedure is schematically shown in Fig. 1. In the first step, the fundamental properties, thermodynamic stability in the phase diagram, and stability against lattice vibration are evaluated for candidate materials. Selected materials are then subject to further investigation in terms of native point defect formation and doping to assess the dopability into p and/or n type. Finally, promising materials as semiconductors are proposed on the basis of these assessments.

Among the series of calculations, the native point defect and dopant calculations are computationally the most demanding and complicated. Therefore, making these calculations more efficient is an urgent requirement for accelerating the screening.

In this study, we have developed and tested computational schemes for point defect calculations. First, we tested a scheme based on non-self-consistent, dielectric-dependent hybrid functional calculations to correct the valence and conduction band edges on top of the calculations using semilocal functionals [2]. This approach allows us to obtain band edge positions with accuracy comparable to standard GW calculations at the random phase approximation level, simultaneously with much

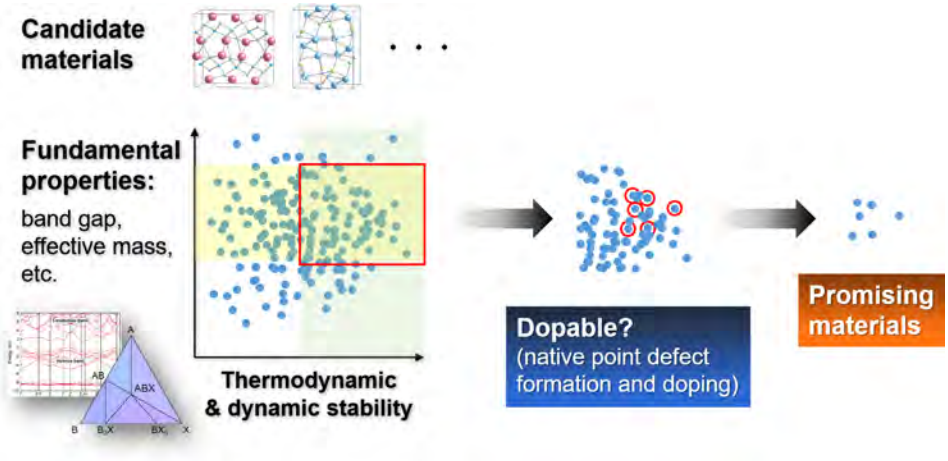

Figure 1: Schematic showing the screening procedure for semiconductors.

reduced computational costs.

Second, a finite cell-size correction scheme that we have developed previously [3], which is an extension of the method proposed by Freysoldt, Neugebauer, and Van de Walle (FNV)[4], was modified so that the corrections can be applied semi-automatically. By correcting electrostatic interactions, the formation energies of charged point defects at the dilute defect limit, in other words, infinite cell-size limit, can be predicted even using supercells with moderate sizes for diverse defects in diverse materials (Fig. 2). This is attained by the twofold extension of the original FNV scheme: (i) Anisotropic screening is taken into account using dielectric tensors and (ii) the corrections for relaxed atomic structures are significantly improved by the use of atomic-site local potential as a potential marker. This year the CPU time was mainly used for testing and establishing the above-mentioned correction schemes. As a result, these schemes are now almost ready for massive calculations toward high-throughput screening of diverse candidates.

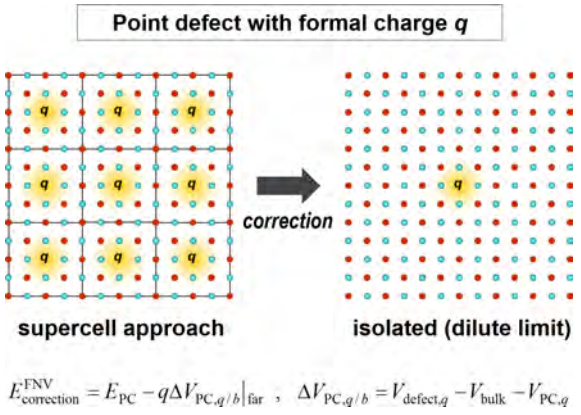

Figure 2: Schematic showing the finite cell-size corrections based on the FNV scheme in charged point defect calculations using a supercell approach.

References

[1] Y. Hinuma, T. Hatakeyama, Y. Kumagai, L. A. Burton, H. Sato, Y. Muraba, S. Iimura, H. Hiramatsu, I. Tanaka, H. Hosono, and F. Oba: Nat. Commun. **7** (2016) 11962.

[2] Y. Hinuma, Y. Kumagai, I. Tanaka, and F. Oba: Phys. Rev. B **95** (2017) 075302.

[3] Y. Kumagai and F. Oba: Phys. Rev. B **89** (2014) 195205.

[4] C. Freysoldt, J. Neugebauer, and C. G. Van de Walle: Phys. Rev. Lett. **102** (2009) 016402.

Quantum Molecular Dynamics Simulation on Electrolyte Solution for Sodium-Ion Battery

Hiromi NAKAI

Faculty of Science and Engineering,

Waseda University, Shinjuku, Tokyo 169-8555

Na-ion batteries (SIBs) receive growing attentions as the alternative to Li-ion batteries (LIBs) with shrinking resources of lithium. Electrolyte solutions, one of the main components of secondary battery, have a crucial impact on the performances of batteries. Within the electrolyte solutions, the superconcentrated solutions attract intense interests as a novel class of electrolyte for the specific favorable characteristics, i.e., high electrochemical (oxidative/reductive) stabilities, fast electrode reactions, low volatility, and so forth [1].

Career ion conductivity is one of the crucial issues in superconcentrated solutions, which generally show high viscosities. Especially, the ion diffusion mechanism is one of the remaining fundamental issues for superconcentrated electrolyte solutions, in which conventional vehicular-type diffusion mechanism cannot take place due to the severely limited number of free solvents.

The present study analyzed concentration dependences of solution structures and diffusion properties of electrolytes for SIB by using molecular dynamics (MD) simulations based on the density-functional tight-binding (DFTB) method.

DFTB-MD simulations were performed with the divide-and-conquer (DC) technique for accelerated computation by using the DC-DFTB-K program package [2] that is designed for massively parallelized computer environment such as the K computer. Modified 3ob parameter was used with so-called DFT-D3 dispersion correction. Dimethoxy ethane (DME) and Na-FSA (bis-fluorosulfonyl amide anion; $N(SO_2F)_2^-$) were employed as solvent and salt, respectively. Dilute and superconcentrated systems with 10% (220 molecules, 3388 atoms) and 40% (215 molecules, 2924 atoms) of salt concentrations were setup with the densities obtained from classical MD simulations. Production runs were performed for 20 ps under NVE ensemble following 10 ps of equilibration runs under NVT ensemble (T = 298.15 K).

The averaged coordination number of Na ion was ca. six for both dilute and superconcentrated systems. Oxygen atoms were dominantly contributed to the coordination. In the dilute (10%) system, the numbers of coordination of DME and FSA to Na ion were

four and two, respectively, while that for the superconcentrated (40%) system were three for both DME and FSA (Fig. 1). The numbers of free DME (FSA) decreased from 77% (6%) to 11% (0%) with increasing concentration of salts from 10% to 40%.

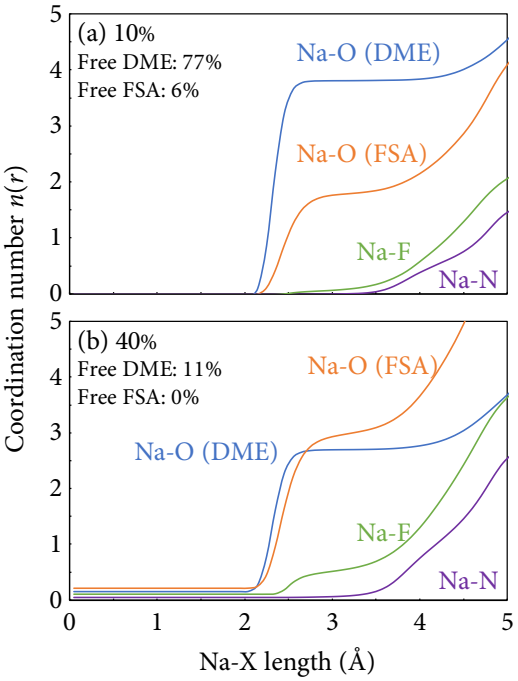

Fig. 1: Coordination numbers of O, F, and N atoms to Na ion.

Table 1: Diffusion coefficients of DME, FSA, and Na in dilute (10%) and concentrated (40%) systems (10^{-10} m^2/sec).

Molar ratio	DME	FSA	Na
10%	25.8	7.6	7.2
40%	6.8	3.3	3.2

The diffusion coefficient of DME decreased to ca. 1/4 in superconcentrated system, while those for Na and FSA decreased by about a half (Table 1). This result indicates the existence of a diffusion path of Na ion, which differs from the conventional vehicular type mechanism. As for such an extra diffusion process, we have newly found ligand (solvent/anion) exchange reactions (Fig. 2).

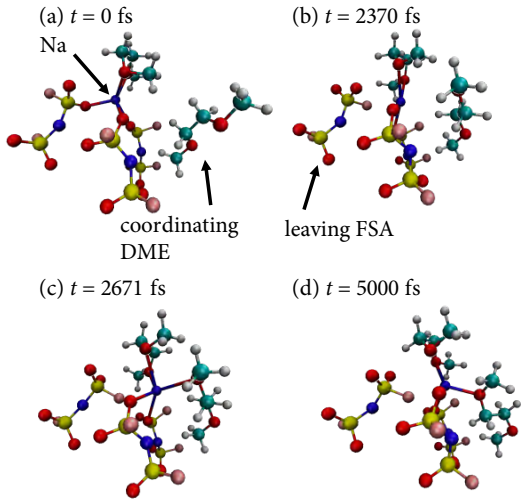

Fig. 2: Snapshots of Na ion diffusion accompanying ligand exchange reactions.

The rates of ligand exchange reactions were evaluated via number of associated/dissociated solvents/anions to Na ions averaged over 20 ps. The reaction rates for 40% and 10% systems were 0.019 (/ps) and 0.010 (/ps), respectively, implying roughly twice as frequent ligand exchange reaction in superconcentrated system.

References

[1] Y. Yamada and A. Yamada: J. Electrochem. Soc. **162** (2015) A2406.

[2] H. Nishizawa, Y. Nishimura, M. Kobayashi, S. Irle, and H. Nakai: J. Comput. Chem. **37** (2016) 1983.

First-principles Study of Magnetic Materials

Takashi MIYAKE

CD-FMat, AIST, Umezono, Tsukuba, Ibaraki 305-8568

Development of new strong magnet compounds have been attracting interests not only as a fundamental science but also for technological importance. Recently, $NdFe_{12}N$ has been successfully synthesized as a film, and it was shown that the compound has larger saturation magnetization and anisotropy filed than $Nd_2Fe_{14}B$ [1]. However, this compound is thermodynamically unstable, and it is necessary to substitute a part of Fe atoms with another element. Various elements, such as Ti, V and Si are known to stabilize the bulk phase.

In the present work, we study $NdFe_{11}M$ for M=Ti, V, Cr, Mn, Co, Ni, Cu and Zn. We have performed a first-principles calculation in DFT-GGA using QMAS code. Nd-4f electrons are treated as open-core. We found that M=Ti and Cr at the 8i site have negative formation energy. This suggests that the system is stabilized by Ti and Cr, which is consistent with experimental observation. We also found that M=Co has negative formation energy. Figure 1 shows the magnetic moment and the second order crystal-field parameter. The magnetic moment is substantially smaller in $NdFe_{11}Ti$ compared to $NdFe_{12}$. This is because Ti is negatively spin-polarized, and local magnetic moment at surrounding Fe sites also changes. In the case of M=Co, on the other hand, the spin moment is comparable to or larger than that of $NdFe_{12}$. The crystal-field parameter is also similar to that of $NdFe_{12}$. These results suggest that Co can be a good stabilizing element in terms of structural stability and magnetization. The system would have strong uniaxial magnetocrystalline anisotropy by interstitial nitrogenation.

References

[1] Y. Hirayama et al., Scripta Materialia **95**, 70 (2015).

[2] Y. Harashima et al., J. Appl. Phys. **120** (2016) 203904.

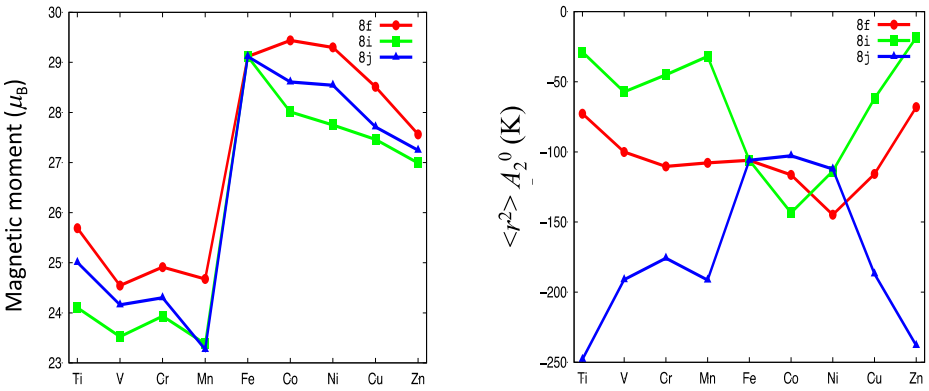

Fig. 1: Magnetic moment and crystal-field parameter in $NdFe_{11}M$.

3.6 Software Advancement Projects and GPGPU Support

Development of numerical library Kω ver.1 and quantum lattice solver $\mathcal{H}\Phi$ ver.2

Takeo Hoshi[1], Youhei Yamaji[2], Mitsuaki Kawamura[3], Kazuyoshi Yoshimi[3], Takahiro Misawa[3], Synge Todo[4], Tomohiro Sogabe[5], Naoki Kawashima[3]
[1] *Department of Applied Mathematics and Physics, Tottori University Koyama-Minami, Tottori 680-8550, Japan*
[2] *Department of Applied Physics, The University of Tokyo Bunkyo-ku, Tokyo, 113-8656, Japan*
[3] *The Institute for Solid State Physics, The University of Tokyo Kashiwa-shi, Chiba, 277-8581,Japan*
[4] *Department of Physics, The University of Tokyo Bunkyo-ku, Tokyo, 113-8656, Japan*
[5] *Department of Computational Science and Engineering, Nagoya University Chikusa-ku, Nagoya, 464-8603, Japan*

The two novel open-source softwares of (i) numerical library Kω ver.1 [1] and (ii) quantum lattice solver $\mathcal{H}\Phi$ ver.2 [2] were developed in Project for advancement of software usability in materials science [3] at the fiscal year of 2016. The project name is 'shifted Krylov-subspace algorithm and novel solvers for computational condensed matter physics'. The project is a interdisciplinary one between computational material science and applied mathematics. The softwares are preinstalled on the supercomputer (Sekirei) at ISSP [3]. The two softwares are closely related, because Kω is a set of numerical linear-algebraic routines and $\mathcal{H}\Phi$ ver.2 supports the use of Kω in the optical spectrum calculations.

Kω is a general numerical library for the Green's function of

$$G^{ab}(\omega) = \langle a| \frac{1}{(E_0 + \omega + i\delta)I - H} |b\rangle, \qquad (1)$$

where H is a large-scale complex-Hermitian or real-symmetric matrix and $|a\rangle, |b\rangle$ are the input vectors. Traditionally, the problem was solved by the Lanczos-based algorithm. In the present solver, instead, the numerical solution of Eq. (1) is obtained from the linear equation of

$$[(E_0 + \omega + i\delta)I - H]\,|x\rangle = |b\rangle \qquad (2)$$

and the solution of $|x\rangle$ is obtained by the novel iterative algorithm, called shifted Krylov-subspace algorithm [4, 5]. The algorithm was used for the excited spectrum of many-body states in a previous paper [5], which motivated us to the present project. The algorithm enables us to control the accuracy of the spectrum $G^{ab}(\omega)$ at a specific frequently ω [5], when one monitors the residual vector of Eq. (2). The method is general and was applied also to many other computational science fields, such as QCD[4], electronic structure calculations, transport calculation with non-equilibrium Green's function theory. Kω is a general numerical library and can be called, in principle, from any material simulator, as well as $\mathcal{H}\Phi$ ver.2. Moreover, a mini-application is included in the package of Kω, so that researchers can evaluate the numerical library before the use in their real researches.

$\mathcal{H}\Phi$ ver.2 is the latest version of $\mathcal{H}\Phi$ [6]. The quantum lattice solver $\mathcal{H}\Phi$ is a program

package based on exact diagonalization applicable to a broad range of quantum lattice models, including the Heisenberg model, the Kitaev model, the Hubbard model and the Kondo-lattice model. In $\mathcal{H}\Phi$ ver.1, the Lanczos method for calculating the ground state and a few excited states, thermal pure quantum (TPQ) states [7] for finite-temperature calculations, and full diagonalization method for checking results of Lanczos and TPQ methods are implemented with an easy-to-use and flexible user interface.

The project in the 2016 fiscal year [3] has supported implementation of the Lanczos and shifted Krylov-subspace algorithm for calculating excitation spectra in the latest version $\mathcal{H}\Phi$ ver.2. The $\mathcal{H}\Phi$ ver.2 call subroutines for the shifted Krylov-subspace algorithm from the library Kω.

As an example tractable by $\mathcal{H}\Phi$ ver.2, we show excitation spectra of an *ab initio* spin hamiltonian of an iridium oxides Na_2IrO_3 [8], which is a so-called Kitaev material and a typical example of frustrated magnets due to magnetic anisotropy. In Fig.1, dynamical spin structure factors calculated for a 24-site cluster of the *ab initio* spin hamiltonian of an iridium oxides Na_2IrO_3 are shown. The continuum in the spectra is the hallmark of the proximity to the Kitaev's quantum spin liquid. The controlled accuracy of the shifted Krylov-subspace algorithm safely resolves the detailed continuum spread over the wide range of frequency, where the typical exchange energy scale of Na_2IrO_3 is 30 meV.

For a future outlook, the successor project in the fiscal year of 2017 [3] will support implementation of real-time dynamics, finite-temperature excitation spectra, and interfaces for data science approaches.

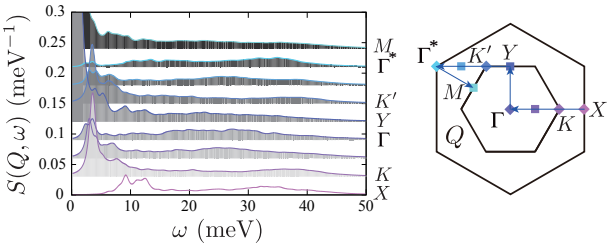

Figure 1: Calculated dynamical structure factors $S(Q,\omega)$ of Na_2IrO_3 [8]. The spectra are vertically shifted depending on Q. The Brillouin zone of Na_2IrO_3 is shown in the right panel.

References

[1] `https://github.com/issp-center-dev/Komega`

[2] `https://github.com/QLMS/HPhi`

[3] `http://www.issp.u-tokyo.ac.jp/supercom/softwaredev`

[4] A. Frommer, BiCGStab(l) for families of shifted linear systems, Computing 70, 87 (2003).

[5] S. Yamamoto, T. Sogabe, T. Hoshi, S.-L. Zhang and T. Fujiwara, 'Shifted conjugate orthogonal conjugate-gradient method and its application to double orbital extended Hubbard model', J. Phys. Soc. Jpn. 77,114713 (2008).

[6] M. Kawamura, K. Yoshimi, T. Misawa, Y. Yamaji, S. Todo, N. Kawashima, 'Quantum Lattice Model Solver HΦ', arXiv:1703.03637, Computer Physics Communications, in press.

[7] S. Sugiura and A. Shimizu, 'Theremal Pure Quantum States at Finite Temperature,' Phys. Rev. Lett. 108, 240401 (2012).

[8] Y. Yamaji, Y. Nomura, M. Kurita, R. Arita, and M. Imada, 'First-principles study of the honeycomb-lattice iridates Na_2IrO_3 in the presence of strong spin-orbit interaction and electron correlations,' Phys. Rev. Lett. 113, 107201 (2014).

Development of open-source software for Many-variable variational Monte Carlo (mVMC) method

Takahiro Misawa
Institute for Solid State Physics, University of Tokyo
Kashiwa-no-ha, Kashiwa, Chiba 277-8581

The variational Monte Carlo (VMC) method is a commonly used method for treating the low-energy effective models of quantum many-body systems such as the Hubbard model and the Heisenberg model [1]. In the VMC method, the many-body correlation factors such as the Gutzwiller and the Jastrow factors are introduced to the one-body wave functions. By optimizing the variational parameters in the many-body wave functions to lower the energy, we can obtain the wave functions for the ground states of the quantum many-body systems.

Because the VMC does not suffer from the negative sign problems, the VMC method is widely used for analyzing the low-energy effective models for quantum many-body systems including the strongly correlated electrons systems. However, it has been pointed out that accuracy of the conventional VMC method is not high due to the strong limitation of the implemented wave functions in the conventional VMC method. To overcome the limitation of the conventional VMC, we have introduced many variational parameters in the one-body part of the wave functions (typically more than ten thousand variational parameters) and have succeeded in relaxing the limitations of the wave functions. We also employ the quantum number projection to recover the symmetries inherent to the systems [2]. By combining the many-variable variational wave functions and the quantum number projections, we have shown that the highly accurate calculations is possible for the wide range of the quantum many-body systems [2, 3]. We call this method *many-variable variational Monte Carlo* (mVMC) method to distinguish the conventional VMC method, whose number of variational parameters is limited to more or less one hundred. Although the optimization of the many variational parameters is difficult in general, it is shown that the optimization of more than ten thousand variational parameters is possible by using the stochastic reconfiguration (SR) method proposed by S. Sorella [4], which is based on the imaginary-time evolution of the wave functions.

The project for advancement of software usability in materials science in the 2016 fiscal year has supported the release of the mVMC as the open-source software [5]. The project has especially supported the improvement of the user interfaces of mVMC and extensions of the wave functions. The latest version of the mVMC is preinstalled on the system B (sekirei) of the supercomputers at ISSP.

By using the software, users can easily start the mVMC calculation by preparing one input file, whose length is typically less than ten lines, for the standard models in the strongly correlated electron systems. As an example, we show the input file for the 4×4 Hubbard model as below:

```
L          = 4
```

```
W       = 4
Lsub    = 2
Wsub    = 2
model   = "FermionHubbard"
lattice = "tetragonal"
U       = 4.0
t       = 1.0
nelec   = 16
```

Here L and W are a linear extents of square lattice, in x and y directions, respectively. The nearest neighbor transfer (on-site Coulomb repulsion) is represented by t (U). Details of the other keywords in the input files can be found in the manuals of mVMC [5]. In Fig. 1, we show the optimization process of the mVMC. As shown in this figure, by preparing the above simple input file, users can easily obtain the wave functions for the ground state whose accuracy is $E_{\mathrm{mVMC}} - E_{\mathrm{exact}} \sim 10^{-3} \times t$. By changing the keywords in the input file slightly, users can easily perform the mVMC calculations for the other standard models such as the Heisenberg model and the Kondo-lattice model. It is also easy to treat more general models in the quantum many-body systems by properly preparing the input files. We hope that the mVMC becomes useful software and will be widely used by the broad spectrum of the researchers in the condensed matter physics as well as the other fields such as the quantum chemistry.

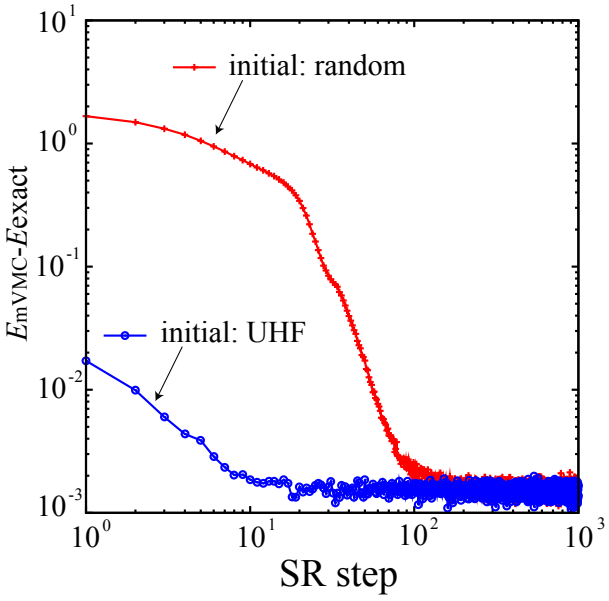

Figure 1: Optimization process of mVMC for 4×4 Hubbard model. The internal energy per site calculated by mVMC (exact diagonalization) is represented by E_{mMVC} (E_{exact}). Exact diagonalization is done by using $\mathcal{H}\Phi$ [6]. We take two different initial states: One is the random initial states (red crosses) whose initial variational parameters are generated by the random numbers and the variational parameters of the another one is generated by results of the unrestricted Hartree-Fock (UHF) calculations (blue circles). Although the two different initial states give nearly the same converged results, the convergence is faster by taking UHF initial states.

References

[1] For a review, see C. Gros, Ann. Phys. 189, 53 (1989).

[2] D. Tahara and M. Imada, J. Phys. Soc. Jpn. 77, 114701 (2008).

[3] T. Misawa and M. Imada, Phys. Rev. B 90, 115137 (2014).

[4] S. Sorella, Phys. Rev. B 64, 024512 (2001).

[5] http://ma.cms-initiative.jp/en/application-list/mvmc/mvmc

[6] http://qlms.github.io/HPhi/index.html

ISSP support service of software optimization for the GPGPU architectures: A case study for molecular dynamics simulation software MODYLAS

Yoshimichi ANDOH
Center of Computational Science, Graduate School of Engineering, Nagoya University
Furo-cho, Chikusa-ku, Nagoya 464-8603

With the GPGPU support service by the ISSP in the 2015 and 2016 fiscal years, our originally developed general-purpose molecular dynamics (MD) simulation software MODYLAS[1] has been optimized for the system B in the ISSP supercomputer center by using the OpenACC directive-based extension for the Fortran language.

Our MD software assumes that calculation system is in the condensed phase, and contains the long-range Coulombic interaction under three dimensional periodic boundary condition. The Coulombic interactions are strictly and e ciently calculated by the fast multipole method[2]. Most time consuming parts in such MD calculations (hot spots) are pairwise additive calculations of the interaction with nearly located atoms (p2p), and the translation from multipole to local expansions (M2L). With preceding optimization with the OpenACC, these hot spots had been already accelerated at the kickoff of the support service. So, the optimizations in this service were mainly applied to the secondary hot spots.

In the 2015 fiscal year, the conversion from point charges to multipoles (p2M) and evaluation of the electric field on particle by local expansions (L2p) were successfully accelerated by nearly 25 times, inserting the OpenACC directives into these secondary hot spots. Further, transfer style of the data of coordinates and force field parameters from the main memory to the GPGPU's on-board memory, which is needed in the first hot spot, was improved. With these tunings, total calculation time for one MD cycle was considerably reduced, if compared with the code before the tunings.

In the 2016 fiscal year, we tried to further accelerate the p2p code by utilizing the Newton's third law, and to introduce task parallelization between CPU and GPGPU. In the former, the atomic operations at the summation of the calculated atom pair forces drastically reduced calculation e ciency. In the latter, grammatical restriction in the OpenACC prevented us from implementing the task parallelization straightforwardly. Consequently, despite our efforts, further acceleration of the code on the GPGPU was not achieved.

In this support program, code structure was changed only locally under a constraint of work time. For further speed-up of the code, it is essential to propose new arithmetic algorithms suited for the parallelization on GPGPU architectures, and if necessary, to implement them with the CUDA platform.

References

[1] Y. Andoh, *et al.* : J. Chem. Theory Comput. **9** (2013) 3201.

[2] L. F. Greengard : *The Rapid Evaluation of Potential Fields in Particle Systems* (MIT Press, 1988).

Implementation of GPGPU codes in Real-space Car-Parrinello Molecular Dynamics (RS-CPMD)

Yasuteru SHIGETA and Jun-ichi IWATA

Center for Computational Sciences,

University of Tsukuba, 1-1-1 Tennodai, Tsukuba, Ibaraki 305-8577, Japan.

Graduate School of Engineering, The University of Tokyo, Hongo 7-3-1, Tokyo, Japan.

The real space density functional theory (RSDFT) developed by one of us has enabled static calculations of several tens of thousands of silicon atoms on K computer [1, 2]. However, in order to describe physical properties of a given system, entropic contribution becomes important as the number of particles increases. Molecular dynamics (MD) simulations are usually used to take it into account. Howver, it is difficult to handle chemical reactions with classical MD. Neverheless, the first-principles MD (FPMD) also has a drawback in required computational costs. In order to avoid them, Car and Parrinello have proposed an efficient method to avoid solving the self-consitent field calculations in FPMD [3].

We have implemented CPMD modules in RSDFT (RS-CPMD), which enables us to simulate thousand atoms FPMD on K computer. In this report, performances of a GPU version of RSCPMD under the support of ISSP (SGI Japn and Ark Information Systems) is presented. The most severe bottleneck in RS-CPMD is evaluation of inner products between wave functions and its velocities ($O(N_{grid}^3)$). Therefore, in the implementation of the last year, we made GPU modules for this inner product calculation. Since BLAS3 routines can be used for this operation, three or four-fold speed-up can be achived by adopting GPU. In this year, GPU versions of several routines in a force evaluation were implimented. By changing the numers of MPIs and threds, we have tested our programs on ISSP system B 64 nodes (512 cores and 128 GPUs) for an organic solvent (1664 atoms) as a target system. For the fastest case it took 6.28 sec for one CPMD step, which is comparable with 5.54 sec with 4096 cores in K computer. For Ewald and local force calculations, drastic speed-up was achieved. While the performance of the GPU version for non-local forces is not high due to a difficulty in load balance and multiple internode communications.

References

[1] Y. Hasegawa *et al.*, *J. High Perform. Comp. Appl.* **28**, 335 (2014).

[2] https://github.com/j-iwata/RSDFT.

[3] R. Car, M. Parrinello, *Phys. Rev. Lett.* **55**, 2471 (1985)

4 PUBLICATION LIST

Example:

LASTNAME, Firstname [project class; # points (B), # points (C)] (Page #)
Project title
1. First paper
   Names of Authors, etc.
2. Second paper
   ...

□ ISSP Joint Research Projects

ADACHI, Takahiro [C class; 3500 (B), 900 (C)] (250)
— *Heat Transfer Characteristics of Condensate Film Flow along Vertical Plates with Microscopic Grooves*

AKAGI, Kazuto [C class; 11000 (B), 0 (C)] (55)
— *Exploration of structure motifs characterizing the metal oxides*
1. Deep electron and hole polarons and bipolarons in amorphous oxide
   M. Kaviani et al.: Phys. Rev. B **94** (2016) 020103(R).

AKAI, Hisazumi [B class; 500 (B), 300 (C)] (140)
— *Electronic structure of light rare earth permanent magnets*
1. Schottky junction studied using Korringa–Kohn–Rostoker Nonequilibrium Green's function method
   M. Ogura and H. Akai: J. Phys. Soc. Jpn. **85** (2016) 104715.
2. Relevance of 4f-3d exchange to finite-temperature magnetism of rare-earth permanent magnets: an ab-initio-based spin model approach for $NdFe_{12}N$
   M. Matsumoto, H. Akai, Y. Harashima, S. Doi and T. Miyake: J. Appl. Phys. **119** (2016) 213901.
3. Electrical resistivity of substitutionally disordered hcp Fe–Si and Fe–Ni alloys: Chemically-induced resistivity saturation in the Earth's core
   H. Gomi, K. Hirose, H. Akai, and Y. Fei: Earth Planet. Sci. Lett. **451** (2016) 51.
4. Monte Carlo analysis for finite-temperature magnetism of $Nd_2Fe_{14}B$ permanent magnet
   Yuta Toga, Munehisa Matsumoto, Seiji Miyashita, Hisazumi Akai, Shotaro Doi, Takashi Miyake, and Akimasa Sakuma: Phys. Rev. B **94** (2016) 174433.
5. Atomistic-model study of temperature-dependent domain walls in the neodymium permanent magnet $Nd_2Fe_{14}B$
   Masamichi Nishino, Yuta Toga, Seiji Miyashita, Hisazumi Akai, Akimasa Sakuma, and Satoshi Hirosawa: Phys. Rev. B **95** (2017) 094429.

AKASHI, Ryosuke [C class; 5500 (B), 800 (C)] (79)
— *Accurate evaluation of electron-phonon coupling in sulfur-hydride superconductors*
1. Possible "Magnéli" Phases and Self-Alloying in the Superconducting Sulfur Hydride
   R. Akashi, W. Sano, R. Arita, and S. Tsuneyuki: Phys. Rev. Lett. **117**, (2016) 075503.
2. Weak Phonon-mediated pairing in BiS_2 superconductor from first principles
   C. Morice, R. Akashi, T. Koretsune, S. S. Saxena, and R. Arita: arXiv:1701.02909; submitted.

ANDO, Yasunobu [C class; 1000 (B), 0 (C)] (139)
— *First-Principles study on the electric-double layer capacitance of MXene compound Ti_2CT_x*

AOYAMA, Kazushi [B class; 1200 (B), 0 (C)] (270)
— *Effects of a magnetic field on spin-lattice-coupled orders in pyrochlore antiferromagnets*
— *Lattice distortion effects on classical Heisenberg antiferromagnets on pyrochlore lattices*

1. Spin-Lattice-Coupled Order in Heisenberg Antiferromagnets on the Pyrochlore Lattice
   K. Aoyama and H. Kawamura: Phys. Rev. Lett. **116** (2016) 257201.

ARAI, Munehito [B class; 2100 (B), 1300 (C)] (257)
— *Computational rational design of novel artificial proteins*
— *Molecular dynamics simulations of proteins*
— *Structure and dynamics of the gliding protein from Mycoplasma mobile*

ARAIDAI, Masaaki [C class; 5500 (B), 2000 (C)] (68)
— *Development and Application of Extended Ensemble Method Coupled With First-Principles Electronic Structure Calculations*

ARAKAWA, Naoya [B class; 700 (B), 0 (C)] (193)
— *Study of interaction and multiband effects in intrinsic spin-Hall effect of an interacting multiorbital metal*

1. Controlling spin Hall effect by using a band anticrossing and nonmagnetic impurity scattering
   T. Mizoguchi and N. Arakawa: Phys. Rev. B **93** (2016) 041304(R).
2. Fermi-surface vs. Fermi-sea contributions to intrinsic anomalous- and spin-Hall effects of multiorbital metals in the presence of Coulomb interaction and spin-Coulomb drag
   N. Arakawa: Phys. Rev. B **93** (2016) 245128.
3. Microscopic theory on charge tranports of a correlated multiorbital system
   N. Arakawa: Phys. Rev. B **94** (2016) 045107.
4. Microscopic theory of Dzyaloshinsky-Moriya interaction in pyrochlore oxides with spin-orbit coupling
   N. Arakawa: Phys. Rev. B **94** (2016) 155139.
5. Vector chirality for effective total momentum J_{eff} in a nonfrustrated Mott insulator: Effects of strong spin-orbit coupling and broken inversion symmetry
   N. Arakawa: Phys. Rev. B **94** (2016) 174416.
6. Magnon dispersion and specific heat of chiral magnets on the pyrochlore lattice
   N. Arakawa: subitted to Phys. Rev. B.

ASAI, Yoshihiro [C class; 5000 (B), 2300 (C)] (69)
— *Large scale computational simulations of non-equilibrium transport phenomena*

1. The effect of a Ta oxygen scavenger layer on HfO2-based resistive switching behavior: thermodynamic stability, electronic structure, and low-bias transport
   X. Zhong, I. Rungger, P. Zapol, H. Nakamura, Y. Asai and O. Heinonen: Phys. Chem. Chem. Phys. **18** (2016) 7502.
2. Competitive effects of oxygen vacancy formation and interfacial oxidation on an ultra-thin HfO2-based resistive switching memory: beyond filament and charge hopping models
   H. Nakamura and Y. Asai: Phys. Chem. Chem. Phys. **18** (2016) 8820.
3. Thermoelectric effect and its dependence on molecular length and sequence in single DNA molecules
   Y. Li, L. Xiang, J. L. Palma, Y. Asai and NJ Tao: Nature Communications, **7** (2016) 11294.
4. Thermal conductance of Teflon and Polyethylene: Insight from an atomistic, single-molecule level
   M. Buerkle and Y. Asai: Sci. Rep. **7** (2017) 41898.
5. The Orbital Selection Rule for Molecular Conductance as Manifested in Tetraphenyl-Based Molecular Junctions
   M. Buerkle, L. Xiang, G. Li, A. Rostamian, T. Hines, S. Guo, G. Zhou, NJ Tao, and Y. Asai: J. Am. Chem. Soc. **139** (2017) 2989.

DEKURA, Haruhiko [C class; 1500 (B), 0 (C)] (49)
— *First-principles calculations of iron solid solution effects on the lattice thermal conductivity of lower mantle minerals*

DINO, Wilson [C class; 5500 (B), 2000 (C)] (67)
— *Surface reactions of hydrogen and oxygen on oxide materials*

1. A DFT+U study on the contribution of 4f electrons to oxygen vacancy formation and migration in Ln-doped CeO_2
   M. Alaydrus, M. Sakaue, H. Kasai: Phys. Chem. Chem. Phys. **18** (2016) 12938.
2. C_2H_4 adsorption on Cu(210), revisited: bonding nature and coverage effects
   S. Amino, E. Arguelles, W. A. Diño, M. Okada, H. Kasai: Phys. Chem. Chem. Phys. **18** (2016) 23621.
3. Experimental and Theoretical Studies on Oxidation of Cu-Au Alloy Surfaces: Effect of Bulk Au Concentration
   M. Okada, Y. Tsuda, K. Oka, K. Kojima, W. A. Diño, A. Yoshigoe, H. Kasai: Sci. Rep. **6** (2016) 31101.
4. Morphology Effect on Proton Dynamics in Nafion® 117 and Sulfonated Polyether Ether Ketone
   J. X. Leong, W. A. Diño, A. Ahmad, W. R. W. Daud, H. Kasai: J. Phys. Soc. Jpn. **85** (2016) 094803.
5. Enhanced Molecular Adsorption of Ethylene on Reduced Anatase TiO_2 (001): Role of Surface O-vacancy
   G. Shukri, W. A. Diño, H. K. Dipojono, M. K. Agusta, H. Kasai: RSC Advances **6** (2016) 92241.
6. CO-induced Pd segregation and the effect of subsurface Pd on CO adsorption on CuPd surfaces
   A. A. B. Padama, R. A. B. Villaos, J. R. Albia, W. A. Diño, H. Nakanishi, H. Kasai: J. Phys.: Condens. Matter **29** (2017) 025005.

EGAMI, Yoshiyuki [C class; 1000 (B), 2000 (C)] (119)
— *Development and application of first-principles simulator for time-dependent electron-transport calculation*

1. First-principles study on electron transport through BN-dimer embedded zigzag carbon nanotubes
   Y. Egami and H. Akera: Physica E **88** (2017) 212.
2. First-principles calculation method and its applications for two-dimensional materials
   Y. Egami, S. Tsukamoto, and T. Ono: Quantum Matter, in press.
3. First-principles study on electron transport through Mn(dmit)2 molecular junction depending on relative angle between ligands
   Y. Egami and M. Taniguchi: submitted to Physica B.

FUCHIZAKI, Kazuhiro [C class; 6500 (B), 0 (C)] (233)
— *Melting phenomena and polyamorphism*

1. A new approach for estimating the density of liquids
   T. Sakagami, K. Fuchizaki, and K. Ohara: J. Phys.: Condens. Matter **28** (2016) 395101.
2. Structure of a molecular liquid GeI_4
   K. Fuchizaki, T. Sakagami, S. Kohara, A. Mizuno, Y. Asano, and N. Hamaya: J. Phys.: Condens. Matter **28** (2016) 445101.
3. Does a network structure exist in molecular liquid SnI_4 and GeI_4?
   T. Sakagami and K. Fuchizaki: J. Phys.: Condens. Matter **29** (2017) 145102.
4. Determination of the Melting Curve of the Modified Lennard-Jones System Using the Nonequilibrium Relaxation Method
   Y. Asano and K. Fuchizaki: J. Phys. Soc. Jpn **86** (2017) 025001.
5. Accurate Critical Parameters for the Modified Lennard-Jones Model
   K. Okamoto and K. Fuchizaki: J. Phys. Soc. Jpn **86** (2017) 034003.

FUJIKAWA, Sachie [C,D class; 1300 (B), 500 (C)] ()
— *Study of band structure for InSbN based dilute nitride semiconductor by using first-principle simulation*

FUJIMOTO, Yoshitaka [C class; 2000 (B), 0 (C)] (121)
— *Atomic structures and electronic properties of atomic-layered materials*

1. Interlayer distances and band-gap tuning of hexagonal boron-nitride bilayers

Y. Fujimoto and S. Saito: Journal of the Ceramic Society of Japan **124**, 584 (2016).
2. Gas adsorption, energetics and electronic properties of boron- and nitrogen-doped bilayer graphenes
Y. Fujimoto and S. Saito: Chem. Phys. **478**, 55 (2016).
3. Band engineering and relative stabilities of hexagonal boron-nitride bilayers under biaxial strains
Y. Fujimoto and S. Saito: Phys. Rev. B **94**, 245427 (2016).
4. Structure, Stabilities, and Electronic Properties of Smart Ceramic Composites
Y. Fujimoto: Sol-Gel Based Nanoceramic Materials: Synthesis, Properties, and Applications (Springer 2017) Chapter 4, pp.113.
5. Energetics and scanning tunneling microscopy images of B and N defects in graphene bilayer
Y. Fujimoto and S. Saito: Springer Proceedings in Physics **186**, 107 (2017).
6. Gas adsorption effects on the stabilities, electronic structures and scanning tunneling microscopy of graphene monolayers doped with B or N
Y. Fujimoto and S. Saito: submitted.

FUKUDA, Jun-ichi [B,D class; 1700 (B), 0 (C)] (266)
— *Calculation of optical properties of ordered structures of soft materials*

FUKUI, Ken-ichi [C class; 4500 (B), 1700 (C)] (82)
— *Microscopic Structure and Dynamics of Solutions Faced to Solid Materials Using First-Principles and Classical Molecular Dynamics*
1. Density Functional Theory Investigations of Ferrocene-Terminated Self-Assembled Monolayers: Electronic State Changes Induced by Electric Dipole Field of Coadsorbed Species
Y. Yokota, S. Akiyama, Y. Kaneda, A. Imanishi, K. Inagaki, Y. Morikawa and K. Fukui: J. Phys. Chem. C, **120**, 8684-8692 (2016).

FURUKAWA, Akira [C class; 4500 (B), 0 (C)] (249)
— *Anomalous rheological behaviors of glassy materials and granular suspensions*
1. Significant Difference in the Dynamics between Strong and Fragile Glass-formers
Akira Furukawa and Hajime Tanaka : Phys. Rev. E, **94**, 052607 (2016).
2. Onset of shear thinning in glassy liquids: Shear-induced small reduction of effective density
Akira Furukawa : Phys. Rev. E **95**, 012613 (2017).

GOHDA, Yoshihiro [B class; 700 (B), 500 (C)] (128)
— *Effects of heavy elements in surface nanostructures*
1. First-Principles Study of the Role of Cu in Improving the Coercivity of Nd-Fe-B Permanent Magnets
Y. Tatetsu, S. Tsuneyuki, and Y. Gohda: Phys. Rev. Appl. **6**, 064029 (2016).
2. Epitaxially stabilized iron thin films via effective strain relief from steps
T. Miyamachi, S. Nakashima, S. Kim, N. Kawamura, Y. Tatetsu, Y. Gohda, S. Tsuneyuki, and F. Komori: Phys. Rev. B **94**, 045439 (2016).

HAGITA, Katsumi [D class; 10000 (B), 0 (C)] (212)
— *2D Scattering Pattern Analysis on Coarse Grained MD Model of Filled Hydrogel*
1. Coarse-Grained Molecular Dynamics Simulation of Filled Polymer Nanocomposites under Uniaxial Elongation
K. Hagita, H. Morita, M. Doi, H. Takano: Macromolecules 49 (2016) 1972-1983.
2. Molecular dynamics simulation study of a fracture of filler-filled polymer nanocomposites
K. Hagita, H. Morita, H. Takano, Polymer, 99 (2016) 368-375.

HAMADA, Ikutaro [C class; 2500 (B), 1300 (C)] (103)
— *Development and application of the large-scale GW calculation code*

HAMAMOTO, Yuji [C class; 2000 (B), 1300 (C)] ()
— *First principles study of the influence of lattice defects on Pt cluster supported on graphene*

HARADA, Kenji [C class; 5000 (B), 0 (C)] (245)
— *Development of tensor network algorithms*

HASHIMOTO, Tamotsu [C class; 5000 (B), 0 (C)] (244)
— *Molecular dynamics simulation of ferroelectrics using a shell model II*

HATSUGAI, Yasuhiro [C class; 6000 (B), 1300 (C)] (229)
— *Numerical studies of bulk-edge correspondence*

1. Edge states of mechanical diamond and its topological origin
   Y. Takahashi, T. Kariyado, Y. Hatsugai: New J. Phys. 19, 035003 (2017).
2. Edge states of hydrogen terminated monolayer materials: silicene, germanene and stanene ribbons
   A. Hattori, S. Tanaya, K. Yada, M. Araidai, M. Sato, Y. Hatsugai, K. Shiraishi, Y. Tanaka: J. Phys. Cond. Mat. 29, 115302 (2017).
3. A Spin Pump Characterized by Entanglement Chern Numbers
   T. Fukui, Y. Hatsugai: J. Phys. Soc. Jpn 85, 083703 (2016).
4. Bulk-edge correspondence in topological pumping
   Y. Hatsugai, T. Fukui: Phys. Rev. B 94, 041102(2016).
5. Lattice realization of the generalized chiral symmetry in two dimensions
   T. Kawarabayashi, H. Aoki, Y. Hatsugai: Phys. Rev. B94, 235307 (2016).
6. Section Chern number for a three-dimensional photonic crystal and the bulk-edge correspondence
   S. Oono, T. Kariyado, Y. Hatsugai: Phys. Rev. B94, 125125 (2016).

HATTORI, Kazumasa [C class; 2000 (B), 0 (C)] (191)
— *Numerical analysis on a transverse-field Ising-Kondo lattice model*

HATTORI, Ken [B class; 1200 (B), 300 (C)] (125)
— *Model calculations in Si surfaces with adsorbates*

HAYAMI, Satoru [C class; 2000 (B), 0 (C)] (189)
— *Study of skyrmion in frustrated magnets with inversion symmetry*

1. Effective bilinear-biquadratic model for noncoplanar ordering in itinerant magnets
   S. Hayami, R. Ozawa, and Y. Motome, submitted to Phys. Rev. B

HIDA, Kazuo [B class; 500 (B), 0 (C)] (280)
— *Numerical Study of One Dimensional Frustrated Quantum Spin Systems*

1. Topological Phases of Spin-1/2 Ferromagnetic–Antiferromagnetic Alternating Heisenberg Chains with Alternating Next-Nearest-Neighbour Interaction
   K. Hida: J. Phys. Soc. Jpn. **85**, 124712 (2016).
2. Ground State Phase Diagram of S=1 Diamond Chains
   K. Hida and K. Takano: J. Phys. Soc. Jpn. **86**, 033707 (2017).

HIRAI, Kunitomo [B class; 200 (B), 100 (C)] (155)
— *Electronic State and Proximity Effects around Interface in Layered Superlattices*

HIRAYAMA, Naomi [C class; 3000 (B), 0 (C)] ()
— *Effects of Impurity Doping on Thermoelectric Transport Properties of Semiconducting Silicides*

HIYAMA, Miyabi [B class; 600 (B), 0 (C)] (278)
— *Electronic states of bioluminescence related molecules*

1. Reverse Stability of Oxyluciferin Isomers in Aqueous Solutions
   Y. Noguchi, M. Hiyama, M. Shiga, O. Sugino and H. Akiyama: J. Phys. Chem. B, **120** (2016) 8776.
2. Theoretical insights into the effect of pH values on oxidation processes in the emission of firefly luciferin in aqueous solution
   M. Hiyama, H. Akiyama and N. Koga, Luminescence: The Journal of Biological and Chemical

Luminescence, in press

3. Effect of dynamical fluctuations of hydration structures on the absorption spectra of oxyluciferin anions in aqueous solution
   M. Hiyama, M. Shiga, N. Koga, O. Sugino, H. Akiyama and Y. Noguchi: Phys. Chem. Chem. Phys., in press.

HOSHI, Takeo [C class; 4500 (B), 500 (C)] (95, 314)

— *Large-scale device-material research by massively parallel electronic structure calculation and data science*

1. Extremely scalable algorithm for 108-atom quantum material simulation on the full system of the K computer
   T. Hoshi, H. Imachi, K. Kumahata, M. Terai, K. Miyamoto, K. Minami and F. Shoji, Proc. ScalA16 in SC16, pp.33-40, (2016)
2. One-hundred-nm-scale electronic structure and transport calculations of organic polymers on the K computer
   H. Imachi, S. Yokoyama, T. Kaji, Y. Abe, T. Tada, AIP Conf. Proc. 1790, 020010, 4pp. (2016)
3. Asymptotic quadratic convergence of the serial block-Jacobi EVD algorithm for Hermitian matrices
   G. Oksa, Y. Yamamoto, M. Vajtersic, Numerische Mathematik, to appear (DOI : 10.1007/s00211-016-0863-5)
4. Performance analysis and optimization of the parallel one-sided block Jacobi SVD algorithm with dynamic ordering and variable blocking
   S. Kudo, Y. Yamamoto, M. Becka, M. Vajtersic, Concurrency and Computation: Practice and Experience, to appear (DOI : 10.1002/cpe.4059)
5. Switching mechanism in resistive random access memory by first-principles calculation using practical model based on experimental results
   T. Moriyama, T. Yamasaki, S. Hida, T. Ohno, S. Kishida, and K. Kinoshita, Jpn. J. Appl. Phys., Accepted.
6. Resistance given by tiling grain surface with micro surface structures inpolycrystalline metal oxide
   T. Moriyama, T. Yamasaki, T. Ohno, S. Kishida, and K. Kinoshita, J. Appl. Phys. **120**, 215302 (2016)
7. Formation mechanism of conducting path in resistive random access memory by first principles calculation using practical model based on experimental results
   T. Moriyama, T. Yamasaki, T. Ohno, S. Kishida, and K. Kinoshita, MRS Advances **1(49)**, 3367 (2016)

HOSHINO, Shintaro [C class; 5500 (B), 0 (C)] (173)

— *Monte Carlo approach to correlated electron and spin systems*

1. Ultrafast switching of composite order in A3C60
   P. Werner, H. Strand, S. Hoshino, M. Eckstein, arXiv:1612.09584, (2016).
2. Spontaneous orbital-selective Mott transitions and the Jahn-Teller metal of A3C60
   S. Hoshino, P. Werner, arXiv:1609.00136, (2016), accepted for publication in Phys. Rev. Lett.
3. A spin-freezing perspective on cuprates
   P. Werner, S. Hoshino, H. Shinaoka, Phys. Rev. B 94, 245134 (2016).
4. Long-range orders, spin- and orbital-freezing in the two-band Hubbard model
   K. Steiner, S. Hoshino, Y. Nomura, P. Werner, Phys. Rev. B 94, 075107 (2016).
5. Tunneling and Josephson effects in odd-frequency superconductor junctions: A study on multi-channel Kondo chain
   S. Hoshino, K. Yada, Y. Tanaka, Phys. Rev. B 93, 224511 (2016).
6. Critical Temperature Enhancement of Topological Superconductors: A Dynamical Mean Field Study
   Y. Nagai, S. Hoshino, Y. Ota, Phys. Rev. B (Rapid Communications) 93, 220505 (2016)
7. Electronic orders in multi-orbital Hubbard models with lifted orbital degeneracy
   S. Hoshino, P. Werner, Phys. Rev. B 93, 155161, (2016).
8. Finite-Temperature Properties of Three-Dimensional Classical Chiral Helimagnets

M. Shinozaki, S. Hoshino, Y. Masaki, J. Kishine, Y. Kato, J. Phys. Soc. Jpn. 85, 074710 (2016).

HOTTA, Takashi [C class; 4000 (B), 400 (C)] (177)
— *Research on Kondo effect in the Peierls-Anderson model*

1. Influence of lattice structure on multipole interactions in Γ 3 non-Kramers doublet systems
   Katsunori Kubo and Takashi Hotta: Phys. Rev. B **95** (2017) 054425-1-6.

HU, Chunping [B class; 800 (B), 500 (C)] ()
— *First-principles simulation of electrolyte diffusion process on constant-potential electrodes*

HUKUSHIMA, Koji [C class; 11500 (B), 1900 (C)] (29)
— *Large-scale Monte Carlo calculation of random spin systems*

1. Irreversible simulated tempering
   Y. Sakai and K. Hukushima: J. Phys. Soc. Jpn. **85** (2016) 104002/1-7.
2. Irreversible simulated tempering algorithm with skew detailed balance conditions: a learning method of weight factors in simulated tempering
   Y. Sakai and K. Hukushima: J. Phys.: Conf. Ser. **750** (2016) 012013/1-5.
3. Phase transitions and ordering structures of a model of chiral helimagnet in three dimensions
   Y. Nishikawa, and K.Hukushima: Phys. Rev. B **94** (2016) 064428/1-11.

IGARASHI, Ryo [C class; 2000 (B), 2000 (C)] ()
— *Monte Carlo simulation using low-rank approximation to long range interaction matrices*
— *Parallelization and GPGPU utilization of MPS program and its application to frustrated systems*

IKUHARA, Yuichi [C class; 6500 (B), 2500 (C)] (63)
— *Study of Atomic Structures and Selective Segregation Behavior at Grain Boundaries in Functional Materials*

1. Atomic structure and electronic properties of MgO grain boundaries in tunnelling magnetoresistive devices
   J. J. Bean, M. Saito, S. Fukami, H. Sato, S. Ikeda, H. Ohno, Y. Ikuhara and K. P. McKenna: Sci. Rep. **7**, (2017) 45594.

IMADA, Masatoshi [D,E class; 50500 (B), 7000 (C)] (157)
— *Numerical Studies on Finite-Temperature Properties of 2D Hubbard and ab initio Models for Cuprates by Finite-Temperature Variational Monte Carlo Methods*
— *Numerical Studies on Mechanisms for Critical Temperature Control at Interfaces of Superconductors*
— *Numerical study of non-equilibrium superconducting states in two-dimensional Hubbard model by the time-dependent multi-variable variational Monte Carlo method*

1. Finite-Temperature Variational Monte Carlo Method for Strongly Correlated Electron Systems
   Kensaku Takai, Kota Ido, Takahiro Misawa, Youhei Yamaji, and Masatoshi Imada: J. Phys. Soc. Jpn.**85** (2016) 034601.
2. Real-space renormalized dynamical mean field theory
   Dai Kubota, Shiro Sakai, and Masatoshi Imada: Phys. Rev. B **93** (2016) 205119.
3. Modulated Helical Metals at Magnetic Domain Walls of Pyrochlore Iridium Oxides
   Youhei Yamaji, Masatoshi Imada: Phys. Rev. B**93** (2016) 195146.
4. Clues and criteria for designing a Kitaev spin liquid revealed by thermal and spin excitations of the honeycomb iridate Na2IrO3
   Youhei Yamaji, Takafumi Suzuki, Takuto Yamada, Sei-ichiro Suga, Naoki Kawashima, and Masatoshi Imada: Phys. Rev. B **93** (2016) 174425.
5. Self-Optimized Superconductivity Attainable by Interlayer Phase Separation at Cuprate Interfaces
   Takahiro Misawa, Yusuke Nomura, Silke Biermann, and Masatoshi Imada: Sci. Adv. **2** (2016) e1600664 .
6. Nonequilibrium Pump-Probe Photoexcitation as a Tool for Analyzing Unoccupied Equilibrium States of Correlated Electrons
   Youhei Yamaji,and Masatoshi Imada: J. Phys. Soc. Jpn. **85** (2016) 094707.

7. Hidden-fermion representation of self-energy in pseudogap and superconducting states of the two-dimensional Hubbard model
   Shiro Sakai, Marcello Civelli, and Masatoshi Imada: Phys. Rev. B.**94** (2016) 115130.
8. Stabilization of topological insulator emerging from electron correlations on honeycomb lattice and its possible relevance in twisted bilayer graphene
   Moyuru Kurita, Youhei Yamaji, and Masatoshi Imada : Phys. Rev. B. **94** (2016) 125131.

INAGAKI, Kouji [C class; 5000 (B), 1800 (C)] (75)
— *First-principles meta-dynamics analysis of Catalyst Referred Etching method (dissociative adsorption reaction barrier at interface between Pt and material surface)*

INAOKA, Takeshi [C class; 2500 (B), 1100 (C)] (106)
— *Search and realization of novel electronic properties of solid surfaces and small particles*
1. STM-enhanced dynamic dipole moments coupled with adsorbate vibration at substrate or tip surfaces
   T. Inaoka and Y. Uehara: submitted to J. Appl. Phys.

ISHII, Fumiyuki [B,C class; 8200 (B), 1300 (C)] (59, 61)
— *First-principles calculations of oxide thin-films and heterostructures*
— *First-principles study of anomalous thermoelectric effect*
— *First-principles design of thermoelectric materials based on Berry curvature landscape*
1. Large Anomalous Nernst Effect in a Skyrmion Crystal
   Y. P. Mizuta and F. Ishii: Sci. Rep. **6** (2016) 28076.
2. First-principles study of Rashba effect in ultra-thin bismuth surface alloys
   N. Yamaguchi, H. Kotaka, and F. Ishii: J. Cryst. Growth, in press.
3. Strain-controlled spin splitting in the conduction band of monolayer WS_2
   M.A.U. Absor, H. Kotaka, F. Ishii, and M. Saito: Phys. Rev. B **94** (2016)115131.
4. First-principles design of the spinel iridate Ir_2O_4 for high-temperature quantum spin ice
   S. Onoda and F. Ishii: arXiv:1612.00553.

ISOBE, Masaharu [B class; 900 (B), 0 (C)] (273)
— *Nonequilibrium phase transition in the large scale dense hard sphere molecular dynamics simulation*
1. Hard Sphere Simulation in Statistical Physics —Methodologies and Applications—
   M. Isobe: Molecular Simulation, — A special issue on nonequilibrium systems —, Mol. Sim. **42** (2016) 1317.
2. Applicability of Dynamic Facilitation Theory to Binary Hard Disk Systems
   M. Isobe, A. S. Keys, D. Chandler, and J. P. Garrahan: Phys. Rev. Lett. **117** (2016) 145701.
3. Hard Sphere Simulation by Event-Driven Molecular Dynamics : Breakthrough, Numerical Difficulty and Overcoming the Issues
   M. Isobe: "Advances in the Comutational Sciences — Proceedings of the Symposium in Honor of Dr Berni Alder's 90th Birthday", edited by Eric Shwegler, Brenda M. Rubenstein, and Stephen B. Libby, World Scientific, Chapter **6** (2017) 83.
4. Clustering Impact Regime with Shocks in Freely Evolving Granular Gas
   M. Isobe: EPJ Web of Conferences, Proceedings of Powders&Grains2017, (2017) in press.

KAGESHIMA, Hiroyuki [C class; 1000 (B), 0 (C)] (138)
— *Study on structure formation and physical properties of multiatomic vacancies and clusters of 2D semiconductors*
1. Theoretical study of multiatomic vacancies in single-layer hexagonal boron nitride
   S. Urasaki, and H. Kageshima, Jpn. J. Appl. Phys. **56**, 025201 (2017).

KAKEHASHI, Yoshiro [B class; 400 (B), 0 (C)] (154)
— *First-Principles Momentum Dependent Local Ansatz and Application to Momentum Distribution and Quasiparticle Bands in Fe Compounds*
1. First-Principles Theory of Momentum Dependent Local Ansatz Approach to Correlated Electron

System
S. Chandra and Y. Kakehashi: J. Phys. Soc. Jpn. **85**, 064714 (2016).
2. First-Principles Momentum Dependent Local Ansatz Approach to the Ground-State Properties of Iron-Group Transition Metals
Y. Kakehashi and S. Chandra: J. Phys. Soc. Jpn. **85**, 084708 (2016).
3. First-Principles Momentum Dependent Local Ansatz Approach to the Momentum Distribution Function in Iron-Group Transition Metals
Y. Kakehashi and S. Chandra: J. Phys. Soc. Jpn. **86**, 034711 (2017).

KAMIHARA, Yoichi [B class; 600 (B), 0 (C)] (151)
— *Theoretical research on dissociation of N2 and H2 for designing new ammonia catalysis supporting Ru*

KAMIYA, Yoshitomo [C class; 6000 (B), 0 (C)] (238)
— *Quantum Monte Carlo study of spin liquids*

KARIYADO, Toshikaze [B class; 600 (B), 0 (C)] (277)
— *Analysis of Topological Systems with Real Space Structures*

KASAMATSU, Shusuke [C class; 5500 (B), 0 (C)] (90)
— *First-principles analysis of the dielectric response of defective interfaces*
1. Electric field response in bilayer graphene: Ab initio investigation
Y. Mori, E. Minamitani, Y. Ando, S. Kasamatsu and S. Watanabe: Appl. Phys. Express **9** (2016) 115104.

KATO, Takeo [B class; 800 (B), 0 (C)] ()
— *Numerical research of one-dimensional interacting electron systems by a quantum Monte Carlo method*

KATO, Yusuke [C class; 7000 (B), 0 (C)] (232)
— *Thermodynamic properties of chiral magnets*
1. Finite-Temperature Properties of Three-Dimensional Chiral Helimagnets
M.Shinozaki, S. Hoshino, Y. Masaki, J. Kishine, and Y. Kato: J. Phys. Soc. Jpn. **85** (2016) 074710.
2. Erratum: Finite-Temperature Properties of Three-Dimensional Chiral Helimagnets
M.Shinozaki, S. Hoshino, Y. Masaki, J. Kishine, and Y. Kato: J. Phys. Soc. Jpn. **86** (2016) 038001.

KAWAKAMI, Norio [C class; 11500 (B), 0 (C)] (165)
— *Skyrmion phases and nonequilibrium phenomena in strongly correlated electron systems with strong spin-orbit interaction*
— *Topological phases and nonequilibrium phenomena in strongly correlated electron systems with strong spin-orbit interaction*
1. Coexistence of light and heavy surface states in a topological multiband Kondo insulator
R. Peters, T. Yoshida, H. Sakakibara, and N. Kawakami: Phys. Rev. B **93**, 235159 (2016)
2. Magnetism in f-electron superlattices
R. Peters, Y. Tada, and N. Kawakami: Phys. Rev. B **94**, 205142 (2016)
3. Reduction of Z classification of a two-dimensional weak topological insulator
T. Yoshida and N. Kawakami: Phys. Rev. B **95**, 045127 (2017)
4. Fate of Majorana modes in CeCoIn5/YbCoIn5 superlattices
T. Yoshida, A. Daido, Y. Yanase, and N. Kawakami: Phys. Rev. Lett. **118**, 147001 (2017)
5. Topological edge Mott insulating state in two dimensions at finite temperatures
T. Yoshida and N. Kawakami: Phys. Rev. B **94**, 085149 (2016)

KAWAMURA, Hikaru [B,C class; 12100 (B), 0 (C)] (204, 206)
— *Novel order in frustrated magnets*
— *Numerical simulations on statistical models of earthquakes*

1. Spin-lattice-coupled order in Heisenberg antiferromagnets on the pyrochlore lattice
   K. Aoyama and H. Kawamura: Phys. Rev. Lett. **116**, 257201 (2016).
2. Finite-temperature crossover phenomenon in the S=1/2 antiferromagnetic Heisenberg model on the kagome lattice
   T. Shimokawa and H. Kawamura: J. Phys. Soc. Jpn. **85**, 113702 (2017).
3. Randomness-Induced Quantum Spin Liquid Behavior in the s = 1/2 Random J1-J2 Heisenberg Antiferromagnet on the Honeycomb Lattice
   K. Uematsu and H. Kawamura: J. Phys. Soc. Jpn. **86**, 044704 (2017).
4. Statistical properties of the one-dimensional Burridge-Knopoff model obeying the date and state dependent friction law
   H. Kawamura, Y. Ueda, S. Kakui, S. Morimoto and T. Yamamoto: Phys. Rev. E **95**, 042122 (2017).

KAWASHIMA, Naoki [E class; 40500 (B), 4700 (C)] (197)
— *Tensor Network Study on Frustrated Quantum Spin Systems*

1. Ground state properties of Na_2IrO_3 determined from *ab initio* Hamiltonian and its extensions containing Kitaev and extended Heisenberg interactions
   Tsuyoshi Okubo, Kazuya Shinjo, Youhei Yamaji, Naoki Kawashima, Shigetoshi Sota, Takami Tohyama, and Masatoshi Imada: arXiv:1611.03614.
2. Quantum Lattice Model Solver HPhi
   M. Kawamuraa, K. Yoshimi, T. Misawa, Y. Yamaji, S. Todo, and N. Kawashima: Comput. Phys. Commun. in press.
3. Clues and criteria for designing a Kitaev spin liquid revealed by thermal and spin excitations of the honeycomb iridate Na2IrO3
   Youhei Yamaji, Takafumi Suzuki, Takuto Yamada, Sei-ichiro Suga, Naoki Kawashima, and Masatoshi Imada: Phys. Rev. B **93**, 174425 (2016).

KITA, Takafumi [C class; 3000 (B), 0 (C)] (259)
— *Microscopic analysis of the Hall effect in superconductors using the augmented quasiclassical equations with the Lorentz force*

KITAO, Akio [C class; 8500 (B), 1000 (C)] (214)
— *Efficient sampling simulation of the soft modes significantly contribute to protein properties*

1. High anisotropy and frustration: the keys to regulating protein function efficiently in crowded environments.
   A. Kitao and K. Takemura: Curr. Opin. Struct. Biol., **42** (2017) 50.
2. Computational Assignment of the Histidine Protonation State in (6-4) Photolyase Enzyme and Its Effect on the Protonation Step.
   H. M. Dokainish and A. Kitao: ACS Catal., **6** (2016) 5500.
3. Dynamic profile analysis to characterize dynamics-driven allosteric sites in enzymes.
   J. Taguchi and A. Kitao: Biophys. Physicobiol., **13** (2016) 117.

KOBAYASHI, Katsuyoshi [B class; 400 (B), 300 (C)] (146)
— *Search for electronic properties of new nanoscale interfaces*

1. Spin-dependent quantum interference in photoemission process from spin-orbit coupled states
   K. Yaji et al.: Nat. Commun. **8** (2017) 14588.

KOBAYASHI, Nobuhiko [C class; 10500 (B), 4300 (C)] (50)
— *First-principles study of quantum transport in nanostructures*

1. First-principles calculations of thermoelectric properties of TiN/MgO superlattices:The route for an enhancement of thermoelectric effects in artificial nanostructures,
   H. Takaki, K. Kobayashi, M. Shimono, N. Kobayashi, and K. Hirose: J. Appl. Phys. 119 014302

(2016).
2. Confinement of the Pt(111) Surface State in Graphene Nanoislands,
H. W. Kim, S. Takemoto, E. Minamitani, T. Okada, T. Takami, K. Motobayashi, M. Trenary, M. Kawai, N. Kobayashi, and Y. Kim: J. Phys. Chem. C 120 345-349 (2016).
3. Emergence of charge coherence in soft molecular organic semiconductors by suppressing thermal fluctuations,
K. Sakai, Y. Okada, T. Uemura, J. Tsurumi, R. Hausermann, H. Matsui, T. Fukami, H. Ishii, N. Kobayashi, K. Hirose and J. Takeya: NPG Asia Materials, 8, e252 (2016).
4. 電気伝導理論、
小林伸彦、石井宏幸、広瀬賢二: 機能構造科学入門、（丸善出版, 2016）p111-121.
5. Electronic band structure of TiN/MgO nanostructures,
K.Kobayashi, H.Takaki, M.Shimono, N.Kobayashi, K.Hirose: Jpn. J. Appl. Phys. 56 04CK06 (2017).
6. First-principles calculations of Seebeck coefficients in a magnetic semiconductor CuFeS2,
H.Takaki, K.Kobayashi, M.Shimono, N.Kobayashi, K.Hirose, N.Tsujii, T.Mori: Appl. Phys. Lett. **110**, 072107 (2017).
7. Charge transport calculations by a wave-packet dynamical approach using maximally localized Wannier functions based on density functional theory: Application to high-mobility organic semiconductors,
H. Ishii, N. Kobayashi, and K. Hirose: Phys. Rev. B **95**, 035433 (2017).

KOGA, Akihisa [C class; 9500 (B), 0 (C)] (169)

— *Dynamical mean-field theory for correlated electron system with orbital degeneracy*

— *Dynamical mean-field theory for strongly correlated electron systems with quasiperiodicity*

1. Spin-Liquid-to-Spin-Liquid Transition in Kitaev Magnets Driven by Fractionalization
J. Nasu, Y. Kato, J. Yoshitake, Y. Kamiya, and Y. Motome: Phys. Rev. Lett. **118**, 137203 (2017).
2. Spontaneously symmetry breaking states in the attractive SU(N) Hubbard model
A. Koga and H. Yanatori: J. Phys. Soc. Jpn. **86**, 034702 (2017).
3. Superconductivity on a Quasiperiodic Lattice: Extended-to-Localized Crossover of Cooper Pairs
S. Sakai, N. Takemori, A. Koga, and R. Arita: Phys. Rev. B **95**, 024509 (2017).
4. Fermionic response from fractionalization in an insulating two-dimensional magnet
J. Nasu, J. Knolle, D. L. Kovrizhin, Y. Motome, and R. Moessner: Nat. Phys. **12**, 912-915 (2016).
5. Magnetic Response and Valence Fluctuations in the Extended Anderson Lattice Model with Quasiperiodicity
R. Shinzaki, J. Nasu, and A. Koga: J. Phys. Soc. Jpn. **85**, 114706 1-6 (2016).
6. Fractional Spin Fluctuation as a Precursor of Quantum Spin Liquids: Majorana Dynamical Mean-Field Study for the Kitaev Model
J. Yoshitake, J. Nasu, and Y. Motome: Phys. Rev. Lett. **117**, 157203 (2016).
7. Magnetic Field Effects in a Correlated Electron System with Spin-State Degree of Freedom - Implication of an Excitonic Insulator-
T. Tatsuno, E. Mizoguchi, J. Nasu, M. Naka, and S. Ishihara: J. Phys. Soc. Jpn. **85**, 083706 (2016).
8. Finite Temperature Phase Transitions in the SU(N) Hubbard model
H. Yanatori and A. Koga: Phys. Rev. B **94**, 041110(R) (2016).
9. Phase transitions in the Hubbard model for the bismuth nickelate
S. Kojima, J. Nasu, A. Koga: Phys. Rev. B **94**, 045103 (2016).
10. Phase diagram and collective excitations in an excitonic insulator from an orbital physics viewpoint
J. Nasu, T. Watanabe, M. Naka, and S. Ishihara: Phys. Rev. B **93**, 205136 (2016).
11. Cluster Size Effects on Electronic Reconstruction in Quasiperiodic System
R. Shinzaki, J. Nasu, and A. Koga: J. Phys.: Conf. Ser. **809**, 012022 (2017).

KOTAKA, Hiroki [C class; 4000 (B), 1700 (C)] ()

— *First-principles study of nontrivial electronic structure*

KOURA, Akihide [C class; 2500 (B), 1200 (C)] (104)

— *Ab initio molecular dynamics study of static structure of glasses*

1. Pressure dependence of the static structure of liquid GeTe based on ab initio molecular dynamics simulations
   A. Koura and F. Shimojo: submitted to LAM-16 Conference Proceedings

KUNISADA, Yuji [C class; 7000 (B), 0 (C)] (72)

— *Reduction of Rare Metals in Fuel Cell Catalysts and Oxygen Sorption Materials*

1. Estimating the dopant distribution in Ca-doped α-SiAlON: statistical HAADF-STEM analysis and large-scale atomic modeling
   N. Sakaguchi, F. Yamaki, G. Saito, Y. Kunisada: Microscopy **65** (2016) 400.
2. Improving the measurement of dielectric function by TEM-EELS: avoiding the retardation effect
   N. Sakaguchi, L. Tanda, Y. Kunisada: Microscopy **65** (2016) 415.
3. Al(111) 表面近傍での水素原子の拡散特性における欠陥及び合金元素の影響
   國貞雄治，坂口紀史: 金属学会誌 **80** (2016) 570.
4. Measurement of the dielectric function of α-Al_2O_3 by transmission electron microscopy-electron energy-loss spectroscopy without Cerenkov radiation effects
   N. Sakaguchi, L. Tanda, and Y. Kunisada: Ultramicroscopy **169** (2016) 37.
5. Twin formation in hematite during dehydration of goethite
   G. Saito, Y. Kunisada, T. Nomura, N. Sakaguchi, T. Akiyama: Phys. Chem. Miner. **43** (2016) 749.
6. Atomic and local electronic structures of $Ca_2AlMnO_{5+\delta}$ as an oxygen storage material
   G. Saito, Y. Kunisada, K. Hayami, T. Nomura, N. Sakaguchi: Chem. Mater. **29** (2017) 648.
7. Three-dimensional analysis of Eu dopant atoms in Ca-α-SiAlON via through-focus HAADF-STEM imaging
   G. Saito, F. Yamaki, Y. Kunisada, N. Sakaguchi, T. Akiyama: Ultramicroscopy **175** (2017) 97.

KUROKI, Kazuhiko [C class; 3500 (B), 1300 (C)] (175)

— *Study on transition metal oxides by combined first-principles and many-body methods*

1. Strong Bilayer Coupling Induced by the Symmetry Breaking in the Monoclinic Phase of BiS_2-Based Superconductors
   M. Ochi, R. Akashi, and K. Kuroki: J. Phys. Soc. Jpn. **85** (2016) 094705.
2. Correlated Band Structure of a Transition Metal Oxide ZnO Obtained from a Many-Body Wave Function Theory
   M. Ochi, R. Arita, and S. Tsuneyuki: Phys. Rev. Lett. **118** (2017) 026402.
3. Two-particle self-consistent analysis for the electron-hole asymmetry of superconductivity in cuprate superconductors
   D. Ogura and K. Kuroki: Phys. Status Solidi C (2017) 1600157.

KUROSAWA, Masashi [C class; 3500 (B), 0 (C)] (112)

— *First-Principles Study on New Group-IV Semiconductor Alloys*

1. Evaluation of energy band offset of $Si_{1-x}Sn_x$ semiconductors by numerical calculation using density functional theory
   Y. Nagae, M. Kurosawa, M. Araidai, O. Nakatsuka, K. Shiraishi, and S. Zaima: Jpn. J. Appl. Phys. **56** (2017) 04CR10.

KUSAKABE, Koichi [C class; 2000 (B), 700 (C)] (184)

— *Topological symmetry in two-body scattering in strongly correlated electron systems*

1. Theoretical Analysis on Pseudo-Degenerate Zero-Energy Modes in Vacancy-Centered Hexagonal Armchair Nanographene
   N. Morishita, G.K. Sunnardianto, S. Miyao, K. Kusakabe, J. Phys. Soc. Jpn., **85**, 084703 (2016).
2. Structure Deformation and Level Splitting in Vacancy-Centered Hexagonal Armchair Nanographene
   S. Miyao, N. Morishita, G.K. Sunnardianto, K. Kusakabe, J. Phys. Soc. Jpn. **86**, 034802 (2017).
3. Systematic study of the effect of H adsorption on the rate of electron transfer in graphene
   G.K. Sunnardianto, I. Maruyama, K. Kusakabe, J. Comput. Theor. Nanosci. **13**, 4883 (2016).

4. Dissociation-chemisorption pathways of H_2 molecule on graphene activated by a hydrogenated mono-vacancy V_{11}
   G.K. Sunnardianto, I. Maruyama, K. Kusakabe, Advanced Science, Engineering and Medicine, **8**, 421 (2016).
5. Storing-hydrogen process on graphene activated by atomic-vacancy
   G.K. Sunnardianto, I. Maruyama, K. Kusakabe, Int. J. Hydrogen Energy (2017) in press.
6. Chemically induced topological zero mode at graphenic armchair edges
   M. Ziatdinov, H. Lim, S. Fujii, K. Kusakabe, M. Kiguchi, T. Enoki, and Y. Kim, Phys. Chem. Chem. Phys. **19**, 5145-5154 (2017).
7. Self-doping effect arising from electron correlations in multi-layer cuprates
   K. Nishiguchi, S. Teranishi, K. Kusakabe, arXiv:1704.04867.
8. An enhancement mechanism of two-particle exchange interactions in single- and multi-layer cuprate superconductors
   S. Teranishi, S. Miyao, K. Nishiguchi, K. Kusakabe, arXiv:1704.06559.

KUWABARA, Akihide [C class; 4500 (B), 0 (C)] ()
— *First-principles calculations of mechanical properties of Li-ion battery materials*

MACHIDA, Manabu [D class; 1500 (B), 0 (C)] (268)
— *Light transport in random media and its application to medical imaging*

MAKINO, Takayuki [C class; 1000 (B), 900 (C)] (123)
— *study on electronic structures in perovskite-type lead-halide mixed crystals*

MASAKI-KATO, Akiko [C class; 9500 (B), 4000 (C)] (202)
— *Development of Quantum Monte Carlo Methods and Application to Critical Phenomena of Dirty Bosons*
— *Development of a parallel quantum Monte Carlo Method and Study of novel quantum phenomena in quantum lattice models*

MATSUKAWA, Hiroshi [C class; 3000 (B), 0 (C)] ()
— *Physics of Friction*

MATSUSHITA, Katsuyoshi [C class; 4000 (B), 0 (C)] (252)
— *Cell Crowding Effects in Collective Cell Migration*
— *Crowding effect on order formation in collective cell migration*

1. Cell-alignment patterns in the collective migration of cells with polarized adhesion
   Katsuyoshi Matsushita: Phys. Rev. E **95** (2017) 032415(12).
2. Model Prediction of Cell-Shape Dependence of Cell Motion
   Katsuyoshi Matsushita: Proceedings of the Symposium on Simulation of Traffic Flow **22**, 5 (2016).

MISAWA, Takahiro [E class; 15000 (B), 1900 (C)] (163, 316)
— *Thermal pure quantum state study on finite-temperature properties of quantum spin liquids*

1. Finite-Temperature Signatures of Spin Liquids in Frustrated Hubbard Model
   T. Misawa and Y. Yamaji, arXiv:1608.09006.
2. Quantum Lattice Model Solver HPhi
   M. Kawamuraa, K. Yoshimi, T. Misawa, Y. Yamaji, S. Todo, and N. Kawashima: Comput. Phys. Commun. in press.

MIYASHITA, Seiji [C class; 5500 (B), 2000 (C)] (227)
— *Development of direct method for quantum response from microscopic Hamiltonian*

1. Effective Floquet-Gibbs states for dissipative quantum systems
   T. Shirai, J. Thingna, T. Mori, S. Denisov, P. Hanggi and S. Miyashita : New J. Phys. **18** (2016) 053008.
2. Extensive increase of entropy in quantum quench.

T. Mori: J. Phys. A **49** (2016) 44403.

3. Quantum states of dark solitons in the 1D Bose gas.
   J. Sato, R. Kanamoto, E. Kaminishi, and T. Deguchi : New J. Phys. **18** (2016) 075008.
4. Temperature dependence of the threshold magnetic field for nucleation and domain wall propagation in an inhomogeneous structure with grain boundary.
   S. Mohakud, S. Andraus, M. Nishino, A. Sakuma, and S. Miyashita: Phys. Rev. B **94** (2016) 054430.
5. Macrostate equivalence of two general ensembles and specific relative entropies
   T. Mori: Phys. Rev. E **94** (2016) 020101(R).
6. Dynamics of open quantum spin systems: An assessment of the quantum master equation approach
   P. Zhao, H. D. Raedt, S. Miyashita, F. Jin, and K. Michielsen : Phys. Rev. E **94** (2016) 022126.
7. Anomalous finite-size effect due to quasidegenerate phases in triangular antiferromagnets with long-range interactions and mapping to the generalized six-state clock model.
   M. Nishino and S. Miyashita : Phys. Rev. B **94** (2016) 184434.
8. Monte Carlo analysis for finite-temperature magnetism of $Nd_2Fe_{14}B$ permanent magnet
   Y. Toga, M. Matsumoto, S. Miyashita, H. Akai, S. Doi, T. Miyake, and A. Sakuma : Phys. Rev. B **94** (2016) 174433.
9. Publisher's Note: Monte Carlo analysis for finite-temperature magnetism of $Nd_2Fe_{14}B$ permanent magnet
   Y. Toga, M. Matsumoto, S. Miyashita, H. Akai, S. Doi, T. Miyake, and A. Sakuma : Phys. Rev. B **94**(2016) 174433.
10. Size and temperature dependence of the line shape of ESR spectra of the XXZ antiferromagnetic chain
    H. Ikeuchi, H. D. Raedt, S. Bertaina, and S. Miyashita : Phys. Rev. B **95**,(2017) 024402.
11. Entanglement prethermalization in an interaction quench between two harmonic oscillators
    T. N.Ikeda, T. Mori, E. kaminishi and M. Ueda : Phys. Rev. E **95** (2017) 022129.
12. Atomistic-model study of temperature-dependent domain walls in the neodymium permanent magnet $Nd_2Fe_{14}B$
    M. Nishino, Y. Toga, S. Miyashita, H. Akai, A. Sakuma and S. Hirosawa : Phys. Rev. B **95** (2017) 094429.
13. Development of direct method for quantum response from microscopic Hamiltonian
    S. Miyashita :

MIZUGUCHI, Tomoko [C class; 2500 (B), 0 (C)] (262)
— *local structure and phase transition in supercooled cyclohexane*

1. Molecular dynamics study of new phase transition in supercooled cyclohexane
   T. Mizuguchi, S. Tatsumi and S. Fujiwara: Proceedings of JSST 2016 - International Conference on Simulation Technology (2016) 41.

MIZUKAMI, Wataru [C class; 3500 (B), 0 (C)] (111)
— *Exploring active sites of Real model catalysis via first principle calculations*

MOMIDA, Hiroyoshi [C class; 3500 (B), 800 (C)] (101)
— *First-principles calculations of electron and spin device materials*

1. Strong Enhancement of Piezoelectric Constants in $Sc_xAl_{1-x}N$: First-Principles Calculations
   H. Momida, A. Teshigahara and T. Oguchi: AIP Advances **6** (2016) 065006.
2. Polar Phase Transitions and Physical Properties in Fresnoite $A_2TiSi_2O_8$ (A = Ba, Sr) by First Principles Calculations
   N. Song, H. Momida, T. Oguchi and B. G. Kim: J. Solid State Chem. **242** (2016) 136.

MORIKAWA, Yoshitada [E class; 25500 (B), 2500 (C)] (38)
— *Analysis of heterogeneous catalysts by combining first-principles simulations and statistical mechanics*

1. First-Principles Molecular Dynamics Analysis of Ligand-Free Suzuki-Miyaura Cross Coupling in Water Solvent: Oxidative Addition Step
   T. Hirakawa, Y. Uramoto, D. Mimura, A. Takeda, S. Yanagisawa, T. Ikeda, K. Inagaki, and Y.

Morikawa: J. Phys. Chem. B, **121**, (2017) 164.
2. Self-consistent van der Waals density functional study of benzene adsorption on Si(100)
Y. Hamamoto, I. Hamada, K. Inagaki, and Y. Morikawa: Phys. Rev. B, **93**, (2016) 245440.
3. Density Functional Theory Investigationsj of Ferrocene-Terminated Self-Assembled Monolayers: Electronic State Changes Induced by Electric Dipole Field of Coadsorbed Species
Y. Yokota, S. Akiyama, Y. Kaneda, A. Imanishi, K. Inagaki, Y. Morikawa, and K. Fukui: J. Phys. Chem. C, **120**, (2016) 8684.
4. Ab-initio moleculer dynamics of solvation effects on reactiveity at electrified interfaces
J.A. Herron, *Y. Morikawa, and *M. Mavrikakis: Proc. Natl. Acad. Sci. U. S. A. **113**, (2016) E4937.
5. Photoelectron Holographic Atomic Arrangement Imaging of Cleaved Bimetal-intercalated Graphite Superconductor Surface
F. Matsui, R. Eguchi, S. Nishiyama, M. Izumi, E. Uesugi, H. Goto, T. Matsushita, K. Sugita, H. Daimon, Y. Hamamoto, I. Hamada, Y. Morikawa, and Y. Kubozono: Sci. Rep. **6**, (2016) 36258.
6. The adsorption of CO_2 on graphene: A combined TPD, XPS, vdW-DF study
K. Takeuchi, S. Yamamoto, Y. Hamamoto, Y. Shiozawa, K. Tashima, H. Fukidome, T. Koitaya, K. Mukai, S. Yoshimoto, M. Suemitsu, Y. Morikawa, J. Yoshinobu, and I. Matsuda: J. Phys. Chem. C **121**, (2017) 2807.
7. Electronic states and growth modes of Zn atoms deposited on Cu(111) studied by XPS, UPS and DFT
T. Koitaya, Y. Shiozawa, Y. Yoshikura, K. Mukai, S. Yoshimoto, S. Torii, F. Muttaqien, Y. Hamamoto, K. Inagaki, Y. Morikawa, and J. Yoshinobu: Surf. Sci. **663**, (2017) 1.

MORIMOTO, Kenichi [C class; 3500 (B), 0 (C)] (256)
— *Development of meshless analysis-based shape optimization method for heat transfer equipments*
— *Development of optimal design methodology of heat and fluid flow devices involving phase-change heat transfer*

1. Meshless Analysis-Based Shape Optimization in Conjugate Heat Transfer Problems
H. Kinoshita, Y. Suzuki and K. Morimoto: Proc. 9th JSME-KSME Thermal Fluids Eng. Conf.(TFEC9), Oct. 2017 (accepted)
2. RANS-Based Adjoint Analysis for Shape Optimization of High-Performance Turbulent Heat Exchangers
K. Morimoto, Y. Goto and Y. Suzuki: Proc. 9th JSME-KSME Thermal Fluids Eng. Conf.(TFEC9), Oct. 2017 (accepted)

MORITA, Satoshi [C class; 4000 (B), 800 (C)] (246)
— *Development of Parallelized Tensor-Network Algorithm and its Applications*

1. Variational Monte Carlo method for fermionic models combined with tensor networks and applications to the hole-doped 2D Hubbard model
H.-H. Zhao, K. Ido, S. Morita and M. Imada: submitted to Phys. Rev. B

MOTOME, Yukitoshi [C,D class; 19500 (B), 2000 (C)] (159, 161)
— *Creation and control of skyrmions with different topological numbers in itinerant magnets*
— *Large-scale simulation for spin-orbital physics in strongly-correlated electron systems*
— *Theoretical study of novel quantum phenomena in strongly-correlated spin-orbit coupled systems*

1. Asymmetric Magnon Excitation by Spontaneous Toroidal Ordering
S. Hayami, H. Kusunose and Y. Motome: J. Phys. Soc. Jpn. **85** (2016) 053705.
2. Topological Insulators from Electronic Superstructures
Y. Sugita and Y. Motome: J. Phys. Soc. Jpn. **85** (2016) 073709.
3. Fermionic response from fractionalization in an insulating two-dimensional magnet
J. Nasu, J. Knolle, D.L. Kovrizhin, Y. Motome, and R. Moessner: Nat. Phys. **12** (2016) 912.
4. Engineering chiral density waves and topological band structures by multiple-Q superpositions of collinear up-up-down-down orders
S. Hayami, R. Ozawa, and Y. Motome: Phys. Rev. B **94** (2016) 024424.
5. Emergent spin-valley-orbital physics by spontaneous parity breaking

S. Hayami, H. Kusunose and Y. Motome: J. Phys.: Cond. Matter **28** (2016) 395601.

6. Vortex Crystals with Chiral Stripes in Itinerant Magnets
   R. Ozawa, S. Hayami, K. Barros, G-W. Chern, Y. Motome, and C. D. Batista: J. Phys. Soc. Jpn. **85** (2016) 103703.
7. Shape of magnetic domain walls formed by coupling to mobile charges
   R. Ozawa, S. Hayami, K. Barros, and Y. Motome: arXiv:1609.07189.
8. Simulated floating zone method
   R. Ozawa, Y. Kato, and Y. Motome: J. Phys.: Conf. Ser. **807** (2017) 102005.
9. Fractional Spin Fluctuations as a Precursor of Quantum Spin Liquids: Majorana Dynamical Mean-Field Study for the Kitaev Model
   J. Yoshitake, J. Nasu, and Y. Motome: Phys. Rev. Lett. **117** (2016) 157203.
10. Incarnation of Majorana Fermions in Kitaev Quantum Spin Lattice
    S.-H. Do, S.-Y. Park, J. Yoshitake, J. Nasu, Y. Motome, Y. S. Kwon, D. T. Ardor, D. J. Voneshen, K. Kim, T.-H. Jang, J.-H. Park, K.-Y. Choi, and S. Ji: arXiv:1703.01081.
11. Magnetoelectric Behavior from S=1/2 Asymmetric Square Cupolas
    Y. Kato, K. Kimura, A. Miyake, M. Tokunaga, A. Matsuo, K. Kindo, M. Akaki, M. Hagiwara, M. Sera, T. Kimura, and Y. Motome: Phys. Rev. Lett. **118** (2017) 107601.
12. Effective bilinear-biquadratic model for noncoplanar ordering in itinerant magnets
    S. Hayami, R. Ozawa, and Y. Motome: arXiv:1703.07690.
13. Thermal Transport in the Kitaev Model
    J. Nasu, J. Yoshitake, and Y. Motome: arXiv:1703.10395.
14. Spin-Liquid-to-Spin-Liquid Transition in Kitaev Magnets Driven by Fractionalization
    J. Nasu, Y. Kato, J. Yoshitake, Y. Kamiya, and Y. Motome: Phys. Rev. Lett. **118** (2017) 137203.
15. Zero-Field Skyrmions with a High Topological Number in Itinerant Magnets
    R. Ozawa, S. Hayami, and Y. Motome: Phys. Rev. Lett. **118** (2017) 147205.

MOTOYAMA, Yuichi [C class; 3000 (B), 600 (C)] (180)
— *Monte Carlo simulation of ^{4}He adsorbed on substrates*

MURASHIMA, Takahiro [E class; 12000 (B), 1800 (C)] (201)
— *Multiscale simulation of polymer melt*

1. Inter Node Parallelization of Multiscale Fluid Particle Simulation towards Large-scale Polymeric Fluid Simulation.
   T. Murashima: Microsyst. Technol. (2017). doi:10.1007/s00542-017-3413-x.

NADA, Hiroki [C class; 5000 (B), 0 (C)] (243)
— *Molecular Dynamics Simulation Study of Morphology Control Mechanism of TiO2 Rutile Crystal by Hydroxy Acid*

1. Heterogeneous Growth of Calcite at Aragonite 001- and Vaterite 001-Melt Interfaces: A Molecular Dynamics Simulation Study
   H. Nada, T. Nishimura, T. Sakamoto and T. Kato: J. Cryst. Growth, **450** (2016) 148.
2. Observing Crystal Growth Processes in Computer Simulation
   H. Nada, H. Miura, J. Kawano and T. Irisawa: Prog. Cryst. Growth Charact. Mater., **62** (2016) 404.
3. Anisotropy in Geometrically Rough Structure of Ice Prismatic Plane Interface During Growth: Development of a Modified Six-Site Model of H2O and a Molecular Dynamics Simulation
   H. Nada: J. Chem. Phys., **145** (2016) 244706.

NAKAMURA, Kazuma [C class; 5000 (B), 0 (C)] (93)
— *Ab initio many-body perturbation calculations for paramagnon excitation*
— *ab initio calculation for superconducting parameters*

1. Ab initio GW plus cumulant calculation for isolated band systems: Application to organic conductor (TMTSF)2PF6 and transition-metal oxide
   Kazuma Nakamura, Yoshiro Nohara, Yoshihide Yoshimoto, and Yusuke Nomura: Phys. Rev. B **93** (2016) 085124.

2. Large enhancement of superconducting transition temperature in single-element superconducting rhenium by shear strain
   M. Mito, H. Matsui, K. Tsuruta, T. Yamaguchi, K. Nakamura, H. Deguchi, N. Shirakawa, H. Adachi, T. Yamasaki, H. Iwaoka, Y. Ikoma, and Z. Horita: Sci. Rep. **6**, (2016) 36337.
3. Uniaxial strain effects on superconducting transition in Re-doped Hg-1223 cuprate superconductors
   M. Mito, K. Ogata, H. Goto, K. Tsuruta, K. Nakamura, H. Deguchi, T. Horide, K. Matsumoto, T. Tajiri, H. Hara, T. Ozaki, H. Takeya, and Y. Takano: Phys. Rev. B **95** (2017) 064503.

NAKAMURA, Kohji [C class; 3000 (B), 0 (C)] (118)
— First principles calculations of electronic structures magnetism and electric field effects in metal thin films and organometallic complexes

1. Search for the ground state electronic configuration of correlated organometallic metallocenes from constraint density functional theory
   K. Nawa, Y. Kitaoka, K. Nakamura, H. Imamura, T. Akiyama, T. Ito, M. Weinert: Phys. Rev. B **94** (2016) 0351361.
2. Interfacial Dzyaloshinskii-Moriya interaction and orbital magnetic moments of metallic multilayer films
   K. Yamamoto, A.-M. Pradipto, K. Nawa, T. Akiyama, T. Ito, T. Ono, K. Nakamura: AIP Advances **7** (2017) 0563021.
3. Effect of heavy-metal insertions at Fe/MgO interfaces on electric-field-induced modification of magnetocrystalline anisotropy
   K. Nakamura, T. Nomura, A.-M. Pradipto, K. Nawa, T. Akiyama, T. Ito: J. Magn. Magn. Mater. **429** (2017) 214.
4. Symmetric and asymmetric exchange stiffnesses of transition-metal thin film interfaces
   K. Nakamura, A.-M. Pradipto, T. Akiyama, T. Ito, M. Weinert: submitted.
5. Role of surface-bound hole states in electric-field-driven superconductivity at diamond (110)
   T. Hattori, K. Nakamura, and K. Sano: submitted.
6. Mechanism and electric-feld-induced modifcation of magnetic exchange stifness in transition-metal thin flms on MgO(001)
   A.-M. Pradipto, T. Akiyama, T. Ito, and K. Nakamura: submitted.

NAKANO, Hiroki [C class; 6000 (B), 2100 (C)] (221)
— Numerical study on low-energy states of quantum spin systems

1. Ferrimagnetism in the Spin-1/2 Heisenberg Antiferromagnet on a Distorted Triangular-Lattice
   H. Nakano and T. Sakai: to be published in J. Phys. Soc. Jpn.
2. Gapless quantum spin liquid of the kagome-lattice antiferromagnet
   T. Sakai and H. Nakano: Polyhedron **126** (2017) 42-44.

NAKAYAMA, Takashi [C class; 4000 (B), 1300 (C)] (91)
— Theory of molecular Rydberg states by light-mass impurities in semiconductors: tunneling current and strong luminescence properties

1. Stability and electronic structures of isoelectronic impurity complexes in Si: First-principles study
   S. Iizuka, T. Nakayama: Jpn. J. Appl. Phys. **55** (2016) 101301.
2. Defect distribution and Schottky barrier at metal/Ge interfaces: Role of metal-induced gap states
   S. Sasaki, T. Nakayama: Jpn. J. Appl. Phys. **55** (2016) 111302.
3. Fundamental processes of exciton scattering at organic solar-cell interfaces:One-dimensional model calculation
   Y. Masugata, H. Iizuka, K. Sato, T. Nakayama: Jpn. J. Appl. Phys. **55** (2016) 081601.
4. Physics of Metal/Ge Interfaces; Interface Defects and Fermi-Level Depinning
   T. Nakayama, S. Sasaki, Y. Asayama: ECS trans. **75** (2016) 643.
5. Metal-atom interactions and clustering in organic semiconductor systems
   Y. Tomita, T. Park, T. Nakayama: J. Electronic Materials, in press (2017) doi:10.1007/s11664-016-5090-4.
6. Ionization and diffusion of metal atoms under electric field at metal/insulator interfaces; First-

principles study
Y. Asayama, M. Hiyama, T. Nakayama: Materials Science in Semiconductor Processing, in press (2017) DOI:10.1016/j.mssp.2016.09.010.

NISHIDATE, Kazume [C class; 3000 (B), 0 (C)] (117)
— *Molecular Dynamics Simulation of Organic Semiconductors*

1. Tuning the work function of graphene with the adsorbed organic molecules: first-principles calculations
   K. Nishidate, N. Yoshimoto, P. Chantngarm, H. Saito and M. Hasegawa: Mol. Phys. **114** (2016) 2993.

NOGUCHI, Hiroshi [C class; 14000 (B), 5000 (C)] (198, 199)
— *Structure formation of biomembranes*

1. Shape deformation of lipid membranes by banana-shaped protein rods: comparison with isotropic inclusions and membrane rupture
   H. Noguchi: Phys. Rev. E **93**, 052404 (2016).
2. Construction of nuclear envelope shape by a high-genus vesicle with pore-size constraint
   H. Noguchi: Biophys. J. **111**, 824 (2016).
3. Nonuniqueness of local stress of three-body potentials in molecular simulations
   K. M. Nakagawa and H. Noguchi: Phys. Rev. E **94**, 053304 (2016).
4. Membrane structure formation induced by two types of banana-shaped proteins
   H. Noguchi and J.-B. fournier: Soft Matter **13**, 4099 (2017).
5. 分子シミュレーションにおける三体ポテンシャルを含んだ系の局所応力テンソルの非一意性
   中川恒: 分子シミュレーション研究会会誌“アンサンブル”**19**, 69 (2017).

NOGUCHI, Yoshifumi [E class; 18500 (B), 2100 (C)] (42)
— *Large scale first-principles GW+Bethe-Salpeter calculations*

1. Reverse Stability of Oxyluciferin Isomers in Aqueous Solutions
   Y. Noguchi, M. Hiyama, M. Shiga, O. Sugino, and H. Akiyama: J. Phys. Chem. B **120** (2016) 8776.
2. GWΓ+ Bethe-Salpeter equation approach for photoabsorption spectra:Importance of self-consistent GWΓ calculations in small atomic systems
   R. Kuwahara, Y. Noguchi, and K. Ohno: Phys. Rev. B **94** (2016) 121116(R).
3. Quantitative characterization of exciton from GW+Bethe-Salpeter calculation
   D. Hirose, Y. Noguchi, and O. Sugino: J. Chem. Phys. **146** (2017) 044303.
4. The effect of dynamical fluctuations of hydration structures on the absorption spectra of oxyluciferin anions in an aqueous solution
   M. Hiyama, M. Shiga, N. Koga, O. Sugino, H. Akiyama, and Y. Noguchi: Phys. Chem. Chem. Phys. **19** (2017) 10028.
5. Molecular Size Insensitivity of Optical Gap of [n]Cycloparaphenylenes (n = 3-16)
   Y. Noguchi and O. Sugino: J. Chem. Phys. **146** (2017) 144304.

OBATA, Shuji [C class; 2500 (B), 600 (C)] (116)
— *Magnetization Processes Based on Magnetic Dipole Moments*

ODA, Tatsuki [C,E class; 18000 (B), 4800 (C)] (40)
— *Analyses on atomic structure magnetism and electronic structure in spintronics materials and molecular magnets*

1. Nonvortical Rashba spin structure on a surface with C1h symmetry
   E. Annese, T. Kuzumaki, B. M?ller, Y. Yamamoto, H. Nakano, H. Kato, A. Araki, M. Ohtaka, T. Aoki, H. Ishikawa, T. Hayashida, J. R. Osiecki, K. Miyamoto, Y. Takeichi, A. Harasawa, K. Yaji, T. Shirasawa, K. Nittoh, W. I. Yang, K. Miki, T, Oda, H. W. Yeom, and K. Sakamoto: Phys. Rev. Lett. **117** (2016) 16803.
2. Tunneling electroresistance of MgZnO-based tunnel junctions
   M. Belmoubarik, M. Al-Mahdawi, M. Obata, D. Yoshikawa, H. Sato, T. Nozaki, T. Oda, and M.

Sahashi: Appl. Phys. Lett. **109** (2016) 173507.

OGUSHI, Fumiko [B class; 500 (B), 0 (C)] (279)
— *Simulation study of membrane system coupled with inner reaction*

OHGOE, Takahiro [C class; 8000 (B), 1900 (C)] (168)
— *Ab-initio study on the role of the electron-phonon interactions in high-temperature curate superconductors*
— *Numerical study on the mechanism of enhanced superconductivity by phonons in cuprates*

1. Competitions of Superconducting, Antiferromagnetic and Charge Orders with Intervention by Phase Separation in 2D Holstein-Hubbard Model
   T. Ohgoe and M. Imada: submitted to Phys. Rev. Lett.

OHMURA, Satoshi [C class; 3500 (B), 0 (C)] (110)
— *Novel Structures of Liquid Metal under Ultrahigh Pressures: ab initio Molecular-Dynamics Simulations*

1. Femtosecond Charge and Molecular Dynamics of I-containing organic molecules Induced by Intense X-Ray Free-Electron Laser Pulses
   K. Nagaya, K. Motomura, E. Kukk, Y. Takahashi, K. Yamazaki, S. Ohmura, H. Fukuzawa, S. Wada, S. Mondal, T. Tachibana, Y. Ito, R. Koga, T. Sakai, K. Matsunami, K. Nakamura, M. Kanno, A. Rudenko, C. Nicolas, X.-J. Liu1, C. Miron1, Y. Zhang, Y. Jiang, J. Chen, M. Anand, D. E. Kim, K. Tono, M. Yabashi, M. Yao, H. Kono and K. Ueda: Faraday Discuss. **194** (2016) 537.
2. Ultrafast dynamics of a nucleobase analogue illuminated by a short intense x-ray free electron laser pulse
   K. Nagaya, K. Motomura, E. Kukk, H. Fukuzawa, S. Wada, T. Tachibana, Y. Ito, S. Mondal, T. Sakai, K. Matsunami, R. Koga, S. Ohmura, Y. Takahashi, M. Kanno, A. Rudenko, C. Nicolas, X.-J. Liu, Y. Zhang, J. Chen, A. Mailam, Y. H. Jiang, D.-E. Kim, K. Tono, M. Yabashi, H. Kono, C. Miron, M. Yao, K. Ueda: Phys. Rev. X **6** (2016) 021035.

OHSAWA, Kazuhito [C class; 1000 (B), 0 (C)] (137)
— *Study of interaction between radiation damage and interstitial atom*

OHTO, Tatsuhiko [C class; 4500 (B), 1600 (C)] (83)
— *Ab initio molecular dynamics simulation of graphene/water interfaces*

1. π^+–π^+ stacking of imidazolium cations enhances molecular layering of room temperature ionic liquid at their interfaces
   Fujie Tang, Tatsuhiko Ohto, Taisuke Hasegawa, Mischa Bonn, and Yuki Nagata: Phys. Chem. Chem. Phys. **19** (2017) 2850.
2. Trimethylamin-N-oxide: Hydration structure, surface activity, and biological function viewed by vibrational spectroscopy
   Tatsuhiko Ohto, Johannes Hunger, Ellen H. G. Backus, Wataru Mizukami, Mischa Bonn, and Yuki Nagata: Phys. Chem. Chem. Phys. **19** (2017) 6909.

OHTSUKI, Tomi [C class; 3500 (B), 1000 (C)] (248)
— *Numerical study of random Dirac/Weyl electron systems*

1. Deep Learning the Quantum Phase Transitions in Random Electron Systems: Applications to Three Dimensions
   Tomi Ohtsuki, Tomoki Ohtsuki: J. Phys. Soc. Jpn. **86**, 044708 (2017)
2. Integer quantum magnon Hall plateau-plateau transition in a spin-ice model
   B. Xu, T. Ohtsuki, R. Shindou: Phys. Rev. B **94**, 220403(R) (2016)
3. Comparative study of Weyl semimetal and topological/Chern insulators: Thin-film point of view
   .Y. Yoshimura, W. Onishi, K. Kobayashi, T. Ohtsuki, K.-I. Imurai: Phys. Rev. B **94**, 235414 (2016)
4. Deep Learning the Quantum Phase Transitions in Random Two-Dimensional Electron Systems

Tomoki Ohtsuki, Tomi Ohtsuki: J. Phys. Soc. Jpn. **85**, 123706 (2016)

5. Estimate of the Critical Exponent of the Anderson Transition in the Three and Four-Dimensional Unitary Universality Classes
   K. Slevin, T. Ohtsuki: J. Phys. Soc. Jpn. **85**, 104712 (2016)
6. Lattice realization of the generalized chiral symmetry in two dimensions
   T. Kawarabayashi, H. Aoki, Y. Hatsugai, Phys. Rev. B **94**, 235307 (2016)

OKITSU, Kouhei [C class; 5000 (B), 400 (C)] (241)
— *A preliminary study on phase determination for protein crystals with the n-beam method*
— *Study on numerical method to solve n-beam Takagi equation with spherical-wave X-ray incidence*

OKUBO, Tatsuya [C class; 2500 (B), 0 (C)] (261)
— *Computer-aided synthesis of zeolites*

1. Energy Analysis of Aluminosilicate Zeolites with Comprehensive Ranges of Framework Topologies, Chemical Compositions, and Aluminum Distributions
   K. Muraoka, W. Chaikittisilp and T. Okubo: J. Am. Chem. Soc. **138** (2016) 6184.
2. Factors Governing the Formation of Hierarchically and Sequentially Intergrown MFI Zeolites by Using Simple Diquaternary Ammonium Structure-Directing Agents
   S. H. Keoh, W. Chaikittisilp, K. Muraoka, R. R. Mukti, A. Shimojima, P. Kumar, M. Tsapatsis and T. Okubo: Chemistry of Materials, 2016, **28**, 8997.
3. Two-Stage Crystallization of Meso- and Macroporous MFI and MEL Zeolites Using Tributylamine-Derived Diquaternary Ammonium Cations as Organic Structure-Directing Agents
   S. H. Keoh, W. Chaikittisilp, A. Endo, A. Shimojima, T. Okubo: Bull. Chem. Soc. Jpn. 2017, **90**, 586.
4. Design and Synthesis of IFR-Type Zeolites with Controlled Locations of Framework Aluminum with the Aid of Theoretical Calculation
   K. Muraoka, W. Chaikittisilp, T. Okubo: The 2016 AIChE annual meeting, 2016.
5. The Energetics of Zeolites with Comprehensive Ranges of Framework Topologies and Different Substituting Tetrahedral Atoms: Towards More Complete Energy Landscapes of Zeolites
   W. Chaikittisilp, K. Muraoka, T. Okubo: The 2016 AIChE annual meeting, 2016.
6. 種々の骨格構造、化学組成、原子位置を有するゼオライトの計算機モデリングによるエネルギー景観
   村岡恒輝, W. Chaikittisilp, 大久保達也: 化学工学会第 48 回秋季大会, 2016.
7. 理論計算支援による有機構造規定剤のゼオライト骨格中 Al 位置制御能の検討
   村岡恒輝, W. Chaikittisilp, 大久保達也: 第 32 回ゼオライト研究発表会, 2016.

OKUBO, Tsuyoshi [C class; 11000 (B), 4300 (C)] (20)
— *Novel orders in frustrated magnets*

1. Ground state properties of Na_2IrO_3 determined from *ab initio* Hamiltonian and its extensions containing Kitaev and extended Heisenberg interactions
   T. Okubo, K. Shinjo, Y. Yamaji, N. Kawashima, S. Sota, T. Tohyama, and M. Imada: arXiv:1611.03614.

OKUMURA, Hisashi [C class; 6000 (B), 0 (C)] (237)
— *Dynamical ordering of amyloid fibrils by molecular dynamics simulations*

1. Structural and fluctuational difference between two ends of A β amyloid fibril: MD simulation predicts only one end has open conformations
   H. Okumura and S. G. Itoh: Sci. Rep. **6** (2016) 38422.
2. Oligomer formation of amyloid-β (29-42) from its monomers using the Hamiltonian replica-permutation molecular dynamics simulation
   S. G. Itoh and H. Okumura: J. Phys. Chem. B **120** (2016) 6555.

ONISHI, Hiroaki [C class; 2000 (B), 0 (C)] (264)
— *Magnetic excitation and spin transport in frustrated quantum spin chain*

1. Variational Wavefunction for the Periodic Anderson Model with Onsite Correlation Factors
   K. Kubo and H. Onishi, J. Phys. Soc. Jpn. **86**, 013701 (2017).

ONO, Tomoya [C class; 14500 (B), 4900 (C)] (43)
— *Development of first-principles electronic-structure and transport calculation method based on real-space finite-difference approach*

1. First-Principles Study on Electron Conduction at 4H-SiC(0001)/SiO_2 Interface
   T. Ono, C. J. Kirkham, and S. Iwase: ECS Trans. **75** (2016) 121.
2. Importance of SiC Stacking to Interlayer States at the SiC/SiO_2 Interface
   C. J. Kirkham and T. Ono: Mater. Sci. Forum **858** (2016) 457.
3. First-principles study on oxidation of Ge and its interface electronic structures
   T. Ono, S. Saito, and S. Iwase: Jpn. J. Appl. Phys. **55** (2016) 08PA01.
4. Intrinsic origin of electron scattering at the 4H-SiC(0001)/SiO_2 interface
   S. Iwase, C. J. Kirkham, and T. Ono: Phys. Rev. B **95** (2017) 041302.
5. First-principles calculation method and its applications for two-dimensional materials
   Y. Egami, S. Tsukamoto, and T. Ono: Quant. Matt. **6** (2017) 4.

ORITA, Nozomi [C class; 1000 (B), 0 (C)] (135)
— *Ab initio calculations of impurity states in the silicon cluster superlattice*

OSHIKAWA, Masaki [C class; 3000 (B), 0 (C)] (258)
— *Computational study of topological properties and realization of quantum spin liquids in metal-organic frameworks*

1. Flux quench in a system of interacting spinless fermions in one dimension
   Yuya O. Nakagawa, Grégoire Misguich, and Masaki Oshikawa: Phys. Rev. B **93** (2016) 174310.

OSHIYAMA, Atsushi [E class; 45500 (B), 4900 (C)] ()
— *Atomic Structures and Electronic Properties of Hard- and Soft-Nano Materials*

1. Multistep Atomic Reaction Enhanced by an Atomic Force Microscope Probe on Si (111) and Ge(111) Surfaces
   B. Enkhtaivan and A. Oshiyama: Phys. Rev. B **94** (2016) 085416.
2. Atomic Force Microscope manipulation of Ag atom on the Si(111) surface
   B. Enkhtaivan and A. Oshiyama: Phys. Rev. B **95** (2017) 035309.
3. Band-unfolding approach to moiré-induced band-gap opening and Fermi-level-velocity reduction in twisted bilayer graphene
   H. Nishi, Y-i. Matsushita, A. Oshiyama: Phys. Rev. B **95** (2017) 085420.
4. First-Principles Calculations that Clarify Energetics and Reactions of Oxygen Adsorption and Carbon Desorption on 4H-SiC ($11\bar{2}0$) Surface
   H. Li, Y.-i. Matsushita, M. Boero and A. Oshiyama: J. Phys. Chem. C **121** (2017) 3920.
5. Microscopic Mechanisms of Initial Formation Process of Graphene on SiC(0001) Surfaces: Selective Si Desorption from Step Edges
   F. Imoto, J.-I. Iwata, M. Boero, A. Oshiyama: J. Phys. Chem. C **121** (2017) 5041.
6. Comprehensive study on band-gap variations in sp^3-bonded semiconductors: roles of electronic states floating in internal space
   Y.-i. Matsushita and A. Oshiyama: J. Phys. Soc. Jpn **86** (2017) 054702.

OTSUKI, Junya [B class; 800 (B), 0 (C)] (192)
— *Electronic structure calculations of strongly correlated Ce compounds using the dynamical mean-field theory*

OZEKI, Yukiyasu [C class; 7500 (B), 0 (C)] (226)
— *Improvement of nonequilibrium relaxation analysis by the use of kernel method*
— *Improvement of nonequilibrium relaxation analysis by the use of kernel method II*

1. Improved dynamical scaling analysis using the kernel method for nonequilibrium relaxation
   Y. Echinaka and Y. Ozeki: Phys. Rev E **94** (2016) 043312

RAEBIGER, Hannes [B class; 700 (B), 0 (C)] (144)
— *Theory of self-organized nano-interfaces for electronic devices*

1. Positron Binding Properties of Glycine and Its Aqueous Complexes
   M. Nummela H. Raebiger D. Yoshida M. Tachikawa, J. Phys. Chem. A **120**, 4037 (2016).
2. Critical metal-insulator transition due to nuclear quantum effects in Mn-doped GaAs
   S. Bae H. Raebiger, Phys. Rev. B **94**, 241115(R) (2016).
3. Defect-Induced Vibration Modes of Ar+-Irradiated MoS2
   Soungmin Bae, Natsuki Sugiyama, Takatoshi Matsuo, Hannes Raebiger, Ken-ichi Shudo, and Koichi Ohno, Phys. Rev. Applied **7**, 024001 (2017).

SAITO, Mineo [C class; 11500 (B), 0 (C)] (54)
— *First Principles Calculations of Muon and Positron in Solids*

1. Spin-Polarized First-Principles Calculation of Momentum Densities of Fe
   I. Sugita and M. Saito: J. Phys. Conf. Ser. **791** (2017) 012037
2. Strain-controlled spin splitting in the conduction band of monolayer WS2
   M.A.U. Absor, H. Kotaka, F. Ishii, and M. Saito: Phys. Rev. B **94** (2016) 115131

SAKAI, Toru [C class; 7500 (B), 3600 (C)] (207, 209)
— *Novel Field Induced Transitions in Low-Dimensional Quantum Spin Systems*
— *Numerical Diagonalization Study on the Quantum Spin Liquid in Frustrated Systems*

1. Ground-state phase diagram of an anisotropic S=1/2 ladder with alternating rung interactions
   T. Tonegawa, K. Okamoto, T. Hikihara and T. Sakai: J. Phys.: Conf. Ser. **683** (2016) 012039.
2. Effect of monomer-monomer interactions on the phase diagrams of the S=1/2 distorted diamond type quantum spin chain
   K. Okamoto, T. Tonegawa and T. Sakai: J. Phys.: Conf. Ser. **683** (2016) 012038.
3. Ground State Phase Diagram of the Bond-Alternating S=2 Quantum Spin Chain with the XXZ and On-Site Anisotropies -Symmetry Protected Topological Phase versus Trivial Phase-
   K. Okamoto, T. Tonegawa and T. Sakai: J. Phys. Soc. Jpn. **85** (2016) 063704.
4. Dzyaloshinsky-Moriya Interaction and the Ground State in S=3/2 Perfect Kagome Lattice Antiferromagnet $KCr_3(OH)_6(SO_4)_2$ (Cr-Jarosite) Studied by X-Band and High-Frequency ESR
   S. Okubo, R. Nakata, S. Idehara, N. Takahashi, T. Sakurai, W. Zhang, H. Ohta, T. Shimokawa, T. Sakai, K. Okuta, S. Hara, and H. Sato: J. Phys. Soc. Jpn. **86** (2017) 024703.
5. Gapless Quantum Spin Liquid of the Kagome-Lattice Antiferromagnet
   T. Sakai and H. Nakano: POLYHEDRON **126** (2017) 42.
6. Exact ground states of frustrated quantum spin systems consisting of spin-dimer units
   T. Hikihara, T. Tonegawa, K. Okamoto and T. Sakai: J. Phys. Soc. Jpn. **86** (2017) 054709.
7. Frustrated S=1/2 Two-Leg Ladder with Different Leg Interactions
   T. Tonegawa, K. Okamoto, T. Hikihara and T. Sakai: J. Phys.: Conf. Ser. **828** (2017) 012003.
8. Ferrimagnetism in the Spin-1/2 Heisenberg Antiferromagnet on a Distorted Triangular Lattice
   H. Nakano and T. Sakai: to appear in J. Phys. Soc. Jpn.
9. Quantum Spin Liquid in the Kagome-Lattice Antiferromagnet and Related Systems
   T. Sakai and H. Nakano: to appear in J. Phys.: Conf. Ser.

SAKAKIBARA, Hirofumi [B class; 600 (B), 400 (C)] (133)
— *A study about the methods for the derivation of effective model in strongly correlated electron system based on the first-principles calculation*

1. Model-Mapped RPA for Determining the Effective Coulomb Interaction
   H. Sakakibara, S.W. Jang, H. Kino, M.J. Han, K. Kuroki, T. Kotani : J. Phys. Soc. Jpn. **86** (2017) 044714.
2. Direct theoretical evidence for weaker correlations in electron-doped and Hg-based hole-doped cuprates
   S.W. Jang, H. Sakakibara, H. Kino, T. Kotani, K. Kuroki, M.J. Han : Sci. Rep. **6** (2016) 33397

SAKASHITA, Tatsuya [B class; 800 (B), 0 (C)] ()
— *Study on Heisenberg-Kitaev model by exact diagonalization package Rokko*

SATO, Tetsuya [C class; 4500 (B), 0 (C)] (99)
— *Study of spontaneous distortion and ferromagnetism in Pd(100) ultrathin films by first-principles calculation*

1. Spontaneous Distortion and Ferromagnetism Induced by Quantum-well States in Pd(100) Ultrathin Films
   Shunsuke Sakuragi, Hiroo Tajiri, Hiroyuki Kageshima, and Tetsuya Sato: submitted to Phys. Rev. Lett.

SATO, Yukio [B class; 600 (B), 0 (C)] ()
— *Computational Catalyst Design for Energy Applications through ab initio Mechanistic Investigation*

1. Manipulation of Optoelectronic Properties and Band Structure Engineering of Ultrathin Te Nanowires by Chemical Adsorption
   A. Roy, K. R. Amin, S. Tripathi, S. Biswas, A. K. Singh, A. Bid, and N. Ravishankar, ACS Applied Materials and Interfaces, (published online: doi: 10.1021/acsami.6b12064)

SHIBA, Hayato [C,D class; 7000 (B), 0 (C)] (231)
— *Debye-law for the density of states and dimensionality dependence of fluctuation at ultra-low-frequencies in amorphous systems*
— *Study of heterogeneous dynamics inducing defect structure formation and deformation glassy materials*

1. Unveiling Dimensionality Dependence of Glassy Dynamics: 2D Infinite Fluctuation Eclipses Inherent Structural Relaxation
   H. Shiba, Y. Yamada, T. Kawasaki, and K. Kim: Phys. Rev. Lett. **117** (2016) 245701.

SHIGETA, Yasuteru [C class; 14000 (B), 4900 (C)] (45, 319)
— *First-principles analyses on protein folding processes using an automatic detection of effective reaction coordinates*
— *First-principles analyses on structural changes of proteins*

SHIMAMURA, Kohei [C class; 2000 (B), 1600 (C)] (105)
— *Generation Mechanism of Organic/Biological Molecules on Early Earth: Ab Initio Molecular Dynamics Simulation*

1. Meteorite Impact-Induced Rapid NH_3 Production on Early Earth: *Ab Initio* Molecular Dynamics Simulation
   K. Shimamura, F. Shimojo, A. Nakano, and S. Tanaka: Sci. Rep. **6** (2016) 38953.
2. Meteorite impacts on ancient oceans opened up multiple NH_3 production pathways
   K. Shimamura, F. Shimojo, A. Nakano, and S. Tanaka: Phys. Chem. Chem. Phys., in press.

SHIMOJO, Fuyuki [C class; 4000 (B), 1600 (C)] (87)
— *First-Principles Molecular-Dynamics Study of Structural and Electronic Properties of Covalent Liquids and Glass under Pressure*

1. The nature of free-carrier transport in organometal halide perovskites
   T. Hakamata, K. Shimamura, F. Shimojo, R. K. Kalia, A. Nakano, and P. Vashishta: Sci. Rep. **6**, 19599 (2016).
2. Doping effect on photoabsorption and charge-separation dynamics in light- harvesting organic molecule
   S. Ohmura, K. Tsuruta, F. Shimojo, and A. Nakano: AIP Adv. **6**, 015305 (2016).
3. Crystalline anisotropy of shock-induced phenomena: omni-directional multiscale shock technique
   K. Shimamura, M. Misawa, S. Ohmura, F. Shimojo, R. K. Kalia, A. Nakano, and P. Vashishta: Appl. Phys. Lett. **108**, 071901 (2016).
4. Dissociation Dynamics of Ethylene Molecules on a Ni Cluster Using *Ab Initio* Molecular Dynamics Simulations
   K. Shimamura, Y. Shibuta, S. Ohmura, Rizal Arifin, and F. Shimojo: J. Phys.: Condens. Matter **28**, 145001 (2016).

5. Rotation mechanism of methylammonium molecules in organometal halide perovskite in cubic phase: an *ab initio* molecular dynamics study
K. Shimamura, T. Hakamata, F. Shimojo, R. K. Kalia, A. Nakano, and P. Vashishta: J. Chem. Phys. **145**, 224503 (2016).

SHIMOKAWA, Tokuro [C class; 8500 (B), 4000 (C)] (203)
— *The effect of bond-randomness on the quantum magnetisms in low dimension*
1. Finite-temperature crossover phenomenon in the S=1/2 antiferromagnetic Heisenberg model on the kagome lattice
T. Shimokawa and H. Kawamura: J. Phys. Soc. Jpn. **85** (2016) 113702.

SHINAOKA, Hiroshi [C class; 3000 (B), 0 (C)] (182)
— *First-principles study on strong electron correlations in 5d transition metal oxides*
1. Continuous-time hybridization expansion quantum impurity solver for multi-orbital systems with complex hybridizations
H. Shinaoka, E. Gull, P. Werner: Computer Physics Communications **215**, 128-136 (2017).
2. A spin-freezing perspective on cuprates
P. Werner, S. Hoshino, H. Shinaoka: Phys. Rev. B **94**, 245134 (2016).
3. Compression of imaginary-time data using intermediate representation of analytical continuation
H. Shinaoka, J. Otsuki, M. Ohzeki, K. Yoshimi: submitted to Phys. Rev. Lett.

SHINOHARA, Yasushi [C class; 6000 (B), 0 (C)] (86)
— *First-principles calculation for spin-charge dynamics induced by ultrashort laser pulse*
— *First-principles simulation for THz generation based on optical rectification*
1. High Harmonic Ellipsometry of Solids
Keisuke Kaneshima, Yasushi Shinohara, Kengo Takeuchi, Nobuhisa Ishii, Kotaro Imasaka, Tomohiro Kaji , Satoshi Ashihara , Kenichi L. Ishikawa, and Jiro Itatani: submitted

SHIOMI, Junichiro [B,C class; 6100 (B), 2500 (C)] (218, 220)
— *Control of phonon and electron transport properties using mechanical strain*
— *Screening for Thermal Functional Materials using Materials Infomatics*
1. Harmonic phonon theory for calculating thermal conductivity spectrum from first-principles dispersion relations
Takuma Shiga, Daisuke Aketo, Lei Feng, and Junichiro Shiomi: Appl. Phys. Lett. **108**, 201903 (2016).
2. Designing nanostructures for interfacial phonon transport via Bayesian optimization
Shenghong Ju, Takuma Shiga, Lei Feng, Zhufeng Hou, Koji Tsuda, and Junichiro Shiomi: Phys. Rev. X, in press.
3. Effects of defects on thermoelectric properties of carbon nanotubes
Masato Ohnishi, Takuma Shiga, and Junichiro Shiomi: Phys. Rev. B **95**, 155405 (2017).

SHIRAISHI, Kenji [C class; 4500 (B), 1700 (C)] ()
— *First Principles Studies toward Guiding Principles of Future New-Types of Memories*

SHISHIDOU, Tatsuya [C class; 5500 (B), 0 (C)] ()
— *First-principles study of magnetic materials*

SUGIYAMA, Takanori [B class; 600 (B), 0 (C)] (275)
— *Evaluation of quantum error correction codes' performance against realistic error models*

SUWA, Hidemaro [C class; 9000 (B), 0 (C)] (216, 217)
— *Magnetization Plateaus Induced by Quantum Phonons*
— *Monte Carlo Spectral Analysis of Quantum Spin Systems with Emergent Excitation*
1. Level spectroscopy in a two-dimensional quantum magnet: linearly dispersing spinons at the deconfined quantum-critical point

H. Suwa, A. Sen, and A. W. Sandvik: Phys. Rev. B **94** (2016) 144416

SUZUKI, Takafumi [E class; 12000 (B), 1800 (C)] (200)
— *Thermal properties and dynamical properties of the Kitaev-Heisenberg model on a honeycomb lattice*

1. Clues and criteria for designing a Kitaev spin liquid revealed by thermal and spin excitations of the honeycomb iridate Na2IrO3
   Youhei Yamaji, Takafumi Suzuki, Takuto Yamada, Sei-ichiro Suga, Naoki Kawashima, and Masatoshi Imada: Phys. Rev. B **93** (2016) 174425.

SUZUKI, Yuji [C class; 2000 (B), 1100 (C)] (114)
— *Orientation of Liquid Crystal Molecules in 3D Electrical Field*

TACHIKAWA, Masanori [C class; 1500 (B), 0 (C)] (124)
— *Theoretical analysis of H/D isotope effect in hydrogen-bonded organic conductor*

1. Theoretical study of H/D isotope effect on phase transition of hydrogen-bonded organic conductor κ-H3(Cat-EDT-TTF)2
   K. Yamamoto, Y. Kanematsu, U. Nagashima, A. Ueda, H. Mori, and M. Tachikawa: Phys. Chem. Chem. Phys. (Communication) **18** (2016) 29673.
2. Multicomponent DFT study of geometrical H/D isotope effect on hydrogen-bonded organic conductor, κ-H3(Cat EDT-ST)2
   K. Yamamoto, Y. Kanematsu, U. Nagashima, A. Ueda, H. Mori, and M. Tachikawa: Chem. Phys. Lett. in press (2017).

TADANO, Terumasa [C class; 6000 (B), 0 (C)] (84)
— *First-principles calculation of anharmonic effects of phonons and related properties in solids*

1. First-Principles Lattice Dynamics Method for Strongly Anharmonic Crystals
   T. Tadano and S. Tsuneyuki: submitted to J. Phys. Soc. Jpn.

TAKAE, Kyohei [B class; 900 (B), 0 (C)] (272)
— *Competition between ferroelectric and antiferroelectric order in anisotropic molecular systems*

1. Ferroelectric glass of spheroidal dipoles with impurities: Polar nanoregions, response to applied electric field, and ergodicity breakdown
   K. Takae and A. Onuki: J. Phys.: Condens. Matter **29** (2017) 165401.

TAKAGI, Noriaki [B class; 1000 (B), 0 (C)] (129, 131)
— *Adsorbed states of magnetic molecules at solid surfaces*
— *Geometric and electronic structures at edge of 2-dimensional honeycomb sheets*

1. Determination of the Geometric Structure of “Multilayer Silicene” Grown on Ag(111) by Dynamical Low Energy Electron Diffraction and Scanning Tunneling Microscopy
   K. Kawahara, T. Shirasawa, C.-L. Lin, R. Nagao, N. Tsukahara, T. Takahashi, R. Arafune, M. Kawai, N. Takagi: Surf. Sci. **651** (2016) 70.
2. Model Hamiltonian approach to magnetic anisotropy of iron phthalocyanine on solid surface
   E. Minamitani, N. Takagi, S. Watanabe: Phys. Rev. B **94** (2016) 205402.
3. Comment on “Rashba Spin-Orbit Coupling in Image Potential States”
   R. Arafune, T. Nakazawa, N. Takagi, M. Kawai, and H. Ishida: Phys. Rev. Lett. **117** (2016) 239701.
4. Surface structure of novel semimetal WTe2
   K. Kawahara, Z. Ni, R. Arafune, T. Shirasawa, C.-L. Lin, E. Minamitani, S. Watanabe, M. Kawai and N. Takagi: Appl. Phys. Express **10** (2017) 045702.

TAKETSUGU, Tetsuya [C class; 4500 (B), 1800 (C)] (78)
— *Ab initio study for designer catalysis based on abundant elements*

TAMURA, Ryo [C class; 7500 (B), 2700 (C)] (210)
— *Magnetocaloric effect in random magnets*
— *Search for applicable external fields of scaling law in magnetic refrigeration*

1. Topological and Dynamical Properties of a Generalized Cluster Model in One Dimension
   T. Ohta, S. Tanaka, I. Danshita, and K. Totsuka: Phys. Rev. B **93** (2016) 165423.
2. Applicability of Scaling Behavior and Power Laws in the Analysis of the Magnetocaloric Effect in Second-Order Phase Transition Materials
   C. Romero-Muñiz, R. Tamura, S. Tanaka, and V. Franco: Phys. Rev. B **94** (2016) 134401.
3. Machine Learning for Atomic Forces in a Crystalline Solid: Transferability to Various Temperatures
   T. Suzuki, R. Tamura, and T. Miyazaki: Int. J. Quantum Chem. **117** (2017) 33.
4. Method for Estimating Spin-Spin Interactions from Magnetization Curves
   R. Tamura and K. Hukushima: Phys. Rev. B **95** (2017) 064407.

TANAKA, Shu [C class; 5000 (B), 2700 (C)] (223)
— *Phase Transitions in Generalized Ising Models*
— *Theoretical study on quantum annealing machine*

1. Topological and Dynamical Properties of a Generalized Cluster Model in One Dimension
   T. Ohta, S. Tanaka, I. Danshita, and K. Totsuka: Phys. Rev. B **93** (2016) 165423.
2. Applicability of Scaling Behavior and Power Laws in the Analysis of the Magnetocaloric Effect in Second-Order Phase Transition Materials
   C. Romero-Muñiz, R. Tamura, S. Tanaka, and V. Franco: Phys. Rev. B **94** (2016) 134401.
3. Machine Learning for Atomic Forces in a Crystalline Solid: Transferability to Various Temperatures
   T. Suzuki, R. Tamura, and T. Miyazaki: Int. J. Quantum Chem. **117** (2017) 33.
4. Method for Estimating Spin-Spin Interactions from Magnetization Curves
   R. Tamura and K. Hukushima: Phys. Rev. B **95** (2017) 064407.

TANUMA, Yasunari [B class; 700 (B), 500 (C)] (269)
— *Study of numerical methods for quantum phenomena of anisotoropic superconductors*

TATENO, Masaru [C class; 3500 (B), 0 (C)] (108)
— *Hybrid ab initio QM/MM calculations of biological systems*

1. Novel strategy for discrimination of transcription factor binding motifs employing mathematical neural network
   A. Sugimoto, J. Kang, T. Sumi, and M. Tateno: J. Phys. Soc. Jpn. in press
2. Effects of a positive feedback loop upon the stability of bi-connected elementary biochemical reaction cycles
   J. Kang and M. Tateno: J. Phys. Soc. Jpn. in press
3. Electronic Structure Rearrangements in Hybrid Ribozyme/Protein Catalysis
   J. Kang, H. Kino, M. J. Field, and M. Tateno: J. Phys. Soc. Jpn. **86** (2017) 044801.
4. Simulated Annealing-Extended Sampling for Multicomponent Decomposition of Spectral Data of DNA Complexed with Peptide
   J. Kang, K. Yamasaki, K. Sano, K. Tsutsui, K. M. Tsutsui, and M. Tateno: J. Phys. Soc. Jpn.**86** (2017) 014802.
5. Complex structure of cytochrome c-cytochrome c oxidase reveals a novel protein-protein interaction mode
   S. Shimada, K. Shinzawa - Itoh, J. Baba, S. Aoe, A. Shimada, E. Yamashita, J. Kang, M. Tateno, S. Yoshikawa, and T. Tsukihara: EMBO J. , **36** (2017) 291.

TATETSU, Yasutomi [C class; 3000 (B), 1200 (C)] (102)
— *Identification of sub phase structures in Nd-Fe-B magnets by first-principles calculations*

1. First-Principles Study of the Role of Cu in Improving the Coercivity of Nd-Fe-B Permanent Magnets
   Y. Tatetsu, S. Tsuneyuki, and Y. Gohda: Phys. Rev. Appl. **6**, 064029 (2016).

TATEYAMA, Yoshitaka [C class; 13000 (B), 2000 (C)] (47)
— *DFT sampling studies on interfacial reactions in catalysts and batteries*

1. Superconcentrated electrolytes for a high-voltage lithium-ion battery
   Jianhui Wang, Yuki Yamada, Keitaro Sodeyama, Ching Hua Chiang, Yoshitaka Tateyama, Atsuo Yamada: Nat. Commun. **7**, 12032 (2016).
2. Catalytic Proton Dynamics at the Water/Solid Interface of Ceria Supported Pt Clusters
   Matteo Farnesi Camellone, Fabio Negreiros Ribeiro, Lucie Szabova, Yoshitaka Tateyama, Stefano Fabris: J. Am Chem. Soc. **138**, 11560 (2016).
3. Hydrate-melt electrolytes for high-energy-density aqueous batteries
   Yuki Yamada, Kenji, Usui, Keitaro Sodeyama, Seongjae Ko, Yoshitaka Tateyama, Atsuo Yamada: Nat. Energy **1**, 16129 (2016).
4. The Solvation Structure of Lithium Ions in an Ether Based Electrolyte Solution from First-Principles Molecular Dynamics
   Martin Callsen, Keitaro Sodeyama, Zdnek Futera, Yoshitaka Tateyama, Ikutaro Hamada: J. Phys. Chem. B, **121**, 180 (2017).
5. Cation Mixing Properties toward Co Diffusion at the LiCoO2 Cathode/ Sulfide Electrolyte Interface in a Solid-State Battery
   Jun Haruyama, Keitaro Sodeyama, Yoshitaka Tateyama: ACS Appl. Mater. Interfaces, **9**, 286 (2017).
6. Enhanced Li-Ion Accessibility in MXene Titanium Carbide by Steric Chloride Termination
   Satoshi Kajiyama, Lucie Szabova, Hiroki Iinuma, Akira Sugahara, Kazuma Gotoh, Keitaro Sodeyama, Yoshitaka Tateyama, Masashi Okubo, Atsuo Yamada: Adv. Energy Mater. **7**, 1601873 (2017).

TERAO, Takamichi [B class; 1000 (B), 700 (C)] (265)
— *Large-scale simulations of semiconductor nanocrystals*

1. Hopping electron model with geometrical frustration: Kinetic Monte Carlo simulations
   T. Terao: Eur. Phys. J. B **89** (2016) 209.
2. Wave propagation in acoustic metamaterial double-barrier structures
   T. Terao: Phys. Status Solidi A **213** (2016) 2773.

TODO, Synge [C class; 5500 (B), 0 (C)] (239)
— *Stochastic Optimization Approach to Phase Transitions and Structure Search*

1. Upper and lower critical decay exponents of Ising ferromagnet with long-range interaction
   T. Horita, H. Suwa, and S. Todo, Phys. Rev. E **95**, 012143 (2017).
2. Updated Core Libraries of the ALPS Project
   A. Gaenko, A. E. Antipov, G. Carcassi, T. Chen, X. Chen, Q. Dong, L. Gamper, J. Gukelberger, R. Igarashi, S. Iskakov, M. Könz, J. P. F. LeBlanc, R. Levy, P. N. Ma, J. E. Paki, H. Shinaoka, S. Todo, M. Troyer, and E. Gull: Comp. Phys. Comm. **213**, 235 (2017).
3. Quantum Lattice Model Solver HPhi
   M. Kawamuraa, K. Yoshimi, T. Misawa, Y. Yamaji, S. Todo, and N. Kawashima: Comput. Phys. Commun. in press.

TOHYAMA, Takami [C class; 5500 (B), 2000 (C)] (224)
— *Dynamical DMRG study of spin dynamics in frustrated quantum spin systems*

1. Phenomenological Magnetic Model in Tsai-Type Approximants
   T. Sugimoto, T. Tohyama, T. Hiroto, and R. Tamura: J. Phys. Soc. Jpn. **85**, (2016) 053701.
2. Density-matrix renormalization group study of Kitaev-Heisenberg model on the triangular lattice
   K. Shinjo, S. Sota, S. Yunoki, K. Totsuka, and T. Tohyama: J. Phys. Soc. Jpn. **85**, (2016) 114710.
3. Static and Dynamic Magnetic Properties of Spin-1/2 Inequilateral Diamond-Chain Compounds $A_3Cu_3AlO_2(SO_4)_4$ (A=K, Rb, and Cs)
   K. Morita, M. Fujihala, H. Koorikawa, T. Sugimoto, S. Sota, S. Mitsuda, and T. Tohyama: Phys. Rev. B, in press.
4. Observation of a dispersive charge mode in hole-doped cuprates using resonant inelastic x-ray

scattering at the oxygen K edge
K. Ishii, T. Tohyama, S. Asano, K. Sato, M. Fujita, S. Wakimoto, K. Tustsui, S. Sota, J. Miyawaki, H. Niwa, Y. Harada, J. Pelliciari, Y. Huang, T. Schmitt, Y. Yamamoto, and J. Mizuki: submitted to Phys. Rev. Lett.

TOKIWA, Hiroaki [C class; 4500 (B), 2500 (C)] (71)
— *Development & Application of Rational Drug Design Method using First-Principles Calculations & Bioinfomatics*

1. Comparative Binding Analysis of Dipeptidyl Peptidase IV (DPP-4) with Antidiabetic Drugs - An Ab Initio Fragment Molecular Orbital Study -
   Nongluk Sriwilaijaroen, Magesh Sadagopan, Akihiro Imamura, Hiromune Ando, Hideharu Ishida, Miho Sakai, Erika Ishitsubo, Takanori Hori, Setsuko Moriya, Takeshi Ishikawa, Kazuo Kuwata, Takato Odagiri, Masato Tashiro, Hiroaki Hiramatsu, Kenji Tsukamoto, Taeko Miyagi, Hiroaki Tokiwa, Makoto Kiso, and Yasuo Suzuki: J.Med.Chem.59(10),4563-4577 (2016).
2. Comparative Binding Analysis of Dipeptidyl Peptidase IV (DPP-4) with Antidiabetic Drugs - An Ab Initio Fragment Molecular Orbital Study -
   Sundaram Arulmozhiraja, Naoya Matsuo, Erika Ishitsubo, Seiji Okazaki, Hitoshi Shimano, and Hiroaki Tokiwa: PLoS One (DOI: 10.1371/journal.pone.0166275) (2016).
3. 高精度第一原理計算による新規抗インフルエンザ薬の合理的設計開発
   常盤広明: 別冊 BioClinica Vol.6(2), p148-154 (2017).
4. In silico analysis of interaction pattern switching in ligand - receptor binding in Golgi α-mannosidase II induced by inhibitors protonation state
   Vladimir Sladek,Juraj Kona,and Hiroaki Tokiwa: Phys.Chem.Chem.Phys. (DOI:10.1039/C7CP01200D) (2017).

TOMITA, Yusuke [C class; 4500 (B), 0 (C)] (247)
— *Numerical study of dynamics in Ising spin models with long-range interactions*

1. Relaxational processes in the one-dimensional Ising model with long-range interactions
   Y. Tomita: Phys. Rev. E **94**, 062142 (2016)

TONEGAWA, Takashi [B,C class; 3700 (B), 0 (C)] (253)
— *Numerical Study of the One-Dimensional Quantum Spin Systems with Spatial Structures*

1. Ground-State Phase Diagram of the Bond-Alternating $S = 2$ Quantum Spin Chain with the XXZ and On-Site Anisotropies —Symmetry Protected Topological Phase versus Trivial Phase—
   K. Okamoto, T. Tonegawa, and T. Sakai: J. Phys. Soc. Jpn. **85** (2016) 063704
2. Frustrated $S = 1/2$ Two-Leg Ladder with Different Leg Interactions
   T. Tonegawa, K. Okamoto, T. Hikihara, and T. Sakai: to be published in J. Phys.: Conf. Series; arXiv:1608.02064
3. Exact Ground States of Frustrated Quantum Spin Systems Consisting of Spin-Dimer Units
   T. Hikihara, T. Tonegawa, K. Okamoto, and T. Sakai: to be published in J. Phys. Soc. Jpn.; arXiv:1612.07515

TOYODA, Masayuki [B class; 600 (B), 0 (C)] (149)
— *Band-gap engineering by forming isotope superlattice and polytypic superlattice*

TSUNEYUKI, Shinji [C class; 7500 (B), 2500 (C)] (14)
— *Development and Application of First-Principles Methods for Spatiotemporally Large-Scale Simulation of Materials*

1. Possible "Magneli" phases and self-alloying in superconducting sulfur hydride
   R. Akashi, W. Sano, R. Arita, S. Tsuneyuki: Phys. Rev. Lett. 117, 075503 (2016).
2. Perovskite-type oxyhydride with a two-dimensional electron system: First-principles prediction of $KTiO_2H$
   N. Sato and S. Tsuneyuki: Appl. Phys. Lett. 109, 172903 (2016).
3. Correlated Band Structure of a Transition Metal Oxide ZnO Obtained from a Many-Body Wave Function Theory

M. Ochi, R. Arita, and S. Tsuneyuki: Phys. Rev. Lett. 118, 026402 (2017).
4. Efficient method for calculating spatially extended electronic states of large systems with a divide-and-conquer approach
S. Yamada, F. Shimojo, R. Akashi, and S. Tsuneyuki: Phys. Rev. B 95, 045106 (2017).
5. Anisotropic superconducting gaps in YNi_2B_2C: A first-principles investigation
M. Kawamura, R. Akashi, and S. Tsuneyuki: Phys. Rev. B 95, 054506 (2017).
6. Numerical investigation of triexciton stabilization in diamond with multiple valleys and bands
H. Katow, J. Usukura, R. Akashi, K. Varga, and S. Tsuneyuki: Phys. Rev. B 95, 125205 (2017).

TSURUTA, Kenji [B class; 500 (B), 0 (C)] (153)
— *Ab-initio Analysis on Structures and Charge States of Amorphous Iron Oxide for Secondary Battery*

UCHIDA, Kazuyuki [C class; 1000 (B), 1700 (C)] (120)
— *First-Principles Study of Moire Patterns in Atomic Layers II*

UCHIDA, Takashi [B class; 200 (B), 500 (C)] (143)
— *First-principles molecular spin dynamics theory of the complex magnetic structures in Mn-Pt alloys*
— *Theory of the magnetic structure of Mn-Pt alloys with CuAu-I type crystal structure*

UDA, Yutaka [B class; 600 (B), 0 (C)] (147)
— *Wear mechanism of diamond tool*

WATANABE, Hiroshi [C class; 6000 (B), 0 (C)] (236)
— *Large-scale molecular dynamics simulations on liquid containing impurity*

1. Direct Observation of Kinetic Equation in Bubble Coarsening
Hiroshi Watanabe, Hajime Inaoka, and Nobuyasu Ito: J. Chem. Phys. **145**, 124707 (2016).
2. Failure of deterministic and stochastic thermostats to control temperature of molecular systems
Hiroshi Watanabe: submitted to J. Phys. Soc. Jpn.

WATANABE, Hiroshi [B class; 400 (B), 0 (C)] (194)
— *Intradimer charge degrees of freedom magnetism and superconductivity in kappa-type molecular conductor*

1. Phase Competition and Superconductivity in κ-(BEDT-TTF)$_2$X: Importance of Intermolecular Coulomb Interactions
H. Watanabe, H. Seo, and S. Yunoki: J. Phys. Soc. Jpn. **86** (2017) 033703.

WATANABE, Kazuyuki [C class; 10500 (B), 0 (C)] (57)
— *First-Principles Study of Excited Electron Dynamics of Nanostructures and Positron States at Surfaces*

1. First-principles study of the dielectric functions of carbon nanotubes with adsorbed water
D. Iwasaki, Y. Suzuki, and K. Watanabe, Appl. Phys. Express **10**, 045101 (2017).
2. Electron transmission through bilayer graphene: A time-dependent first-principles study
H. Miyauchi, Y. Ueda, Y. Suzuki, and K. Watanabe, Phys. Rev.B **95**, 125425 (2017).
3. Mechanism of Electron Excitation and Emission from a Nanoribbon under Pulsed Laser Irradiation: Time-Dependent First-Principles Study
S. Miyauchi and K. Watanabe, J. Phys. Soc. Jpn. **86**, 035003 (2017).
4. Positron States at Li- and O-adsorbed Fe(001) Ferromagnetic Surfaces Studied by Two-Component Density Functional Theory
S. Hagiwara and K. Watanabe, J. Phys. Soc. Jpn. **85**, 114703 (2016).
5. Bohmian mechanics in the exact factorization of electron-nuclear wave functions
Y. Suzuki and K. Watanabe, Phys. Rev. A **94**, 032517 (2016).
6. Quantum dynamics of charge state in silicon field evaporation
E.P. Silaeva, K. Uchida, and K. Watanabe, AIP Advances **6** 085202 (2016).
7. Quantum dynamics of secondary electron emission from nanographene
Y. Ueda, Y. Suzuki, and K. Watanabe, Phys. Rev. B **94**, 035403 (2016).

8. Electrostatic-field-enhanced photoexfoliation of bilayer benzene: A first-principles study
K. Uchida, E.P. Silaeva, and K. Watanabe, Appl. Phys. Express **9**, 065101 (2016).

WATANABE, Satoshi [C class; 12500 (B), 1700 (C)] (52)
— *Theoretical Analyses on Ionic Transport Properties Electrical Properties and Interfacial Electronic States of Nanostructures*

1. Electric field response in bilayer graphene: Ab initio investigation
Y. Mori, E. Minamitani, Y. Ando, S. Kasamatsu, and S. Watanabe: Applied Physics Express **9** (2016) 115104.
2. Surface phonon excitation on clean metal surfaces in scanning tunneling microscopy
E. Minamitani, R. Arafune, N. Tsukahara, Y. Ohda, S. Watanabe, M. Kawai, H. Ueba, and N. Takagi: Phys. Rev. B **93** (2016) 085411.
3. Model Hamiltonian approach to the magnetic anisotropy of iron phthalocyanine at solid surfaces
E. Minamitani, N. Takagi, and S. Watanabe: Phys. Rev. B **94** (2016) 205402.
4. Surface structure of novel semimetal WTe_2
K. Kawahara, Z. Ni, R. Arafune, T. Shirasawa, C.-L. Lin, E. Minamitani, S. Watanabe, M. Kawai, and N. Takagi: Appl. Phys. Express **10** (2017) 045702.
5. Controlled Modification of Superconductivity in Epitaxial Atomic Layer–Organic Molecule Heterostructures
S. Yoshizawa, E. Minamitani, S. Vijayaraghavan, P. Mishra, Y. Takagi, T. Yokoyama, H. Oba, J. Nitta, K. Sakamoto, S. Watanabe, T. Nakayama, and T. Uchihashi: Nano Lett. **17** (2017) 2287.
6. スパースモデリングによるナノデバイスシミュレーション解析
安藤康伸, 藤掛 壮, W. Li and 渡邉 聡: 電子情報通信学会誌 **99** (2016) 461.
7. Germanene and stanene on two-dimensional substrates: Dirac cone and Z_2 invariant
Z. Ni, E. Minamitani, Y. Ando, and S. Watanabe: submitted to Phys. Rev. B.
8. Cu diffusion in amorphous Ta_2O_5 studied with a simplified neural network potential
W. Li, Y. Ando, and S. Watanabe: submitted to J. Chem. Phys.

YAMADA, Atsuo [C class; 4500 (B), 0 (C)] (98)
— *Theoretical study on electrode materials for sodium ion batteries*

1. Sodium Iron(II) Pyrosilicate $Na_2Fe_2Si_2O_7$: A Potential Cathode Material in the Na2O-FeO-SiO2 System
A. Panigrahi,S. Nishimura,T. Shimada, E. Watanabe, W. Zhao, G. Oyama,and A. Yamada: submitted to Chemistry of Materials

YAMADA, Atsushi [C class; 4000 (B), 0 (C)] (179)
— *Superconductivity and magnetic properties in the strongly correlated electron systems*

1. A study of the magnetic properties in the Hubbard model on the honeycomb lattice by variational cluster approximation
Atsushi Yamada: Int. J. Mod. Phys. B**30** (2016) 1650158.

YAMAGUCHI, Shu [C class; 6500 (B), 0 (C)] (76)
— *Research about Protonic Activity on the hydrated surface of acid-base oxide catalysts*

1. Effect of CO_2 Adsorption on Proton Migration on Hydrated ZrO_2 Surface: an *Ab Initio* Molecular Dynamic Study
R. Sato, Y. Shibuta, F. Shimojo, S. Yamaguchi: submitted to Phys. Chem. Chem. Phys.

YAMAJI, Youhei [C class; 6000 (B), 2100 (C)] (171)
— *Numerical Studies on Excitation Spectra of Strongly Correlated Topological Materials*

1. Finite-Temperature Variational Monte Carlo Method for Strongly Correlated Electron Systems
K. Takai, K. Ido, T. Misawa, Y. Yamaji, and M. Imada: J. Phys. Soc. Jpn. **85** (2016) 034601.
2. Modulated helical metals at magnetic domain walls of pyrochlore iridium oxides
Y. Yamaji and M. Imada: Phys. Rev. B **93** (2016) 195146.
3. Clues and criteria for designing a Kitaev spin liquid revealed by thermal and spin excitations of the honeycomb iridate Na_2IrO_3

Y. Yamaji, T. Suzuki, T. Yamada, S. Suga, N. Kawashima, and M. Imada: Phys. Rev. B **93** (2016) 174425.

4. Finite-Temperature Signatures of Spin Liquids in Frustrated Hubbard Model
   T. Misawa and Y. Yamaji: arXiv:1608.09006, submitted.
5. Ground state properties of Na_2IrO_3 determined from *ab initio* Hamiltonian and its extensions containing Kitaev and extended Heisenberg interactions
   T. Okubo, K. Shinjo, Y. Yamaji, N. Kawashima, S. Sota, T. Tohyama, and M. Imada: arXiv:1611.03614.
6. Realizing quantum spin liquid phases in spin-orbit driven correlated materials
   A. Catuneanu, Y. Yamaji, G. Wachtel, H.-Y. Kee, and Y. B. Kim: arXiv:1701.07837, submitted.
7. Quantum Lattice Model Solver HPhi
   M. Kawamuraa, K. Yoshimi, T. Misawa, Y. Yamaji, S. Todo, and N. Kawashima: Comput. Phys. Commun. in press.

YAMASHITA, Koichi [C class; 5500 (B), 0 (C)] (88)
— *Large scale ab initio calculations on the fundamental processes of solar energy convergence devices and on designing principles for new materials*

1. Theoretical investigation of [Ru(tpy)2]2+2]2+, [Ru(tpy)(bpy)(H2O)]2+2+ and [Ru(tpy)(bpy)(Cl)]++ complexes in acetone revisited: Inclusion of strong spin?orbit couplings to quantum chemistry calculations
   K. Mishima, T. Kinoshita, M. Hayashi, R. Jono, H. Segawa, K. Yamashita: J. Theor. Comput. Chem. **15** (2016) 1650001.
2. Photon-absorbing charge-bridging states in organic bulk heterojunctions consisting of diketopyrrolopyrrole derivatives and PCBM
   M. Fujii, W. Shin, T. Yasuda, K. Yamashita: Phys. Chem. Chem. Phys. **18** (2016) 9514.
3. Dipole Analyses for Short-Circuit Current in Organic Photovoltaic Devices of Diketopyrrolopyrrole-Based Donor and PCBM
   S. Koda, M. Fujii, S. Hatamiya, K. Yamashita: Theor. Chem. Acc. **135** (2016) 115.
4. Does organic/organic interface mimic band bending by deforming structure?
   R. Jono, E. Watanabe, M. Fujii, K. Yamashita: J. Photochem. Photobiol. A: Chem. **330** (2016) 181.
5. The Effects of the Organic-Inorganic Interactions on the Thermal Transport Properties of CH3NH3PbI3
   T. Hata, G. Giorgi, K. Yamashita: Nano Lett. **16** (2016) 2749.
6. Thermal effect on the morphology and performance of organic photovoltaics
   E. Kawashima, M. Fujii, K. Yamashita: Phys. Chem. Chem. Phys. **18** (2016) 26456.
7. Anion Ordering in CaTaO2N: Structural Impact on the Photocatalytic Activity. Insights from First-Principles
   A. Kubo, G. Giorgi, K. Yamashita: Chem. Mater. **29** (2017) 539.
8. Charge Carrier Trapping at Surface Defects of Perovskite Solar Cell Absorbers: A First-Principles Study
   H. Uratani, K. Yamashita: J. Phys. Chem. Lett. **8** (2017) 742.
9. Synthesis of Quinoidal Fused Oligosiloles by Rhodium-Catalyzed Stitching Reaction and Theoretical Investigation of Their Properties
   R. Shintani, N. Misawa, T. Tsuda, R. Iino, M. Fujii, K. Yamashita, K. Nozaki: J. Am. Chem. Soc. **139)** (2017) 3861.

YAMASHITA, Tomoki [C class; 3000 (B), 1800 (C)] (97)
— *Search for magnet and spintronics materials based on materials informatics*

YAMAUCHI, Jun [B class; 800 (B), 500 (C)] (127)
— *First-principles study on the defects in semiconductors*

1. X-ray photoelectron spectroscopy analysis of boron defects in silicon crystal: a first-principles study
   J. Yamauchi, Y. Yoshimoto, and Y. Suwa: J. Appl. Phys., **119** (2016) 175704.

YAMAUCHI, Kunihiko [C class; 6500 (B), 2200 (C)] (64)
— *Search and design for topological materials based on evolutionary algorithm*

1. Topological phase transition coupled with spin-valley physics in ferroelectric oxide heterostructures
   Kunihiko Yamauchi, Paolo Barone, and Silvia Picozzi: Phys. Rev. B 95, 035146 (2017).
2. Superexchange interaction in the A-site ordered perovskite YMn3Al4O12
   K. Nakayama, M. Kuno, K. Yamauchi, S. Souma, K. Sugawara, T. Oguchi, T. Sato, and T. Takahashi: Phys. Rev. B 95, 125204 (2017).
3. Magnetodielectric detection of magnetic quadrupole order in Ba(TiO)Cu4(PO4)4 with Cu4O12 square cupolas
   K. Kimura, P. Babkevich, M. Sera, M. Toyoda, K. Yamauchi, G.S. Tucker, J. Martius, T. Fennell, P. Manuel, D.D. Khalyavin, R.D. Johnson, T. Nakano, Y. Nozue, H.M. Ronnow, and T. Kimura: Nat. Commun. 7, 13039 (2016).

YANAGISAWA, Susumu [C class; 5000 (B), 1800 (C)] (73)
— *Theoretical investigation on electronic structure of organic semiconductor solids*

1. First-Principles Molecular Dynamics Analysis of Ligand-Free Suzuki-Miyaura Cross Coupling in Water Solvent: Oxidative Addition Step
   T. Hirakawa, Y. Uramoto, D. Mimura, A. Takeda, S. Yanagisawa, T. Ikeda, K. Inagaki and Y. Morikawa: J. Phys. Chem. B **121** (2017) 164
2. Determination of geometric and electronic structures of organic crystals from first principles: Role of the molecular configuration on the electronic structure
   S. Yanagisawa and I. Hamada: J. Appl. Phys. **121** (2017) 045501

YANAGISAWA, Takashi [B class; 1300 (B), 800 (C)] (187)
— *Quantum Monte Carlo and first principles study of strongly correlated electron systems*

1. Crossover from weakly to strongly correlated regions in the two-dimensional Hubbard model
   T. Yanagisawa: J. Phys. Soc. Jpn. 85 (2016) 114707.a
2. One way to design a valence-skip compound
   I. Hase, T. Yanagisawa and K. Kawashima: Nanoscale Research Letters 12 (2017) 127.
3. Isotope shift of the ferromagnetic transition temperature in itinerant ferromagnets
   T. Yanagisawa, I. Hase and K. Odagiri: Physics Letters A381 (2017) 737.a
4. Chiral sine-Gordon model
   T. Yanagisawa: EPL 113 (2016) 41001.
5. Nambu-Goldstone-Leggett and Higgs modes in multi-condensate superconductors
   T. Yanagisawa: J. Superconductivity and Novel MAgnetism 29 (2016) 3099.
6. Electronic structure of InTe, SnAs and PbSb: Valence-skip compound or not?
   I. Hase, K. Yasutomi, T. Yanagisawa and K. Odagiri: Physica C527 (2016) 85.
7. Electronic Structure of SnF_3: An Example of Valence Skipper which Forms Charge-Density Wave
   I. Hase, T. Yanagisawa and K. Kawashima: Physica C530 (2016) 11.
8. Duality in Spin Fluctuations in Correlated Electron Systems
   T. Yanagisawa and I. Hase: Physica C530 (2016) 1.
9. Magnetism, Fluctuations and mechanism of high-temperature superconductivity
   T. Yanagisawa, I. Hase, M. Miyazaki and K. Yamaji: J. Phys. Conf. Series (2017) in press.a
10. Evolution of the CDW gap in valence skipper RbTlX3 (X = F, Cl, Br): A first-principles study
    I. Hase and T. Yanagisawa: J. Phys. Conf. Series (2017) in press.

YASUDA, Chitoshi [C class; 3500 (B), 0 (C)] (255)
— *Randomness Effects on Quantum Spin Systems Coupled to Lattice Degrees of Freedom*

YASUOKA, Kenji [C class; 7500 (B), 0 (C)] (65)
— *The role of Ti interstitial in adsorption of O2 on reduced rutile TiO2 (110) surface*
— *The role of excess electrons in adsorption of O2 on rutile TiO2 (110) surface*

1. Stability of Excess Electrons Introduced by Ti Interstitial in Rutile TiO2(110) Surface
   K. Morita, T. Shibuya, and K. Yasuoka: J. Phys. Chem. C **121** (2017) 1602-1607.

YOSHIDA, Tsuneya [C class; 11000 (B), 0 (C)] (166)
— *Correlation effects on surface states of topological phases*
— *Study of topological phases in strongly correlated systems*

1. Restoration of topological properties at finite temperatures in a heavy-fermion system
   Tsuneya Yoshida, and Robert Peters, and Norio Kawakami: Phys. Rev. B. **93** (2016) 045138
2. Coexistence of light and heavy surface states in a topological multiband Kondo insulator
   R. Peters, T. Yoshida, H. Sakakibara, and N. Kawakami: Phys. Rev. B **93**, 235159 (2016)
3. Reduction of Z classification of a two-dimensional weak topological insulator
   T. Yoshida and N. Kawakami: Phys. Rev. B **95**, 045127 (2017)
4. Fate of Majorana modes in CeCoIn5/YbCoIn5 superlattices
   T. Yoshida, A. Daido, Y. Yanase, and N. Kawakami: Phys. Rev. Lett. **118**, 147001 (2017)
5. Topological edge Mott insulating state in two dimensions at finite temperatures
   T. Yoshida and N. Kawakami: Phys. Rev. B **94**, 085149 (2016)

YOSHIDOME, Takashi [C class; 4500 (B), 1700 (C)] (235)
— *A construction of the Markov state model of protein folding using the manifold theory*

YOSHIZAWA, Kanako [C class; 2500 (B), 1800 (C)] (100)
— *Structural analysis of titanium dioxide by first-principles calculation*

□ SCCMS Projects

AKAI, Hisazumi [1000 (B), 1000 (C)] (140)

— *First-principles calculation on f-electron systems*

1. Schottky junction studied using Korringa–Kohn–Rostoker Nonequilibrium Green's function method
   M. Ogura and H. Akai: J. Phys. Soc. Jpn. **85** (2016) 104715.
2. Relevance of 4f-3d exchange to finite-temperature magnetism of rare-earth permanent magnets: an ab-initio-based spin model approach for $NdFe_{12}N$
   M. Matsumoto, H. Akai, Y. Harashima, S. Doi and T. Miyake: J. Appl. Phys. **119** (2016) 213901.
3. Electrical resistivity of substitutionally disordered hcp Fe–Si and Fe–Ni alloys: Chemically-induced resistivity saturation in the Earth's core
   H. Gomi, K. Hirose, H. Akai, and Y. Fei: Earth Planet. Sci. Lett. **451** (2016) 51.
4. Monte Carlo analysis for finite-temperature magnetism of $Nd_2Fe_{14}B$ permanent magnet
   Yuta Toga, Munehisa Matsumoto, Seiji Miyashita, Hisazumi Akai, Shotaro Doi, Takashi Miyake, and Akimasa Sakuma: Phys. Rev. B **94** (2016) 174433.
5. Atomistic-model study of temperature-dependent domain walls in the neodymium permanent magnet $Nd_2Fe_{14}B$
   Masamichi Nishino, Yuta Toga, Seiji Miyashita, Hisazumi Akai, Akimasa Sakuma, and Satoshi Hirosawa: Phys. Rev. B **95** (2017) 094429.

FUJITA, Takatoshi [1000 (B), 0 (C)] (303)

— *Excited-state calculations for molecular aggregates based on Greenfs function method*

1. Coherent Dynamics of Mixed Frenkel and Charge-Transfer Excitons in Dinaphtho[2,3-*b*:2′3′-*f*]thieno[3,2-*b*]-thiophene Thin Films: The Importance of Hole Delocalization
   T. Fujita, J. Huh, S K. Saikin, and A. Aspuru-Guzik: J. Phys. Chem. Lett. **7** (2016) 546.
2. Emulation of complex open quantum systems using superconducting qubits
   S. Mostame, J. Huh, C. Kreisbeck, A. J. Kerman, T. Fujita, A. E. Eisfeld, A. Aspuru-Guzik: Quantum Inf. Proc. **16** (2017) 44.

FUKUSHIMA, Tetsuya [5000 (B), 2500 (C)] (304)

— *Design of spintronics materials by order-N screened KKR Green function method*

1. Supercomputer System at ISSP

2. Local energies and energy fluctuations - applied to the high entropy alloy CrFeCoNi
   T. Fukushima, H. Katayama-Yoshida, K. Sato, M. Ogura, R. Zeller, and P. H. Dederichs: submitted to J. Phys. Soc. Jpn.
3. Structure of the high-entropy alloy AlxCrFeCoNi: fcc versus bcc
   M. Ogura, T. Fukushima, R. Zeller, and P. H. Dederichs: submitted to J. Alloy Compd.

IMADA, Masatoshi [25000 (B), 10000 (C)] (287)

— *Interfacial high-Tc superconductivity and nonequilibrium superconductivity*

— *Superconducting correlations of nonequilibrium states*

1. Finite-Temperature Variational Monte Carlo Method for Strongly Correlated Electron Systems
   Kensaku Takai, Kota Ido, Takahiro Misawa, Youhei Yamaji, and Masatoshi Imada: J. Phys. Soc. Jpn.**85** (2016) 034601.
2. Real-space renormalized dynamical mean field theory
   Dai Kubota, Shiro Sakai, and Masatoshi Imada: Phys. Rev. B **93** (2016) 205119.
3. Modulated Helical Metals at Magnetic Domain Walls of Pyrochlore Iridium Oxides
   Youhei Yamaji, Masatoshi Imada: Phys. Rev. B**93** (2016) 195146.
4. Clues and criteria for designing a Kitaev spin liquid revealed by thermal and spin excitations of the honeycomb iridate Na2IrO3
   Youhei Yamaji, Takafumi Suzuki, Takuto Yamada, Sei-ichiro Suga, Naoki Kawashima, and Masatoshi Imada: Phys. Rev. B **93** (2016) 174425.

5. Self-Optimized Superconductivity Attainable by Interlayer Phase Separation at Cuprate Interfaces
Takahiro Misawa, Yusuke Nomura, Silke Biermann, and Masatoshi Imada: Sci. Adv. **2** (2016) e1600664 .
6. Nonequilibrium Pump-Probe Photoexcitation as a Tool for Analyzing Unoccupied Equilibrium States of Correlated Electrons
Youhei Yamaji,and Masatoshi Imada: J. Phys. Soc. Jpn. **85** (2016) 094707.
7. Hidden-fermion representation of self-energy in pseudogap and superconducting states of the two-dimensional Hubbard model
Shiro Sakai, Marcello Civelli, and Masatoshi Imada: Phys. Rev. B.**94** (2016) 115130.
8. Stabilization of topological insulator emerging from electron correlations on honeycomb lattice and its possible relevance in twisted bilayer graphene
Moyuru Kurita, Youhei Yamaji, and Masatoshi Imada : Phys. Rev. B. **94** (2016) 125131.

KAWASHIMA, Naoki [5000 (B), 2500 (C)] (298)
— *Search for novel quantum phases and transitions by tensor network methods and quantum Monte Carlo methods*

1. Ground state properties of Na2IrO3 determined from ab initio Hamiltonian and its extensions containing Kitaev and extended Heisenberg interactions
Tsuyoshi Okubo, Kazuya Shinjo, Youhei Yamaji, Naoki Kawashima, Shigetoshi Sota, Takami Tohyama, and Masatoshi Imada: arXiv:1611.03614.
2. Quantum Lattice Model Solver HPhi
Mitsuaki Kawamura, Kazuyoshi Yoshimi, Takahiro Misawa, Youhei Yamaji, Synge Todo, and Naoki Kawashima: Comput. Phys. Commun., in press.
3. Clues and criteria for designing a Kitaev spin liquid revealed by thermal and spin excitations of the honeycomb iridate Na2IrO3
Youhei Yamaji, Takafumi Suzuki, Takuto Yamada, Sei-ichiro Suga, Naoki Kawashima, and Masatoshi Imada: Phys. Rev. B **93**, 174425 (2016).

KOHYAMA, Masanori [25000 (B), 12500 (C)] (289, 290)
— *First-principles phase field mapping*

1. Relationship between cap structure and energy gap in capped carbon nanotubes
S. Ono, K. Tanikawa, R. Kuwahara, and K. Ohno: J. Chem. Phys. 145, 024702 (2016).
2. Ab initio molecular dynamics simulation study of successive hydrogenation reactions of carbon monoxide producing methanol
T. N. Pham, S. Ono, and K. Ohno: J. Chem. Phys. 144, 144309 (2016).
3. Momentum-dependent band spin splitting in semiconducting MnO2: a density functional calculation
Y. Noda, K. Ohno, and S. Nakamura: Phys. Chem. Chem. Phys. 18, 13294 (2016).
4. Growth of Graphene Nanocoil in a SiC Container: A Molecular Dynamics Study
S. Battacharyya, S. Otake, S. Ono, R. Kuwahara, and K. Ohno: Advances in Materials Physics and Chemistry 6, 113 (2016).
5. A self-consistent GW approach to the van der Waals potential for a helium dimer
T. Shoji, R. Kuwahara, S. Ono, and K. Ohno: Phys. Chem. Chem. Phys. 18, 24477 (2016).
6. GWγ+ Bethe-Salpeter equation approach for photoabsorption spectra: Importance of self-consistent GWγ calculations in small atomic systems
R. Kuwahara, Y. Noguchi, and K. Ohno: Phys. Rev. B 94, 121116(R) (2016).
7. A simple derivation of the exact quasiparticle theory and its extension to arbitrary initial excited eigenstates
K. Ohno, S. Ono, and T. Isobe: J. Chem. Phys. 146, 084108 (2017).

MISAWA, Takahiro [10000 (B), 5000 (C)] (295)
— *Many-variable variational Monte Carlo study for interfaces of high-Tc superconductors*
— *Many-variable variational Monte Carlo study for degenerate two-orbital Hubbard model with inverted Hund coupling*

1. Self-optimized superconductivity attainable by interlayer phase separation at cuprate interfaces

T. Misawa, Y. Nomura, S. Biermann, and M. Imada, Sci. Adv. **2**, e1600664 (2016)

MIYAKE, Takashi [5400 (B), 0 (C)] (311)
— *First-principles study of magnetic materials*

1. First-principles study on stability and magnetism of NdFe11M and NdFe11MN for M = Ti, V, Cr, Mn, Fe, Co, Ni, Cu, Zn
   Yosuke Harashima, Kiyoyuki Terakura, Hiori Kino, Shoji Ishibashi, and Takashi Miyake: J. Appl. Phys. **120** (2016) 203904.

NAKAI, Hiromi [0 (B), 5000 (C)] (309)
— *Quantum molecular dynamics simulation on electrolyte solution for sodium-ion battery*

NOBUSADA, Katsuyuki [15000 (B), 7500 (C)] (285)
— *Nano-optical response theory and computational design of photo-electronic functional devices*

1. An atomic-level insight into the basic mechanism responsible for the enhancement of the catalytic oxidation of carbon monoxide on a Cu/CeO2 surface
   K. Koizumi, K. Nobusada and M. Boero: Phys. Chem. Chem. Phys. **19**, 3498 (2017).
2. Simple but efficient method for inhibiting sintering and aggregation of catalytic Pt nanoclusters on metal-oxide supports
   K. Koizumi, K. Nobusada and M. Boero: Chem. Eur. J. **23**, 1531 (2017).
3. The absence of a gap state and enhancement of the Mars-van Krevelen reaction on oxygen defective Cu/CeO2 surfaces
   K. Koizumi, K. Nobusada and M. Boero: Phys. Chem. Chem. Phys. **18**, 20708 (2016).

OBA, Fumiyasu [10000 (B), 0 (C)] (307)
— *Exploration of novel semiconductors by first-principles screening*

OGATA, Shuji [5000 (B), 2500 (C)] (299)
— *Simulation of organic-inorganic interfaces*

1. Enhanced Si-O Bond Breaking in Silica Glass by Water Dimer: A Hybrid Quantum-Classical Simulation Study
   T. Kouno, S. Ogata, T. Shimada, T. Tamura, and R. Kobayashi: J. Phys. Soc. Jpn. **85** (2016) 054601.
2. Moisture-Induced Reduction of Adhesion Strength between Surface Oxidized Al and Epoxy Resin: Dynamics Simulation with Electronic Structure Calculation
   S. Ogata and Y. Takahashi: J. Phys. Chem. C **120** (2016) 13630.

OGUCHI, Tamio [10000 (B), 5000 (C)] (306)
— *Materials exploration for sodium secondary batteries*

OKAZAKI, Kei-ichi [1500 (B), 0 (C)] (302)
— *Multiscale simulations of bio-membrane shape-changing dynamics*

OKAZAKI, Susumu [5000 (B), 2500 (C)] (301)
— *Conversion and storage of energy - Fuel cells and secondary batteries: Research and development of fundamental technologies of battery simulators*

1. Evaluation of atomic pressure in the multiple time-step integration algorithm
   Y. Andoh, N. Yoshii, A. Yamada, S. Okazaki: J. Comput. Chem. **38** , 704 (2017)
2. Structural ordering of lipid bilayers induced by surfactant molecules with small hydrophilic head group
   Y. Andoh, S. N. S. Mohamed, S. Kite, S. Okazaki: Mol. Siml., in press
3. Transferable coarse-grained model for perfluorosulfonic acid polymer membranes
   A. Kuo, S. Okazaki, W. Shinoda: Soft Matter, submitted.
4. Molecular dynamics study of the morphology of hydrated perfluorosulfonic acid polymer membranes

A. Kuo, W. Shinoda, S. Okazaki: J. Phys. Chem. C, **120**, 25832 (2017)

OSHIYAMA, Atsushi [25000 (B), 12500 (C)] (283)
— *First-principles electronic-structure calculations and device-process simulations*

1. Multistep Atomic Reaction Enhanced by an Atomic Force Microscope Probe on Si (111) and Ge(111) Surfaces
   B. Enkhtaivan and A. Oshiyama: Phys. Rev. B **94** (2016) 085416.
2. Atomic Force Microscope manipulation of Ag atom on the Si(111) surface
   B. Enkhtaivan and A. Oshiyama: Phys. Rev. B **95** (2017) 035309.
3. Band-unfolding approach to moiré-induced band-gap opening and Fermi-level-velocity reduction in twisted bilayer graphene
   H. Nishi, Y-i. Matsushita, A. Oshiyama: Phys. Rev. B **95** (2017) 085420.
4. First-Principles Calculations that Clarify Energetics and Reactions of Oxygen Adsorption and Carbon Desorption on 4H-SiC ($11\bar{2}0$) Surface
   H. Li, Y.-i. Matsushita, M. Boero and A. Oshiyama: J. Phys. Chem. C **121** (2017) 3920.
5. Microscopic Mechanisms of Initial Formation Process of Graphene on SiC(0001) Surfaces: Selective Si Desorption from Step Edges
   F. Imoto, J.-I. Iwata, M. Boero, A. Oshiyama: J. Phys. Chem. C **121** (2017) 5041.
6. Comprehensive study on band-gap variations in sp^3-bonded semiconductors: roles of electronic states floating in internal space
   Y.-i. Matsushita and A. Oshiyama: J. Phys. Soc. Jpn **86** (2017) 054702.

SAITO, Susumu [5000 (B), 2500 (C)] (149)
— *Materials design using B, C, and N for next-generation device*

SHIBA, Hayato [10000 (B), 5000 (C)] (292)
— *Simulation of liquid materials properties using hybrid classical modeling*
— *Mesoscale dynamics study of rheology and friction in composite electrolyte solutions*

SHIGETA, Yasuteru [5000 (B), 2500 (C)] (296)
— *First-principles analyses on crystal growth mechanism of GaN*

SUGINO, Osamu [15000 (B), 2500 (C)] (291)
— *Energy conversion and storage – electric energy*

TAKETSUGU, Tetsuya [10000 (B), 5000 (C)] (78)
— *Catalytic activity of abundant-metal clusters supported by an oxide substrate*

TOHYAMA, Takami [0 (B), 2500 (C)] (224)
— *Cooperation research with big experimental Facilities*

1. Phenomenological Magnetic Model in Tsai-Type Approximants
   T. Sugimoto, T. Tohyama, T. Hiroto, and R. Tamura: J. Phys. Soc. Jpn. **85**, (2016) 053701.
2. Density-matrix renormalization group study of Kitaev-Heisenberg model on the triangular lattice
   K. Shinjo, S. Sota, S. Yunoki, K. Totsuka, and T. Tohyama: J. Phys. Soc. Jpn. **85**, (2016) 114710.
3. Static and Dynamic Magnetic Properties of Spin-1/2 Inequilateral Diamond-Chain Compounds $A_3Cu_3AlO_2(SO_4)_4$ (A=K, Rb, and Cs)
   K. Morita, M. Fujihala, H. Koorikawa, T. Sugimoto, S. Sota, S. Mitsuda, and T. Tohyama: Phys. Rev. B, in press.
4. Observation of a dispersive charge mode in hole-doped cuprates using resonant inelastic x-ray scattering at the oxygen K edge
   K. Ishii, T. Tohyama, S. Asano, K. Sato, M. Fujita, S. Wakimoto, K. Tustsui, S. Sota, J. Miyawaki, H. Niwa, Y. Harada, J. Pelliciari, Y. Huang, T. Schmitt, Y. Yamamoto, and J. Mizuki: submitted to Phys. Rev. Lett.

YABANA, Kazuhiro [5000 (B), 2500 (C)] (297)
— *Dynamics in nano-interface excited by high-intensity pulsed light*

YAMADA, Atsuo [5000 (B), 0 (C)] (98)
— *Analysis of elementary cathode reactions towards high-voltage sodium ion batteries*

1. Sodium Iron(II) Pyrosilicate $Na_2Fe_2Si_2O_7$: A Potential Cathode Material in the Na2O-FeO-SiO2 System
   A. Panigrahi,S. Nishimura,T. Shimada, E. Watanabe, W. Zhao, G. Oyama,and A. Yamada: submitted to Chemistry of Materials

YAMASHITA, Koichi [5000 (B), 2500 (C)] (300)
— *Large scale calculations on the fundamental processes of organic and perovskite solar cells and their optimization in conversion efficiency*

1. Theoretical investigation of [Ru(tpy)2]2+2]2+, [Ru(tpy)(bpy)(H2O)]2+2+ and [Ru(tpy)(bpy)(Cl)]++ complexes in acetone revisited: Inclusion of strong spin?orbit couplings to quantum chemistry calculations
   K. Mishima, T. Kinoshita, M. Hayashi, R. Jono, H. Segawa, K. Yamashita: J. Theor. Comput. Chem. **15** (2016) 1650001.
2. Photon-absorbing charge-bridging states in organic bulk heterojunctions consisting of diketopyrrolopyrrole derivatives and PCBM
   M. Fujii, W. Shin, T. Yasuda, K. Yamashita: Phys. Chem. Chem. Phys. **18** (2016) 9514.
3. Dipole Analyses for Short-Circuit Current in Organic Photovoltaic Devices of Diketopyrrolopyrrole-Based Donor and PCBM
   S. Koda, M. Fujii, S. Hatamiya, K. Yamashita: Theor. Chem. Acc. **135** (2016) 115.
4. Does organic/organic interface mimic band bending by deforming structure?
   R. Jono, E. Watanabe, M. Fujii, K. Yamashita: J. Photochem. Photobiol. A: Chem. **330** (2016) 181.
5. The Effects of the Organic-Inorganic Interactions on the Thermal Transport Properties of CH3NH3PbI3
   T. Hata, G. Giorgi, K. Yamashita: Nano Lett. **16** (2016) 2749.
6. Thermal effect on the morphology and performance of organic photovoltaics
   E. Kawashima, M. Fujii, K. Yamashita: Phys. Chem. Chem. Phys. **18** (2016) 26456.
7. Anion Ordering in CaTaO2N: Structural Impact on the Photocatalytic Activity. Insights from First-Principles
   A. Kubo, G. Giorgi, K. Yamashita: Chem. Mater. **29** (2017) 539.
8. Charge Carrier Trapping at Surface Defects of Perovskite Solar Cell Absorbers: A First-Principles Study
   H. Uratani, K. Yamashita: J. Phys. Chem. Lett. **8** (2017) 742.
9. Synthesis of Quinoidal Fused Oligosiloles by Rhodium-Catalyzed Stitching Reaction and Theoretical Investigation of Their Properties
   R. Shintani, N. Misawa, T. Tsuda, R. Iino, M. Fujii, K. Yamashita, K. Nozaki: J. Am. Chem. Soc. **139** (2017) 3861.

YOSHIMI, Kazuyoshi [10000 (B), 2500 (C)] (293)
— *Promotion of joint researches through Project for advancement of software usability in materials science in 2015*
— *Analysis of spin relaxation phenomena in quantum dots*

1. Quantum Lattice Model Solver HPhi
   Mitsuaki Kawamura, Kazuyoshi Yoshimi, Takahiro Misawa, Youhei Yamaji, Synge Todo, and Naoki Kawashima: Comput. Phys. Commun., in press.

□ Doctor theses

1. **ALAYDRUS, Musa**
   Theoretical investigation of ionic conduction in rare-earth oxide materials
   Osaka University, 2016-03

2. **BUI, Van Pho**
   Study on the Mechanism of Plutinum-Assisted Hydrofluoric Acid/Water Etching of SiC
   Osaka University, 2016-08

3. **ENKHTAIVAN, Batnyam**
   First-Principles Study on Microscopic Mechanism of Atom Manipulation by Atomic Force Microscope
   the University of Tokyo, 2017-03

4. **HAGIWARA, Satoshi**
   Positron States in Solids and At Surfaces Studied by Two-component Density Functional Theory
   Tokyo University of Science, 2017-03

5. **HIROSE, Daichi**
   Development and application of the GW+Bethe-Salpeter method for the study of excitonic states in molecules
   the University of Tokyo, 2017-03

6. **IMACHI, Hiroto**
   Numerical Methods for Large-scale Quantum Material Simulations
   Tottori University, 2017-03

7. **ISOHASHI, Ai**
   Development of Catalyst-Assisted Etching in Pure Water
   Osaka University, 2017-01

8. **MORIYAMA, Takumi**
   Study on switching mechanism of resistive random access memories using polycrystalline metal oxide films
   Tottori University, 2017-03

9. **OBATA, Masao**
   Development and application of spin dependent van der Waals density functional method
   Kanazawa University, 2016-09

10. **OZAWA, Ryo**
    Topological spin textures emergent from spin-charge coupling
    the University of Tokyo, 2017-03

11. **SAKAGAMI, Takahiro**
    Structure of liquid ZI_4 (Z=Sn, Ge) under ambient pressure
    Ehime University, 2016-03

12. **SAKURAGI, Shunsuke**
    Ferromagnetism Induced by Quantum-Well States in Pd(100) Ultrathin Films
    Keio University, 2017-03

13. **SATO, Nobuya**

Theoretical predictions of perovskite-type oxyhydrides based on first-principles calculations
the University of Tokyo, 2016-03

14. **SHUKRI, Ganes**
Theoretical Study on the Effect of Oxygen Vacancy on Ethylene and Acetylene Interaction with Anatase TiO_2 (001) Surface
Osaka University, 2016-09

15. **SUNNARDIANTO, Gagus Ketut**
An Effective Way of Storing and Releasing Hydrogen via Graphene Vacancy for Hydrogen Storage Applications
Osaka University, 2017-03

16. **SUZUKI, Takafumi**
Nonequilibrium current fluctuation in interacting mesoscopic systems
the University of Tokyo, 2017-03

17. **UEKI, Hikaru**
Microscopic Theory of the Flux-Flow Hall Effect in Type-II@Superconductors
Hokkaido University, 2017-06

18. **YAMADA, Shunsuke**
First-principles calculations of spatially extended electronic states for nanostructures with a divide-and-conquer method
the University of Tokyo, 2016-03

□ Master Theses

1. **ADACHI, Daiki**
   Combined optimization method using X-ray diffraction data and ab initio calculation
   the University of Tokyo, 2017-03

2. **ASAYAMA, Yoshihiro**
   Ionization and penetration of metal atoms at metal/insulator interfaces in electric field and effects of metal alloying
   Chiba University, 2016-03

3. **FUNATO, Yosuke**
   First-principles study on the electronic structures in Tl/Ag(111) surface and solid oxygen
   Kanazawa University, 2017-03

4. **GOTO, Yuki**
   Shape optimization in high Reynolds number problems using adjoint turbulence models
   the University of Tokyo, 2017-03

5. **HAMAGUCHI, Motoyuki**
   First-principles analysis of the electronic structure of olivine type $LiFePO_4$ and rock-salt type Li_2MTiO_4 (M=V, Mn, Fe, Co, Ni)
   Osaka University, 2017-03

6. **HASEGAWA, Miki**
   Dissociative adsorption of water molecule at kink site of GaN(0001)
   Osaka University, 2017-03

7. **HASHIMOTO, Toshio**
   Numerical Simulation using CLSVOF method of Nucleate Boiling in Forced Convection of FC-72
   Saga University, 2017-03

8. **IMAI, Masaya**
   Local Structuring and Molecular Dynamics at Electric Double Layer of Aqueous Electrolytes Faced to Graphite Electrode Analyzed by MD Calculation
   Osaka University, 2016-03

9. **KAWABATA, Kohei**
   Adsorption and charging of metal atoms in organic molecular solids
   Chiba University, 2016-03

10. **MAEDA,Takahiro**
    First-principles calculations of electronic structures of single-crystal organic semiconductors
    University of Tsukuba, 2017-03

11. **MARUYAMA, Shohei**
    Loop Optimization for Tensor Network Renormalization and Its Application to Various Lattices
    the University of Tokyo, 2017-03-23

12. **MISHCHENKO, Petr**
    Thermodynamic properties of the Kitaev model on a hyperoctagon lattice: Large-scale Monte Carlo study
    the University of Tokyo, 2017-03

13. **MORI, Yutaro**
the University of Tokyo, 2017-03

14. **MORIKAWA, Yusuke**
Sodium-ion Intercalation Mechanism into Hard Carbon
the University of Tokyo, 2017-03

15. **MORIYA, Tomotaka**
the University of Tokyo, 2017-03

16. **NAGANO, Yoshihiro**
Numerical study on the critical properties of the antiferromagnetic classical Heisenberg model on the stacked-triangular lattice
Osaka University, 2017-03

17. **NAGASAWA, Akito**
First-principles study on stability of boron clusters in BaSi2
Chiba University, 2016-03

18. **NAKAUCHI, Shiryu**
Analysis of ordered states in iridium oxides on a honeycomb lattice
Tokyo Institute of Technology, 2017-03

19. **NISHI, Hirofumi**
Theoretical Study on Twisted Bilayaer Grpahene Using the Band Unfolding Method
the University of Tokyo, 2017-03

20. **OBA, Yusuke**
First-principles study of phonon anharmonicity and negative thermal expansion in ScF_3
the University of Tokyo, 2016-03

21. **OKADA, Katsuya**
Theoretical Study on Crystal Growth of MoS_2 Cluster
Shimane University, 2017-3

22. **OKAMOTO, Kazuma**
A two-phase simulation trial for determining phase boundaries
Ehime University, 2016-03

23. **SAKATANI, Fuminori**
First-principles study of spin-orbit splitting in III-V compound semiconductor
Kanazawa University, 2017-03

24. **SHIMAGAKI, Kai**
Performance analysis of parameter inference using unsteady relaxation and application to inverse Ising problem
the University of Tokyo, 2017-03

25. **SHINZAKI, Ryu**
Theoretical study for heavy fermion systems on quasiperiodicity
Tokyo Institute of Technology, 2017-03

26. **TODA, Marika**
Control of band gaps in electronic systems of two-dimensional layered materials
Ochanomizu University, 2017-03

27. **TONARI, Ken**
Development of Cluster-expansion method inducing sparsity based on semi-analytical cross validation method
Tokyo Institute of Technology, 2017-03

28. **TSUTSUMI, Kentaro**
First-principles calculation of superconducting transition temperatures including the effect of spin fluctuations
the University of Tokyo, 2016-03

29. **UEMATSU, Kazuki**
Quantum spin liquid behavior of the random J1-J2 Heisenberg model on the honeycomb lattice
Osaka University, 2017-03

30. **URASAKI, Syu**
Stabilities and Electronic Structures of Vacancies in 2D Materials: h-BN and MoS_2
Shimane University, 2017-03

31. **WATANABE, Saki**
Calculation of photoelectron excitation in monolayer transition-metal chalcogenides
Ochanomizu University, 2017-03

32. **YAMADA, Masahiko G.**
Designing various quantum spin liquids in metal-organic frameworks
the University of Tokyo, 2017-03

33. **YAMAMOTO, Kaichi**
Yokohama City University, 2017-03

34. **YAMAMOTO, Maho**
Numerical simulations on the inhomogeneous one-dimensional spring-block model mimicking the subduction zone
Osaka University, 2017-03